



# Valence intermédiaire induite par un lanthanide divalent dans des complexes hétérobimétalliques : Impact sur la réactivité de métaux de transition

Maxime Tricoire

## ► To cite this version:

Maxime Tricoire. Valence intermédiaire induite par un lanthanide divalent dans des complexes hétérobimétalliques : Impact sur la réactivité de métaux de transition. Coordination chemistry. Institut Polytechnique de Paris, 2022. English. NNT : 2022IPPAX027 . tel-04482748

**HAL Id: tel-04482748**

**<https://theses.hal.science/tel-04482748>**

Submitted on 28 Feb 2024

**HAL** is a multi-disciplinary open access archive for the deposit and dissemination of scientific research documents, whether they are published or not. The documents may come from teaching and research institutions in France or abroad, or from public or private research centers.

L'archive ouverte pluridisciplinaire **HAL**, est destinée au dépôt et à la diffusion de documents scientifiques de niveau recherche, publiés ou non, émanant des établissements d'enseignement et de recherche français ou étrangers, des laboratoires publics ou privés.

# Divalent lanthanide-induced intermediate valence in heterobimetallic complexes: Impact on transition metal reactivities

Thèse de doctorat de l'Institut Polytechnique de Paris  
préparée à l'École Polytechnique

École doctorale n°626 École Doctorale de l'Institut Polytechnique de  
Paris (ED IP Paris)  
Spécialité de doctorat : Chimie

Thèse présentée et soutenue à Palaiseau, le 19 avril 2022, par

**Maxime Tricoire**

Composition du Jury :

Rodrigue Lescouëzec Professeur des Universités, Sorbonne Université Institut Parisien de Chimie Moléculaire	Président
Richard Layfield Professeur des Universités, University of Sussex Department of Chemistry	Rapporteur
Victor Mougel Professeur des Universités, ETH Zürich Department of Chemistry and Applied Biosciences	Rapporteur
Lucile Chatelain Maîtresse de conférences, Université de Bretagne Occidentale Laboratoire de Chimie, Electrochimie Moléculaires et Chimie Analytique	Examinatrice
Grégory Nocton Chargé de recherche, École Polytechnique Laboratoire de Chimie Moléculaire	Directeur de thèse
Grégory Danoun Chargé de recherche, École Polytechnique Laboratoire de Chimie Moléculaire	Invité
Carine Clavaguéra Chargée de recherche, Université Paris-Saclay Laboratoire de Chimie Physique	Invitée



# Divalent lanthanide-induced intermediate valence in heterobimetallic complexes: Impact on transition metal reactivities



**Maxime Tricoire**

*LCM, CNRS, Ecole Polytechnique, Institut Polytechnique de Paris*



Manuscript submitted for the degree of Doctor of Philosophy

April 2022

A work funded by:



**European Research Council**

Established by the European Commission





## Acknowledgments

Now that this PhD thesis manuscript has been defended and corrected, the time to thank all the people who made this possible has come. During a bit more than four years in total, I had the luck to be surrounded by a lot of people who helped me to become the chemist I am now, but also helped me to endure some more difficult times by spending a lot of happy moments outside of the lab.

The first person to thank is undoubtedly Greg as he allowed me to start this adventure. Eight years ago, I would not have imagined that I was meeting my future PhD advisor in the student bar I was “working” a bit too much in the basements of the 45 rue d’Ulm. A few years later, I saw that you were proposing a PhD position while I was looking for one and although I was a bit lost and in lack of confidence, I dared to contact you again to see if we could make it work. We decided to start with a five months tryout and quickly agreed to continue for three more years. During all this time, you not only taught me most of what I know about f-element chemistry but you also constantly pushed me further to make me a better chemist. I was lucky and proud to have you as my supervisor and I will hopefully continue to strengthen this small amount of self-confidence you helped me to build.

During the last two years of my studies, I also had the luck to interact a lot with Bibi who became kind of a second advisor. During our ~~too~~ long and ~~too~~ numerous cigarette breaks, I not only discovered a great chemist filled with ideas, but also a friend eager to discuss about any topic. Your enthusiasm and motivation helped me to handle the pressure when needed and all these discussions allowed me to discover a lot about many types of chemistry that I was not familiar with, as well as really challenging board games. Thanks for everything, I wish you the best for the future, have fun continuing your journey in the f-elements world!

I would also like to thank a lot the rest of the members of the jury who accepted to evaluate my work as well as for the really nice discussion session we had after my presentation: Prof. Richard Layfield and Prof. Victor Mougel as reviewers, and Dr. Lucile Chatelain and Prof. Rodrigue Lescouëzec as examiners. I was especially proud to be able to present my work in front of Rodrigue who first taught me about molecular magnetism back when I was his student and intern during my master studies in Paris. I want to also thank Dr. Carine Clavaguéra for accepting my invitation and attending to my defense. It was really important for me as you taught me how to launch my first computations and I owe you most of my understanding of theoretical chemistry.

I would also like to thank Dr. Jean-Claude Berthet for accepting to tag along Rodrigue to attend to my mid-term “mini-defense” and give me important advices in order to finish properly my PhD.

Then of course I would not have made it until the end without all the members of the lab I crossed over these four years. First comes of course the people from Lab 1: the Crazy Lanthanide team! Back when I was still a clumsy intern, “Mommy” Violaine was always patient enough to

answer a lot of my questions. I had the luck to also share the lab with “Captain” Mathieu who taught me a lot on the rigor needed when you work with divalent lanthanides but also introduced me to whisky tasting when we were not having beers with other labmates. “Big bro” Ding watched over my back when I was still (re)discovering inert atmosphere conditions and helped me to perform my first experiments. That allowed me to start my PhD and I enjoyed to share these more than two years in the lab with you either side by side in the glovebox or around beers at the bar. At the end of my internship arrived Jules our first ERC post-doc. You quickly became a real friend and you perfectly succeeded in transforming us three young PhD students into distillation machines! Thanks to your motivation, I was also able to enjoy some nice time outside the lab bouldering at Arkose or (re)tasting all the tap beers at the Sham. Thanks for everything! Aside of Ding, I also had the luck to share the lab during most of my stay with my other PhD brother Valeriu. Your kindness and cheerfulness never left you during all these three years during which I saw you slowly joining the dark side of computational chemists haha. Thanks for all the support, I wish the best for you, Sarah and the parrots. Although it was sad to let Jules leave us, we got really lucky to welcome Thomas as our second post-doc in the ERC crew. You never ceased to amaze me with your determination and your patience either when a glovebox needed some attention or when we needed to improve the lab’s daily management. You carried us through many issues and allowed us to grow as chemists. Thanks for everything and congratulation again for your CNRS position, you deserve it and I am sure you will be a great PI. The crazy lanthanide lab would not have been complete without the Cnt team. Nolwenn who grew from being my ~~intern~~ padawan into a wonderful PhD ~~student~~ knight with reducing hands. I wish you good luck and I am looking forward to see the end of the difficult stories you started when you decided to synthesize “molecules that are not supposed to exist”. Oleh our post-doc who decided that bending one Cnt was not enough so he made propeller complexes. Good luck with your new projects in Lab 7. I did not have the luck to share much time with you Kuba since you arrived when I had to avoid the lab to write the upcoming pages of this manuscript. I hope you will have fun continuing some of the work I did and that you will surprise me with some unexpected reactivities! I also have a thought for Adrien who will soon start his three years run in the group. Good luck with your Cerium chemistry! I also want to thank all the interns I had the luck to work with in the lab: Jules, Sébastien, Junghan, Grégoire, Thomas, Audrey, Zeyu, Lamise, Adrien, Lily, Rafaela, Marie, Jean-Christophe and others. A special mention to Mathilde who enlightened the lab during both of her stays, I really enjoyed the board game or beer evenings and I wish you the best for the future.

I have also a lot of people to thank outside of Lab 1 as they constituted the rest of the foster family I found at the lab. Louis aka Loulou, your kindness has no equal but your sense of humor. You’ve been the leader of the LCM party crew during all our shared stay in the lab, your best creation being the now famous “melted cheese night”, the second one being the “we leave for beers at the CC

in 15 mins?”, a sentence that I tried to share to the next generation of students. Céline aka Cécé, if Ding was the big bro you definitely were the big sis. Always motivated to go running/playing volleyball/partying/smoking with me and Bibi (note that I always ingeniously evaded the first two propositions). I hope everything is going well for you in Wisconsin. P-A who decided that his short stay in the lab would last for more than two years. Thanks for all the moments we shared with and without your partner in crime Mathilde. Then comes the younger students that I had the luck to welcome in the lab. Pauline who always had some kind words to support me when I was not feeling great. Thanks a lot for the help you gave me with Mathilde in the last days prior to my defense. Mengyu and her ability to always keep a smiling and happy face. Thibault with whom I shared a lot of worrying moments taking care of the NMR maintenance as well as a lot of more cheerful ones when you invited everyone at your place. You guys are the next ones in line, thanks for everything and good luck for these last months I am sure you will all do great! As I do not want to forget the upstairs team. Thanks to Zsuzsanna, Radhika and Silvia now followed by Cate, Noman and Ling Hui for the moments we shared.

I also want to thank a lot the permanent staff of the lab. Of course, the people from XRD platform, Marie who helped me to discover the diffractometer and to understand its maintenance and even more Nicolas who replaced her. Your kindness, your calm and your patience are probably your best qualities but you have so much of them that the choice is difficult. Thanks for all the moments we shared in and out of the lab. I wish you to have a lot of fun and much less trouble with the new machine. I will always be happy to share with you some “Star Wars” images of diffraction. How to mention the XRD service without thanking my former desk neighbor Louis R. for all the things he taught me about crystallography. I will miss our discussions on difficult structures and a lot of other stuff. I hope you are doing well! Then comes the administrative staff of the lab, Anne-Flo. You literally were my paperwork mummy and you saved me from a lot of administrative traps. Thank you for your kindness and patience. Thanks also to Thérèse who retired at the beginning of my third year, I hope you enjoy it. I also want to deeply thank Corinne and Cédric the two successive heads of the lab for their help with the teaching or the doctoral school paperwork. Cédric, I wish you the best for all the nice projects you planned to make the lab an even better place. I also want to thank Duncan who always had kind words and nice anecdotes about molar scale syntheses. Thanks also to Audrey with whom I shared my first large scale teaching experiences for the Bachelor program. Then comes the upstairs team who welcomed me warmly during all my writing. Sophie and Christophe who also performed some Mass experiments when I was having a hard time with some deuterium-labelled experiments. Stéphane and his impressive guitar skills. Edith, Cindy, Elodie and Sylvaine who were always cheerful. Jean-Michel our glassblower who tirelessly repaired our broken J. Young NMR

tubes, Olivier and Jean-Marc who taught me some plumbing skills when we dealt with the Ar lines, Gilles A. who took care of my computer needs, but also Gilles F., Gilles O., David and Vincent.

Je me permets aussi quelques mots en français pour remercier toutes les personnes en dehors du labo qui m'ont permis de m'évader quelques temps de ma thèse quand j'en avais besoin. La fameuse « Dynastie » créée il y a maintenant sept ans avec Kajetan. Merci à toi mais aussi à Marion, Clément, Chems, Sélène, Audran, Enora et les derniers arrivés Mathis et Ulysse pour les bons moments passés à chacun de nos restos. Vient ensuite la team chill avec qui j'allais oublier la chimie chaque été à Fermanville, Noirmoutier ou encore Torchefelon. Merci à Axelle, Romain, Joran, Marie, Marc, Oscar, Matthieu, Adrien, Amiel, Sylvain, Sevan, Sarah, Pierre, Maguelone et tous les autres en espérant vous revoir très vite malgré mon déménagement en Suisse.

Enfin, pour terminer ces remerciements, j'en arrive aux personnes qui me sont les plus chères. Merci à toute ma famille de m'avoir toujours soutenu et permis d'en arriver jusque-là. Merci Papa et Maman d'avoir cru en moi, même quand j'étais en moins bonne forme. Merci à Marion et Julie de nous avoir fait devenir avec Clément les plus heureux des tontons du monde. Et pour finir un petit coucou à mes twins préférés du haut de leurs 13 mois, Maël et Noam. Au moment de finir ces lignes, j'ai enfin eu la chance de vous voir pour la première fois. J'ai hâte de vous voir grandir.

# Table of Contents

List of abbreviations .....	11
<b>Chapter I Intermediate valence in lanthanide compounds .....</b>	<b>13</b>
<b>I. Introduction .....</b>	<b>13</b>
I.A. Lanthanide ions' intrinsic properties .....	13
I.B. From a formal oxidation state to intermediate valence .....	15
<b>II. Spectroscopic and computational singularities .....</b>	<b>17</b>
II.A. The LnCp <sub>3</sub> case, Ln = Yb, Eu and Ce .....	17
II.B. Cerocene, a computational debate .....	19
II.C. Ytterbocene adducts of N-heterocyclic redox-active ligands .....	21
<b>III. Rationalization and utility of intermediate valence .....</b>	<b>22</b>
III.A. Energy and symmetry considerations .....	22
III.B. Chemical ramifications: Impact on reactivities .....	25
III.C. Going further with heterobimetallic architectures .....	27
<b>IV. Conclusion and objectives .....</b>	<b>28</b>
<b>References .....</b>	<b>30</b>
<b>Chapter II New trivalent organolanthanide precursors supported by large aromatic ligands .....</b>	<b>37</b>
<b>I. Background on sandwich complexes .....</b>	<b>37</b>
I.A. Pioneer works with the cyclopentadienyl ligand .....	37
I.B. Toward bigger ligands: cyclooctatetraenyl and arene derivatives .....	38
I.C. The cyclononatetraenyl ligand .....	39
<b>II. Synthesis and characterization of (Cot)Ln(Cnt) heteroleptic complexes .....</b>	<b>40</b>
II.A. Synthesis of the (Cot)LnX(thf) <sub>n</sub> precursors .....	40
II.B. Synthesis and characterization of (Cot)Ln(Cnt) heteroleptic sandwich complexes .....	42
<b>III. The magnetic interest of the (Cot)Ln(Cnt) architecture .....</b>	<b>49</b>
III.A. Brief introduction on single molecule magnets .....	49
III.B. Magnetic properties and theoretical studies across the (Cot)Ln(Cnt) series of complexes .....	52
<b>IV. Conclusion and perspectives .....</b>	<b>55</b>

References .....	57
<b>Chapter III Original heterobimetallic complexes of Yb and Pt as models for group 10 reactivity .....</b>	<b>61</b>
<b>I. Background on platinum chemistry .....</b>	<b>61</b>
I.A. Pioneer works, toward Shilov's chemistry .....	61
I.B. The Catalytica system .....	63
I.C. Recent works and objectives of the project .....	64
<b>II. Synthesis and characterization of heterobimetallic Yb-Pt complexes .....</b>	<b>65</b>
II.A. Synthesis and structural analysis .....	65
II.B. Experimental electronic structure studies .....	67
II.C. Modulation of the high-valent Pt coordinating environment .....	71
<b>III. Reactivity studies .....</b>	<b>77</b>
III.A. Trials for mild condition C-H activation of methane and intrinsic reactivity of the high valent species .....	77
III.B. Exploring other reactivities .....	79
<b>IV. Conclusion and perspectives .....</b>	<b>83</b>
References .....	85
<b>Chapter IV Low-valent N-heteroaromatic-Ni catalysts for alkene isomerization .....</b>	<b>89</b>
<b>I. Background on homogeneous Ni catalysis .....</b>	<b>89</b>
I.A. Nickel-catalyzed cross-couplings .....	89
I.B. Toward alkene isomerization .....	93
<b>II. Heterobimetallic Yb-Ni catalyst for alkene isomerization .....</b>	<b>94</b>
II.A. Developing facile access to a low-valent Ni center.....	94
II.B. Catalytic reactivity of the <i>in-situ</i> formed Yb-Ni species .....	95
II.C. Mechanistic insights .....	99
<b>III. Conclusion and perspectives.....</b>	<b>108</b>
References .....	110
<b>Chapter V Synthesis and characterization of tetraalkyl palladium complexes .....</b>	<b>113</b>

<b>I. Background on high-valent palladium complexes.....</b>	<b>113</b>
I.A. An elusive +IV oxidation state .....	113
I.B. Selectivity of the reductive elimination .....	114
I.C. Isolated stable high-valent alkyl palladium species .....	117
<b>II. Synthesis and characterization .....</b>	<b>118</b>
II.A. Development of the synthetic protocol.....	118
II.B. Solid- and solution-state characterization.....	119
<b>III. Stability and reactivity studies .....</b>	<b>122</b>
III.A. <sup>1</sup> H NMR monitoring of the degradation .....	122
III.B. Selectivity of the reductive elimination.....	127
<b>IV. Conclusion and perspectives .....</b>	<b>129</b>
<b>References .....</b>	<b>131</b>
<b>Chapter VI General conclusion and perspectives.....</b>	<b>133</b>
I. A study across group 10 transition metals .....	133
II. But what about other metal groups? .....	135
<b>Appendices .....</b>	<b>141</b>
<b>A. Synthesizes and characterization data .....</b>	<b>143</b>
General considerations: .....	143
Chapter II .....	144
Chapter III.....	149
Chapter IV .....	152
Chapter V.....	174
<b>B. Crystallographic data .....</b>	<b>177</b>
General details:.....	177
Chapter II .....	178
Chapter III.....	182
Chapter IV .....	184
Chapter V.....	185
References:.....	186
<b>C. Published articles .....</b>	<b>189</b>





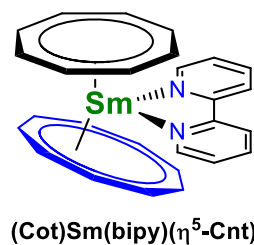
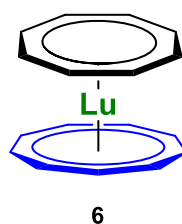
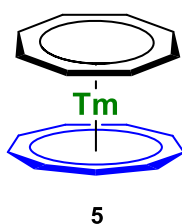
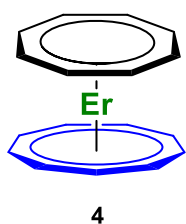
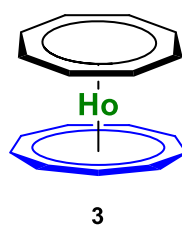
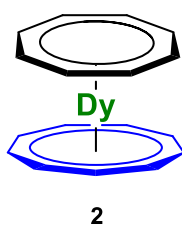
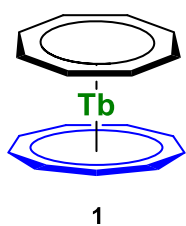
## List of abbreviations

<i>ab-initio</i>	Latin term = from the beginning
ABz	Allylbenzene
bipy	2,2'-bipyridine
bipym	2,2'-bipyrimidine
<i>ca.</i>	<i>circa</i> = around
CASSCF	Complete active space self-consistent field
CASPT2	Second order Complete active space perturbation theory
Cnt	cyclononatetrenyl
Cod	1,5-cyclooctadiene
Cot	cyclooctadienyl
Cp	cyclopentadienyl
Cp''	bis(trimethylsilyl)cyclopentadienyl
Cp*	pentamethylcyclopentadienyl
Cp <sup>ttt</sup>	tris(tert-butyl)cyclopentadienyl
Cp <sup>BIG</sup>	pentaphenylcyclopentadienyl
Ctr	Centroid
dad	diazadiene
DFT	Density functional theory
EPR	Electron paramagnetic resonance
Et	ethyl
<i>et al.</i>	<i>et alia</i> = and others
FLP	Frustrated Lewis pair
HAT	Hydrogen atom transfer
HBCat	catecholborane
Hbimpm	2-pyrimidin-2-yl-1H-benzimidazole
HMabiq	macrocyclic biquinazoline
HOMO	Highest occupied molecular orbital
<i>in situ</i>	Latin term = on site
Int	Intermediate
<i>i</i> Pr	isopropyl
LEDs	Light-emitting diode
Ln	Lanthanide
LUMO	Lowest unoccupied molecular orbital

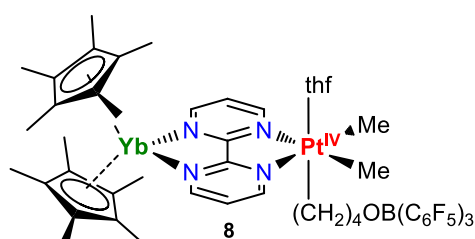
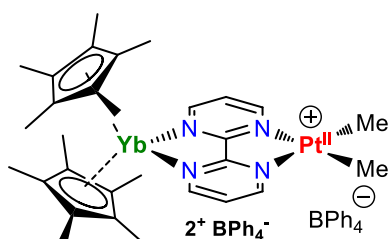
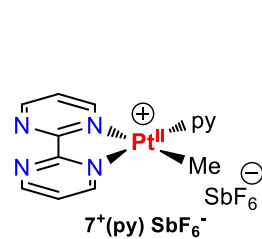
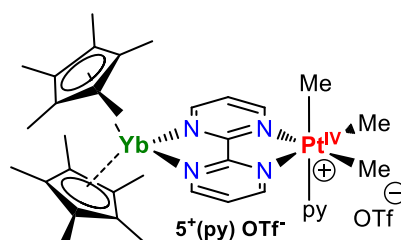
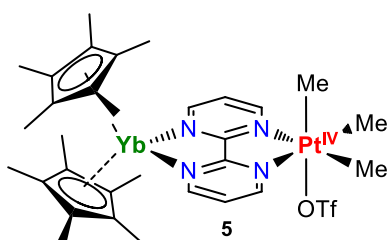
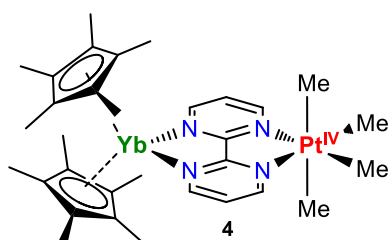
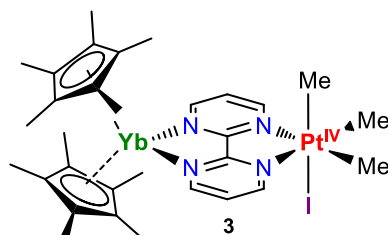
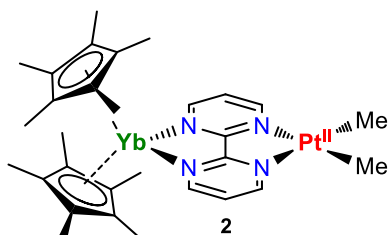
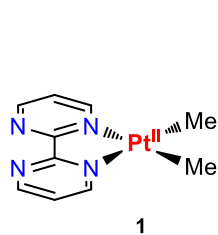
Me	methyl
NHC	N-heterocyclic carbene
NHE	Normal hydrogen electrode
NMR	Nuclear magnetic resonance
ORTEP	Oak Ridge thermal ellipsoid plot
OTf	triflate
Pc	phtalocyanine
PES	Photoelectron spectroscopy
Ph	phenyl
phen	1,10-phenantroline
py	pyridine
QTAIM	Quantum theory of atoms in molecules
QTM	Quantum tunneling of the magnetization
RAL	Redox-active ligand
salen	contraction of salicylaldehyde (sal) and ethylenediamine (en)
SCE	Saturated calomel electrode
SIM	Single-ion magnet
SMM	Single-molecule magnet
SQUID	Superconducting quantum interference device
taphen	4,5,9,10-tetraazaphenanthrene
T <sub>B</sub>	Blocking temperature
<i>t</i> Bu	tert-butyl
TIP	Temperature-independent paramagnetism
TM	Transition metal
tmeda	tetramethylethylenediamine
Tp	Trispyrazolylborate
tpy	terpyridine
TS	Transition state
U <sub>eff</sub>	Energy barrier for a spin state reversal
VT	Variable temperature
XANES	X-ray absorption near edge structure
XRD	X-ray diffraction

# Index of synthesized molecules

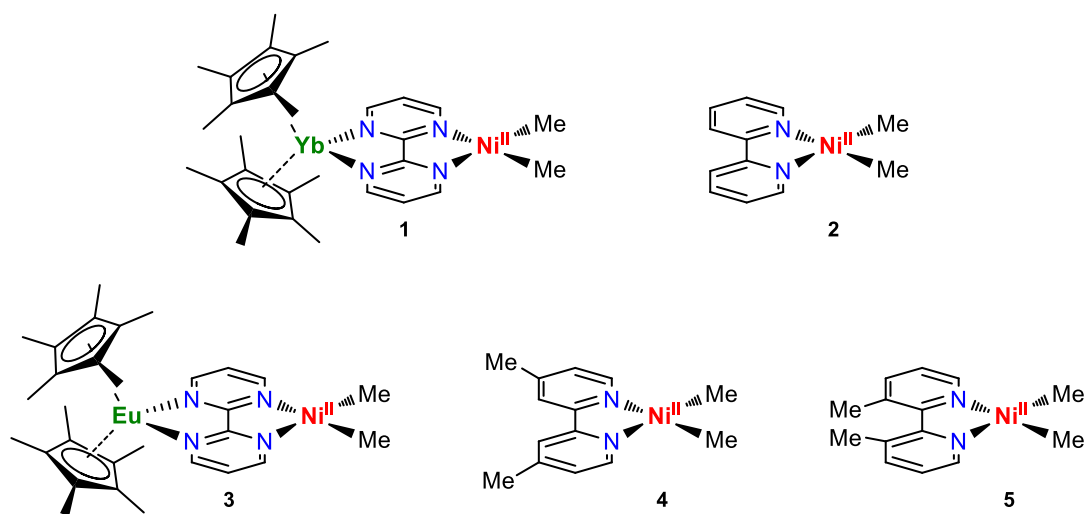
## Chapter II



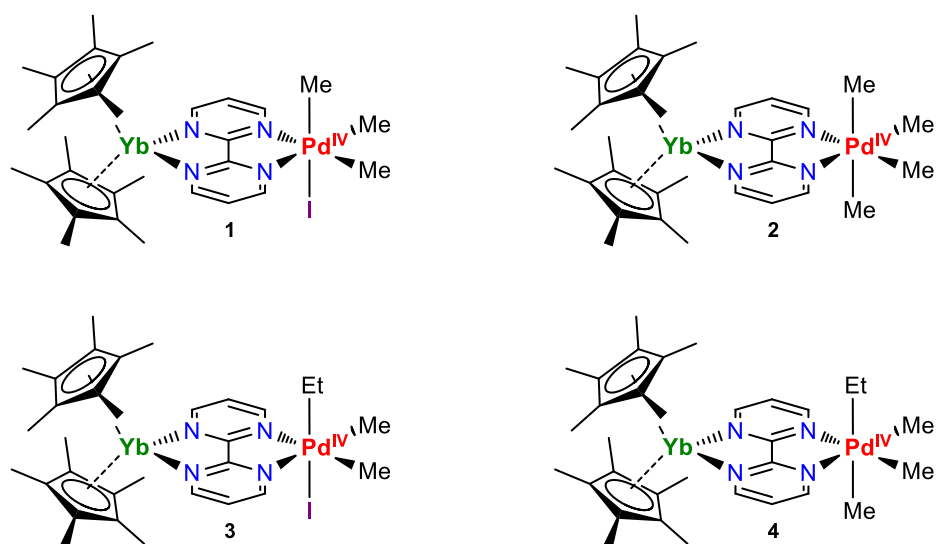
## Chapter III



■ Chapter IV



■ Chapter V



# Chapter I

## Intermediate valence in lanthanide compounds

### I. Introduction

The lanthanide series is composed of 15 elements, from lanthanum to lutetium ( $57 \leq Z \leq 71$ ),<sup>1</sup> they are mostly found at the 0, +II or +III oxidation states, the latter being the most stable. With the addition of scandium and yttrium they form the family of the rare earth elements. This name was inherited from their presence, promethium excepted, in small proportion in most metal ores as mixed  $\text{Ln}_2\text{O}_3$  oxides. Discovered during the XIX<sup>th</sup> century, these elements puzzled Mendeleev when he attempted to include them in his theory of elemental periodicity while their overall similarities complexified greatly their separation.<sup>2</sup> However, “rare” can be qualified as a poor naming choice considering their global abundance in the earth’s crust, cerium being as abundant as nickel.<sup>3</sup> From an economical point of view,<sup>4</sup> this abundance is really important considering the growing needs of rare earth elements in various fields of application such as ethylene polymerization,<sup>5,6</sup> LEDs or magnets manufacturing,<sup>7,8</sup> among others.<sup>9,10</sup>

#### I.A. Lanthanide ions’ intrinsic properties

As the first elements of the periodic table involving f-orbitals, lanthanide ions’ properties are relatively different from transition metals. At their 0<sup>th</sup> oxidation state, their electronic structure is either  $4f^{n+1}5d^06s^2$  or  $4f^n5d^16s^2$  and upon oxidation they are therefore drawn to be most stable at the +III oxidation state  $4f^n5d^06s^0$  (Table I.1).<sup>11</sup> Divalent lanthanide chemistry is also known since the 60s but remained limited for a long time to three elements for which such reduced state is stabilized, the half-filled shell  $4f^7 \text{Eu}^{II+}$ , the filled shell  $4f^{14} \text{Yb}^{II+}$  and the close to half-filled shell  $4f^6 \text{Sm}^{II+}$  ions.<sup>12–</sup>

<sup>16</sup> While the coordination chemistry of the so-called “classical” divalent lanthanide ions was mostly developed in 80s by the groups of Andersen and Evans,<sup>17,18</sup> Kagan explored their potential as reagents for organic syntheses.<sup>19</sup> It was only in 1997 that the first molecular compound of divalent thulium was isolated by Bochkarev *et al.*<sup>20</sup> This category of the molecular complexes of “non-classical” divalent lanthanide ions was, no so long after, extended to dysprosium and neodymium.<sup>21–24</sup> Finally, after Lappert’s report of the successful isolation of a divalent lanthanum complex obtained after the reduction of bis(trimethylsilyl)cyclopentadienyl (Cp’’) trivalent precursors,<sup>25</sup> the group of Evans completed the series, to the exception of the radioactive promethium element. While they followed a similar strategy, they observed that the ground state of these new compounds was  $4f^n5d^1$  instead of the observed  $4f^{n+1}5d^0$  state for the less reductive ones.<sup>26–29</sup> Also known to be accessible but mostly limited to molecular cerium species such as cerocene,<sup>30–32</sup> due to the relatively accessible  $4f^05d^06s^0$  ground state,<sup>33</sup> the tetravalent state was also recently reached with molecular terbium and praseodymium compounds.<sup>34–39</sup> This variety of accessible oxidation states coupled to preferred monoelectronic transformations in such a large category of similar yet different elements is the reason why coordination chemists are always trying unlock the access to a larger amount of species at unusual oxidation states (Table I.1).

**Table I.1.** Updated table of accessible oxidation states for molecular lanthanide complexes.<sup>40,41</sup> Classical divalent lanthanides in green, recently isolated tetravalent elements in red, radioactive Pm in grey.

<sup>57</sup> La	<sup>58</sup> Ce	<sup>59</sup> Pr	<sup>60</sup> Nd	<sup>61</sup> Pm	<sup>62</sup> Sm	<sup>63</sup> Eu	<sup>64</sup> Gd	<sup>65</sup> Tb	<sup>66</sup> Dy	<sup>67</sup> Ho	<sup>68</sup> Er	<sup>69</sup> Tm	<sup>70</sup> Yb	<sup>71</sup> Lu
	+4	+4						+4						
+3	+3	+3	+3		+3	+3	+3	+3	+3	+3	+3	+3	+3	+3
+2	+2	+2	+2		+2	+2	+2	+2	+2	+2	+2	+2	+2	+2
0		0	0		0		0	0	0	0	0			0

As it is the source of the various chemical reactivities observed at each oxidation states, understanding the physical properties of these different lanthanide ions is of paramount importance. Being heavy elements of the 6<sup>th</sup> row, the spin-orbit coupling can no longer be neglected, the appropriate quantum number is  $J$  and the ligand field is significantly smaller than the spin-orbit coupling. Additionally, 4f orbitals present a rather small radial expansion resulting in a core nature of the aforementioned  $4f^n$  valence shell.<sup>42</sup> As a consequence, most textbook argue that, due to minimal overlap between Lewis base ligands and 4f orbitals, their energy is only marginally impacted upon coordination. Lanthanides are then mostly involved in pure ionic bonding contrary to transition metals.<sup>43–45</sup> This could imply that the ligand choice is mostly governed by a steric hindrance-based paradigm. However, with the multiplication of isolated species at unusual oxidation states, both in the low and high-valent cases, every report of unexpected physical properties challenges this

paradigm, indicating that there are aspects of the lanthanide-ligand bonding that might have been underestimated. This naturally calls for the addition of symmetry and energetic considerations to the sterics-governed model, constituting a singularity in the textbook guidelines for lanthanide chemistry.

## I.B. From a formal oxidation state to intermediate valence

When it comes to standard coordination chemistry with low-valent lanthanide ions, the ligand choice has mostly been driven by solubility and stability considerations. The most striking example lies in lanthanide-cyclopentadienyl (Cp) chemistry, where most guidebooks would state: “the bulkier, the better”, when it comes to stabilize non-classical divalent elements.<sup>24,40</sup> The extensive literature on substituted Cp or hetero-Cp-based divalent lanthanide complexes also hinted toward the electronic non-innocence of such ligands in reductive reactivity. While most divalent samarium complexes do not react with N<sub>2</sub> or CO, the thf adduct of decamethylsamarocene (Cp\*<sub>2</sub>Sm(thf)<sub>2</sub>) was found to achieve such reductions, although the latter is reversible.<sup>46,47</sup> The same complex was also found to reduce pyridine to form a C-C bonded dimeric complex [Cp\*<sub>2</sub>Sm(C<sub>5</sub>H<sub>5</sub>N)]<sub>2</sub>[μ-(NC<sub>5</sub>H<sub>5</sub>-C<sub>5</sub>H<sub>5</sub>N)], a reactivity not observed when switching to a phosphyl analog ligand, and illustrating the importance of the metal-ligand pair choice. This energetic relationship in the lanthanide-ligand pair is undoubtedly echoing to the theory of covalency in metal complexes,<sup>48</sup> thus questioning the aforementioned ionic nature of lanthanide-ligand interactions. Actually, contrary to transition metals, this particularity of the bonding in lanthanide compounds prevents the formation of a metal-ligand fully delocalized orbital when both fragments are of similar energies. This lack of covalency force the electrons to adopt a statistical distribution, therefore having similar probabilities to be found on the metal or the ligand (Figure I.1).

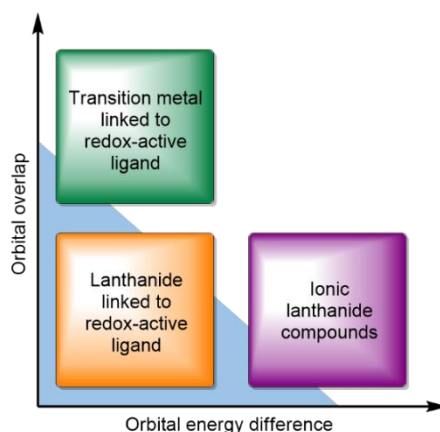


**Figure I.1.** Representative orbital overlap versus orbital energy difference plot and related compound categories, adapted from ref<sup>49</sup>. The blue section illustrates the intermediate valence realm.

The resulting wavefunctions are therefore the sum of the multiple possible configurations, in which the oxidation state of the lanthanide center and the ligands vary. While this phenomenon is not



limited to 4f-elements, it is less rare than in transition metal species since it is not restricted to cases where the metal and ligand orbitals are almost orthogonal, preventing covalent interaction, as highlighted by several works from Wiegardt and coworkers as well as our group's (Figure I.1).<sup>49–57</sup> The superposition of these multiple electronic configurations is also impacting the physical properties of the resulting compounds and the use of a formal oxidation state has to be questioned since none of the limit forms properly describe the species' behaviors. As proposed by Dolg, Fulde, Maron and Andersen, pioneers in this field, a more appropriate term: “intermediate valence” accurately embraces the complexity of such systems.<sup>58–62</sup> Among their investigations, the computational studies they performed most notably contributed to build nowadays guidelines to treat such multiconfigurational systems. Contrary to traditional transition metal cases, the choice of the method is rather important as density-based models remain limited to single component wave-functions they only give an approximated picture of the delocalized density and most of the time fail to reproduce the observed spectroscopic signatures. This is what led Field to first introduce the concept of “super-configurations” in 1982 to deal with the particular features observed due to low-lying electronic states in diatomic molecules of lanthanides.<sup>63</sup> It is only in the late 1980s that Fulde and coworkers rationalized the formation of diradical open-shell singlets and/or low-lying multiplets states by using the interaction between two partners (metal-metal or metal-ligand).<sup>58,64</sup> As an analogy to Kondo singlet-state known in solid-state physics, this approach provided the possibility to rationalize the observed experimental singularities.<sup>65,66</sup>

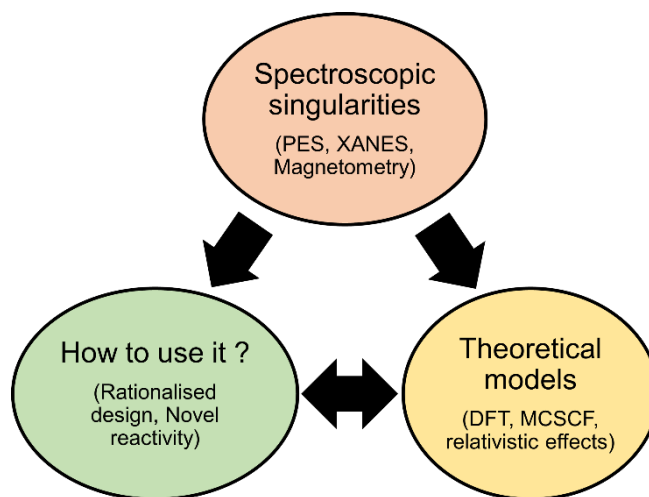


**Figure I.2.** Intermediate valence in lanthanide compounds, from spectroscopic singularities to theoretical models aiming to rationalize the phenomenon.

## II. Spectroscopic and computational singularities

### II.A. The LnCp<sub>3</sub> case, Ln = Yb, Eu and Ce

Following the report of the first metallocene,<sup>67</sup> the synthesis of the LnCp<sub>3</sub> organolanthanide series of compounds was achieved by Wilkinson and Birmingham in the late 1950s.<sup>68–70</sup> To probe the Ln-Cp bonding nature, their reactivity toward FeCl<sub>2</sub> was tested and resulted in quantitative formation of ferrocene, FeCp<sub>2</sub>. This confirmed the expected ionic bonding resulting from the dominant electrostatic metal-ligand interactions.<sup>71</sup> Additionally, further investigations permitted to measure the effective magnetic moments and, to the exception of YbCp<sub>3</sub>, all values were concurring with the expected ones for the free-ions. Indeed, the measured value of 4.0  $\mu_B$ , at three different temperatures by the Gouy method,<sup>72</sup> for YbCp<sub>3</sub> is significantly lower than the expected 4.54  $\mu_B$  for such <sup>2</sup>F<sub>7/2</sub> Yb<sup>III</sup> ground state.<sup>73</sup> This first singular result called for extended investigations on this compound to understand the origin of such deviation. Much latter, gas-phase photoelectron spectroscopy (PES) was performed at variable energies throughout the LnCp<sub>3</sub> series (Ln = Ce, Pr, Nd, Sm, Yb and Lu).<sup>74–78</sup> This technique is especially performant to investigate the electronic structure of lanthanide complexes due to the signature of the ionized products. For instance, a 4f<sup>n</sup> ground state compound will be directly identified by its related 4f<sup>n-1</sup> ionized cation as observed with the LuCp<sub>3</sub> complex, a 4f<sup>14</sup> ground state, for which both <sup>2</sup>F<sub>7/2</sub> and <sup>2</sup>F<sub>5/2</sub> ions states of its 4f<sup>13</sup> cationic form were identified.<sup>76</sup> A less trivial example is found with the YbCp<sub>3</sub> complex, since signals corresponding to both 4f<sup>12</sup> (Yb<sup>IV</sup>) and 4f<sup>13</sup> (Yb<sup>III</sup>) ionized products are observed, which is indicative of the intermediate valence of the formed [YbCp<sub>3</sub>]<sup>+</sup> cation. The question remains as whether these signatures are due to the multiconfigurational character of the YbCp<sub>3</sub> starting complex (initial-state effect), or to its ionized version (final-state effect). The propensity of Yb to form divalent species was thought to be a strong support of an initial-state induced intermediate valence, and the ground state of YbCp<sub>3</sub> was estimated to be of 88% 4f<sup>13</sup> character and 12% of 4f<sup>14</sup> character.<sup>77</sup> To reinforce this initial-state hypothesis, similar values were also obtained by rigorous EPR investigations, including hyperfine coupling interaction of both <sup>13</sup>C and <sup>171</sup>Yb nucleus, as well as modern magnetic susceptibility measurements that corrected the previously measured  $\mu_{\text{eff}}$  value to 3.53  $\mu_B$  measured in the 20–300 K range (Figure II.1).

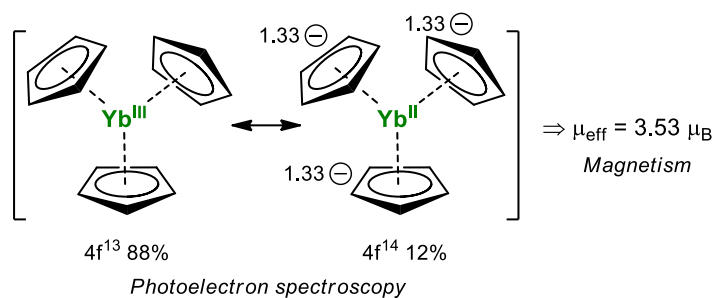


**Figure II.1.** Spectroscopic singularities observed for YbCp<sub>3</sub>.

As the  $\text{Ln}^{3+}/\text{Ln}^{2+}$  redox potential is 0.8 V higher when switching from Yb to Eu, -0.35 V and -1.15 V respectively versus NHE (normal hydrogen electrode),<sup>79</sup> a similar intermediate valence can also be expected with the EuCp<sub>3</sub> complex. In this case, <sup>151</sup>Eu Mössbauer spectroscopy is a first choice technique to probe the electronic properties of the Eu ion.<sup>80</sup> The analysis of an EuCp<sub>3</sub>(thf) sample revealed a strong interaction between the Eu 4f orbitals and the Cp ligands which was estimated to account for approximately 14% of divalent 4f<sup>7</sup> character.<sup>81</sup>

Contrary to the two previous cases, CeCp<sub>3</sub> was studied because of its enhanced oxidative reactivity, in presence of air traces, compared to the rest of the series, an observation echoing to the aforementioned accessibility to a 4f<sup>0</sup>5d<sup>0</sup>6s<sup>0</sup> ground state by the oxidation of a 4f<sup>1</sup> Ce<sup>III</sup> ion.<sup>68,69</sup> Magnetic data confirmed the <sup>2</sup>F<sub>5/2</sub> ground state of CeCp<sub>3</sub> with a measured magnetic moment of 2.46  $\mu_B$  versus the expected 2.54  $\mu_B$  value. However, gas phase variable photon energy photoelectron studies permitted to probe the electronic structure of the CeCp<sub>3</sub><sup>+</sup> cation and surprisingly, two different final states were observed, a result in contradiction with the only possible 4f<sup>0</sup> ground state for such oxidized compound.<sup>74</sup> While this phenomenon was already reported for solid inorganic Ce samples,<sup>82–84</sup> in agreement with the magnetic measurements, it was attributed in this case to a final-state effect resulting from an the intrinsic intermediate valence of the [CeCp<sub>3</sub>]<sup>+</sup> cation. Computations indicated that if the latter is expected to formally be a Ce<sup>IV</sup> species with no pure 4f orbital being occupied, significant 4f electronic density arises from the population of delocalized  $\delta$  bonding and antibonding Ce-Cp orbitals.<sup>75</sup> This report is perfectly illustrating the semantic issue when using the “formal oxidation state” term for such species. In this case neither the Ce<sup>III</sup> nor the Ce<sup>IV</sup> designations are accurate since both “Ce<sup>III</sup> with no pure f orbital” and “Ce<sup>IV</sup> with 4f electronic density” statements are challenging the textbook definitions (Figure II.2).

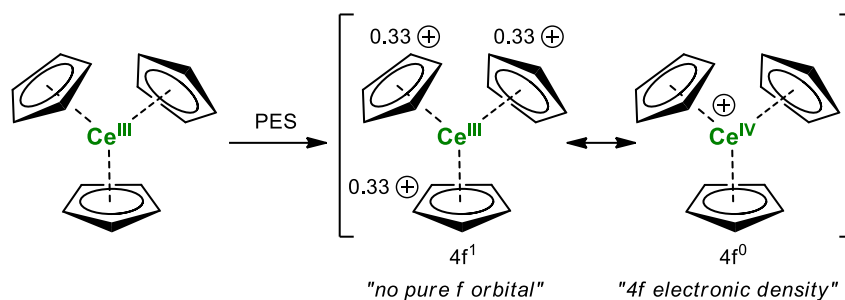


**Figure II.2.** Odd spectroscopic or computed features for the CeCp<sub>3</sub> species.

## II.B. Cerocene, a computational debate

If the LnCp<sub>3</sub> series remain the first occurrence of singular spectroscopic signatures observed with organolanthanide complexes, the most studied and discussed case is the cerocene's (biscyclooctatetraenyl cerium, Ce(Cot)<sub>2</sub>). As previously discussed, this compound was first isolated in 1976 by Cesca and coworkers,<sup>30</sup> the synthetic protocol being latter improved by the groups of Streitwieser and Andersen.<sup>31,32</sup> Substituted Cot analog species were also characterized in the meantime (Figure II.3).<sup>85,86</sup> Several spectroscopic and structural features, among which XRD-obtained metrics or photoelectron spectrum,<sup>87,88</sup> were in favor of a formal Ce<sup>IV</sup> oxidation state, while UV-Vis and luminescence studies were indicative of Ce<sup>III</sup> characteristics.<sup>89</sup>

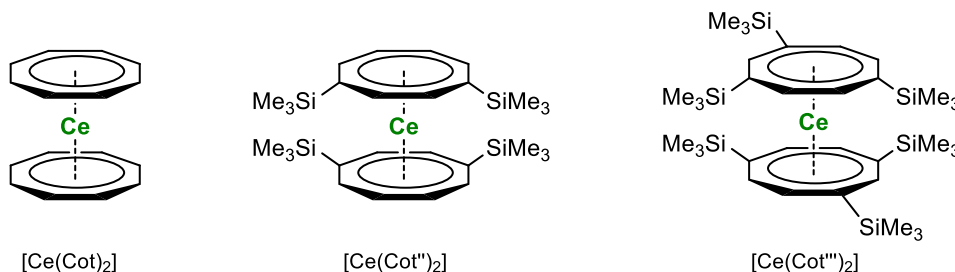


**Figure II.3.** The cerocene complex and its substituted derivatives.

To solve this problem, X-ray absorption near edge structure (XANES) spectroscopy investigations were conducted,<sup>32,90–92</sup> as it is another performant tool to determine the oxidation state of a metal center as well as the extent of the bonding character of f-orbitals in lanthanide and actinide complexes.<sup>93–97</sup> With both the original Ce(Cot)<sub>2</sub> and its substituted versions, XANES data supported an intermediate valence with both Ce<sup>III</sup> and Ce<sup>IV</sup> signatures.<sup>90,91</sup> And if the same initial-state versus final-state effects question is at stake, most studies consider the former to be the cause of the observed multiple contributions. By fitting the data obtained with the Ce(Cot)<sub>2</sub> sample, the 4f<sup>0</sup> (Ce<sup>IV</sup>) and 4f<sup>1</sup> (Ce<sup>III</sup>) contributions were estimated to 11% and 89% respectively (Figure II.4),  $n_f = 0.89$  ( $n_f$  representing the weight of the open-shell configuration), a value questioned by a recent study that estimated the contribution from the 4f<sup>1</sup> configuration to be lower,  $n_f = 0.51$ .<sup>92</sup>

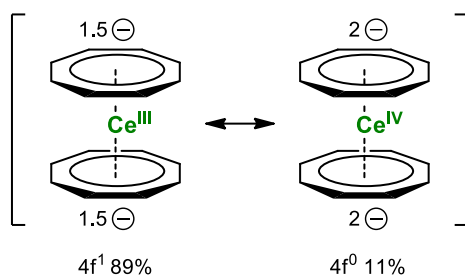


**Figure II.4.** Configuration admixture ratios resulting from XANES fitted data.

If from the experimental side, XANES studies permitted to confirm the intermediate valence of the  $\text{Ce}(\text{Cot})_2$  complex, theoretical chemists did not wait such advanced spectroscopic investigations to open cerocene's Pandora box, in which the numerous questions about its oxidation state were concealed. Based on the study of Roesch and Streitwieser in which a formal  $\text{Ce}^{\text{IV}}$  oxidation state was proposed,<sup>98</sup> Neumann and Fulde estimated the  $\text{Ce}^{\text{III}}$   $4f^1$  contribution to be dominant because being more stable according to their more advanced, yet still semi-empirical, computations.<sup>99</sup> By the early 1990s, relativistic pseudo-potentials developed for f-elements finally allowed theoreticians to use *ab-initio* multiconfigurational computational methodologies,<sup>100–103</sup> such as complete active space self-consistent field (CASSCF)<sup>104</sup> and second-order complete active space perturbation theory (CASPT2).<sup>105</sup> Investigations led by Dolg and coworkers thus validated the intermediate valence of cerocene and even estimated the  $4f^0$  and  $4f^1$  contributions, respectively 17% and 83%,  $n_f = 0.83$ ,<sup>59,60,106</sup> in good agreement with the XANES results obtained a decade later. However, this was the start of long discussion between the groups of Dolg and Kerridge, to find the best way to estimate these contributions. The latter reported an admixture of three states,  $\text{Ce}^{\text{II}}/\text{Ce}^{\text{III}}/\text{Ce}^{\text{IV}}$ , with respective contributions of 9%/23%/60% to the wavefunction.<sup>107</sup> This proposition of a dominant  $\text{Ce}^{\text{IV}}$  character, although not concurring with the experience, was later supported by CASSCF-derived quantum theory of atom in molecules (QTAIM)<sup>108</sup> topological studies,<sup>109</sup> where the odd  $\text{Ce}^{\text{III}}$  spectroscopic features were attributed to metal-ligand “degeneracy-driven covalency” as well as to the first excited state that presents a  $4f^1$  character. Mooßen and Dolg corrected these propositions by arguing that the CASSCF wavefunction remained invariant upon unitary transformation of the orbital space, such as a simple rotation.<sup>110</sup> Within this framework they demonstrated that both the  $\text{Ce}^{\text{III}}$  and  $\text{Ce}^{\text{IV}}$  representations proposed earlier are only limit cases obtained at precise rotation angle values  $\alpha$  (Figure II.5). The infinite number of combinations accessible in between these values would just result in intermediate results, illustrating perfectly the need of the “intermediate valence” term. To definitely end up the cerocene oxidation state debate, Dolg concluded that the choice between the  $\text{Ce}^{\text{III}}$  and  $\text{Ce}^{\text{IV}}$  representations is “to a certain extent a matter of taste”, which, for a pioneer of the field, is quite meaningful.

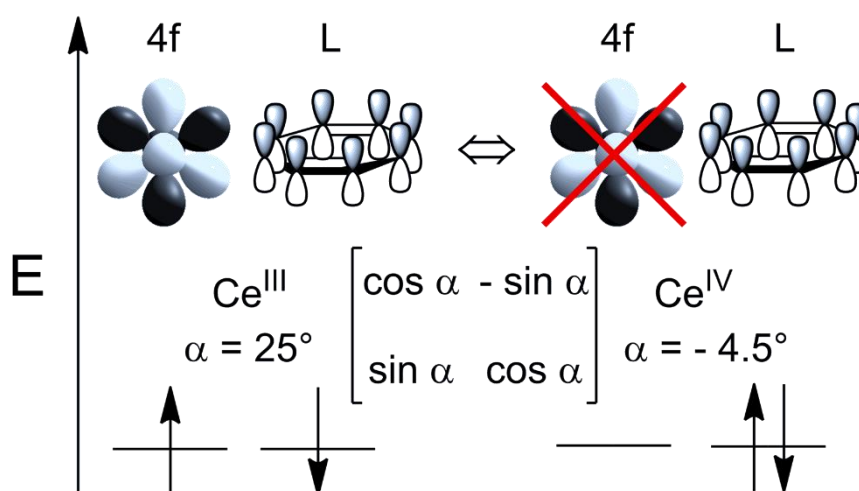


**Figure II.5.** Impact of the rotated CASSCF orbitals on the computed electronic structures.

## II.C. Ytterbocene adducts of N-heterocyclic redox-active ligands

In both  $\text{LnCp}_3$  and  $\text{Ce}(\text{Cot})_2$  systems, intermediate valence states have been reached with Hückel aromatic carbon-based ligands. However, the group of Andersen also investigated the odd spectroscopic behaviors of ytterbocene adducts  $[\text{Cp}^*_2\text{Yb}(\text{L})]$  formed with well-known redox non-innocent ligands, L, such as 2,2'-bipyridyl (bipy), 1,10-phenanthroline (phen) or diazabutadiene (dad) derivatives (Figure II.6).<sup>61,62,111–118</sup>

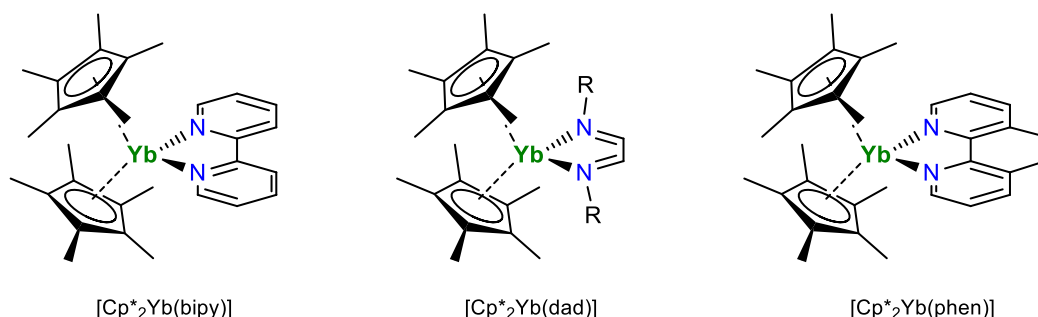


**Figure II.6.** Different ytterbocene adducts with N-heteroaromatic redox active ligands.

Although the redox potential of the  $\text{Yb}^{3+}/\text{Yb}^{2+}$  couple alone is not supposed to be sufficient to reduce such ligands,<sup>119</sup> XRD metrics as well as magnetic and spectroscopic measurements indicated that the redox-active ligand could be formally reduced, - or not, depending on the ligands used: both the Cp derivatives and the N-heterocyclic ligands choices matter. For instance, with the bipy ligand, XRD analysis of the  $\text{Cp}^*_2\text{Yb}(\text{bipy})$  complex revealed a shortened bridging C-C bond distance, 1.43 Å versus 1.49 Å for the free ligand and the oxidized  $[\text{Cp}^*_2\text{Yb}(\text{bipy})]^+$  cation. The effective magnetic moment was measured to be  $2.4 \mu_B$  in the neutral case, far from the  $4.2 \mu_B$  obtained with the cation or the  $4.54 \mu_B$  expected value for a free  $\text{Yb}^{\text{III}}$  ion. Added to all the spectroscopic singularities, IR absorption bands typical of a bipyridine radical or paramagnetic nature of the  $^1\text{H}$  NMR spectrum but deviating from the Curie-Weiss law upon variation of the temperature among others, it was first

proposed that both  $\text{Yb}^{\text{II}} 4\text{f}^{14}$  and  $\text{Yb}^{\text{III}} 4\text{f}^{13}$  configurations were contributing to the ground state, an hypothesis supported few years later by XANES, with an estimated  $n_{\text{f}} = 0.83$ , extended magnetic measurements and CASSCF theoretical studies.<sup>61,111</sup> As per magnetic considerations, if the effective magnetic moment alone is already strongly hinting toward intermediate valence, many of those ytterbocene adducts presents a temperature-independent, - or Van Vleck, paramagnetism (TIP) at low temperature. This phenomenon arises from a second order perturbation of the Hamiltonian ruling the interaction between an electron and an external magnetic field.<sup>120</sup> Since in most of those systems, the singlet-triplet energy gap is of the same order of magnitude than  $k_{\text{B}}T$ , it allows the observation of this phenomenon where, until the temperature upon which the triplet starts to be populated, the magnetic susceptibility remains constant. Once the impurity-induced “Curie tail” behavior is corrected, this particular susceptibility value  $\chi_{\text{TIP}}$  is used to estimate the energy gap with several models, a methodology that will be further explained in the third chapter of this manuscript.<sup>121,122</sup> Having these spectroscopic facts in mind, further investigations were conducted to evaluate the impact of the ligand tuning in such ytterbocene adducts. It allowed to understand the origin of the phenomenon and unveil new reactivities, a consequence of the relative energy and symmetry of the orbitals of both the Yb and the redox active ligands.<sup>116–118</sup>

### III. Rationalization and utility of intermediate valence

#### III.A. Energy and symmetry considerations

If the spectroscopic singularities are now well-known and often well-understood with the support of forever more robust theoretical methodologies, there is still a need for a rationalization of the respective weights of each configuration involved in the intermediate valence states of lanthanide compounds. To understand the impact of the energy of the involved orbitals, it is necessary to look back to the covalency present in such architectures. As defined by Equation (1),<sup>48</sup> two main parameters rule this interaction: the metal-ligand orbital overlap and the energy gap between both fragments. As aforementioned, the core character of f-orbitals implies a minimized overlap. Yet, when it comes to the energy gap, covalency arises when it is minimized yielding the “degeneracy driven covalency” that was suggested by Kerridge in the cerocene case.<sup>109</sup> This electronic density delocalization implies that both the ligand and the metal center receive partial spin densities resulting in an intermediate valence state.



$$\sigma = \frac{\varphi_M + \lambda \varphi_L}{\sqrt{1 + 2\lambda S_{ML} + \lambda^2}} \quad \text{with} \quad \lambda = \frac{H_{ML}}{E_M^0 - E_L^0} \quad (1)$$

$\sigma$  is the mixing between the metal and the ligand orbitals from perturbation theory of the ionic limit,  $\varphi_M$  is the metal orbital and  $\varphi_L$  the ligand orbital, both characterized by the metal and ligand energies,  $E_M^0$  and  $E_L^0$ .  $S_{ML}$  is the orbital overlap,  $\lambda$  the mixing co-efficient and  $H_{ML}$  the off-diagonal matrix element of the Hamiltonian. Note that in the Hückel theory,  $H_{ML}$  is proportional to  $S_{ML}$ .

In both Ce and Yb compounds, this model is easily represented in the simplest cases with three different configurations. One is composed of an empty or full shell,  $4f^0$  for Ce and  $4f^{14}$  for Yb while the two others result from the interaction between the open-shell  $4f^1$  (Ce) or  $4f^{13}$  (Yb) and the ligand configurations. As represented in Figure III.1 (left), the intermediate valence arises from the stabilized admixture of both singlet configurations while both  $\Delta_{SS}$  and  $\Delta_{ST}$ , the closed shell singlet-open-shell singlet and singlet-triplet energy gaps, are ruling the weight of each configuration in the ground state and the thermally accessible excited states. In the precise case of the ytterbocene adducts presented in the last part, the  $\Delta_{SS}$  can be expected to be closely related to the redox potentials of both Yb and N-heterocyclic fragments. If in the case of  $\text{Cp}^*_2\text{Yb}(\text{bipy})$ , the  $n_f$  was estimated to 0.83 from XANES data, further studies on methyl substituted bipy ligands allowed to modulate  $n_f$  confirming the impact of the redox potentials on  $\Delta_{SS}$ , when the redox potential of the ligand is decreased, so is the value of  $n_f$  (Figure III.2).<sup>62,115</sup> If this case is rather simple, several ligands, such as 1,10-phenantroline or 4,5-diazafluorene,<sup>116,118</sup> not only involve one but two or three  $\pi^*$  orbitals in the interaction with the lanthanide fragment (Figure III.1.right).

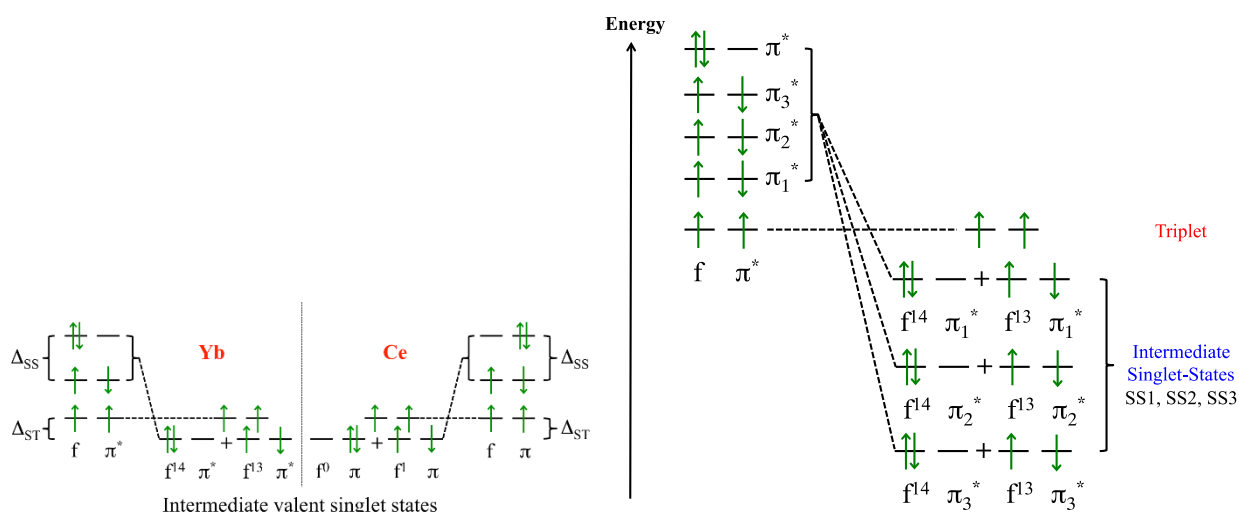


**Figure III.1.** Qualitative energy diagrams for intermediate-valent Yb and Ce species (left) and less trivial case of ytterbocene adducts with several  $\pi^*$  orbitals involved (right).

This leads to less trivial situations with several intermediate-valent singlets, each having its own  $n_f$ , lying below the lowest triplet state. The intermediate valence then becomes temperature dependent upon the successive population of the several singlet states and has to be fitted by a



Boltzmann distribution and compared to the XANES and magnetic data sets. If the  $n_f$  values are indeed correlated to the redox potential of the ligand, a closer look at Figure III.2 reveals that this relationship is different upon changing the core structure of the ligand, yielding drastically distinct mean line slopes.

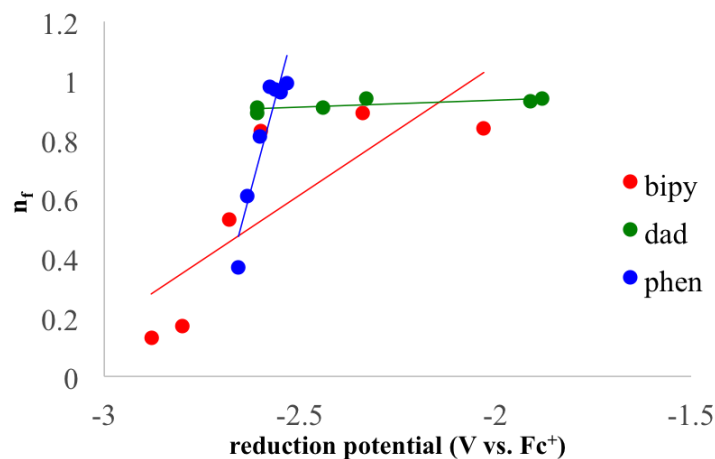


**Figure III.2.** Plot of the redox potentials of the different bipy, phen and dad derivatives versus the measured  $n_f$  for each series of ytterbocene complexes.<sup>115,123–125</sup>

This means that energy gaps alone cannot rationalize the  $n_f$  value and other parameters have to be considered. For instance, the fact that the correlation is reasonably good for each series of substituted ligands means the symmetry of the interacting orbital(s) is also impacting the intermediate valence. This was especially highlighted with the phen ligand since two  $\pi^*$  orbitals of different symmetry,  $b_1$  and  $a_2$ , can interact with the ytterbocene fragment. While the  $b_1$  orbital has the same symmetry and shape than the  $b_1 \pi^*$  orbital of a bipy with much density on the nitrogen atoms, the electronic density is mostly localized on the 4,7 positions for the  $a_2$  orbital and a node is present on the 3,8 positions (Figure III.3.left). These differences of symmetry allow precise tuning of each orbital energies explaining the different ground state observed for the substituted phen ligands (Figure III.3.right).<sup>117,118</sup> Upon methylation of the 3,8 positions, the  $b_1$  orbital energy is slightly increased while the  $a_2$  orbital remains unchanged resulting in relatively small change compared to the unsubstituted case ( $n_f = 0.96$  instead of 0.99), the same result was obtained with the methylation of the 5,6 positions. However, when the 4,7 positions are substituted (where most density is located), the relative energies of the  $a_2$  and  $b_1$  orbitals are reversed since the energy of the  $a_2$  orbital is significantly increased while the coordination of the Yb fragment stabilize the  $b_1$  orbital, yielding to an intermediate valence for the ground state.

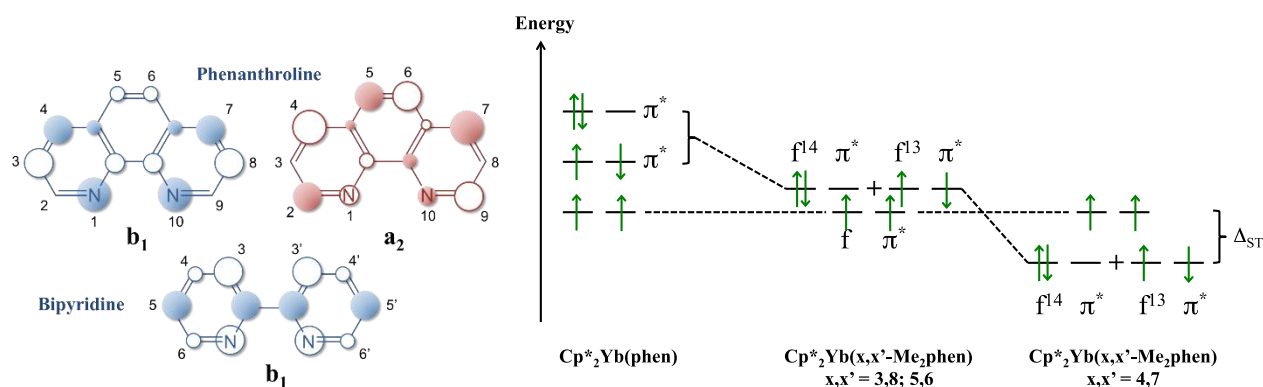


**Figure III.3.** Representation of the bipy and phen  $\pi^*$  orbitals (left) and qualitative energy diagram illustrating the impact of the different substitution of the phenanthroline ligand (right).

### III.B. Chemical ramifications: Impact on reactivities

If tuning an electronic structure is an important aspect in fundamental chemistry, it would also be interesting to relate these singular electronic structures to their chemical behavior. Inspired by the works of Andersen and coworkers, previous results obtained in the group came from a strong collaboration with him until his passing in June 2019.<sup>126</sup> From the work performed during this period,<sup>115–118</sup> the attention given to the symmetry of the redox active ligand orbitals was reinforced by the different reactivity observed upon switching from the historical bipy to the 4,5-diazafluorene and phen ligands. Slow hydrogen evolution was observed with the  $Cp^*_2Yb(4,5\text{-diazfluorene})$  complex, yielding the  $Cp^*_2Yb(4,5\text{-diazfluorenyl})$  compound.<sup>116</sup> This was attributed to the intermediate valence character of the starting complex with three  $\pi^*$  orbitals of different symmetry interacting with the Yb fragment,  $b_1$  for the LUMO and LUMO+1 and  $a_2$  for the LUMO +2. Among the three intermediate-valent singlet states, the second one has a  $n_f = 0.39$ , indicating a significant biradical character, and is thermally populated at room temperature. This explains the radical elimination of  $\frac{1}{2} H_2$  since significant spin density is found on the C9 atom, the position at which the C-H bond is broken (Figure III.4).

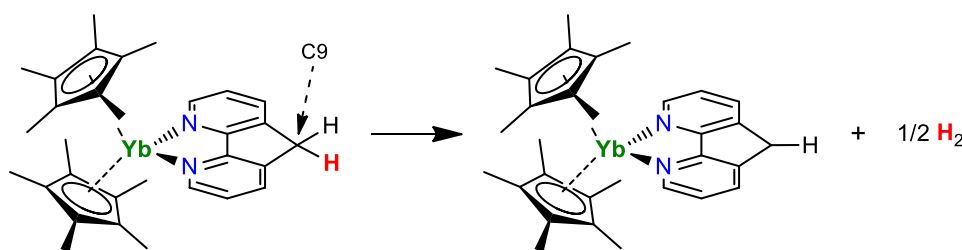


**Figure III.4.** Thermal dihydrogen elimination from the 4,5-diazafluorene ligand.

A further indication that reactivity of such intermediate-valent species is governed by the symmetry of their orbitals was evidenced with the aforementioned series of  $Cp^*_2Yb(x,x'-Me_2phen)$ . While the origin of their different electronic ground state was already discussed, the position at which

the methylation was performed triggered a reaction dichotomy between the 3,8 or 5,6 positions and the 4,7 one (Figure III.5). While the 3,8 version was shown to be able to reversibly dimerize by the mean of a radical C-C coupling in position 4,7 (Figure III.6.top),<sup>118</sup> the 5,6 one was most likely too hindered to do so. In contrast, the 4,7 one performed a bimolecular hydrogen atom transfer (HAT) reaction echoing to the H<sub>2</sub> formed in the 4,5-diazafluorene case (Figure III.6.bottom).<sup>117</sup> The C-C coupling can easily be related to the symmetry of their stabilized  $a_2$  orbital: the highest spin densities are found on the symmetrical C4 and C7 atoms and this density is large enough in the unsubstituted phen and 3,8-Me<sub>2</sub>phen cases to trigger the radical coupling. In the other case, the 4,7 substitution prevents the C-C coupling since overcoming the steric hindrance in a hypothetical dimer would be more expensive in energy than the stabilization resulting from the  $\sigma$  bond formation. The trigger of the HAT is then the delocalization of the C4  $\pi^*$  spin density to its neighboring  $\sigma^*C4-H$  orbital, the weakened C-H bond is then ready to perform the observed bimolecular rearrangement.

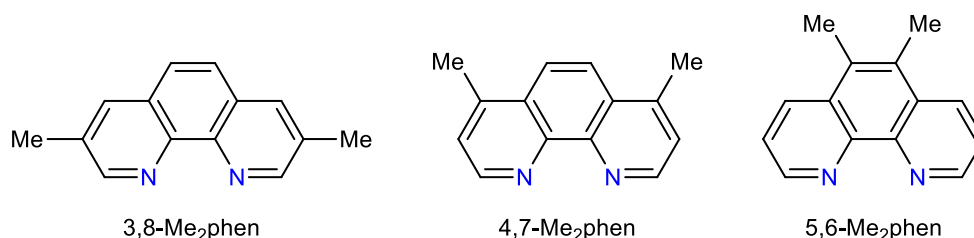


**Figure III.5.** The different dimethyl phenanthroline involving different reactivity upon coordination to a divalent organoytterbium fragment.

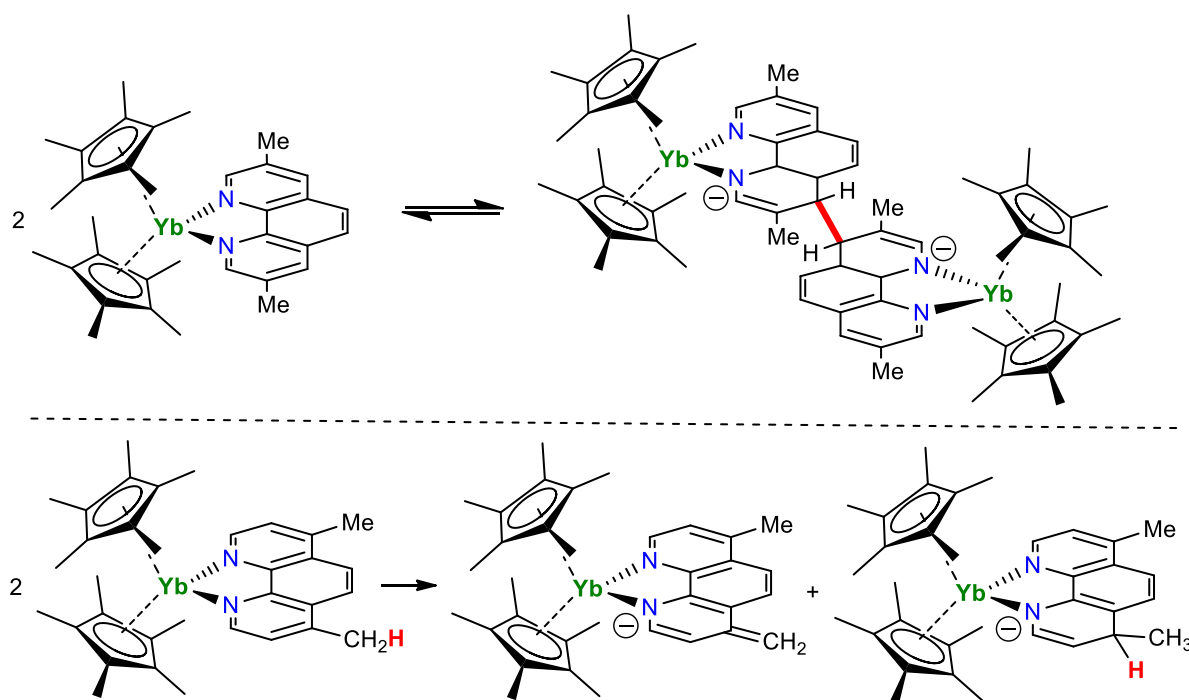


**Figure III.6.** Two different reactivity pathways depending on the position of the methyl substituents of the phen ligand. (top) Reversible radical C-C coupling, (bottom) bimolecular HAT.

### III.C. Going further with heterobimetallic architectures

Taking advantage of this in-depth knowledge of the energetic and symmetry driven reactivities, a further application of the tunable intermediate valence state of such ytterbocene adducts was recently developed in the group. By switching from bipy and phen ligands to 2,2'-bipyrimidine (bipym) and 4,5,9,10-tetraazaphenanthrene (taphen), ligands having a second coordination site, the objective was to build heterobimetallic complexes composed of divalent Yb and transition metal (TM) fragments. The resulting compounds would allow to evaluate the impact of the intermediate valence on the TM reactivity and hopefully unveil new transformations. The proof of concept of this project was published in 2017 with the novel  $\text{Cp}^*_2\text{Yb}(\text{L})\text{PdMe}_2$  complexes ( $\text{L} = \text{bipym}$  or  $\text{taphen}$ ). Echoing to the bipy and phen adducts, the bipym version was found intermediate-valent with a mixed singlet state and a low-lying triplet state while the taphen presented a pure triplet ground state due to their respective orbital symmetry (Figure III.7).<sup>127</sup> To evaluate the impact of such different electronic structures, both compounds were treated with MeI to trigger an oxidative addition. While the formed taphen- $\text{Pd}^{\text{IV}}$  complex was not resistant to reductive elimination of ethane, the bipym version presented a much higher stability than its mononuclear analog isolated in 1986 ( $\text{bipy})\text{PdMe}_3\text{I}$ .<sup>128,129</sup> From an orbital point of view this stability arises from the significant spin density held by the four nitrogen atoms, and consequently the two that support the Pd center while this characteristic is not present with the taphen ligand.

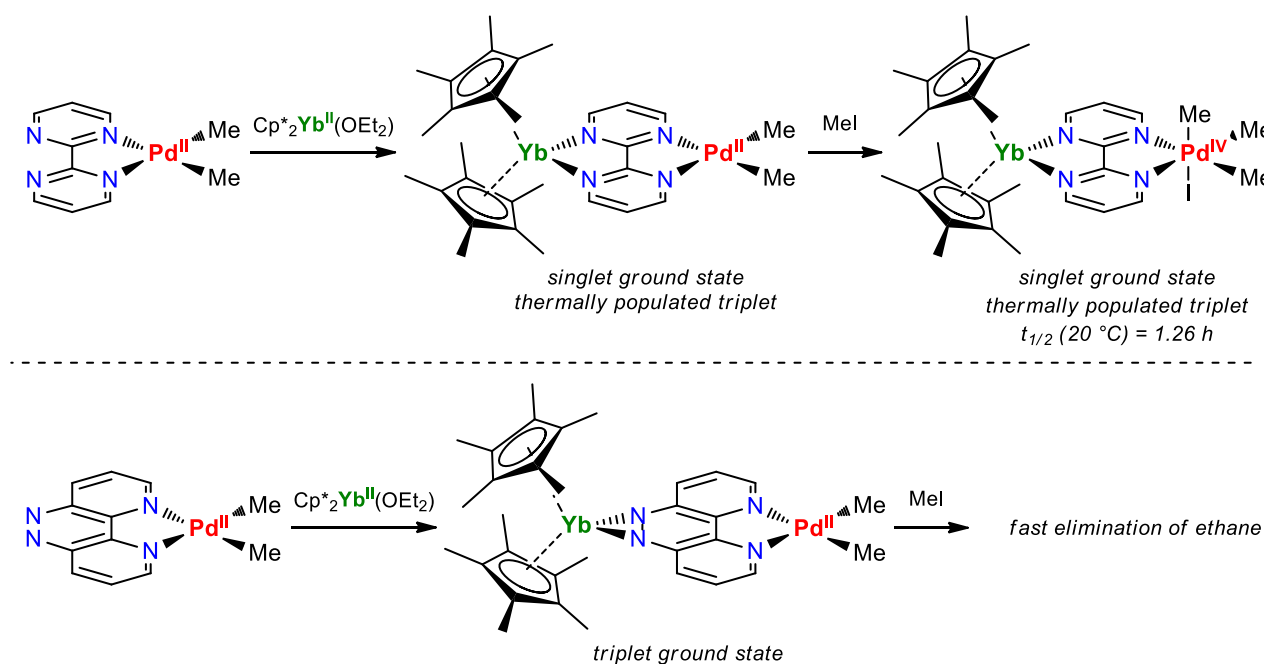


**Figure III.7.** Heterobimetallic complexes of Yb and Pd, stabilization of the unusual  $\text{Pd}^{\text{IV}}$  oxidation state.

Extension of this strategy to nickel lead to a comparative reactivity study toward CO with the  $\text{Cp}^*_2\text{Yb}(\text{bipym})\text{NiMe}_2$  and its  $(\text{bipym})\text{NiMe}_2$  precursor.<sup>130</sup> The ytterbocene fragment was found to

stabilize the expected acyl intermediate resulting from the CO migratory insertion in the Ni-Me bond, most likely through a similar process that the one discussed for the Yb-Pd<sup>IV</sup> compound. These two studies combined confirmed the relevance of such heterobimetallic architectures in the study and stabilization of elusive reaction intermediates, a topic further investigated in this manuscript.

To widen the scope of bridging ligand used (Figure III.8), other members of the group proposed to use the L<sub>3</sub>X dissymmetric 2-pyrimidin-2-yl-1H-benzimidazole (Hbimp) ligand (Figure III.8.left). Contrary to the two previous studies, this example unveiled that the ytterbocene fragment was influencing the position at which radical C-C coupling reactivity was observed upon reduction of the deprotonated bimp<sup>-</sup> ligand by either the Yb moiety of KC<sub>8</sub>.<sup>131</sup> Lately a collaborative project with the Hess group allowed to study the intermediate valence of the novel [Cp\*<sub>2</sub>Yb(Mabiq)Ni]<sup>+</sup> cation,<sup>132</sup> HMabiq being a macrocyclic biquinazoline ligand (Figure III.8.right),<sup>133</sup> and evaluate the tuned photophysical properties of the (Mabiq)Ni fragment.<sup>134</sup>

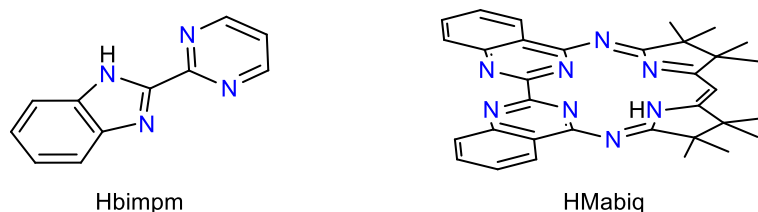


**Figure III.8.** The Hbimp and HMabiq ligands recently used to synthesize heterobimetallic complexes.

## IV. Conclusion and objectives

This introduction gathers the most illustrative examples investigated for their odd spectroscopic signatures now fully incorporated as features of the intermediate valence found in lanthanide compounds. These properties not only surprised experimental chemists, they also challenged theoretical chemists and robust computational methodologies were developed to model this specific phenomenon. All these contributions allowed the rationalization of such original electronic architectures and guidelines to design intermediate-valent species for which an electronic state is composed of several configurations. Finally, the extensive studies conducted on N-heterocyclic adducts of ytterbocene eventually opened the way to the project in which this thesis work is included: the synthesis of divalent lanthanide induced intermediate-valent heterobimetallic complexes with transition metals in order to evaluate the impact of the 4f-element fragment on the reactivity of the TM center (Figure IV.1). An extended version of this introductory chapter can be found in our recently published minireview on the topic.<sup>135</sup>

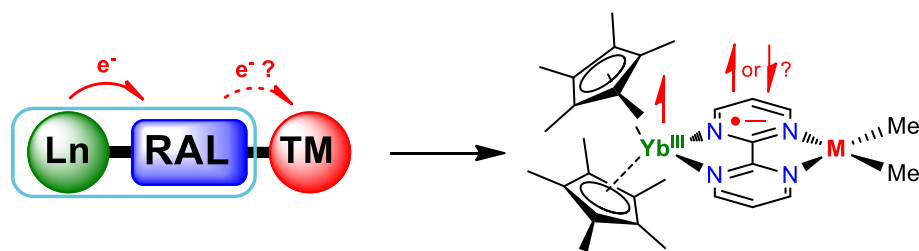


**Figure IV.1.** Design of intermediate-valent heterobimetallic complexes.

Following the recent works conducted in the group this Ph.D. manuscript will mainly deal with two aspects. **Chapter II** will focus on the synthesis of new precursors of trivalent lanthanide ions with large aromatic ligands representing a potential alternative to the traditional Cp-based organolanthanide complexes used to design intermediate-valent compounds. This work permitted to further study the coordination chemistry of the rarely used cyclononatetraenyl (Cnt) ligand and uncover a lanthanide size-induced hapticity switch in the series of prepared compounds.<sup>136</sup> In order to fully cover the group 10 transition metal that can be involved in  $\text{Cp}^*_2\text{Yb}(\text{bipym})\text{MMe}_2$  type of complex, **Chapter III** will present the extensive characterization and reactivity studies conducted with platinum where the observed modulation of the intermediate valence upon variation of the coordination environment of the Pt center is directly related to the collaborative work performed with the Andersen group. The reactivity trials conducted with Yb-Pt compounds led to the investigation of low-valent Ni reactivity toward alkene isomerization presented in **Chapter IV**, allowing to discover an original mechanism based on the shuttle of electrons between the Yb, the bipym and the Ni center. Finally, **Chapter V** will present the synthesis and characterization of unprecedented tetraalkyl Pd complexes with a high stability, the study of its degradation opening new perspectives for  $\text{Csp}^3\text{-Csp}^3$  coupling reactions.

## References

- (1) *Chem. Int. -- Newsmag. IUPAC* **2005**, 27 (6), 25–26. <https://doi.org/doi:10.1515/ci.2005.27.6.25>.
- (2) Cheisson, T.; Schelter, E. J. *Science* (80-. ). **2019**, 363 (6426), 489–493. <https://doi.org/10.1126/science.aau7628>.
- (3) Wedepohl, K. H. *Geochim. Cosmochim. Acta* **1995**, 59 (7), 1217–1232. [https://doi.org/10.1016/0016-7037\(95\)00038-2](https://doi.org/10.1016/0016-7037(95)00038-2).
- (4) Zhou, B.; Li, Z.; Chen, C. *Minerals* **2017**, 7(11), 203. <https://doi.org/10.3390/min7110203>.
- (5) Zeimentz, P. M.; Arndt, S.; Elvidge, B. R.; Okuda, J. *Chem. Rev.* **2006**, 106 (6), 2404–2433. <https://doi.org/10.1021/cr050574s>.
- (6) Wang, H.; Cue, J. M. O.; Calubaquib, E. L.; Kularatne, R. N.; Taslimy, S.; Miller, J. T.; Stefan, M. C. *Polym. Chem.* **2021**, 12 (47), 6790–6823. <https://doi.org/10.1039/D1PY01270C>.
- (7) Yang, Y.; Walton, A.; Sheridan, R.; Güth, K.; Gauß, R.; Gutfleisch, O.; Buchert, M.; Steenari, B.-M.; Van Gerven, T.; Jones, P. T.; Binnemans, K. *J. Sustain. Metall.* **2017**, 3 (1), 122–149. <https://doi.org/10.1007/s40831-016-0090-4>.
- (8) Wang, L.; Zhao, Z.; Wei, C.; Wei, H.; Liu, Z.; Bian, Z.; Huang, C. *Adv. Opt. Mater.* **2019**, 7 (11), 1801256. <https://doi.org/10.1002/adom.201801256>.
- (9) Kuriki, K.; Koike, Y.; Okamoto, Y. *Chem. Rev.* **2002**, 102 (6), 2347–2356. <https://doi.org/10.1021/cr010309g>.
- (10) Bottrill, M.; Kwok, L.; Long, N. J. *Chem. Soc. Rev.* **2006**, 35 (6), 557–571. <https://doi.org/10.1039/B516376P>.
- (11) Lang, P. F.; Smith, B. C. *J. Chem. Educ.* **2010**, 87 (8), 875–881. <https://doi.org/10.1021/ed100215q>.
- (12) Fischer, E. O.; Fischer, H. *Angew. Chemie Int. Ed. English* **1964**, 3 (2), 132–133. <https://doi.org/10.1002/anie.196401322>.
- (13) Fischer, E. O.; Fischer, H. *J. Organomet. Chem.* **1965**, 3 (3), 181–187. [https://doi.org/10.1016/S0022-328X\(00\)87500-2](https://doi.org/10.1016/S0022-328X(00)87500-2).
- (14) Howell, J. K.; Pytlewski, L. L. *J. Less Common Met.* **1969**, 18 (4), 437–439. [https://doi.org/10.1016/0022-5088\(69\)90017-4](https://doi.org/10.1016/0022-5088(69)90017-4).
- (15) Watt, G. W.; Gillow, E. W. *J. Am. Chem. Soc.* **1969**, 91 (3), 775–776. <https://doi.org/10.1021/ja01031a061>.
- (16) Girard, P.; Namy, J. L.; Kagan, H. B. *J. Am. Chem. Soc.* **1980**, 102 (8), 2693–2698. <https://doi.org/10.1021/ja00528a029>.
- (17) Tilley, T. D.; Andersen, R. A.; Spencer, B.; Ruben, H.; Zalkin, A.; Templeton, D. H. *Inorg. Chem.* **1980**, 19 (10), 2999–3003. <https://doi.org/10.1021/ic50212a031>.
- (18) Evans, W. J.; Hughes, L. A.; Hanusa, T. P. *Organometallics* **1986**, 5 (7), 1285–1291. <https://doi.org/10.1021/om00138a001>.
- (19) Kagan, H. B.; Namy, J. L. B. T.-H. on the P. and C. of R. E. In *Handbook on the Physics and Chemistry of Rare Earths*; Elsevier, 1984; Vol. 6, pp 525–565. [https://doi.org/10.1016/S0168-1273\(84\)06007-4](https://doi.org/10.1016/S0168-1273(84)06007-4).
- (20) Bochkarev, M. N.; Fedushkin, I. L.; Fagin, A. A.; Petrovskaya, T. V.; Ziller, J. W.; Broomhall-Dillard, R. N. R.; Evans, W. J. *Angew. Chemie Int. Ed. English* **1997**, 36 (1–2), 133–135. <https://doi.org/10.1002/anie.199701331>.
- (21) Bochkarev, M. N.; Fagin, A. A. *Chem. – A Eur. J.* **1999**, 5 (10), 2990–2992. [https://doi.org/10.1002/\(SICI\)1521-3765\(19991001\)5:10<2990::AID-CHEM2990>3.0.CO;2-U](https://doi.org/10.1002/(SICI)1521-3765(19991001)5:10<2990::AID-CHEM2990>3.0.CO;2-U).
- (22) Evans, W. J.; Allen, N. T.; Ziller, J. W. *J. Am. Chem. Soc.* **2000**, 122 (47), 11749–11750. <https://doi.org/10.1021/ja0034949>.
- (23) Bochkarev, M. N.; Fedushkin, I. L.; Dechert, S.; Fagin, A. A.; Schumann, H. *Angew. Chemie Int. Ed.* **2001**, 40 (17), 3176–3178. [https://doi.org/10.1002/1521-3773\(20010903\)40:17<3176::AID-ANIE3176>3.0.CO;2-Y](https://doi.org/10.1002/1521-3773(20010903)40:17<3176::AID-ANIE3176>3.0.CO;2-Y).
- (24) Nief, F. *Dalt. Trans.* **2010**, 39 (29), 6589–6598. <https://doi.org/10.1039/C001280G>.

- (25) Hitchcock, P. B.; Lappert, M. F.; Maron, L.; Protchenko, A. V. *Angew. Chemie Int. Ed.* **2008**, *47* (8), 1488–1491. <https://doi.org/10.1002/anie.200704887>.
- (26) MacDonald, M. R.; Ziller, J. W.; Evans, W. J. *J. Am. Chem. Soc.* **2011**, *133* (40), 15914–15917. <https://doi.org/10.1021/ja207151y>.
- (27) MacDonald, M. R.; Bates, J. E.; Fieser, M. E.; Ziller, J. W.; Furche, F.; Evans, W. J. *J. Am. Chem. Soc.* **2012**, *134* (20), 8420–8423. <https://doi.org/10.1021/ja303357w>.
- (28) MacDonald, M. R.; Bates, J. E.; Ziller, J. W.; Furche, F.; Evans, W. J. *J. Am. Chem. Soc.* **2013**, *135* (26), 9857–9868. <https://doi.org/10.1021/ja403753j>.
- (29) Fieser, M. E.; Ferrier, M. G.; Su, J.; Batista, E.; Cary, S. K.; Engle, J. W.; Evans, W. J.; Lezama Pacheco, J. S.; Kozimor, S. A.; Olson, A. C.; Ryan, A. J.; Stein, B. W.; Wagner, G. L.; Woen, D. H.; Vitova, T.; Yang, P. *Chem. Sci.* **2017**, *8* (9), 6076–6091. <https://doi.org/10.1039/C7SC00825B>.
- (30) Greco, A.; Cesca, S.; Bertolini, W. *J. Organomet. Chem.* **1976**, *113* (4), 321–330. [https://doi.org/10.1016/S0022-328X\(00\)96143-6](https://doi.org/10.1016/S0022-328X(00)96143-6).
- (31) Streitwieser, A.; Kinsley, S. A.; Jenson, C. H.; Rigsbee, J. T. *Organometallics* **2004**, *23* (22), 5169–5175. <https://doi.org/10.1021/om049743+>.
- (32) Walter, M. D.; Booth, C. H.; Lukens, W. W.; Andersen, R. A. *Organometallics* **2009**, *28* (3), 698–707. <https://doi.org/10.1021/om7012327>.
- (33) Piro, N. A.; Robinson, J. R.; Walsh, P. J.; Schelter, E. J. *Coord. Chem. Rev.* **2014**, *260*, 21–36. <https://doi.org/10.1016/j.ccr.2013.08.034>.
- (34) Palumbo, C. T.; Zivkovic, I.; Scopelliti, R.; Mazzanti, M. *J. Am. Chem. Soc.* **2019**, *141* (25), 9827–9831. <https://doi.org/10.1021/jacs.9b05337>.
- (35) Rice, N. T.; Popov, I. A.; Russo, D. R.; Bacsá, J.; Batista, E. R.; Yang, P.; Telser, J.; La Pierre, H. S. *J. Am. Chem. Soc.* **2019**, *141* (33), 13222–13233. <https://doi.org/10.1021/jacs.9b06622>.
- (36) Willauer, A. R.; Palumbo, C. T.; Fadaei-Tirani, F.; Zivkovic, I.; Douair, I.; Maron, L.; Mazzanti, M. *J. Am. Chem. Soc.* **2020**, *142* (12), 5538–5542. <https://doi.org/10.1021/jacs.0c01204>.
- (37) Willauer, A. R.; Palumbo, C. T.; Scopelliti, R.; Zivkovic, I.; Douair, I.; Maron, L.; Mazzanti, M. *Angew. Chemie Int. Ed.* **2020**, *59* (9), 3549–3553. <https://doi.org/10.1002/anie.201914733>.
- (38) Gompa, T. P.; Ramanathan, A.; Rice, N. T.; La Pierre, H. S. *Dalt. Trans.* **2020**, *49* (45), 15945–15987. <https://doi.org/10.1039/D0DT01400A>.
- (39) Li, N.; Zhang, W.-X. *Chinese J. Chem.* **2020**, *38* (11), 1449–1450. <https://doi.org/10.1002/cjoc.202000258>.
- (40) Evans, W. J. *Organometallics* **2016**, *35* (18), 3088–3100. <https://doi.org/10.1021/acs.organomet.6b00466>.
- (41) Cloke, F. G. N. *Chem. Soc. Rev.* **1993**, *22* (1), 17–24. <https://doi.org/10.1039/CS9932200017>.
- (42) Friedman, H. G.; Choppin, G. R.; Feuerbacher, D. G. *J. Chem. Educ.* **1964**, *41* (7), 354. <https://doi.org/10.1021/ed041p354>.
- (43) Raymond, K. N.; Eigenbrot, C. W. *Acc. Chem. Res.* **1980**, *13* (8), 276–283. <https://doi.org/10.1021/ar50152a005>.
- (44) Karraker, D. G. *J. Chem. Educ.* **1970**, *47* (6), 424. <https://doi.org/10.1021/ed047p424>.
- (45) Cotton, S. A. *Lanthanide and Actinide Chemistry*; Wiley, Chichester, England, **2006**. <https://doi.org/10.1002/0470010088>.
- (46) Evans, W. J.; Grate, J. W.; Hughes, L. A.; Zhang, H.; Atwood, J. L. *J. Am. Chem. Soc.* **1985**, *107* (12), 3728–3730. <https://doi.org/10.1021/ja00298a060>.
- (47) Evans, W. J.; Ulibarri, T. A.; Ziller, J. W. *J. Am. Chem. Soc.* **1988**, *110* (20), 6877–6879. <https://doi.org/10.1021/ja00228a043>.
- (48) Neidig, M. L.; Clark, D. L.; Martin, R. L. *Coord. Chem. Rev.* **2013**, *257* (2), 394–406. <https://doi.org/10.1016/j.ccr.2012.04.029>.



- (49) Tomson, N. C.; Crimmin, M. R.; Petrenko, T.; Rosebrugh, L. E.; Sproules, S.; Boyd, W. C.; Bergman, R. G.; Debeer, S.; Toste, F. D.; Wieghardt, K. *J. Am. Chem. Soc.* **2011**, *133* (46), 18785–18801. <https://doi.org/10.1021/ja206042k>.
- (50) Ray, K.; Weyhermüller, T.; Neese, F.; Wieghardt, K. *Inorg. Chem.* **2005**, *44* (15), 5345–5360. <https://doi.org/10.1021/ic0507565>.
- (51) Ray, K.; Petrenko, T.; Wieghardt, K.; Neese, F. *Dalt. Trans.* **2007**, No. 16, 1552–1566. <https://doi.org/10.1039/B700096K>.
- (52) Scarborough, C. C.; Wieghardt, K. *Inorg. Chem.* **2011**, *50* (20), 9773–9793. <https://doi.org/10.1021/ic2005419>.
- (53) Scarborough, C. C.; Sproules, S.; Weyhermüller, T.; DeBeer, S.; Wieghardt, K. *Inorg. Chem.* **2011**, *50* (24), 12446–12462. <https://doi.org/10.1021/ic201123x>.
- (54) Tomson, N. C.; Williams, K. D.; Dai, X.; Sproules, S.; DeBeer, S.; Warren, T. H.; Wieghardt, K. *Chem. Sci.* **2015**, *6* (4), 2474–2487. <https://doi.org/10.1039/C4SC03294B>.
- (55) England, J.; Bill, E.; Weyhermüller, T.; Neese, F.; Atanasov, M.; Wieghardt, K. *Inorg. Chem.* **2015**, *54* (24), 12002–12018. <https://doi.org/10.1021/acs.inorgchem.5b02415>.
- (56) Wolff, C.; Gottschlich, A.; England, J.; Wieghardt, K.; Saak, W.; Haase, D.; Beckhaus, R. *Inorg. Chem.* **2015**, *54* (10), 4811–4820. <https://doi.org/10.1021/acs.inorgchem.5b00285>.
- (57) Mustieles Marín, I.; Cheisson, T.; Singh-Chauhan, R.; Herrero, C.; Cordier, M.; Clavaguéra, C.; Nocton, G.; Auffrant, A. *Chem. – A Eur. J.* **2017**, *23* (71), 17940–17953. <https://doi.org/10.1002/chem.201703390>.
- (58) Neumann, C. S.; Fulde, P. *Zeitschrift für Phys. B Condens. Matter* **1989**, *74* (3), 277–278. <https://doi.org/10.1007/BF01307872>.
- (59) Dolg, M.; Fulde, P.; Küchle, W.; Neumann, C. S.; Stoll, H. *J. Chem. Phys.* **1991**, *94* (4), 3011–3017. <https://doi.org/10.1063/1.459824>.
- (60) Dolg, M.; Fulde, P.; Stoll, H.; Preuss, H.; Chang, A.; Pitzer, R. M. *Chem. Phys.* **1995**, *195* (1), 71–82. [https://doi.org/10.1016/0301-0104\(94\)00363-F](https://doi.org/10.1016/0301-0104(94)00363-F).
- (61) Booth, C. H.; Walter, M. D.; Kazhdan, D.; Hu, Y.-J.; Lukens, W. W.; Bauer, E. D.; Maron, L.; Eisenstein, O.; Andersen, R. A. *J. Am. Chem. Soc.* **2009**. <https://doi.org/10.1021/ja809624w>.
- (62) Booth, C. H.; Kazhdan, D.; Werkema, E. L.; Walter, M. D.; Lukens, W. W.; Bauer, E. D.; Hu, Y.-J.; Maron, L.; Eisenstein, O.; Head-Gordon, M.; Andersen, R. A. *J. Am. Chem. Soc.* **2010**, *132* (49), 17537–17549. <https://doi.org/10.1021/ja106902s>.
- (63) Field, R. W. *Berichte der Bunsengesellschaft für Phys. Chemie* **1982**, *86* (9), 771–779. <https://doi.org/10.1002/bbpc.19820860903>.
- (64) Fulde, P.; Keller, J.; Zwicknagl, G. *Theory of Heavy Fermion Systems*, Elsevier, Amsterdam, Netherlands, **1988**; 41, pp 1–150. [https://doi.org/10.1016/S0081-1947\(08\)60378-1](https://doi.org/10.1016/S0081-1947(08)60378-1).
- (65) Riseborough, P. S. *Adv. Phys.* **2000**, *49* (3), 257–320. <https://doi.org/10.1080/000187300243345>.
- (66) Gilbert, A.; Vidhyadhiraja, N. S.; Logan, D. E. *J. Phys. Condens. Matter* **2007**, *19* (10), 106220. <https://doi.org/10.1088/0953-8984/19/10/106220>.
- (67) Kaely, T. J.; Pauson, P. L. *Nature* **1951**, *168* (4285), 1039–1040. <https://doi.org/10.1038/1681039b0>.
- (68) Wilkinson, G.; Birmingham, J. M. *J. Am. Chem. Soc.* **1954**, *76* (23), 6210. <https://doi.org/10.1021/ja01652a114>.
- (69) Birmingham, J. M.; Wilkinson, G. *J. Am. Chem. Soc.* **1956**, *78* (1), 42–44. <https://doi.org/10.1021/ja01582a009>.
- (70) Schumann, H.; Meese-Marktscheffel, J. A.; Esser, L. *Chem. Rev.* **1995**, *95* (4), 865–986. <https://doi.org/10.1021/cr00036a004>.
- (71) Andersen, R. A.; Boncella, J. M.; Burns, C. J.; Green, J. C.; Hohl, D.; Rösch, N. *J. Chem. Soc. Chem. Commun.* **1986**, No. 5, 405–407. <https://doi.org/10.1039/C39860000405>.
- (72) Baddar, F. G.; Hilal, O. M. M.; Sugden, S. *J. Chem. Soc.* **1949**, No. 0, 132–135. <https://doi.org/10.1039/JR9490000132>.

- (73) Benelli, C.; Gatteschi, D. *Introduction to Molecular Magnetism: From Transition Metals to Lanthanides*, Wiley, Weinheim, Germany, **2015**, p 71. <https://doi.org/10.1002/9783527690541>.
- (74) Coreno, M.; de Simone, M.; Green, J. C.; Kaltsoyannis, N.; Narband, N.; Sella, A. *Chem. Phys. Lett.* **2006**, *432* (1), 17–21. <https://doi.org/10.1016/j.cplett.2006.10.029>.
- (75) Coates, R.; Coreno, M.; DeSimone, M.; Green, J. C.; Kaltsoyannis, N.; Kerridge, A.; Narband, N.; Sella, A. *Dalt. Trans.* **2009**, No. 30, 5943–5953. <https://doi.org/10.1039/B902263E>.
- (76) Coreno, M.; de Simone, M.; Coates, R.; Denning, M. S.; Denning, R. G.; Green, J. C.; Hunston, C.; Kaltsoyannis, N.; Sella, A. *Organometallics* **2010**, *29* (21), 4752–4755. <https://doi.org/10.1021/om100240m>.
- (77) Denning, R. G.; Harmer, J.; Green, J. C.; Irwin, M. *J. Am. Chem. Soc.* **2011**, *133* (50), 20644–20660. <https://doi.org/10.1021/ja209311g>.
- (78) Coreno, M.; de Simone, M.; Green, J. C.; Kaltsoyannis, N.; Coates, R.; Hunston, C.; Narband, N.; Sella, A. *Dalt. Trans.* **2014**, *43* (13), 5134–5141. <https://doi.org/10.1039/C3DT53512F>.
- (79) Morss, L. R. *Chem. Rev.* **1976**, *76* (6), 827–841. <https://doi.org/10.1021/cr60304a007>.
- (80) Grandjean, F.; Long, G. J. Long, G. J., Grandjean, F., *Mössbauer Spectroscopy of Europium-Containing Compounds*, Springer US: Boston, MA, **1989**, pp 513–597. [https://doi.org/10.1007/978-1-4899-2289-2\\_11](https://doi.org/10.1007/978-1-4899-2289-2_11).
- (81) Depaoli, G.; Russo, U.; Valle, G.; Grandjean, F.; Williams, A. F.; Long, G. J. *J. Am. Chem. Soc.* **1994**, *116* (13), 5999–6000. <https://doi.org/10.1021/ja00092a073>.
- (82) Baer, Y.; Hauger, R.; Zürcher, C.; Campagna, M.; Wertheim, G. K. *Phys. Rev. B* **1978**, *18* (8), 4433–4439. <https://doi.org/10.1103/PhysRevB.18.4433>.
- (83) Franciosi, A.; Weaver, J. H.; Mårtensson, N.; Croft, M. *Phys. Rev. B* **1981**, *24* (6), 3651–3654. <https://doi.org/10.1103/PhysRevB.24.3651>.
- (84) Allen, J. W.; Oh, S. J.; Gunnarsson, O.; Schönhammer, K.; Maple, M. B.; Torikachvili, M. S.; Lindau, I. *Adv. Phys.* **1986**, *35* (3), 275–316. <https://doi.org/10.1080/00018738600101901>.
- (85) Boussie, T. R.; Eisenberg, D. C.; Rigsbee, J.; Streitwieser, A.; Zalkin, A. *Organometallics* **1991**, *10* (6), 1922–1928. <https://doi.org/10.1021/om00052a044>.
- (86) Kilimann, U.; Herbst-Irmer, R.; Stalke, D.; Edelmann, F. T. *Angew. Chemie Int. Ed. English* **1994**, *33* (15–16), 1618–1621. <https://doi.org/10.1002/anie.199416181>.
- (87) Hodgson, K. O.; Raymond, K. N. *Inorg. Chem.* **1972**, *11* (12), 3030–3035. <https://doi.org/10.1021/ic50118a031>.
- (88) Streitwieser, A.; Kinsley, S. A.; Rigsbee, J. T.; Fragala, I. L.; Ciliberto, E. *J. Am. Chem. Soc.* **1985**, *107* (25), 7786–7788. <https://doi.org/10.1021/ja00311a108>.
- (89) Amberger, H.-D.; Reddmann, H.; Edelmann, F. T. *J. Organomet. Chem.* **2005**, *690* (9), 2238–2242. <https://doi.org/10.1016/j.jorganchem.2005.01.066>.
- (90) Edelstein, N. M.; Allen, P. G.; Bucher, J. J.; Shuh, D. K.; Sofield, C. D.; Kaltsoyannis, N.; Maunder, G. H.; Russo, M. R.; Sella, A. *J. Am. Chem. Soc.* **1996**, *118* (51), 13115–13116. <https://doi.org/10.1021/ja962915c>.
- (91) Booth, C. H.; Walter, M. D.; Daniel, M.; Lukens, W. W.; Andersen, R. A. *Phys. Rev. Lett.* **2005**, *95* (26), 267202. <https://doi.org/10.1103/PhysRevLett.95.267202>.
- (92) Smiles, D. E.; Batista, E. R.; Booth, C. H.; Clark, D. L.; Keith, J. M.; Kozimor, S. A.; Martin, R. L.; Minasian, S. G.; Shuh, D. K.; Stieber, S. C. E.; Tylliszczak, T. *Chem. Sci.* **2020**, *11* (10), 2796–2809. <https://doi.org/10.1039/C9SC06114B>.
- (93) Sarrao, J. L.; Immer, C. D.; Fisk, Z.; Booth, C. H.; Figueroa, E.; Lawrence, J. M.; Modler, R.; Cornelius, A. L.; Hundley, M. F.; Kwei, G. H.; Thompson, J. D.; Bridges, F. *Phys. Rev. B* **1999**, *59* (10), 6855–6866. <https://doi.org/10.1103/PhysRevB.59.6855>.
- (94) Vitova, T.; Kvashnina, K. O.; Nocton, G.; Sukharina, G.; Denecke, M. A.; Butorin, S. M.; Mazzanti, M.; Caciuffo, R.; Soldatov, A.; Behrends, T.; Geckeis, H. *Phys. Rev. B* **2010**, *82* (23), 235118. <https://doi.org/10.1103/PhysRevB.82.235118>.

- (95) Löble, M. W.; Keith, J. M.; Altman, A. B.; Stieber, S. C. E.; Batista, E. R.; Boland, K. S.; Conradson, S. D.; Clark, D. L.; Lezama Pacheco, J.; Kozimor, S. A.; Martin, R. L.; Minasian, S. G.; Olson, A. C.; Scott, B. L.; Shuh, D. K.; Tyliczszak, T.; Wilkerson, M. P.; Zehnder, R. A. *J. Am. Chem. Soc.* **2015**, *137* (7), 2506–2523. <https://doi.org/10.1021/ja510067v>.
- (96) Altman, A. B.; Pacold, J. I.; Wang, J.; Lukens, W. W.; Minasian, S. G. *Dalt. Trans.* **2016**, *45* (24), 9948–9961. <https://doi.org/10.1039/C6DT00358C>.
- (97) Minasian, S. G.; Batista, E. R.; Booth, C. H.; Clark, D. L.; Keith, J. M.; Kozimor, S. A.; Lukens, W. W.; Martin, R. L.; Shuh, D. K.; Stieber, S. C. E.; Tyliczszak, T.; Wen, X. *J. Am. Chem. Soc.* **2017**, *139* (49), 18052–18064. <https://doi.org/10.1021/jacs.7b10361>.
- (98) Roesch, N.; Streitwieser, A. *J. Am. Chem. Soc.* **1983**, *105* (25), 7237–7240. <https://doi.org/10.1021/ja00363a004>.
- (99) Neumann, C.-S.; Fulde, P. *Z. Physik B - Condensed Matter* **1989**, *74*, 277–278. <https://doi.org/10.1007/BF01307872>.
- (100) Dolg, M.; Stoll, H. *Theor. Chim. Acta* **1989**, *75* (5), 369–387. <https://doi.org/10.1007/BF00526695>.
- (101) Dolg, M.; Stoll, H.; Preuss, H. *J. Chem. Phys.* **1989**, *90* (3), 1730–1734. <https://doi.org/10.1063/1.456066>.
- (102) Küchle, W.; Dolg, M.; Stoll, H.; Preuss, H. *J. Chem. Phys.* **1994**, *100* (10), 7535–7542. <https://doi.org/10.1063/1.466847>.
- (103) Dolg, M.; Cao, X. *Chem. Rev.* **2012**, *112* (1), 403–480. <https://doi.org/10.1021/cr2001383>.
- (104) Roos, B. O.; Taylor, P. R.; Sigbahn, P. E. M. *Chem. Phys.* **1980**, *48* (2), 157–173. [https://doi.org/10.1016/0301-0104\(80\)80045-0](https://doi.org/10.1016/0301-0104(80)80045-0).
- (105) Andersson, K.; Malmqvist, P. A.; Roos, B. O.; Sadlej, A. J.; Wolinski, K. *J. Phys. Chem.* **1990**, *94* (14), 5483–5488. <https://doi.org/10.1021/j100377a012>.
- (106) Dolg, M.; Fulde, P. *Chem. – A Eur. J.* **1998**, *4* (2), 200–204. [https://doi.org/10.1002/\(SICI\)1521-3765\(19980210\)4:2<200::AID-CHEM200>3.0.CO;2-X](https://doi.org/10.1002/(SICI)1521-3765(19980210)4:2<200::AID-CHEM200>3.0.CO;2-X).
- (107) Kerridge, A.; Coates, R.; Kaltsoyannis, N. *J. Phys. Chem. A* **2009**, *113* (12), 2896–2905. <https://doi.org/10.1021/jp807804w>.
- (108) Bader, R. F. W. *Atoms in Molecules: A Quantum Theory*, Clarendon Press, Oxford, UK, **1994**. <https://global.oup.com/academic/product/atoms-in-molecules-9780198558651?cc=fr&lang=en&>
- (109) Kerridge, A. *Dalt. Trans.* **2013**, *42* (46), 16428–16436. <https://doi.org/10.1039/C3DT52279B>.
- (110) Mooßen, O.; Dolg, M. *Chem. Phys. Lett.* **2014**, *594*, 47–50. <https://doi.org/10.1016/j.cplett.2014.01.022>.
- (111) Schultz, M.; Boncella, J. M.; Berg, D. J.; Tilley, T. D.; Andersen, R. A. *Organometallics* **2002**, *21* (3), 460–472. <https://doi.org/10.1021/om010661k>.
- (112) Walter, M. D.; Schultz, M.; Andersen, R. A. *New J. Chem.* **2006**, *30* (2), 238–246. <https://doi.org/10.1039/B512865J>.
- (113) Walter, M. D.; Berg, D. J.; Andersen, R. A. *Organometallics* **2006**, *25* (13), 3228–3237. <https://doi.org/10.1021/om051051d>.
- (114) Walter, M. D.; Berg, D. J.; Andersen, R. A. *Organometallics* **2007**, *26* (9), 2296–2307. <https://doi.org/10.1021/om0610142>.
- (115) Nocton, G.; Booth, C. H.; Maron, L.; Andersen, R. A. *Organometallics* **2013**, *32* (19), 5305–5312. <https://doi.org/10.1021/om400528d>.
- (116) Nocton, G.; Booth, C. H.; Maron, L.; Andersen, R. A. *Organometallics* **2013**, *32* (5), 1150–1158. <https://doi.org/10.1021/om300876b>.
- (117) Nocton, G.; Booth, C. H.; Maron, L.; Ricard, L.; Andersen, R. A. *Organometallics* **2014**, *33* (23), 6819–6829. <https://doi.org/10.1021/om500843z>.
- (118) Nocton, G.; Lukens, W. W.; Booth, C. H.; Rozenel, S. S.; Medling, S. A.; Maron, L.; Andersen, R. A. *J. Am. Chem. Soc.* **2014**, *136* (24), 8626–8641. <https://doi.org/10.1021/ja502271q>.

- (119) Finke, R. G.; Keenan, S. R.; Watson, P. L. *Organometallics* **1989**, *8* (2), 263–277. <https://doi.org/10.1021/om00104a001>.
- (120) Van Vleck, J. H. *The Theory of Electric and Magnetic Susceptibilities*, Clarendon Press, Oxford, UK, **1965**.
- (121) O'Connor, C. J. *Magnetochemistry—Advances in Theory and Experimentation*, Wiley, New York, NY, USA, **1982**, pp 203–283. <https://doi.org/10.1002/9780470166307.ch4>.
- (122) Lukens, W. W.; Magnani, N.; Booth, C. H. *Inorg. Chem.* **2012**, *51* (19), 10105–10110. <https://doi.org/10.1021/ic300037q>.
- (123) Booth, C. H.; Walter, M. D.; Kazhdan, D.; Hu, Y.-J.; Lukens, W. W.; Bauer, E. D.; Maron, L.; Eisenstein, O.; Andersen, R. A. *J. Am. Chem. Soc.* **2009**, *131* (18), 6480–6491. <https://doi.org/10.1021/ja809624w>.
- (124) Krishnan, C. V.; Creutz, C.; Schwarz, H. A.; Sutin, N. *J. Am. Chem. Soc.* **1983**, *105* (17), 5617–5623. <https://doi.org/10.1021/ja00355a015>.
- (125) Ferreira, H.; Conradie, M. M.; von Eschwege, K. G.; Conradie, J. *Polyhedron* **2017**, *122*, 147–154. <https://doi.org/10.1016/j.poly.2016.11.018>.
- (126) Carmona, E. *Organometallics* **2019**, *38* (23), 4523–4532. <https://doi.org/10.1021/acs.organomet.9b00756>.
- (127) Goudy, V.; Jaoul, A.; Cordier, M.; Clavaguéra, C.; Nocton, G. *J. Am. Chem. Soc.* **2017**, *139* (31), 10633–10636. <https://doi.org/10.1021/jacs.7b05634>.
- (128) Byers, P. K.; Canty, A. J.; Skelton, B. W.; White, A. H. *J. Chem. Soc. Chem. Commun.* **1986**, No. 23, 1722–1724. <https://doi.org/10.1039/C39860001722>.
- (129) Canty, A. J.; Watson, A. A.; Skelton, B. W.; White, A. H. *J. Organomet. Chem.* **1989**, *367* (3), C25–C28. [https://doi.org/10.1016/0022-328X\(89\)87065-2](https://doi.org/10.1016/0022-328X(89)87065-2).
- (130) Wang, D.; Moutet, J.; Tricoire, M.; Cordier, M.; Nocton, G. *Inorganics* **2019**, *7* (5), 58. <https://doi.org/10.3390/inorganics7050058>.
- (131) Wang, D.; Tricoire, M.; Cemortan, V.; Moutet, J.; Nocton, G. *Inorg. Chem. Front.* **2021**, *8* (3), 647–657. <https://doi.org/10.1039/D0QI00952K>.
- (132) Boyce, S. A. J.; Moutet, J.; Niederegger, L.; Simler, T.; Nocton, G.; Hess, C. R. *Inorg. Chem.* **2021**, *60* (1), 403–411. <https://doi.org/10.1021/acs.inorgchem.0c03058>.
- (133) Banerjee, P.; Company, A.; Weyhermüller, T.; Bill, E.; Hess, C. R. *Inorg. Chem.* **2009**, *48* (7), 2944–2955. <https://doi.org/10.1021/ic8020172>.
- (134) Grübel, M.; Bosque, I.; Altmann, P. J.; Bach, T.; Hess, C. R. *Chem. Sci.* **2018**, *9* (13), 3313–3317. <https://doi.org/10.1039/C7SC05320G>.
- (135) Tricoire, M.; Mahieu, N.; Simler, T.; Nocton, G. *Chem. – A Eur. J.* **2021**, *27* (23), 6860–6879. <https://doi.org/10.1002/chem.202004735>.
- (136) Tricoire, M.; Münzfeld, L.; Moutet, J.; Mahieu, N.; La Droite, L.; Moreno-Pineda, E.; Gendron, F.; Hilgar, J. D.; Rinehart, J. D.; Ruben, M.; Le Guennic, B.; Cador, O.; Roesky, P. W.; Nocton, G. *Chem. – A Eur. J.* **2021**, *27* (54), 13558–13567. <https://doi.org/10.1002/chem.202101599>.



# Chapter II

## New trivalent organolanthanide precursors supported by large aromatic ligands

### I. Background on sandwich complexes

#### I.A. Pioneer works with the cyclopentadienyl ligand

The first report of the synthesis of a metallocene compound dates from 1951 with Pauson and Kealy's synthesis of ferrocene by the mean of a cyclopentadienyl (Cp) Grignard reagent.<sup>1</sup> The overall linear geometry was proposed with two independent works from Fischer and Wilkinson which resulted in them being awarded the Nobel prize in 1973.<sup>2-4</sup> In the few following years, the completed XRD analysis of the complex confirmed their findings.<sup>5,6</sup> This gave birth to the now well-known "molecular sandwich" term for such architecture. The remarkable symmetry and geometry of this complex led the scientific community to explore further this sort of species. From the study of physical properties of such compounds to their use in terms of reactivity, they are now widely used across all the periodic table for various applications.<sup>7,8</sup> Yet Cp-based ligands being small L<sub>2</sub>X ligands, they tend to form bent architectures when used outside of the d-block, with the bigger lanthanide ions for example.<sup>9-16</sup> In this precise case, the first step toward perfectly axial architectures involved very bulky Cp ligands: C<sub>5</sub>H<sub>2</sub>(*t*Bu)<sub>3</sub> (Cp<sup>ttt</sup>), C<sub>5</sub>(*i*Pr)<sub>5</sub> (Cp<sup>*i*Pr5</sup>) and C<sub>5</sub>(Ph)<sub>5</sub> (Cp<sup>BIG</sup>) to sterically prevent adduct formation and intermolecular interactions that favor bent structures (Figure I.1).<sup>17-21</sup>

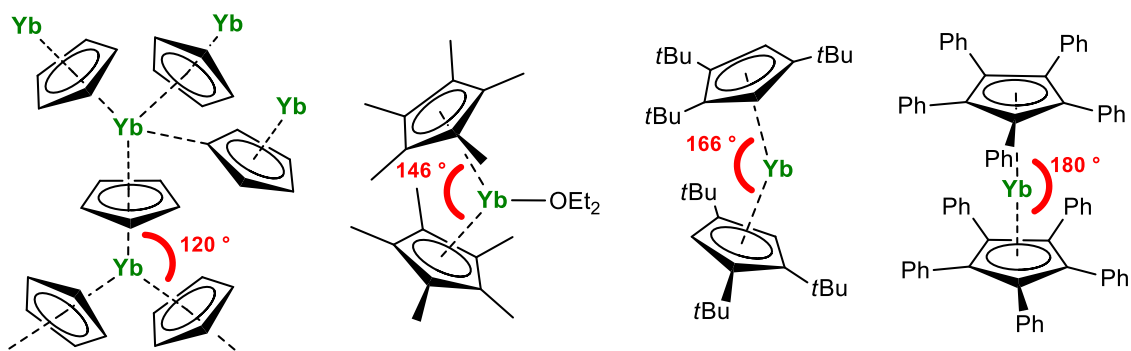


**Figure I.1.** Trend in bent CpYb structures from  $[\text{Cp}_2\text{Yb}]_n$  to  $(\text{Cp}^{\text{BIG}})_2\text{Yb}$ .

## I.B. Toward bigger ligands: cyclooctatetraenyl and arene derivatives

In the series of carbon-based Hückel aromatic ligands, the use of larger aromatic rings was thought as another solution to control the steric environment of the f-elements. This idea was developed by Streitwieser in the late 60s with the isolation of the neutral uranocene ( $\text{U}(\text{Cot})_2$ ) thanks to the dianionic cyclooctatetraenyl (Cot) ligand.<sup>22,23</sup> This architecture was extended to lanthanide ions a decade later with the isolation of cerocene ( $\text{Ce}(\text{Cot})_2$ ) (Figure I.2).<sup>24</sup> The Cot ligand, however, is not perfectly suited for the stabilization of the most common +II and +III oxidation states of lanthanide ions. Indeed, the formation of anionic species with alkali counter cations leads, upon crystallization, to packing interactions that can induce a bending of the linear geometry.<sup>25–27</sup> This does not however prevent such axial or near-axial architectures to be actively studied for their magnetic properties, as it will be explained later in this chapter.<sup>28–32</sup>

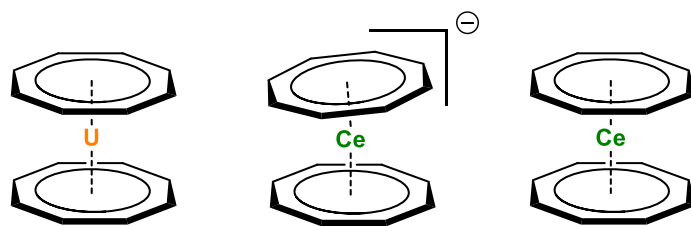


**Figure I.2.** First linear sandwich complexes involving the Cot ligand, uranocene and cerocene. The anionic cerocene precursor  $\text{K}^+[(\text{Cot})_2\text{Ce}]^-$  is bent.

Outside of the  $\text{Cot}^{2-}$  ligand, benzene derivatives were also known since the 50's to form bis-arene complexes with transition metals.<sup>33–35</sup> On first thoughts, neutral arenes should not fit properly with the standard +II and +III lanthanide oxidation states. However, the group of Cloke managed to isolate the remarkable series of  $\text{Ln}(\text{tBu}_3\text{C}_6\text{H}_3)_2$  complexes at the 0 oxidation state with  $\text{Ln} = \text{La}, \text{Pr}, \text{Nd}, \text{Sm}, \text{Gd}, \text{Tb}, \text{Dy}, \text{Ho}, \text{Er}, \text{and Lu}$ .<sup>36–38</sup> On top of extending the possible strategies to achieve linear sandwich architectures, these studies remain nowadays the only examples of isolated “zero-valent” molecular complexes of lanthanide ions.

## I.C. The cyclononatetraenyl ligand

Since the strategy using Hückel aromatic ligands was proven efficient toward the synthesis of linear sandwich architecture, the next larger monoanionic aromatic ring, the cyclononatetraenyl (Cnt) ligand was a promising choice in order to form neutral divalent “lanthanidocenes”. The ligand synthesis was described in the 1960’s by Katz and Garratt<sup>39,40</sup> and depending on the reaction conditions the alkali salt  $[M^+Cnt^-]$  can be formed as mixture of *cis,cis,cis,trans*-Cnt<sup>-</sup> (*trans*-Cnt) and *cis,cis,cis,cis*-Cnt<sup>-</sup> (*cis*-Cnt), the latter being thermodynamically more stable.<sup>41</sup> This isomerization process was already investigated and rationalized by Boche *et al.* in 1978 (Figure I.3).<sup>42–44</sup>

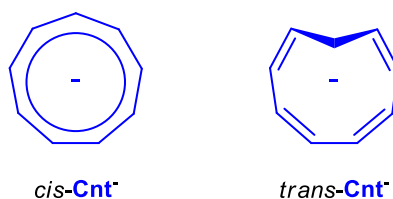


**Figure I.3.** The two isomers *cis*-Cnt<sup>-</sup> and *trans*-Cnt<sup>-</sup>.

To the exception of a study with titanium species<sup>45</sup> it’s only decades later that the Cnt ligand was used in coordination chemistry by the group of Sitzmann who characterized the promising  $\eta^9$ -coordinated  $Ba(\eta^9-Cnt)_2$  complex<sup>46</sup> while another report was made a bit after with a tetranuclear  $[Pd_4(\eta^4-Cnt)(\eta^4-Cot)]^-$  species characterized (Figure I.4.left).<sup>47</sup> This is not surprising considering the Cnt<sup>-</sup> ligand is likely to reorganize itself as the more stable indenyl ligand when protonated or when not meeting suitable coordination environment (Figure I.4.right).<sup>48,49</sup>

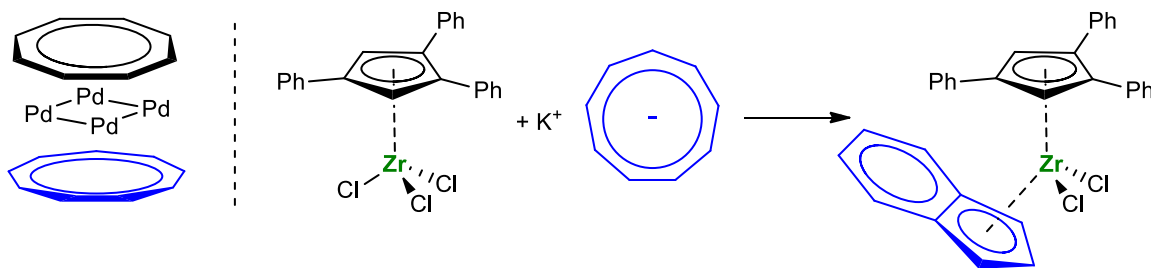


**Figure I.4.** Examples from previous works with the Cnt<sup>-</sup> ligand.

In 2017, while the group was already investigating the use of this promising ligand with lanthanide ions, Nakajima *et al.* reported the difficult synthesis of  $Eu(\eta^9-Cnt)_2$  (4 % yield) and how its geometry impacted the luminescence properties of europium.<sup>50</sup> A year after, the series was completed by members of the group with the isolation of the other classical divalent lanthanide analog compounds  $Yb(\eta^9-Cnt)_2$ ,  $Sm(\eta^9-Cnt)_2$ , with the addition of  $Tm(\eta^9-Cnt)_2$  (Figure I.5).<sup>51</sup> In this study, the importance of isolating the ligand salt with the *trans*-Cnt as the major isomer as well as the fine control of the isomerization of the latter was shown to be key to reach higher yields for the perfectly



*cis*-Cnt complexes. The surprising stability of these new Yb and Sm species in dichloromethane compared to other divalent lanthanide precursors<sup>52,53</sup> was also a proof that the Cnt ligand was highly impacting the reactivity of such species. It was therefore needed to study other lanthanide systems involving the Cnt ligand to get better insights on its potential as a contender for Cp based ligands in the design of future organometallic species considering the large number of fields where lanthanide ions are of high interest.

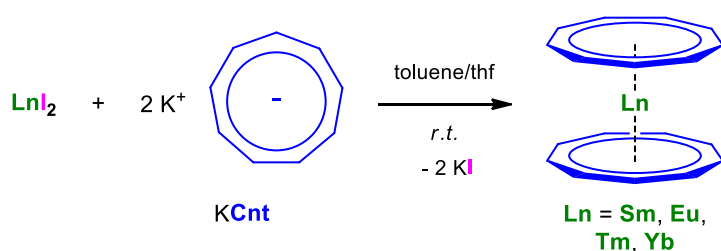


**Figure I.5.** Synthesis of the divalent lanthanidocenes series.

## II. Synthesis and characterization of (Cot)Ln(Cnt) heteroleptic complexes

In order to adapt these findings to fit the more common trivalent oxidation state of lanthanide ions, the idea to combine the large Cot and Cnt ligands to access to heteroleptic linear complexes was the next logical step since heteroleptic Cot-Cp systems had already shown promising properties.<sup>28</sup> Unfortunately, Münzfeld *et al.* published the synthesis of such ( $\eta^8$ -Cot)Ln( $\eta^9$ -Cnt) complexes, with Ln = Nd, Sm, Dy and Er, while we were performing the characterization of these highly sought species.<sup>54</sup> The magnetic study of the erbium compound revealed that it is a nicely performing single ion magnet (SIM) with a blocking temperature  $T_B = 10$  K on par with other Cot-Er systems.<sup>29,31,55,56</sup> Yet, in this study, the coordination mode of the Cnt ligand was not trivial to attribute because of a crystallographic disorder for the late lanthanide ions. While there was strong evidence of an  $\eta^9$ -Cnt coordination mode for the early neodymium and samarium ions, the conclusion remained uncertain for dysprosium and erbium. A collaborative work was therefore started between our two groups and led to the results presented hereafter.

### II.A. Synthesis of the (Cot)LnX(thf)<sub>n</sub> precursors

For the late lanthanide ions, the choice was made to use the protocol proposed by Hilgar *et al.*<sup>56</sup> instead of the elegant procedure published for early 4f-elements Ln = La, Ce, Pr, Nd and Sm by Mashima and co-workers.<sup>57</sup> After an overnight metathesis reaction between the LnI<sub>3</sub> and K<sub>2</sub>Cot salts in thf, crystalline product was isolated after proper removal of the KI salt formed and this protocol

allowed the synthesis of the desired “piano stool” (Cot)LnI(thf)<sub>2</sub> precursors for Ln = Tb, Dy, Ho, Er and Tm (Figure II.1).

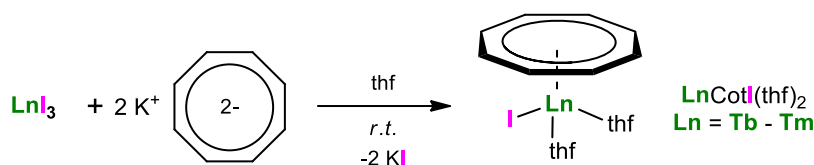


**Figure II.1.** Synthesis of the (Cot)LnI(thf)<sub>n</sub> precursors.

For Lu, the same procedure was not successful starting from LuCl<sub>3</sub> so it was decided to first get a borohydride salt instead of a halogenated one to increase its solubility and thus its reactivity with the K<sub>2</sub>Cot salt. Using the procedure reported for Nd,<sup>58,59</sup> [Lu(BH<sub>4</sub>)<sub>3</sub>(thf)<sub>3</sub>] was synthesized by salt metathesis and reaction in thf with K<sub>2</sub>Cot led to the formation of a dimeric [Lu(Cot)(BH<sub>4</sub>)(thf)]<sub>2</sub> precursor after recrystallisation in toluene (Figure II.2). It is important to note that the purity of the [Lu(BH<sub>4</sub>)<sub>3</sub>(thf)<sub>3</sub>] salt is of paramount importance to get this dimer. When chloride ions were still partially present, the isolated product was (Cot)Ln(BH<sub>4</sub>)<sub>1-x</sub>(Cl)<sub>x</sub>(thf)<sub>2</sub>, a precursor from which the yields obtained at the next step were lowered, most likely because of a worse solubility.

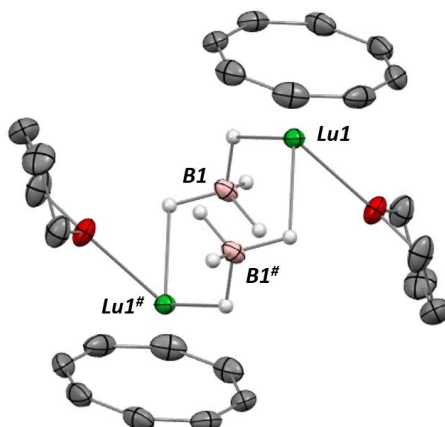


**Figure II.2.** ORTEP of [Lu(Cot)(BH<sub>4</sub>)(THF)]<sub>2</sub>. Thermal ellipsoids are depicted at 50 % probability level. Carbon atoms are in grey, boron atoms in pink, oxygen atoms in red, and lutetium atoms in light green. Hydrogen atoms except on the boron atoms have been removed for clarity.

To finish the series of those late trivalent precursors, Yb is still missing. Several protocols were tried but almost all of them led to divalent Yb species due to the reductive potential of the Cot<sup>2-</sup> ligand. Even when Mashima's protocol was used with Yb, it yielded a bright pink solid insoluble in most common organic solvents to the exception of pyridine in which it can be recrystallized as (Cot)Yb(py)<sub>3</sub>.<sup>60</sup> Oxidation trials in pyridine to form trivalent (Cot)YbX species with silver salts remained unsuccessful. It only led to the isolation of YbI<sub>2</sub>(py)<sub>4</sub> salt when AgI was used. One remaining option to get such trivalent Yb precursors would consist in using a similar method that the one used by the groups of Roesky or Eldemann who isolated heteroleptic (Cot)Yb<sup>3+</sup> complexes by

using bulky amidinate or bis(phosphinimino)methanide ligands.<sup>61–63</sup> The question yet remains about whether or not these complexes would be reactive toward a salt metathesis with the KCnt salt.

## II.B. Synthesis and characterization of (Cot)Ln(Cnt) heteroleptic sandwich complexes

### ▪ Synthesis of the title compounds

In order to achieve high yields and rapid isolation of the aimed complexes, a variation of the protocol developed for the divalent bis-Cnt complexes was used.<sup>51</sup> Salt metathesis reactions between the (Cot)LnX(thf)<sub>n</sub> precursors and KCnt salt were performed in a toluene-acetonitrile mixture for Ln = Tb (**1**), Dy (**2**), Ho (**3**), Er (**4**) and Tm (**5**) (Figure II.3). The main difference to the aforementioned bis-Cnt protocol is that both *cis*-Cnt and *trans*-Cnt isomers could be used and were dissolved in acetonitrile to form a solution that is added to the suspension of the (Cot)Ln precursors in toluene. The use of acetonitrile allowed a faster isomerization of the *trans*-Cnt isomer to its *cis* form ensuring the completion of the reaction in 12 h. For the synthesis of (Cot)Lu(Cnt) (**6**), the most efficient protocol was found by putting to reflux for 16 h a suspension of both reactants in toluene probably because the coordination of the Cnt ligand is less likely to happen with such smaller ion (Figure II.3<sup>a</sup>). The most important step in order to get clean base free (Cot)Ln(Cnt) was the removal of all the volatiles under reduced pressure including the coordinating solvents (acetonitrile for **1-5**, thf for **6**). Crystalline products were then isolated in good yields by several extractions with large amount of toluene, filtration, concentration and cooling of the resulting solution at -40 °C overnight. A smooth color evolution was observed along the series from pale yellow **1** to salmon-orange **5** while **6** is pale yellow. Solution and solid-state analyses of the species were performed to investigate the coordination mode of the Cnt and are discussed in the following sections of this chapter.

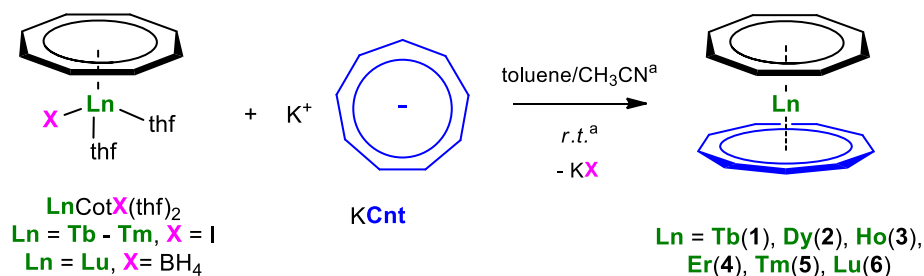


**Figure II.3.** Synthesis of the (Cot)Ln(Cnt) complexes **1-6**.

<sup>a</sup> No acetonitrile used in the case of **6** and temperature was risen to 115 °C.

### ▪ Solution state characterization

Room temperature  $^1\text{H}$  NMR characterization of complexes **1-5** were performed even though they are highly paramagnetic. For all compounds, two similar broad signals were observed which is coherent with average  $\eta^8\text{-Cot}$  and  $\eta^9\text{-Cnt}$  coordination modes in solution. The attribution of the signals to the Cot or the Cnt ligand was possible for **1-3** by integrating the broad peaks, the Cot signals were found at 245.9, 118.7 and 90.5 ppm respectively, while the Cnt signals appeared at 101.5, 72.9 and 59.2 ppm respectively. For **4** and **5**, the broadness of the signals did not allow any attribution of the -5.01, -128.7 ppm and -23.2, -235.8 ppm respective pairs of peaks. One shall note that lanthanide ions in **1-3** have oblate, axially elongated, electronic density while it is prolate, equatorially elongated, for **4-5**, and that these intrinsic properties impact greatly their magnetic properties as it will be explained later in this chapter.<sup>64</sup> This influence was nicely illustrated by the chemical shifts' signs being positive for the oblate ions and negative for the prolate ones. The study of the diamagnetic Lu compound (**6**) did not offer more answers regarding hapticity switching in solution. The room temperature signals at 5.83 (Cot) and 6.54 ppm (Cnt) were not showing any fluctuation between +80 and -80 °C. This absence of coalescence indicated that, if there was a structural change in solution across the series, the energy barrier of such rearrangement was too low to be observed within this temperature range.<sup>65</sup>

For the terbium complex, an intriguing behavior was observed upon evolution of the NMR solution at room temperature. After several days, a new set of 6 signals appeared, at 404.0, 230.1, 203.6, 196.2, 165.1 and -169.5 ppm, indicating a thermodynamic evolution from **1** to another species **1'**. Even though the signals are highly paramagnetic, the estimated 2:8:2:2:1:2 ratio observed for the integrations of this new set of signals was concurring with the isomerization of a *cis*-Cnt moiety to its *trans*-Cnt form while the Cot ligand remained a singlet since this reorganization did not impact the symmetry of the compound (Figure II.4). The *cis:trans* ratio was estimated to be 66:34 after 3 days, 60:40 after 20 days and did not evolve further at increased timings. This isomerization of the Cnt ligand was confirmed when crystals of **1'** were isolated as red blocks different from the pale-yellow needles of **1** with an estimated *cis:trans* ratio of 79:21 in **1'**.

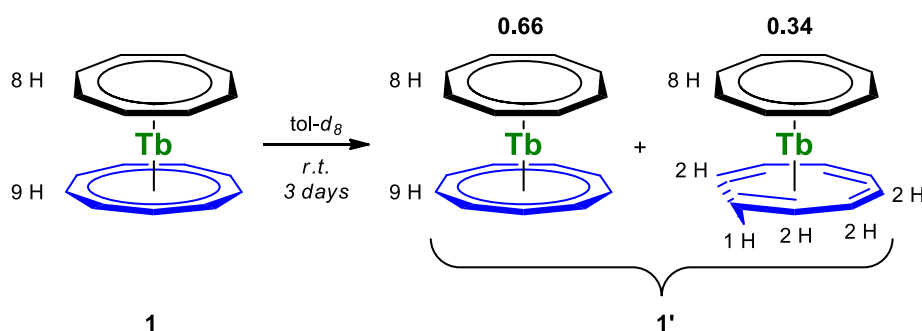


**Figure II.4.** Isomerization of **1** in **1'** in  $\text{tol-}d_8$  and its impact on NMR signals.

This phenomenon was found rather surprising considering Boche's previous works on the isomerization of different alkali salts of the  $\text{Cnt}^-$  anion in different conditions.<sup>42–44</sup> All results pointed toward a thermodynamically more stable *cis*-Cnt form with  $\Delta G^\ddagger$  values ranging between 29.6 and 34.8 kcal mol<sup>-1</sup>. The fact that upon coordination of a Tb cation, a supposedly contra-thermodynamic isomerization could be triggered was counter intuitive and is currently under study in the group to see if thermodynamic barriers can be determined and if this transformation is reproducible with the larger early lanthanide ions. The understanding and the control of this phenomenon could be the key to access different reactivities thanks to the different solubility and electronic structures of the two isomers.

#### ▪ X-ray diffraction analysis

From the crystal structure study, the first note is that **1** and **2-6** were not isomorphous. The terbium complex crystallized in the *Pnma* space group while the five others unit cells corresponded to the *P2<sub>1</sub>/n* space group. This resulted in the lanthanide ions being close to an inversion center with an 0.5 occupancy for compounds **2-6**. The rest of the asymmetric unit was composed of the two disordered carbon rings embedded with an occupancy of 0.5 as well. Before addressing the disorder, careful modeling of the carbon aromatic rings needed to be performed in order to separate them without too many restraints. To respect the aromaticity of the ligand, a soft SADI restraint (equidistance between named atoms) was applied to all the C-C bond distances of the C<sub>8</sub> or the C<sub>9</sub> rings respectively. This ensured reasonable positional freedom throughout the refinement cycles while preventing scrambling of the carbon atoms between the two ligands. Although aromaticity is often associated to planarity, this case perfectly exemplified that such assumption should always be carefully considered when solving a structure. When used, the FLAT instruction that forces the coplanarity of the selected atoms, induced a significant increase of the refinement's indicators and have to be removed to respect the experimental dataset. With all these considerations in mind, a first statement could be made, the Cot ligand appeared to be planar while the Cnt presented a bent conformation (Figure II.5.a). Moreover, this fact combined with the lanthanide ion not being centered with both ligands suggested that one of them was adopting a lower coordination mode than the expected  $\eta^8$  and  $\eta^9$  hapticity. To properly address this issue, a second asymmetric unit was constructed thanks to the inversion center (Figure II.5.b). By removing the disorder on the ligands (Figure II.5.c), two crystallographically correct solutions were then accessible depending on which symmetrically equivalent Ln ion was removed (Figure II.5.d-e). On the first one, the bent Cnt ligand had a lower hapticity, while it was the opposite for the second one. Lowering the space group symmetry to *PI* did not solve the problem. The asymmetric unit only got more crowded by the addition of 3 other disordered moiety with an 0.5 occupancy since *Z'* (the number of molecules in the asymmetric unit)

was increased from 0.5 to 2. The question was then simple: which of the two solutions was the correct one from a chemical point of view?

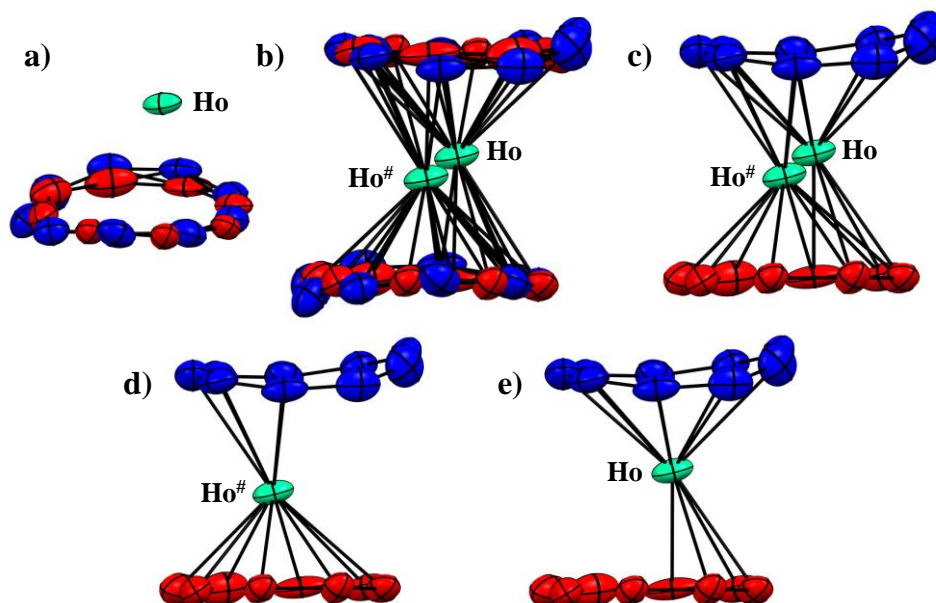


**Figure II.5.** Step by step crystallographic resolution of the structure of **5**. Cot ligand in red, Cnt ligand in blue and Ho in green.

The fact that the Cnt ligand in the first solution showed a deviation from a standard planar geometry expected for aromatic ligands was a first hint pointing toward this solution instead of the other. The Ln-Ctr distance (Ctr for centroid) was another one since it is supposed to be lower for the dianionic  $\text{Cot}^{2-}$  moiety than the monoanionic  $\text{Cnt}^-$  fragment. The holmium case shown above illustrated well this point: in the first solution the distances were  $\text{Ho-Ctr}_{\text{Cot}} = 1.735 \text{ \AA}$  and  $\text{Ho-Ctr}_{\text{Cnt}} = 2.222 \text{ \AA}$  while they were  $\text{Ho-Ctr}_{\text{Cot}} = 2.153 \text{ \AA}$  and  $\text{Ho-Ctr}_{\text{Cnt}} = 1.775 \text{ \AA}$  for the second one. Another hint came from obtaining a lowered hapticity for the Cnt in a sample of **2**, which was not perfectly dried upon crystallization in DCM. The compound was characterized by XRD as **2(MeCN)**, in which the asymmetric unit was composed of one disordered molecule of **2** and a non-disordered acetonitrile adduct of the same complex (Figure II.6).

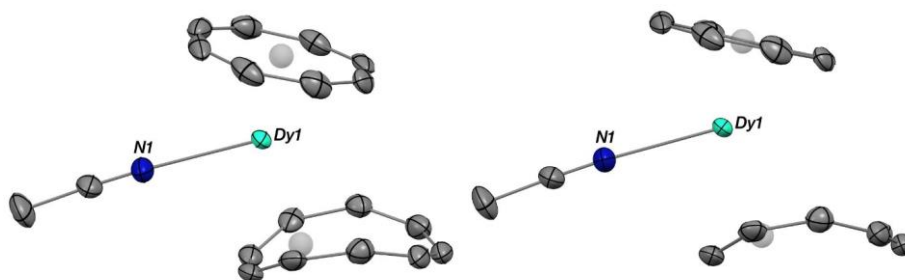


**Figure II.6.** ORTEP of **2(MeCN)** at 150 K, two orientations of the molecule. Thermal ellipsoids are depicted at 50 % probability level. Carbon atoms are in grey, the nitrogen atom in blue, and the dysprosium atom in light green. Only the adduct part of the asymmetric unit is shown, co-crystallized DCM and hydrogen atoms have been removed for clarity.

With this accumulation of pieces of evidence, the second solution was definitely discarded. In the case of compound **1**, the *Pnma* space group completely changed the analysis. The terbium ion was now included in a symmetry plane that contained the centroids of both rings. The ligands were cut into two symmetrical and planar parts, resulting in a more planar Cnt ligand. This change of symmetry was attributed to the increased hapticity of the Cnt ligand thanks to the larger ionic radii of earlier lanthanide ions which are therefore more suited to fit to an  $\eta^9$ -coordination mode.

**Table II.1.** Main metric parameters for **1–6** at 150 K:

	<b>Tb (1, <math>\eta^9</math>)</b>	<b>Dy (2, <math>\eta^8</math>)</b>	<b>Ho (3, <math>\eta^6</math>)</b>	<b>Er (4, <math>\eta^6</math>)</b>	<b>Tm (5, <math>\eta^6</math>)</b>	<b>Lu (6, <math>\eta^6</math>)</b>
Ln-C(Cnt)	2.775(7)	2.68(2)	2.56(2)	2.55(3)	2.54(3)	2.50(2)
	2.775(7)	2.72(2)	2.61(2)	2.59(3)	2.57(2)	2.54(2)
	2.79(1)	2.74(2)	2.62(2)	2.61(3)	2.64(2)	2.6(2)
	2.82(3)	2.74(2)	2.72(2)	2.69(3)	2.73(2)	2.68(2)
	2.83(1)	2.79(2)	2.82(2)	2.88(3)	2.875(13)	2.943(12)
	2.84(2)	2.86(2)	3.02(3)	3.10(2)	3.11(2)	3.14(2)
	2.85(3)	2.86(2)	3.212(14)	3.443(13)	3.449(9)	3.59(10)
	2.85(1)	2.95(2)	3.37(2)	3.60(2)	3.594(12)	3.719(13)
	2.86(2)	2.96(2)	3.47(2)	3.76 (2)	3.769(8)	3.930(9)
$\eta(\text{Ln-C(Cnt)}_{\text{max}} - \text{LnC(Cnt)}_{\text{min}})$	0.094	0.284	0.906	1.213	1.228	1.426
Ln-C( $\eta$ -Cnt) <sup>a</sup> ave	2.82(3)	2.79(9)	2.73(17)	2.74(21)	2.74(21)	2.73(26)
C( $\eta$ -Cnt)-Ln-C( $\eta$ -Cnt) <sup>a</sup>	<b>177.4</b>	<b>172.0</b>	<b>169.6</b>	<b>174.7</b>	<b>173.8</b>	<b>174.2</b>
Ln-C(Cnt) ave	<b>2.82(3)</b>	<b>2.81(10)</b>	<b>2.93(33)</b>	<b>3.02(44)</b>	<b>3.03(44)</b>	<b>3.07(55)</b>
Ln-C(Cot) range	2.57(3)- 2.63(2)	2.52(2)- 2.64(2)	2.46(2)- 2.65(2)	2.45(2)- 2.55(3)	2.43(3)- 2.54(3)	2.44(2)- 2.50(2)
Ln-C(Cot) ave	<b>2.58(2)</b>	<b>2.58(4)</b>	<b>2.55(7)</b>	<b>2.50(4)</b>	<b>2.48(3)</b>	<b>2.46(1)</b>
Ln-C( $\eta$ -all) <sup>a</sup> ave	<b>2.71</b>	<b>2.69</b>	<b>2.63</b>	<b>2.60</b>	<b>2.59</b>	<b>2.58</b>

<sup>a</sup> Only the carbon atoms formally  $\eta$ -coordinated (see below discussions) were considered in the average calculation.

To get a closer look at this proposed hapticity switching observed for the Cnt ligand several metric parameters were studied (Table II.1). First, the Ln-C<sub>Cot</sub> distances showed that for the C<sub>8</sub> ligand each carbon atoms were within the same range of distance from their respective lanthanide: 2.57(3)-2.63(2) Å in **1**, 2.52(2)-2.64(2) Å in **2**, 2.46(2)-2.65(2) Å in **3**, 2.45(2)-2.55(3) Å in **4**, 2.43(3)-2.54(3) Å in **5** and 2.44(2)-2.50(2) Å in **6**. The Ln-C<sub>Cot</sub> average distances evolving from 2.58(2) Å for **1** to 2.46(1) Å for **6** was considered as a consequence of the lanthanide ionic radii contraction across the series.<sup>66</sup> The situation was rather different with the Ln-C<sub>Cnt</sub> distances. They ranged between 2.775(7) and 2.86(2) in **1**, 2.68(2)-2.96(2) Å in **2**, 2.56(2)-3.47(2) Å in **3**, 2.55(3)-3.76(2) Å in **4**, 2.54(3)-3.769(8) Å in **5** and 2.50(2)-3.930(9) Å in **6**. This resulted in their average value evolving from 2.82(3) Å for **1** to 3.07(6) in **6** which was contradictory considering the lanthanide contraction and therefore numerically demonstrating that the  $\eta^9$ -coordination mode was not respected across the series. To get



a hand on formal coordination numbers and quantify the hapticity evolution in the series, several geometrically constructed parameters were studied, from measurements performed at both 150 K and 300 K. First, two mean planes were constructed out of the six closest carbon atoms of the Cnt ligand on one hand and the three furthest carbon atoms of the Cnt ligand on the other hand (Figure II.7). By analyzing the angle measured between those two planes, the deviation from planarity was quantified from 4.80 ° in **1** to 34.2 ° in **6** at 150 K (3.2 ° in **1** to 25.3 ° in **6** at 300 K). This clearly illustrated how the Cnt ligand bent as the ionic radius of the lanthanide ion decreased and the temperature's impact on the metrics remained scarce. To conclude on this matter a 5 K measurement on **1** was performed and did not show any sign of symmetry break thus invalidating a hypothetical temperature-induced phase transition from the orthorhombic cell to the monoclinic one.

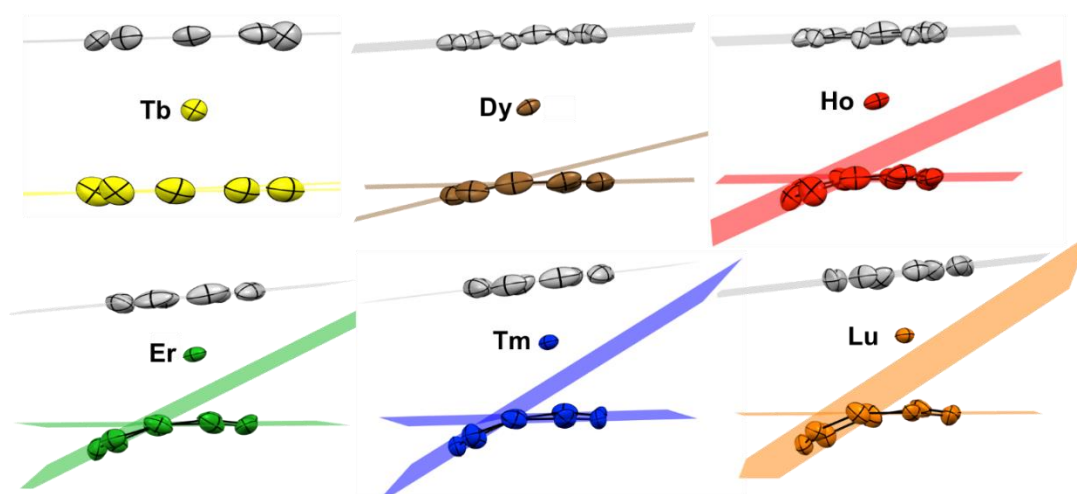


**Figure II.7.** Mean planes constructed in **1–6** to illustrate Cnt ligand's bending. The grey plane is constructed with the eight carbon atoms of the Cot ligand.

In order to propose formal coordination modes for these six compounds another set of constructed metric parameters were studied by considering the Cot centroid and three different centroids for the Cnt ligand, one with the six closest, a second with the eight closest and the last with all nine carbon atoms of the C<sub>9</sub> ligand (Ctr6, Ctr8 and Ctr9 respectively). As shown in Table II.2 and as expected from the results of Table II.1 the Ln-Cot<sub>Ctr</sub> are 1.804 Å in **1**, 1.772 Å in **2**, 1.735 Å in **3**, 1.701 Å in **4**, 1.681 Å in **5** and 1.653 Å in **6** which was coherent regarding the lanthanide contraction trend. Note that to the exception of **1** this Ln-Cot<sub>Ctr</sub> distances were slightly shorter yet close to the one obtained within the (Cot)LnX(thf)<sub>n</sub> series (X = I or BH<sub>4</sub>): 1.81 Å (Tb), 1.80 Å (Dy), 1.78 Å (Ho), 1.76 Å (Er), 1.75 Å (Tm) and 1.724 Å (Lu). On the Ln-Cnt<sub>Ctr</sub> side, at 150 K, the Ctr6 was the closest for **3–6** while Ctr8 and Ctr9 were the closest for **2** and **1** respectively. Moreover, the same centroids were highlighted by considering the highest Cot<sub>Ctr</sub>-Ln-Cnt<sub>Ctr</sub> angles. This rather straightforward and conclusive metric analysis of the centroids allowed the attribution of the formal η<sup>6</sup>-coordination mode for **3–6**, η<sup>8</sup>-coordination mode for **2** and η<sup>9</sup>-coordination mode for **1** at 150 K (Figure II.8). Thanks to



this definition it was noticed that, by considering the average Ln-C distance only with formally  $\eta$ -coordinated carbon atoms, the lanthanide contraction was respected (Table II.1).

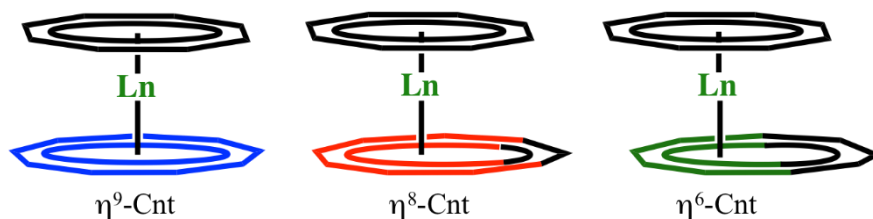


**Figure II.8.** Representation of the three formal coordination modes of the Cnt ligand.

It is also important to note that this conclusion was only slightly different when the sum of the van der Waals radii was considered. Carbon atoms were considered  $\eta$ -coordinated if their Ln-C distance was lower than the sum van der Waals radii which ranged from 1.80 to 1.72 Å from Tb to Lu while the radius of an aromatic C atom was 1.70 Å. This resulted in maximum distances for  $\eta$ -coordinated carbon atoms to be between 3.42 Å for **6** to 3.47 Å for **1**, leading to **4-6** being  $\eta^6$ , **3**  $\eta^8$  and **1-2**  $\eta^9$ .

**Table II.2.** Centroid metric parameters for **1-6** at 150 and 300 K:  
The smallest distances and highest angles for each complex are given in bold red.

	Tb (1) <sup>a</sup>	Dy (2)	Ho (3)	Er (4)	Tm (5)	Lu (6)
Plane angles	4.80	12.5	23.7	29.7	31.3	34.2
Ln-Ctr(6-C/Cnt)	2.130	2.082	<b>2.054</b>	<b>2.065</b>	<b>2.070</b>	<b>2.066</b>
Ln-Ctr(8-C/Cnt)	1.979	<b>1.997</b>	2.102	2.193	2.197	2.239
Ln-Ctr(9-C/Cnt)	<b>1.970</b>	2.016	2.184	2.309	2.314	2.375
Ln-Cot(Ctr)	1.804	1.772	1.735	1.701	1.681	1.653
Ln-Cot-(6-C/Cnt)	157.5	161.0	<b>169.6</b>	<b>174.7</b>	<b>173.8</b>	<b>174.2</b>
Ln-Cot-(8-C/Cnt)	173.6	<b>172.0</b>	166.7	163.1	163.5	161.3
Ln-Cot-(9-C/Cnt)	<b>177.4</b>	170.5	161.4	157.6	158.1	156.0
Ln-Ln <sup>#</sup>	0	0.248	0.635	0.912	0.896	1.095
	1, 300 K	2, 300 K	3, 300 K	4, 300 K	5, 300 K	6, 300 K
Plane angles	3.2	14.8	15.0	17.7	19.8	25.3
Ln-Ctr(6-C/Cnt)	2.142	2.158	2.137	<b>2.105</b>	<b>2.121</b>	<b>2.135</b>
Ln-Ctr(8-C/Cnt)	1.985	<b>2.072</b>	<b>2.117</b>	2.182	2.203	2.278
Ln-Ctr(9-C/Cnt)	<b>1.967</b>	2.092	2.167	2.269	2.293	2.398
Ln-Cot(Ctr)	1.802	1.778	1.705	1.687	1.667	1.627
Ln-Cot-(6-C/Cnt)	154.3	160.3	165.0	<b>174.0</b>	<b>168.6</b>	<b>171.9</b>
Ln-Cot-(8-C/Cnt)	170.2	<b>170.2</b>	<b>173.3</b>	167.0	163.2	161.9
Ln-Cot-(9-C/Cnt)	<b>177.4</b>	169.4	169.2	161.3	158.5	156.8
Ln-Ln <sup>#</sup>	0	0.366	0.602	0.882	0.876	1.137

<sup>a</sup> The Tb parameters are the average distances and angles between the two disordered parts.

To conclude this structural study, it is important to keep in mind that these proposed formal coordination modes can vary depending on the limiting criteria chosen. These limit forms were not observed in the solution state yet, their solid-state properties might be tuned by this original behavior of the Cnt ligand.

### III. The magnetic interest of the (Cot)Ln(Cnt) architecture

#### III.A. Brief introduction on single molecule magnets

- *From cluster chemistry to lanthanide single ion magnets*

The report of a “Magnetic bistability in a metal-ion cluster” by Sessoli and coworkers in 1993 opened the door of the molecular world for magnets.<sup>67</sup> The now-famous Mn<sub>12</sub> cluster was the first example of a molecule showing hysteresis opening upon magnetization thus retaining magnetic information for a certain amount of time even though the external field has been removed. Although this phenomenon was only observed below 5 K, this led to the still ongoing quest to make this behavior accessible at higher temperatures with relaxation times long enough to actually build molecular-based data storage devices.<sup>68</sup> To achieve that, the strategy consists in making the energy barrier for the spin state reversal ( $U_{\text{eff}}$ ) the highest possible, this not only slows down the relaxation process but also increases the blocking temperature under which the phenomenon can be observed.<sup>69</sup> For transition metals, this barrier can be approximated to be proportional to both the square of the total spin value  $S$  and the axial magnetic anisotropy  $D$  of the system (Equation 1).

$$U = |D|S^2, S = \text{integer}, U = |D|\left(S^2 - \frac{1}{4}\right), S = \text{non - integer} \quad (1)$$

Therefore, a good single molecule magnet (SMM) must have high enough values to generate a decent barrier that can induce a slow relaxation process, which is well illustrated by a double well diagram (Figure III.1). Historically, following the report of the  $S = 10$  Mn<sub>12</sub> cluster, maximizing the spin was the predominant paradigm.<sup>70</sup> But this did not always lead to interesting SMMs because it was often realized at the cost of the magnetic anisotropy.<sup>71</sup>

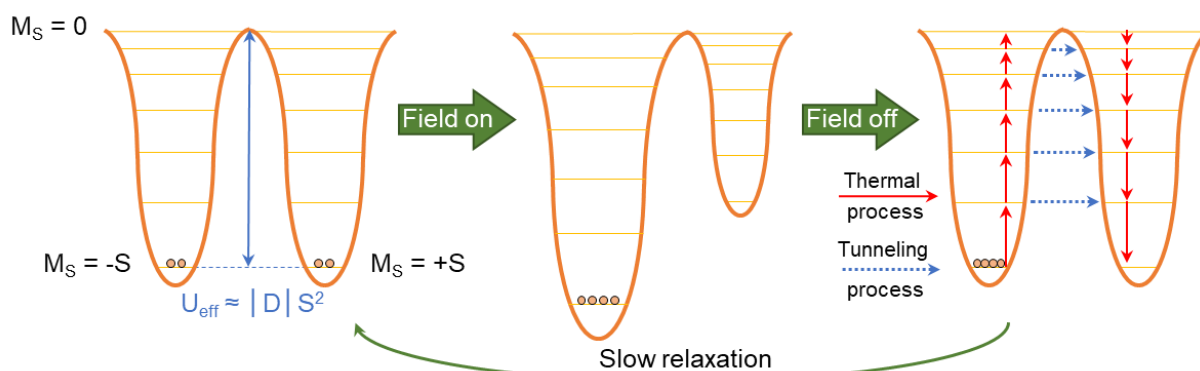


**Figure III.1.** Double well diagram illustrating the magnetization and magnetic relaxation processes of SMMs (adapted from ref<sup>72</sup>).

This paradigm started to shift toward maximizing the axial magnetic anisotropy due to the findings of Ishikawa *et al.* in 2003.<sup>73</sup> They reported the magnetic study of sandwich complexes composed of two dianionic phthalocyanine ligands (Pc) and a trivalent lanthanide ion ( $[\text{Ln}(\text{Pc})_2]^+[\text{NBu}_4]^-$ ). The Tb and Dy versions of the compound were revealed to behave as SMMs thus becoming the first-ever observed single-ion magnets (SIMs). Parallel investigations to renew and change the focus toward maximizing the anisotropy and not the spin state reinforced this discovery.<sup>72,74–76</sup> Since lanthanide ions are naturally presenting high spin and high single-ion anisotropy thanks to their unquenched orbital angular momentum<sup>66</sup> they were considered to represent the best candidates one can think of to design future SMMs respecting this new paradigm.

#### ▪ Rationalization of the design of lanthanide-based single molecule magnets

The key concepts for the design of performant lanthanide single-molecule magnets were summarized by Rinehart and Long in 2011.<sup>64</sup> When considering the electronic states involved in the slow relaxation process, crystal field splitting in f-elements has to be considered as a perturbation of the strong spin-orbit coupling splitting. Hence, the crystal field splitting creates the last level of degeneracy before the Zeeman effect and therefore rules the properties of the relaxation process.

Since the interaction between the free ion and the crystal field is what impacts the most the resulting  $m_J$  states, a simple electrostatic model was proposed to get a straightforward visualization of the best-suited crystal field, for each lanthanide ion, in order to maximize its anisotropy. From the shape of electronic clouds of  $4f^n$  systems ( $n = 1-14$  from Ce to Lu, in their trivalent states), three categories of lanthanide ions arise: the oblate ones (mostly equatorial charge distribution), the isotropic ones (spherical cloud) and the prolate ones (axial charge distribution) (Figure III.2).

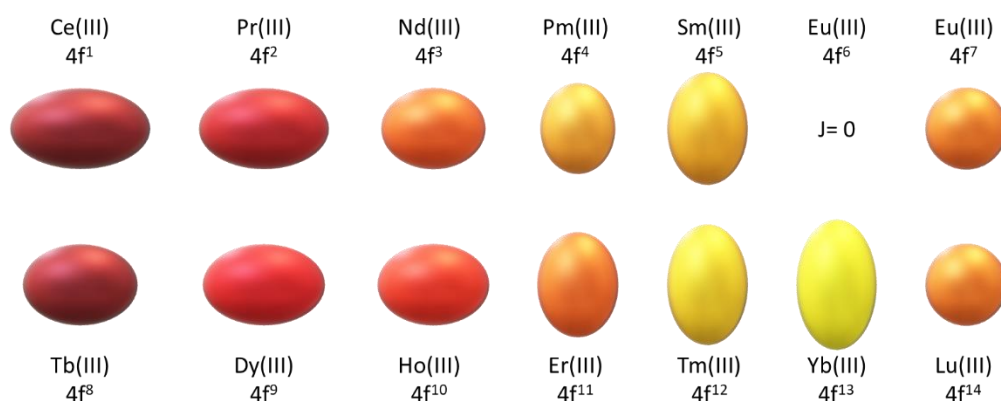


**Figure III.2.** Approximated electronic distribution across the trivalent lanthanide series (adapted from ref<sup>64</sup>).

Hence, to maximize the magnetic properties of such ions, the crystal field should enhance these charge distributions by avoiding repulsive interactions that would hamper their anisotropy. This leads to a simple statement: axial crystal fields are preferred for oblate ions and equatorial crystal fields are best-fitting prolate ions, a concept that was later reinforced by rigorous theoretical studies (Figure III.3.A-B).<sup>77,78</sup> Thanks to these findings the oblate  $\text{Dy}^{3+}$  cation tackled record-breaking blocking temperature one after another with bulky  $\text{Cp}^{\text{III}}$  ligands in a first example.<sup>79</sup> More recently the groundbreaking report of the heteroleptic  $[(\text{Cp}^{\text{IPr5}})\text{Dy}(\text{Cp}^*)]^+$  cation finally broke the liquid nitrogen barrier with  $T_B = 80$  K, thus reinforcing the hopes for data storage applications.<sup>80</sup>

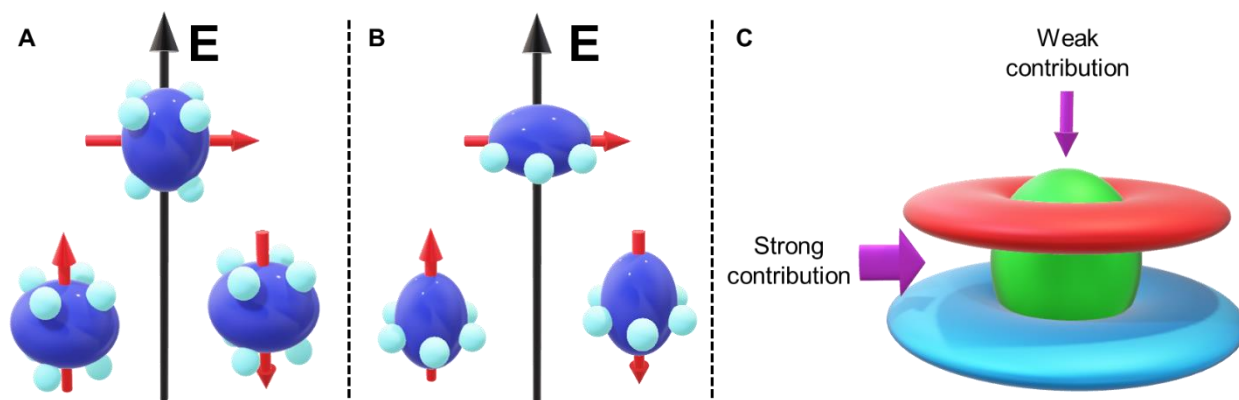


**Figure III.3.** Best fitting crystal fields for either an oblate ion (A) or a prolate one (B), lowest energy states are achieved by applying axial (A) or equatorial (B) restraints. (adapted from ref<sup>64</sup>). Illustration of the electrostatic influence of large aromatic ligands on a prolate ion (C).

Interestingly, sandwiches architectures are also of great interest for prolate ions since large aromatic ligands are mostly equatorially contributing to the crystal field thanks to their  $\pi$  electronic cloud (Figure III.3.C). Noteworthy examples were reported using the Cot ligand and the  $\text{Er}^{3+}$ ,  $\text{Tm}^{3+}$  ions.<sup>28–31,55,56</sup> This strategy was even extended to  $\text{Tm}^{2+}$  (isoelectronic to the prolate  $\text{Yb}^{3+}$ )<sup>32</sup> making it the second divalent lanthanide SIM after the remarkable  $(\text{Cp}^{\text{IPr5}})_2\text{Tb}$  complex.<sup>81</sup>

### III.B. Magnetic properties and theoretical studies across the (Cot)Ln(Cnt) series of complexes

As reported in the paper published by Münzfeld *et al.* the erbium compound **4**,<sup>54</sup> which was the most promising of the series, is behaving as a single molecule magnet below  $T_B = 10$  K thanks to its  $m_J = \pm 15/2$  states being stabilized by the equatorial crystal field. The spin reversal energy barrier was measured to be  $U_{\text{eff}} = 251(1) \text{ cm}^{-1}$ , yet no coercive field was observed. This was attributed to the efficiency of the quantum tunneling of the magnetization (QTM), which is not rare in 4f-elements systems.<sup>82</sup> Those results were confronted to complete active space self-consistent field (CASSCF) calculations realized with a DFT optimized structure, in which the Cnt ligand is considered  $\eta^9$ -coordinated. Although the hapticity was proven to be lower in the solid-state study presented earlier, these *ab initio* results reproduced quite well the experimental results with the first and second excited states  $m_J = \pm 13/2$  and  $\pm 1/2$  being 140 and 268  $\text{cm}^{-1}$  above the ground state. An Arrhenius analysis was then performed and led to consider a relaxation pathway dominated by an Orbach process<sup>83</sup> followed by a QTM through the  $m_J = \pm 1/2$  states (Figure III.4). These calculated values were therefore in reasonable agreement with the experimentally measured value of the barrier. Noteworthy, the fact that Raman spectroscopy allowed to measure the antisymmetric vibration of the C<sub>8</sub>/C<sub>9</sub> rings at a similar energy (240  $\text{cm}^{-1}$ ) was making echo to the very recent works of the Chilton group who investigated the influence of vibrational modes' resonance on the Orbach relaxation process.<sup>84</sup>

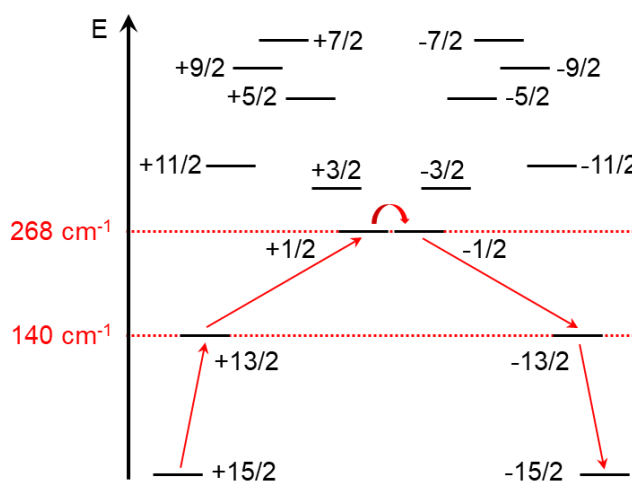


**Figure III.4.** Most probable magnetic relaxation pathway for **4** as *ab initio* computed in ref<sup>54</sup>.

The magnetic investigations were performed on the rest of the series **1-3** and **5** and are depicted in Figure III.5. The measured  $\chi T$  values at room temperature fell in the expected range of the Curie constants for each ion's ground state:  $^7F_6$  (Tb(III), **1**, 11.82  $\text{cm}^3 \text{ K mol}^{-1}$ ,  $g_J = 3/2$ ),  $^6H_{15/2}$  (Dy(III), **2**, 14.17  $\text{cm}^3 \text{ K mol}^{-1}$ ,  $g_J = 4/3$ ),  $^5I_8$  (Ho(III), **3**, 14.07  $\text{cm}^3 \text{ K mol}^{-1}$ ,  $g_J = 5/4$ ) and  $^3H_6$  (Tm(III), **5**, 7.15

$\text{cm}^3 \text{ K mol}^{-1}$ ,  $g_J = 7/6$ ). No other slow relaxation process than the one detected with the Erbium complex, **4**, was found.

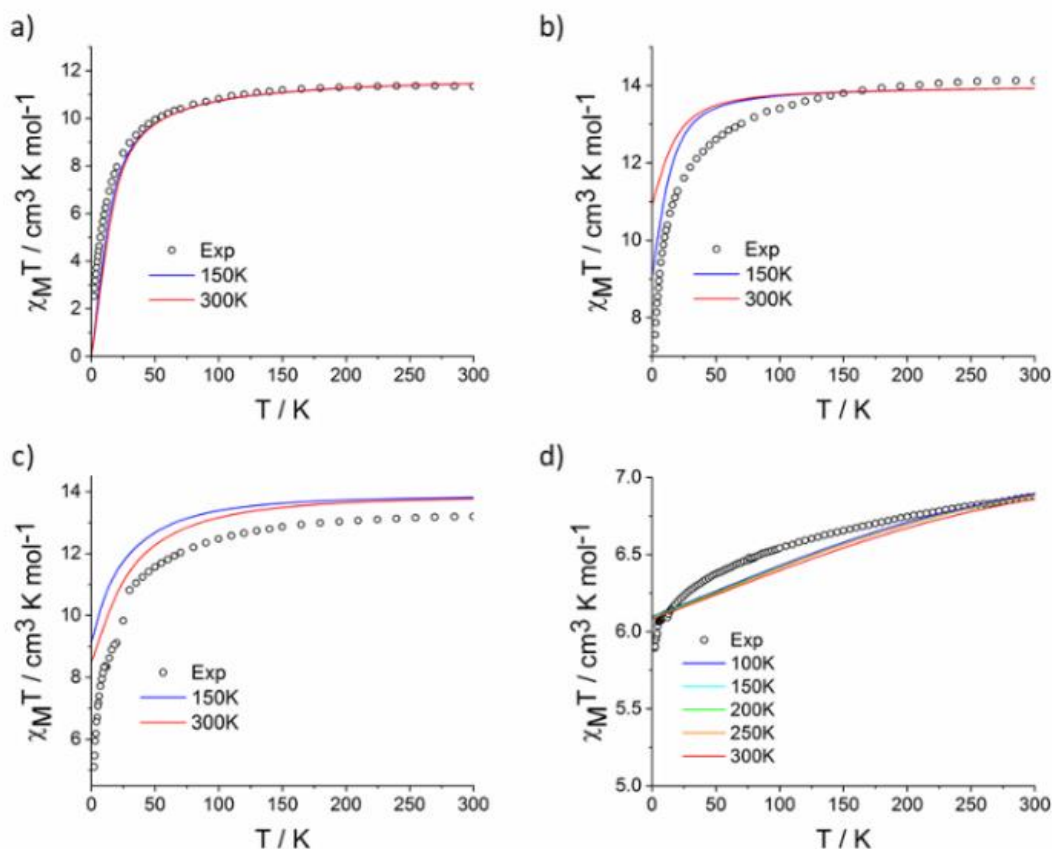


**Figure III.5.** Temperature dependent  $\chi T$  values for compound **1** (a), **2** (b), **3** (c) and **5** (d) in dots with the calculated curves from the different structures obtained at various temperature in colored lines.

With the disorder freed XRD structures at several temperatures, new theoretical studies were performed to get a better evaluation of the modulated hapticity's impact on the magnetic properties, especially for the prolate ions in **4** and **5**. In the case of **1-3**, the results illustrated well why they were not SMMs. The ground states calculated for **1** was pure  $m_J = \pm 0$  with low lying  $m_J = \pm 1$  states ( $27$  and  $61 \text{ cm}^{-1}$ ) and the total splitting of the  $2J+1$  states on  $873 \text{ cm}^{-1}$  gave satisfactory modeling of the experimental  $\chi T$  values. **2** and **3** had mixed ground states with main components:  $m_J = \pm 15/2$  (68 %) and  $m_J = \pm 11/2$  (13 %) for **2** and  $m_J = \pm 8$  (65 %) and  $m_J = \pm 6$  (14 %) for **3**. The first excited states for **2** and **3** were also low lying, 6 states were accessible within a  $109 \text{ cm}^{-1}$  range for **2** and 5 degenerated states were found within  $136 \text{ cm}^{-1}$  for **3**. The differences observed between 150 K and 300 K models of the temperature-dependent susceptibility was easily explained by the variation of the ratios of the mixed ground states because of the geometry evolution. Yet the curves were reasonably comparable to experimental values. It was likely that the mixing of the ground states combined with low-lying excited states was the reason for having no retention of the magnetization. The anisotropy axes represented in Figure III.6 are good evidence that the electrostatic prediction was indeed verified.



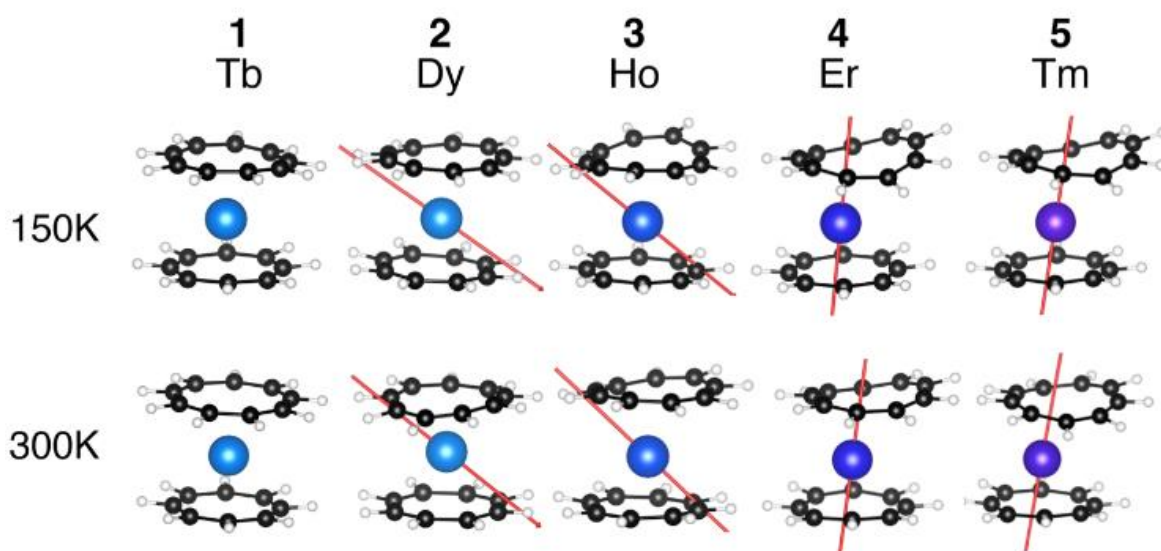


**Figure III.6.** Computed structures of **1-5** at 150 and 300 K and ground-state anisotropy axis (not represented for Tb due to planar anisotropy).

With **4**, even though the DFT optimized  $\eta^9$ -coordinated Cnt geometry gave satisfactory results, the lower hapticity present in the XRD structure induced mixing in between excited  $m_J$  states. While the ground state remained pure  $m_J = \pm 15/2$ , the first excited state was 98 %  $m_J = \pm 13/2$  and the second excited states a combination of 68 %  $m_J = \pm 1/2$  and 20 %  $m_J = \pm 3/2$ . The energy gaps were 170 and 251  $\text{cm}^{-1}$  respectively, which was in excellent agreement with the measured value considering the thermally induced QTM through the second excited state process proposed earlier. Compared to the  $\eta^9$ -coordinated Cnt geometry of **4** in which the anisotropy axis was perfectly orthogonal to both carbon rings, the  $\eta^6$  hapticity found in XRD induced a bending of this axis. This correction being considered, the anisotropy axis was slightly impacted and crossed the ligands in the position of the centroids  $\text{Cot}_{\text{ctr}}$  and  $\text{Ctr6}$  used earlier for the XRD metric study (Figure III.6). With **5**, the computation indicated a pure  $m_J = \pm 6$  ground state, which is concurring with the  $\chi T$  value at low temperature. The first excited state was also pure,  $m_J = \pm 5$ , 431  $\text{cm}^{-1}$  above the ground state, yet this was not coherent with the experimental data. From 2 K to 50 K, the shape of the curve indicated that low excited states are gradually populated which should not be the case with an electronic gap of this extent.

In conclusion, these computational studies demonstrated that the promising prolate ions were not too much influenced by the mixing of excited states arising from the hapticity switching across the series. However, they brought a smooth improvement of the model which was important to understand properly the versatility of the Cnt ligand as well as its impact on the lanthanide properties.

## IV. Conclusion and perspectives

The synthesis and characterization of new precursors of trivalent late lanthanide ions (to the exception of Yb) supported by the dianionic Cot and the monoanionic Cnt ligands resulted in unveiling original fluxional behaviors of the latter. The Tb complex **1** was perfectly linear with  $\eta^8$  and  $\eta^9$  hapticities for the Cot and the Cnt ligands respectively. Nevertheless, a “contra-thermodynamic” partial isomerization of the C<sub>9</sub> ligand was observed in both solution and solid-state leading to a *trans*-Cnt ligand being only  $\eta^8$ -coordinated. Another type of hapticity switch was found in the **2-6** series of compounds. The careful resolution of the highly disordered XRD structures demonstrated that either the Cot or the Cnt was in a lower coordination mode than the expected  $\eta^9$  (Figure IV.1).

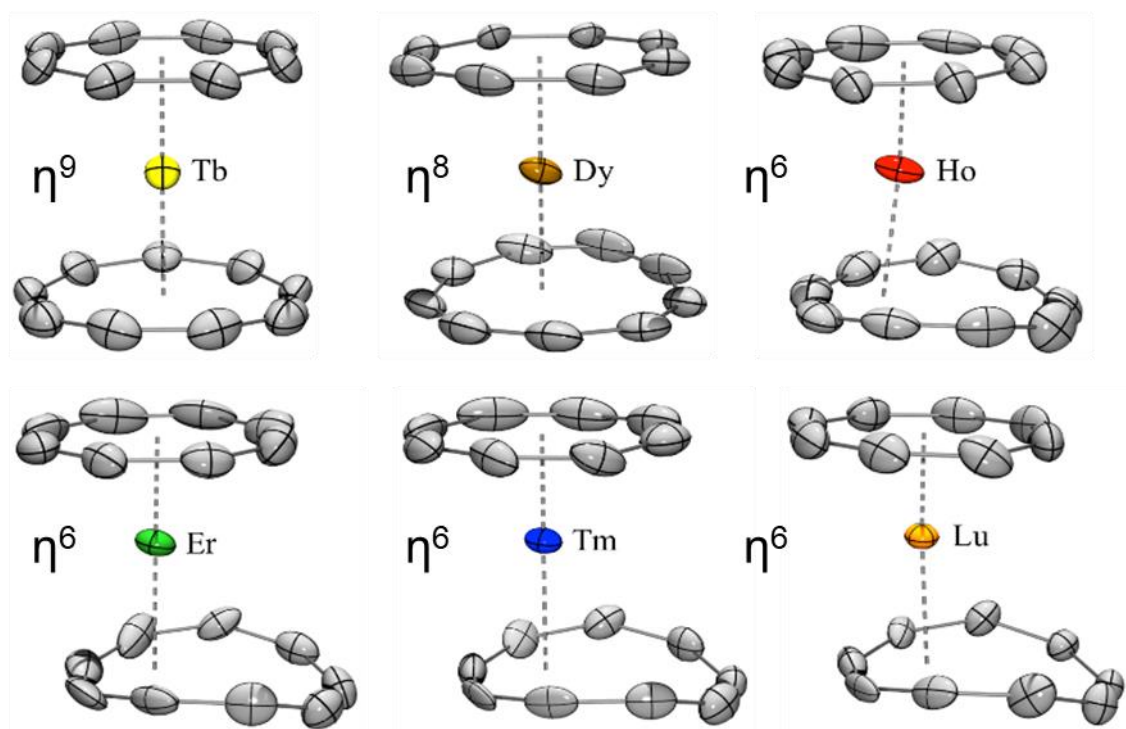


**Figure IV.1.** ORTEPs of **1-6** at 150 K. Thermal ellipsoids are depicted at 50 % probability level. Carbon atoms are in grey, and lanthanides are in several colors, as labelled. Hydrogen atoms have been removed for clarity.

A bond metric study and the isolation of the adduct **2(MeCN)** pointed toward the more flexible C<sub>9</sub> ring being more and more distorted across the series concurring with the lanthanide contraction. These compounds being of great interest for their potential SMM behavior, their magnetic properties were probed and it resulted in the prolate Er and Tm complexes being the best-fitting lanthanides in this crystal field, as expected considering the electrostatic model and the theoretical investigations. Yet, only the Er version presented slow magnetic relaxation properties as it was previously reported.<sup>54</sup> This study should help upcoming works on the versatile Cnt ligand since the fluxional behaviors



presented in this work will surely be great tools to tune the physical properties of future lanthanide complexes supported by this ligand.

As it was already done with the  $(\text{Cnt})_2\text{Ln}$  complexes,<sup>85</sup> reactions with the classic 2,2'-bipyridine (bipy) ligand were performed to probe if further coordination chemistry was possible with those compounds. Although the resulting species was found highly insoluble. An XRD acquisition was achieved after crystals were finally isolated by slow diffusion of a bipy solution in a  $(\text{Cot})\text{Sm}(\text{Cnt})$  solution yielding the expected adduct **(Cot)Sm(bipy)( $\eta^5$ -Cnt)** (Figure IV.2).

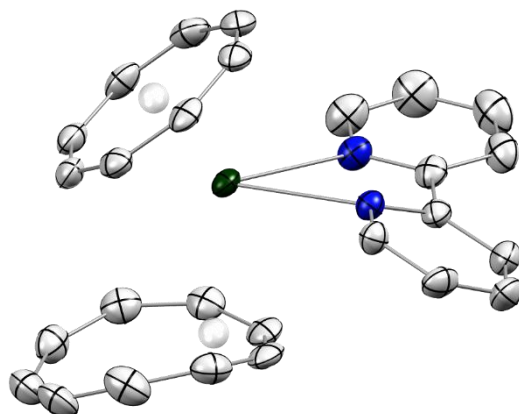


**Figure IV.2.** ORTEP of **(Cot)Sm(Cnt)(bipy)** at 150 K. Thermal ellipsoids are depicted at 50 % probability level. Carbon atoms are in grey, nitrogen atoms in blue, and the samarium atom in dark green. Hydrogen atoms have been removed for clarity.

The low solubility of both divalent  $(\text{Cnt})_2\text{Ln}$  and trivalent  $(\text{Cot})\text{Ln}(\text{Cnt})$  precursors is currently preventing further coordination studies to compare the Cnt ligand to the widely used  $\text{Cp}^*$  ligand. One of the keys to overcome this issue might reside in trying to add substituents on the Cnt ligand in order to increase its solubility and get on par with substituted Cp ligands. With such objective in mind, it should be reminded that the few substituted Cnt ligands reported to date are extremely temperature-sensitive in their protonated form, making their synthesis and further use in coordination chemistry really challenging.<sup>48</sup> Lastly, a more ambitious synthetic strategy could imply engaging substituted Cot ligands<sup>86,87</sup> in Katz and Garratt's procedure. Indeed, after having witnessed the versatility of this  $\text{C}_9$  ring, who would not dream of getting his hands on its permethylated  $\text{Cnt}^*$  version?

## References

- (1) Kealy, T. J.; Pauson, P. L. *Nature* **1951**, *168* (4285), 1039–1040. <https://doi.org/10.1038/1681039b0>.
- (2) Wilkinson, G.; Rosenblum, M.; Whiting, M. C.; Woodward, R. B. *J. Am. Chem. Soc.* **1952**, *74* (8), 2125–2126. <https://doi.org/10.1021/ja01128a527>.
- (3) Fischer, E. O.; Pfab, W. *Zeitschrift für Naturforsch. B* **1952**, *7* (7), 377–379. <https://doi.org/doi:10.1515/zn-1952-0701>.
- (4) The Nobel Prize in Chemistry **1973**. <https://www.nobelprize.org/prizes/chemistry/1973/summary/>.
- (5) Dunitz, J. D.; Orgel, L. E. *Nature* **1953**, *171* (4342), 121–122. <https://doi.org/10.1038/171121a0>.
- (6) Dunitz, J. D.; Orgel, L. E.; Rich, A. *Acta Crystallogr.* **1956**, *9* (4), 373–375. <https://doi.org/10.1107/S0365110X56001091>.
- (7) Togni, A.; Halterman, R. L. *Metallocenes: Synthesis Reactivity Applications* Wiley, Weinheim, Germany, **1998**, p 832. <https://doi.org/10.1002/9783527619542>.
- (8) Chirik, P. J. *Organometallics* **2010**, *29* (7), 1500–1517. <https://doi.org/10.1021/om100016p>.
- (9) Wilkinson, G.; Birmingham, J. M. *J. Am. Chem. Soc.* **1954**, *76* (23), 6210. <https://doi.org/10.1021/ja01652a114>.
- (10) Birmingham, J. M.; Wilkinson, G. *J. Am. Chem. Soc.* **1956**, *78* (1), 42–44. <https://doi.org/10.1021/ja01582a009>.
- (11) Fischer, E. O.; Fischer, H. *J. Organomet. Chem.* **1965**, *3* (3), 181–187. [https://doi.org/10.1016/S0022-328X\(00\)87500-2](https://doi.org/10.1016/S0022-328X(00)87500-2).
- (12) Apostolidis, C.; Deacon, G. B.; Dornberger, E.; Edelmann, F. T.; Kanellakopulos, B.; MacKinnon, P.; Stalke, D. *Chem. Commun.* **1997**, No. 11, 1047–1048. <https://doi.org/10.1039/A700531H>.
- (13) Eggers, S. H.; Kopf, J.; Fischer, R. D. *Acta Crystallogr. Sect. C* **1987**, *43* (12), 2288–2290. <https://doi.org/10.1107/S0108270187088036>.
- (14) Deacon, G. B.; Mackinnon, P. I.; Hambley, T. W.; Taylor, J. C. *J. Organomet. Chem.* **1983**, *259* (1), 91–97. [https://doi.org/10.1016/0022-328X\(83\)85160-2](https://doi.org/10.1016/0022-328X(83)85160-2).
- (15) Tilley, T. D.; Andersen, R. A.; Spencer, B.; Ruben, H.; Zalkin, A.; Templeton, D. H. *Inorg. Chem.* **1980**, *19* (10), 2999–3003. <https://doi.org/10.1021/ic50212a031>.
- (16) Evans, W. J.; Hughes, L. A.; Hanusa, T. P. *Organometallics* **1986**, *5* (7), 1285–1291. <https://doi.org/10.1021/om00138a001>.
- (17) Sitzmann, H.; Dezember, T.; Schmitt, O.; Weber, F.; Wolmershäuser, G.; Ruck, M. *Zeitschrift für Anorg. und Allg. Chemie* **2000**, *626* (11), 2241–2244. [https://doi.org/10.1002/1521-3749\(200011\)626:11<2241::AID-ZAAC2241>3.0.CO;2-0](https://doi.org/10.1002/1521-3749(200011)626:11<2241::AID-ZAAC2241>3.0.CO;2-0).
- (18) Weber, F.; Schultz, M.; Sofield, C. D.; Andersen, R. A. *Organometallics* **2002**, *21* (15), 3139–3146. <https://doi.org/10.1021/om0108705>.
- (19) Jaroschik, F.; Nief, F.; Ricard, L. *Chem. Commun.* **2006**, No. 4, 426–428. <https://doi.org/10.1039/B514818A>.
- (20) Deacon, G. B.; Forsyth, C. M.; Jaroschik, F.; Junk, P. C.; Kay, D. L.; Maschmeyer, T.; Masters, A. F.; Wang, J.; Field, L. D. *Organometallics* **2008**, *27* (18), 4772–4778. <https://doi.org/10.1021/om800501z>.
- (21) Kelly, R. P.; Bell, T. D. M.; Cox, R. P.; Daniels, D. P.; Deacon, G. B.; Jaroschik, F.; Junk, P. C.; Le Goff, X. F.; Lemerrier, G.; Martinez, A.; Wang, J.; Werner, D. *Organometallics* **2015**, *34* (23), 5624–5636. <https://doi.org/10.1021/acs.organomet.5b00842>.
- (22) Streitwieser, A.; Mueller-Westerhoff, U. *J. Am. Chem. Soc.* **1968**, *90* (26), 7364–7364. <https://doi.org/10.1021/ja01028a044>.
- (23) Zalkin, A.; Raymond, K. N. *J. Am. Chem. Soc.* **1969**, *91* (20), 5667–5668. <https://doi.org/10.1021/ja01048a055>.
- (24) Greco, A.; Cesca, S.; Bertolini, W. *J. Organomet. Chem.* **1976**, *113* (4), 321–330. [https://doi.org/10.1016/S0022-328X\(00\)96143-6](https://doi.org/10.1016/S0022-328X(00)96143-6).

- (25) Hodgson, K. O.; Raymond, K. N. *Inorg. Chem.* **1972**, *11* (12), 3030–3035. <https://doi.org/10.1021/ic50118a031>.
- (26) Kinsley, S. A.; Streitwieser, A.; Zalkin, A. *Organometallics* **1985**, *4* (1), 52–57. <https://doi.org/10.1021/om00120a010>.
- (27) Boussie, T. R.; Eisenberg, D. C.; Rigsbee, J.; Streitwieser, A.; Zalkin, A. *Organometallics* **1991**, *10* (6), 1922–1928. <https://doi.org/10.1021/om00052a044>.
- (28) Jiang, S.-D.; Wang, B.-W.; Sun, H.-L.; Wang, Z.-M.; Gao, S. *J. Am. Chem. Soc.* **2011**, *133* (13), 4730–4733. <https://doi.org/10.1021/ja200198v>.
- (29) Le Roy, J. J.; Korobkov, I.; Murugesu, M. *Chem. Commun.* **2014**, *50* (13), 1602–1604. <https://doi.org/10.1039/C3CC48557A>.
- (30) Harriman, K. L. M.; Korobkov, I.; Murugesu, M. *Organometallics* **2017**, *36* (23), 4515–4518. <https://doi.org/10.1021/acs.organomet.7b00449>.
- (31) Hilgar, J. D.; Bernbeck, M. G.; Rinehart, J. D. *J. Am. Chem. Soc.* **2019**, *141* (5), 1913–1917. <https://doi.org/10.1021/jacs.8b13514>.
- (32) Moutet, J.; Schleinitz, J.; La Droite, L.; Tricoire, M.; Pointillart, F.; Gendron, F.; Simler, T.; Clavaguéra, C.; Le Guennic, B.; Cador, O.; Nocton, G. *Angew. Chemie Int. Ed.* **2021**, *60* (11), 6042–6046. <https://doi.org/10.1002/anie.202015428>.
- (33) Fischer, E. O.; Hafner, W. *Zeitschrift für Naturforsch. B* **1955**, *10* (12), 665–668. <https://doi.org/doi:10.1515/znB-1955-1201>.
- (34) Fischer, E. O.; Stahl, H.-O. *Chem. Ber.* **1956**, *89* (8), 1805–1808. <https://doi.org/10.1002/cber.19560890802>.
- (35) Fischer, E. O.; Kögler, H. P. *Chem. Ber.* **1957**, *90* (2), 250–255. <https://doi.org/10.1002/cber.19570900218>.
- (36) Brennan, J. G.; Cloke, F. G. N.; Sameh, A. A.; Zalkin, A. *J. Chem. Soc. Chem. Commun.* **1987**, No. 21, 1668–1669. <https://doi.org/10.1039/C39870001668>.
- (37) Anderson, D. M.; Cloke, F. G. N.; Cox, P. A.; Edelstein, N.; Green, J. C.; Pang, T.; Sameh, A. A.; Shalimoff, G. *J. Chem. Soc. Chem. Commun.* **1989**, No. 1, 53–55. <https://doi.org/10.1039/C39890000053>.
- (38) Cloke, F. G. N. *Chem. Soc. Rev.* **1993**, *22* (1), 17–24. <https://doi.org/10.1039/CS9932200017>.
- (39) Katz, T. J.; Garratt, P. J. *J. Am. Chem. Soc.* **1963**, *85* (18), 2852–2853. <https://doi.org/10.1021/ja00901a041>.
- (40) Katz, T. J.; Garratt, P. J.; 86, V. *J. Am. Chem. Soc.* **1964**, *86* (23), 5194–5202. <https://doi.org/10.1021/ja01077a032>.
- (41) Boche, G.; Martens, D.; Danzer, W. *Angew. Chemie Int. Ed. English* **1969**, *8* (12), 984. <https://doi.org/10.1002/anie.196909841>.
- (42) Boche, G.; Weber, H.; Martens, D.; Bieberbach, A. *Chem. Ber.* **1978**, *111* (7), 2480–2496. <https://doi.org/10.1002/cber.19781110703>.
- (43) Boche, G.; Weber, H.; Bieberbach, A. *Chem. Ber.* **1978**, *111* (8), 2833–2849. <https://doi.org/10.1002/cber.19781110810>.
- (44) Boche, G.; Bieberbach, A. *Chem. Ber.* **1978**, *111* (8), 2850–2858. <https://doi.org/10.1002/cber.19781110811>.
- (45) Verkouw, H. T.; Veldman, M. E. E.; Groenenboom, C. J.; Van Oven, H. O.; De Leifde Meijer, H. J. *J. Organomet. Chem.* **1975**, *102* (1), 49–56. [https://doi.org/10.1016/S0022-328X\(00\)90259-6](https://doi.org/10.1016/S0022-328X(00)90259-6).
- (46) Walter, M. D.; Wolmershäuser, G.; Sitzmann, H. *J. Am. Chem. Soc.* **2005**, *127* (49), 17494–17503. <https://doi.org/10.1021/ja0550071>.
- (47) Murahashi, T.; Inoue, R.; Usui, K.; Ogoshi, S. *J. Am. Chem. Soc.* **2009**, *131* (29), 9888–9889. <https://doi.org/10.1021/ja903679f>.
- (48) Bonny, A.; Stobart, S. R. *J. Chem. Soc. Dalt. Trans.* **1979**, No. 5, 786–791. <https://doi.org/10.1039/DT9790000786>.
- (49) Schäfer, S.; Bauer, H.; Becker, J.; Sun, Y.; Sitzmann, H. *Eur. J. Inorg. Chem.* **2013**, *2013* (33), 5694–5700. <https://doi.org/10.1002/ejic.201300885>.

- (50) Kawasaki, K.; Sugiyama, R.; Tsuji, T.; Iwasa, T.; Tsunoyama, H.; Mizuhata, Y.; Tokitoh, N.; Nakajima, A. *Chem. Commun.* **2017**, 53 (49), 6557–6560. <https://doi.org/10.1039/C7CC03045B>.
- (51) Xémard, M.; Zimmer, S.; Cordier, M.; Goudy, V.; Ricard, L.; Clavaguéra, C.; Nocton, G. *J. Am. Chem. Soc.* **2018**, 140 (43), 14433–14439. <https://doi.org/10.1021/jacs.8b09081>.
- (52) Tilley, T. D.; Andersen, R. A. *Inorg. Chem.* **1981**, 20 (10), 3267–3270. <https://doi.org/10.1021/ic50224a025>.
- (53) Finke, R. G.; Keenan, S. R.; Watson, P. L. *Organometallics* **1989**, 8 (2), 263–277. <https://doi.org/10.1021/om00104a001>.
- (54) Münzfeld, L.; Schoo, C.; Bestgen, S.; Moreno-Pineda, E.; Köppe, R.; Ruben, M.; Roesky, P. W. *Nat. Commun.* **2019**, 10 (1), 3135. <https://doi.org/10.1038/s41467-019-10976-6>.
- (55) Hilgar, J. D.; Flores, B. S.; Rinehart, J. D. *Chem. Commun.* **2017**, 53 (53), 7322–7324. <https://doi.org/10.1039/C7CC02356A>.
- (56) Hilgar, J. D.; Bernbeck, M. G.; Flores, B. S.; Rinehart, J. D. *Chem. Sci.* **2018**, 9 (36), 7204–7209. <https://doi.org/10.1039/C8SC01361F>.
- (57) Mashima, K.; Nakayama, Y.; Nakamura, A.; Kanehisa, N.; Kai, Y.; Takaya, H. *J. Organomet. Chem.* **1994**, 473 (1), 85–91. [https://doi.org/10.1016/0022-328X\(94\)80108-8](https://doi.org/10.1016/0022-328X(94)80108-8).
- (58) Cendrowski-Guillaume, S. M.; Nierlich, M.; Lance, M.; Ephritikhine, M. *Organometallics* **1998**, 17 (5), 786–788. <https://doi.org/10.1021/om9709446>.
- (59) Cendrowski-Guillaume, S. M.; Le Gland, G.; Nierlich, M.; Ephritikhine, M. *Organometallics* **2000**, 19 (26), 5654–5660. <https://doi.org/10.1021/om000558f>.
- (60) Wayda, A. L.; Mukerji, I.; Dye, J. L.; Rogers, R. D. *Organometallics* **1987**, 6 (6), 1328–1332. <https://doi.org/10.1021/om00149a032>.
- (61) Panda, T. K.; Zulys, A.; Gamer, M. T.; Roesky, P. W. *Organometallics* **2005**, 24 (9), 2197–2202. <https://doi.org/10.1021/om0491138>.
- (62) Edelmann, A.; Lorenz, V.; Hrib, C. G.; Hilfert, L.; Blaurock, S.; Edelmann, F. T. *Organometallics* **2013**, 32 (5), 1435–1444. <https://doi.org/10.1021/om3010993>.
- (63) He, M.; Chen, X.; Bodenstein, T.; Nyvang, A.; Schmidt, S. F. M.; Peng, Y.; Moreno-Pineda, E.; Ruben, M.; Fink, K.; Gamer, M. T.; Powell, A. K.; Roesky, P. W. *Organometallics* **2018**, 37 (21), 3708–3717. <https://doi.org/10.1021/acs.organomet.8b00412>.
- (64) Rinehart, J. D.; Long, J. R. *Chem. Sci.* **2011**, 2 (11), 2078–2085. <https://doi.org/10.1039/C1SC00513H>.
- (65) Cotton, F. A. *Acc. Chem. Res.* **1968**, 1 (9), 257–265. <https://doi.org/10.1021/ar50009a001>.
- (66) Cotton, S. A. *Lanthanide and Actinide Chemistry*; Wiley, Chichester, England; **2006**. <https://doi.org/10.1002/0470010088>.
- (67) Sessoli, R.; Gatteschi, D.; Caneschi, A.; Novak, M. A. *Nature* **1993**, 365 (6442), 141–143. <https://doi.org/10.1038/365141a0>.
- (68) Affronte, M. *J. Mater. Chem.* **2009**, 19 (12), 1731–1737. <https://doi.org/10.1039/B809251F>.
- (69) Zabala-Lekuona, A.; Seco, J. M.; Colacio, E. *Coord. Chem. Rev.* **2021**, 441, 213984. <https://doi.org/10.1016/j.ccr.2021.213984>.
- (70) Murugesu, M.; Habrych, M.; Wernsdorfer, W.; Abboud, K. A.; Christou, G. *J. Am. Chem. Soc.* **2004**, 126 (15), 4766–4767. <https://doi.org/10.1021/ja0316824>.
- (71) Ako, A. M.; Hewitt, I. J.; Mereacre, V.; Clérac, R.; Wernsdorfer, W.; Anson, C. E.; Powell, A. K. *Angew. Chemie Int. Ed.* **2006**, 45 (30), 4926–4929. <https://doi.org/10.1002/anie.200601467>.
- (72) Neese, F.; Pantazis, D. A. *Faraday Discuss.* **2011**, 148 (0), 229–238. <https://doi.org/10.1039/C005256F>.
- (73) Ishikawa, N.; Sugita, M.; Ishikawa, T.; Koshihara, S.; Kaizu, Y. *J. Am. Chem. Soc.* **2003**, 125 (29), 8694–8695. <https://doi.org/10.1021/ja029629n>.
- (74) Waldmann, O. *Inorg. Chem.* **2007**, 46 (24), 10035–10037. <https://doi.org/10.1021/ic701365t>.

- (75) Ruiz, E.; Cirera, J.; Cano, J.; Alvarez, S.; Loose, C.; Kortus, J. *Chem. Commun.* **2008**, No. 1, 52–54. <https://doi.org/10.1039/B714715E>.
- (76) Cirera, J.; Ruiz, E.; Alvarez, S.; Neese, F.; Kortus, J. *Chem. – A Eur. J.* **2009**, *15* (16), 4078–4087. <https://doi.org/10.1002/chem.200801608>.
- (77) Chilton, N. F.; Collison, D.; McInnes, E. J. L.; Winpenny, R. E. P.; Soncini, A. *Nat. Commun.* **2013**, *4* (1), 2551. <https://doi.org/10.1038/ncomms3551>.
- (78) Goodwin, C. A. P.; Reta, D.; Ortu, F.; Chilton, N. F.; Mills, D. P. *J. Am. Chem. Soc.* **2017**, *139* (51), 18714–18724. <https://doi.org/10.1021/jacs.7b11535>.
- (79) Goodwin, C. A. P.; Ortu, F.; Reta, D.; Chilton, N. F.; Mills, D. P. *Nature* **2017**, *548* (7668), 439–442. <https://doi.org/10.1038/nature23447>.
- (80) Guo, F. S.; Day, B. M.; Chen, Y. C.; Tong, M. L.; Mansikkamäki, A.; Layfield, R. A. *Science* (80-. ). **2018**, *362* (6421), 1400–1403. <https://doi.org/10.1126/science.aav0652>.
- (81) Gould, C. A.; McClain, K. R.; Yu, J. M.; Groshens, T. J.; Furche, F.; Harvey, B. G.; Long, J. R. *J. Am. Chem. Soc.* **2019**, *141* (33), 12967–12973. <https://doi.org/10.1021/jacs.9b05816>.
- (82) Dey, A.; Kalita, P.; Chandrasekhar, V. *ACS Omega* **2018**, *3* (8), 9462–9475. <https://doi.org/10.1021/acsomega.8b01204>.
- (83) Abragam, A.; Bleaney, B. *Electron Paramagnetic Resonance of Transition Ions*; Clarendon press, Oxford, UK, **1970**. <https://global.oup.com/academic/product/electron-paramagnetic-resonance-of-transition-ions-9780199651528?cc=fr&lang=en&>
- (84) Reta, D.; Kragoskow, J. G. C.; Chilton, N. F. *J. Am. Chem. Soc.* **2021**, *143* (15), 5943–5950. <https://doi.org/10.1021/jacs.1c01410>.
- (85) Xémard, M. , Ph.D. thesis, Université Paris-Saclay, **2018**. <https://pastel.archives-ouvertes.fr/tel-02265243v1>.
- (86) Maier, G.; Schneider, M.; Kreiling, G.; Mayer, W. *Chem. Ber.* **1981**, *114* (12), 3922–3934. <https://doi.org/10.1002/cber.19811141215>.
- (87) Kilimann, U.; Herbst-Irmer, R.; Stalke, D.; Edelmann, F. T. *Angew. Chemie Int. Ed. English* **1994**, *33* (15–16), 1618–1621. <https://doi.org/10.1002/anie.199416181>.

## Chapter III

# Original heterobimetallic complexes of Yb and Pt as models for group 10 reactivity

## I. Background on platinum chemistry

### I.A. Pioneer works, toward Shilov's chemistry

The origin of organoplatinum chemistry can be tracked back to the first half of the 19<sup>th</sup> century when Zeise isolated yellow crystalline product as the result of the reaction between  $\text{PtCl}_4$  and EtOH in presence of KCl salt.<sup>1</sup> Since the “metallic, astringent and long lasting” taste of the unidentified product did not allow its identification, the formulation  $\text{K}[(\text{C}_2\text{H}_4)\text{PtCl}_3]\cdot\text{H}_2\text{O}$  was only unveiled thirty years later, proving that Zeise's salt was indeed the first ever organometallic compound isolated.<sup>2</sup>

It was however only a century later that the reactivity studies of such organoplatinum compounds were conclusive, opening the road toward catalysis,<sup>3–5</sup> up to the activation of saturated hydrocarbon compounds.<sup>6</sup> In 1969 Shilov and coworkers reported the C-H activation of inert alkanes by a metal complex.<sup>7</sup> In this system, the  $\text{Pt}^{\text{II}}$  catalyst ( $\text{PtCl}_2$ ) performed the activation of  $\text{CH}_4$  in acidic aqueous environment to end up with  $\text{CH}_3\text{OH}$  as the valuable product of the reaction. Since then, a remarkable amount of work have been performed to elucidate the nature of this C-H activation.<sup>8,9</sup> The initial studies were in favor of a three step mechanism: (i) C-H activation at a  $\text{Pt}^{\text{II}}$  center to form a  $\text{Pt}^{\text{II}}$ -alkyl species, (ii) fast oxidation by a stoichiometric amount of  $\text{Pt}^{\text{IV}}$  that yield a  $\text{Pt}^{\text{IV}}$ -methyl intermediate and (iii) reductive elimination of  $\text{CH}_3\text{OH}$  with regeneration of  $\text{Pt}^{\text{II}}\text{Cl}_2$  (Figure I.1).

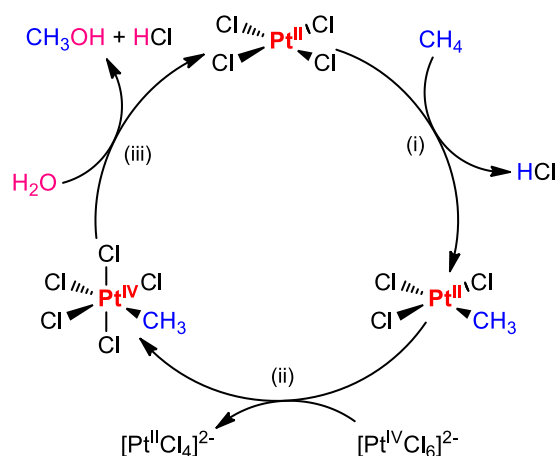


**Figure I.1.** The Shilov system for methane oxidation in methanol.

This breakthrough significantly influenced platinum chemistry for the following decades yet improvements were necessary to make this process industrially relevant: replace the stoichiometric amount of Pt<sup>IV</sup> with another cheaper oxidant. This is what led Bercaw and Labinger, who extensively studied the Shilov system in the 90's. While the two last steps were easily demonstrated, assessing the nature of the C-H activation in step (i) remained a tough challenge. On one side, Shilov initially proposed that the Pt<sup>II</sup>-alkyl complex was formed through oxidative addition of the C-H bond followed by a reductive elimination of HCl.<sup>10</sup> On the other side, Labinger and Bercaw preferred to consider first an electrophilic activation of a  $\sigma$ -bonded CH<sub>4</sub> molecule thanks to the favorable liberation of a proton in the acidic environment.<sup>11</sup> However they later studied several model systems and reaction conditions leading to the following statement: if both the  $\sigma$ -CH<sub>4</sub>-Pt and the alkyl-Pt<sup>IV</sup>-H species were involved in the mechanism they were in equilibrium with each other and only the latter produced the Pt<sup>II</sup>-alkyl intermediate (Figure I.2).<sup>12,13</sup> A short summary of these studies was published in 2015, as a tribute, six months after Shilov passed away.<sup>14</sup> As an additional note, in this retrospective, Labinger and Bercaw greatly thanked him for his pioneer studies, "it all started with his work, and we greatly value our memories of him".

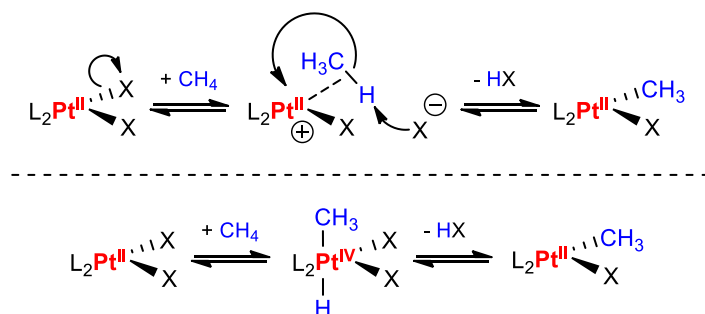


**Figure I.2.** The two discussed mechanism for step (i) of the Shilov system, (top) the electrophilic activation and (bottom) the oxidative addition pathways.

## I.B. The Catalytica system

With the mechanism of the Shilov system well-known, several studies were starting to point toward the possible replacement of the stoichiometric  $\text{Pt}^{\text{IV}}$  oxidant with  $\text{O}_2$  being a possible candidate.<sup>15</sup> Capitalizing on their experience obtained on a  $\text{Hg}^{\text{II}}\text{-H}_2\text{SO}_4$  system developed in 1993 for the oxidation of  $\text{CH}_4$ ,<sup>16</sup> Periana and coworkers finally solved the oxidant issue with their groundbreaking report in 1998 of the now-known as “Catalytica” system yielding up to 72%  $\text{CH}_4$  conversion to methyl bisulfate  $\text{CH}_3\text{OSO}_3\text{H}$  (Figure I.3).<sup>17</sup> In this study, Periana used the bidentate 2,2'-bipyrimidyl (bipym) ligand with a stronger acidic environment, hot  $\text{H}_2\text{SO}_4$ , that also behaved as the oxidant in the system. It has to be noted that the system was also efficient with  $\text{NH}_3$  ligands but the complex degraded after a short time ( $t_{1/2} \approx 15$  mins) to insoluble  $\text{PtCl}_2$  polymer.

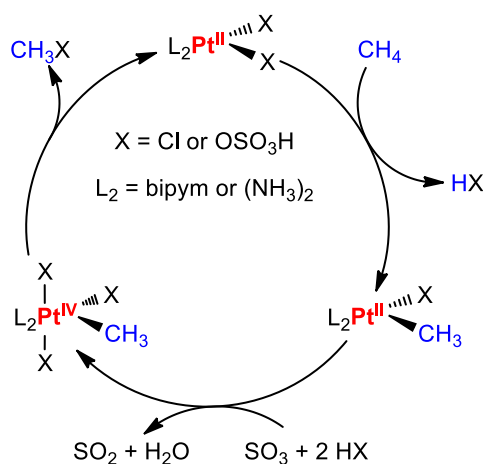


**Figure I.3.** The Catalytica system, as presented in ref<sup>17</sup>.

Theoretical studies on the thermodynamics of the reaction showed that the bipym ligand had to be considered in its protonated forms,  $\text{bipymH}^+$  or  $\text{bipymH}_2^{2+}$ , in the reaction mixture,<sup>18,19</sup> and a later experimental study from the Sanford group, where they replaced sulfuric acid by dimethyl sulfate, reinforced this proposition (Figure I.4).<sup>20</sup> The resulting protonated, or methylated in Sanford's work, species were stabilized which was not the case with  $\text{NH}_3$  ligands and degradation to  $\text{PtCl}_2$  by elimination of  $\text{NH}_4^+$  was thermodynamically favorable, which was not the case with the bipym ligand. Interestingly, it was also lowering the C-H activation energy highlighting the non-innocence of the bidentate ligand. If this C-H activation was first proposed as an electrophilic substitution between  $\text{R}^\cdot$  and an  $\text{X}^-$  ligand ( $\text{X} = \text{Cl}, \text{HSO}_4$ ), it was later corrected that the oxidative addition was more probable when they added explicit solvent molecule to the calculation.<sup>21</sup>



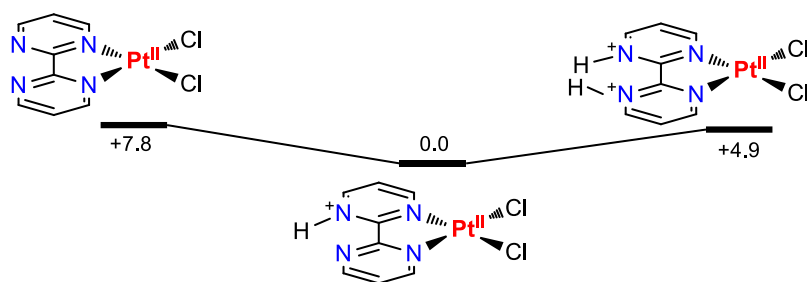


**Figure I.4.** Comparative stability of the neutral and protonated forms of the (bipym)PtCl<sub>2</sub> complex.  $\Delta G$  values in kcal mol<sup>-1</sup> calculated at 453 K<sup>18</sup>.

### I.C. Recent works and objectives of the project

While the Catalytica system was still suffering from drawbacks such as a relatively high catalyst loading (~ 3-4 mol%) and the inherent inhibition of the reaction upon reaching ~1 M concentration of the product, the number of Pt-mediated C-H activation studies started to decrease to the profit of cheaper first and second row transition metals.<sup>22,23</sup> The activity of Pt chemistry was therefore mostly oriented toward stoichiometric reactivity and mechanistic investigations with few examples of original catalytic applications. Among the reactivities studied figure the reductive elimination step where the C-O bond is formed in the Shilov and Catalytica systems (Figure I.5, left),<sup>24,25</sup> while other investigations were conducted on the oxygenation of the Pt-C bond as an alternative pathway for the C-O bond formation (Figure I.5, right).<sup>15,26-30</sup> On the catalysis side, the combination of a C-H oxidative addition of benzene derivatives with ethylene insertion in a Pt-Ar bond,<sup>31,32</sup> resulted in elegant hydroarylation of olefin systems.<sup>33,34</sup>

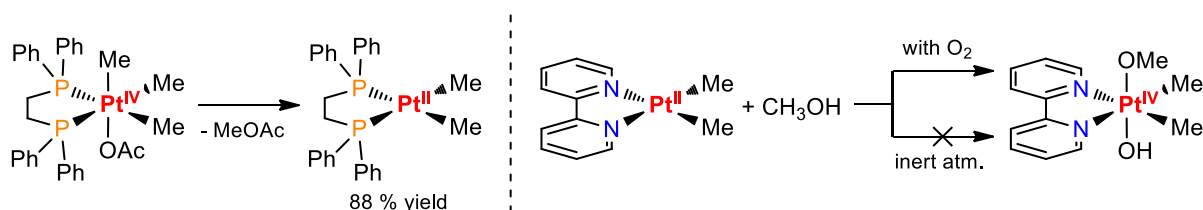


**Figure I.5.** (left) Selective C-O vs C-C reductive elimination as observed in ref<sup>24</sup> and (right) aerobic oxidation of a Pt<sup>II</sup> center with an oxygen atom insertion to form a C-O bond<sup>15</sup>.

As observed so far, the oxidative addition process is at the core of C-H activation-oriented platinum chemistry and Periana's findings might have not been possible without the careful study of this step. Indeed, the fine understanding of X-H and R-Y reactivities (X and Y being heteroatoms) toward various Pt<sup>II</sup> species was needed to isolate species similar to the intermediates proposed in the Catalytica system, a key point to further enhance its performances. This resulted in the literature on the topic being greatly enriched in the last quarter of the twentieth century. During this period, Puddephatt and coworkers notably contributed to this effort with N-donor ligand systems and summarized it in a review in 1997 (Figure I.6).<sup>35</sup> This not only resulted in original reactivities but

also the characterization of numerous model compounds for the more elusive Pd chemistry when it comes to high oxidation states.<sup>36,37</sup>

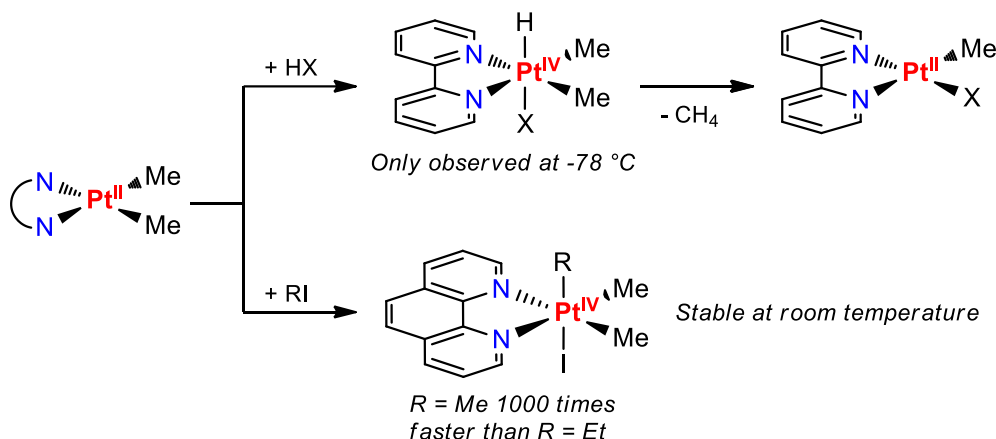


**Figure I.6.** Selected examples of oxidative additions from ref<sup>35</sup>.

Considering the recent results obtained in the group with the synthesis of  $\text{Cp}^*\text{Yb}(\text{bipym})\text{MMe}_2$  compounds of group 10 metals ( $\text{M} = \text{Ni}$  and  $\text{Pd}$ ),<sup>38,39</sup> the next step was to switch to Pt to complete the series. The first objective consisted in using platinum's enhanced stability to perform the fine characterization of the intermediate valence states of various Yb-Pt architectures, notably at high oxidation state, in order to better understand the impact of the transition metal fragment on such behavior. Additionally, after having isolated a series of different multiconfigurational architectures, a second goal became to evaluate the resulting modulation of the reactivity, having as an ultimate goal the C-H activation of methane thanks to the tuned electronic environment of the Pt center that should favor the oxidative addition step by stabilizing its hypothetical product, with a  $\text{Pt}^{\text{IV}}\text{Me}_3\text{H}$  fragment.

## II. Synthesis and characterization of heterobimetallic Yb-Pt complexes

### II.A. Synthesis and structural analysis

Contrary to the other group 10 metals, the synthesis of the  $(\text{bipym})\text{PtMe}_2$  precursor, **1**, was already reported and was performed in  $\text{CH}_2\text{Cl}_2$  starting from the dimer  $[\text{Pt}(\text{SMe}_2)\text{Me}_2]_2$  precursor.<sup>40–43</sup> Excess of the bipym ligand was used to reduce the final amount of the undesired  $\text{Me}_2\text{Pt}(\text{bipym})\text{PtMe}_2$  dimer. The crystallization step was mandatory to remove the remaining free ligand. Indeed, as specified in the Pd and Ni case,<sup>38,39</sup> any free ligand contamination of **1** resulted in the formation of the also undesired  $\text{Cp}^*_2\text{Yb}(\text{bipym})\text{YbCp}^*_2$  dimer upon addition of the  $\text{Cp}^*_2\text{Yb}(\text{OEt}_2)$  precursor.<sup>44</sup> Note that in that case, the double reduction of the bipym ligand by two  $\text{Cp}^*_2\text{Yb}$  fragments

resulted in a closed-shell singlet dianionic ligand.<sup>45</sup> This thermodynamic driving force thus prevents the isolation of any monomeric  $\text{Cp}^*_2\text{Yb}(\text{bipym})$  precursor. With this purity prerequisite respected, the  $\text{Cp}^*_2\text{Yb}(\text{bipym})\text{PtMe}_2$ , **2**, complex was synthesized in toluene with the same protocol used for his Ni and Pd analogs (Figure II.1).<sup>38,39</sup> After the addition of a toluene solution of  $\text{Cp}^*_2\text{Yb}(\text{OEt}_2)$  to a toluene suspension of **1**, **2** was isolated as dark greenish-black X-ray suitable crystals in 86% yield from the dark brownish-green resulting mixture after a night at  $-40^\circ\text{C}$ .

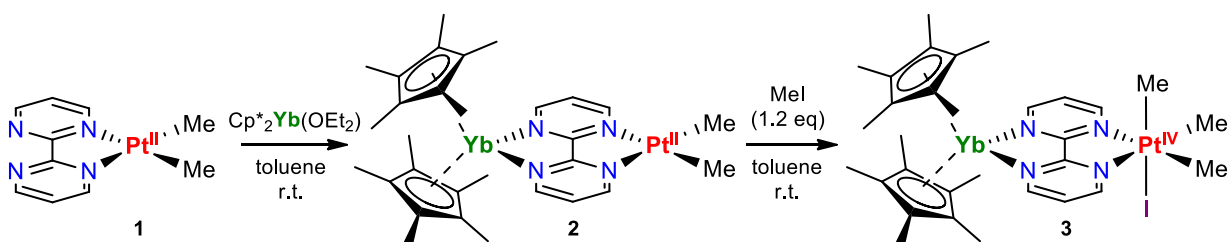


**Figure II.1.** Synthesis of  $\text{Cp}^*_2\text{Yb}(\text{bipym})\text{PtMe}_2$ , **2** and  $\text{Cp}^*_2\text{Yb}(\text{bipym})\text{PtMe}_3\text{I}$ , **3**.

The comparison of **1** and **2** XRD structures allowed to observe that the divalent Yb transferred its electron to the bipym ligand (Figure II.2 and Table II.1). As it is typical for these species,<sup>38,39</sup> upon coordination the C-C bond bridging the two pyrimidine rings was shortened by almost  $0.1\text{ \AA}$ ,  $1.49(2)\text{ \AA}$  for **1** vs  $1.408(5)\text{ \AA}$  for **2**. This was a first indication of the formal ligand reduction because the electron was transferred to the  $b_1$  LUMO of **1** ( $\text{C}_{2v}$  symmetry) in which most of the electronic density was found on the C-C bridging bond. Another metric parameter indicative of the oxidation of the Yb center was the Yb- $\text{Cp}^*_{\text{ctr}}$  distance. The  $2.31(1)\text{ \AA}$  found in **2** was coherent with a formal  $\text{Yb}^{\text{III}}$  oxidation state.<sup>38,39,46</sup> On the Pt side, no significant change was found Pt-N distances of  $2.09(2)\text{ \AA}$  for **1** and  $2.088(4)\text{ \AA}$  for **2** while Pt-Me distances was  $2.05(3)\text{ \AA}$  in **1** and  $2.037(9)\text{ \AA}$  in **2**.

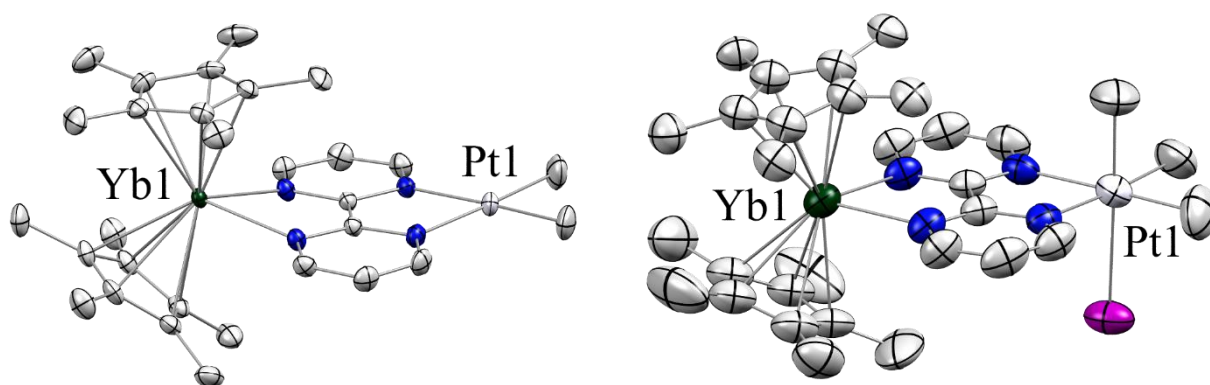


**Figure II.2.** ORTEPs of (left) **2** and (right) **3** with thermal ellipsoids at 50 % level. Carbon atoms are in grey, nitrogen atoms in blue, the iodide atom in purple, the platinum atom in white, and the ytterbium atom in olive green. Hydrogen atoms and co-crystallized toluene molecules have been removed for clarity.

Upon addition of MeI to a toluene solution of **2**, the coloration of the solution turned to brown and X-ray suitable needles were grown overnight at  $-40\text{ }^{\circ}\text{C}$  in 92% yield. The XRD study of these crystals was found rather difficult. At 150 K, images indicative of several twins were recorded. This was thought to be due to toluene cavities and decent data was only obtained at 280 K. The oxidative addition led to the  $\text{Cp}^*_2\text{Yb}(\text{bipym})\text{PtMe}_3\text{I}$  complex, **3**, in which the  $C_2$  axis left place to a mirror plane leading to a  $C_s$  symmetry. The resulting distances on the Pt center were slightly modified the Pt-Me distance was  $2.06(4)\text{ \AA}$  while the Pt-N distance was  $2.15(1)\text{ \AA}$ . Those values were within the standard range for a  $\text{Pt}^{\text{IV}}$  ion.<sup>47–49</sup>

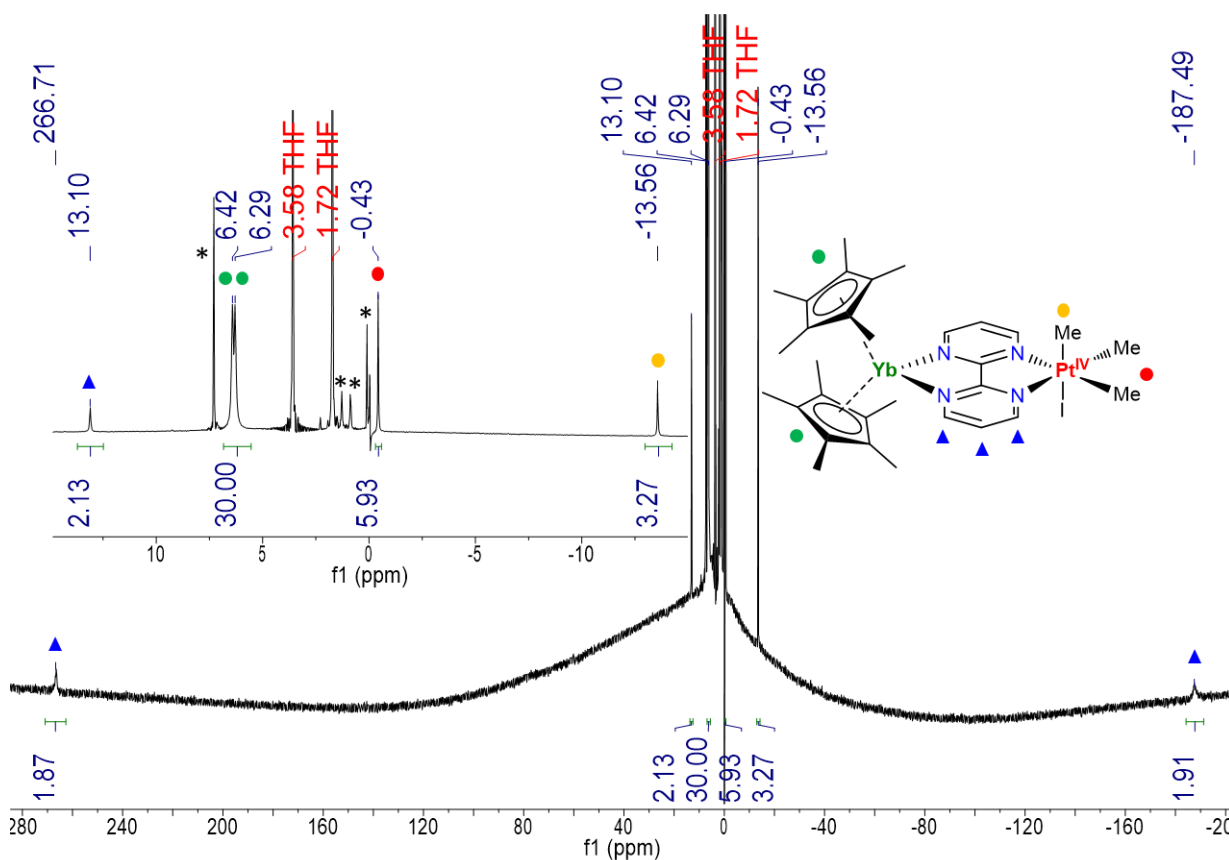
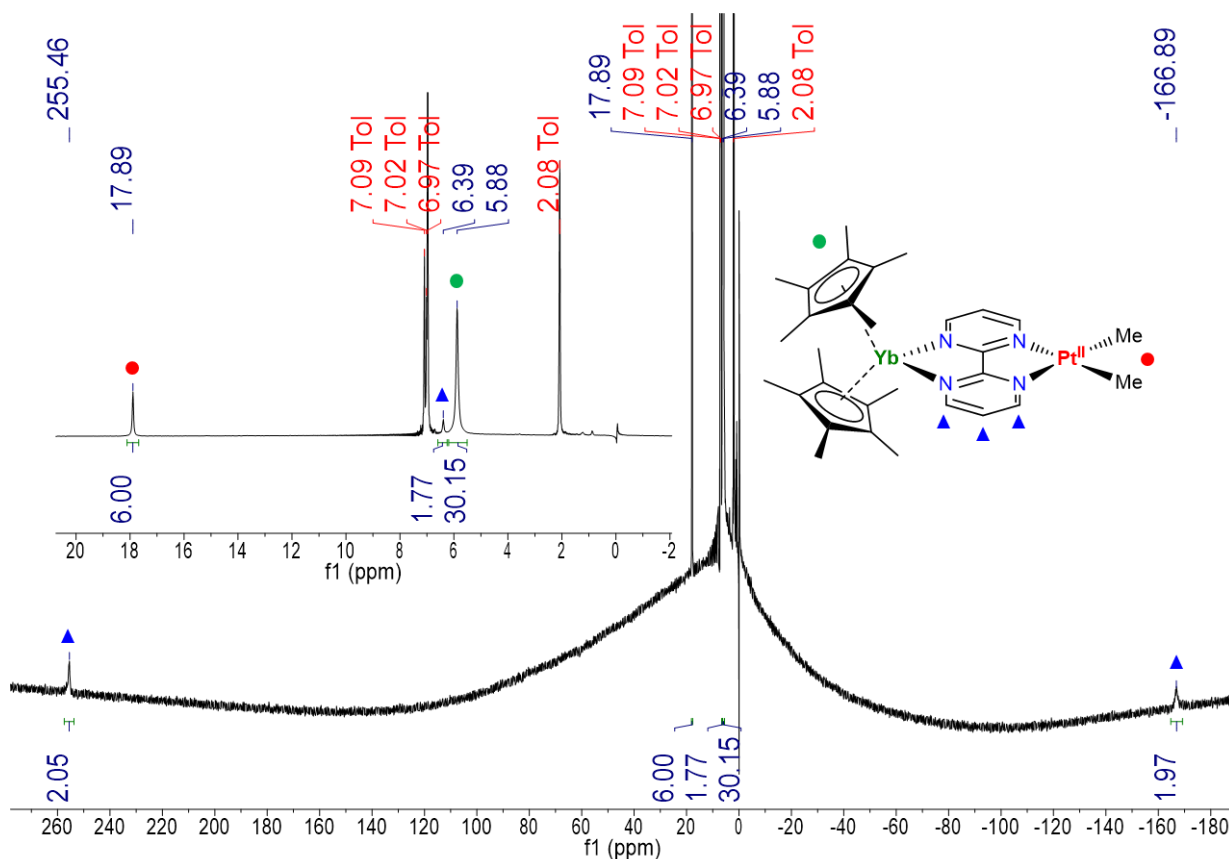
**Table II.1.** Main metric parameters in  $\text{\AA}$  for the free bipym ligand and complexes **1-3**:

Atoms	bipym	1	2	3
C-C <sub>bipym</sub>	1.501(1)	1.49(2)	1.408(5)	1.41(1)
Pt-N <sub>bipym</sub>	/	2.09(2)	2.088(4)	2.15(1)
Pt-C <sub>Me</sub>	/	2.05(3)	2.037(9)	2.06(4)
Yb-Cp* <sub>ctr</sub>	/	/	2.31	2.36
Yb-N <sub>bipym</sub>	/	/	2.361(3)	2.35(1)

## II.B. Experimental electronic structure studies

In the  $^1\text{H}$  NMR spectrum of **2**, recorded at  $20\text{ }^{\circ}\text{C}$  in  $\text{tol-}d_8$ , a 30 H integrated  $\text{Cp}^*$  signal was found at 5.88 ppm, the two first signals of the bipym signals were highly shifted at 255.46 and -166.89 ppm while the last one was found at 6.39 ppm. Lastly, the signal for the two methyl groups was found at 17.89 ppm (Figure II.3). This was concurring with the  $C_{2v}$  symmetry observed in the solid-state. The high chemical shifts for the first two peaks of the bipym were the consequence of the paramagnetic behavior of **2**. This would not be the case with a divalent  $\text{Yb}^{\text{II}}$  ( $f^{14}$ ) ion. The solution-state NMR was therefore in agreement with the solid-state XRD analysis, the Yb was formally oxidized ( $f^{13}$ ) and the bipym ligand was better described as a radical anion.

The  $^1\text{H}$  NMR spectrum of **3** recorded in  $\text{thf-}d_8$  presented a similar paramagnetic behavior that the one observed with **2**. However, since the  $C_{2v}$  symmetry was lowered to  $C_s$  after the oxidative addition, the two  $\text{Cp}^*$  signals were now nicely split, one was found at 6.29 ppm while the other was at 6.42 ppm. The bipym signals were also slightly shifted at 266.71, -187.49 and 13.10 ppm respectively. The two equatorial Me groups were found at -0.43 ppm and the axial one was at -13.56 ppm (Figure II.4). Noteworthy, contrary to its Pd analog,<sup>38</sup> **3** was found indefinitely stable at room temperature in both the solid and solution state.



To probe the electronic ground state of **2** and **3** further investigations were needed. To present such paramagnetic character, both compounds had to be either in a triplet state ( $S = 1$ ) or in a singlet state ( $S = 0$ ) with a room temperature populated low-lying triplet (Figure II.5). To quickly probe that, a variable temperature (VT) NMR study was performed and all the chemical shifts of **2** and **3** were plotted versus  $1/T$  (Figure II.6). As it was already observed in similar systems, the plots were showing a deviation from the Curie-Weiss law.<sup>38,39,50–52</sup> This was symptomatic of the magnetic exchange coupling between the two single electrons but still not answering the question about the ground state of the two complexes.

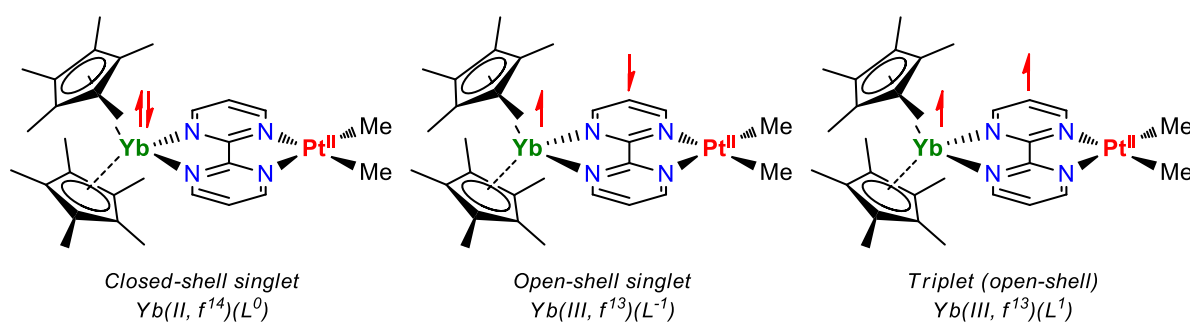


**Figure II.5.** Different possible electronic configurations of **2**.

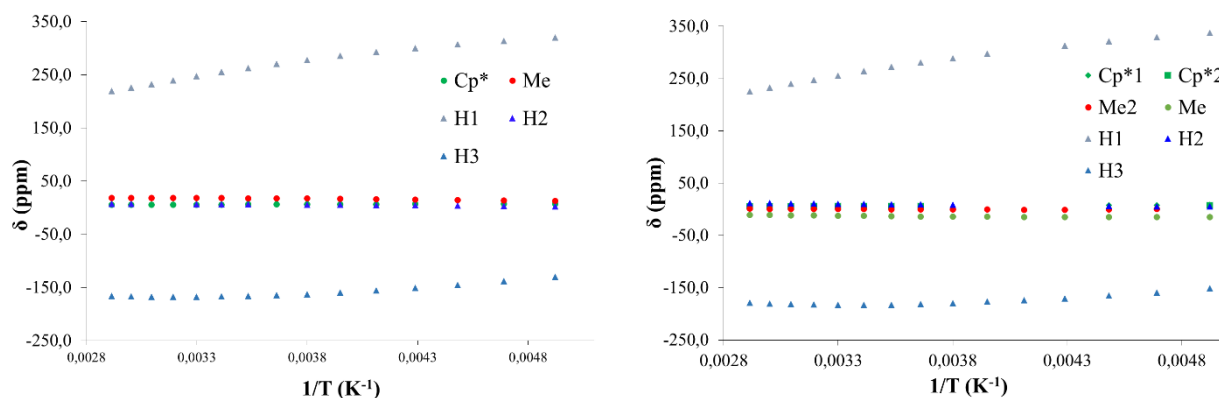


**Figure II.6.** Variable temperature  $^1\text{H}$  NMR of **2** (left) and **3** (right) in  $\text{tol-}d_8$ ,  $\delta$  vs  $1/T$  plots in the 203–343 K range.

Solid-state magnetic studies were therefore conducted to study the species on a larger temperature range, between 2 and 300 K. The  $\chi T$  versus  $T$  plot recorded under a 0.5 T field showed clearly a  $\chi T$  value going toward 0 at 0 K, meaning that the ground state of **2** was a singlet. Then with the increasing temperature, the  $\chi T$  value increased toward a room temperature value of  $2.44 \text{ cm}^3 \text{ K mol}^{-1}$  (Figure II.7, left). This value was close to the expected value for an isolated  $^2\text{F}_{7/2} \text{Yb}^{\text{III}}$  paramagnet  $2.57 \text{ cm}^3 \text{ K mol}^{-1}$  at 300 K.<sup>46</sup> This was the consequence of the triplet state being gradually populated upon the temperature increase. While Ni and Pd analogs were found to behave in a similar fashion, in this precise case, it could also be observed upon freezing a dark brownish-green solution of **2** in liquid nitrogen. The triplet state was then only marginally populated and the frozen solution turned orange.

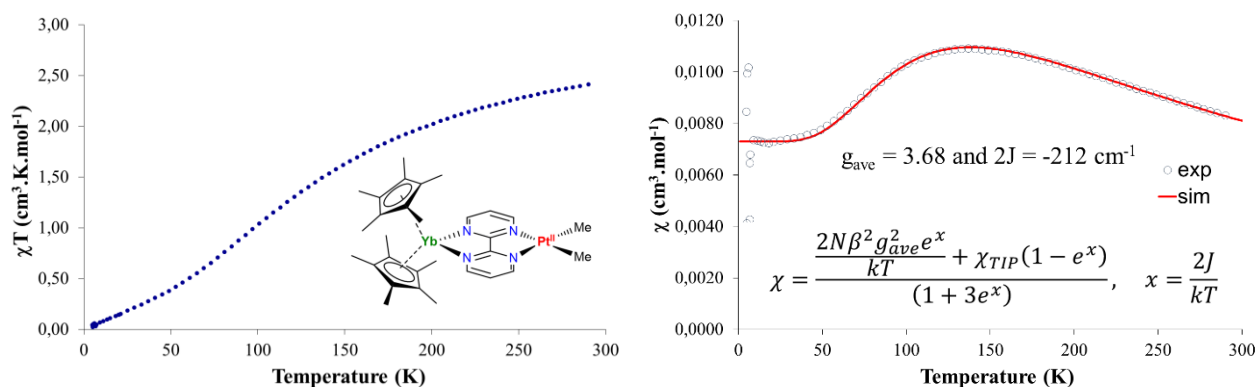


**Figure II.7.** Solid-state temperature dependent magnetic susceptibility of **2** recorded at 0.5 T: (left)  $\chi T$  vs  $T$  plot and (right)  $\chi$  vs  $T$  plot and its simulation with the TIP-including Bleaney-Bowers equation.

By plotting  $\chi$  versus  $T$ , several additional observations were obtained. At low temperature, a temperature independent paramagnetism (TIP) or van Vleck paramagnetism was observed,<sup>53</sup> such behavior was caused by the small energy gap between the ground state and the low-lying excited state. Then the susceptibility rose to reach a maximum of around 130 K before decreasing as the temperature continued to be increased which was normal Curie-Weiss behavior. Since the susceptibility value during the TIP regime  $\chi_{TIP}$  was caused by the small singlet-triplet energy gap, its incorporation in a Bleaney-Bowers equation permitted an estimation of the energy gap (Figure II.7, right).<sup>54</sup> Considering the  $\chi_{TIP}$  value of  $0.0073 \text{ cm}^3 \text{ mol}^{-1}$ , the  $\chi$  plot versus  $T$  is fitted with a  $g_{ave}$  value of 3.68 which was relatively close to similar systems, 3.315 for instance for the  $\text{Cp}^*_2\text{Yb}(\text{bipy})^+$  cation.<sup>55</sup> The curve was then fitted as close as possible to the experimental one by varying the  $2J$  energy gap which was then estimated to be  $-212 \text{ cm}^{-1}$ . This was consistent with the triplet state being significantly populated at room temperature since  $k_B T = 203.7 \text{ cm}^{-1}$  at 293.15 K. Considering that the  $\chi_{TIP}$  and  $g_{ave}$  values were indicative of a high anisotropy, another model was developed by Lukens *et al.* to estimate the  $2J$  energy gap for strongly coupled electrons.<sup>56</sup> To do so, they considered a two-state approximated wavefunction for the  $\text{Cp}^*_2\text{Yb}(\text{bipy})$  system:  $\Psi = c_1 |f^{13}, \text{bipy}^{\bullet-}\rangle + c_2 |f^{14}, \text{bipy}^0\rangle$ . By assuming that the Yb ion was purely trivalent  $f^{13}$ ,  $c_1^2$  was fixed to 1 and by injecting the  $g$ -tensor values of the similar  $\text{Cp}^*_2\text{Yb}(\text{bipy})^+$  cation in equation (1) ( $g_z = 7.05$ ,  $g_y = 1.731$  and  $g_x = 1.165$ ),<sup>55</sup>  $2J$  was then estimated to  $-202.6 \text{ cm}^{-1}$ . Noteworthy, while the Bleaney-Bowers model usually tends to overestimate the  $2J$  value, the second one is likely to underestimate it. The fact that in that case both estimations were really close to each other meanted that the real electronic structure of **2** is really close to the two-states approximated models used.

$$2J = c_1^2 \frac{N\beta^2}{6\chi_{TIP}} \sum_{i=x,y,z} \frac{g_J(g_i - g_{\text{bipy}^{\bullet-}})^2}{g_i(1 - g_J)} \quad \text{with} \quad g_J = \frac{3}{2} + \frac{S(S+1) - L(L+1)}{2J(J+1)} \quad (1)$$



Since in the Pd case, the oxidative addition of MeI did not result in a change of ground state, the same result was expected with **3**. However, the room temperature  $\chi T$  value of  $2.67 \text{ cm}^3 \text{ K mol}^{-1}$  was indicative of a triplet state being populated and upon temperature decrease, this value only went down to  $1.31 \text{ cm}^3 \text{ K mol}^{-1}$  at 2 K due to the thermal depopulation of the crystal-field split states (Figure II.8). The ground state of **3** was therefore a pure triplet ( $S = 1$ ). Although the reason of this change of ground state is still under investigation, the impact on the accessible reactivity on the Pt center could be important. Switching from multistate to single state electronic structure could enhance a triplet triggered reactivity and/or shutdown singlet triggered reaction pathways, a mean to further lower the energy barrier of challenging C-H bond activation such as the targeted methane molecule.

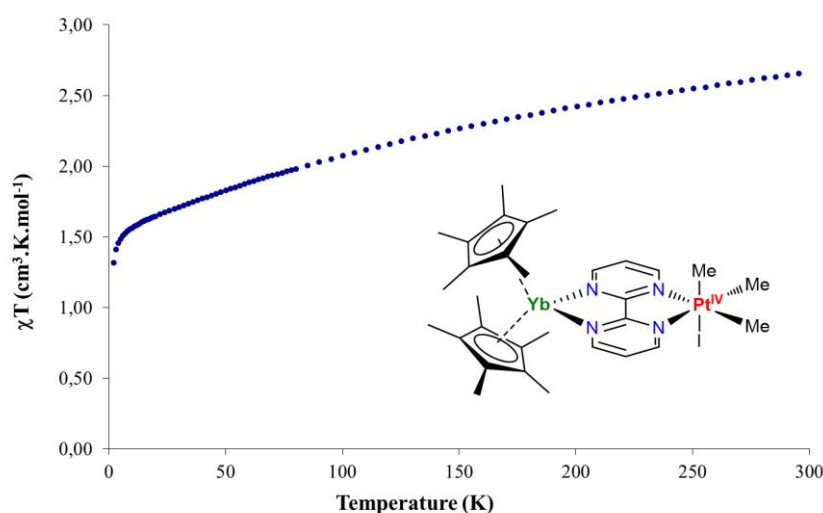


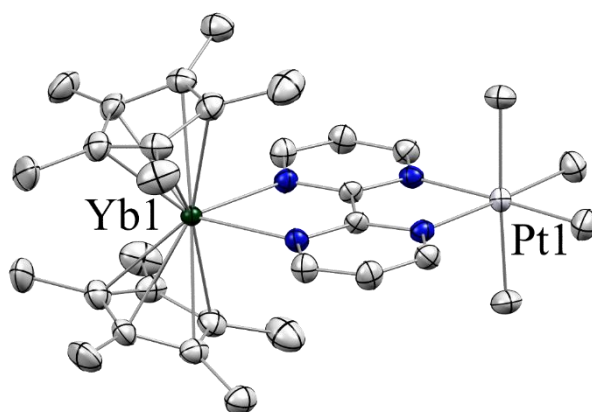
**Figure II.8.** Solid-state temperature dependent magnetic susceptibility of **3** recorded at 0.5 T:  $\chi T$  vs T plot.

### II.C. Modulation of the high-valent Pt coordinating environment

To study more in-depth this phenomenon two other heterobimetallic  $\text{Pt}^{\text{IV}}$  species were targeted. First, thanks to the improved stability of the **3** compared to its Pd analog,<sup>38</sup> the substitution of the iodide in **3** by a fourth methyl ligand was investigated since Puddephatt reported some interesting photo-triggered reactivity.<sup>57,58</sup> Thanks to the thermal robustness of **3**, the addition at room temperature of solid MeLi to a solution of **3** in toluene induced a slow color change of the solution from brown to dark red while some off-white solid slowly appeared. Although toluene might not be the best solvent to perform a reaction with MeLi, it was used to ease the removal of the expected LiI salt. This choice did not come without any drawback since the reaction needed at least 24 h of stirring to be completed on a relatively small scale ( $\sim 0.1 \text{ mmol}$ ). After treatment, XRD suitable dark red prisms of  $\text{Cp}^*_2\text{Yb}(\text{bipym})\text{PtMe}_4$ , **4**, were isolated in a 63 % yield (Figure II.9). The resulting metrics were slightly impacted by the substitution of the iodide by a methyl group. The C-C bond bridging the two pyrimidine rings was almost  $0.02 \text{ \AA}$  longer in **4** than in **2** or **3** ( $1.427(8) \text{ \AA}$  versus  $1.408(5) \text{ \AA}$  and



1.41(1) Å respectively), this could be indicative of some variation of the electronic ground state of **4** compared to **3**. On the Yb side, the Yb-Cp\*<sub>ctr</sub> distance of 2.29 Å was still in the trivalent range and the most important changes were found on the Pt side. The Pt-N distance was 2.099(4) Å which was significantly closer to the distance found in **2** (2.088(4) Å) than in **3** (2.15(1) Å). The average Pt-C distance was lengthened to 2.09(3) Å which was explained by the axial methyl groups being further (2.113(6) Å) than the equatorial ones (2.064(6) Å) (Table II.2). This was considered as the result of the *trans* effect of the bipyrimidine ligand and was rather common for such high-valent Pt or Pd centers.<sup>59</sup>

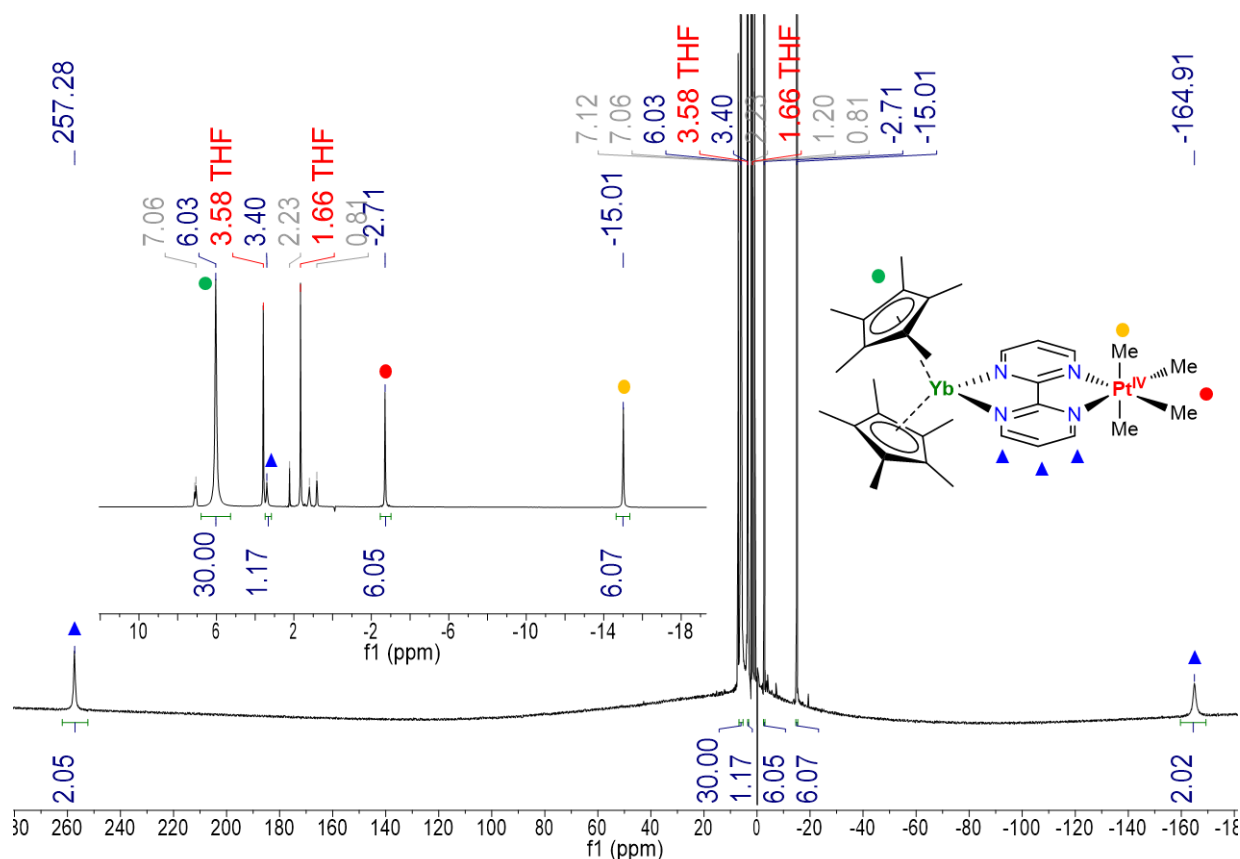


**Figure II.9.** ORTEP of **4** with thermal ellipsoids at 50 % level. Carbon atoms are in grey, nitrogen atoms in blue, the platinum atom in white, and the ytterbium atom in olive green. Hydrogen atoms have been removed for clarity.

The <sup>1</sup>H NMR spectrum of **4** was acquired in thf-*d*<sub>8</sub> and presents the same typical paramagnetic behavior as **2** and **3**. Only one Cp\* peak was found at 6.03 ppm which was indicative of the return to a C<sub>2v</sub> symmetry as expected with the substitution of the iodide by a methyl group. The bipym ligand peaks were found at 257.28, 3.40 and -164.91 ppm while the methyl signals both integrating for 6 H were found at -2.71 ppm for the equatorial ones, *trans* to the bipym ligand, and -15.01 ppm for the axial ones. This attribution was inherited from the respective axial and equatorial distribution of the peaks in **3** where the axial methyl group was found at -13.56 ppm while the equatorial ones were found at -0.43 ppm.

**Table II.2.** Main metric parameters in Å for the complexes **2-5** and **5<sup>+</sup>(py) OTf<sup>-</sup>**:

Atoms	2	3	4	5	5 <sup>+</sup> (py) OTf <sup>-</sup>
C-C <sub>bipym</sub>	1.408(5)	1.41(1)	1.427(8)	1.40(2)	1.41(1)
Pt-N <sub>bipym</sub>	2.088(4)	2.15(1)	2.099(4)	2.15(1)	2.15(1)
Pt-C <sub>Me</sub>	2.037(9)	2.06(4)	2.09(3)	2.03(3)	2.04(2)
Yb-Cp* <sub>ctr</sub>	2.31	2.36	2.29	2.29	2.30
Yb-N <sub>bipym</sub>	2.361(3)	2.35(1)	2.364(4)	2.354(9)	2.35(3)

**Figure II.10.** <sup>1</sup>H NMR spectrum of **4** recorded at 20 °C in thf-*d*<sub>8</sub>. Co-crystallized toluene and pentane impurities are labelled in grey.

The solid-state magnetic measurements were conducted on **4** and contrary to **3**, the  $\chi T$  versus  $T$  plot recorded at 0.5 T reaches a value close to 0 cm<sup>3</sup> K mol<sup>-1</sup> at 0 K this means **4** presents a singlet ground state (Figure II.11). The value of  $\chi T$  at room temperature, 2.00 cm<sup>3</sup> K mol<sup>-1</sup> indicated that a triplet state was populated but in a lesser proportion than what was observed in **2**. To confirm this rapid observation, the  $2J$  gap was estimated with the  $\chi_{TIF}$  value being 0.00578 cm<sup>3</sup> mol<sup>-1</sup>. This resulted in the Bleaney-Bowers model to give a value of -315 cm<sup>-1</sup> with a  $g_{ave}$  fitted to 3.45 while the model from Lukens *et al.* resulted in a value of -256 cm<sup>-1</sup>. Those values, while not being contradictory, left a relatively large range for the real value to be found. This could mean that contrary to what was observed with **2**, the two-states approximated models were not enough to fully describe the electronic structure of **4**.

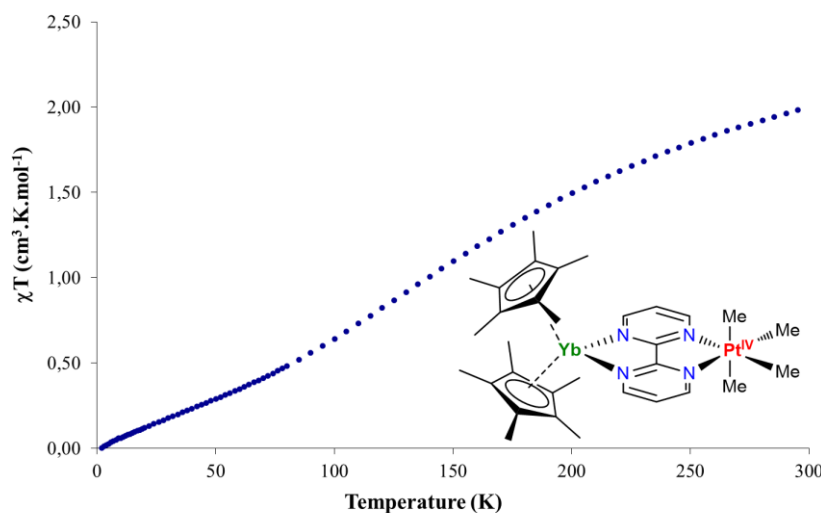


**Figure II.11.** Solid-state temperature dependent magnetic susceptibility of **4** recorded at 0.5 T:  $\chi T$  vs  $T$  plot.

To go further again and isolate the third variant of high-valent Pt species with this heterobimetallic architecture, MeOTf was used instead of MeI to perform the oxidative addition on **2**. As triflate is a more weakly coordinating anion than I<sup>-</sup> this was thought to be an adequate strategy to achieve electrophilic C-H activation. It was also tried with the Pd analog of **2** but it always led to fast degradation that prevented the isolation of the expected Pd<sup>IV</sup> product.<sup>38</sup> The structural characterization of the expected Cp\*<sub>2</sub>Yb(bipym)PtMe<sub>3</sub>OTf complex, **5**, was achieved upon performing the oxidative addition in Et<sub>2</sub>O. The product was almost insoluble in such solvent and with a vapour diffusion of MeOTf on a solution of **2** at -40 °C, tiny yellow XRD suitable needles appeared within a few hours (Figure II.12). The scaling up of the synthesis was achieved by the direct addition of MeOTf to a rapidly stirred Et<sub>2</sub>O suspension of **2**. Note that the same result was also obtained later, by replacing Et<sub>2</sub>O with toluene, to the only difference that the product was slightly soluble in toluene.

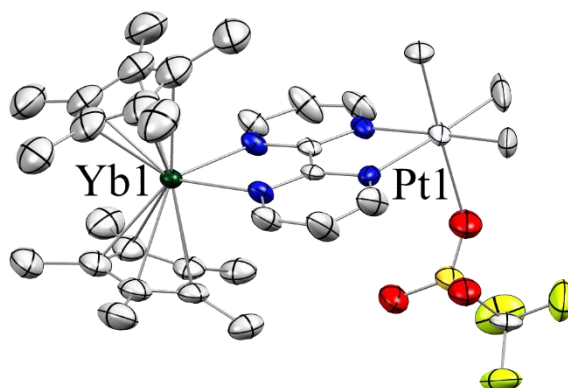


**Figure II.12.** ORTEP of **5** with thermal ellipsoids at 50 % level. Carbon atoms are in grey, nitrogen atoms in blue, oxygen atoms in red, the sulfur atom in orange, fluorine atoms in yellow, the platinum atom in white, and the ytterbium atom in olive green. Hydrogen atoms have been removed for clarity.

The  $^1\text{H}$  NMR spectrum of **5** was performed in  $\text{thf-}d_8$  and the spectrum of isolated **5** was rather clean (Figure II.13). However, the highly shifted bipym ligand peaks were twinned and not integrating for the same values, which meant that two similar heterobimetallic species were observed. It is important to note that although the solubility of **5** was worse in  $\text{C}_6\text{D}_6$ , only one set of signals was found in such a non-coordinating solvent. With that statement in mind, the overlapped  $\text{Cp}^*$  signals seemed to be the sum of two split  $\text{Cp}^*$  signals as expected for a similar  $\text{C}_s$  symmetry than the one observed in **3** and one other  $\text{Cp}^*$  signal not showing any splitting. If the former hinted toward the expected product **5** as isolated in XRD, the latter was either resulting from a  $\text{C}_{2v}$  symmetry either from another  $\text{C}_s$  isomeric form of **5**, **5'**, where the triflate anion was not in axial position but equatorial one, the  $\text{Cp}^*$  being equivalent in this case. This ligand shuffle was known to happen and was observed with the oxidative addition at low temperature of alkyl halides in strongly coordinating solvents such as acetone- $d_6$  or  $\text{MeCN-}d_3$  but it was not reported with the oxidative addition of  $\text{MeOTf}$  in  $\text{Et}_2\text{O}$  on the 4,4'- $t\text{Bu}_2\text{bipyPtMe}_2$  complex.<sup>60</sup>

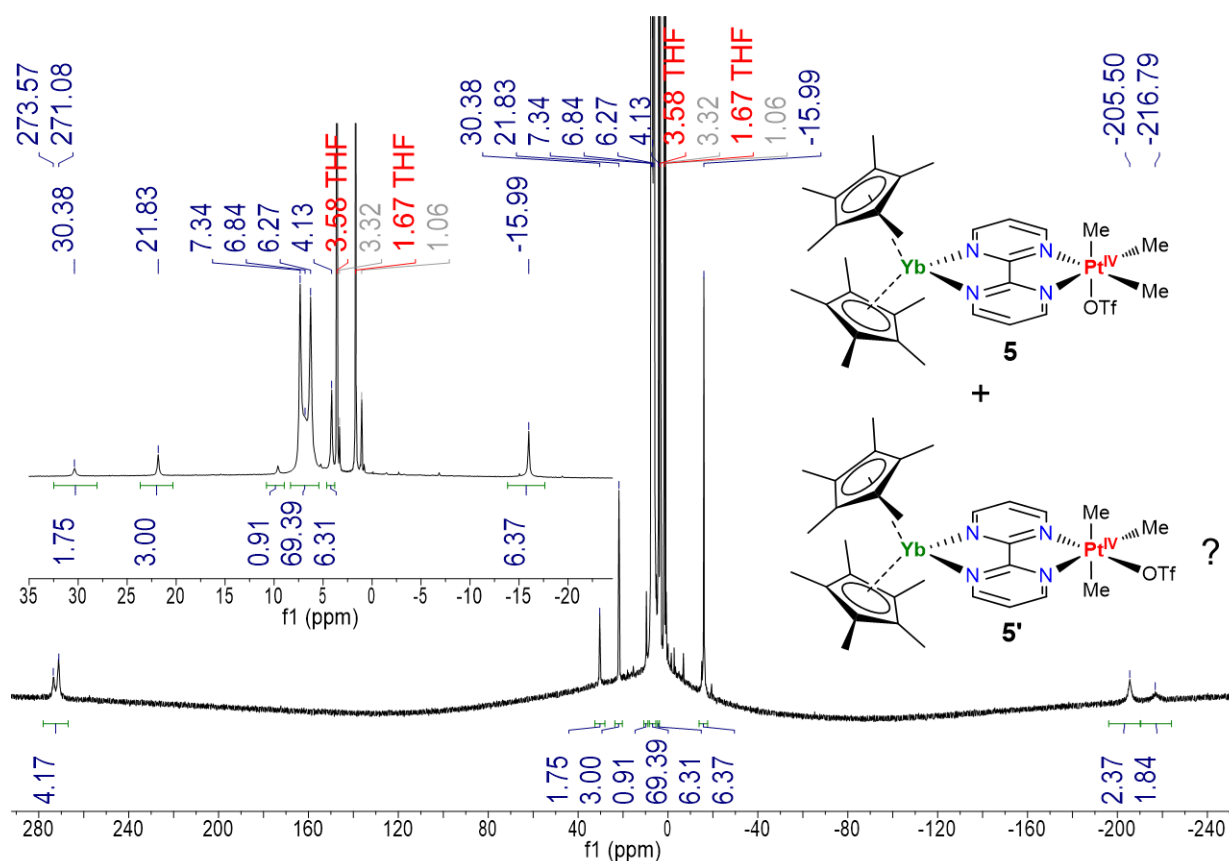


**Figure II.13.**  $^1\text{H}$  NMR spectrum of crystals of **5** recorded at 20 °C in  $\text{thf-}d_8$ .

Another kind of  $\text{C}_s$  symmetry resulted from this ligand scrambling, where the  $\text{Cp}^*$  signal was not split anymore while the bipym ligand signals should be. A reason why the splitting of the highly shifted bipym peaks of **5'** was not observed might result from them being overlapped with the peaks of **5**. The fact that both species were observable at the NMR time scale might mean that the

dissociation of **5** in **5<sup>+</sup>(thf) OTf<sup>-</sup>** was the rate-limiting step of the isomerization equilibrium. While no crystal of the expected **5<sup>+</sup>(thf) OTf<sup>-</sup>** intermediate was isolated, when a stronger coordinating solvent pyridine (py) was added to a toluene suspension of **5** it completely displaced the triflate ligand. This led to the isolation of XRD suitable dark brown blocks of the  $[\text{Cp}^*_2\text{Yb}(\text{bipym})\text{PdMe}_3(\text{py})]^+ \text{OTf}^-$  compound, **5<sup>+</sup>(py) OTf<sup>-</sup>** (Figure II.14).

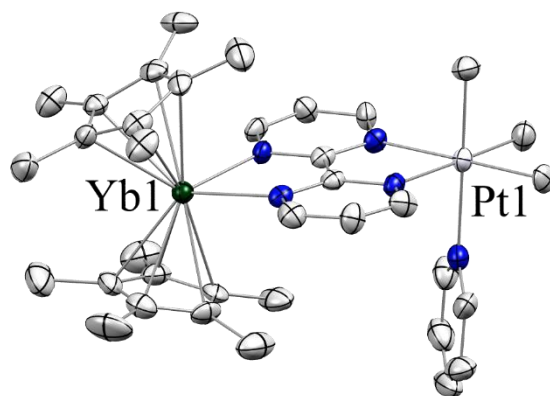


**Figure II.14.** ORTEP of **5<sup>+</sup>(py)** with thermal ellipsoids at 50 % level. Carbon atoms are in grey, nitrogen atoms in blue, the platinum atom in white, and the ytterbium atom in olive green. Hydrogen atoms have been removed for clarity.

Both **5** and **5<sup>+</sup>(py) OTf<sup>-</sup>** were analyzed by SQUID magnetometry. Both  $\chi T$  versus  $T$  plot recorded at 0.5 T revealed singlet ground states but the room temperature  $\chi T$  values were rather different (Figure II.15). In the case of **5<sup>+</sup>(py) OTf<sup>-</sup>**, the  $\chi T$  value at room temperature was  $2.21 \text{ cm}^3 \text{ K mol}^{-1}$  which means a less populated triplet state and, with the Bleaney-Bowers fit or the Lukens *et al.* model, the  $2J$  energy gap was estimated to be in between  $-240 \text{ cm}^{-1}$  and  $-220 \text{ cm}^{-1}$ . For **5**, the measured  $2.71 \text{ cm}^3 \text{ K mol}^{-1}$  value indicated that the triplet state was strongly populated which was close to the recorded value for **3** that have a triplet ground state ( $2.68 \text{ cm}^3 \text{ K mol}^{-1}$ ). The singlet-triplet energy gap was estimated, with the same methodology as before, to be in between  $-240 \text{ cm}^{-1}$  and  $-168 \text{ cm}^{-1}$ . This meant that replacing the iodide anion by a triflate fragment, opened back the access to singlet state reactivity without shutting down possible triplet state pathways. This result, added to the increased lability of the triflate anion, was thought to be the key to tackle down original reactivities and electrophilic C-H activation of methane.

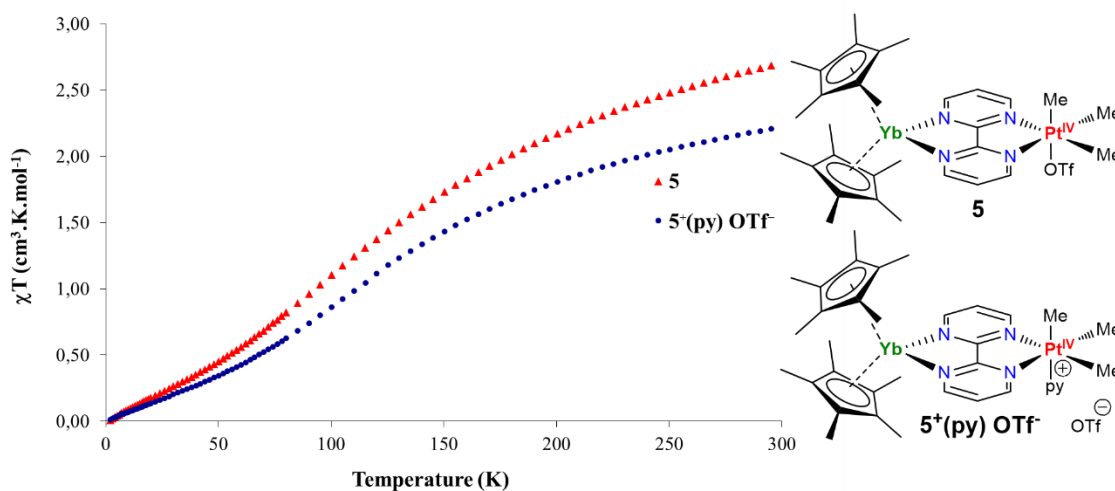


**Figure II.15.** Solid-state temperature-dependent magnetic susceptibility of **5** and **5<sup>+</sup>(py) OTf<sup>-</sup>** recorded at 0.5 T:  $\chi T$  vs T plot.

### III. Reactivity studies

#### III.A. Trials for mild condition C-H activation of methane and intrinsic reactivity of the high valent species

As **2** and **3**, were easily synthesized thanks to the group's experience on Pd and Ni analogous compounds, their reactivity toward methane was tested at relatively low pressure, at room temperature (1.2 bar), and monitored by  $^1\text{H}$  NMR. On one hand, **2** was thought to be able to perform the oxidative addition due to the stabilization of the  $\text{Pt}^{\text{IV}}$  oxidation state. On the other hand, **3** could be electrophilic enough to perform methane exchange reactions as reported with a Lu complex for instance.<sup>61</sup> Unfortunately, under these conditions, the hoped C-H oxidative addition of  $\text{CH}_4$  on **2**, the key step of Shilov or Periana systems, was not observed and no more success was encountered with **3**, even upon heating the solution. To definitely confirm this, trials will have to be performed at higher working pressure. To do so, one can think of reproducing Goldberg's group protocol since they published a study in which they performed similar reactions with ethene at pressure up to  $\sim 10$  bars in NMR tubes.<sup>62</sup> Although the violent thaw of  $\text{CH}_4$  upon unfreezing is not riskless, this could be an elegant alternative to a pressure bomb setup allowing to keep access to  $^1\text{H}$  NMR as it is the most relevant tool to observe potential reactivity.

Before performing the same methane reactivity test with **4**, its reactivity in solution in  $\text{tol-}d_8$ , under UV irradiation, was probed. In Puddephatt's work with the  $(\text{bipy})\text{PtMe}_4$  complex,<sup>57</sup> the photo-reactivity was proposed to result from the excitation of a Pt-C  $\sigma$  electron to the  $\pi^*$  system of the bipy ligand. Having strongly modified the ligand's electronic structure, the reactivity was expected to be

different with **4** and original. In the absence of any substrates **4** transformed slowly to a relatively clean set of signals from the  $^1\text{H}$  NMR point of view (Figure III.1).

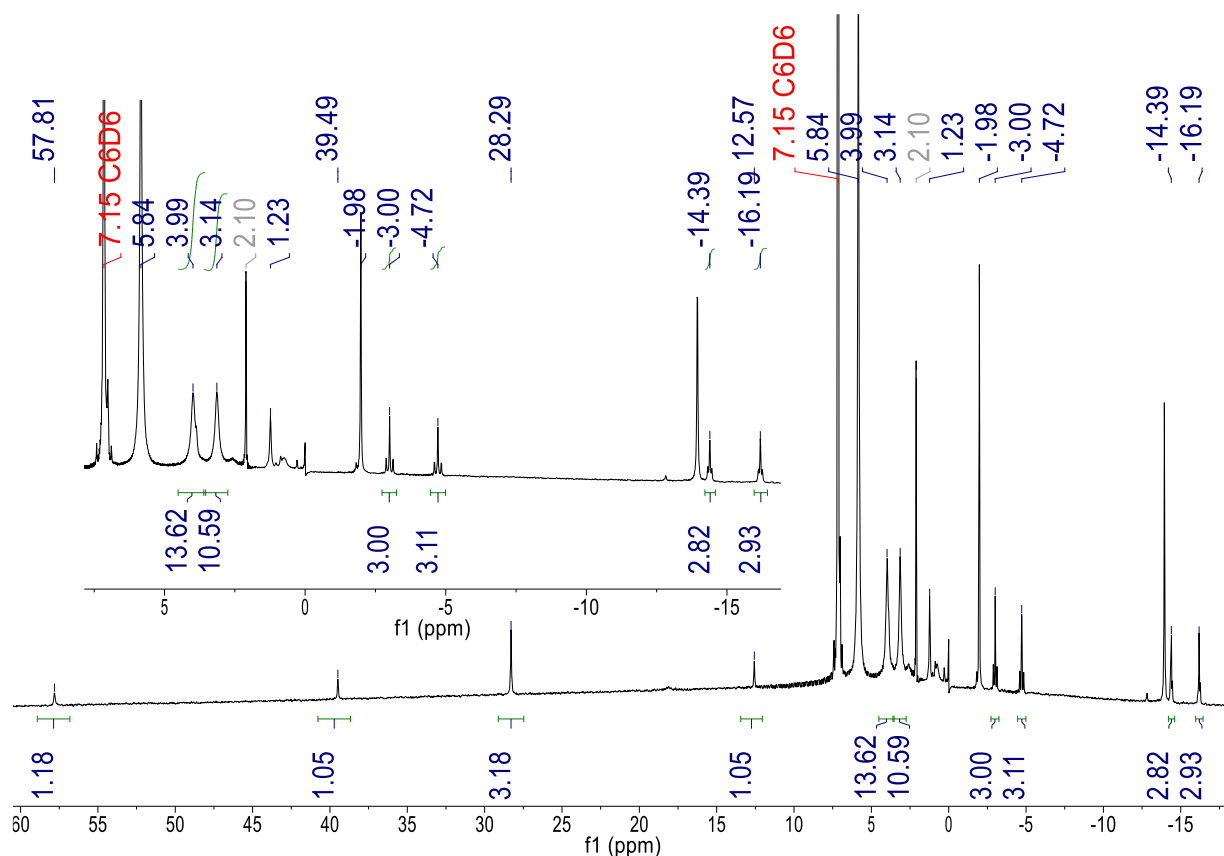


**Figure III.1.**  $^1\text{H}$  NMR spectrum of **4** recorded at 20 °C in  $\text{C}_6\text{D}_6$  after 2 hours under irradiation at 400 nm.

After two hours under irradiation at 400 nm, from a solution of **4** ( $\sim 5.10^{-4}$  M) in  $\text{C}_6\text{D}_6$ , the  $\text{Cp}^*$  signal was split into two signals that were shifted from 5.84 ppm to 3.99 ppm and 3.14 ppm with close to 15 H integrations each. While this was indicative of the loss of the  $\text{C}_{2v}$  symmetry, the alkyl signals were also split into two sets and found at -3.00 and -4.72 ppm for the equatorial ones and -14.39 and -16.19 ppm for the axial ones, all of them were integrated to *ca.* 3H. This means that not only the equatorial symmetry plane found in **4** was broken but also the axial one. Note that this transformation led to the only spectrum in which the  $^2J(^{195}\text{Pt}-\text{CH})$  coupling constants were observed for such paramagnetic species and were typical of tetraalkyl platinum species, 74 Hz for the equatorial  $J(\text{Pt}-\text{CH})$  and 43 Hz for the axial one.<sup>59,63</sup> In addition to these split signals another set of 4 signals was growing at 57.81 ppm (1H), 39.49 ppm (1H), 28.29 (3H), 12.57 (1H). The fact that both  $\text{Cp}^*$  signals and the four methyl signals were conserved was also indicating that the transformation most likely occurred on the bipym ligand body. With those observations in mind, a proposed formed complex would have a monofunctionalized bipym ligand by a methyl radical formed at the  $\text{Pt-Me}_4$  center of a second complex **4**. This would result in two different species, **4-hv** and **4-hv'**,  $\text{Cp}^*_2\text{Yb}(\text{Mebipym})\text{PtMe}_4$  and  $\text{Cp}^*_2\text{Yb}(\text{bipym})\text{PtMe}_3$  respectively (Figure III.2). It could also be



argued that **4-hv'** should also be observed but its paramagnetic nature might make it silent or its low stability could result in immediate degradation. Further UV irradiation to get a higher conversion toward these proposed species led to more products being formed, most likely because **4-hv** and **4-hv'** were not so stable under such conditions, and degradation of the sample was observed when the irradiation time was too long. Crystallization trials remained unsuccessful at different irradiation timing since it resulted in either recrystallisation of starting complex **4** or isolation of polycrystalline samples of no interest for single crystal XRD analysis. Eventually, **4** was tested toward methane activation (1.2 bar) and no sign of C-H activation was observed with or without UV irradiation.

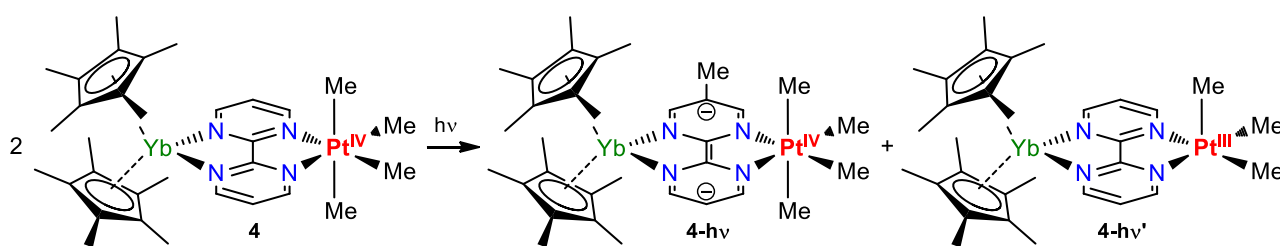


**Figure III.2.** Proposed reactivity of **4** under irradiation.

In the case of **5**, several solvents, such as thf-*d*<sub>8</sub>, C<sub>6</sub>D<sub>6</sub> or tol-*d*<sub>8</sub>, have been tested for reaction time of about 18 hours at room temperature. At this time of the reaction, characteristic <sup>1</sup>H NMR signals of **4** slowly appeared upon the disappearance of **5**. This transformation was not quantitative and was attributed to a ligand exchange between two complexes **5** due to the lability of the triflate anion. Unfortunately, the other expected product from such transformation a hypothetical Cp\*<sub>2</sub>Yb(bipym)PtMe<sub>2</sub>(OTf)<sub>2</sub> complex, **6**, was not observed nor isolated. The possible formation of **6** as a really unstable electrophilic intermediates was thought to be another reasonable candidate for mild conditions (1.2 bar) C-H activation of methane. Since nothing was observed with CH<sub>4</sub>, CD<sub>4</sub> was also used but no proton-deuterium scrambling was observed indicating that C-H activation remained unsuccessful for the whole series of compounds. Several subsequent trials were made to synthesize the expected Cp\*<sub>2</sub>Yb(bipym)PtMe<sub>3</sub>H starting from **3** in presence of KH or KBHEt<sub>3</sub> but the isolation of the obtained products from these attempts also remained unsuccessful. It however did not prevent the study of other type of reactivities, in order to use platinum's stability as a model compound for its Ni or Pd analogs.

### III.B. Exploring other reactivities

- *Trying to get a cationic monomethyl Pt<sup>II</sup> center.*

Knowing that the Pt<sup>II</sup> center in the system described herein should become more reactive by abstracting one of the Me groups as it was demonstrated by Bercaw and Labinger,<sup>13</sup> two strategies



were investigated to get our hands on a hypothetical  $[\text{Cp}^*_2\text{Yb}(\text{bipym})\text{PtMeL}]^+$  cation, L being a neutral coordinating ligand. The first one was to follow a similar protocol to the one used for the synthesis of **2**, but using the  $(\text{SMe}_2)_2\text{PtMeCl}$ .<sup>64</sup> This led to the isolation of the  $(\text{bipym})\text{PtMeCl}$  complex, **7**, and chloride abstraction by  $\text{AgSbF}_6$  salt yielded its cationic version  $(\text{bipym})\text{PtMe}(\text{py})$ , **7<sup>+</sup>(py) SbF<sub>6</sub><sup>-</sup>** (Figure III.3). However, from this point two issues had to be addressed. The first was the thermal instability of such compounds at room temperature in solution, probably due to intramolecular C-H activation of the pyridine ligand,<sup>13</sup> this should be solved by working at lower temperatures. The second problem was the presence of the divalent lanthanide incompatible fluorinated  $\text{SbF}_6^-$  anion. To solve this problem the  $\text{BPh}_4^-$  should be preferred but this hypothesis still has to be tested.

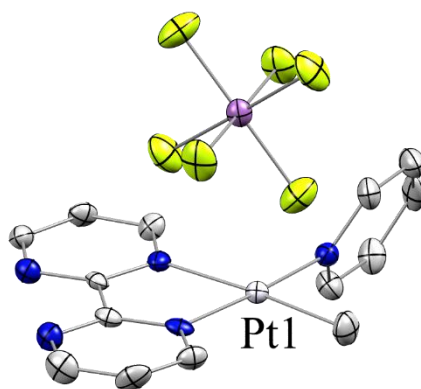


**Figure III.3.** ORTEP of **7<sup>+</sup> SbF<sub>6</sub><sup>-</sup>** with thermal ellipsoids at 50 % level. Carbon atoms are in grey, nitrogen atoms in blue, fluorine atoms in yellow, the antimony atom in pink, and the platinum atom in white. Hydrogen atoms have been removed for clarity.

Since this strategy seemed not trivial at the time, starting directly from **2** and abstracting one of its methyl groups was preferred. Two reagents were tested,  $\text{B}(\text{C}_6\text{F}_5)_3$  and  $\text{Ph}_3\text{C}^+ \text{BPh}_4^-$ ,<sup>65–68</sup> since the typical Brookhart's acid pathway was obviously incompatible with  $\text{Cp}^*$  ligands. Surprisingly both tests resulted in unexpected species and, in both cases, **2** got oxidized. On one hand  $\text{Ph}_3\text{C}^+ \text{BPh}_4^-$  led to a **2<sup>+</sup> BPh<sub>4</sub><sup>-</sup>** ionic pair and the XRD analysis revealed a  $\text{C}-\text{C}_{\text{bipym}}$  distance of 1.472(8) Å, indicating that the oxidation occurred on the bipym fragment. On the other hand,  $\text{B}(\text{C}_6\text{F}_5)_3$  assisted the  $\text{Pt}^{\text{II}}$  center into the activation of a *thf-d<sub>8</sub>* molecule, which was the solvent of the reaction, to form compound **8** (Figure III.4).

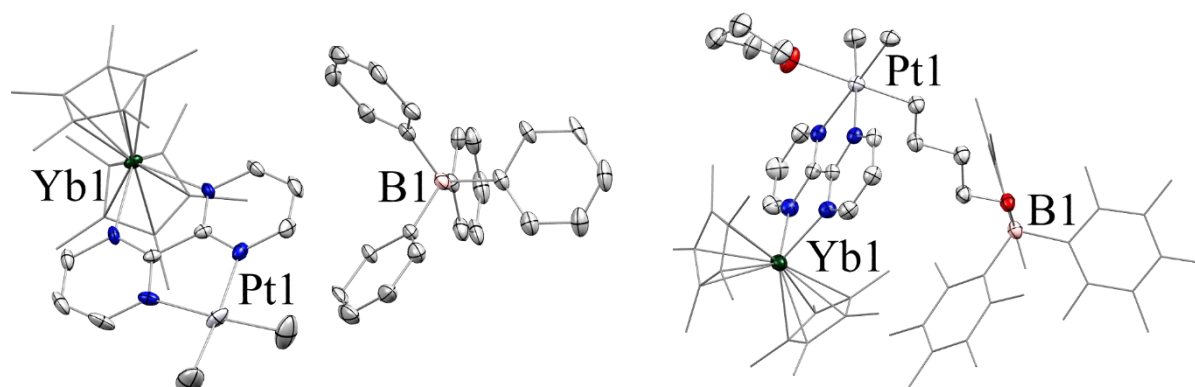


**Figure III.4.** ORTEPs of (left) **2**<sup>+</sup> **BPh<sub>4</sub>**<sup>-</sup> and (right) **8** with thermal ellipsoids at 50 % level. Carbon atoms are in grey, nitrogen atoms in blue, the platinum atom in white, and the ytterbium atom in olive green. Cp\* and C<sub>6</sub>F<sub>5</sub> ligands are represented in wireframe while hydrogen atoms have been removed for clarity.

This latter reactivity is typical of frustrated Lewis pair.<sup>69,70</sup> A comparative reaction with **1** and B(C<sub>6</sub>F<sub>5</sub>)<sub>3</sub> led to the same reactivity, although the transformation looked slower and only poorly diffracting crystals were obtained. This was not surprising considering that the Cp\*<sub>2</sub>Yb(bipym) fragment is most likely accelerating the reaction by stabilizing the resulting Pt<sup>IV</sup> center. Achieving such FLP reactivity remained of relative importance in that case, since more abundant metals are capable of doing so and the addition of the lanthanide moiety did not seem to induce a great change.<sup>71</sup> However, such behavior with Pt<sup>II</sup> was not reported, and it might deserve to be explored a bit further. As starting guesses, trials in absence of thf and in presence of more valuable FLP-reactive substrates, such as H<sub>2</sub> or terminal alkynes,<sup>72,73</sup> have to be prioritized to fully evaluate the potential of this system. Lastly, considering that these strategies to abstract a methyl group from **2** remained unsuccessful, although interesting, solving the issues with the pathway involving the cationization of **7**<sup>+</sup>(py) **SbF<sub>6</sub>**<sup>-</sup> probably is the best option left at hand to fulfill this goal.

#### ▪ *Reactivity toward simple borane reagents and hydroboration trials*

Since the investigations on the C-H activation of methane were found unfruitful, the reactivities of **1** and **2** toward X-H bonds (X = Si or B) were probed to potentially perform the hydrofunctionalization of double bonds. If silicon and boron-based reactivities were extensively studied with Pt,<sup>74</sup> they were mostly observed at the 0 oxidation state with silane or diboron species. While the several silane reagents tried were found non-reactive, the addition of catecholborane (HBcat) to **2** triggered a reaction. Although <sup>1</sup>H NMR analysis and crystallization trials did not allow the identification of the formed paramagnetic species, the hydroboration trial was attempted with a simple alkene, allylbenzene (ABz), to probe the reactivity of the in-situ formed species. Interestingly, at a 5 mol% loading of **2**, hydroboration of the allylbenzene was performed. However, the conversion

was only partial and another well-defined organic product, ( $\beta$ -methyl)styrene was easily identified (Figure III.5).

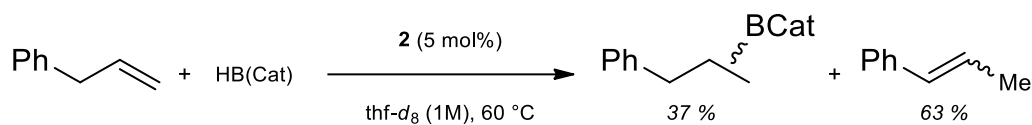


**Figure III.5.** First trial of catalyzed hydroboration of ABz with **2**.

This meant that in these conditions, there was a competition between the isomerization of the double bond to its thermodynamically more stable position and the hydroboration and the same result was obtained by replacing **2** with **1**. To quench one of those pathways, the HBcat amount was lowered from 100 to 5 mol% and the loading in Pt (**1** or **2**) was also decreased to 1 mol%. After 31h, a conversion of 73 % of the ABz was observed and almost complete conversion (<99 %) was obtained after 3 days (Figure III.6).

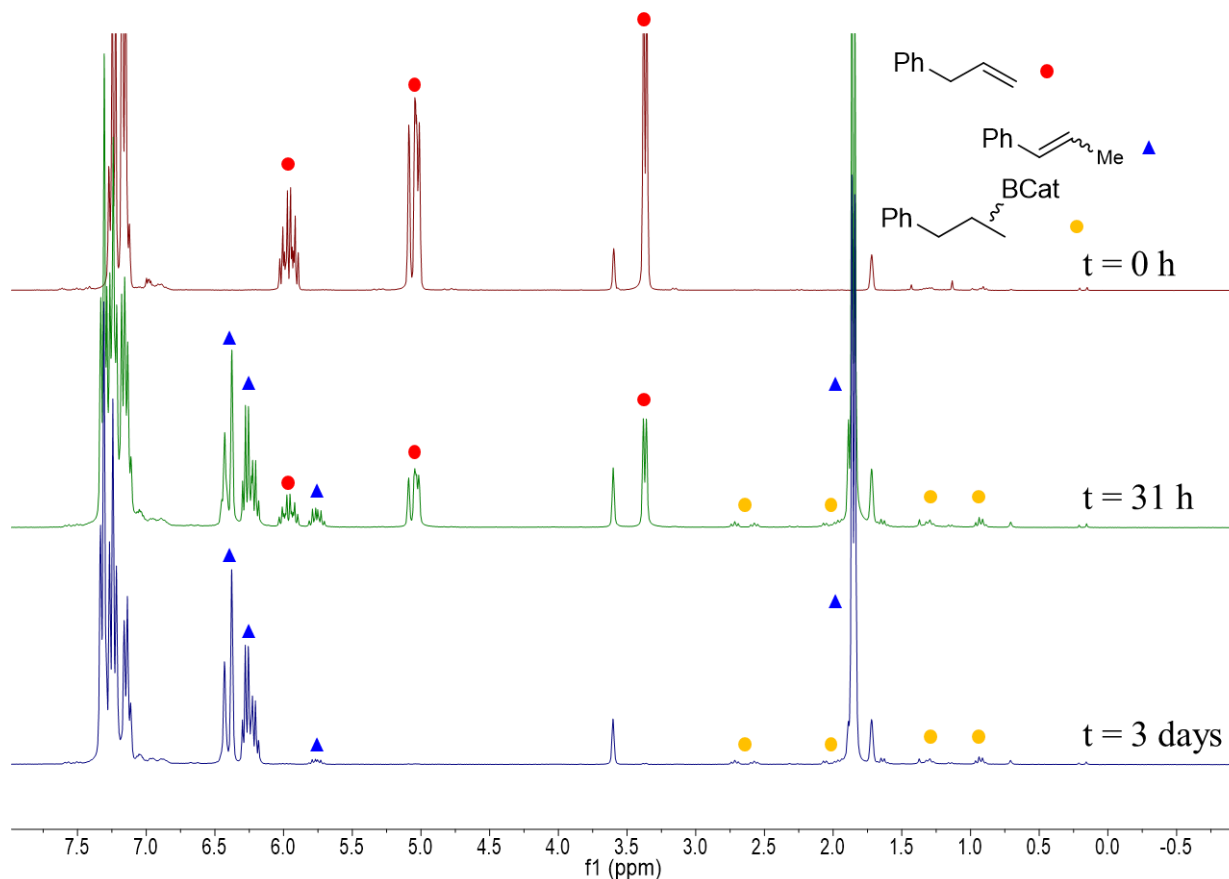


**Figure III.6.**  $^1\text{H}$  NMR monitored isomerization of ABz by 1 mol% of **2** in  $\text{thf-}d_8$ .

In these conditions only 2% of the ABz was hydroborated and to reduce this amount the loading in HBcat was later reduced to 2 mol %. To assess whether the  $\text{Cp}^*\text{Yb(bipym)}$  fragment was impacting the catalysis, both systems were monitored by  $^1\text{H}$  NMR overnight with another substrate the 4-phenyl-1-butene to also probe the chain walking potential of this transformation. As it can be observed in

Figure III.7, both systems evolved almost identically and no decent chain walking isomerization was observed. At this point, considering our system's performances, the lack of lanthanide-induced originality in the process and the fact that the most probable active species was a Pt-hydride which is a well-known catalyst for alkene isomerization, this catalytic system was not studied further to prioritize other projects. However, if its catalytic application remains to be enhanced, the reactivity between **1** or **2** and HBcat borane was a rare example of a B-H activation at a +II oxidation state group 10 metal center, especially with Pt, and was found to be a great tool to form in-situ reactive species from our heterobimetallic architectures.<sup>75–80</sup>

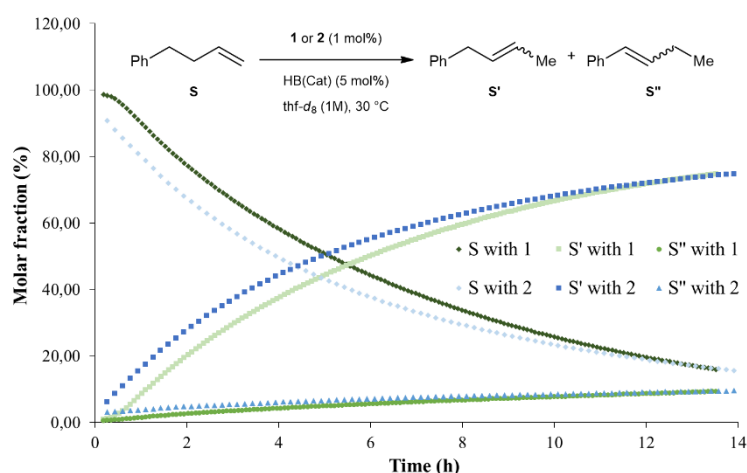


**Figure III.7.** Comparative conversion rates of the isomerization of 4-Ph-1-butene by 1 mol% of **1** (green labels) and **2** (blue labels).

## IV. Conclusion and perspectives

In this chapter, the platinum version of the Cp\*<sub>2</sub>Yb(bipym)MMe<sub>2</sub>, M being a group 10 transition metal, was synthesized as well as several resulting products of its oxidation by small molecules such as MeI or MeOTf. Intermediate valence behavior was characterized for all of them but **3**. This well-known phenomenon was triggered by the presence of a singlet ground state and a low-lying triplet state and was shown to be tunable upon ligand exchange on the Pt center, echoing to previous results on substituted redox-active ligand (RAL) systems.<sup>81</sup> The possibility to tune the singlet-triplet energy gap in such compounds was thought to be a prerequisite in order to control electronic-state-specific reactivity and activate or quench the undesired pathways at will. The increased electronic density surrounding the Pt center due to the bipym ligand reduction did not allow the C-H activation of methane under mild conditions. However, the parallel investigations led on the self-induced reactivity of **4** and **5** allowed to propose their most probable degradation product, **4-hv** and **6**. If the latter remains an elusive specie, its enhanced potential as an electrophilic activator, compared to **5**, needs to be explored to a greater extent. Preliminary reactivity trials toward the hydrofunctionalization of

alkenes were performed with cyclohexene but time constraints prevented further investigations. In the case of the photodegradation of **4**, although the fact that the reduced bipym ligand was most likely able to trap an in-situ formed radical was not desired, it constituted an original way to perform such reaction, echoing to a recent study made in the group where a similar reactivity was observed with a divalent samarium reduced benzophenone radical.<sup>82</sup> Comparative experiment with other in-situ photogenerated radical as well as with other Ln(II)-RAL systems are therefore needed to fully validate this hypothesis and, if applicable, evaluate the efficiency of such novel protocol (Figure IV.1). In a similar fashion, the investigations conducted on the isolation of a more reactive monomethyl cationic version of the heterobimetallic architecture did lead to unexpected results. While the FLP reactivity was intriguing and probably deserves some further attention, the most promising synthetical pathway remains to access a divalent lanthanide-compatible Pt precursor.

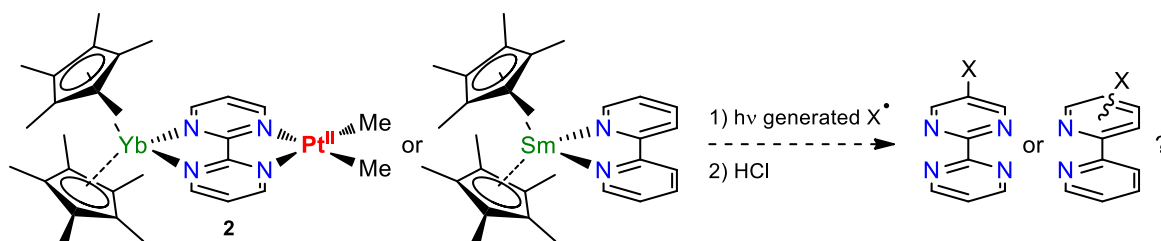


**Figure IV.1.** Perspective on photo-triggered mono-functionalization of bipym or bipy ligands.

Eventually, the reactivity study on B-H bond activation led to the first catalytic system ever developed with this kind of Ln-RAL-TM species, and while the catalytic performances was not improved by the addition of a lanthanide fragment, most likely because of platinum's redox chemistry being too rigid. These model reactivity studies with Pt remained to be extended, by switching to the more redox flexible Pd and especially Ni, as it will be illustrated in the upcoming chapter with the Ni analog of **2** as well as in the following one with the Pd analog of **4**.

## References

- (1) Seyferth, D. *Organometallics* **2001**, 20 (1), 2–6. <https://doi.org/10.1021/om000993+>.
- (2) Hunt, L. *Platin. Met. Rev.* **1894**, 28 (2), 76–84.
- (3) Anderson, J. S. *J. Chem. Soc.* **1934**, No. 0, 971–974. <https://doi.org/10.1039/JR9340000971>.
- (4) Flynn, J. H.; Hulburt, H. M. *J. Am. Chem. Soc.* **1954**, 76 (13), 3393–3396. <https://doi.org/10.1021/ja01642a010>.
- (5) Smidt, J.; Hafner, W.; Jira, R.; Sieber, R.; Sedlmeier, J.; Sabel, A. *Angew. Chemie Int. Ed. English* **1962**, 1 (2), 80–88. <https://doi.org/10.1002/anie.196200801>.
- (6) Halpern, J. *Discuss. Faraday Soc.* **1968**, 46 (0), 7–19. <https://doi.org/10.1039/DF9684600007>.
- (7) Goldshleger, F. N.; Tyabin, M. B.; Shilov, A. E.; Shteinman, A. A. *Russ. J. Phys. Chem.* **1969**, 43 (8), 1222–+.
- (8) Shilov, A. E. *Activation of Saturated Hydrocarbons by Transition Metal Complexes*; Springer, Netherlands, **1984**. <https://link.springer.com/book/9789027716286>.
- (9) Shilov, A. E.; Shul'pin, G. B. *Chem. Rev.* **1997**, 97 (8), 2879–2932. <https://doi.org/10.1021/cr9411886>.
- (10) Shilov, A. E.; Shteinman, A. A. *Coord. Chem. Rev.* **1977**, 24 (2–3), 97–143. [https://doi.org/10.1016/S0010-8545\(00\)80336-7](https://doi.org/10.1016/S0010-8545(00)80336-7).
- (11) Labinger, J. A.; Herring, A. M.; Lyon, D. K.; Luinstra, G. A.; Bercaw, J. E.; Horvath, I. T.; Eller, K. *Organometallics* **1993**, 12 (3), 895–905. <https://doi.org/10.1021/om00027a045>.
- (12) Stahl, S. S.; Labinger, J. A.; Bercaw, J. E. *J. Am. Chem. Soc.* **1996**, 118 (25), 5961–5976. <https://doi.org/10.1021/ja960110z>.
- (13) Holtcamp, M. W.; Labinger, J. A.; Bercaw, J. E. *J. Am. Chem. Soc.* **1997**, 119 (4), 848–849. <https://doi.org/10.1021/ja9620595>.
- (14) Labinger, J. A.; Bercaw, J. E. *J. Organomet. Chem.* **2015**, 793, 47–53. <https://doi.org/10.1016/j.jorganchem.2015.01.027>.
- (15) Rostovtsev, V. V.; Labinger, J. A.; Bercaw, J. E.; Lasseter, T. L.; Goldberg, K. I. *Organometallics* **1998**, 17 (21), 4530–4531. <https://doi.org/10.1021/om980541l>.
- (16) Periana, R. A.; Taube, D. J.; Evitt, E. R.; Löffler, D. G.; Wentrcek, P. R.; Voss, G.; Masuda, T. *Science (80-. )*. **1993**, 259 (5093), 340–343. <https://doi.org/10.1126/science.259.5093.340>.
- (17) Periana, R. A.; Taube, D. J.; Gamble, S.; Taube, H.; Satoh, T.; Fujii, H. *Science (80-. )*. **1998**, 280 (5363), 560–564. <https://doi.org/10.1126/science.280.5363.560>.
- (18) Kua, J.; Xu, X.; Periana, R. A.; Goddard, W. A. *Organometallics* **2002**, 21 (3), 511–525. <https://doi.org/10.1021/om0101691>.
- (19) Xu, X.; Kua, J.; Periana, R. A.; Goddard, W. A. *Organometallics* **2003**, 22 (10), 2057–2068. <https://doi.org/10.1021/om0202165>.
- (20) Villalobos, J. M.; Hickman, A. J.; Sanford, M. S. *Organometallics* **2010**, 29 (1), 257–262. <https://doi.org/10.1021/om900889k>.
- (21) Ahlquist, M.; Periana, R. A.; Goddard III, W. A. *Chem. Commun.* **2009**, No. 17, 2373–2375. <https://doi.org/10.1039/B821854D>.
- (22) Khan, M. S.; Haque, A.; Al-Suti, M. K.; Raithby, P. R. *J. Organomet. Chem.* **2015**, 793, 114–133. <https://doi.org/10.1016/j.jorganchem.2015.03.023>.
- (23) Labinger, J. A. *Chem. Rev.* **2017**, 117 (13), 8483–8496. <https://doi.org/10.1021/acs.chemrev.6b00583>.
- (24) Williams, B. S.; Holland, A. W.; Goldberg, K. I. *J. Am. Chem. Soc.* **1999**, 121 (1), 252–253. <https://doi.org/10.1021/ja982211y>.
- (25) Williams, B. S.; Goldberg, K. I. *J. Am. Chem. Soc.* **2001**, 123 (11), 2576–2587. <https://doi.org/10.1021/ja003366k>.

- (26) Vedernikov, A. N.; Binfield, S. A.; Zavalij, P. Y.; Khusnutdinova, J. R. *J. Am. Chem. Soc.* **2006**, *128* (1), 82–83. <https://doi.org/10.1021/ja0575171>.
- (27) Grice, K. A.; Goldberg, K. I. *Organometallics* **2009**, *28* (4), 953–955. <https://doi.org/10.1021/om8011272>.
- (28) Vedernikov, A. N. *Acc. Chem. Res.* **2012**, *45* (6), 803–813. <https://doi.org/10.1021/ar200191k>.
- (29) Sberegava, A. V.; Liu, W.-G.; Nielsen, R. J.; Goddard, W. A.; Vedernikov, A. N. *J. Am. Chem. Soc.* **2014**, *136* (12), 4761–4768. <https://doi.org/10.1021/ja501213w>.
- (30) Scheuermann, M. L.; Goldberg, K. I. *Chem. – A Eur. J.* **2014**, *20* (45), 14556–14568. <https://doi.org/10.1002/chem.201402599>.
- (31) Johansson, L.; Tilset, M.; Labinger, J. A.; Bercaw, J. E. *J. Am. Chem. Soc.* **2000**, *122* (44), 10846–10855. <https://doi.org/10.1021/ja0017460>.
- (32) MacDonald, M. G.; Kostelansky, C. N.; White, P. S.; Templeton, J. L. *Organometallics* **2006**, *25* (19), 4560–4570. <https://doi.org/10.1021/om060137j>.
- (33) McKeown, B. A.; Foley, N. A.; Lee, J. P.; Gunnoe, T. B. *Organometallics* **2008**, *27* (16), 4031–4033. <https://doi.org/10.1021/om8006008>.
- (34) Luedtke, A. T.; Goldberg, K. I. *Angew. Chemie Int. Ed.* **2008**, *47* (40), 7694–7696. <https://doi.org/10.1002/anie.200800524>.
- (35) Rendina, L. M.; Puddephatt, R. J. *Chem. Rev.* **1997**, *97* (6), 1735–1754. <https://doi.org/10.1021/cr9704671>.
- (36) Byers, P. K.; Canty, A. J.; Skelton, B. W.; White, A. H.; Whitelb, A. H. *Organometallics* **1990**, *9* (3), 826–832. <https://doi.org/10.1021/om00117a044>.
- (37) Canty, A. J.; Gardiner, M. G.; Jones, R. C.; Rodemann, T.; Sharma, M. *J. Am. Chem. Soc.* **2009**, *131* (21), 7236–7237. <https://doi.org/10.1021/ja902799u>.
- (38) Goudy, V.; Jaoul, A.; Cordier, M.; Clavaguéra, C.; Nocton, G. *J. Am. Chem. Soc.* **2017**, *139* (31), 10633–10636. <https://doi.org/10.1021/jacs.7b05634>.
- (39) Wang, D.; Moutet, J.; Tricoire, M.; Cordier, M.; Nocton, G. *Inorganics* **2019**, *7* (5), 58. <https://doi.org/10.3390/inorganics7050058>.
- (40) Scott, J. D.; Puddephatt, R. J. *Organometallics* **1983**, *2* (11), 1643–1648. <https://doi.org/10.1021/om50005a028>.
- (41) Sutcliffe, V. F.; Young, G. B. *Polyhedron* **1984**, *3* (1), 87–94. [https://doi.org/10.1016/S0277-5387\(00\)84718-X](https://doi.org/10.1016/S0277-5387(00)84718-X).
- (42) Scott, J. D.; Puddephatt, R. J. *Organometallics* **1986**, *5* (8), 1538–1544. <https://doi.org/10.1021/om00139a005>.
- (43) Mironov, O. A.; Bischof, S. M.; Konnick, M. M.; Hashiguchi, B. G.; Ziatdinov, V. R.; Goddard, W. A.; Ahlquist, M. M.; Periana, R. A. *J. Am. Chem. Soc.* **2013**, *135* (39), 14644–14658. <https://doi.org/10.1021/ja404895z>.
- (44) Berg, D. J.; Boncella, J. M.; Andersen, R. A. *Organometallics* **2002**, *21* (22), 4622–4631. <https://doi.org/10.1021/om020477e>.
- (45) Berg, D. J.; Boncella, J. M.; Andersen, R. A. *Organometallics* **2002**, *21* (22), 4622–4631. <https://doi.org/10.1021/om020477e>.
- (46) Schultz, M.; Boncella, J. M.; Berg, D. J.; Tilley, T. D.; Andersen, R. A. *Organometallics* **2002**, *21* (3), 460–472. <https://doi.org/10.1021/om010661k>.
- (47) Nabavizadeh, S. M.; Habibzadeh, S.; Rashidi, M.; Puddephatt, R. J. *Organometallics* **2010**, *29* (23), 6359–6368. <https://doi.org/10.1021/om100810t>.
- (48) Nasser, N.; Fard, M. A.; Boyle, P. D.; Puddephatt, R. J. *J. Organomet. Chem.* **2018**, *858*, 67–77. <https://doi.org/10.1016/j.jorganchem.2017.12.043>.
- (49) Mala, B.; Murtagh, L. E.; Farrow, C. M. A.; Akien, G. R.; Halcovich, N. R.; Allinson, S. L.; Platts, J. A.; Coogan, M. P. *Inorg. Chem.* **2021**, *60* (10), 7031–7043. <https://doi.org/10.1021/acs.inorgchem.0c03553>.
- (50) Schultz, M.; Boncella, J. M.; Berg, D. J.; Tilley, T. D.; Andersen, R. A. *Organometallics* **2002**, *21* (3), 460–472. <https://doi.org/10.1021/om010661k>.

- (51) Booth, C. H.; Kazhdan, D.; Werkema, E. L.; Walter, M. D.; Lukens, W. W.; Bauer, E. D.; Hu, Y.-J.; Maron, L.; Eisenstein, O.; Head-Gordon, M.; Andersen, R. A. *J. Am. Chem. Soc.* **2010**, *132* (49), 17537–17549. <https://doi.org/10.1021/ja106902s>.
- (52) Walter, M. D.; Berg, D. J.; Andersen, R. A. *Organometallics* **2006**, *25* (13), 3228–3237. <https://doi.org/10.1021/om051051d>.
- (53) Van Vleck, J. H. *The Theory of Electric and Magnetic Susceptibilities*, Clarendon Press, Oxford, UK, **1965**.
- (54) O'Connor, C. J. *Progress in Inorganic Chemistry*. January 1, **1982**, pp 203–283. <https://doi.org/10.1002/9780470166307.ch4>.
- (55) Lukens, W. W.; Walter, M. D. *Inorg. Chem.* **2010**, *49* (10), 4458–4465. <https://doi.org/10.1021/ic100120d>.
- (56) Lukens, W. W.; Magnani, N.; Booth, C. H. *Inorg. Chem.* **2012**, *51* (19), 10105–10110. <https://doi.org/10.1021/ic300037q>.
- (57) Hux, J. E.; Puddephatt, R. J. *J. Organomet. Chem.* **1988**, *346* (1), C31–C34. [https://doi.org/10.1016/0022-328X\(88\)87020-7](https://doi.org/10.1016/0022-328X(88)87020-7).
- (58) Hux, J. E.; Puddephatt, R. J. *J. Organomet. Chem.* **1992**, *437* (1), 251–263. [https://doi.org/10.1016/0022-328X\(92\)83448-Q](https://doi.org/10.1016/0022-328X(92)83448-Q).
- (59) Clegg, D. E.; Hall, J. R.; Swile, G. A. *J. Organomet. Chem.* **1972**, *38* (2), 403–420. [https://doi.org/10.1016/S0022-328X\(00\)83343-4](https://doi.org/10.1016/S0022-328X(00)83343-4).
- (60) Hill, G. S.; Puddephatt, R. J. *J. Am. Chem. Soc.* **1996**, *118* (36), 8745–8746. <https://doi.org/10.1021/ja961404n>.
- (61) Watson, P. L. *J. Am. Chem. Soc.* **1983**, *105* (21), 6491–6493. <https://doi.org/10.1021/ja00359a023>.
- (62) Luedtke, A. T.; Goldberg, K. I. *Inorg. Chem.* **2007**, *46* (21), 8496–8498. <https://doi.org/10.1021/ic701504z>.
- (63) Hux, J. E.; Puddephatt, R. J. *Inorganica Chim. Acta* **1985**, *100* (1), 1–5. [https://doi.org/10.1016/S0020-1693\(00\)88287-0](https://doi.org/10.1016/S0020-1693(00)88287-0).
- (64) Hill, G. S.; Irwin, M. J.; Levy, C. J.; Rendina, L. M.; Puddephatt, R. J.; Andersen, R. A.; Mclean, L. *Inorganic Syntheses*. **1998**, pp 149–153. <https://doi.org/10.1002/9780470132630.ch25>.
- (65) Bochmann, M.; Lancaster, S. J. *J. Organomet. Chem.* **1992**, *434* (1), C1–C5. [https://doi.org/10.1016/0022-328X\(92\)83360-T](https://doi.org/10.1016/0022-328X(92)83360-T).
- (66) Hill, G. S.; Rendina, L. M.; Puddephatt, R. J. *J. Chem. Soc. Dalt. Trans.* **1996**, No. 9, 1809–1813. <https://doi.org/10.1039/DT9960001809>.
- (67) Piers, W. E.; Chivers, T. *Chem. Soc. Rev.* **1997**, *26* (5), 345–354. <https://doi.org/10.1039/CS9972600345>.
- (68) Campos, J.; López-Serrano, J.; Peloso, R.; Carmona, E. *Chem. – A Eur. J.* **2016**, *22* (19), 6432–6457. <https://doi.org/10.1002/chem.201504483>.
- (69) Chapman, A. M.; Haddow, M. F.; Wass, D. F. *J. Am. Chem. Soc.* **2011**, *133* (45), 18463–18478. <https://doi.org/10.1021/ja207936p>.
- (70) Zhao, X.; Lough, A. J.; Stephan, D. W. *Chem. – A Eur. J.* **2011**, *17* (24), 6731–6743. <https://doi.org/10.1002/chem.201100203>.
- (71) Stephan, D. W. *Science (80-. )*. **2016**, *354* (6317), aaf7229. <https://doi.org/10.1126/science.aaf7229>.
- (72) Stephan, D. W. W.; Erker, G. *Angew. Chemie Int. Ed.* **2010**, *49* (1), 46–76. <https://doi.org/10.1002/anie.200903708>.
- (73) Stephan, D. W. *J. Am. Chem. Soc.* **2021**, *143* (48), 20002–20014. <https://doi.org/10.1021/jacs.1c10845>.
- (74) Obligacion, J. V.; Chirik, P. J. *Nature Reviews Chemistry* **2018**, pp 15–34. <https://doi.org/10.1038/s41570-018-0001-2>.
- (75) Kabalka, G. W.; Narayana, C.; Reddy, N. K. *Synth. Commun.* **1994**, *24* (7), 1019–1023. <https://doi.org/10.1080/00397919408020777>.
- (76) Pereira, S.; Srebnik, M. *Tetrahedron Lett.* **1996**, *37* (19), 3283–3286. [https://doi.org/10.1016/0040-4039\(96\)00576-X](https://doi.org/10.1016/0040-4039(96)00576-X).



- (77) Pender, M. J.; Wideman, T.; Carroll, P. J.; Sneddon, L. G. *J. Am. Chem. Soc.* **1998**, *120* (35), 9108–9109. <https://doi.org/10.1021/ja981622b>.
- (78) Lillo, V.; Mata, J. A.; Segarra, A. M.; Peris, E.; Fernandez, E. *Chem. Commun.* **2007**, No. 21, 2184–2186. <https://doi.org/10.1039/B700800G>.
- (79) Yu, X.-H.; Cao, K.; Huang, Y.; Yang, J.; Li, J.; Chang, G. *Chem. Commun.* **2014**, *50* (35), 4585–4587. <https://doi.org/10.1039/C3CC49203F>.
- (80) Touney, E. E.; Van Hoveln, R.; Buttke, C. T.; Freidberg, M. D.; Guzei, I. A.; Schomaker, J. M. *Organometallics* **2016**, *35* (20), 3436–3439. <https://doi.org/10.1021/acs.organomet.6b00652>.
- (81) Nocton, G.; Booth, C. H.; Maron, L.; Ricard, L.; Andersen, R. A. *Organometallics* **2014**, *33* (23), 6819–6829. <https://doi.org/10.1021/om500843z>.
- (82) Jaoul, A.; Yang, Y.; Casaretto, N.; Clavaguéra, C.; Maron, L.; Nocton, G. *Chem. Commun.* **2020**, *56* (79), 11875–11878. <https://doi.org/10.1039/D0CC05164K>.

# Chapter IV

## Low-valent N-heteroaromatic-Ni catalysts for alkene isomerization

### I. Background on homogeneous Ni catalysis

#### I.A. Nickel-catalyzed cross-couplings

- *Pioneering works before decades past in the shade of palladium*

One of the first occurrences of homogeneous catalysis involving organonickel species was discovered in the 1920s with the report of an odd reactivity when catalytic amounts of  $\text{NiCl}_2$  were exposed to a  $\text{PhMgBr}$  reagent triggering the “absorption” of ethylene.<sup>1</sup> It has to be noted that the presence of ethylbenzene, styrene or biphenyl products, already implied at that time an uncontrolled nickel catalyzed C-C coupling reaction (Figure I.1).

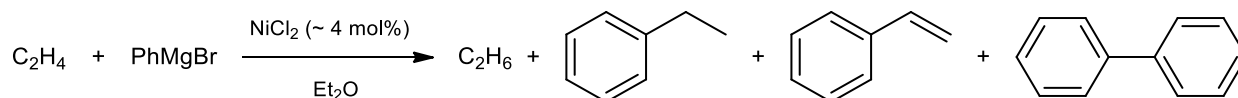


**Figure I.1.** André Job's preliminary observations.

This curious behavior remained mostly unnoticed but led Corriu and Masse to rationalize this reactivity in 1972 thus becoming the historical fathers of Ni catalyzed cross-coupling reactions along with Kumada *et al.* who reported similar findings at the same time (Figure I.2).<sup>2,3</sup> However, because of the capricious nature of nickel that 1912 Nobel Prize winner Paul Sabatier described as a “Spirited horse”,<sup>4</sup> the more docile palladium quickly replaced it as the center of attention in this type of reactions.<sup>5</sup> Indeed, palladium systems were easier to handle and to understand, hence facilitating the development of more efficient catalysts in most described coupling reactions.<sup>6,7</sup> This overall

superiority of palladium versus nickel led to numerous industrial applications.<sup>8–11</sup> Ultimately in 2010, the Nobel Prize in Chemistry was delivered to R. F. Heck, E. Negishi, and A. Suzuki “for palladium-catalyzed cross couplings in organic synthesis” thus witnessing the utmost importance of their findings.<sup>12</sup> Yet, palladium was remaining a rare and expensive metal. Therefore, the need for more sustainable processes slowly led nickel catalysis to be back in the game over the last 20 years.<sup>13,14</sup>

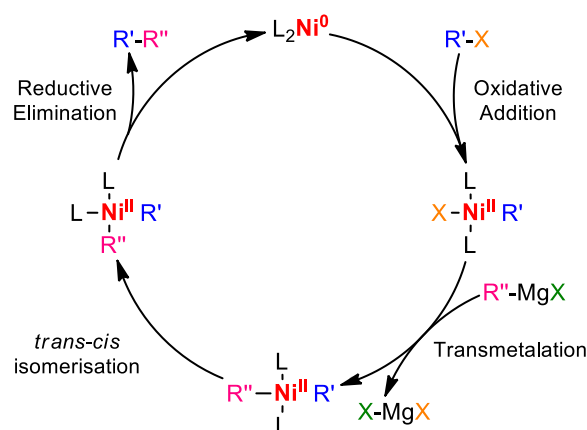


**Figure I.2.** Kumada-Corriu catalytic cycle, a proposed  $\text{Ni}^0/\text{Ni}^{\text{II}}$  mechanism.

▪ *A renewal through unusual oxidation states reactivity*

If the rich redox chemistry of nickel was first assessed as a drawback in earlier works, it is now more thought of as a tool to trigger original reactivities.<sup>7,15</sup> It was notably highlighted by works from the groups of Sanford and Mézailles who isolated high valent nickel complexes at the formal oxidation states +III and +IV.<sup>16,17</sup> This resulted in original C-C and C-F bonds formation with standard two-electron processes involving  $\text{Ni}^{\text{I}}/\text{Ni}^{\text{III}}$  oxidation states instead of the traditional  $\text{Ni}^0/\text{Ni}^{\text{II}}$  (Figure I.3 and Figure I.4).<sup>18</sup>

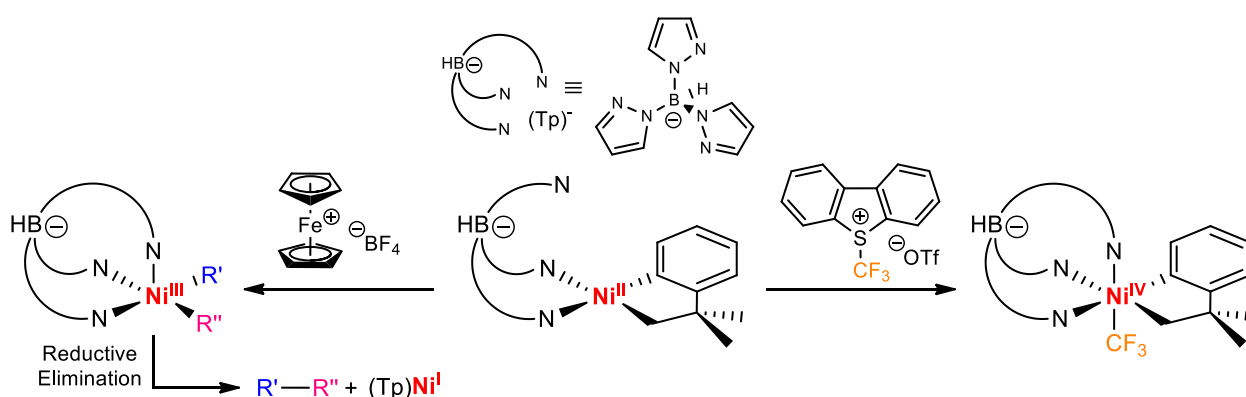


**Figure I.3.** Sanford and coworkers' tris(pyrazolyl)borate-based high-valent Ni complexes.<sup>16,18</sup>

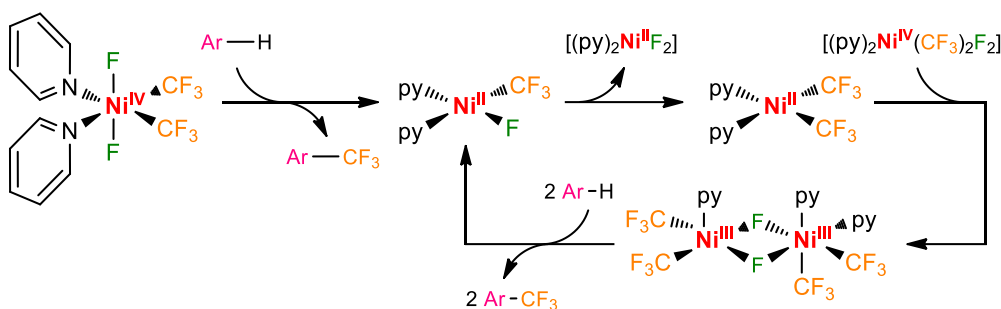


**Figure I.4.** Mézailles and coworkers' Ni-mediated trifluoromethylation of aromatic C(sp)<sup>2</sup>-H bonds.<sup>17</sup>

Additionally, these systems were also found to be involved in successive one-electron processes for radical C-C bond formation.<sup>17,19</sup> This potency to perform radical reactivity was notably developed independently by the groups of Hu and Weix.<sup>20,21</sup> They both unveiled the importance of the already proposed alkyl radical formation from halogenoalkane at a Ni<sup>II</sup> center<sup>22</sup> and applied it in catalytic systems.<sup>23</sup> Another outstanding example of the use of one electron processes in nickel catalysis was reported by the groups of Doyle and MacMillan who developed dual iridium-nickel photocatalysis.<sup>24</sup> In their system, both two electrons related Ni<sup>0</sup>/Ni<sup>II</sup> and Ni<sup>I</sup>/Ni<sup>III</sup> couples were used in typical oxidative addition/reductive elimination steps that were linked by one-electron processes triggered by the iridium photoredox cycle (Figure I.5).

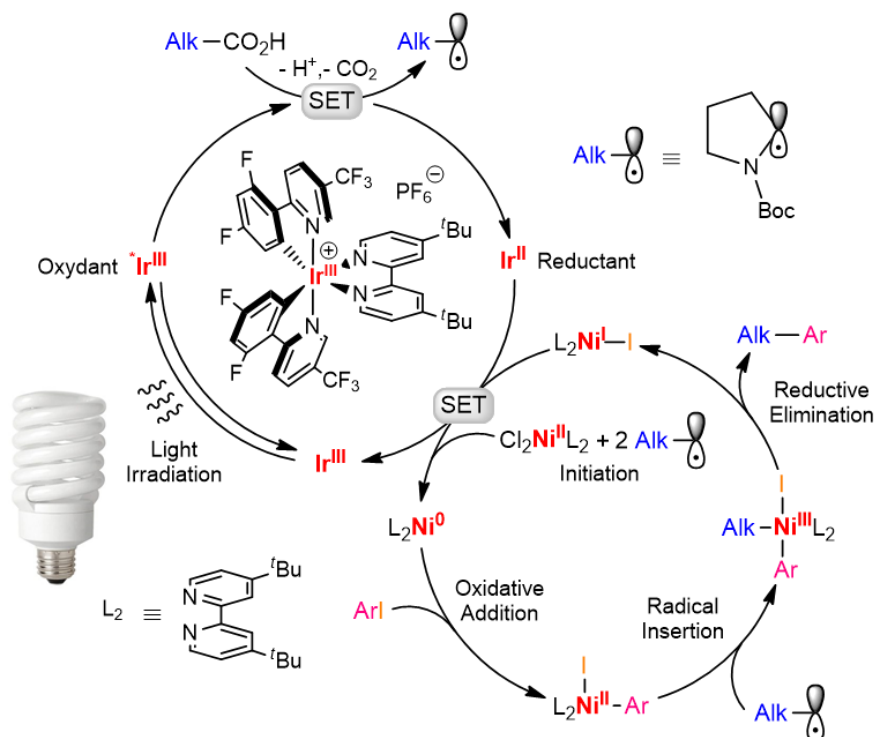


**Figure I.5.** MacMillan-Doyle dual photocatalysis system (adapted from ref<sup>24</sup>).

The tour-de-force in this system resided in achieving to merge those two cycles together. If this process was also developed with other transition metals,<sup>25–29</sup> the fine-tuning of the photoredox processes<sup>30–32</sup> combined with non-innocent ligands-based Ni complexes opened the way for the

development of multiple new systems making dual photocatalysis with nickel efficient toward an increasing number of transformations and substrates.<sup>33</sup>

▪ *The importance of the metal-ligand pair*

The fine choice of the ligand is a key step in nickel catalysis and redox-active ligands are known to tune the properties of a transition metal center.<sup>34,35</sup> A perfect example of this metal-ligand pair behavior can be found in Vicic *et al.* works on terpyridine (tpy) Ni complexes.<sup>36,37</sup> In those (tpy)NiX systems, X being a monoanionic ancillary ligand, two limit mesomeric forms had to be considered to judge whether the nickel was in +I or +II oxidation state: (tpy<sup>•-</sup>)Ni<sup>II</sup>X or (tpy)Ni<sup>I</sup>X (Figure I.6). When X = Me, the radical was mostly localized on the tpy  $\pi^*$  body thanks to the  $\sigma$ -donating properties of the Me ligand while when X = Br, the electronic density was best found on the  $d_{x^2-y^2}$  orbital of the metal.<sup>38</sup> However, these descriptions remained limit forms, since in the Me case 10% residual spin density was still localized on the Ni center.

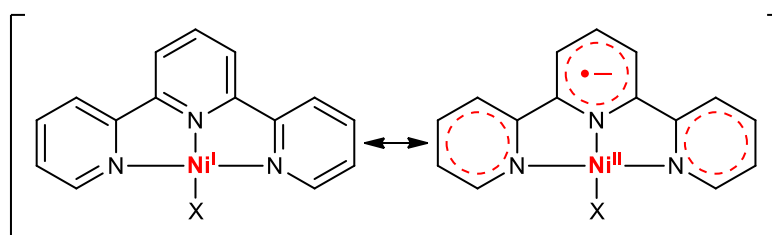


**Figure I.6.** Mesomeric forms of (tpy)NiX complexes.

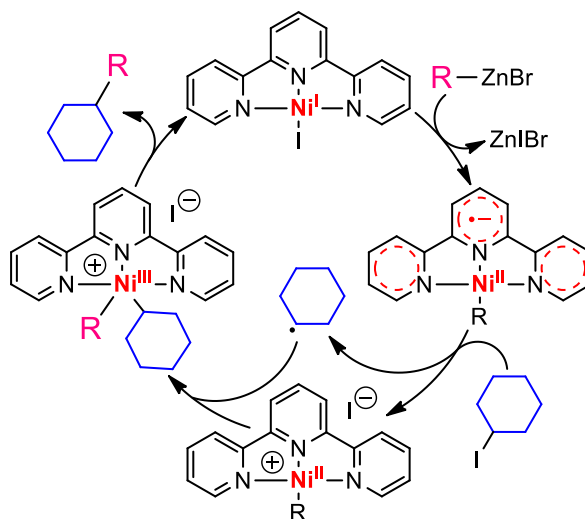


**Figure I.7.** Proposed catalytic system by Vicic and coworkers for the (tpy)Ni-mediated Negishi coupling.

The mechanistic and theoretical studies of (tpy)NiMe induced Negishi-type cross coupling reactions with alkyl halides unveiled the importance of such difference.<sup>39,40</sup> It ended up with a proposed mechanism not involving a typical Ni<sup>0</sup>/Ni<sup>II</sup> mechanism but rather a “significantly ligand-

based” radical reactivity of the  $(\text{tpy}^{\bullet})\text{Ni}^{\text{II}}\text{R}$  ( $\text{R}$  = alkyl ligand) toward the alkyl iodine coupling partner (Figure I.7).

Yet, in the latter statement, something remains to be questioned. Although the spin density was mainly localized on the ligand, this kind of behavior could also rise from a multi-state reactivity since the remaining 10% spin density localized on the nickel center could be the trigger of the reactivity. In other terms, since from the EPR and DFT point of view, the  $(\text{tpy})\text{NiR}$  complex was roughly considered as  $= 0.9 (\text{tpy}^{\bullet})\text{Ni}^{\text{II}}\text{R} + 0.1 (\text{tpy})\text{Ni}^{\text{I}}\text{R}$ , which mesomeric form, the former or the latter, was triggering the reactivity? At the moment no multiconfigurational study has been reported to tackle this question however recent studies are always going further to get a better understanding of these radical transformations at  $\text{Ni}^{\text{I}}$  centers.<sup>41–43</sup>

## I.B. Toward alkene isomerization

### ▪ Recent breakthroughs with low-valent Ni catalysts

With this growing interest for  $\text{Ni}^{\text{I}}$  species in catalysis,<sup>15</sup> one striking original development was recently published by Schoenebeck and coworkers who developed an olefin isomerization catalytic system using a simple dimeric N-heterocyclic carbene (NHC)  $\text{Ni}^{\text{I}}$  precursor (Figure I.8.left).<sup>44</sup> Historically, alkene isomerization was mostly dominated by the high performances of rare and precious metals hydrides.<sup>45</sup> In a similar fashion as coupling catalysis, there has been a recent growth in interest for the early-transition metals in this field.<sup>46</sup> In this context Schoenebeck’s findings of an efficient, E-selective NHC- $\text{Ni}^{\text{I}}$  catalyst applicable to a wide range of substrates in mild conditions was really astonishing. Thanks to a newly proposed metalloradical induced 1,3-H atom relocation mechanism, their system was even capable of performing chain walking isomerization.<sup>47–49</sup> More recently a  $\text{Ni}^0$ -phosphine system was also reported with in-depth mechanistic investigations and a proposed reaction pathway with two alkenes reacting together at the same Ni center (Figure I.8.right).<sup>50</sup>

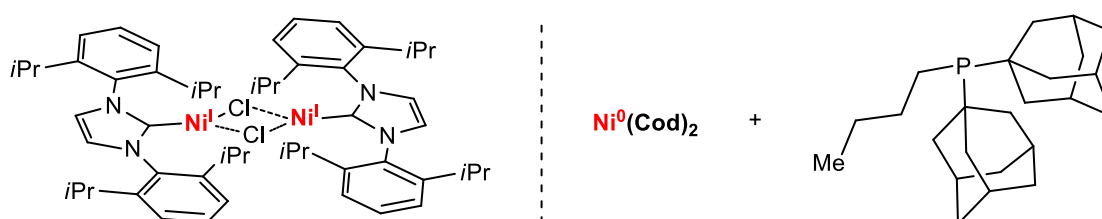


**Figure I.8.** Schoenebeck's (left) and Iwamoto's (right) catalysts.

▪ *A heterobimetallic architecture to tune the metal-ligand pair electronics*

In those two systems, only ancillary ligands were used at two different oxidation states, hence questioning whether the  $\text{Ni}^{\text{I}}$  oxidation state was the trigger of the reactivity or a remarkable enhancement of low-valent nickel's propensity to perform such transformation. Moreover, the metal-ligand pair's influence on cross-coupling systems had already been discussed. It was therefore thought-provoking to also imagine how the tuning of a redox-active ligands' electronic properties would influence another transformation such as alkene isomerization.

Among the heterobimetallic complexes recently synthesized in the group,  $\text{Cp}^*_2\text{Yb}(\text{bipym})\text{NiMe}_2$  complex,<sup>51</sup> **1**, was studied for its reactivity with CO and it was concluded that the  $\text{Ni}^{\text{II}}$ -acyl intermediate after CO insertion was stabilized thanks to the  $\pi$ -donating properties of the lanthanide-bipym moiety (Figure I.9). However, the impact of such electron rich environment on low-valent Ni catalysis remained to be studied. A supposed  $\text{Ni}^0$  species was formed by the reductive elimination of acetone in the preceding example. Yet, the *in-situ* formed ketone was thought to be a potential threat for the lanthanide-bipym moiety that could trigger the reversibility of the electron transfer upon its coordination to the oxophilic lanthanide ion.<sup>52–54</sup> That is why another reductive reactivity was searched to easily form bimetallic Yb-Ni species with a low-valent Ni center that could be engaged in alkene isomerization.

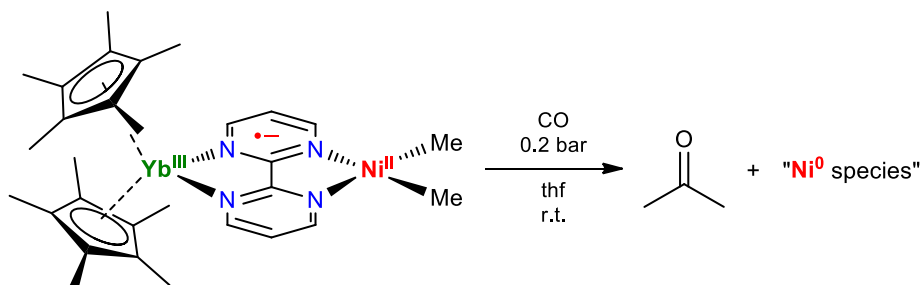


Figure I.9. Previous results obtained with the  $\text{Cp}^*_2\text{Yb}(\text{bipym})\text{NiMe}_2$  complex **1**.<sup>51</sup>

## II. Heterobimetallic Yb-Ni catalyst for alkene isomerization

### II.A. Developing facile access to a low-valent Ni center

Inspired by the results obtained in Chapter III, the reactivity of **1** with boranes was probed and **1** was found to react instantaneously with catecholborane (HBCat) in thf. If  $^1\text{H}$  NMR spectroscopy analysis in  $\text{thf-}d_8$  of the reaction mixture did not present any peaks that could be attributed to a resulting organometallic species, new diamagnetic signals were found. A multiplet characteristic of a catecholboron body yet slightly shifted compared to HBCat and two singlets at 0.65 ppm and 0.17 ppm. The relative integrations of the two former signals were 4:3 while the latter signal corresponded

to methane meaning that methylcatecholborane (MeBCat) was also formed during the reaction.<sup>55</sup> This reactivity was likely the result of oxidative addition of the B-H bond to the Ni<sup>II</sup> center followed by two reductive eliminations yielding the two aforementioned products and a low-valent Yb-Ni species. A titration of **1** by HBCat monitored by <sup>1</sup>H NMR in thf-*d*<sub>8</sub> confirmed this hypothesis, one equivalent of HBCat was enough to suppress the signals of **1** while 1 eq. of MeBCat and methane were quantitatively formed (Figure II.1). Similar results were obtained by titrating the monometallic analogous complex (bipy)NiMe<sub>2</sub>, **2**, however dark solid appeared rapidly. This was attributed to the decomposition of **2** since lacking the stabilizing and solubility enhancing Cp\*<sub>2</sub>Yb moiety. To further confirm the Ni<sup>0</sup> oxidation state, HBCat was added to **2** in presence of the Ni<sup>0</sup> stabilizing 1,5-cyclooctadiene (Cod) ligand. It immediately resulted in the deep blue coloration of the mixture due to the formation of the known (bipy)Ni(Cod) complex which was identified by <sup>1</sup>H NMR.<sup>56</sup>

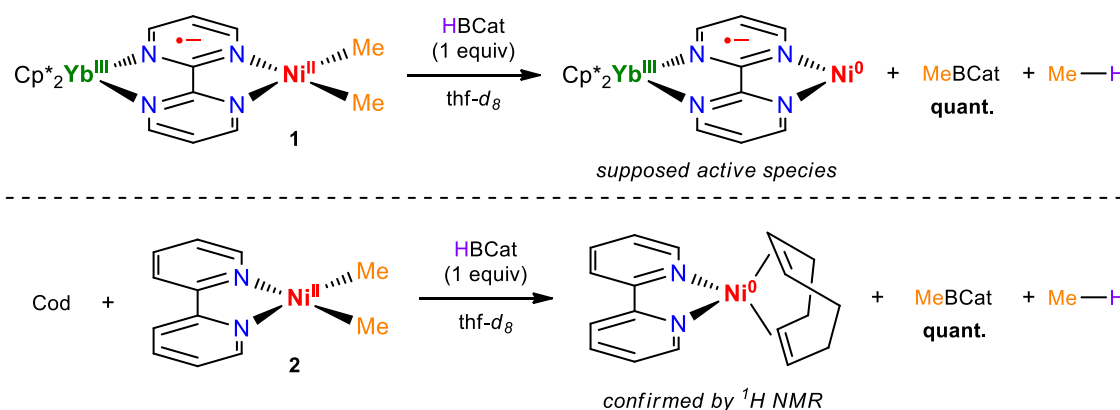


**Figure II.1.** Reduction of **1** and **2** to low-valent Ni species mediated by HBCat.

This 0 formal oxidation state for **2** was also confirmed by theoretical computations performed at the DFT level of theory on the (bipy)Ni(Cod) complex. As expected for a 3d<sup>10</sup> Ni(0) complex, the 5 HOMOs were mainly centered on the metal while the LUMO was mainly composed of the b<sub>2</sub> symmetry π\* orbital of the bipy ligand. Although the oxidation state of the Ni center seemed clear for **2**, no similar Cod trapping was observed with **1**, the obtained silent <sup>1</sup>H NMR spectrum indicated the presence of highly paramagnetic species and doubt remained on whether a Ni<sup>0</sup> center was indeed formed or not.

## II.B. Catalytic reactivity of the *in-situ* formed Yb-Ni species

### ▪ Optimization of the conditions

To evaluate and compare the reactivity of both **1** and **2**, test reactions were launched with 1 mol% of the pre-catalyst, 5 mol% of HBCat, and the allylbenzene (**A**) reference substrate at 30 °C in thf-*d*<sub>8</sub> and monitored by <sup>1</sup>H NMR spectroscopy.<sup>57</sup> The reaction was surprisingly clean and selective



toward alkene isomerization, almost no trace of side products was observed (< 1% hydroboration). While **1** was found to be an efficient pre-catalyst considering the low catalyst loading (98 % conversion in 3.5 days), **2** only showed low activity (25 % conversion after 3.5 days). Screening of the optimal conditions was therefore performed only with **1** and the results are summarized in Table II.1. Out of the three solvents tested (thf, toluene and chlorobenzene), thf turned out to be the best choice. Increasing the catalyst loading to 2 mol% only led to a more viscous mixture with poor improvement of the reaction rates while 0.5 mol% loading was considered to induce a too significant decrease of the conversion speed. It is however important to note that a decent conversion (86%) was achieved with such low loading after 3.5 days and that the catalyst was still active after 4.5 days which illustrated well the robustness of this heterobimetallic system. At 1 mol% loading, increasing the temperature to 60 °C fastened the reaction without impacting the stability of the catalyst.

**Table II.1.** Summary of the screening of the best catalytic conditions on **A**:

Entry	Solvent	Pre-catalyst	Time	Catalyst loading	Temperature	Conversion
1	thf- <i>d</i> <sub>8</sub>	<b>1</b>	16 h	1%	30 °C	55%
			22.5 h			67%
			3.5 days			97%
2	thf- <i>d</i> <sub>8</sub>	<b>2</b>	16 h	1%	30 °C	5%
			22.5 h			7%
			3.5 days			18%
3	thf- <i>d</i> <sub>8</sub>	<b>1</b>	16 h	2%	30 °C	64%
			22.5 h			74%
			3.5 days			95%
4	thf- <i>d</i> <sub>8</sub>	<b>1</b>	16 h	0.5%	30 °C	26%
			22.5 h			35%
			3.5 days			76%
			4.5 days			83%
5	thf- <i>d</i> <sub>8</sub>	<b>1</b>	16 h	1%	60 °C	>99 %
6	tol- <i>d</i> <sub>8</sub>	<b>1</b>	16 h	1%	30 °C	25%
			22.5 h			30%
			3.5 days			57%
7	PhCl	<b>1</b>	1.5 h	1%	60 °C	13 %
			15 h			58 %
			21 h			59 %
			3.5 days			76 %

To assess whether the catalysis was homo or heterogeneous, a mercury drop test was performed and the initial rates of the reaction were compared to the one from the standard procedure. Since no difference was observed, it was concluded that the process was homogeneous.

▪ *Probing of the reactivity for different substrates*

With the optimal conditions at hand (Figure II.3), various substrates were chosen to test the selectivity and the limits of the catalyst (Table II.2). Only unfunctionalized substrates were considered to avoid compatibility issues between the organoytterbium fragment and oxygenated or halogenated functional groups.

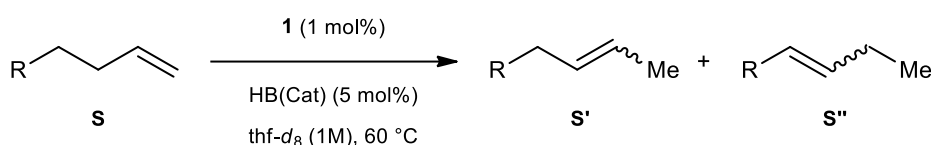


**Figure II.2.** Optimal catalytic conditions and isomerization patterns.

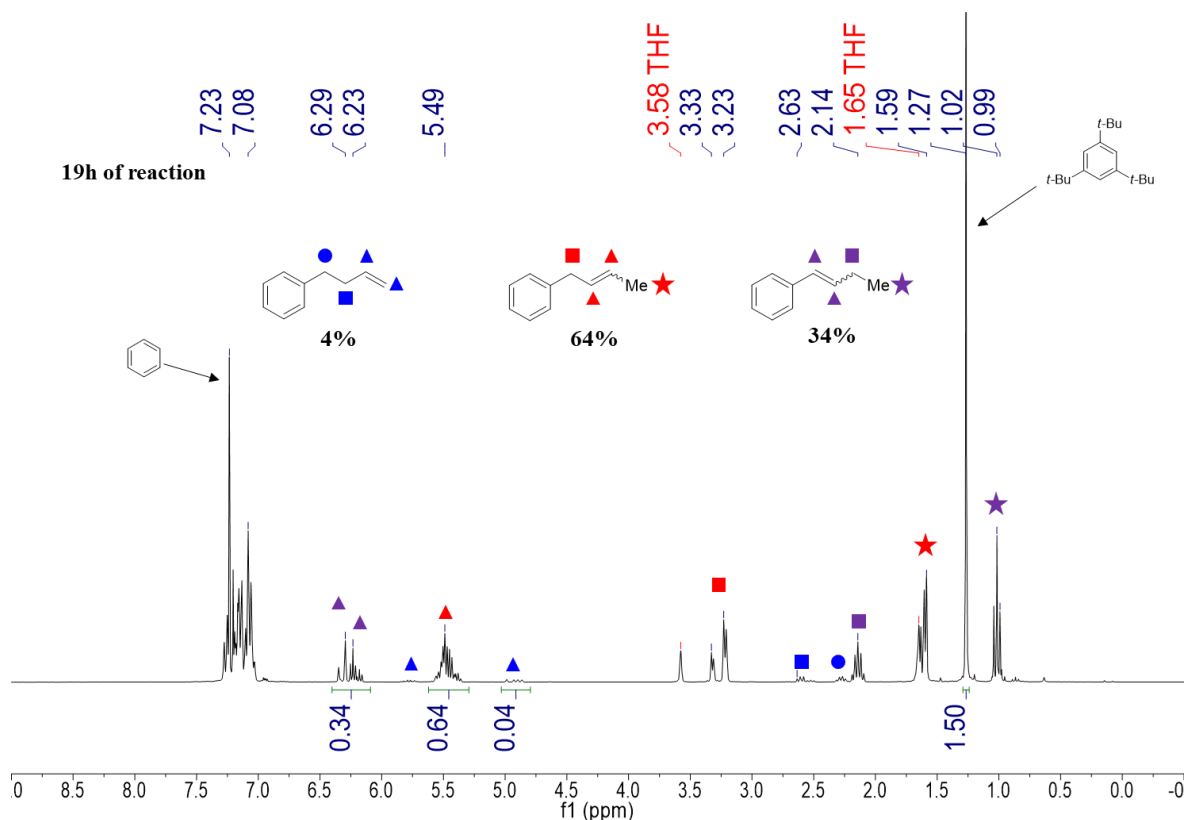


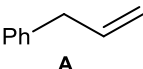
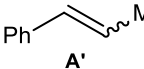
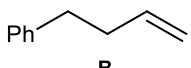
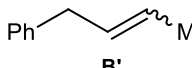
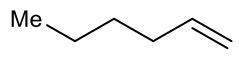
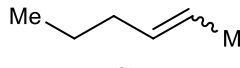
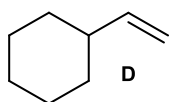
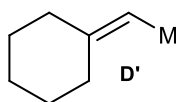
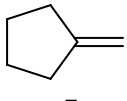
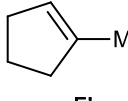
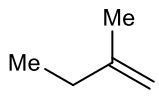
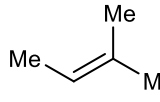
**Figure II.3.** <sup>1</sup>H NMR spectrum in thf-*d*<sub>8</sub> of the isomerization of **B** by 1 mol% of **1** at 60 °C, t=19 h. Relevant peaks are assigned and (tBu)<sub>3</sub>benzene serves as internal reference.

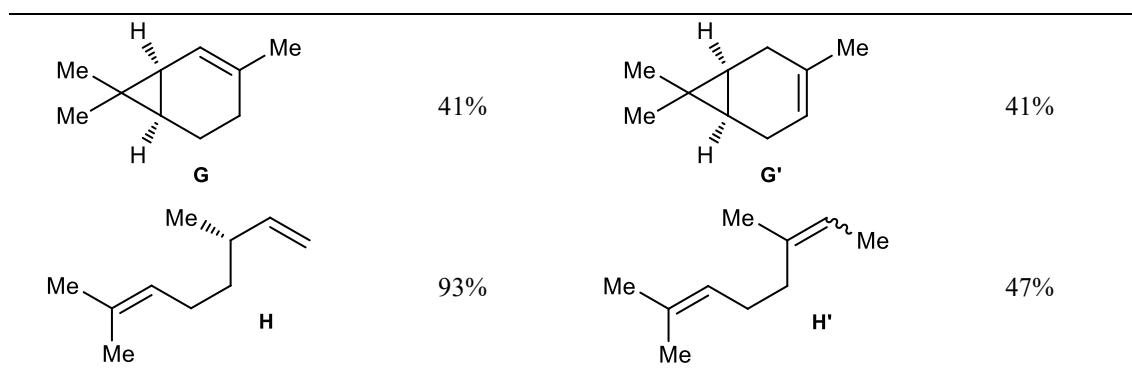
The conversion of 4-phenyl-1-butene (**B**) was close to total (96 %) after 19 h resulting in a mixture of the two possible isomerized products 1-phenyl-2-butene (**B'**) and 1-phenyl-1-butene (**B''**) with a 67% selectivity in favor of **B'**, decreased to 49% after 5.5 days of reaction. This result

highlighted the impact of the sterics of the substrates on the reaction rates while unveiling a controllable selectivity for the mono-isomerization product (Figure II.3).

This selectivity was improved when the thermodynamic driving force of the reaction, the formation of the styrene fragment, was removed as observed with 1-hexene (**C**). 2-hexene (**C'**) was the major product, formed with 85% yield after 19 h of reaction when 96% of **C** was converted. The selectivity only slightly decreased upon reaching a conversion of 98%, with a yield of 79% for **C'** after 5.5 days, while the quantity of 3-hexene (**C''**) rose from 11% to 19% in the meantime. To further probe the steric influence of the olefin substrates, vinylcyclohexane (**D**) was used. The allylic substitution was shown to induce a slight decrease of conversion compared to **C** (83.5% in 19 h and 98% after 5.5 days). In a similar fashion, bulkier substrates, methylenecyclopentane (**E**), 2-methylbutene (**F**) and (+)-2-carene (**G**), were not fully isomerized even after 5.5 days. Few diene substrates were also tested such as vinylcyclohexene and 1,7-octadiene. In the first case, the conversion was surprisingly low compared to **D** while the interpretation of the isomerization of 1,7-octadiene remained limited due to the overlapping between the peaks of the nine possible isomers. The last substrate studied, (+)-citronellene (**H**), was found to be an excellent example to observe the different isomers formed while confirming the mono-isomerization selectivity toward **H'**.

**Table II.2.** Conversion and yield for the major products<sup>a</sup>:

Substrate	Conversion <sup>b</sup>	Main product	Selectivity <sup>b</sup>
 <b>A</b>	>99% <sup>c</sup>	 <b>A'</b>	/
 <b>B</b>	96%, <sup>d</sup> >99%	 <b>B'</b>	64%, <sup>d</sup> 49%
 <b>C</b>	96%, <sup>d</sup> 98%	 <b>C'</b>	85%, <sup>d</sup> 79%
 <b>D</b>	99%	 <b>D'</b>	50%
 <b>E</b>	84%	 <b>E'</b>	70%
 <b>F</b>	73%	 <b>F'</b>	/



<sup>a</sup>Reaction conditions: alkene (0.5 mmol), **1** (5  $\mu$ mol), HBCat (25  $\mu$ mol) in *thf-d*<sub>8</sub> (1M) at 60°C during 5.5 days.

<sup>b</sup>Determined by <sup>1</sup>H NMR using 1,3,5-tri-(*tert*-butyl)benzene or benzene as internal standards.

<sup>c</sup>After 3.5 days of reaction. <sup>d</sup>After 19 h of reaction.

## II.C. Mechanistic insights

This novel catalytic system was found rather efficient with various substrates which was different from the Ni<sup>0</sup>-phosphine recently reported (the reactivity was limited to allylbenzene derivatives). Yet, compared to the Ni<sup>I</sup>-NHC system, it didn't perform as well in term of conversion speed and chain-walking isomerization. This intermediate position in terms of performances could be the result of the odd metal-ligand pair at stake here and therefore questioned which reaction mechanism was followed as well as the role of the oxidation state of the Ni center present in each system.

### ■ The known mechanisms

Among the different mechanisms proposed for alkene isomerization systems, two main families can be found: the metal-hydride-based mechanisms and the  $\pi$ -allyl hydride shift ones.<sup>58</sup> The first type is characterized by the presence *in-situ* of an external metal-hydride complex that performs a 1,2 oxidative addition on the C-C double bond, leading to a metal-alkyl complex that regenerates the catalyst upon  $\beta$ -hydride elimination (Figure II.4.A). This is the main mechanism presented in the literature and it is mostly found with precious metal hydride catalyst,<sup>45</sup> although some examples are also reported with Co and Ni.<sup>59–61</sup> In this metal-hydride family, a diradical mechanism has also been proposed for a Co-salen complex that is able to perform radical hydrogen atom transfer (HAT) (Figure II.4.B).<sup>62</sup> In the other main family, the  $\pi$ -allyl hydride shift, upon coordination of the metal center to the C-C double bond, a C-H activation occurs with the formation of a metal-allyl-hydride intermediate that performs a 1,3-HAT to yield the isomerized product (Figure II.4.C). In this mechanism, there is, therefore, no external hydride species since the mechanism is concerted. Examples of this mechanism are found with Zr, Ru or the Ni<sup>0</sup>-phosphine aforementioned.<sup>47,50,63</sup> By carefully studying their Ni<sup>I</sup>-

NHC system, Schoenebeck *et al.* reported a variation of this mechanism involving a metalloradical intermediate (Figure II.4.D). This made the C-H bond cleavage and H-atom relocation much more efficient allowing fast conversion at room temperature with a 5 mol% catalyst loading. In order to identify this mechanism, they performed several experiments such as deuterium labeling studies and radical clock tests.

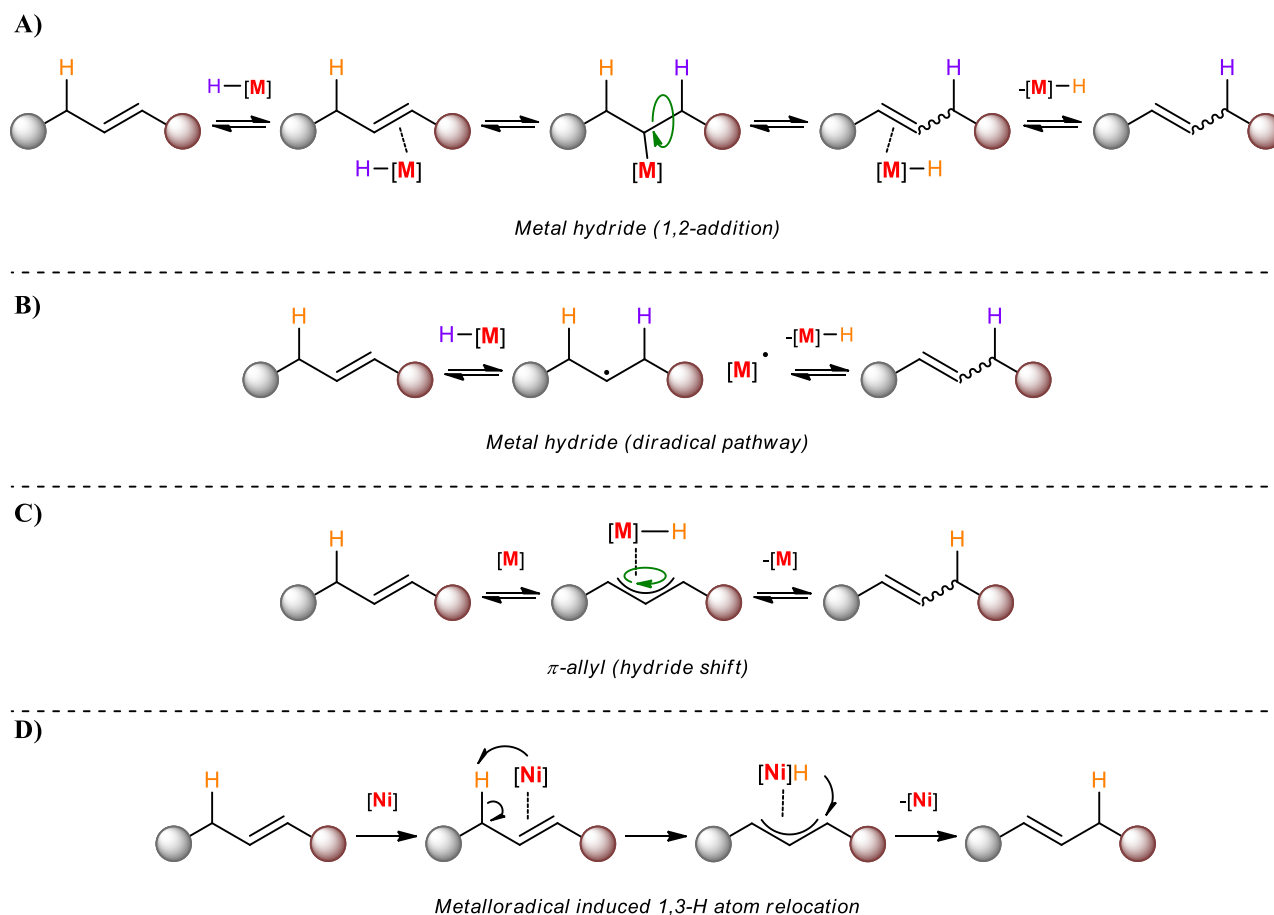


**Figure II.4.** The different proposed mechanisms for the alkene isomerization.

To assess which type of mechanism was at stake with pre-catalyst **1**, a first test was performed by adding  $\text{CCl}_4$  right after the addition of HBCat. The presence of  $\text{CCl}_4$  triggered an instantaneous degradation of the catalyst, yet no chloroform was observed as it should have been the case with persistent metal-hydride species. A similar test with 9,10-dihydroanthracene added to the catalytic system did not hamper the kinetics of the system, also pointing toward a  $\pi$ -allyl sort of mechanism.

#### ▪ Deuterium labelling studies

To get a deeper understanding of this system, deuterium-labeled experiments were conducted. No deuterium incorporation from the solvent was detected, and when the experiment was performed with **A- $d_2$**  (deuterated on the allylic positions), the isomerization yielded no sign of the intermolecular hydrogen shift proposed by Iwamoto *et al.* for their  $\text{Ni}^0$ -phosphine system.<sup>50</sup> To definitely discard a

potential metal-hydride type of mechanism, a deuterium scrambling control experiment between **A**- $d_2$  and **B** was also started (Figure II.5). Considering the similar rates of reaction for both substrates, if an external metal-hydride was performing the isomerization, the resulting products would be **A'**- $d_{2-x-y}$ , **B'**- $d_x$  and **B''**- $d_y$  (x and y representing the deuterium incorporation in **B'** and **B''**). The absence of these partially deuterated **B'**- $d_x$  and **B''**- $d_y$  products was confirmed by the  $^1\text{H}$  NMR analysis of the reaction mixture while no deuterium loss was observed in the formed **A'**- $d_2$ . These results added to the  $\text{CCl}_4$  and the 9,10-dihydroanthracene tests permitted to definitely discard the possible metal-hydride pathway in favor of a  $\pi$ -allyl mechanism.

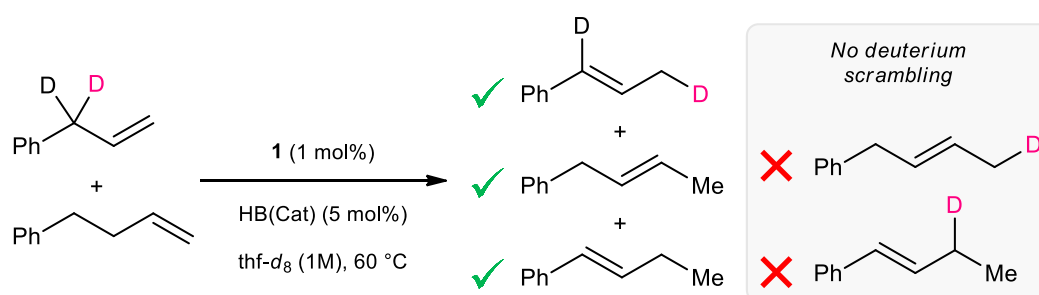


**Figure II.5.** Deuterium labelling cross-over experiment between **A**- $d_2$  and **B**.

#### ▪ Radical clock experiments

At this point a thought-provoking question remained about the role of the lone electron lying on the  $\pi^*$ -system of the bipym ligand, which was antibonding with the Ni d-orbital. In group 10 chemistry, this is known to stabilize +II and especially +IV oxidation states for the metal centers thanks to the increased  $\pi$ -donating properties of the ligands.<sup>51,53</sup> Moreover, some of these redox-active ligands were shown to circumvent the metal reactivity by inducing a ligand triggered radical reactivity as discussed before.<sup>35,64,65</sup> A radical clock experiment with the substituted vinylcyclopropane substrate **cis-I** was conducted with **1**, as reported in Schoenebeck's paper. They proposed that thanks to the metalloradical species formed on the carbon atom next the cyclopropane, the latter was opened, leaving the phenyl group in free rotation and allowing the isomerization to **trans-I** (Figure II.6).<sup>66,67</sup> After several hours of reaction with **1**, signal for the **trans-I** compound were observed and up to 34 % conversion was obtained after 12 days.

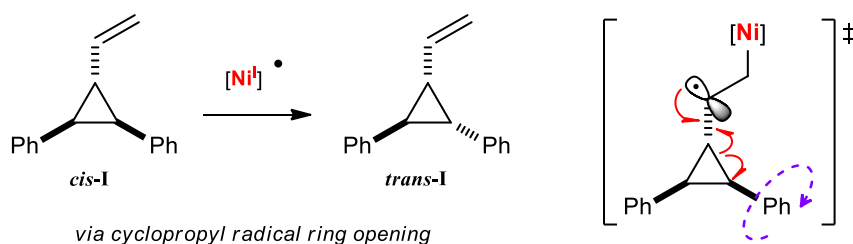


**Figure II.6.** Isomerization of **cis-I** due to the radical ring opening of the cyclopropane.

Since the test was positive, it pointed either toward a formal  $\text{Ni}^{\text{I}}$  active species or a  $\text{Ni}^0$  induced radical reactivity. To address this question, the synthesis of the new heterobimetallic  $\text{Cp}^*_2\text{Eu}(\text{bipym})\text{NiMe}_2$ , **3**, was performed. Since the  $\text{Cp}^*_2\text{Eu}$  fragment is known to be way less reductive than its ytterbium analog (-1.22 V vs SCE and -1.78 V vs SCE respectively),<sup>68</sup> it should result in the Eu center staying divalent and the bipym ligand remaining neutral. After a crystallization in benzene, the XRD analysis revealed the expected compound **3** (Figure II.7).

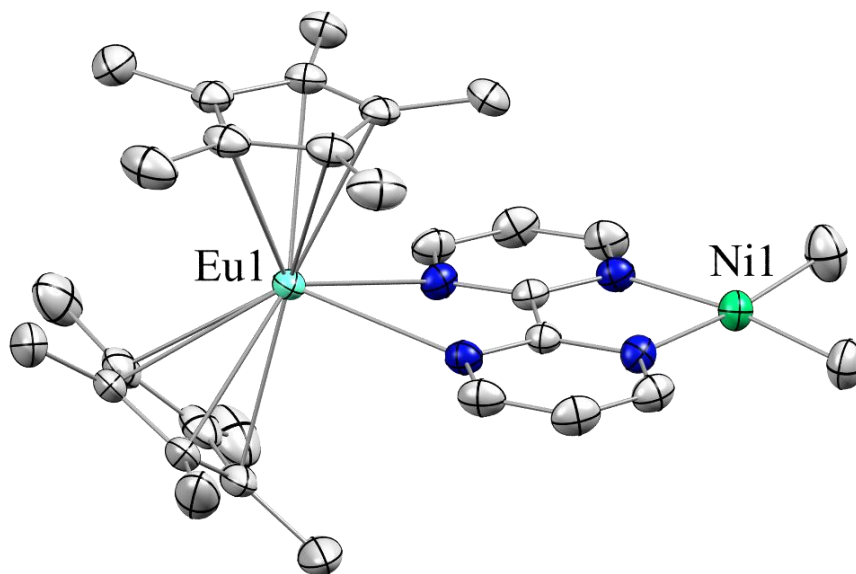


**Figure II.7.** ORTEP of **3** with thermal ellipsoids at 50 % level.

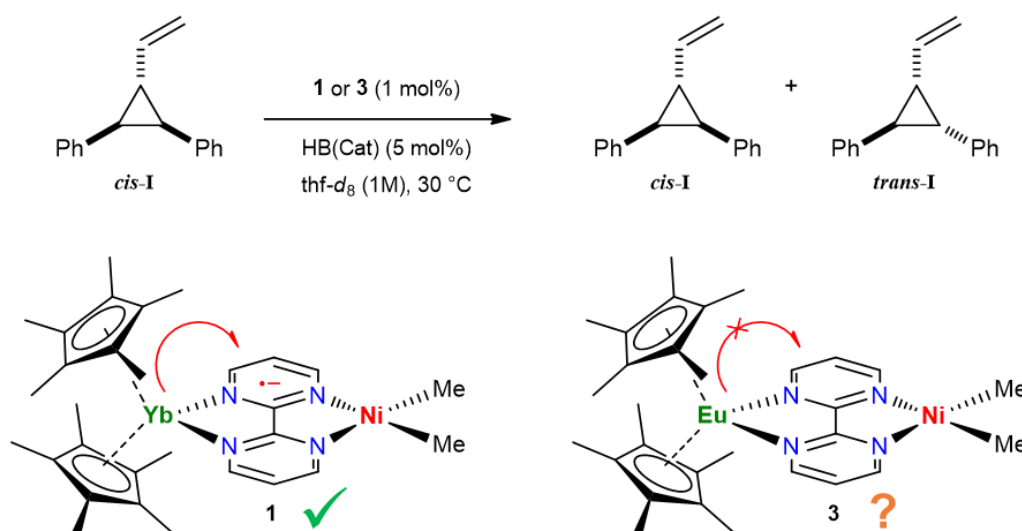
Carbon atoms are in grey, nitrogen atoms in blue, the nickel atom in green, and the europium atom in light blue. Hydrogen atoms and co-crystallized benzene molecules have been removed for clarity.

The  $^1\text{H}$  NMR spectrum of the isolated compound was silent which is typical for  $4f^7$  divalent europium compounds, thus indicating that the bipym ligand was not reduced in **3**. To confirm that, the XRD metrics of **1**, **2** and **3** were compared with the  $(\text{bipym})\text{NiMe}_2$  precursor (Table II.3). The first distance to look at in those systems was the one between the two carbon atoms bridging the two pyrimidyl fragments ( $\text{C-C}_{\text{bipym}}$ ). In the  $(\text{bipym})\text{NiMe}_2$  complex, the distance was 1.482(5) Å,<sup>51</sup> which was similar to the 1.466(2) Å distance observed for **2**. In **1**, the reduction of the ligand was shortening this distance to 1.403(4) Å because of the added electronic density on the C-C bond.<sup>51,53,69,70</sup> The 1.465(4) Å distance observed with **3** was therefore indicating that no reduction of the bipym ligand occurred. This was further confirmed by the  $\text{Ln-Cp}^*_{\text{Ctr}}$  distances (Ctr for centroid), 2.31(1) Å in **1** indicating a formal trivalent state versus 2.53(2) Å in **3** which was coherent with a divalent state.<sup>51,71,72</sup>

**Table II.3.** Main metric parameters distances in Å and angles in ° for **1-3**:

Atoms	1	2	3
Ni-Me	1.925(1)	1.928(2)	1.917(5)
Ni-N	1.956(3)	1.958(1)	1.959(4)
C-C <sub>bipy(m)</sub>	1.403(4)	1.466(2)	1.465(4)
Ln-N	2.359(1)	/	2.694(3)
Ln-Cp* <sub>ctr</sub>	2.31(1)	/	2.53(2)
NC <sup>^</sup> CN <sub>bipy(m)</sub> torsion Ni side	0.2(4)	1.8(1)	2.7(3)

Having proven that no electron was transferred on the bipym in **3**, a Cod trapping experiment was performed to confirm the Ni<sup>0</sup> oxidation state and led to a slight color change, pointing toward a similar result than the one obtained with **2**. However, no further characterization was achieved, the <sup>1</sup>H NMR remained silent and crystallization trials were unsuccessful. A second radical clock experiment was performed with **3** and only traces of *trans*-**I** product (<2%) were observed. Although no conversion occurred in the absence of Ni or with the other systems tested, the Yb-Pt one from Chapter III or the ones tested by Schoenebeck and coworkers, this was considered to be a too ambiguous result to conclude about the possibility to perform radical reactivity with **3** (Figure II.8).

**Figure II.8.** Positive radical clock experiments with **1** and ambiguous result with **3**.

#### ▪ EPR study

In another attempt to address this issue about the oxidation state of the Ni center in **1**, *in-situ* EPR was performed at low temperature (5 K) on frozen THF samples taken shortly after the addition of the HBCat without (sample 1) and in the presence of the alkene substrate (sample 2). Very broad samples are typical of Yb<sup>III</sup>, f<sup>13</sup> ion, showing strong anisotropy. This is problematic since it can mask



any signal that would be informative on the electronic structure of the catalytic resting state. Sample 1 was simulated with a single Yb<sup>III</sup> ion possessing a rhombic g tensor of 5.95, 2.41, and 1.64 with anisotropic hyperfine coupling. This well corresponded to a Cp\*<sub>2</sub>Yb<sup>III</sup> fragment coordinated to an N-heteroaromatic ligand,<sup>52</sup> but the radical on the bipym ligand was not observed. It was thus likely that the radical was coupled at low temperature with the Yb<sup>III</sup> fragment. Sample 2 presented two species and was fitted with two Yb<sup>III</sup> ions possessing rhombic g tensors of 5.76, 2.77, and 1.78 and 4.40, 2.42, 1.18, respectively. The presence of two ytterbium species under catalytic conditions was not surprising but similarly, as in Sample 1, the spectrum remained uninformative on the electronic structure of the active species (Figure II.6).

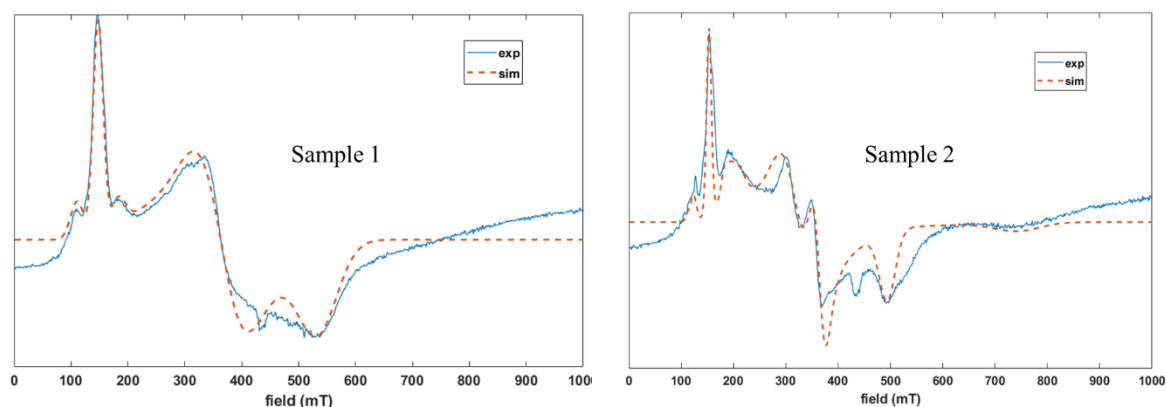


**Figure II.9.** Comparison between experimental (blue) and simulated (orange) EPR spectra of samples 1 (left) and 2 (right) at 10 K. Conditions: 9.64 GHz frequency, 0.250 mW power and a 29 dB gain.

■ *Hypothesis for the role of the ytterbium-bipyrimidine electronics*

Since one electron from the divalent Yb was transferred to the  $\pi^*$ -system of the bipym ligand it was hypothesized that the  $\pi$ -donating properties were reinforced in the latter to the cost of its  $\pi$ -accepting ability. Hence, it was envisioned that the supposed electron richer Ni<sup>0</sup> center in **1** was keener to give some electronic density to a coordinated alkene than in the case of **2** and **3**. It follows that **1**'s behavior could be achieved with a simpler N-heteroaromatic ligand with limited  $\pi$ -accepting properties (Figure II.9).

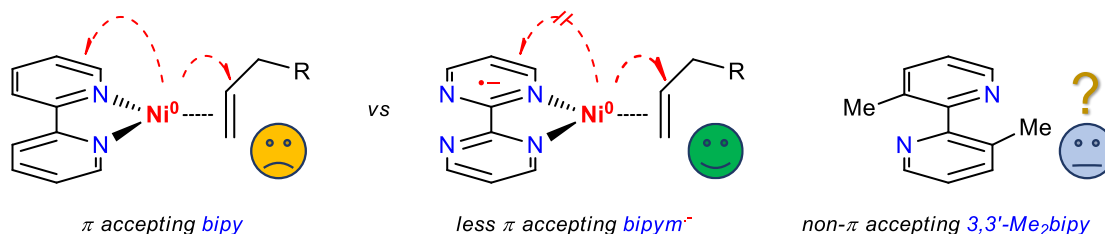


**Figure II.10.** Conjecture on  $\pi$ -accepting properties' influence on reactivity.

To validate this conjecture, two new complexes were synthesized, the (4,4'-Me<sub>2</sub>bipy)NiMe<sub>2</sub>, **4**, and the (3,3'-Me<sub>2</sub>bipy)NiMe<sub>2</sub>, **5**. Upon coordination to a metal center, the steric hindrance induced by the two methyl groups of 3,3'-Me<sub>2</sub>bipy was already shown to twist the NC^CN torsion angle and to limit the  $\pi$ -accepting properties.<sup>73</sup> Both complexes, **4** and **5**, were characterized by XRD and the NC^CN torsion angles were respectively 2° and 33.5° (Figure II.10).

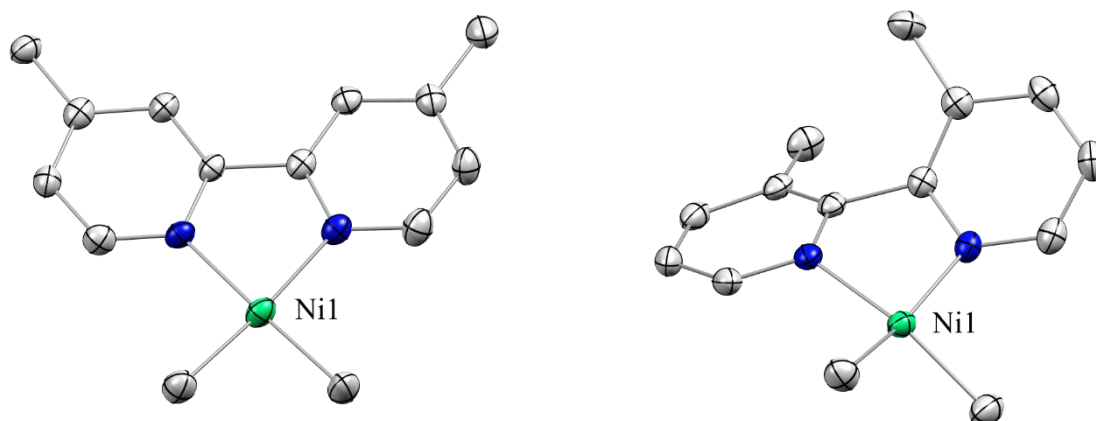


**Figure II.11.** ORTEPs of **4** and **5** with thermal ellipsoids at 50 % level. Carbon atoms are in grey, nitrogen atoms in blue, and the nickel atom in green. Hydrogen atoms have been removed for clarity.

Since **4** and **5** had similar solubilities, they were both engaged in the isomerization of **B** and compared. The beginning of the reactions was monitored by <sup>1</sup>H NMR indicating that **4** did not perform greatly, as **2** and **3**, 9% conversion of **B** in 12.5 h at 30 °C versus 4% and 15% for **2** and **3**, respectively. In contrast, **5** was way more efficient, 54% conversion in the same conditions, which was not far from the performance of **1**, 64% in 12.5 h. The comparison of the initial rates of **1** and **5** also showed that if **5** starts much faster than **1**, its activity was decreasing faster a result attributed to a worse stability in absence of the Cp\*<sub>2</sub>Yb fragment (Figure II.11).

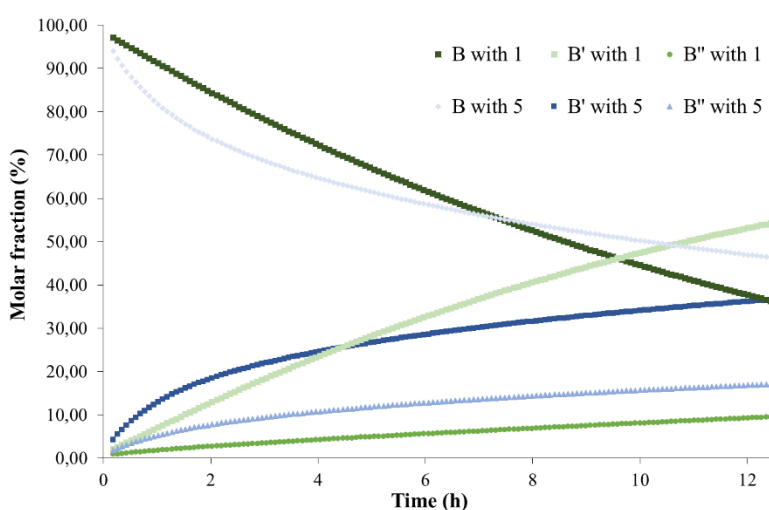


**Figure II.12.** Comparison of the conversion rates of **B** upon isomerization by **1** (green labels) or **5** (blue labels).

To evaluate if **5** was following a metalloradical pathway, another radical clock test was performed, and, similarly to **3**, only traces of conversion to *trans*-**I** were observed (<3%). As in the EuNi case, no conclusion about the radical nature of the transformation was possible and the conjectured Ni<sup>0</sup>-triggered radical reactivity remained unproven. In the absence of conclusive experimental investigations to propose a mechanism, theoretical analysis of the reaction pathways for **1** and **5** became mandatory.

▪ *Theoretical studies of the mechanism*

Computational study of the mechanism was performed at the DFT level for **1**, in collaboration with the group of Prof. Maron. Surprisingly, upon reduction by HBCat, **1** was found to be best described by a Ni<sup>I</sup> center and a dianionic bipym ligand. This result was the consequence of the incompatibility between a reductive Ni<sup>0</sup> center and a monoreduced bipym ligand. The former preferred to transfer its one electron to the latter and such electron shuttle yielded a mesomeric form of the conjectured Ni<sup>0</sup> species (Figure II.13). The presence of two highly paramagnetic Yb<sup>III</sup> and Ni<sup>I</sup> centers could justify the silent <sup>1</sup>H NMR at room temperature, a characteristic not expected for intermediate-valent Yb species and if the EPR measurements did not explicitly support the presence of a Ni<sup>I</sup>, the broadness of the Yb signals could be masking it.

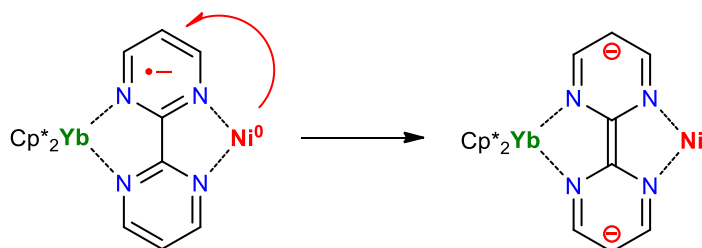


**Figure II.13.** Electron shuttle, which forms the active Yb-Ni<sup>I</sup> active species from the hypothesized Yb-Ni<sup>0</sup>.

After the coordination of the alkene, the C-H activation was found as the rate-determining step (TS1) with a barrier of 34.9 kcal mol<sup>-1</sup>, 10.8 kcal mol<sup>-1</sup> above Schoenebeck's Ni<sup>I</sup>-NHC system, resulting in a  $\pi$ -allyl coordination mode where the spin density was delocalized over both the bipym and Ni fragment but also the Yb one. This relatively high barrier was concurring with the slow reactivity at room temperature, explaining the need to heat to get optimal conditions. After the C-H activation (Int3), the bipym-Ni pair performed another electron shuttle to yield a monoanionic bipym and a Ni<sup>II</sup>-H species, inducing a barrierless relocation of the hydride close to the terminal methylene group (Int4). Upon the formation of the terminal C-H bond, the electronic structure switched back to a bipym<sup>2-</sup>-Ni<sup>I</sup> description (TS2) that evolved toward the mono-isomerized product (Int5) which was slightly more stable by 1.5 kcal mol<sup>-1</sup> than the starting intermediate (Int2). This small energy difference explained well why the kinetics did not strictly follow a first order but a pseudo-first order

kinetics, when the concentration of the terminal alkene decreased the exchange equilibrium between Int5 and Int2 became less favored and the rate slowed down (Figure II.12). The second isomerization followed a similar pathway, to the main difference that the final di-isomerized product was found 9.7 kcal mol<sup>-1</sup> above Int5. The second isomerization was therefore endothermic, explaining well the preference for mono-isomerization when the thermodynamics of the reaction was not strongly in favor of further isomerized products. The unusual electronic structure of a Ni(I) center coordinating alkenes was likely to play a role in this feature. This was rather interesting and provided a way to adapt the selectivity by adapting the ligand electronics to disfavor the internal alkene coordination.

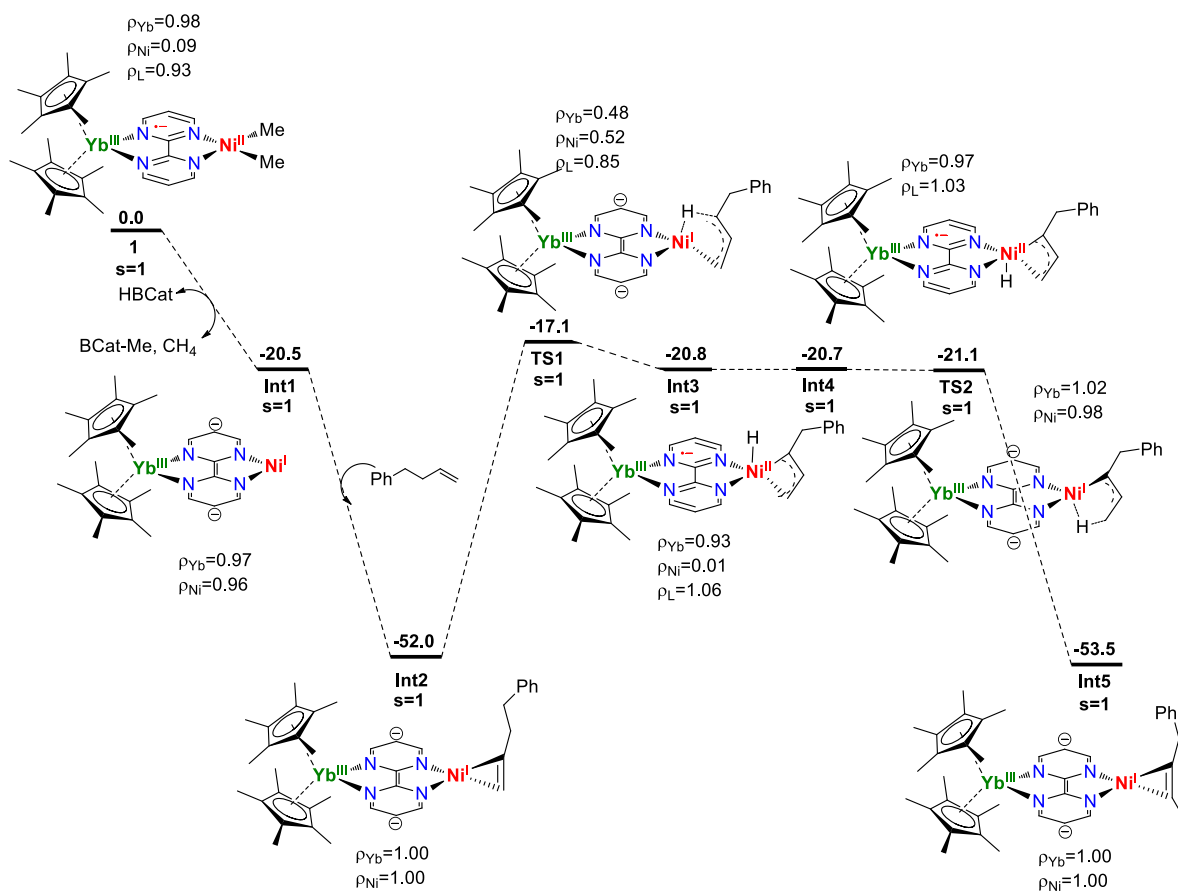


**Figure II.14.** Energy profile and mechanism of the first isomerization of **B** induced by **1**. Relative energies are expressed in kcal mol<sup>-1</sup>.

Since the origin of the  $\pi$ -accepting conjecture got severely hit by these results, similar computations were performed with **5** to understand its performance. This time, the HBcat mediated reduction led to the expected Ni<sup>0</sup> oxidation state. However, the C-H activation rate-determining step was eased by the decooordination of one-half of the ligand, most likely due to the important torsion angle found in **5**. While this phenomenon could explain the lower stability of the active species due to the possible decooordination of the second half of the 3,3'-Me<sub>2</sub>bipy resulting in the formation of nanoparticles, it also enhanced the kinetics of the reaction. The total activation energy was estimated to 26.6 kcal mol<sup>-1</sup>, much lower than in the preceding case. This explained why the initial rates

observed with **5** were surprisingly higher than with **1**. The rest of the mechanism was found to follow a somehow standard  $\pi$ -allyl pathway to the exception that the overall mono-isomerization was endothermic by 11.1 kcal mol<sup>-1</sup>. While this value could seem important, it was echoing to the loss of activity observed after few hours. This was considered in reasonable agreement with a pseudo-first order reaction yielding a kinetic product, the rates of the transformation were then slowly hampered by the decreasing concentration of the starting material (Figure II.13).

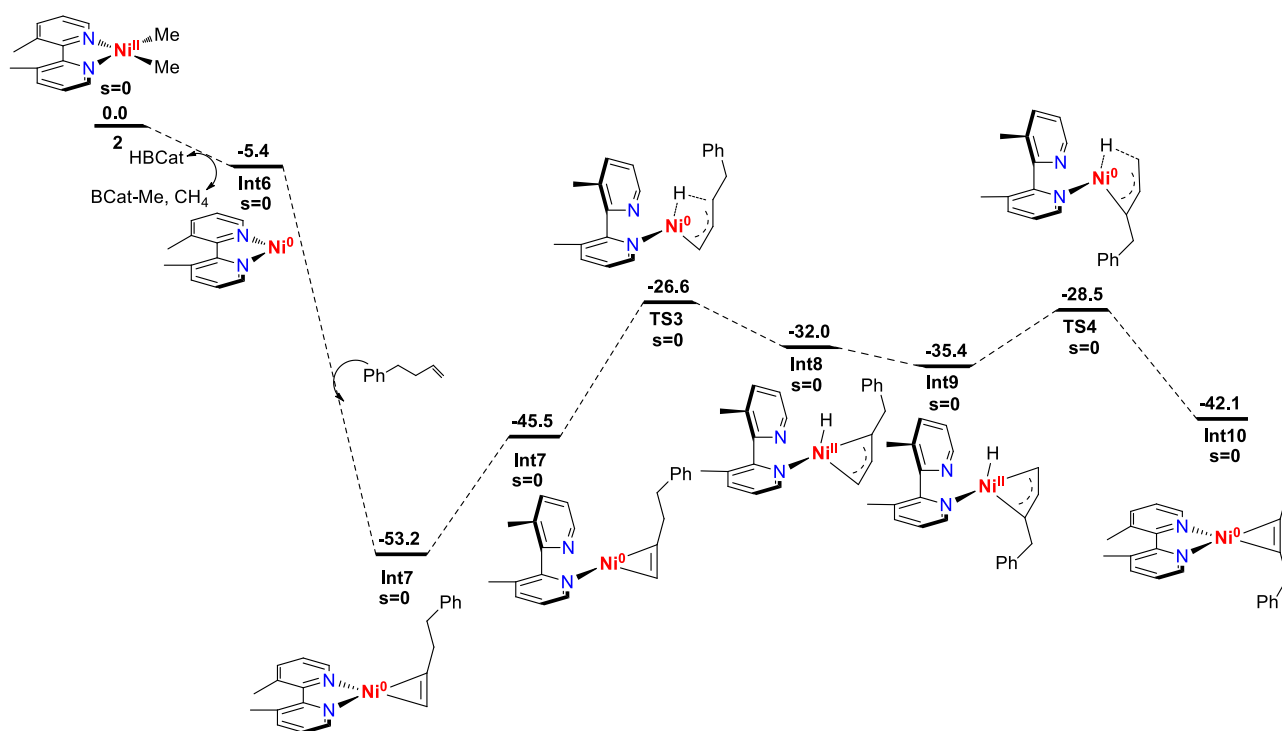


**Figure II.15.** Energy profile and mechanism of the first isomerization of **B** induced by **5**. Relative energies are expressed in kcal mol<sup>-1</sup>.

While these two computational studies definitely invalidated the conjecture that led to the study of pre-catalyst **5**, both different reaction pathways were found to be concurring with the observed kinetics and selectivity toward mono-isomerization. The control of the electron shuttle pathway for **1** but also of the hemilability of the ligand observed with **5** calls for further studies to enhance the performances of each different system. Finally, the last issue remains to be investigated; the validity or not of the radical clock experiments. If the observed traces of *trans*-**I** products, with **3** and **5**, were not enough to consider a radical transformation, the fact that formal Ni<sup>0</sup> species were able to isomerize, even slightly, such cyclopropyl substrate was puzzling and further theoretical investigations are on their way to understand this singular result.

### III. Conclusion and perspectives

In this work the reductive reactivity of complex **1** was extended thanks to the study of the interaction with a simple borane reagent, HBCat. This led to the *in-situ* formation of a low-valent Yb-Ni bimetallic species thanks to the elimination of MeBCat and CH<sub>4</sub>. Having developed this simple and clean protocol, complex **1** and its monometallic analog **2** were tested in catalysis of simple alkene isomerization. While **1** was performing well, at low catalyst loading, with a surprising stability and a significant selectivity for mono-isomerization, **2** was found almost non-reactive. Careful mechanistic investigations revealed that, with **1**, the formed species validated the same test performed to validate the recently proposed metalloradical induced 1,3-H atom relocation mechanism.<sup>44</sup> The synthesis of **3**, where the divalent Eu ion was not reducing the bipym ligand revealed that this radical behavior was not observed without such reduction. This led to an original hypothesis about the role of the N-heteroaromatic ligand in such systems that allowed to find a promising monometallic pre-catalyst supported by the rarely used 3,3'-Me<sub>2</sub>bipy, with performances almost on par with **1** and still at a low catalytic loading (1 mol%). Since no strong experimental evidence was found to choose one mechanism or another, theoretical computation of the reaction pathway was performed. It invalidated the conjectured importance of the  $\pi$ -properties of the ligand and confirmed the presence of a formal Ni<sup>I</sup> center in the case of **1**. This study demonstrated nicely that, on top of being a powerful stabilizing tool, the Cp\*<sub>2</sub>Yb fragment is also of great importance when it comes to influence low-valent N-heteroaromatic-Ni species. To enhance the observed selectivity, several options can be envisioned like tuning the redox potential of the Yb and/or N-heteroaromatic ligand fragments, allowing also to control the steric environment of the Ni center. Several substituted bipym ligands are planned to be studied with this objective in mind (Figure III.1).

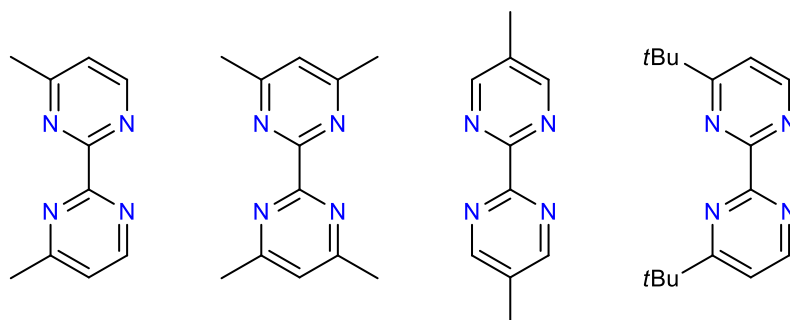


**Figure III.1.** Ligands considered to tune the steric and electronic properties of the bipym ligand.

When it comes to the decoordination pathway unveiled with pre-catalyst **5**, preliminary results with the more labile tetramethylethylenediamine (tmeda) ligand were obtained and almost identical reaction rates were observed. Radical clock experiments with such a system revealed a conversion of *cis*-**I** to *trans*-**I** up to 9%, confirming the necessity to study further the relevance of this test. Investigations with other labile ligands such as the 2-(dimethylaminomethyl)-pyridine or substituted 3,3'-Me<sub>2</sub>bipy,<sup>74</sup> both experimentally and theoretically, will hopefully solve this problem.

## References

- (1) Job, A.; Reich, R. C. R. *Heb. Seances Acad. Sci.* **1924**, 179, 330–332. <https://gallica.bnf.fr/ark:/12148/bpt6k31328/f330.item>.
- (2) Corriu, R. J. P.; Masse, J. P. *J. Chem. Soc. Chem. Commun.* **1972**, No. 3, 144a–144a. <https://doi.org/10.1039/C3972000144A>.
- (3) Tamao, K.; Sumitani, K.; Kumada, M. *J. Am. Chem. Soc.* **1972**, 94 (12), 4374–4376. <https://doi.org/10.1021/ja00767a075>.
- (4) Sabatier, P. *Berichte der Dtsch. Chem. Gesellschaft* **1911**, 44 (3), 1984–2001. <https://doi.org/10.1002/cber.19110440303>.
- (5) Johansson Seechurn, C. C. C.; Kitching, M. O.; Colacot, T. J.; Snieckus, V. *Angew. Chemie Int. Ed.* **2012**, 51 (21), 5062–5085. <https://doi.org/10.1002/anie.201107017>.
- (6) Li, H.; Johansson Seechurn, C. C. C.; Colacot, T. J. *ACS Catal.* **2012**, 2 (6), 1147–1164. <https://doi.org/10.1021/cs300082f>.
- (7) Ananikov, V. P. *ACS Catal.* **2015**, 5 (3), 1964–1971. <https://doi.org/10.1021/acscatal.5b00072>.
- (8) Nicolaou, K. C.; Sorensen, E. J. *Classics in Total Synthesis : Targets, Strategies, Methods*, Wiley, Weinheim, Germany, **1996**. <https://www.wiley.com/en-gb/Classics+in+Total+Synthesis:+Targets,+Strategies,+Methods-p-9783527292318>.
- (9) Torborg, C.; Beller, M. *Adv. Synth. Catal.* **2009**, 351 (18), 3027–3043. <https://doi.org/10.1002/adsc.200900587>.
- (10) Magano, J.; Dunetz, J. R. *Chem. Rev.* **2011**, 111 (3), 2177–2250. <https://doi.org/10.1021/cr100346g>.
- (11) Naso, F.; Babudri, F.; Farinola, G. M. *Pure Appl. Chem.* **1999**, 71 (8), 1485–1492. <https://doi.org/doi:10.1351/pac199971081485>.
- (12) The Nobel Prize in Chemistry **2010**. <https://www.nobelprize.org/prizes/chemistry/2010/summary/>.
- (13) Tasker, S. Z.; Standley, E. A.; Jamison, T. F. *Nature* **2014**, 509 (7500), 299–309. <https://doi.org/10.1038/nature13274>.
- (14) Obligacion, J. V.; Chirik, P. J. *Nature Reviews Chemistry*, **2018**, pp 15–34. <https://doi.org/10.1038/s41570-018-0001-2>.
- (15) Lin, C.-Y.; Power, P. P. *Chem. Soc. Rev.* **2017**, 46 (17), 5347–5399. <https://doi.org/10.1039/C7CS00216E>.
- (16) Camasso, N. M.; Sanford, M. S. *Science (80-. )*. **2015**, 347 (6227), 1218–1220. <https://doi.org/10.1126/science.aaa4526>.
- (17) D'Accrisio, F.; Borja, P.; Saffon-Merceron, N.; Fustier-Boutignon, M.; Mézailles, N.; Nebra, N. *Angew. Chemie Int. Ed.* **2017**, 56 (42), 12898–12902. <https://doi.org/10.1002/anie.201706237>.
- (18) Bour, J. R.; Camasso, N. M.; Meucci, E. A.; Kampf, J. W.; Canty, A. J.; Sanford, M. S. *J. Am. Chem. Soc.* **2016**, 138 (49), 16105–16111. <https://doi.org/10.1021/jacs.6b10350>.
- (19) Bour, J. R.; Ferguson, D. M.; McClain, E. J.; Kampf, J. W.; Sanford, M. S. *J. Am. Chem. Soc.* **2019**, 141 (22), 8914–8920. <https://doi.org/10.1021/jacs.9b02411>.
- (20) Breitenfeld, J.; Ruiz, J.; Wodrich, M. D.; Hu, X. *J. Am. Chem. Soc.* **2013**, 135 (32), 12004–12012. <https://doi.org/10.1021/ja4051923>.
- (21) Biswas, S.; Weix, D. J. *J. Am. Chem. Soc.* **2013**, 135 (43), 16192–16197. <https://doi.org/10.1021/ja407589e>.
- (22) Hegedus, L. S.; Miller, L. L. *J. Am. Chem. Soc.* **1975**, 97 (2), 459–460. <https://doi.org/10.1021/ja00835a061>.
- (23) Everson, D. A.; Weix, D. J. *J. Org. Chem.* **2014**, 79 (11), 4793–4798. <https://doi.org/10.1021/jo500507s>.
- (24) Zuo, Z.; Ahneman, D. T.; Chu, L.; Terrett, J. A.; Doyle, A. G.; MacMillan, D. W. C. *Science (80-. )*. **2014**, 345 (6195), 437–440. <https://doi.org/10.1126/science.1255525>.
- (25) Osawa, M.; Nagai, H.; Akita, M. *Dalt. Trans.* **2007**, No. 8, 827–829. <https://doi.org/10.1039/B618007H>.



- (26) Kalyani, D.; McMurtrey, K. B.; Neufeldt, S. R.; Sanford, M. S. *J. Am. Chem. Soc.* **2011**, *133* (46), 18566–18569. <https://doi.org/10.1021/ja208068w>.
- (27) Rueping, M.; Koenigs, R. M.; Poscharny, K.; Fabry, D. C.; Leonori, D.; Vila, C. *Chem. – A Eur. J.* **2012**, *18* (17), 5170–5174. <https://doi.org/10.1002/chem.201200050>.
- (28) Sahoo, B.; Hopkinson, M. N.; Glorius, F. *J. Am. Chem. Soc.* **2013**, *135* (15), 5505–5508. <https://doi.org/10.1021/ja400311h>.
- (29) Shu, X.; Zhang, M.; He, Y.; Frei, H.; Toste, F. D. *J. Am. Chem. Soc.* **2014**, *136* (16), 5844–5847. <https://doi.org/10.1021/ja500716j>.
- (30) Koike, T.; Akita, M. *Inorg. Chem. Front.* **2014**, *1* (8), 562–576. <https://doi.org/10.1039/C4QI00053F>.
- (31) Terrett, J. A.; Cuthbertson, J. D.; Shurtleff, V. W.; MacMillan, D. W. C. *Nature* **2015**, *524* (7565), 330–334. <https://doi.org/10.1038/nature14875>.
- (32) Tian, L.; Till, N. A.; Kudisch, B.; MacMillan, D. W. C.; Scholes, G. D. *J. Am. Chem. Soc.* **2020**, *142* (10), 4555–4559. <https://doi.org/10.1021/jacs.9b12835>.
- (33) Twilton, J.; Le, C. (Chip); Zhang, P.; Shaw, M. H.; Evans, R. W.; MacMillan, D. W. C. *Nat. Rev. Chem.* **2017**, *1* (7), 52. <https://doi.org/10.1038/s41570-017-0052>.
- (34) Luca, O. R.; Crabtree, R. H. *Chem. Soc. Rev.* **2013**, *42* (4), 1440–1459. <https://doi.org/10.1039/C2CS35228A>.
- (35) Jacquet, J.; Desage-El Murr, M.; Fensterbank, L. *ChemCatChem* **2016**, *8* (21), 3310–3316. <https://doi.org/10.1002/cctc.201600616>.
- (36) Anderson, T. J.; Jones, G. D.; Vicic, D. A. *J. Am. Chem. Soc.* **2004**, *126* (26), 8100–8101. <https://doi.org/10.1021/ja0483903>.
- (37) Jones, G. D.; McFarland, C.; Anderson, T. J.; Vicic, D. A. *Chem. Commun.* **2005**, No. 33, 4211–4213. <https://doi.org/10.1039/B504996B>.
- (38) Ciszewski, J. T.; Mikhaylov, D. Y.; Holin, K. V.; Kadirov, M. K.; Budnikova, Y. H.; Sinyashin, O.; Vicic, D. A. *Inorg. Chem.* **2011**, *50* (17), 8630–8635. <https://doi.org/10.1021/ic201184x>.
- (39) Lin, X.; Phillips, D. L. *J. Org. Chem.* **2008**, *73* (10), 3680–3688. <https://doi.org/10.1021/jo702497p>.
- (40) Budnikova, Y. H.; Vicic, D. A.; Klein, A. *Inorganics* . 2018. <https://doi.org/10.3390/inorganics6010018>.
- (41) Adhikari, D.; Mossin, S.; Basuli, F.; Huffman, J. C.; Szilagyi, R. K.; Meyer, K.; Mindiola, D. J. *J. Am. Chem. Soc.* **2008**, *130* (11), 3676–3682. <https://doi.org/10.1021/ja7108486>.
- (42) Lin, Q.; Diao, T. *J. Am. Chem. Soc.* **2019**, *141* (44), 17937–17948. <https://doi.org/10.1021/jacs.9b10026>.
- (43) Lin, Q.; Fu, Y.; Liu, P.; Diao, T. *J. Am. Chem. Soc.* **2021**, *143* (35), 14196–14206. <https://doi.org/10.1021/jacs.1c05255>.
- (44) Kapat, A.; Sperger, T.; Guven, S.; Schoenebeck, F. *Science* (80-. ). **2019**, *363* (6425), 391–396. <https://doi.org/10.1126/science.aav1610>.
- (45) Larionov, E.; Li, H.; Mazet, C. *Chem. Commun.* **2014**, *50* (69), 9816–9826. <https://doi.org/10.1039/C4CC02399D>.
- (46) Liu, X.; Li, B.; Liu, Q. *Synthesis (Stuttg.)* **2019**, *51* (06), 1293–1310. <https://doi.org/10.1055/s-0037-1612014>.
- (47) Grotjahn, D. B.; Larsen, C. R.; Gustafson, J. L.; Nair, R.; Sharma, A. *J. Am. Chem. Soc.* **2007**, *129* (31), 9592–9593. <https://doi.org/10.1021/ja073457i>.
- (48) Larionov, E.; Lin, L.; Guénée, L.; Mazet, C. *J. Am. Chem. Soc.* **2014**, *136* (48), 16882–16894. <https://doi.org/10.1021/ja508736u>.
- (49) Lin, L.; Romano, C.; Mazet, C. *J. Am. Chem. Soc.* **2016**, *138* (32), 10344–10350. <https://doi.org/10.1021/jacs.6b06390>.
- (50) Iwamoto, H.; Tsuruta, T.; Ogoshi, S. *ACS Catal.* **2021**, *11* (11), 6741–6749. <https://doi.org/10.1021/acscatal.1c00908>.
- (51) Wang, D.; Moutet, J.; Tricoire, M.; Cordier, M.; Nocton, G. *Inorganics* **2019**, *7* (5), 58.



<https://doi.org/10.3390/inorganics7050058>.

- (52) Nocton, G.; Lukens, W. W.; Booth, C. H.; Rozenel, S. S.; Medling, S. A.; Maron, L.; Andersen, R. A. *J. Am. Chem. Soc.* **2014**, *136* (24), 8626–8641. <https://doi.org/10.1021/ja502271q>.
- (53) Goudy, V.; Jaoul, A.; Cordier, M.; Clavaguéra, C.; Nocton, G. *J. Am. Chem. Soc.* **2017**, *139* (31), 10633–10636. <https://doi.org/10.1021/jacs.7b05634>.
- (54) Jaoul, A.; Tricoire, M.; Moutet, J.; Cordier, M.; Clavaguéra, C.; Nocton, G. *Chem. squared* **2019**, *3*, 1. <https://doi.org/10.28954/2019.csq.06.001>.
- (55) Ishida, K.; Yamazaki, H.; Hagiwara, C.; Abe, M.; Kusama, H. *Chem. – A Eur. J.* **2020**, *26* (6), 1249–1253. <https://doi.org/10.1002/chem.201904635>.
- (56) Binger, P.; Doyle, M. J.; McMeeking, J.; Krüger, C.; Tsay, Y.-H. *J. Organomet. Chem.* **1977**, *135* (3), 405–414. [https://doi.org/10.1016/S0022-328X\(00\)88092-4](https://doi.org/10.1016/S0022-328X(00)88092-4).
- (57) Hassam, M.; Taher, A.; Arnott, G. E.; Green, I. R.; van Otterlo, W. A. L. *Chem. Rev.* **2015**, *115* (11), 5462–5569. <https://doi.org/10.1021/acs.chemrev.5b00052>.
- (58) Crabtree, R. H. *The Organometallic Chemistry of the Transition Metals*, **2014**, pp 224–258. <https://doi.org/10.1002/9781118788301.ch9>.
- (59) Goetz, R. W.; Orchin, M. *J. Am. Chem. Soc.* **1963**, *85* (10), 1549–1550. <https://doi.org/10.1021/ja00893a046>.
- (60) Lochow, C. F.; Miller, R. G. *J. Org. Chem.* **1976**, *41* (18), 3020–3022. <https://doi.org/10.1021/jo00880a020>.
- (61) Weber, F.; Schmidt, A.; Röse, P.; Fischer, M.; Burghaus, O.; Hilt, G. *Org. Lett.* **2015**, *17* (12), 2952–2955. <https://doi.org/10.1021/acs.orglett.5b01230>.
- (62) Crossley, S. W. M.; Barabé, F.; Shenvi, R. A. *J. Am. Chem. Soc.* **2014**, *136* (48), 16788–16791. <https://doi.org/10.1021/ja5105602>.
- (63) Negishi, E.; Miller, S. R. *J. Org. Chem.* **1989**, *54* (26), 6014–6016. <https://doi.org/10.1021/jo00287a008>.
- (64) Broere, D. L. J.; de Bruin, B.; Reek, J. N. H.; Lutz, M.; Dechert, S.; van der Vlugt, J. I. *J. Am. Chem. Soc.* **2014**, *136* (33), 11574–11577. <https://doi.org/10.1021/ja502164f>.
- (65) Jacquet, J.; Cheaib, K.; Ren, Y.; Vezin, H.; Orio, M.; Blanchard, S.; Fensterbank, L.; Desage-El Murr, M. *Chem. – A Eur. J.* **2017**, *23* (60), 15030–15034. <https://doi.org/10.1002/chem.201704049>.
- (66) Cahard, E.; Schoenebeck, F.; Garnier, J.; Cutulic, S. P. Y.; Zhou, S.; Murphy, J. A. *Angew. Chemie Int. Ed.* **2012**, *51* (15), 3673–3676. <https://doi.org/10.1002/anie.201200084>.
- (67) Choi, S.-Y.; Toy, P. H.; Newcomb, M. *J. Org. Chem.* **1998**, *63* (23), 8609–8613. <https://doi.org/10.1021/jo981020a>.
- (68) Finke, R. G.; Keenan, S. R.; Watson, P. L. *Organometallics* **1989**, *8* (2), 263–277. <https://doi.org/10.1021/om00104a001>.
- (69) Wolff, C.; Gottschlich, A.; England, J.; Wieghardt, K.; Saak, W.; Haase, D.; Beckhaus, R. *Inorg. Chem.* **2015**, *54* (10), 4811–4820. <https://doi.org/10.1021/acs.inorgchem.5b00285>.
- (70) England, J.; Bill, E.; Weyhermüller, T.; Neese, F.; Atanasov, M.; Wieghardt, K. *Inorg. Chem.* **2015**, *54* (24), 12002–12018. <https://doi.org/10.1021/acs.inorgchem.5b02415>.
- (71) Schultz, M.; Boncella, J. M.; Berg, D. J.; Tilley, T. D.; Andersen, R. A. *Organometallics* **2002**, *21* (3), 460–472. <https://doi.org/10.1021/om010661k>.
- (72) Moore, J. A.; Cowley, A. H.; Gordon, J. C. *Organometallics* **2006**, *25* (22), 5207–5209. <https://doi.org/10.1021/om060793j>.
- (73) Nocton, G.; Booth, C. H.; Maron, L.; Andersen, R. A. *Organometallics* **2013**, *32* (19), 5305–5312. <https://doi.org/10.1021/om400528d>.
- (74) Varela, J. A.; Castedo, L.; Maestro, M.; Mahía, J.; Saá, C. *Chem. – A Eur. J.* **2001**, *7* (23), 5203–5213. [https://doi.org/10.1002/1521-3765\(20011203\)7:23<5203::AID-CHEM5203>3.0.CO;2-R](https://doi.org/10.1002/1521-3765(20011203)7:23<5203::AID-CHEM5203>3.0.CO;2-R).

## Synthesis and characterization of tetraalkyl palladium complexes

### I. Background on high-valent palladium complexes

#### I.A. An elusive +IV oxidation state

As discussed in the introduction of the precedent chapter, palladium-mediated transformations are of paramount interest as highlighted by the 2010 Nobel Prize in Chemistry.<sup>1</sup> Most of the time these processes are involving Pd<sup>0</sup> and Pd<sup>II</sup> species. However, similarly as with Ni, the less common +I, +III and +IV oxidation states are accessible although they are often elusive.<sup>2-9</sup> Because of the remarkable possibilities offered by the easily accessed Pt<sup>IV</sup> species discussed in Chapter III, studying analogous species with the increased versatility of Pd in terms of redox chemistry should allow to access different reaction pathways. The necessity to achieve the isolation of such highly unstable Pd<sup>IV</sup> compounds is thus key for experimental understanding and developing original reactivities. In 1986, the first-ever XRD characterized Pd<sup>IV</sup> complex, a *fac*-(bipy)PdMe<sub>3</sub>I, was reported by Canty and coworkers. Inspired by Pt<sup>IV</sup> chemistry, they managed to do so by treating the (bipy)PdMe<sub>2</sub> precursor with MeI to trigger an oxidative addition, and obtain a complex stable only below -20 °C.<sup>10</sup> The reason of such instability was found by monitoring the oxidative addition at low temperature by <sup>1</sup>H NMR spectroscopy. The lability of the iodide ligand, especially in coordinating solvent such as acetonitrile, permitted to observe an equilibrium between the (bipy)PdMe<sub>3</sub>I complex and its [(bipy)PdMe<sub>3</sub>(CD<sub>3</sub>CN)]<sup>+</sup> I<sup>-</sup> cationic form (Figure I.1).<sup>11</sup>

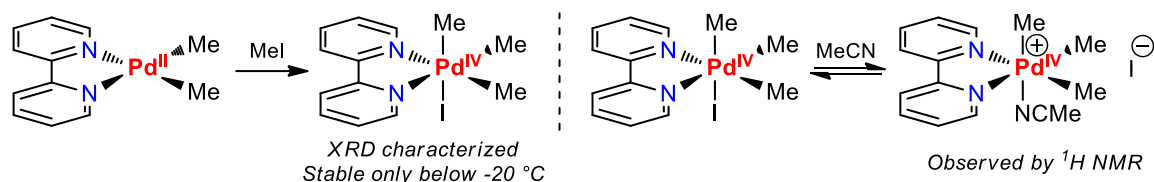


**Figure I.1.** First XRD characterized  $\text{Pd}^{\text{IV}}$  complex and its solution-state behavior.

In acetone- $d_6$ , the addition of  $\text{MeI-}d_3$  allowed to detect a scrambling between the methyl substituents, most likely a consequence of the lability of the iodide ion. The following study by De Graaf *et al.* also permitted to observe such cationic forms with the  $(\text{tmeda})\text{PdMe}_2$  complex while the fast scrambling of the methyl groups only permitted the observation of a single average  $^1\text{H}$  NMR signal for the three Me groups above  $-20^\circ\text{C}$ , the temperature at which a coalescence was observed in  $\text{MeCN-}d_3$ .<sup>12</sup>

### I.B. Selectivity of the reductive elimination

Benefiting from the experience obtained through this first study, Canty *et al.* multiplied the oxidative addition tests with other halogenoalkanes.<sup>13–15</sup> From these studies, several other well defined species were isolated such as  $(\text{bipy})\text{PdMe}_2(\text{CH}_2\text{Ar})\text{I}$ , the Ar group being  $\text{C}_6\text{F}_5$ ,  $p\text{-C}_6\text{H}_4\text{Me}$  or  $p\text{-C}_6\text{H}_4\text{Br}$ . The study of its reductive elimination allowed to report the possibility to marginally control the selectivity of the reductive elimination step since the selectivity for ethane formation was decreased from 100% to 90% and 78% when the bipy ligand was replaced by a phenantroline ligand in the case of the xylol and bromobenzyl substituents respectively (Figure I.2). Further tuning of the ligand even allowed to get a 60:40 ratio of products.<sup>16</sup>

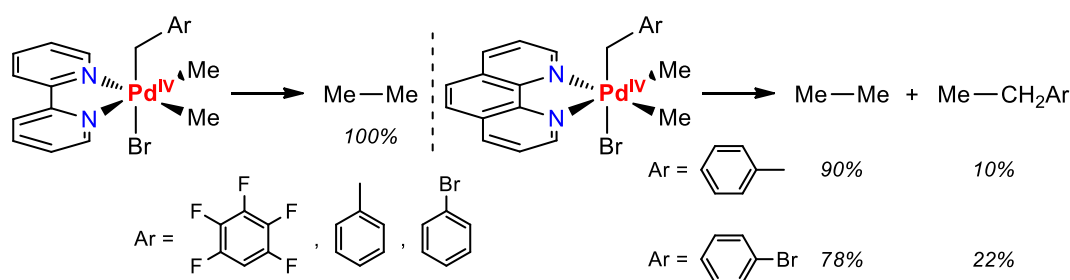


**Figure I.2.** The first results pointed toward a controllable selectivity of the reductive elimination.

A favored reductive elimination step being crucial when thinking about alkyl-alkyl cross coupling reactions, Canty also investigated the oxidative addition of ethyl iodide.<sup>17</sup> This time the kinetics of the reaction did not allow to isolate the expected  $(\text{bipy})\text{PdMe}_2\text{EtI}$  species and was only briefly observed by  $^1\text{H}$  NMR. This was most likely because the rate of the addition was much lowered, as observed with analogous Pt compounds for which reaction with  $\text{EtI}$  was a thousand times slower than with  $\text{MeI}$  due to steric considerations.<sup>18</sup> The analysis of the organic decomposition products

revealed the formation of ethane and propane but also the presence of ethene. This latter product, the result of a  $\beta$ -hydride elimination was proposed to be formed only by the (bipy)PdEtI since appearing only when approaching the end of the reaction (Figure I.3). However, this could also be due to the slower kinetics of the Pd<sup>IV</sup>-triggered  $\beta$ -hydride elimination compared to the reductive elimination. If confirmed, the possibility for Pd<sup>IV</sup> species to avoid this  $\beta$ -hydride elimination pathway due to the absence of a free coordination site would then be a huge asset since it is rarely the case for a Pd<sup>II</sup> center.<sup>19</sup>

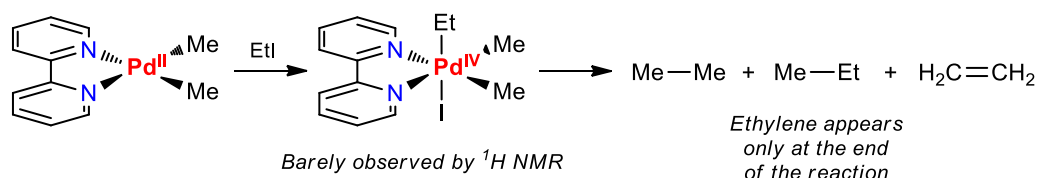


**Figure I.3.** Degradation of the elusive (bipy)PdMe<sub>2</sub>EtI complex.

To further probe this selectivity, an opposite synthetic route was used since substrates such as PhI were not performing an oxidative addition on a PdMe<sub>2</sub> fragment. However, adding MeI to a (bipy)PdMePh precursors allowed the formation of a (bipy)PdMe<sub>2</sub>PhI intermediate.<sup>20</sup> The <sup>1</sup>H NMR monitoring of the reaction allowed to observe two isomers in *ca.* 1:1 ratio, the first one had its Ph group in an axial position while it was found in an equatorial position in the second (Figure I.4). From this mixture of isomers, the reductive elimination produced 80% of ethane and 20% of toluene confirming that the formation of the heavier and potentially more valuable product was once again less favored. In a similar fashion, when the same precursor was treated with benzylbromide, no ethylbenzene was observed and only toluene appeared after the degradation of the Pd<sup>IV</sup> intermediate.

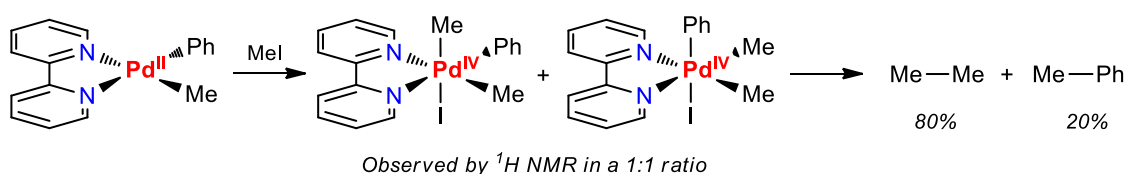


**Figure I.4.** Selectivity of the reductive elimination toward ethane instead of toluene.

Within this same article, another interesting result was the study of the ligand exchange reaction between the (bipy)PdMe<sub>2</sub> and (bipy)PdMePh(CH<sub>2</sub>Ph)Br complexes yielding the (bipy)PdMe<sub>2</sub>(CH<sub>2</sub>Ph)Br and (bipy)PdMePh (Figure I.5.top). This type of reaction, already known with similar Pt complexes,<sup>21</sup> was recently shown to involve a cationic dimer intermediate formed after dissociation of the relatively labile halide ligand.<sup>22</sup> From the precedent example (Figure I.4), this phenomenon could partially explain the selectivity observed for the reductive elimination. When toluene was formed from the high-valent (bipy)PdMe<sub>2</sub>PhI complex, its (bipy)PdMeI byproduct can react with the remaining Pd<sup>IV</sup> species to preferentially yield (bipy)PdMe<sub>3</sub>I from which only ethane is

formed (Figure I.5.bottom). In parallel, the selectivity observed in the (bipy)PdMePh(CH<sub>2</sub>Ph)Br example was attributed to a possible ligand scrambling since the reductive elimination was proposed to only occur between an axial and an equatorial ligand. However, no other <sup>1</sup>H NMR signature than the one attributed to the complex having its benzyl group in axial position was observed.

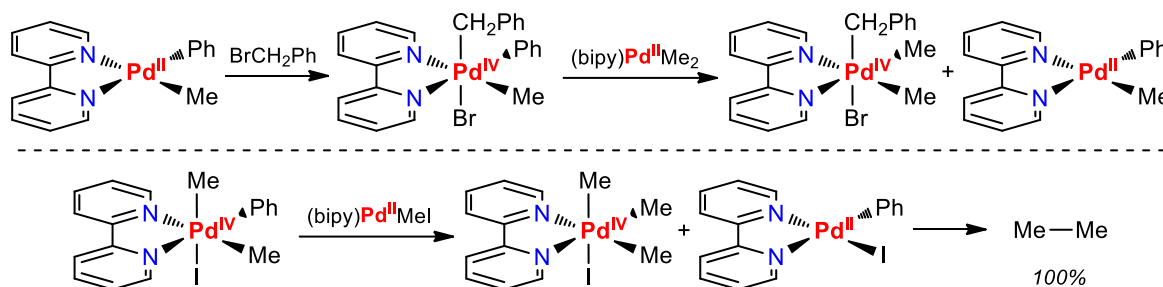


**Figure I.5.** Observed Pd<sup>IV</sup>-Pd<sup>II</sup> ligand exchange (top) and possible explanation of the selectivity observed in Figure I.4 (bottom).

A later strategy employed to reverse the selectivity was found when the 8-(bromomethyl)quinoline organohalide was used.<sup>23</sup> Considering that the reductive elimination is occurring between an axial and an equatorial ligand, the control of the coordination sphere of the Pd center is key to tuning the selectivity. In this case, the coordinating nitrogen atom of the methylquinoline motif forced the Br<sup>-</sup> ion to remain in the outer-sphere while forcing an axial-equatorial coordination that almost prevented ligand scrambling to occur during the reductive elimination step (Figure I.6). The major product was therefore the ethylquinoline (65%) and not ethane (35%), which was really interesting, yet this strategy remained limited to really similar substrates.

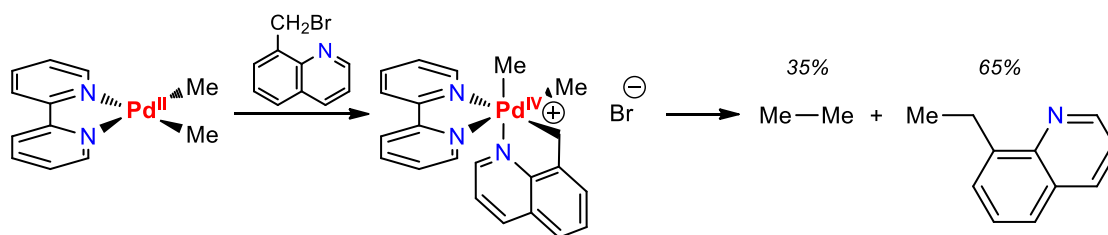


**Figure I.6.** The first example of a reversed selectivity of the reductive elimination thanks to the coordination of the nitrogen of the methylquinoline fragment.

Further works from the group of Canty with other ligands and or with other oxidative reagents allowed to further enrich the variety of observable Pd<sup>IV</sup> species.<sup>24-27</sup> Yet, such compounds remained unstable and rarely isolated and platinum was often used to get an idea of their structural characterization. Among these examples, the remarkably selective C-C coupling from a proposed intermediate (bipy)Pd(alkyl)(aryl)(alkynyl)(OTf) complex was reported with >90% of aryl-alkynyl product and was explained by theoretical studies in which the lower transition state could not lead to the more stable alkyl-aryl product due to the axial position of the alkynyl substituent (Figure I.7).<sup>28</sup>

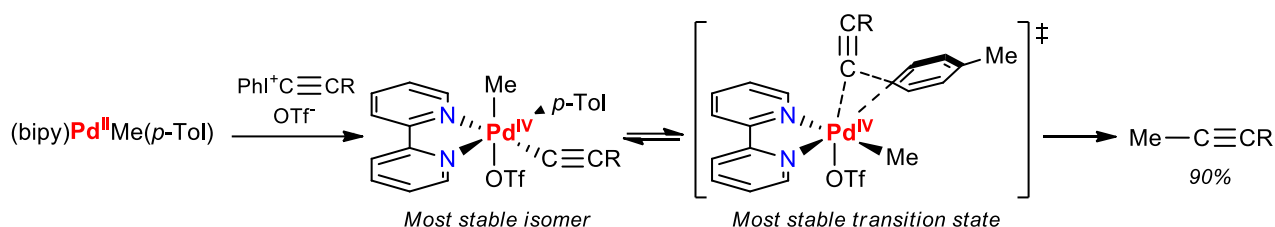


**Figure I.7.** Preference for the formation of the alkynyl-alkyl product due to the most stable intermediate.

Outside of these specific examples of  $\text{Csp}^3\text{-Csp}^3$  bond formation, high-valent palladium chemistry has known significant advances in the past decade.<sup>29–31</sup> Among those contributions, interestingly stable  $\text{Pd}^{\text{IV}}$  species were isolated by the group of Sanford for instance, yet not containing alkyl groups.<sup>32</sup> Such examples of stable  $\text{Pd}(\text{alkyl})_n$  compounds remain extremely rare, even nowadays.

### I.C. Isolated stable high-valent alkyl palladium species

If Canty's findings permitted to isolate several of those elusive  $\text{Pd}^{\text{IV}}$  intermediates formed by oxidative additions, further ligand design and synthetic strategies had to be developed to stabilize such reactive species in order to be able to study them at room temperature. Following the first report from Vedernikov and coworkers,<sup>33</sup> the group of Mirica fully characterized the stable trialkyl  $\text{Pd}^{\text{IV}}$  complex and rationalized its formation via aerobic oxidation of a  $\text{Pd}^{\text{II}}\text{Me}_2$  compound supported by a triazacyclononane ligand (Figure I.8.left).<sup>34</sup> A recent other example was published by the group of Sanford in collaboration with Canty.<sup>35</sup> In this work they managed to oxidize a  $\text{Pd}^{\text{II}}$  precursor supported by trispyrazolyl (Tp) and cycloneophyl ligands to get the highly stable high-valent corresponding species, resisting to reductive elimination of benzocyclobutane even when it was heated for several weeks at 70 °C in MeCN (Figure I.8.right). It has to be noted that these two systems were taking the advantage of having partially labile ligands with three coordination sites to stabilize such species.

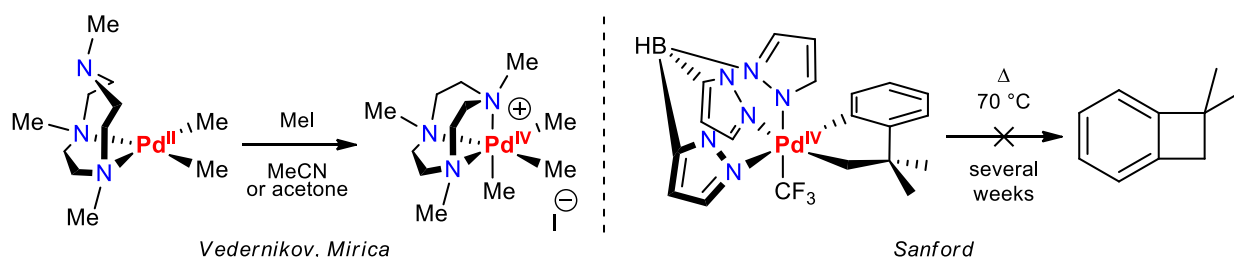


**Figure I.8.** Two examples of highly stable alkyl  $\text{Pd}^{\text{IV}}$  species.

Based on the group's experience with intermediate valent lanthanide architecture, the synthesis of heterobimetallic complexes combining a divalent ytterbium fragment and a palladium center was achieved.<sup>36</sup> Both the  $\text{Cp}^*\text{Yb}(\text{bipym})\text{PdMe}_2$  and the  $\text{Cp}^*\text{Yb}(\text{taphen})\text{PdMe}_2$  compounds were then

treated with MeI to study the stability of the resulting high-valent complexes. While the reduction of the taphen ligand did not affect much the stability of the formed Pd<sup>IV</sup> center, the particular symmetry of the populated bipym  $\pi^*$  orbital fastened the oxidative addition and stabilized the resulting Cp\*<sub>2</sub>Yb(bipym)PdMe<sub>3</sub>I complex. Its half-life at room temperature was measured to be as long as 75 min, a remarkable improvement compared to the monometallic (bipym)PdMe<sub>3</sub>I species ( $t_{1/2} \approx 5$  min) (Figure I.9). Studies with CD<sub>3</sub>I revealed scrambling of the deuterated methyl positions, similarly to what was reported by Canty,<sup>10</sup> thus confirming the lability of the iodide ion. Inspired by the relatively simple synthesis of the tetramethyl platinum complex described in Chapter III, the isolation of its palladium analog was targeted, with the hope to reach even higher stability due to the removal of the halide triggering the reductive elimination.

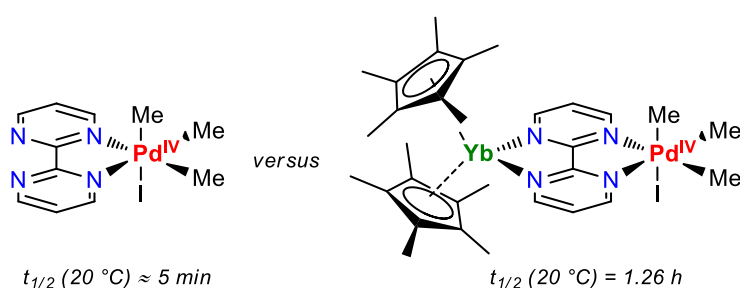


**Figure I.9.** Stabilization of a high-valent Pd center thanks to the coordination of divalent ytterbium fragment.

## II. Synthesis and characterization

### II.A. Development of the synthetic protocol

Considering the sensitivity of the Cp\*<sub>2</sub>Yb(bipym)PdMe<sub>3</sub>I complex, **1**, the straightforward room temperature protocol used with platinum was considerably modified and first trials were launched on very small scale (<10  $\mu\text{mol}$ ). The layering at -40  $^{\circ}\text{C}$  of a freshly prepared MeLi solution in THF on top of solution of **1** also in THF permitted to slowly observe a vague color change of the deep brown solution. Few XRD suitable dark brown blocks were obtained overnight after the concentration of the resulting mixture at -40  $^{\circ}\text{C}$  and confirmed the formation of the expected Cp\*<sub>2</sub>Yb(bipym)PdMe<sub>4</sub> complex, **2**. However, no further isolation and characterization were achieved at this point due to the scale at which the reaction was performed. The upscaling of this protocol was tried several times and always led to impure batches even when the layering was carried out at *ca.* -100  $^{\circ}\text{C}$ . Several issues were identified, first, the removal of the formed LiI salts was extremely tedious yet switching to toluene prevented the formation of **2**, most likely because the C-H benzylic position was too reactive under such conditions, resulting in transmetalation reactions yielding unstable species. Second, the salt metathesis with MeLi was thought to be too rough at a larger scale and switching to the smoother methyl Grignard reagent was tested. The addition at -40  $^{\circ}\text{C}$  of a solution of MeMgI in Et<sub>2</sub>O and a

solution of **1** in THF, pleasingly led to the fast formation of an off-white precipitate accompanied by a slight color change upon leaving the solution for 1h at -40 °C. After filtration, concentration and layering of the resulting solution with cold pentane, dark blocks of **2** were isolated with a 77% yield on a 0.5 mmol scale (Figure II.1). Additionally, a one-pot synthesis of **2** was achieved starting from the (bipym)PdMe<sub>2</sub> precursor with successive additions of Cp\*<sub>2</sub>Yb(OEt<sub>2</sub>), MeI and MeMgI, since all steps of the synthesis were found to be quantitative from <sup>1</sup>H NMR point of view, thus confirming the robustness of this protocol.

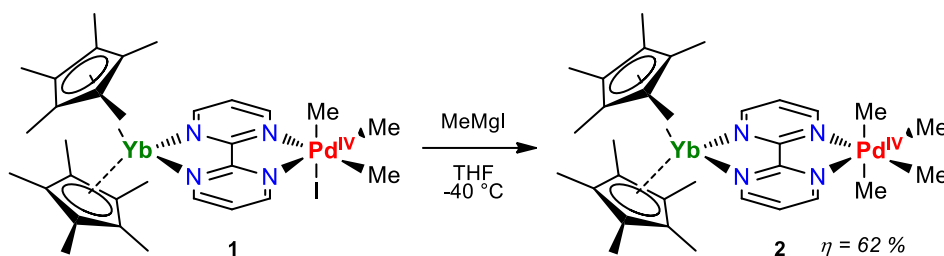


**Figure II.1.** Optimized protocol for the synthesis of **2**.

## II.B. Solid- and solution-state characterization

XRD analysis indicated that **2** crystallized in the P2<sub>1</sub>/n space group with three molecules in the asymmetric unit each accompanied by one co-crystallized thf molecule (Figure II.2). The study of the metrics revealed that the average distance for the C-C bridging bond between the two pyrimidine halves of the bipym ligand measured 1.41(2) Å and was slightly longer than the one found in **1** (1.35(1) Å (Table II.1). This variation did not question the fact that the bipym ligand remained formally reduced but was rather indicative of the tuning of the electronic ground state upon substitution of the iodide ligand as observed with the high-valent platinum series. Similarly, the Pd-Me distances were impacted by the *trans* effect of the bipym ligand,<sup>37</sup> 2.03(2) Å in average for the equatorial ones and 2.12(2) Å for the axial ones and the Pd-N distances were rather similar in **1** and **2**, 2.185(6) Å and 2.17(2) Å respectively. On the Yb side, the average Yb-Cp\*<sub>Ctr</sub> distance of 2.31 Å was still in the trivalent range, as expected.

**Table II.1.** Main metric parameters in Å for the free bipym ligand and the complexes (bipym)PdMe<sub>3</sub>I, **1** and **2**:

Atoms	bipym	(bipym)PdMe <sub>3</sub> I	<b>1</b> <sup>36</sup>	<b>2</b>
C-C <sub>bipym</sub>	1.501(1)	1.496(5)	1.35(1)	1.41(2)
Pd-N <sub>bipym</sub>	/	2.206(8)	2.185(6)	2.17(2)
Pd-C <sub>Me_eq</sub>	/	2.038(7)	2.035(8)	2.03(2)
Pd-C <sub>Me_ax</sub>	/	2.046(4)	2.04(1)	2.12(2)
Yb-Cp* <sub>Ctr</sub>	/	/	2.29	2.31
Yb-N <sub>bipym</sub>	/	/	2.359(5)	2.34(1)



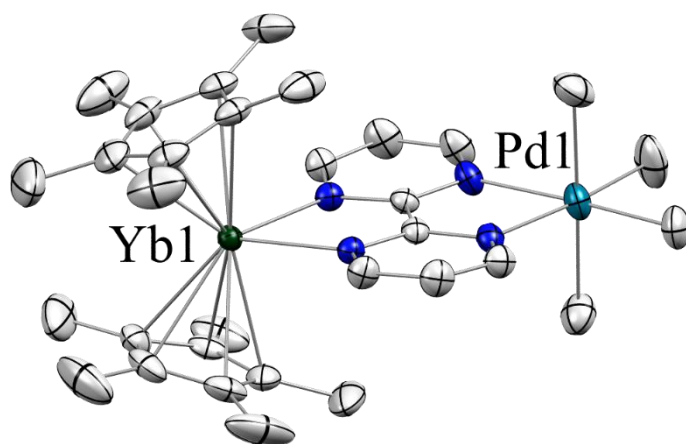


**Figure II.2.** ORTEP of **2** with thermal ellipsoids at 50 % level. Carbon atoms are in grey, nitrogen atoms in blue, the palladium atom in dark blue, and the ytterbium atom in olive green. Hydrogen atoms and co-crystallized thf molecules have been removed for clarity.

The  $^1\text{H}$  NMR spectrum of **2** was rather similar to its platinum analog and typical of such paramagnetic species. Only one  $\text{Cp}^*$  signal was found at 6.01 ppm concurring with a  $\text{C}_{2v}$  symmetry while the bipym ligand peaks were found at 254.66, -1.41 and -149.73 ppm respectively. The signals for the methyl groups were found at -3.53 for the equatorial ones and -15.01 ppm for the axial ones (Figure II.3).

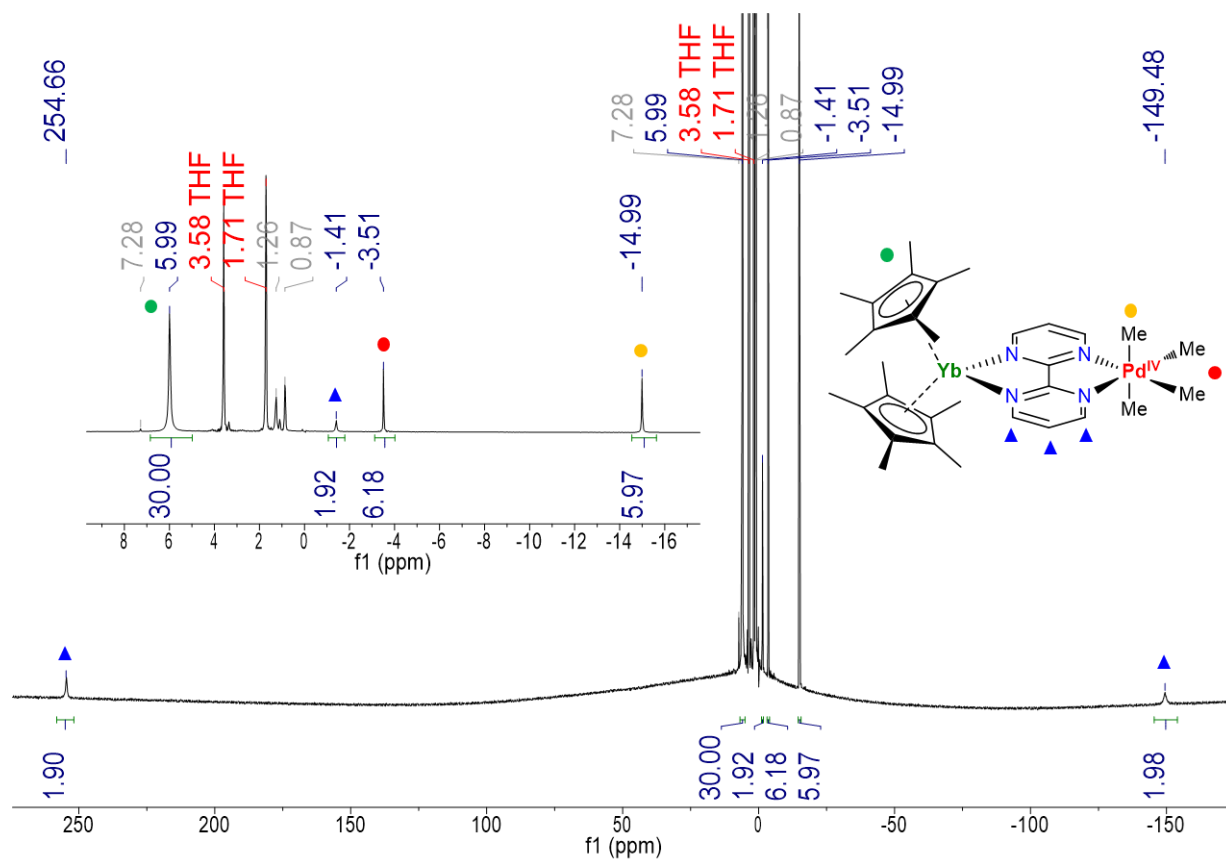


**Figure II.3.**  $^1\text{H}$  NMR spectrum of **2** recorded at 20 °C in  $\text{thf-d}_8$ .

To get the first observations on the magnetic behavior of **2**, a variable temperature (VT) NMR study was performed and the measured chemical shifts were plotted versus  $1/T$  (Figure II.4). As observed with most similar systems, the curves slightly deviated from the linear behavior expected for a Curie-Weiss paramagnet, thus calling for solid-state measurements over a larger temperature range.

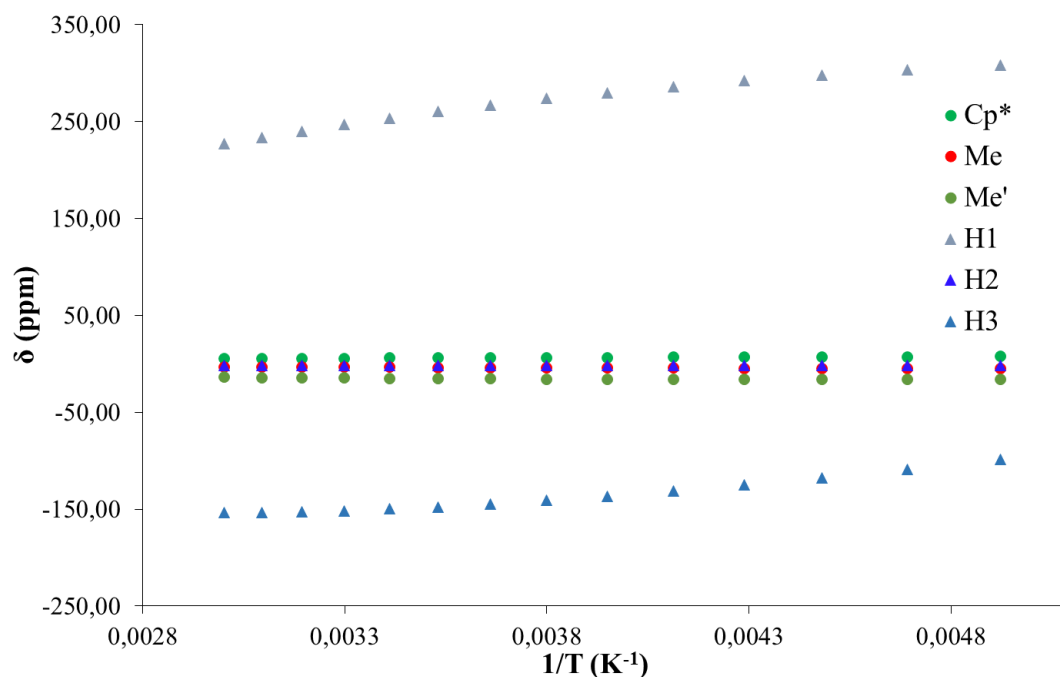


**Figure II.4.** Variable temperature  $^1\text{H}$  NMR of **2** in  $\text{thf-}d_8$ ,  $\delta$  vs  $1/T$  plots in the 193-333 K range.

The  $\chi T$  versus  $T$  plot recorded at 0.1 T between 2 and 300 K, obtained from solid-state magnetic measurements, revealed that **2** was best described as a singlet ground state since  $\chi T$  tends toward  $0 \text{ cm}^3 \text{ K mol}^{-1}$  at 0 K, with a low-lying triplet state being gradually populated above 75 K (Figure II.5.left). The  $\chi T$  value of  $1.828 \text{ cm}^3 \text{ K mol}^{-1}$  at room temperature was significantly lower than the expected  $2.57 \text{ cm}^3 \text{ K mol}^{-1}$  and indicated that the singlet-triplet gap was higher than the one observed with **1**,  $\chi T_{300\text{K}} = 2.49 \text{ cm}^3 \text{ K mol}^{-1}$ . From the  $\chi$  versus  $T$ , a temperature-independent paramagnetism as observed with a  $\chi_{\text{TIP}}$  value of  $0.0045 \text{ cm}^3 \text{ mol}^{-1}$ . The simulated curve with the parameters  $g_{\text{ave}} = 3.48$  and  $2J = -327 \text{ cm}^{-1}$  fitted well with the experimental one which was consistent with only a partial population of the triplet state at room temperature since  $k_{\text{B}}T = 203.7 \text{ cm}^{-1}$  at 293.15 K (Figure II.5.right). The model developed by Lukens *et al.*<sup>38</sup> estimated the  $2J$  gap to  $-332 \text{ cm}^{-1}$ , which was rather close to the fitted value.

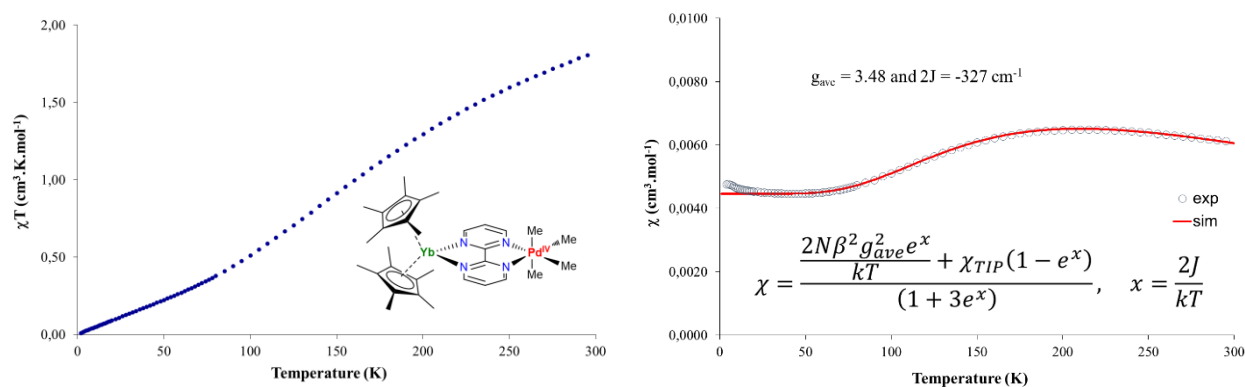


**Figure II.5.** Solid-state temperature-dependent magnetic data of **2** recorded at 0.1 T: (left)  $\chi T$  vs  $T$  plot and (right)  $\chi$  vs  $T$  plot and its simulation with the TIP-including Bleaney-Bowers equation.

### III. Stability and reactivity studies

#### III.A. $^1\text{H}$ NMR monitoring of the degradation

Since removing the iodide ligand was thought to be the key to even further stabilizing a  $\text{Pd}^{\text{IV}}$  center by increasing the activation barrier of the reductive elimination, degradation studies at 20 °C were performed by  $^1\text{H}$  NMR monitoring over 61 h of samples at known concentrations in  $\text{thf-}d_8$ . An important note about the treatment of the obtained data sets is that applying a linear correction for all the integrations is mandatory to avoid overestimation of the percentage of the remaining compound, especially near the end of the reaction or at low concentration. This being said, at  $1 \cdot 10^{-2}$  M, the full degradation was reached after the end of the monitoring since only 5% of the compound was left while 76% of the  $\text{Cp}^*_2\text{Yb}(\text{bipym})\text{PdMe}_2$  precursor was regenerated (Figure III.1).

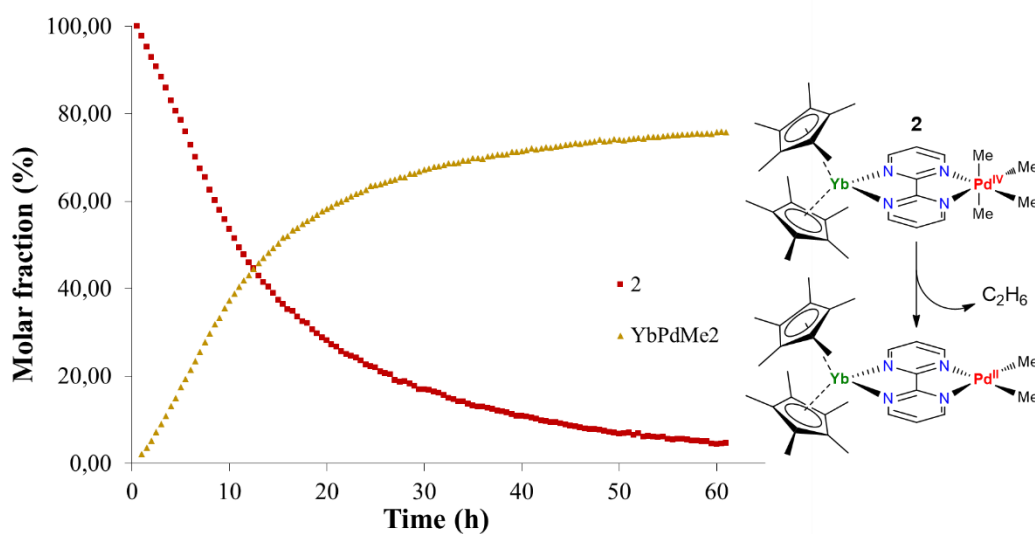


**Figure III.1.**  $^1\text{H}$  NMR monitored degradation of **2**, at 20 °C in  $\text{thf-}d_8$ .

This nicely confirmed that **2** was significantly more stable than **1**, yet still able to perform a reductive elimination. The half-life of **2** at this concentration was 11 h at room temperature, a value that could be increased to 19 h, 36 h and 45 h upon lowering the concentration to  $5.10^{-3}$  M,  $1.10^{-3}$  M and  $5.10^{-4}$  M respectively (Figure III.2). These concentration-dependent half-lives were indicating that the degradation was not following a first-order pathway and the logarithm of the molecular fraction of **2**, was more pointing toward a pseudo-first-order reaction (Figure III.3). It directly implied that the proposed mechanism for the reductive elimination step of **1**, would be triggered by the decoordination of the iodide ligand was not entirely followed in the case of **2**. This was not surprising since such lability was not expected for a methyl group.

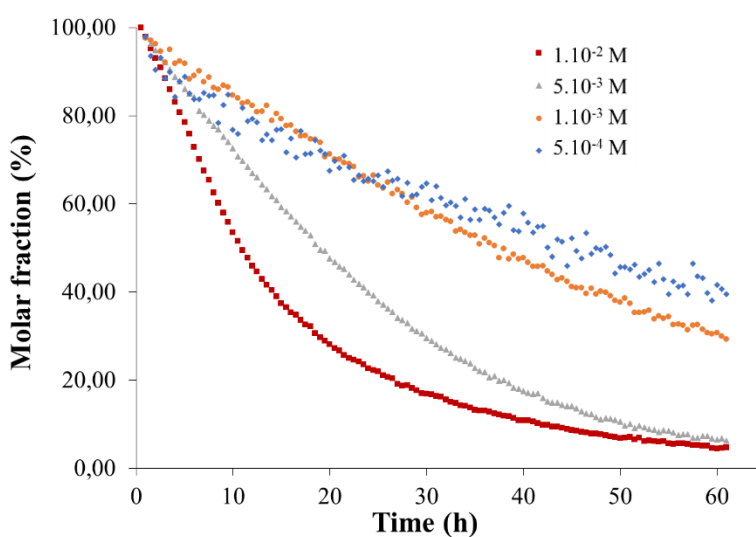


**Figure III.2.**  $^1\text{H}$  NMR monitored degradation of **2**, at 20 °C in  $\text{thf-}d_8$ , comparison between several starting concentrations.

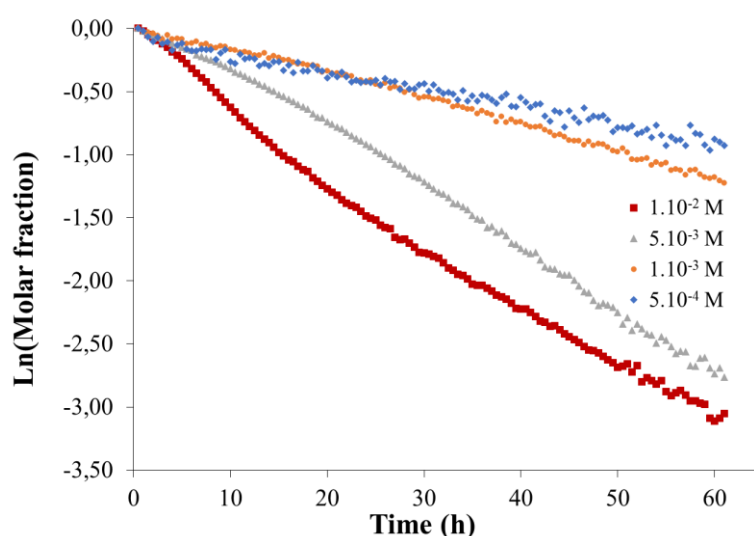


**Figure III.3.** Logarithm of the molar fraction  $[\mathbf{2}]/[\mathbf{2}]_{t=0\text{h}}$  at several starting concentrations.

To confirm this statement, the synthesis of **2-d<sub>3</sub>** was performed by using CD<sub>3</sub>MgI instead of MeMgI. The <sup>1</sup>H NMR spectra recorded right after its dissolution in thf-*d*<sub>8</sub> indicated a 5.76:3.12 ratio between the integrated protons of the equatorial and axial methyl groups (Figure III.4), a ratio indicating that almost no scrambling occurred during the synthesis, contrary to what was observed for **1-d<sub>3</sub>** synthesized with CD<sub>3</sub>I.<sup>36</sup>

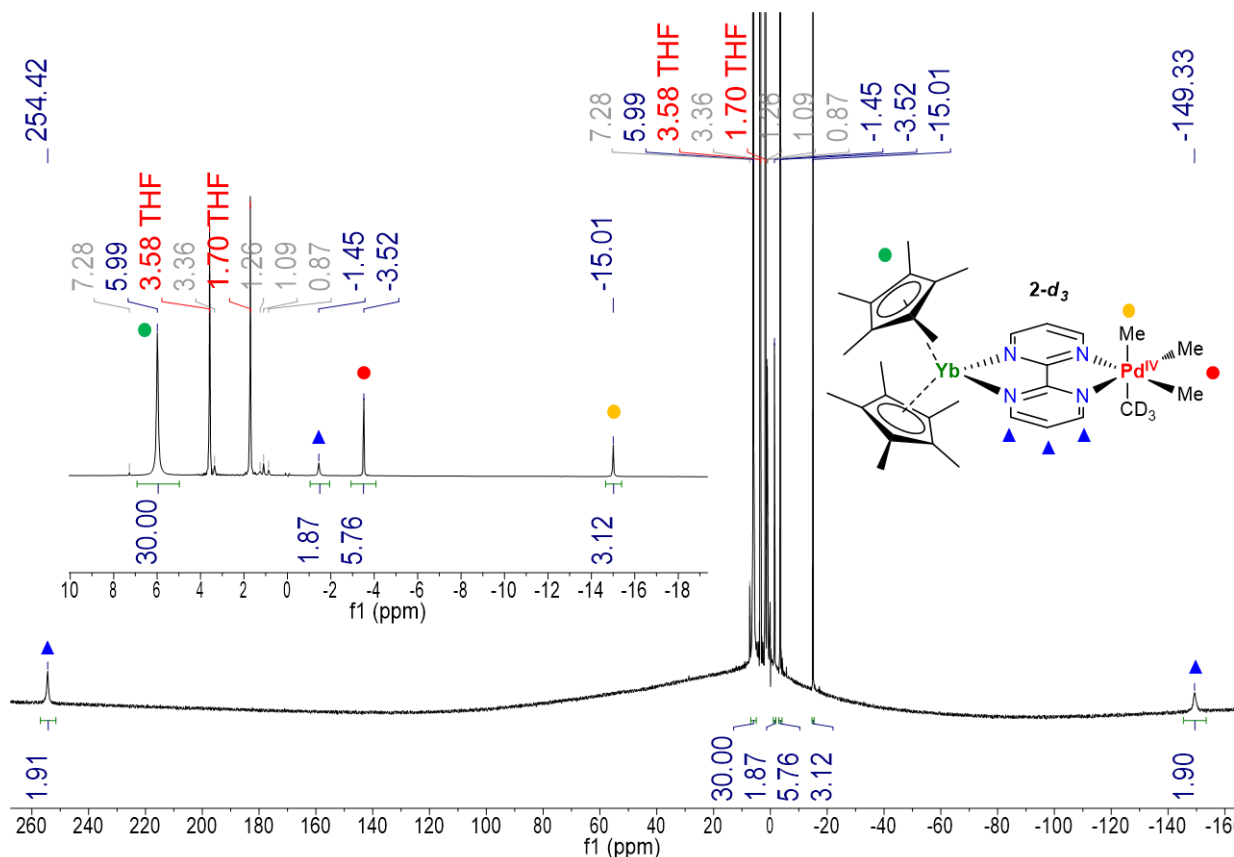


**Figure III.4.** <sup>1</sup>H NMR spectrum of **2-d<sub>3</sub>** recorded at 20 °C in thf-*d*<sub>8</sub>.

However, upon degradation, this ratio slowly evolved to 4.68:3.23 after 15 h (residual protio signal of the thf-*d*<sub>8</sub> served as internal reference). Although the elimination of ethane-*d*<sub>3</sub> could be favored compared to ethane-*d*<sub>0</sub> such unilateral evolution was in better agreement with a slow scrambling of the methyl groups. Several pathways were considered. First, a dissociative one where the methyl group, although being less labile than a halide ligand, allowed intramolecular scrambling via a cationic intermediate that could also eliminate ethane (Figure III.5.top). Second, a bimolecular ligand exchange between two Pd<sup>IV</sup> centers, such phenomenon could also explain the deviation from the first order pathway since a concerted reductive elimination might also happen (Figure III.5.middle). The third and last possibility, a ligand exchange between a Pd<sup>IV</sup> center and a Pd<sup>II</sup>, as observed by Canty (Figure III.5.bottom), such phenomenon however had no impact on the degradation of **2** since all its methyl groups are identical.<sup>20,22</sup>

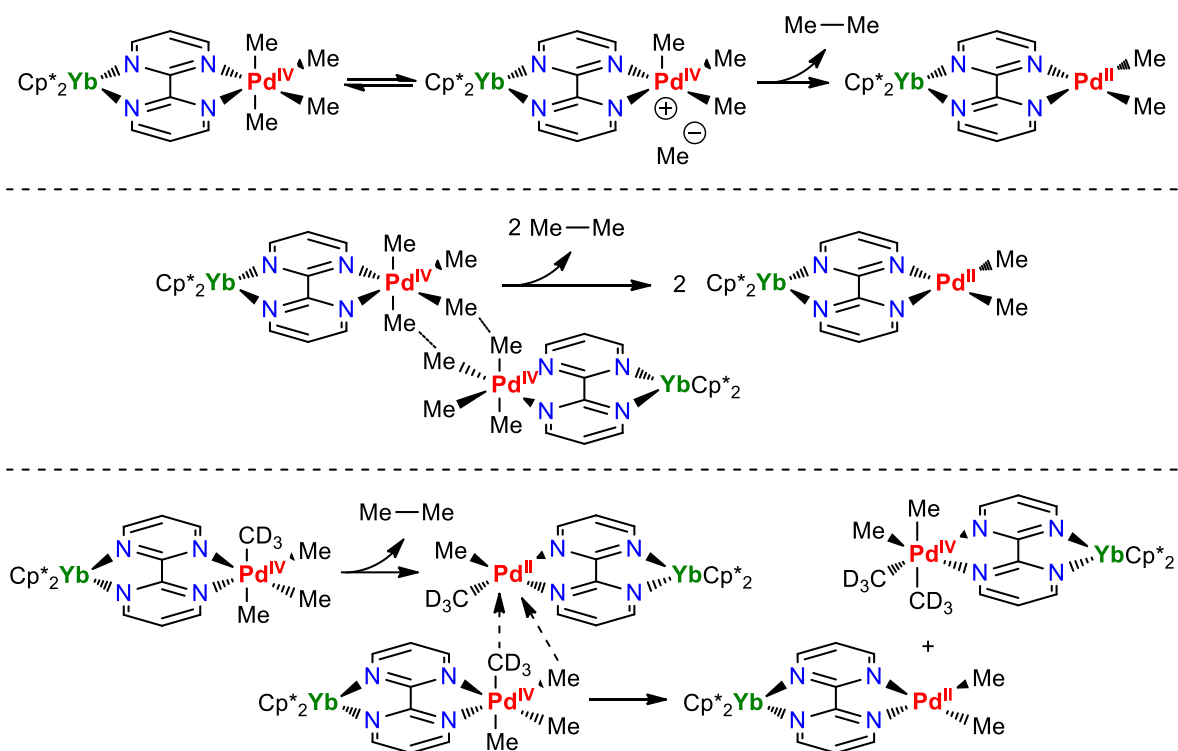


**Figure III.5.** Possible reductive elimination mechanisms (top and middle) and possible ligand scrambling (bottom).

While the first two possible pathways could not be deconvoluted with the monitoring of the degradation, the occurrence of the third one was investigated by dissolving together  $\text{Cp}^*_2\text{Yb}(\text{bipym})\text{PdMe}_2$  and a fully deuterated version of **2**,  $\text{Cp}^*_2\text{Yb}(\text{bipym})\text{Pd}(\text{CD}_3)_4$ , **2-*d*<sub>12</sub>**. While the formation of **2** was not obvious since it was most likely consumed faster than it was formed, clear evidence of a ligand exchange was observed. First the stable  $\text{PdMe}_2$  center methyl signal decreased in intensity over the course of the degradation of **2-*d*<sub>12</sub>** and its integration versus the residual protio signal of the *thf-d*<sub>8</sub> decreased by 5% overnight and by 20% after 4.5 days, time at which almost all **2-*d*<sub>12</sub>** was consumed. Second the appearance of ethane-*d*<sub>3</sub>, as a small shouldering peak next to the residual pentane present at the start of the experiment, could only result from a ligand scrambling (Figure III.6 and Figure III.7).

A crossover experiment between **2** and **2-*d*<sub>12</sub>** was consecutively launched to hopefully observe proofs of a bimolecular pathway. However, if this experiment also revealed the formation of ethane-*d*<sub>3</sub>, the presence of this hemi-deuterated product could be the consequence of the ligand scrambling observed within the previous experiment as well as the bimolecular elimination already mentioned. Overall, these experimental investigations did not allow to certainly propose a mechanism. As it was the case in the former chapter, this situation indicated the need for theoretical studies, both at the singlet and triplet states, to further conclude on the mechanism.

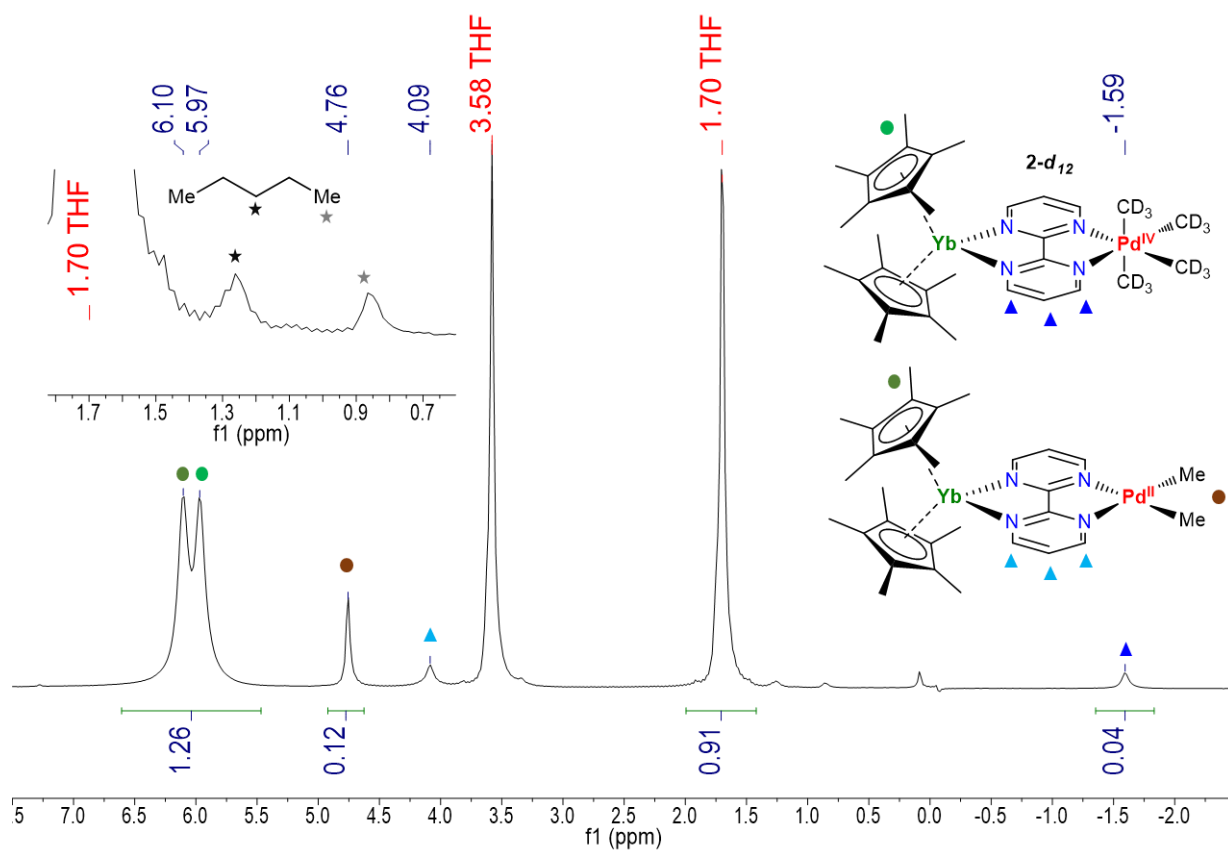


Figure III.6. Ligand exchange between the  $2\text{-d}_{12}$  and  $\text{Cp}^*_2\text{Yb}(\text{bipym})\text{PdMe}_2$  complexes,  $t = 0\text{h}$ .

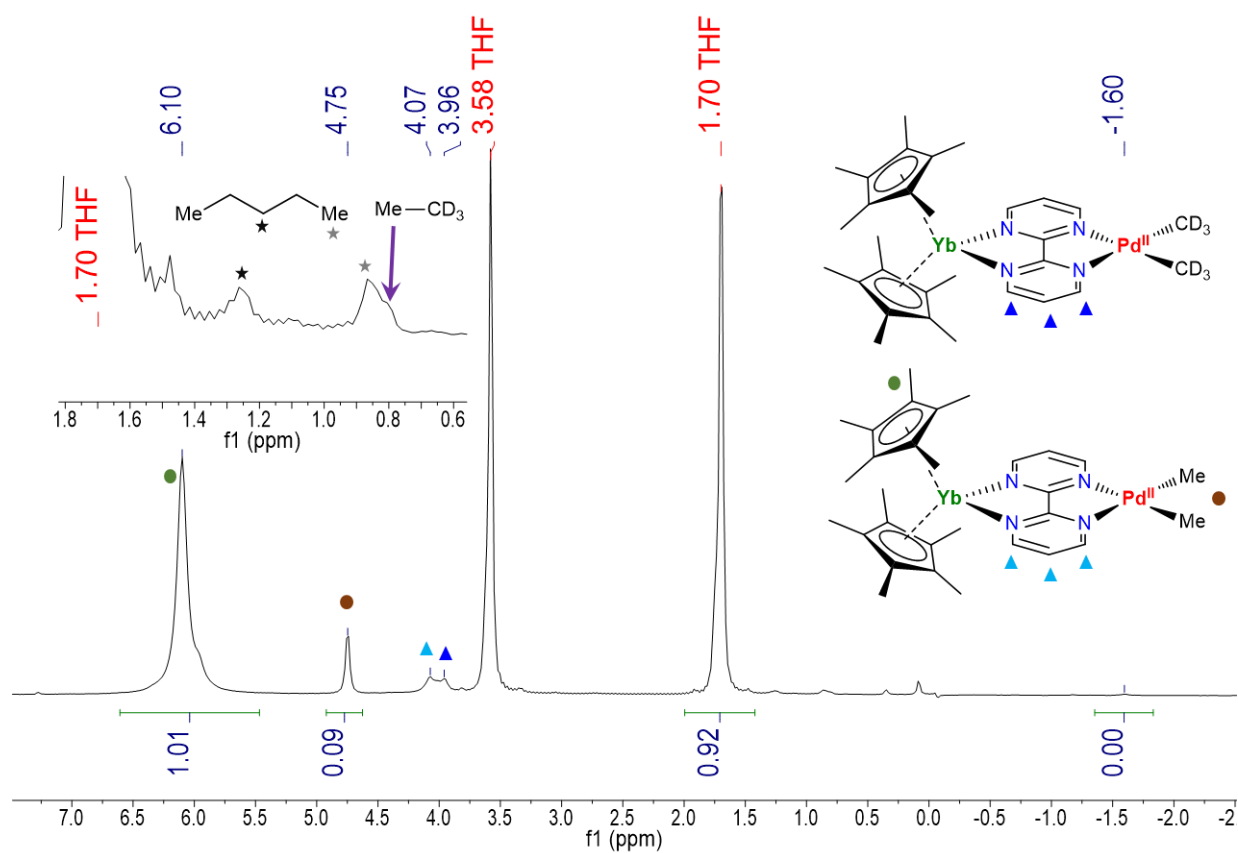
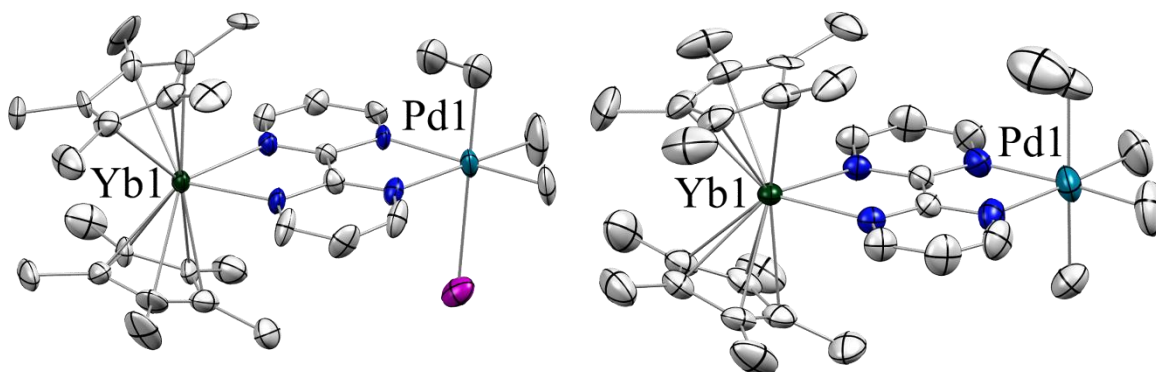


Figure III.7. Ligand exchange between the  $2\text{-d}_{12}$  and  $\text{Cp}^*_2\text{Yb}(\text{bipym})\text{PdMe}_2$  complexes,  $t = 4.5\text{ days}$ .

### III.B. Selectivity of the reductive elimination

To probe the selectivity of the reductive elimination, several derivatives of **2** were synthesized. First, treating **1** with other Grignard reagents such as EtMgI, *i*PrMgI or PhMgI was tried. While in the first two cases, the  $^1\text{H}$  NMR were indicating an unexpected reactivity, the phenyl Grignard reagent seemed to react steadily and form the expected  $\text{Cp}^*_2\text{Yb}(\text{bipym})\text{PdMe}_3\text{Ph}$  complex, **3**. However, the latter was not isolated and further studies are needed to confirm this result. Considering that using Grignard reagents that can perform a  $\beta$ -hydride elimination upon reacting with the Pd center was a limitation, another synthetic strategy was used. Instead of starting from **1**, the  $\text{Cp}^*_2\text{Yb}(\text{bipym})\text{PdMe}_2\text{EtI}$  complex, **4**, was isolated by switching from MeI to EtI. Although the reaction seemed slower for the aforementioned reasons,<sup>18</sup> the lower energy barrier due to the reduced bipym fragment allowed to isolate a few tens of milligrams of **4** as XRD suitable crystals after a few days of reaction. In the solid-state, the ethyl group was only found in axial position and no significant changes were observed upon studying the metrics (Figure III.8.left). In solution, however, a mixture of ethyl in axial (major isomer) and equatorial (minor isomer) positions was observed.



**Figure III.8.** ORTEPs of **4** and **5** with thermal ellipsoids at 50 % level.

Carbon atoms are in grey, nitrogen atoms in blue, the iodide atom in purple, the palladium atom in dark blue, and the ytterbium atom in olive green. Hydrogen atoms have been removed for clarity.

The reaction of MeMgI with **4** at  $-40\text{ }^{\circ}\text{C}$  led smoothly to the targeted  $\text{Cp}^*_2\text{Yb}(\text{bipym})\text{PdMe}_3\text{Et}$  complexes, **5**, as XRD suitable crystals that also revealed an Et group only found in an axial position in the solid-state (Figure III.8.right). The  $^1\text{H}$  NMR spectra, however, was consistent with the presence of the two isomers in which the ethyl group was either in axial ( $\mathbf{5}_{\text{ax}}$  ~66%) or equatorial position ( $\mathbf{5}_{\text{eq}}$  ~33%) (Figure III.9).



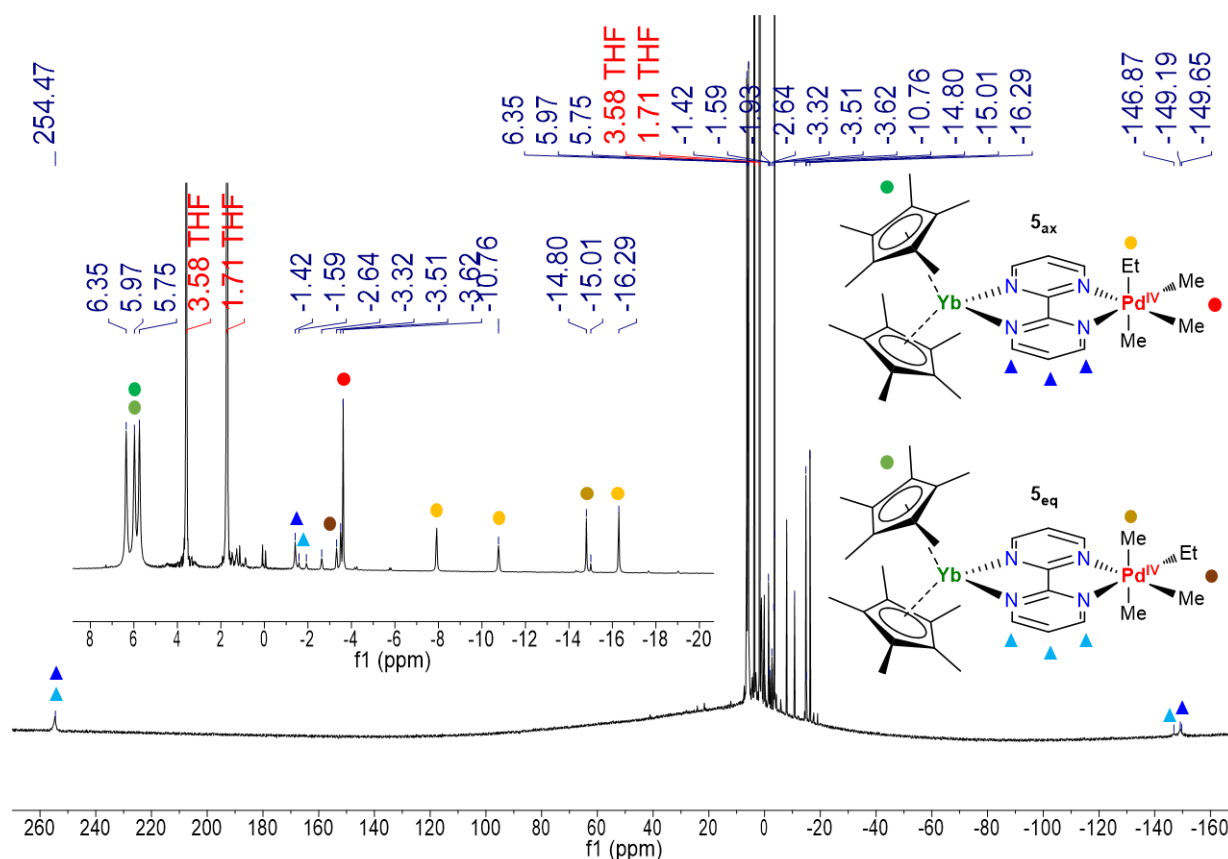


**Figure III.9.**  $^1\text{H}$  NMR spectrum of **5** recorded at 20 °C in  $\text{thf-}d_8$ . A proposed attribution of the peaks is made and the ratio between the two isomers **5<sub>ax</sub>** and **5<sub>eq</sub>** is roughly estimated to 2:1 by comparing the  $\text{Cp}^*$  signals.

This was not surprising and unavoidable with such protocol since it was the direct consequence of the easy scrambling possible in **4**. However, unavoidable does not mean uncontrollable and the final ratio of isomers might be modulated in the future. Tuning the reaction conditions such as performing the oxidative addition of  $\text{EtI}$  and the addition of  $\text{MeMgI}$  in  $\text{Et}_2\text{O}$  is an option, since it is a solvent in which the iodide lability should be reduced. Contrary to what was observed in Canty's case,<sup>17</sup> no ethylene was formed, meaning the complete absence of  $\beta$ -hydride elimination. Only propane and ethane were observed as the reaction products, in a *ca.* 65%:35% ratio (Figure III.10).

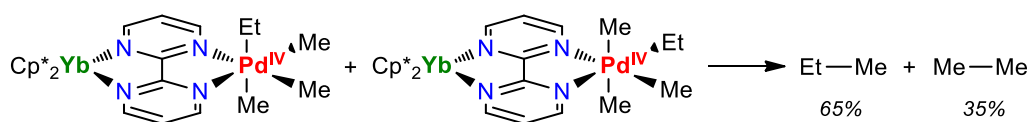


**Figure III.10.** Selective reductive elimination of propane instead of ethane with complex **5**, a mixture of **5<sub>ax</sub>** and **5<sub>eq</sub>**.

This first result, although preliminary, was really encouraging since significant selectivity was achieved. The obtained ratio of products seemed related to the roughly estimated ratio of isomers **5<sub>ax</sub>**:**5<sub>eq</sub>**. If further studies confirm this observation, this would mean that the reductive elimination from **5<sub>ax</sub>** was highly in favor of the formation of propane, similarly to what Canty observed with his

Pd(alkyl)(aryl)(alkynyl) system.<sup>28</sup> To confirm this hypothesis, computational studies should once again be performed.

## IV. Conclusion and perspectives

To conclude, the synthesis of unprecedented tetraalkyl Pd<sup>IV</sup> complexes was performed thanks to the stabilization of high-valent transition metal centers conferred by the Cp\*<sub>2</sub>Yb(bipym) fragment. A really robust synthetic protocol was developed, even allowing facile and quantitative one pot synthesis of **2** from the simple (bipym)PdMe<sub>2</sub> precursor. The substitution of the labile iodide ligand by an alkyl group greatly enhanced the stability of the Pd<sup>IV</sup> center with the half-life of **2** estimated to be ten times higher than the previously studied complex **1**. The investigations conducted with deuterated versions of **2**, in order to elucidate the mechanism of the reductive elimination, supported a pseudo-first order type of reaction most likely resulting from different competing processes. Yet, since the experiences were not conclusive enough to choose between those pathways, computational studies are now needed. While the direct synthesis of derivatives of **2** was probed with other Grignard reagents, only PhMgI seemed to perform as planned. Therefore, a reverse synthetic protocol was developed to isolate the Cp\*<sub>2</sub>Yb(bipym)PdMe<sub>3</sub>Et complex, **5** and confirm its incapacity to perform a  $\beta$ -hydride elimination. The latter complex was however only observed as a mixture of isomers resulting from the easy scrambling of the alkyl ligand when its precursor **4** was left in solution in coordinating solvents. The only organic products observed upon degradation were propane and ethane in a *ca.* 65%:35% ratio, this preliminary result being a rare example of selectivity toward the formation of the heavier product instead of ethane. Theoretical investigations are now needed to get a better understanding of this selectivity.

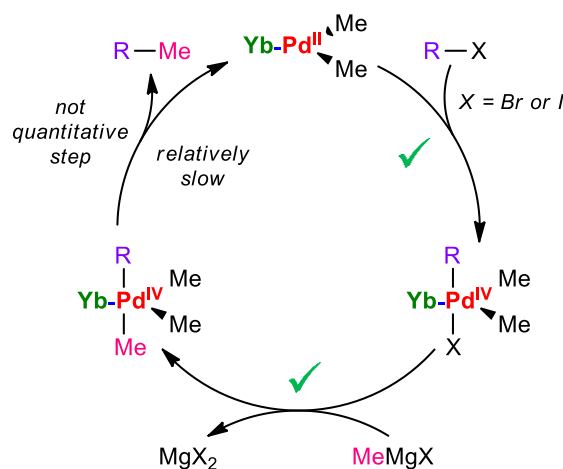


Figure IV.1. Possible catalytic cycle and current limitations.

Among the further investigations planned with such tetraalkyl species, the synthesis of more derivatives of **2** is planned. This will hopefully generalize the possibility to control the selectivity of the reductive elimination and guide it toward the formation of heavier and more valuable products. Once this point is verified, catalytic trials should be performed since the heterometallic product, the  $\text{Cp}^*_2\text{Yb}(\text{bipym})\text{PdMe}_2$  precursor of **1** is regenerated upon the degradation of **2** which is formed quantitatively from its precursors (Figure IV.1). Yet, the regeneration of the  $\text{PdMe}_2$  compound is actually only partial so the turnover number of such a system will remain low as long as this issue is not dealt with. The understanding of the mechanism of the reductive elimination is thus key to solving this problem and reaching high performances. On the positive side, preliminary tests have shown that the Grignard reagent is compatible with the  $\text{PdMe}_2$  fragment and even that the two first steps can be performed simultaneously by adding a  $\text{MeI} + \text{MeMgI}$  solution directly on the  $\text{Cp}^*_2\text{Yb}(\text{bipym})\text{PdMe}_2$  complex to quantitatively form its tetramethyl oxidized form.

## References

- (1) The Nobel Prize in Chemistry **2010**. <https://www.nobelprize.org/prizes/chemistry/2010/summary/>.
- (2) Uson, R.; Fornies, J.; Navarro, R. *J. Organomet. Chem.* **1975**, 96 (2), 307–312. [https://doi.org/10.1016/S0022-328X\(00\)83563-9](https://doi.org/10.1016/S0022-328X(00)83563-9).
- (3) Byers, P. K.; Canty, A. J.; Skelton, B. W.; White, A. H. *J. Chem. Soc. - Ser. Chem. Commun.* **1986**, 3 (1722), 1722–1724. <https://doi.org/10.1039/C39860001722>.
- (4) Vilar, R.; Mingos, D. M. P.; Cardin, C. J. *J. Chem. Soc. Dalt. Trans.* **1996**, No. 23, 4313–4314. <https://doi.org/10.1039/DT9960004313>.
- (5) Cotton, F. A.; Gu, J.; Murillo, C. A.; Timmons, D. J. *J. Am. Chem. Soc.* **1998**, 120 (50), 13280–13281. <https://doi.org/10.1021/ja9832313>.
- (6) Liu, J.; Bollmeyer, M. M.; Kim, Y.; Xiao, D.; MacMillan, S. N.; Chen, Q.; Leng, X.; Kim, S. H.; Zhao, L.; Lancaster, K. M.; Deng, L. *J. Am. Chem. Soc.* **2021**, 143 (28), 10751–10759. <https://doi.org/10.1021/jacs.1c04965>.
- (7) Powers, D. C.; Ritter, T. *Nat. Chem.* **2009**, 1 (4), 302–309. <https://doi.org/10.1038/nchem.246>.
- (8) Deprez, N. R.; Sanford, M. S. *J. Am. Chem. Soc.* **2009**, 131 (31), 11234–11241. <https://doi.org/10.1021/ja904116k>.
- (9) Khusnutdinova, J. R.; Rath, N. P.; Mirica, L. M. *J. Am. Chem. Soc.* **2010**, 132 (21), 7303–7305. <https://doi.org/10.1021/ja103001g>.
- (10) Byers, P. K.; Canty, A. J.; Skelton, B. W.; White, A. H.; Whitelb, A. H. *Organometallics* **1990**, 9 (3), 826–832. <https://doi.org/10.1021/om00117a044>.
- (11) Byers, P. K.; Canty, A. J.; Skelton, B. W.; White, A. H. *Organometallics* **1990**, 9 (3), 826–832. <https://doi.org/10.1021/om00117a044>.
- (12) De Graaf, W.; Boersma, J.; Smeets, W. J. J.; Spek, A. L.; Van Koten, G. *Organometallics* **1989**, 8 (12), 2907–2917. <https://doi.org/10.1021/om00114a028>.
- (13) Canty, A. J.; Watson, A. A.; Skelton, B. W.; White, A. H. *J. Organomet. Chem.* **1989**, 367 (3), C25–C28. [https://doi.org/10.1016/0022-328X\(89\)87065-2](https://doi.org/10.1016/0022-328X(89)87065-2).
- (14) Byers, P. K.; Canty, A. J.; Skelton, B. W.; Traill, P. R.; Watson, A. A.; White, A. H. *Organometallics* **1990**, 9 (12), 3080–3085. <https://doi.org/10.1021/om00162a020>.
- (15) Byers, P. K.; Canty, A. J.; Skelton, B. W.; Traill, P. R.; Watson, A. A.; White, A. H. *Organometallics* **1992**, 11 (9), 3085–3088. <https://doi.org/10.1021/om00045a023>.
- (16) van Asselt, R.; Rijnberg, E.; Elsevier, C. J. *Organometallics* **1994**, 13 (2), 706–720. <https://doi.org/10.1021/om00014a049>.
- (17) Byers, P. K.; Canty, A. J.; Traill, P. R.; Watson, A. A. *J. Organomet. Chem.* **1990**, 390 (3), 399–407. [https://doi.org/10.1016/0022-328X\(90\)85108-B](https://doi.org/10.1016/0022-328X(90)85108-B).
- (18) Monaghan, P. K.; Puddephatt, R. J. *J. Chem. Soc. Dalt. Trans.* **1988**, No. 3, 595–599. <https://doi.org/10.1039/DT9880000595>.
- (19) Cárdenas, D. J. *Angew. Chemie Int. Ed.* **1999**, 38 (20), 3018–3020. [https://doi.org/10.1002/\(SICI\)1521-3773\(19991018\)38:20<3018::AID-ANIE3018>3.0.CO;2-F](https://doi.org/10.1002/(SICI)1521-3773(19991018)38:20<3018::AID-ANIE3018>3.0.CO;2-F).
- (20) Markies, B. A.; Janssen, M. D.; Boersma, J.; van Koten, G.; Canty, A. J.; Spek, A. L. *Recl. des Trav. Chim. des Pays-Bas* **1991**, 110 (11), 477–479. <https://doi.org/10.1002/recl.19911101108>.
- (21) Aye, K.-T.; Canty, A. J.; Crespo, M.; Puddephatt, R. J.; Scott, J. D.; Watson, A. A. *Organometallics* **1989**, 8 (6), 1518–1522. <https://doi.org/10.1021/om00108a024>.
- (22) Canty, A. J.; Ariafard, A. *J. Organomet. Chem.* **2018**, 872, 110–113. <https://doi.org/10.1016/j.jorganchem.2018.07.036>.

- (23) Canty, A. J.; Hoare, J. L.; Patel, J.; Pfeffer, M.; Skelton, B. W.; White, A. H. *Organometallics* **1999**, *18* (14), 2660–2667. <https://doi.org/10.1021/om990130k>.
- (24) Canty, A. J.; Honeyman, R. T.; Roberts, A. S.; Traill, P. R.; Colton, R.; Skelton, B. W.; White, A. H. *J. Organomet. Chem.* **1994**, *471* (1), C8–C10. [https://doi.org/10.1016/0022-328X\(94\)88139-1](https://doi.org/10.1016/0022-328X(94)88139-1).
- (25) Canty, A. J.; Jin, H.; Roberts, A. S.; Skelton, B. W.; Traill, P. R.; White, A. H. *Organometallics* **1995**, *14* (1), 199–206. <https://doi.org/10.1021/om00001a031>.
- (26) Canty, A. J.; Rodemann, T.; Skelton, B. W.; White, A. H. *Organometallics* **2006**, *25* (16), 3996–4001. <https://doi.org/10.1021/om0601495>.
- (27) Canty, A. J. *Dalt. Trans.* **2009**, No. 47, 10409–10417. <https://doi.org/10.1039/B914080H>.
- (28) Sharma, M.; Ariaferd, A.; Canty, A. J.; Yates, B. F.; Gardiner, M. G.; Jones, R. C. *Dalt. Trans.* **2012**, *41* (38), 11820–11828. <https://doi.org/10.1039/C2DT31086D>.
- (29) Xue, L.; Lin, Z. *Chem. Soc. Rev.* **2010**, *39* (5), 1692–1705. <https://doi.org/10.1039/B814973A>.
- (30) Sehnal, P.; Taylor, R. J. K.; Fairlamb, I. J. S. *Chem. Rev.* **2010**, *110* (2), 824–889. <https://doi.org/10.1021/cr9003242>.
- (31) Zhang, B.; Yan, X.; Guo, S. *Chem. – A Eur. J.* **2020**, *26* (43), 9430–9444. <https://doi.org/10.1002/chem.202001074>.
- (32) Dick, A. R.; Kampf, J. W.; Sanford, M. S. *J. Am. Chem. Soc.* **2005**, *127* (37), 12790–12791. <https://doi.org/10.1021/ja0541940>.
- (33) A. Sobanov, A.; N. Vedernikov, A.; Dyker, G.; N. Solomonov, B. *Mendeleev Commun.* **2002**, *12* (1), 14–15. <https://doi.org/10.1070/MC2002v012n01ABEH001530>.
- (34) Khusnutdinova, J. R.; Qu, F.; Zhang, Y.; Rath, N. P.; Mirica, L. M. *Organometallics* **2012**, *31* (13), 4627–4630. <https://doi.org/10.1021/om300426r>.
- (35) Camasso, N. M.; Canty, A. J.; Ariaferd, A.; Sanford, M. S. *Organometallics* **2017**, *36* (22), 4382–4393. <https://doi.org/10.1021/acs.organomet.7b00613>.
- (36) Goudy, V.; Jaoul, A.; Cordier, M.; Clavaguéra, C.; Nocton, G. *J. Am. Chem. Soc.* **2017**, *139* (31), 10633–10636. <https://doi.org/10.1021/jacs.7b05634>.
- (37) Clegg, D. E.; Hall, J. R.; Swile, G. A. *J. Organomet. Chem.* **1972**, *38* (2), 403–420. [https://doi.org/10.1016/S0022-328X\(00\)83343-4](https://doi.org/10.1016/S0022-328X(00)83343-4).
- (38) Lukens, W. W.; Magnani, N.; Booth, C. H. *Inorg. Chem.* **2012**, *51* (19), 10105–10110. <https://doi.org/10.1021/ic300037q>.

## General conclusion and perspectives

### I. A study across group 10 transition metals

If the intermediate valence in lanthanide compounds has now been broadly studied in various situations, from  $\text{Ce}^{\text{IV}}$  to  $\text{Yb}^{\text{II}}$ , using such phenomenon to tune a transition metal reactivity remained limited to the two examples of the  $\text{Cp}^*_2\text{Yb}(\text{bipym})\text{PdMe}_2$  and analogous Yb-Ni system when the projects presented in this manuscript were started. As a first objective, considering the perspectives opened after the synthesis of the lanthanidocenes series of sandwich complexes with the cyclononatetraenyl (Cnt) ligand, the extension of the Ln-Cnt coordination chemistry to the trivalent state was investigated and resulted in the synthesis of the  $(\text{Cot})\text{Ln}(\text{Cnt})$  series of complexes (Ln = Sm, Tb, Dy, Ho, Er, Tm and Lu, Cot = cyclooctatetraenyl). If such compounds were first targeted to widen the scope of accessible organolanthanide precursors and to potentially involve them in multimetallic architectures, their structural study allowed to unveil a size-induced hapticity switch of the versatile Cnt ligand (Figure I.1). The rigorous study of this fluctuational behavior permitted to further refine the theoretical estimation of their promising magnetic properties.

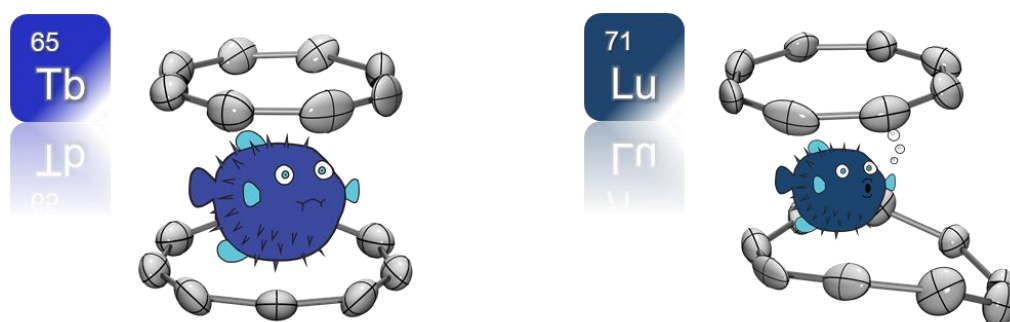


**Figure I.1.** Schemed representation of the size-induced hapticity switch in the  $(\text{Cot})\text{Ln}(\text{Cnt})$  series.

To extend the results obtained with the Yb-Pd and Yb-Ni heterobimellatic complexes, investigations on Yb-Pt analogous systems were conducted. This work was mainly performed having

in mind the potential of such species to be able to perform methane C-H activation due their original electronic architecture. Benefiting from the natural stability of  $\text{Pt}^{\text{IV}}$  species, four different high-valent  $\text{Pt}(\text{alkyl})$  complexes were synthesized and their characterization permitted to observe the modulation of their electronic ground state. The possibility to finely tune the electronic density surrounding the platinum center might become a great asset in the development of electronic-state-specific reactivities. Although trials of methane activation remained unsuccessful, the intrinsic reactivities observed for two of the  $\text{Yb-Pt}^{\text{IV}}$  complexes were rationalized and now needs to be further studied to evaluate the potential of these transformations, especially in the case of the photofunctionalization of the bipym ligand (Figure I.2).

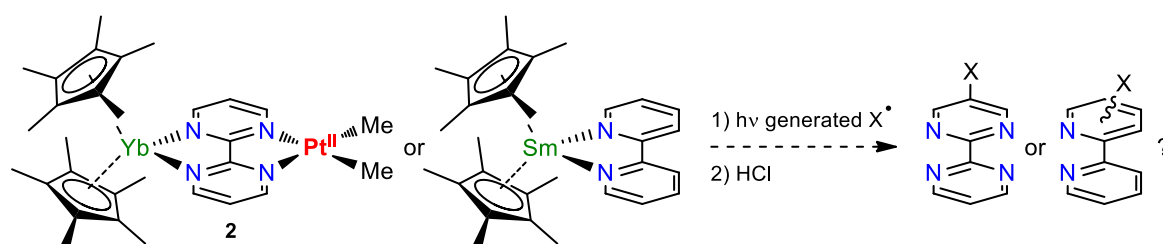


**Figure I.2.** Perspective on photo-triggered mono-functionalization of bipym or bipy ligands.

Benefiting from the experience obtained through the reactivity trials conducted with platinum, the transposition of the reactivity observed with the simple catecholborane reagent to  $\text{Yb-Ni}$  species permitted to develop a low-valent  $\text{Ni}$  catalytic system for alkene isomerization (Figure I.3). While the transformation was almost not performed in absence of the  $\text{Cp}^*_2\text{Yb}$  fragment, its coordination to the  $(\text{bipym})\text{Ni}$  moiety allowed the reaction to be run at low loading and with significant selectivity for the mono-isomerization. From extended mechanistic investigations, no strong proof was obtained to conclude on the oxidation state of the in-situ formed low-valent  $\text{Ni}$  center in the bimetallic case. A hypothesis on  $\pi$ -accepting properties of the redox-active ligand was however proposed and resulted in the synthesis of a promising monometallic pre-catalyst with the rarely used 3,3'- $\text{Me}_2\text{bipy}$  ligand. Theoretical investigations performed on both systems revealed that although the two systems presented similar performances, two different reaction pathways were at stake. In the  $\text{Yb-Ni}$  case, a  $\text{Ni}^{\text{I}}$  center was formed due to the intermediate valence of the  $\text{Yb-bipym}$  fragment, such electron shuttle being reversed at several steps of the mechanism. The selectivity toward the mono-isomerization was rationalized since the second double bond migration was found to be endothermic. To further enhance such selectivity, the tuning of the electronic and steric properties of the bipym bridging ligand will be investigated. Regarding the 3,3'- $\text{Me}_2\text{bipy}$  ligand case, its distortion-triggered hemilability lowered the activation barrier and enabled the C-H activation of the allylic proton followed by a somehow classical, yet endothermic,  $\pi$ -allyl mechanism. This was found to tag along well with the observed slow loss of activity of the catalyst.

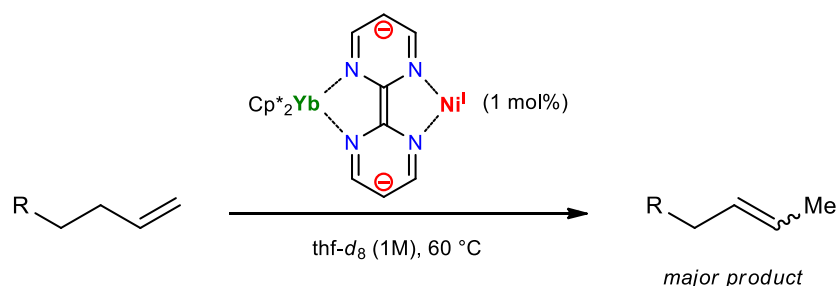


**Figure I.3.** Electron shuttle-triggered formation of an active  $\text{Ni}^{\text{I}}$  center in alkene isomerization.

As a second idea gained from the works conducted with platinum complexes, the synthesis of unprecedented tetraalkyl palladium species was attempted. Although the development of a robust and reproducible synthetic protocol was non-trivial due to the instability of such high-valent species, a simple addition of  $\text{MeMgI}$  to a solution of the  $\text{Yb-PdMe}_3\text{I}$  precursors yielded quantitatively the desired  $\text{PdMe}_4$  center. As expected, the substitution of the labile iodide ligand by a methyl group greatly enhanced the stability of such  $\text{Yb-Pd}^{\text{IV}}$  complex. The monitoring of its degradation revealed a new type of mechanism, unveiled by a deviation from first order kinetics. Such behavior remains however to be fully elucidated and confirmed by computational studies. Benefiting from the divalent lanthanide-enhanced stability, the synthesis of the heteroleptic  $\text{Yb-PdMe}_3\text{Et}$  was also achieved although a modified synthetic protocol was used, since switching from the methyl to the ethyl Grignard reagent was not successful. Preliminary studies of the selectivity of the reductive elimination step were performed and indicated a preference for propane formation instead of ethane, such result was found to be really encouraging and catalytic reactivity trials are on their way since out the three expected steps, two were proven to be fast and quantitative while only the last one, the reductive elimination, needs to be better understood to achieve high performances.

## II. But what about other metal groups?

After having explored all the group 10 metals, a logical idea was to move to the neighbor column where lies the group 9 cobalt, rhodium and iridium elements. As most of the investigations conducted on this topic are still preliminary they will only be discussed briefly here and hopefully be explored further in the future. As was done with palladium, the starting point was to choose a robust, soluble and reactivity-promising monometallic precursor. The choice was quickly made and the synthesis of the well-known  $[\text{Cp}^*\text{Ir}^{\text{III}}\text{Cl}_2]_2$  dimeric precursor was performed in order to associate it with a bipym ligand. Luckily, this step was rendered really simple since the resulting  $[(\text{bipym})\text{Ir}^{\text{III}}\text{Cp}^*\text{Cl}]^+ \text{Cl}^-$  was formed readily as a solid insoluble in THF, the solvent of the reaction. At this point, the idea was to remove the chlorine ions to avoid any unwanted reaction with a divalent ytterbium fragment. Two methods were employed: reduction with sodium and salt metathesis with



silver hexafluoroantimonate. The first yielded the (bipym)Ir<sup>I</sup>Cp\* precursor, while the second resulted in the formation of the [(bipym)Ir<sup>III</sup>Cp\*(NCMe)]<sup>2+</sup> 2 SbF<sub>6</sub><sup>-</sup> compound (Figure II.1).

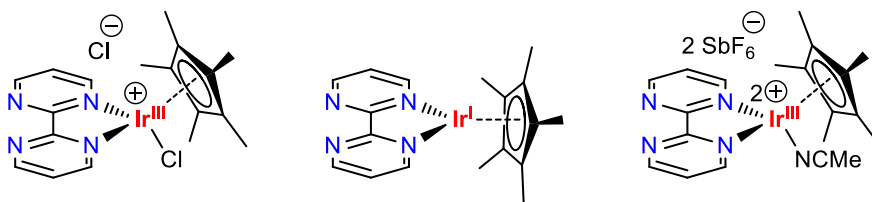


**Figure II.1.** Synthesized bipym-Ir precursors.

With these three different precursors, the addition of the divalent ytterbium fragment was performed to form the desired heterobimetallic species. While the latter dicationic precursor did not lead to such species, due to the presence of the SbF<sub>6</sub><sup>-</sup> anions, the Cp\*<sub>2</sub>Yb(bipym)Ir<sup>I</sup>Cp\* complex was obtained by mixing the Cp\*<sub>2</sub>Yb(OEt<sub>2</sub>) and (bipym)Ir<sup>I</sup>Cp\* precursors together in toluene (Figure II.2. left). The XRD analysis of the crystals confirmed that significant electronic density was transferred from the organoytterbium fragment to the bipym ligand. However, when the same reaction was performed with the [(bipym)Ir<sup>III</sup>Cp\*Cl]<sup>+</sup> Cl<sup>-</sup> salt, the Cp\*<sub>2</sub>Yb(bipym)IrCp\*]<sup>+</sup> [Cp\*<sub>2</sub>YbCl<sub>2</sub>]<sup>-</sup> ionic pair was isolated (Figure II.2.right).

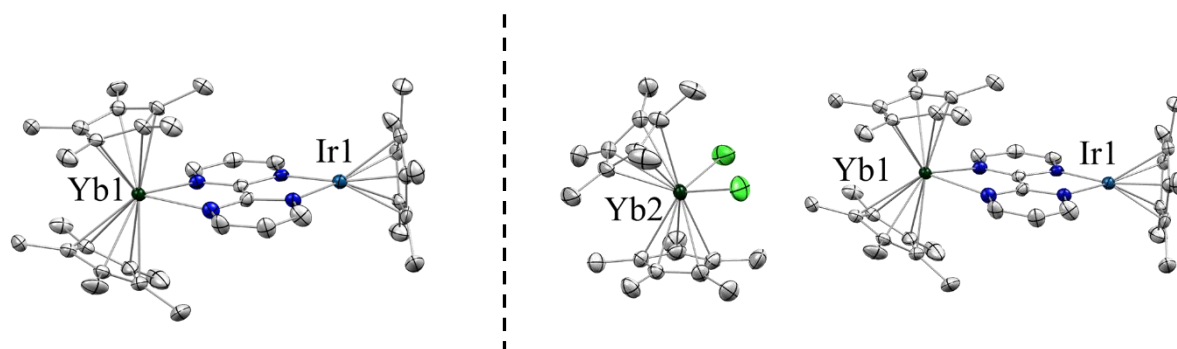


**Figure II.2.** Preliminary structural characterization of two new Yb-Ir bimetallic compounds.

On first thoughts, since the XRD data was also in favor of a formally trivalent ytterbium fragment, as well as a reduced bipym ligand, the Ir center was considered to be at the rarely observed +II oxidation state. However, a more realistic hypothesis might consist in considering that two equivalents of divalent ytterbium consecutively reduced the Ir<sup>III</sup> to an Ir<sup>I</sup> center and that the seemingly reduced bipym fragment is only the result of a strongly delocalized bonding molecular orbital between the formally +I Ir ion and the redox-active ligand (Figure II.3).

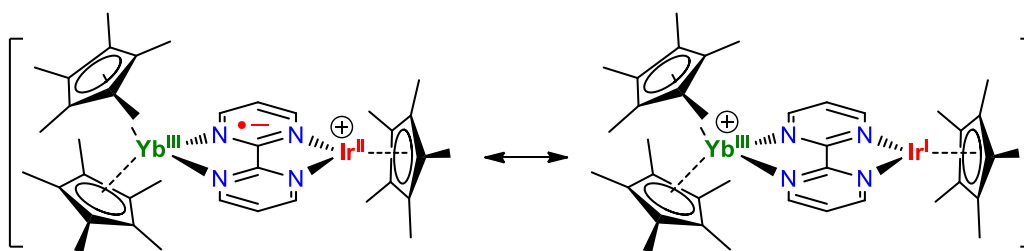


**Figure II.3.** Two possible limit forms of the  $\text{Cp}^*_2\text{Yb}(\text{bipym})\text{IrCp}^*$  cation.

To ascertain which hypothesis is the correct one, the same characterization methodology used throughout this manuscript will have to be followed and considering the surprising electron shuttle observed with the low-valent Ni system, surprising results can be expected. As the last preliminary results on this project, switching from Yb to Eu did lead once again to two other species:  $\text{Cp}^*_2\text{Eu}(\text{bipym})\text{IrCp}^*$  for which the Eu seemed to remain divalent and the surprising  $\text{Cp}^*_2\text{EuCl}_2\text{Cp}^*\text{Eu}(\text{bipym})\text{IrCp}^*$  trinuclear complex with unattributed oxidation state for the Eu center due to the poor quality of the XRD data (Figure II.4).

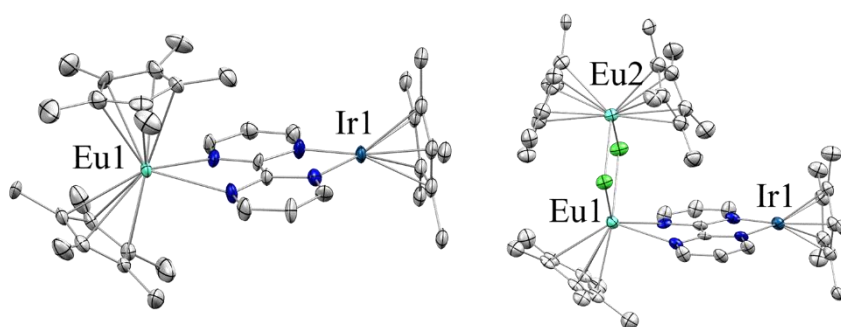


**Figure II.4.** Preliminary structural characterization of two new Eu-Ir bimetallic compounds.

Since iridium is also famous as a photocatalyst, the synthesis of a photoactive bipym-Ir precursor supported by phenylpyridine (ppy) ligands was attempted. Starting from the well-known dimer  $[(\text{ppy})_2\text{Ir}(\mu\text{-Cl})]_2$ , the  $[(\text{bipym})\text{Ir}(\text{ppy})_2]^+ \text{BPh}_4^-$  complex was obtained and then associated to a  $\text{Cp}^*_2\text{Yb}$  fragment, to form the expected  $\text{Cp}^*_2\text{Yb}(\text{bipym})\text{Ir}(\text{ppy})_2]^+ \text{BPh}_4^-$  ionic pair in THF (Figure II.5).

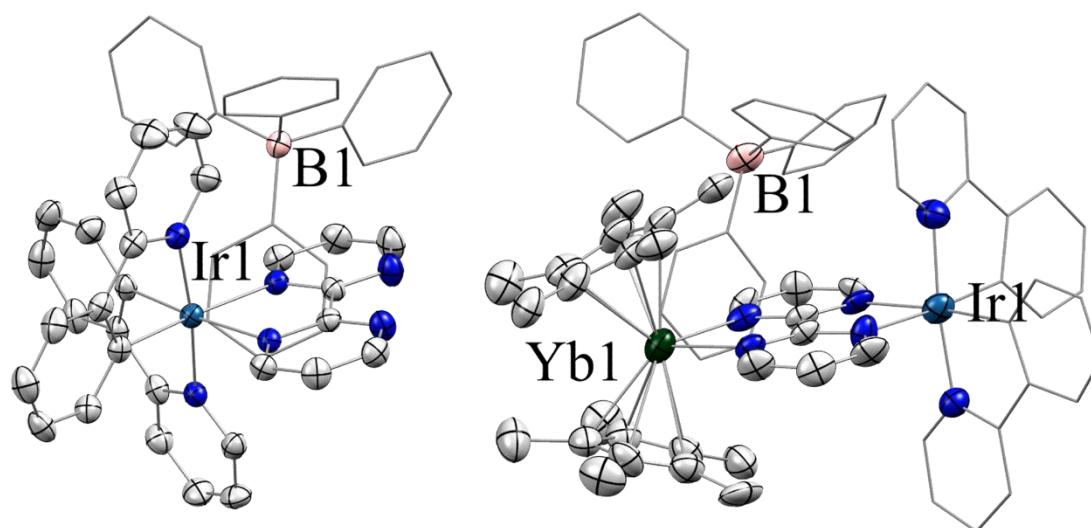


**Figure II.5.** Preliminary structural characterization of the  $[(\text{bipym})\text{Ir}(\text{ppy})_2]^+ \text{BPh}_4^-$  and  $[\text{Cp}^*_2\text{Yb}(\text{bipym})\text{Ir}(\text{ppy})_2]^+ \text{BPh}_4^-$  species

After a change of color was observed upon overnight irradiation at 400 nm, the crystallization of the resulting species was achieved and unraveled an unexpected reactivity. The photoactivation resulted in the functionalization of the bipym ligand by a  $\text{BPh}_2$  group (Figure II.6). Such transformation was not observed in the absence of the lanthanide fragment while the appearance of such functionalized bipym ligand is echoing to what was proposed in chapter III to explain the photoreactivity observed with the  $\text{Yb-PtMe}_4$  complex. A hypothetical mechanism could imply the formation of a formal  $\text{Ir}^{\text{IV}}$  center that would oxidize the  $\text{BPh}_4^-$  anion. This would result in the elimination of biphenyl while the remaining  $\text{BPh}_2$  fragment would have no other option than going on the bipym ligand to replace a hydrogen atom that was eliminated as  $\text{H}_2$  (Figure II.7).

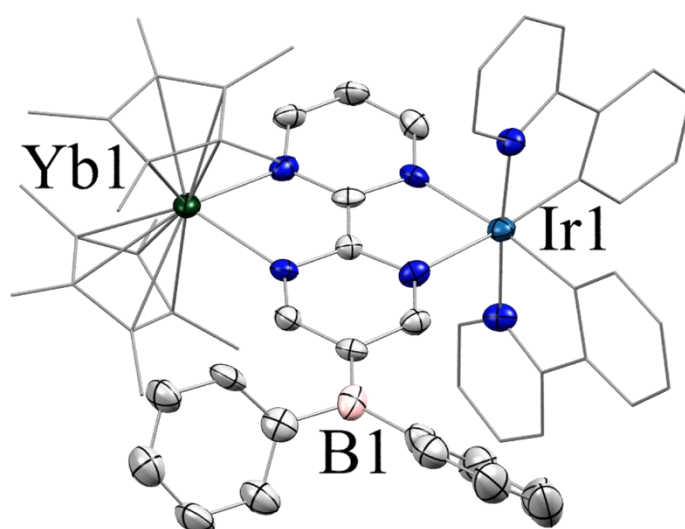


**Figure II.6.** Preliminary structural characterization of the photoproduct

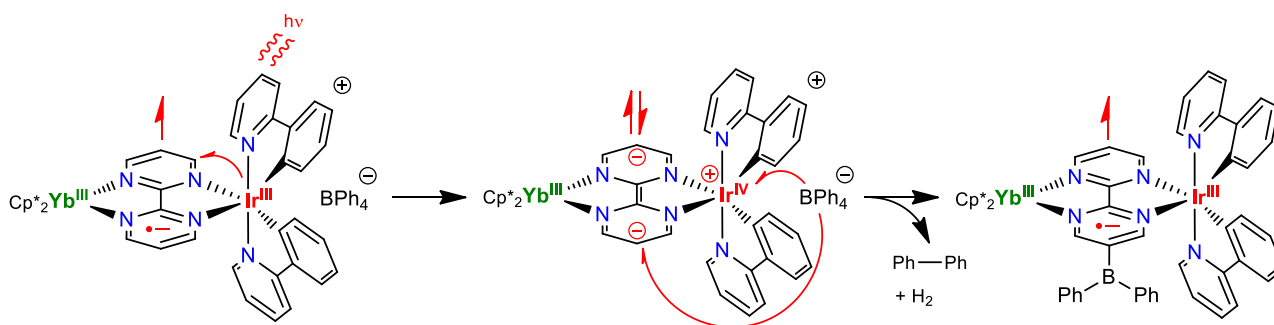


**Figure II.7.** Possible mechanism of the photo-triggered reaction.

Overall, these investigations conducted on Yb-Ir were really promising and deserve to be continued in the future. Their extension to rhodium or even cobalt would also be of great interest and might lead to original reactivities. In a broader perspective, the association of a divalent lanthanide to other groups of transition metal would lead to a greater amount of original electronic architectures and hopefully many novel reactivities.



## **Appendices**



# Synthesizes and characterization data

## General considerations:

All reactions were performed using standard Schlenk-line techniques or in an argon- or nitrogen-filled glovebox (MBraun, Garching, Germany). All glassware was dried at 140 °C for at least 12 h prior to use. All solvents used were either dried over sodium/benzophenone or  $\text{CaH}_2$ , degassed by freeze-pump-thaw cycles and distilled under reduced pressure in a cold flask.  $^1\text{H}$  and  $^{13}\text{C}$  NMR spectra were recorded in 5 mm tubes adapted with a J. Young valve on Bruker Advance III-300 MHz (Bruker, Billerica, MA, USA). Chemical shifts are expressed relative to residual protio signal of the deuterated solvent in ppm.<sup>1</sup> Infrared (IR) spectra were recorded at room temperature under argon on a Thermo Scientific Nicolet iS5 spectrometer equipped with the iD7 ATR – Diamond unit. Elemental analyses were obtained from Mikroanalytisches Labor Pascher (Remagen, Germany). Magnetic susceptibility measurements were made for all samples on a Quantum Design SQUID magnetometer (Cryogenic, London, UK). Diamagnetic corrections were made using Pascal's constants.<sup>2</sup> Temperature dependent magnetic measurements were obtained in sealed quartz tube on a Quantum Design SQUID under fixed DC fields between 0.1 and 2 T. "Curie tail" behavior at low temperature were corrected by considering the contribution of small  $\text{Yb}^{3+}$  impurities.<sup>3,4</sup>



## Chapter II

### ▪ Syntheses:

K<sub>2</sub>Cot and KCnt were prepared as previously described.<sup>5,6</sup> TmI<sub>3</sub>, ErI<sub>3</sub>, HoI<sub>3</sub>, DyI<sub>3</sub>, TbI<sub>3</sub> and LuCl<sub>3</sub> were purchased from Sigma Aldrich and used without further purification.

**Er(Cot)I(thf)** was synthesized as previously described and a similar procedure was used for the other late lanthanides.<sup>7</sup>

**Lu(BH<sub>4</sub>)<sub>3</sub>(thf)<sub>3</sub>** was synthesized using the procedure reported for the Nd analog.<sup>8</sup>

**Tb(Cot)I(thf):** A cold thf solution (-40 °C) of K<sub>2</sub>Cot (4 mL, 117 mg, 0.64 mmol, 1 equiv) was added to a stirred cold (-40 °C) thf suspension of TbI<sub>3</sub> (3 mL, 346 mg, 0.64 mmol, 1 equiv). The mixture was allowed to warm to room temperature (r.t.) and was stirred for 16 h. The resultant light-yellow suspension was filtered through a frit and the filtrate dried under reduced pressure. The solids were suspended in 5 mL thf and heated to 60 °C forming a deep yellow solution. Diethyl ether was layered on the top and the solution was stored at -40 °C. Yellow needles of the desired compound formed slowly (181 mg, 53 %). **<sup>1</sup>H NMR** (300 MHz, thf-d<sub>8</sub>, 293 K): δ (ppm), 194.92 (s br, 8H), *coordinated thf molecules are not visible*. **IR (ATR):**  $\tilde{\nu}$  = 2970 (br m), 2889 (m), 1859 (w), 1753 (w), 1616 (w), 1556 (w), 1444 (br m), 1343 (w), 1309 (w), 1245 (w), 1180 (w), 1011 (vs), 895 (s), 860 (vs), 775 (m), 749 (m), 708 (vs), 667 (s), 573 (m) cm<sup>-1</sup>. **Anal. Calcd.** for C<sub>16</sub>H<sub>24</sub>IO<sub>2</sub>Tb (534.19): C, 35.97; H, 4.53; Found: C, 35.77; H, 4.56.

**Dy(Cot)I(thf):** A cold thf solution (-40 °C) of K<sub>2</sub>Cot (5 mL, 138 mg, 0.76 mmol, 1 equiv) was added to a stirred cold (-40 °C) thf suspension of DyI<sub>3</sub> (10 mL, 411 mg, 0.76 mmol, 1 equiv). The mixture was allowed to warm to r.t. and was stirred for 16 h. The resultant light-yellow suspension was filtered through a frit and the filtrate dried under reduced pressure. The solids were suspended in 8 mL thf and heated to 60 °C forming a deep yellow solution. Diethyl ether was layered on the top and the solution was stored at -40 °C. Yellow needles of desired compound formed slowly (265 mg, 63 %). **<sup>1</sup>H NMR** (300 MHz, thf-d<sub>8</sub>, 293 K): δ (ppm), 88.66 (s br, 8H), *coordinated thf molecules are not visible*. **IR (ATR):**  $\tilde{\nu}$  = 2951 (br m), 2889 (m), 1858 (w), 1752 (w), 1614 (w), 1554 (w), 1453 (br m), 1343 (w); 1309 (w), 1256 (w), 1178 (w), 1010 (vs), 895 (s), 860 (vs), 750 (m), 705 (vs), 670 (s), 575 (m) cm<sup>-1</sup>. **Anal. Calcd.** for C<sub>15.4</sub>H<sub>19.2</sub>IO<sub>2</sub>Dy (537.77): C, 33.03; H, 3.91; Found: C, 32.94; H, 4.07. The number of thf was decreased upon drying.

**Ho(Cot)I(thf):** A cold thf solution (-40 °C) of K<sub>2</sub>Cot (5 mL, 223 mg, 1.22 mmol, 1 equiv) was added to a stirred cold (-40 °C) thf suspension of HoI<sub>3</sub> (668 mg, 1.2 mmol, 1 equiv). The mixture was allowed to warm to r.t. and was stirred for 16 h. The resultant light-yellow suspension was filtered through a frit and the filtrate dried under reduced pressure. The solids were suspended in 7 mL thf and heated to 60 °C forming a deep yellow solution. Diethyl ether was layered on the top and the solution was stored at -40 °C. Yellow needles of desired compound formed slowly (583 mg, 88 %). **<sup>1</sup>H NMR** (300 MHz, thf-d<sub>8</sub>, 293 K):  $\delta$  (ppm), 70.88 (s br, 8H), *coordinated thf molecules are not visible*. **IR (ATR):**  $\tilde{\nu}$  = 2969 (br m), 2888 (m), 1852 (w), 1747 (w), 1601 (w), 1441 (br m), 1343 (w), 1212 (br w), 1008 (vs), 856 (vs), 750 (m), 704 (vs), 645 (s) cm<sup>-1</sup>. **Anal. Calcd.** for C<sub>16</sub>H<sub>24</sub>IO<sub>2</sub>Ho (540.20): C, 35.57; H, 4.48; Found: C, 35.63; H, 4.53.

**Tm(Cot)I(thf):** A cold solution (-40 °C) of K<sub>2</sub>Cot (3 mL, 32 mg, 0.17 mmol, 1 equiv) was added to a stirred cold (-40 °C) thf suspension of TmI<sub>3</sub> (5 mL, 95 mg, 0.17 mmol, 1 equiv). The mixture was allowed to warm to r.t. and was stirred for 16 h. The resultant light-yellow suspension was filtered through a frit and the filtrate dried under reduced pressure. The solids were suspended in 7 mL thf and heated to 60 °C forming a deep yellow solution. Diethyl ether was layered on the top and the solution was stored at -40 °C. Yellow needles of desired compound formed slowly (54 mg, 57 %). The **<sup>1</sup>H NMR** (300 MHz, thf-d<sub>8</sub>, 293 K) remained silent. The compound was previously published by Fedushkin *et al.*<sup>9</sup>

**[Lu(Cot)(BH<sub>4</sub>)(thf)]<sub>2</sub>:** A cold solution (-40 °C) of K<sub>2</sub>Cot (61 mg, 0.33 mmol, 1 equiv) was added to a stirred cold (-40 °C) thf solution of [Lu(BH<sub>4</sub>)<sub>3</sub>(thf)<sub>3</sub>] (145 mg, 0.33 mmol, 1 equiv). The mixture was allowed to warm to r.t. and was stirred for 16 h. The resultant light-yellow suspension was filtered through a Teflon syringe filter. The filtrate was concentrated under reduced pressure until incipient crystallization and stored at -40 °C to afford the title compound as light-yellow crystals (117 mg, 0.27 mmol, 81 %). Recrystallization from toluene led to the decoordination of one thf molecule and formation of [(Cot)Lu(BH<sub>4</sub>)(thf)]<sub>2</sub> as colorless crystals suitable for X-ray diffraction studies. **<sup>1</sup>H NMR** (300 MHz, thf-d<sub>8</sub>, 293 K):  $\delta$  (ppm), 6.31 (s, 8H, Cot), 3.68-3.59 (m, ca. 4H, OCH<sub>2</sub> coordinated thf), 1.84-1.74 (m, ca. 4H, OCH<sub>2</sub>CH<sub>2</sub> coordinated thf), 0.04 (1:1:1:1 quartet <sup>1</sup>J<sub>BH</sub>=83.0 Hz, 4H, BH<sub>4</sub>). **<sup>13</sup>C NMR** (75 MHz, thf-d<sub>8</sub>, 293 K):  $\delta$  (ppm), 92.6 (Cot), 68.0 (OCH<sub>2</sub> coordinated thf), 26.1 (OCH<sub>2</sub>CH<sub>2</sub> coordinated thf). **IR (ATR):**  $\tilde{\nu}$  = 3021 (w), 2989 (w), 2930 (br m), 2889 (m), 2426 (m), 2272 (s), 2239 (s), 2164 (m), 2040 (w), 1855 (w), 1746 (w), 1610 (w), 1494 (w), 1453 (m), 1316 (br m), 1245 (m), 1213 (w), 1092 (s), 1012 (vs), 898 (s), 877 (vs), 752 (m), 706 (vs) cm<sup>-1</sup>. No satisfactory EA was obtained.

**Tb(Cot)(Cnt) (1):** A brown acetonitrile solution of KCnt (2 mL, 42 mg, 0.27 mmol, 1.1 equiv) was added at r.t. to a toluene suspension of Tb(Cot)I(thf)<sub>2</sub> (10 mL, 149 mg, 0.25 mmol, 1 equiv). The resulting suspension was left to stir at r.t. for 12 h and was then dried under reduced pressure. The pale-yellow residue was suspended in toluene (5 mL). After 1 h of stirring, the volatiles were removed under reduced pressure and the residue was further dried for 5 h at r.t. and extracted in several crops with large amounts of toluene. The pale-yellow solution was filtered and cooled at -40 °C yielding X-ray suitable pale-yellow needles of **1** (32 mg, 29 %). **<sup>1</sup>H NMR** (300 MHz, toluene-d<sub>8</sub>, 293 K): δ (ppm), 246.3 (s, 8H, Cot), 101.6 (s, 9H, Cnt). The <sup>1</sup>H NMR evolves with time and crystals of **1'** can be obtained after few days. **IR (ATR):**  $\tilde{\nu}$  = 3006 (m) 2920 (s), 2851 (s), 1935 (w), 1853 (w), 1746 (w), 1602 (w), 1551 (w), 1493 (w), 1457 (m), 1375 (w), 1313 (w), 1018 (w), 892 (vs), 846 (w), 772 (m), 747 (s), 704 (vs), 654 (vs) cm<sup>-1</sup>. **Anal. Calcd.** for C<sub>17</sub>H<sub>17</sub>Tb.0.2 Toluene (398.67): C, 55.43; H, 4.70; Found: C, 55.35; H, 5.03.

**Dy(Cot)(Cnt) (2):** A brown acetonitrile solution of KCnt (2 mL, 47 mg, 0.30 mmol, 1.1 equiv) was added at r.t. to a toluene suspension of Dy(Cot)I(thf)<sub>2</sub> (10 mL, 146 mg, 0.27 mmol, 1 equiv). The resulting suspension was left to stir at r.t. for 12 h and was then dried under reduced pressure. The yellow residue was suspended in toluene (5 mL). After 1 h of stirring, the volatiles were removed under reduced pressure and the residue was further dried for 5 h at r.t. and extracted in several crops with large amounts of toluene. The yellow solution was filtered and cooled at -40 °C yielding X-ray suitable yellow needles of **2** (62.5 mg, 60 %). **<sup>1</sup>H NMR** (300 MHz, toluene-d<sub>8</sub>, 293 K): δ (ppm), 118.7 (s, 8H, Cot), 72.90 (s, 9H, Cnt). **IR (ATR):**  $\tilde{\nu}$  = 3005 (br m), 2917 (m), 1970 (w), 1851 (w), 1744 (w), 1601 (w), 1456 (m), 1373 (w), 1313 (w), 1018 (w), 892 (vs), 848 (w), 773 (m), 748 (s), 706 (vs), 654 (vs), 507 (w) cm<sup>-1</sup>. **Anal. Calcd.** for C<sub>17</sub>H<sub>17</sub>Dy (383.82): C, 53.20; H, 4.46; Found: C, 53.14; H, 4.48.

**Ho(Cot)(Cnt) (3):** A brown acetonitrile solution of KCnt (2 mL, 60 mg, 0.39 mmol, 1.05 equiv) was added at r.t. to a toluene suspension of Ho(Cot)I(thf)<sub>2</sub> (15 mL, 189 mg, 0.35 mmol, 1 equiv). The resulting suspension was left to stir at r.t. for 12 h and was then dried under reduced pressure. The pale-orange residue was suspended in toluene (5 mL). After 1 h of stirring, the volatiles were removed under reduced pressure and the residue was further dried for 5 h at r.t. and extracted in several crops with large amounts of toluene. The pale-orange solution was filtered and cooled at -40 °C yielding X-ray suitable pale-orange needles of **3** (77.8 mg, 67 %). **<sup>1</sup>H NMR** (300 MHz, toluene-d<sub>8</sub>, 293 K): δ (ppm), 90.45 (s, 8H, Cot), 59.17 (s, 9H, Cnt). **IR (ATR):**  $\tilde{\nu}$  = 3003 (br m), 2920 (m), 1969 (w), 1852 (w), 1745 (w), 1602 (w), 1455 (w), 1374 (w), 1313 (w), 1016 (m), 892 (s), 850 (w), 776 (m), 748 (m), 704 (vs), 656 (vs), 506 (m) cm<sup>-1</sup>. **Anal. Calcd.** for C<sub>17</sub>H<sub>17</sub>Ho (386.25): C, 52.86; H, 4.44; Found: C, 52.34; H, 4.53.

**Er(Cot)(Cnt) (4):** A brown acetonitrile solution of KCnt (2 mL, 65 mg, 0.42 mmol, 1.05 equiv) was added at r.t. to a toluene suspension of Er(Cot)I(thf)<sub>2</sub> (15 mL, 215 mg, 0.40 mmol, 1 equiv). The resulting suspension was left to stir at r.t. for 12 h and was then dried under reduced pressure. The orange residue was suspended in toluene (5 mL). After 1 h of stirring, the volatiles were removed under reduced pressure and the residue was further dried for 5 h at r.t. and extracted in several crops with large amounts of toluene. The orange solution was filtered and cooled at -40 °C yielding X-ray suitable orange needles of **4** (73.6 mg, 63 %). **<sup>1</sup>H NMR** (300 MHz, toluene-d<sub>8</sub>, 293 K): δ (ppm), -5.01 (br s), -128.7 (br s). **IR (ATR):**  $\tilde{\nu}$  = 3030 (br m), 2959 (s), 2921 (m), 2851 (m), 1966 (w), 1854 (w), 1748 (w), 1604 (br w), 1451 (w), 1376 (w), 1313 (w), 1259 (s), 1087 (s), 1014 (s), 892 (s), 797 (s), 748 (m), 702 (vs), 657 (vs), 505 (m) cm<sup>-1</sup>. **Anal. Calcd.** for C<sub>17</sub>H<sub>17</sub>Er (388.58): C, 52.55; H, 4.41; Found: C, 52.80; H, 5.04.

**Tm(Cot)(Cnt) (5):** A brown acetonitrile solution of KCnt (2 mL, 65 mg, 0.42 mmol, 1.05 equiv) was added at r.t. to a toluene suspension of Tm(Cot)I(thf)<sub>2</sub> (15 mL, 217 mg, 0.40 mmol, 1 equiv). The resulting suspension was left to stir at r.t. for 12 h and was then dried under reduced pressure. The salmon-orange residue was suspended in toluene (5 mL). After 1 h of stirring, the volatiles were removed under reduced pressure and the residue was further dried for 5 h at r.t. and extracted in several crops with large amounts of toluene. The salmon-orange solution was filtered and cooled at -40 °C yielding X-ray suitable salmon-orange needles of **5** (74.6 mg, 48 %). **<sup>1</sup>H NMR** (300 MHz, toluene-d<sub>8</sub>, 293 K): δ (ppm), -23.21 (br s), -235.8 (br s). **IR (ATR):**  $\tilde{\nu}$  = 2998 (br m), 2920 (m), 2852 (m), 1965 (w), 1856 (w), 1753 (w), 1451 (w), 1314 (w), 1259 (w), 1016 (m), 893 (s), 781 (s), 749 (m), 703 (vs), 658 (vs), 505 (m) cm<sup>-1</sup>. **Anal. Calcd.** for C<sub>17</sub>H<sub>17</sub>Tm (390.25): C, 52.32; H, 4.39; Found: C, 52.80; H, 4.64.

**Lu(Cot)(Cnt) (6):** A mixture of [Lu(Cot)(BH<sub>4</sub>)(thf)]<sub>2</sub> (146 mg, 0.33 mmol) and KCnt (52 mg, 0.33 mmol) in toluene (15 mL) was heated at 110 °C for 16 h and was then dried under reduced pressure for 2 h. The light-yellow residue was extracted with hot toluene. The yellow filtrate was stored at -40 °C yielding yellow needles of **6** suitable for X-ray diffraction studies (44 mg, 0.11 mmol, 34 %). **<sup>1</sup>H NMR** (300 MHz, toluene-d<sub>8</sub>, 293 K): δ (ppm), 6.54 (s, 9H, Cnt), 5.83 (s, 8H, Cot). **<sup>13</sup>C NMR** (75 MHz, toluene-d<sub>8</sub>, 293 K): δ (ppm), 107.8 (Cnt), 93.5 (Cot). **IR (ATR):**  $\tilde{\nu}$  = 2992 (br m), 1963 (w), 1857 (w), 1748 (w), 1604 (w), 1490 (w), 1447 (w), 1375 (w), 1313 (w), 1158 (w), 1018 (w), 892 (vs), 780 (m), 750 (m), 704 (vs), 662 (vs), 502 (w) cm<sup>-1</sup>. **Anal. Calcd.** for C<sub>17</sub>H<sub>17</sub>Lu (396.29): C, 51.52; H, 4.32; Found: C, 51.16; H, 4.34.

**(Cot)Sm(bipy)( $\eta^5$ -Cnt):** Few dark XRD suitable crystals were obtained by the slow diffusion of a toluene solution of 2,2'-bipyrimidine layered on top of a toluene solution of Sm(Cot)(Cnt) prepared with the same protocol reported for the other compounds.

## Chapter III

### ▪ Syntheses:

2,2'-bipyrimidine was purchased from TCI and sublimed prior use. MeLi was purchased from Sigma Aldrich as a 1.6 M diethyl ether solution from which solid MeLi was obtained as a white powder after evaporation over several hours ( $10^{-3}$  mbar).  $[\text{Pt}(\text{SMe}_2)\text{Me}_2]_2$ ,  $(\text{SMe}_2)\text{PtMeCl}$  and  $\text{Ph}_3\text{C}^+ \text{BPh}_4^-$  were synthesized as described in the literature.<sup>10,11</sup>  $\text{B}(\text{C}_6\text{F}_5)_3$  was purchased from Sigma Aldrich and used as received.

**(bipym)PtMe<sub>2</sub> (1):** Synthesis adapted from the literature.<sup>12,13</sup> To a colorless solution of 2,2'-bipyrimidine (250 mg, 1.58 mmol, 2 eq./Pt center) in  $\text{CH}_2\text{Cl}_2$  (30 mL) a beige solution of  $\text{Pt}_2(\text{SMe}_2)\text{Me}_4$  (230 mg, 0.4 mmol, 1 eq.) in  $\text{CH}_2\text{Cl}_2$  (30 mL) was added dropwise under vigorous stirring. The solution slowly turns to deep red. After 2h of reaction, the dark red suspension is filtered through a frit to obtain a deep red solution and remove the black powder corresponding to the insoluble  $[(\text{bipym})\text{Pt}_2\text{Me}_4]$  dimer. The latter is concentrated to a volume of 20 mL and covered with 70 mL of  $\text{Et}_2\text{O}$  and let stand overnight at  $-20^\circ\text{C}$ . XRD suitable red needles are obtained overnight (190 mg, 0.50 mmol, 63%). A real care has to be taken to remove all remaining bipym ligand through this crystallization process since it will react with the lanthanide moiety in the further steps. **<sup>1</sup>H NMR** (300 MHz,  $\text{thf}-d_8$ ,  $20^\circ\text{C}$ ):  $\delta$  (ppm) = 9.44 (m, 2H, bipym), 9.29 (m, 2H, bipym), 7.70 (t, 2H, bipym), 1.02 (s, 6H, Pt-CH<sub>3</sub>,  $J_{\text{Pt-H}} = 87.5$  Hz). **Anal. Calcd.** for  $\text{C}_{10}\text{H}_{12}\text{N}_4\text{Pt}$  : C, 31.33; H, 3.16; N, 14.62; found: C, 31.62; H, 3.27; N, 14.3.

**Cp\*<sub>2</sub>Yb(bipym)PtMe<sub>2</sub>(toluene) (2):** To a red solution of (bipym)PtMe<sub>2</sub> (115 mg, 0.3 mmol, 1 eq.) in toluene (10 mL) a green solution of Cp\*<sub>2</sub>Yb(OEt<sub>2</sub>) (158.3 mg, 0.3 mmol, 1 eq.) in toluene (10 mL) was added dropwise under vigorous stirring. After 5 min of reaction, the dark brownish-green solution was left at  $-40^\circ\text{C}$  overnight to yield dark crystals (217 mg, 0.26 mmol, 86%). **<sup>1</sup>H NMR** (300 MHz,  $\text{tol}-d_8$ ,  $20^\circ\text{C}$ ):  $\delta$  (ppm) = 255.46 (s, 2H, bipym), 6.39 (s, 2H, bipym), -166.89 (s, 2H, bipym), 17.89 (s, 6H, Pt-CH<sub>3</sub>), 5.88 (s, 30H, Cp\*). **Anal. Calcd.** for  $\text{C}_{30}\text{H}_{42}\text{N}_4\text{PtYb} + \text{C}_7\text{H}_8$  : C, 48.36; H, 5.48; N, 6.10; found: C, 48.24; H, 5.52; N, 6.21.

**Cp\*<sub>2</sub>Yb(bipym)PtMe<sub>3</sub>I(toluenes)<sub>0.5</sub> (3):** To a dark green solution of Cp\*<sub>2</sub>Yb(bipym)PtMe<sub>2</sub> (166 mg, 0.18 mmol) in toluene (5 mL), two drops of MeI (excess) were added under vigorous stirring. The dark brownish-green solution turned instantly brown and was left stirring for 5min at room temperature before being left at  $-40^\circ\text{C}$  overnight to yield brown needles (167 mg, 0.16 mmol, 92%). **<sup>1</sup>H NMR** (300 MHz,  $\text{thf}-d_8$ ,  $20^\circ\text{C}$ ):  $\delta$  (ppm) = 266.18 (s, 2H, bipym), 13.25 (s, 2H, bipym), -187.50 (s, 2H, bipym), -0.24 (s, 6H, Pt-(CH<sub>3</sub>)<sub>2</sub>), -13.45 (s, 3H, Pt-CH<sub>3</sub>), 6.47 (s, 15H, Cp\*<sub>1</sub>), 6.32 (s,

15H, Cp\*<sub>2</sub>). **Anal. Calcd.** for C<sub>34.5</sub>H<sub>49</sub>N<sub>4</sub>IPtYb + (C<sub>7</sub>H<sub>8</sub>)<sub>0.5</sub>: C, 40.83; H, 4.87; I, 12.51; N, 5.52; Pt, 19.22; Yb, 17.05 ; found: C, 40.61; H, 4.86; N, 5.32.

**Cp\*<sub>2</sub>Yb(bipym)PtMe<sub>4</sub> (4)**: To a brown solution of Cp\*<sub>2</sub>Yb(bipym)PtMe<sub>3</sub>I (56 mg, 55 μmol, 1eq.) in toluene (4 mL), solid MeLi (3.6 mg, 0.17 mmol, 3 eq.) was added at room temperature under vigorous stirring. The resulting suspension slowly turned dark red over several hours and was filtered after 24 h of stirring. The resulting solution was concentrated under vacuum and left overnight at -40 °C to yield XRD suitable dark red prisms (33 mg, 35 μmol, 63%). **<sup>1</sup>H NMR** (300 MHz, thf-*d*<sub>8</sub>, 20 °C): δ (ppm) = 257.28 (s, 2H, bipym), 3.40 (s, 2H, bipym), -164.91 (s, 2H, bipym), -2.71 (s, 6H, Pt-(CH<sub>3</sub>)<sub>2</sub>), -15.01 (s, 6H, Pt-(CH<sub>3</sub>)<sub>2</sub>), 6.03 (s, 30H, Cp\*). No satisfactory EA was obtained.

**Cp\*<sub>2</sub>Yb(bipym)PtMe<sub>3</sub>OTf (5)**: To a dark green suspension of Cp\*<sub>2</sub>Yb(bipym)PtMe<sub>2</sub> (240 mg, 0.26 mmol) in Et<sub>2</sub>O (8 mL), four drops of MeOTf (excess) were added under vigorous stirring. The dark brownish-green solution rapidly turned to a yellow-brown suspension and was left stirring for 15 min at room temperature before being left at -40 °C overnight to yield a brown microcrystalline powder (251 mg, 0.25 mmol, 96%). XRD suitable crystals can be grown by gas phase slow diffusion of MeOTf over a solution of Cp\*<sub>2</sub>Yb(bipym)PtMe<sub>2</sub> in Et<sub>2</sub>O. **<sup>1</sup>H NMR** (300 MHz, thf-*d*<sub>8</sub>, 20 °C): two isomers were present, no attribution was made (see the corresponding chapter). **Anal. Calcd.** for C<sub>32</sub>H<sub>45</sub>F<sub>3</sub>N<sub>4</sub>O<sub>3</sub>PtSYb : C, 38.79; H, 4.58; N, 5.65; found: C, 39.15; H, 4.71; N, 5.54.

**[Cp\*<sub>2</sub>Yb(bipym)Pt(py)Me<sub>3</sub>]<sup>+</sup>OTf<sup>-</sup>(toluene) (5<sup>+</sup>(py) OTf<sup>-</sup>)**: To a light brown suspension of Cp\*<sub>2</sub>Yb(bipym)PtMe<sub>3</sub>OTf (58 mg, 59 μmol) in toluene (5 mL), four drops of pyridine (excess) were added at -40 °C and left to diffuse slowly at room temperature. The solution slowly turned deep red and dark XRD suitable crystals started to appear. The product was isolated after concentration of the solution to ~ 1 mL (53 mg, 46 μmol, 78%). **<sup>1</sup>H NMR** was not recorded. **Anal. Calcd.** for C<sub>39.1</sub>H<sub>52.4</sub>F<sub>3</sub>N<sub>5</sub>O<sub>3</sub>PtSYb: C, 42.78; H, 4.81; N, 6.38 found: C, 42.65; H, 4.78; N, 6.38. Approximately 0.7 molecules of toluene upon drying.

**[(bipym)PtMe(py)]<sup>+</sup> SbF<sub>6</sub><sup>-</sup> (7<sup>+</sup>(py) SbF<sub>6</sub><sup>-</sup>)**: To a beige solution of (SMe<sub>2</sub>)PtMeCl (200 mg, 0.54 mmol, 1eq.) in thf (8 mL), a colorless solution of 2,2'-bipyrimidine (86 mg, 0.54 mmol, 1eq.) in thf (8 mL) was added under vigorous stirring. A brick red suspension slowly formed and was filtered after 5 h, the resulting brick red solid was dried under vacuum (152 mg, 0.38 mmol, 70 %). **<sup>1</sup>H NMR** (300 MHz, thf-*d*<sub>8</sub>, 20 °C, slightly soluble): δ (ppm) = 9.78 (m, 1H, bipym), 9.47 (m, 1H, bipym), 9.30 (m, 1H, bipym), 9.25 (m, 1H, bipym), 7.87 (m, 1H, bipym), 7.67 (m, 1H, bipym), 1.11 (s, 3H, Pt-(CH<sub>3</sub>), J<sub>Pt-H</sub> = 81.0 Hz).

Pyridine (5 mL) was added at -40 °C to a solid mixture of (bipym)PtMeCl (21.5 mg, 53  $\mu$ mol, 1 eq.) and AgSbF<sub>6</sub> (27.3 mg, 80  $\mu$ mol, 1.5 eq.), the resulting suspension was stirred for 2 days at -40 °C. Then, pentane (4 mL) was added and an off-white solid precipitated. After careful removing of the liquid phase, the solid was dried under vacuum, suspended in CH<sub>2</sub>Cl<sub>2</sub>, filtered and the resulting solution was vacuumed to yield an off-white solid (31 mg, 45  $\mu$ mol, 86%). The solid was found to be temperature and/or light sensitive it must be kept in the dark in the glovebox fridge. <sup>1</sup>H NMR was not recorded.

**[Cp\*<sub>2</sub>Yb(bipym)PtMe<sub>2</sub>] (2<sup>+</sup> BPh<sub>4</sub><sup>-</sup>):** To a dark green solution of Cp\*<sub>2</sub>Yb(bipym)PtMe<sub>2</sub> (5 mg, 5  $\mu$ mol) in thf-*d*<sub>8</sub> (0.4 mL), solid Ph<sub>3</sub>C<sup>+</sup> BPh<sub>4</sub><sup>-</sup> (excess) was added. The solution immediately turned dark brown and XRD suitable needles of the same color appeared in few minutes at room temperature. <sup>1</sup>H NMR (300 MHz, thf-*d*<sub>8</sub>, 20 °C):  $\delta$  (ppm) = 249.43 (s, 2H, bipym), 10.02 (s, 2H, bipym), -124.39 (s, 2H, bipym), 13.71 (s, 6H, Pt-(CH<sub>3</sub>)<sub>2</sub>), 5.43 (s, 30H, Cp\*), 14.65 (s, 8H, BPh<sub>4</sub>), 12.33 (s, 8H, BPh<sub>4</sub>), 11.16 (s, 4H, BPh<sub>4</sub>).

**Cp\*<sub>2</sub>Yb(bipym)PtMe<sub>3</sub>(CD<sub>2</sub>)<sub>4</sub>OB(C<sub>6</sub>F<sub>5</sub>)<sub>3</sub> (8):** To a dark green solution of Cp\*<sub>2</sub>Yb(bipym)PtMe<sub>2</sub> (8 mg, 9  $\mu$ mol, 1 eq.) in thf-*d*<sub>8</sub> (0.4 mL), solid B(C<sub>6</sub>F<sub>5</sub>)<sub>3</sub> (4.2 mg, 9  $\mu$ mol, 1 eq.) was added. The solution immediately turned dark brown and XRD suitable plates of the same color appeared in few minutes at room temperature. <sup>1</sup>H NMR (300 MHz, thf-*d*<sub>8</sub>, 20 °C):  $\delta$  (ppm) = 273.97 (s, 2H, bipym), 27.97 (s, 2H, bipym), -216.95 (s, 2H, bipym), 5.97 (s, 6H, Pt-(CH<sub>3</sub>)<sub>2</sub>), 6.63 (s, 15H, Cp\*<sub>1</sub>), 6.26 (s, 15H, Cp\*<sub>2</sub>).



## Chapter IV

### ▪ *Additional considerations:*

All commercially available alkene substrates were dried on  $\text{CaH}_2$ , distilled and degassed before being transferred in the glovebox. The purity of the alkenes has to be very high since the catalyst **1** is sensitive and used at low catalyst loading (1 mol%). All other reagents were prepared according to literatures procedures as reported hereafter. Column chromatography was performed on Biotage Isolera Prime with Biotage SNAP cartridge KP-Sil 25g as silica gel column. X-band EPR measurements were conducted on a Bruker ELEXSYS 500 spectrometer equipped with a Bruker ER 4116DM X band resonator, an Oxford Instruments continuous flow ESR 900 cryostat, and an Oxford ITC 503 temperature control system. The parameters used were  $T=10\text{ K}$ , MW freq.=9.640 GHz, MW power=0.250 mW, MA = 8 Gauss, Gain=29 dB.

### ▪ *Syntheses:*

The following complexes  $(\text{bipym})\text{NiMe}_2$ , **1**, **2** and  $\text{Cp}^*_2\text{Eu}(\text{OEt}_2)$  were synthesized according to literature procedures.<sup>14–16</sup> All N-heterocyclic ligands used were sublimed before use.

**( $\text{Cp}^*_2\text{Eu}(\text{bipym})\text{Me}_2$ ) (3):** To a dark suspension of  $(\text{bipym})\text{NiMe}_2$  (56 mg, 0.23 mmol, 1 eq.) in benzene (2 mL), a pink solution of  $\text{Cp}^*_2\text{Eu}(\text{OEt}_2)$  (120 mg, 0.24 mmol, 1.05 eq.) in benzene (4 mL) was added dropwise under vigorous stirring. After 10 min of reaction, the resulting dark solution was mixed with 4 mL of pentane and left overnight at  $-40\text{ }^\circ\text{C}$  to yield dark XRD suitable crystals that were washed twice with 3 mL of pentane (141 mg, 0.13 mmol, 58%).  **$^1\text{H NMR}$**  remained silent. **IR (ATR):**  $\tilde{\nu} = 3049\text{ (m)}, 2945\text{ (m)}, 2900\text{ (br s)}, 2846\text{ (br s)}, 2720\text{ (w)}, 2650\text{ (w)}, 1981\text{ (w)}, 1959\text{ (w)}, 1934\text{ (w)}, 1816\text{ (w)}, 1563\text{ (w)}, 1544\text{ (w)}, 1477\text{ (m)}, 1436\text{ (m)}, 1410\text{ (m)}, 1391\text{ (vs)}, 1325\text{ (w)}, 1292\text{ (w)}, 1198\text{ (m)}, 1146\text{ (m)}, 1034\text{ (w)}, 1015\text{ (s)}, 849\text{ (w)}, 813\text{ (m)}, 784\text{ (m)}, 744\text{ (s)}, 697\text{ (s)}, 680\text{ (vs)}, 648\text{ (m)}\text{ cm}^{-1}$ . **Anal. calcd.** for  $\text{C}_{36}\text{H}_{48}\text{EuN}_4\text{Ni}$ : C, 57.85; H, 6.47; N, 7.50; found: C, 57.18; H, 6.46; N, 7.33. The number of co-crystallized benzene decrease to 1 instead of 1.5 upon drying.

**(4,4'-Me<sub>2</sub>-2,2'-bipyridineNiMe<sub>2</sub>) (4):** To a yellow suspension of  $(\text{tmeda})\text{NiMe}_2$  (78 mg, 0.38 mmol, 1 eq.) in benzene (1.5 mL), a colorless solution of 4,4'-dimethyl-2,2'-bipyridine (67 mg, 0.36 mmol, 0.95 eq) in benzene (3.5 mL) was added dropwise under vigorous stirring. After 2 h of reaction, the resulting deep green solution was mixed with 5 mL of pentane and left at  $-40\text{ }^\circ\text{C}$  overnight to yield XRD suitable needles that are washed once with 2 mL of cold  $\text{Et}_2\text{O}$  to remove traces of Ni precursor and twice with 3 mL of pentane (25 mg, 0.09 mmol, 26%).  **$^1\text{H NMR}$**  (300 MHz, 293 K,  $\text{thf}-d_8$ ):  $\delta$  (ppm) = -0.16 (6H, s), 2.33 (6H, s), 7.29 (2H, d), 7.91 (2H, s), 8.80 (2H, d). **IR (ATR):**  $\tilde{\nu}$

= 3112 (w), 3055 (w), 2914 (br s), 2892 (br s), 2781 (s), 2516 (w), 2233 (br w), 1939 (w), 1908 (w), 1767 (br w), 1709 (w), 1613 (vs), 1550 (m), 1478 (m), 1441 (s), 1412 (vs), 1374 (s), 1300 (m), 1277 (s), 1240 (m), 1220 (m), 1147 (m), 1110 (br w), 1038 (m), 955 (w), 921 (m), 816 (vs), 759 (br m), 725 (m), 641 (vs)  $\text{cm}^{-1}$ . **Anal. calcd.** for  $\text{C}_{14}\text{H}_{18}\text{N}_2\text{Ni}$ : C, 61.59; H, 6.65; N, 10.26; found: C, 59.31; H, 6.32; N, 9.93.

**(3,3'-Me<sub>2</sub>-2,2'-bipyridineNiMe<sub>2</sub>) (5):** To a yellow solution of (tmeda)NiMe<sub>2</sub> (71 mg, 0.35 mmol, 1 eq.) in benzene (1.5 mL), a colorless solution of 3,3'-dimethyl-2,2'-bipyridine (61 mg, 0.33 mmol, 0.95 eq.) in benzene (2.5 mL) was added dropwise under vigorous stirring. After 2 h of reaction, the resulting deep green solution is mixed with 4 mL of pentane and left at -40 °C overnight to yield XRD suitable needles that were washed once with 2 mL of cold Et<sub>2</sub>O to remove traces of Ni precursor and twice with 3 mL of pentane (20 mg, 0.07 mmol). Yield: 22 %. <sup>1</sup>H NMR (300 MHz, 293 K, thf-*d*<sub>8</sub>):  $\delta$  (ppm) = -0.34 (6H, s), 2.32 (6H, s), 7.40 (2H, dd), 7.79 (2H, d), 8.74 (2H, d). **IR (ATR):**  $\tilde{\nu}$  = 3078 (w), 2983 (w), 2903 (br s), 2809 (br s), 1948 (w), 1901 (w), 1855 (w), 1763 (w), 1718 (br w), 1612 (w), 1572 (m), 1519 (m), 1440 (vs), 1401 (s), 1377 (s), 1300 (m), 1237 (m), 1177 (m), 1150 (m), 1118 (s), 1068 (w), 1038 (s), 991 (m), 929 (m), 789 (vs), 727 (vs), 651 (vs)  $\text{cm}^{-1}$ . **Anal. calcd.** for  $\text{C}_{14}\text{H}_{18}\text{N}_2\text{Ni}$ : C, 61.59; H, 6.65; N, 10.26; found: C, 60.56; H, 6.51; N, 10.3.

NMR spectra of 4 and 5:

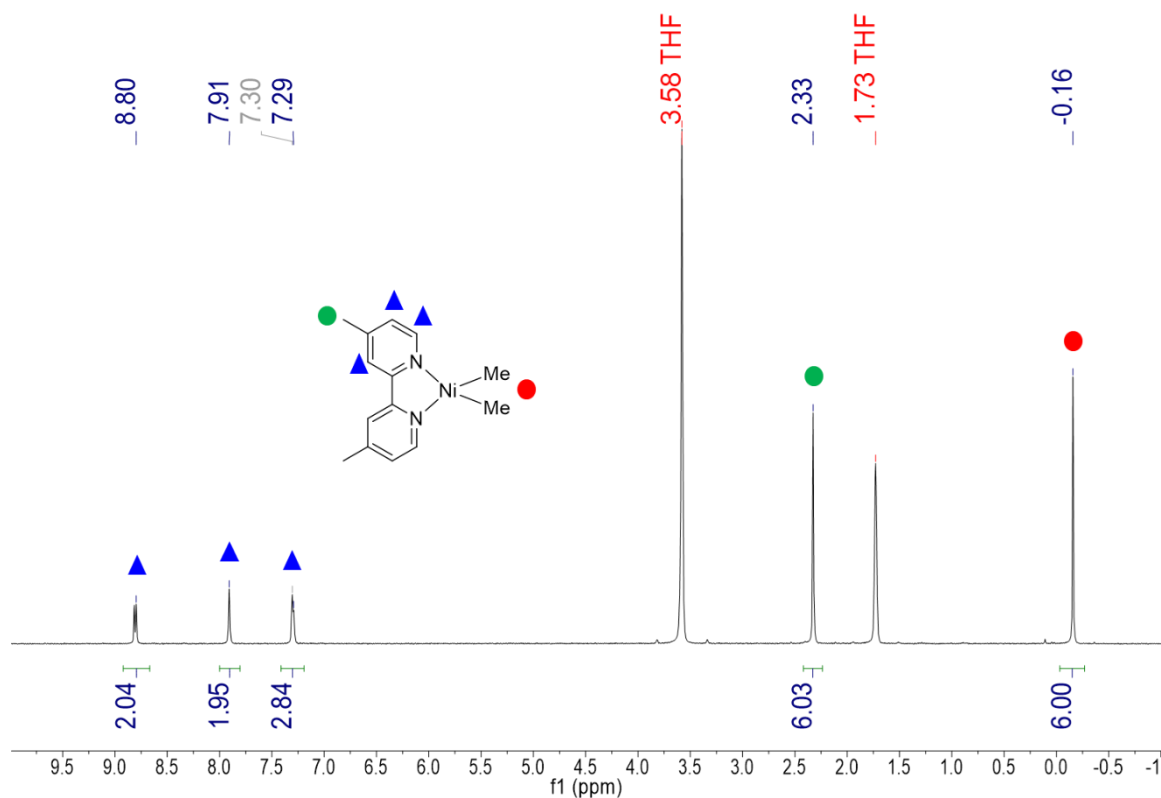


**Figure A1.** <sup>1</sup>H NMR spectrum of 4 in thf-*d*<sub>8</sub> at 20 °C. Solvent peaks are indicated in red, benzene impurities are indicated in grey.

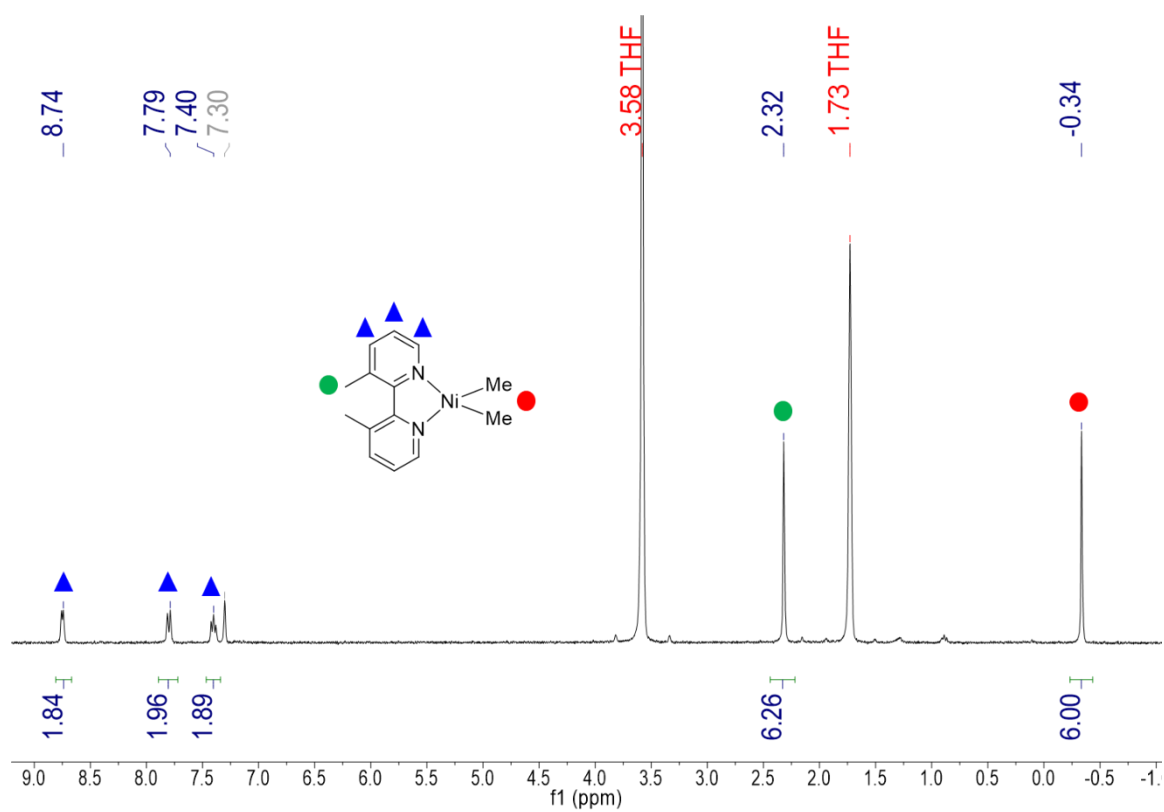


**Figure A2.** <sup>1</sup>H NMR spectrum of **5** in thf-*d*<sub>8</sub> at 20 °C. Solvent peaks are indicated in red, benzene impurities are indicated in grey.

## In-situ NMR characterization of (bipy)Ni(Cod):

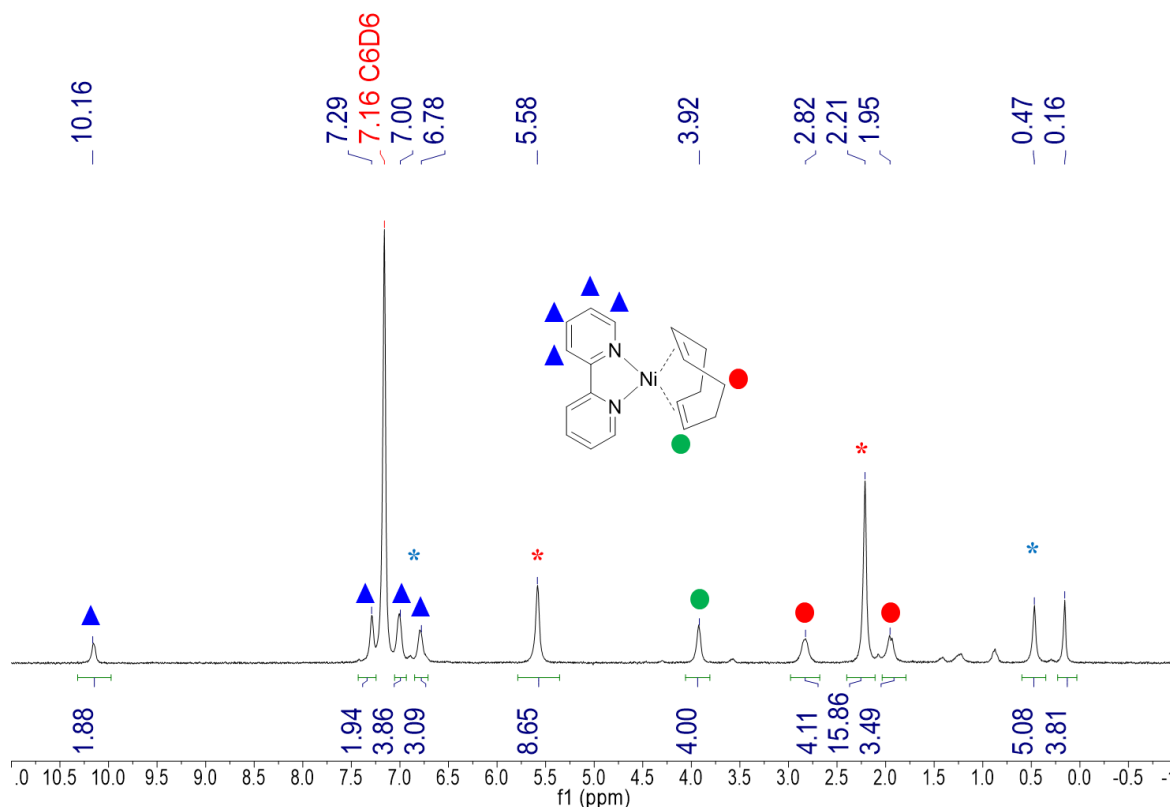


**Figure A3.**  $^1\text{H}$  NMR spectrum of **2** in  $\text{C}_6\text{D}_6$  after addition of Cod then HBCat. In-situ formed (bipy)Ni(Cod) peaks are labelled while free Cod and MeBcat are identified by red and blue asterisks respectively.

■ *Scope study:*

Conditions of the reaction:

In the glovebox, the substrate (0.5 mmol) and internal standard (tri-*tert*-butylbenzene (13.7 mg, 0.06 mmol) and/or benzene (7.5  $\mu\text{L}$ , 0.08 mmol)) were dissolved in  $\text{thf-}d_8$  (0.5 mL). The resulting solution was then used to dissolve successively **1** (4 mg, 5  $\mu\text{mol}$ ) then HBCat (3 mg, 25  $\mu\text{mol}$ ) before being transferred to a 5 mm NMR tube adapted with a J. Young valve. The NMR tube was then removed from the glovebox and heated at 60  $^\circ\text{C}$  in an oil bath. The consumption and yield of the reaction were followed by  $^1\text{H}$  NMR at the indicated times.

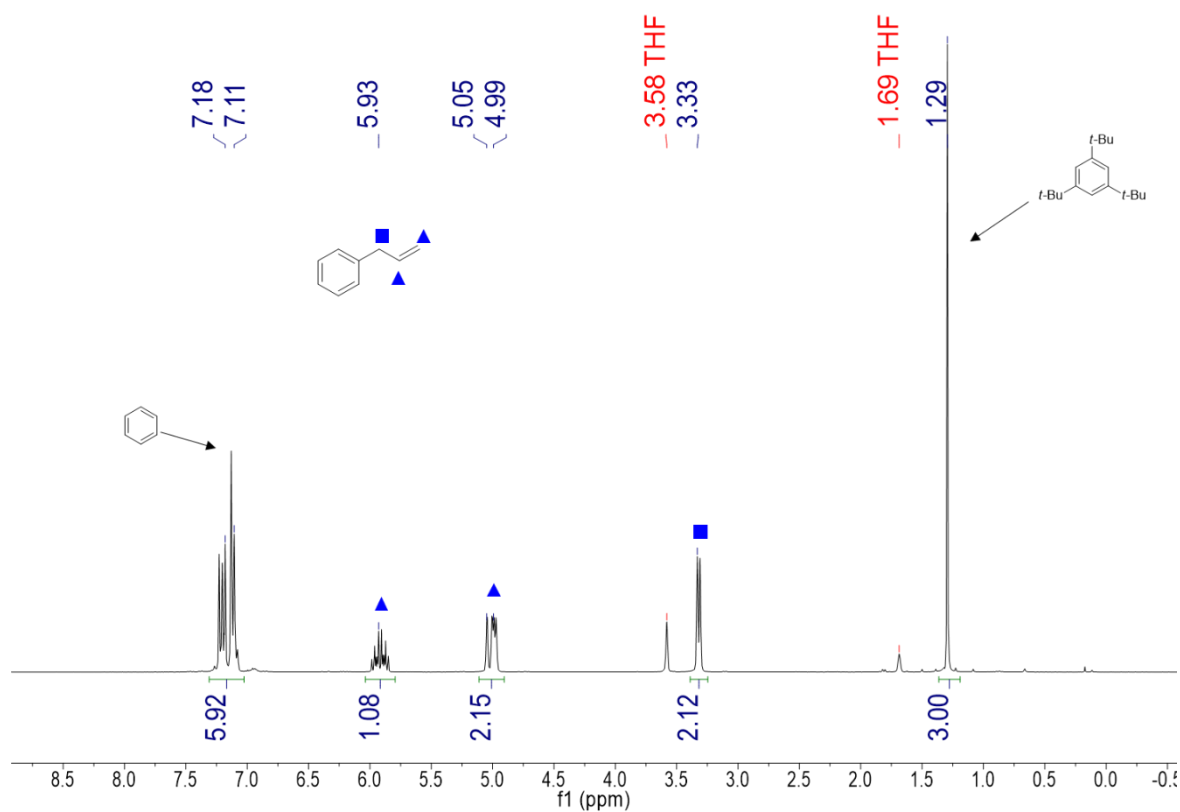


**Figure A4.** <sup>1</sup>H NMR spectrum in thf-*d*<sub>8</sub> of the isomerization of **A** by 1 mol% of **1** at 60 °C, t=0 h. Relevant peaks are assigned and (tBu)<sub>3</sub>benzene serves as internal reference.

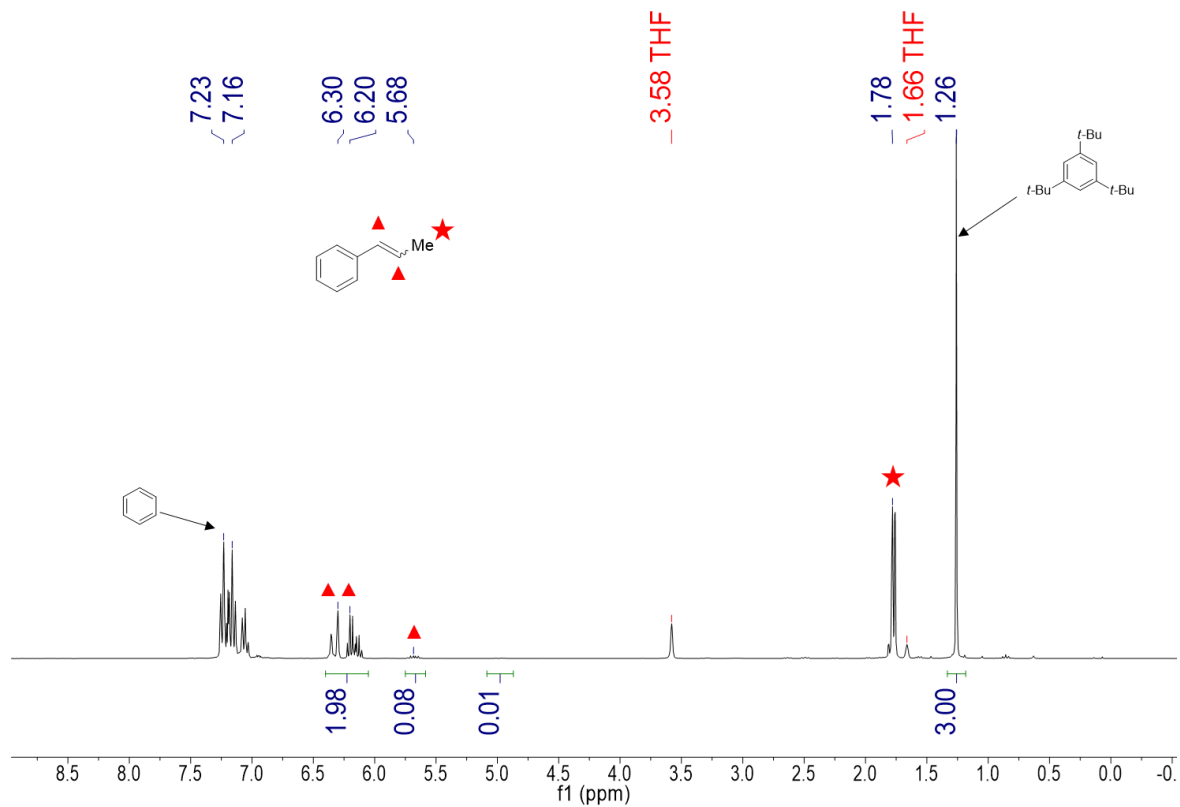


**Figure A5.** <sup>1</sup>H NMR spectrum in thf-*d*<sub>8</sub> of the isomerization of **A** by 1 mol% of **1** at 60 °C, t=16 h. Relevant peaks are assigned and (tBu)<sub>3</sub>benzene served as an internal reference.

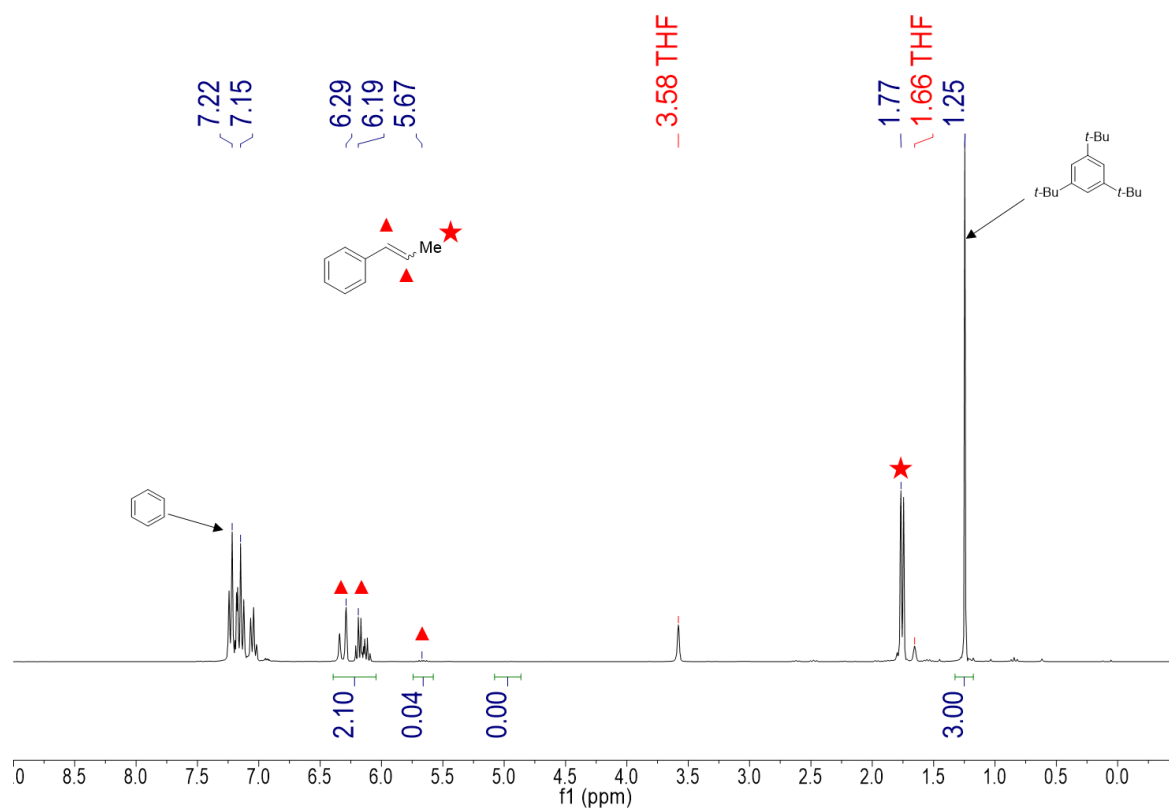


**Figure A6.** <sup>1</sup>H NMR spectrum in thf-*d*<sub>8</sub> of the isomerization of **A** by 1 mol% of **1** at 60 °C, *t*=3.5 days. Relevant peaks are assigned and (tBu)<sub>3</sub>benzene served as an internal reference.

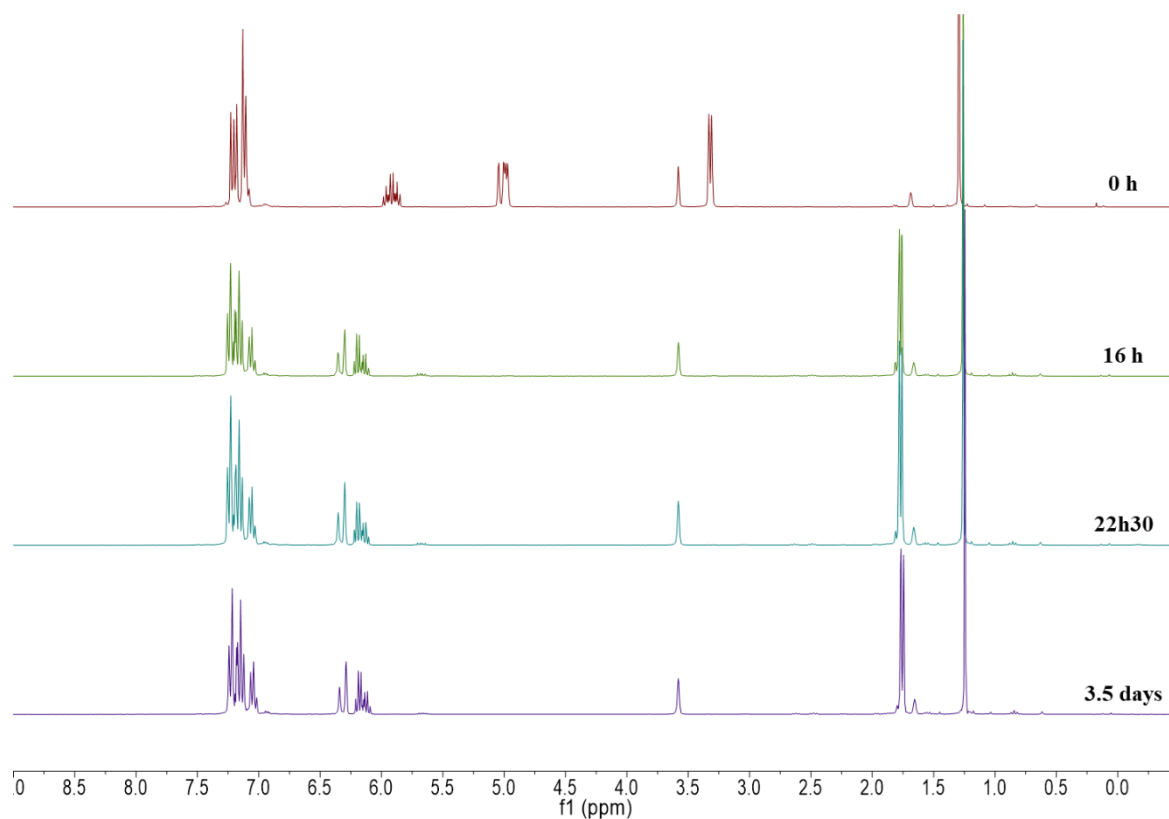


**Figure A7.** Stacked <sup>1</sup>H NMR spectra in thf-*d*<sub>8</sub> of the isomerization of **A** by 1 mol% of **1** at 60 °C, different timings are compared.

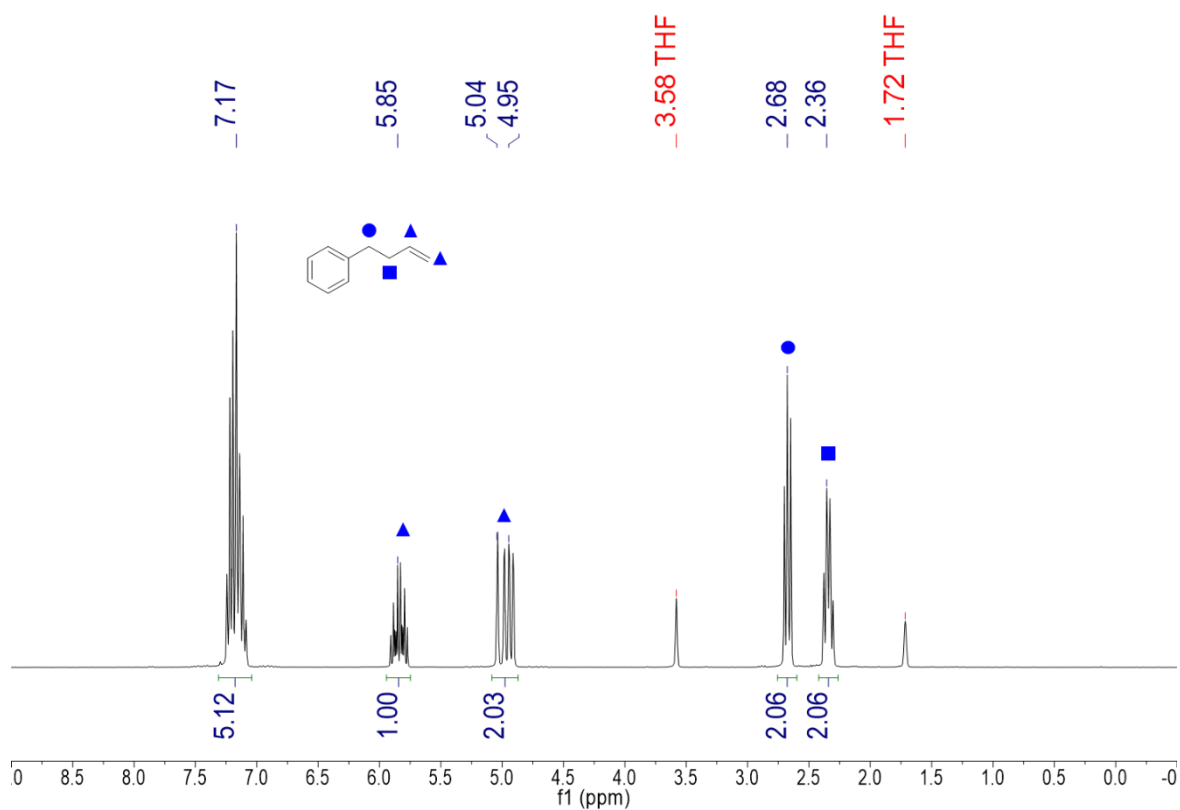


**Figure A8.** <sup>1</sup>H NMR spectrum in thf-*d*<sub>8</sub> of **B**.

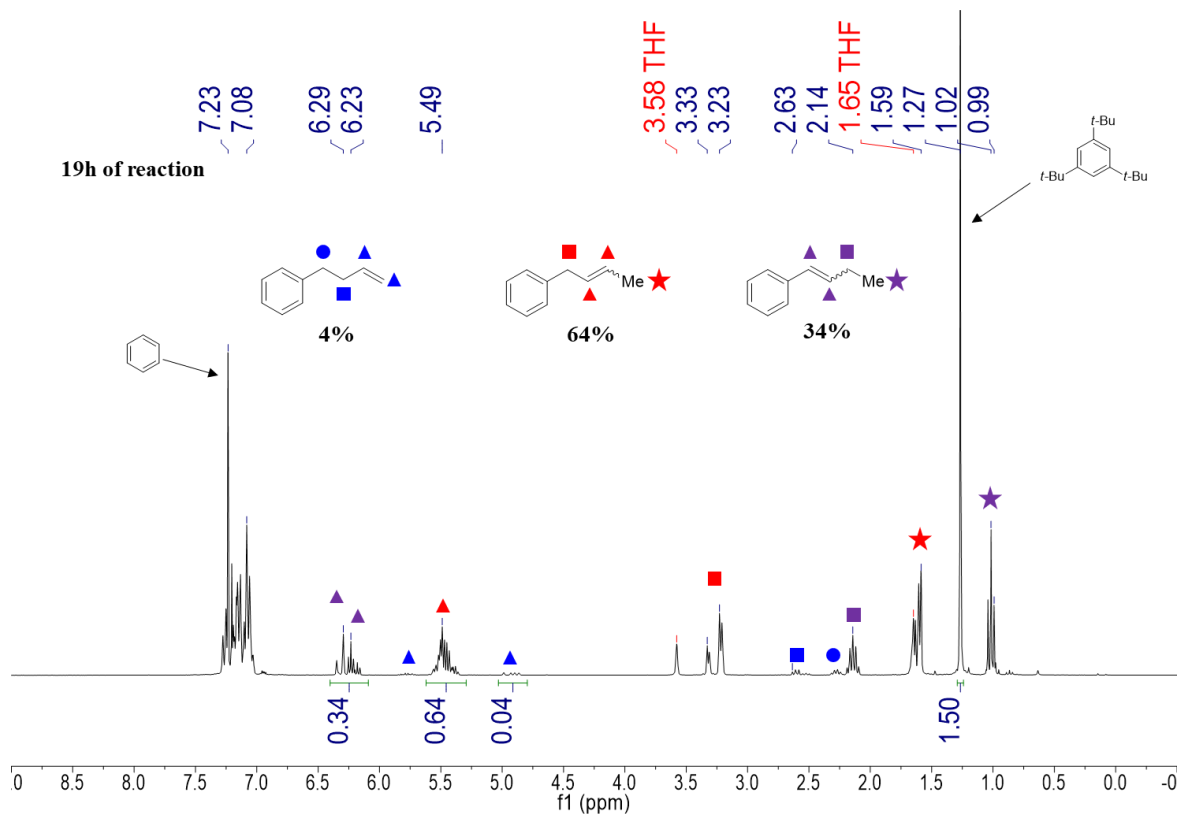


**Figure A9.** <sup>1</sup>H NMR spectrum in thf-*d*<sub>8</sub> of the isomerization of **B** by 1 mol% of **1** at 60 °C, t=19 h. Relevant peaks are assigned and (tBu)<sub>3</sub>benzene served as an internal reference.

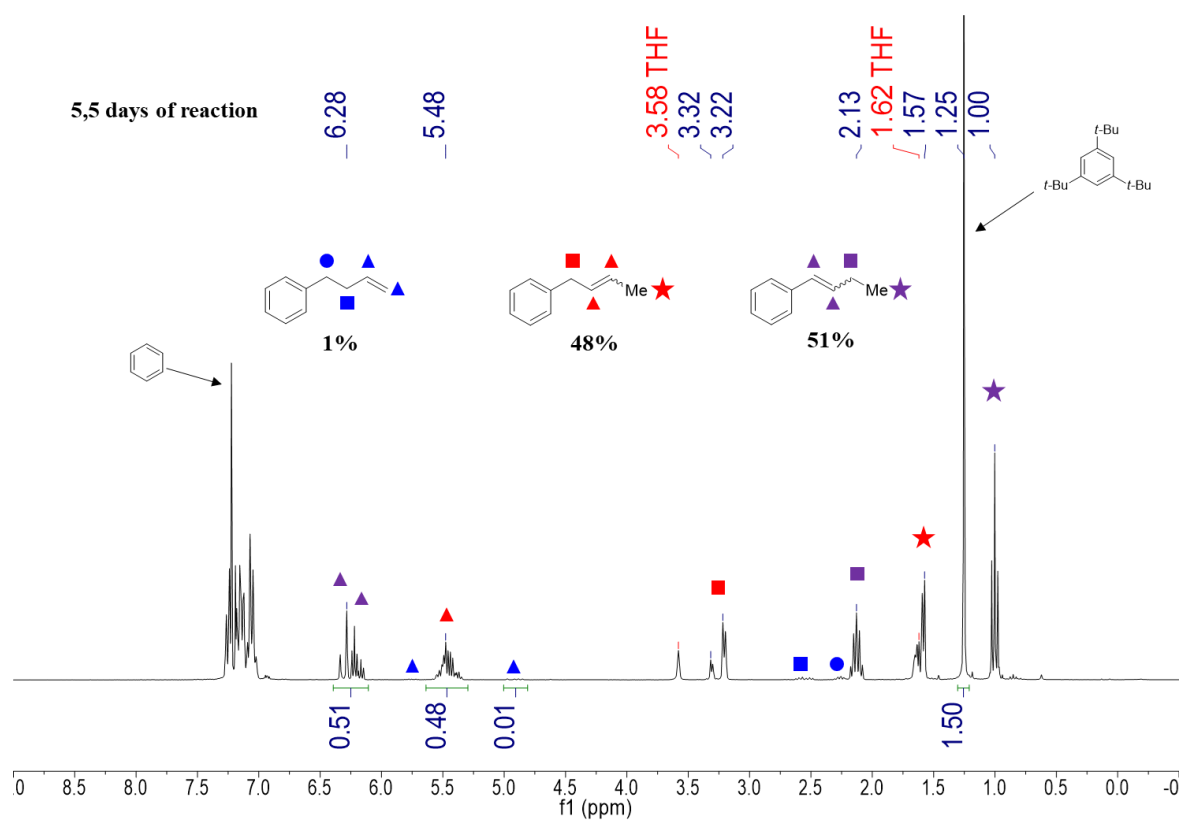


**Figure A10.**  $^1\text{H}$  NMR spectrum in  $\text{thf-}d_8$  of the isomerization of **B** by 1 mol% of **1** at 60 °C,  $t=5.5$  days. Relevant peaks are assigned and  $(t\text{Bu})_3\text{benzene}$  served as an internal reference.

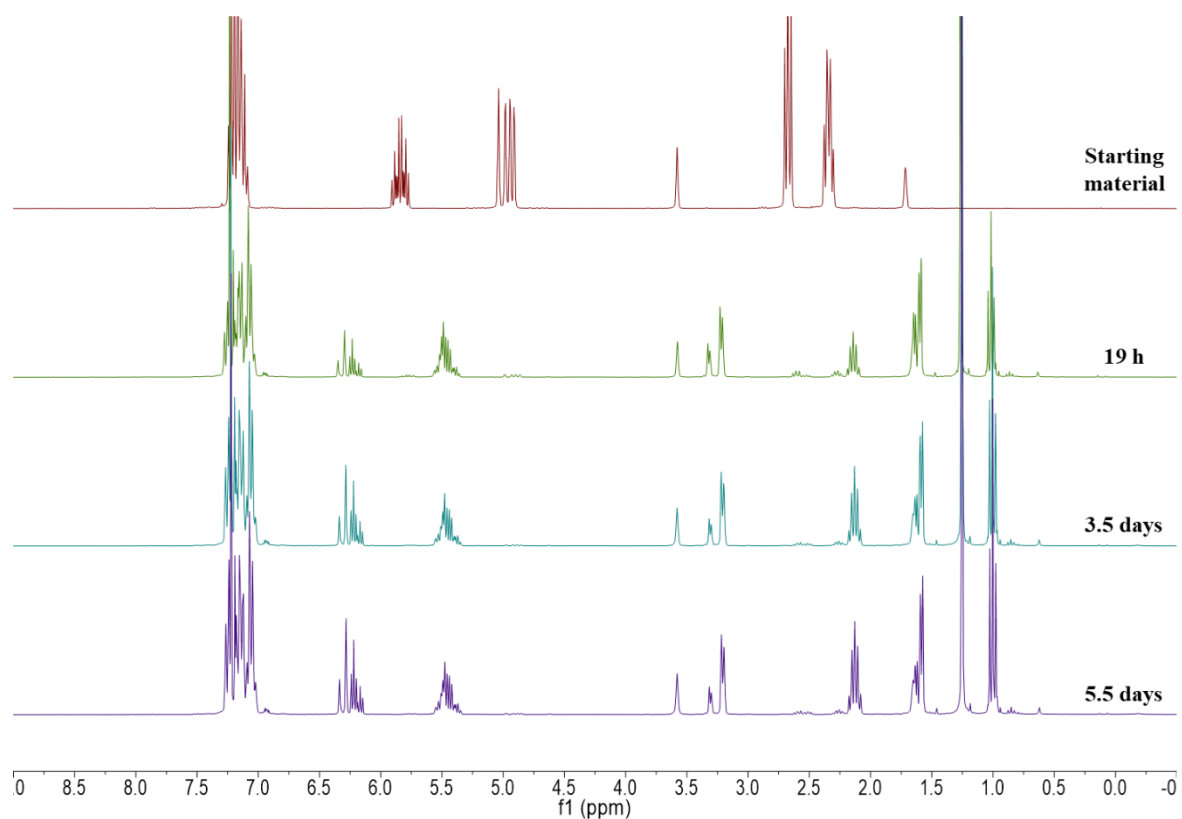


**Figure A11.** Stacked  $^1\text{H}$  NMR spectra in  $\text{thf-}d_8$  of the isomerization of **B** by 1 mol% of **1** at 60 °C, different timings are compared.



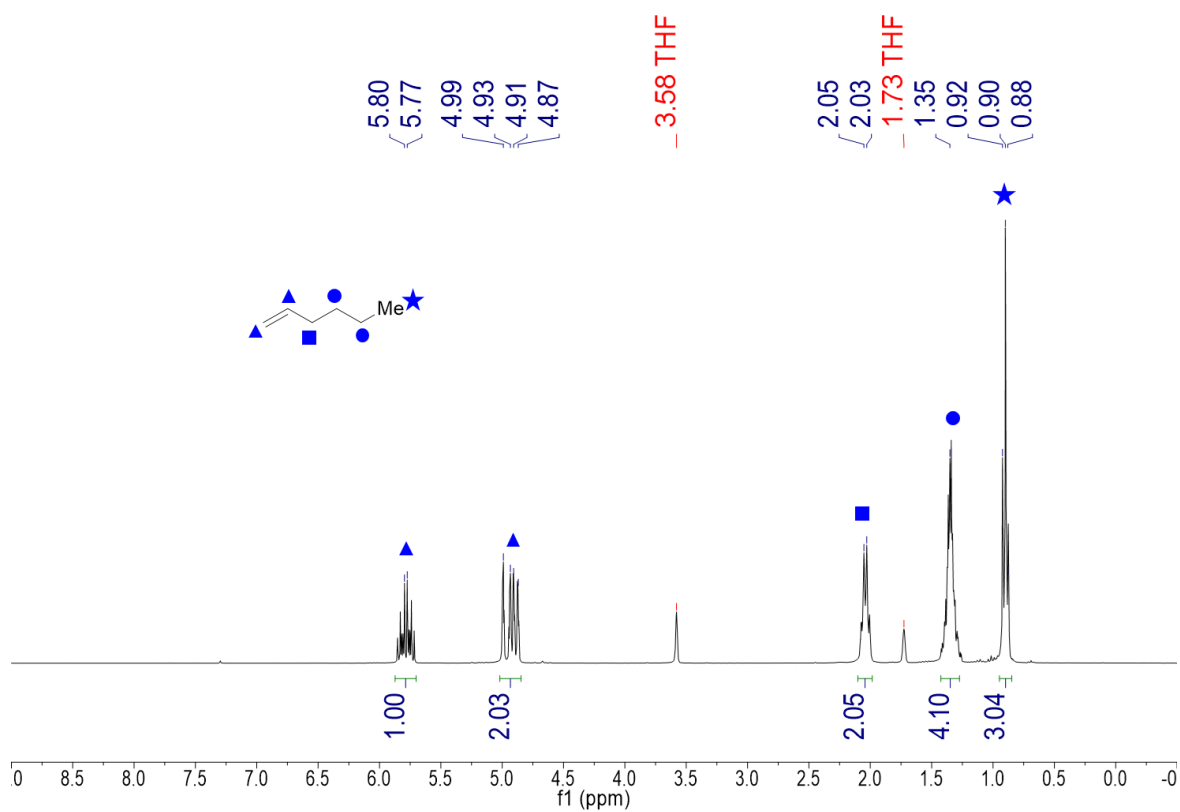


**Figure A12.** <sup>1</sup>H NMR spectrum in thf-*d*<sub>8</sub> of **C**.

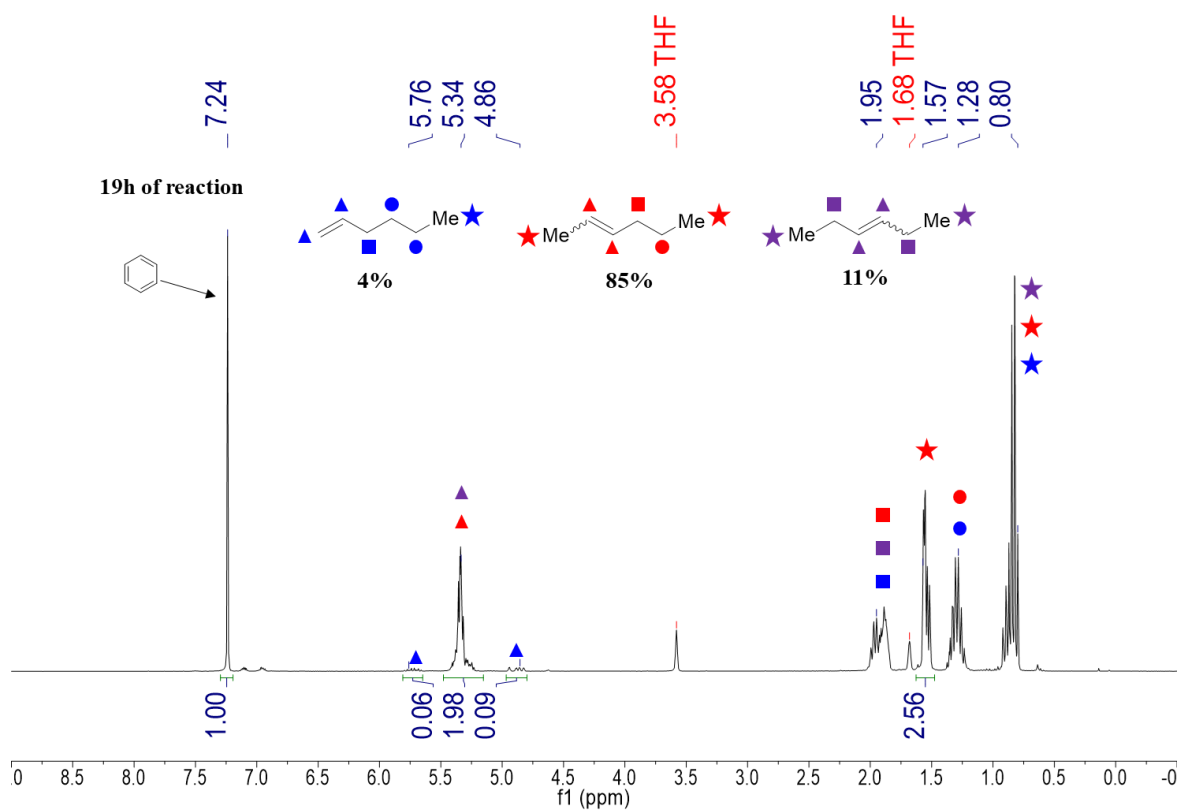


**Figure A13.** <sup>1</sup>H NMR spectrum in thf-*d*<sub>8</sub> of the isomerization of **C** by 1 mol% of **1** at 60 °C, t=19 h. Relevant peaks are assigned and benzene served as an internal reference.

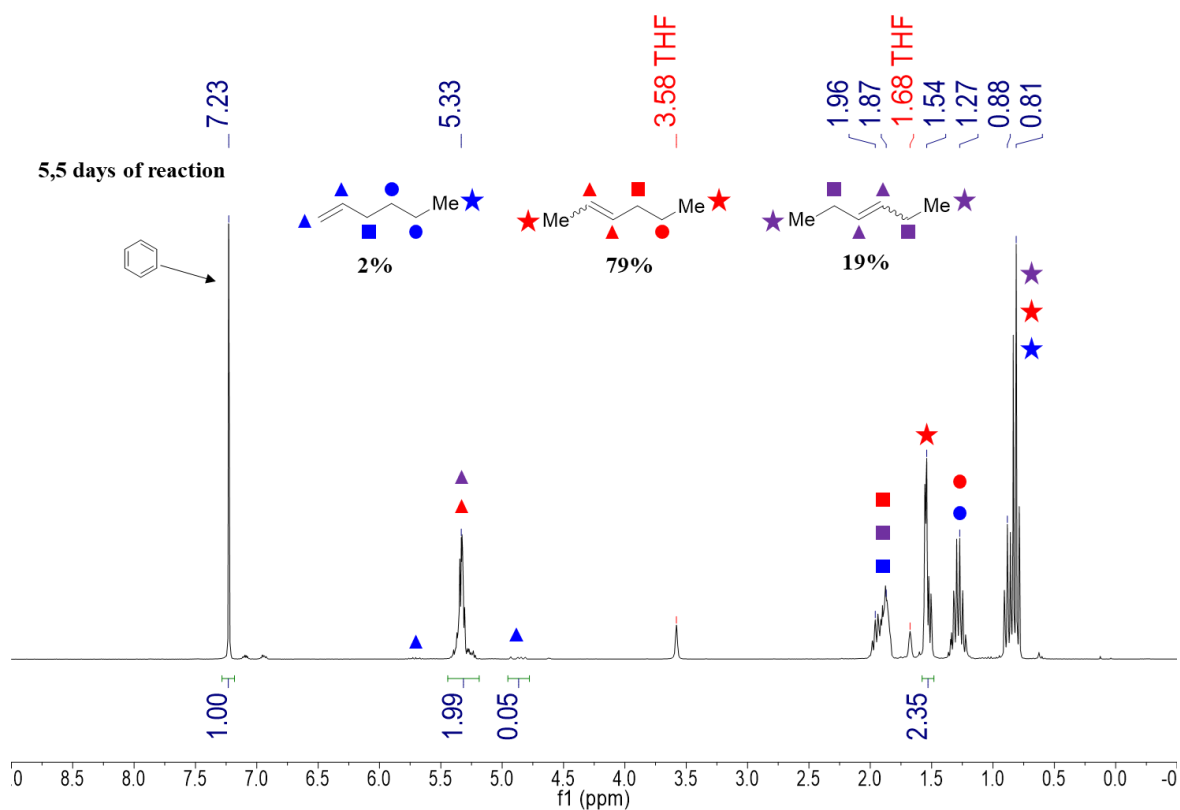


**Figure A14.**  $^1\text{H}$  NMR spectrum in  $\text{thf-}d_8$  of the isomerization of **C** by 1 mol% of **1** at 60 °C,  $t=5.5$  days. Relevant peaks are assigned and benzene served as an internal reference.

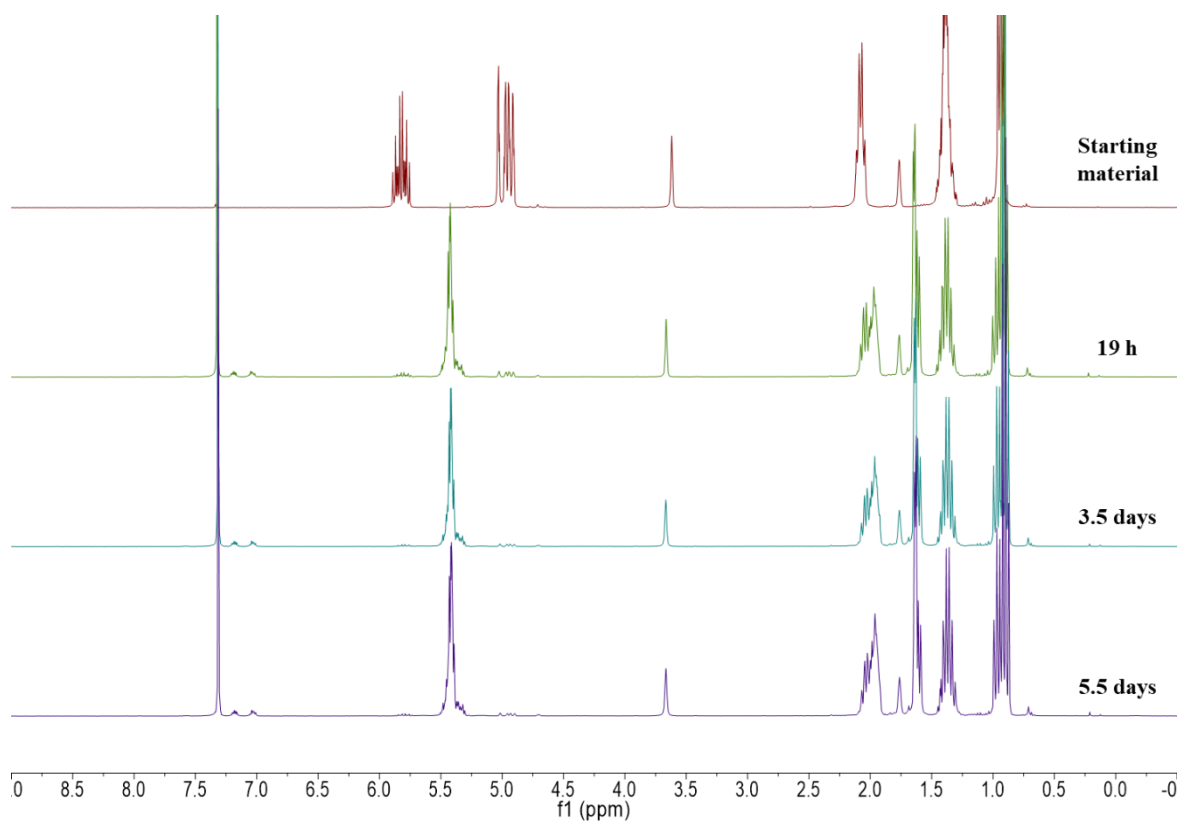


**Figure A15.** Stacked  $^1\text{H}$  NMR spectra in  $\text{thf-}d_8$  of the isomerization of **C** by 1 mol% of **1** at 60 °C, different timings are compared.

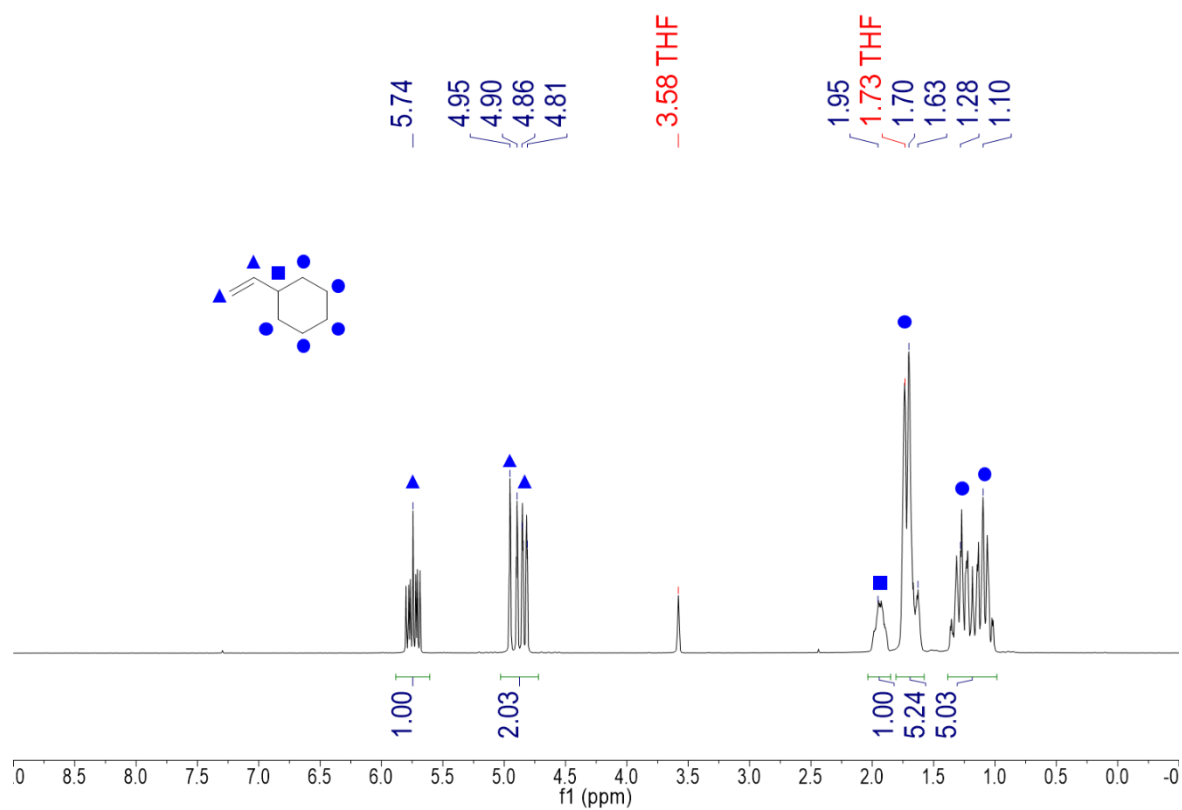


**Figure A16.**  $^1\text{H}$  NMR spectrum in  $\text{thf-}d_8$  of **D**.

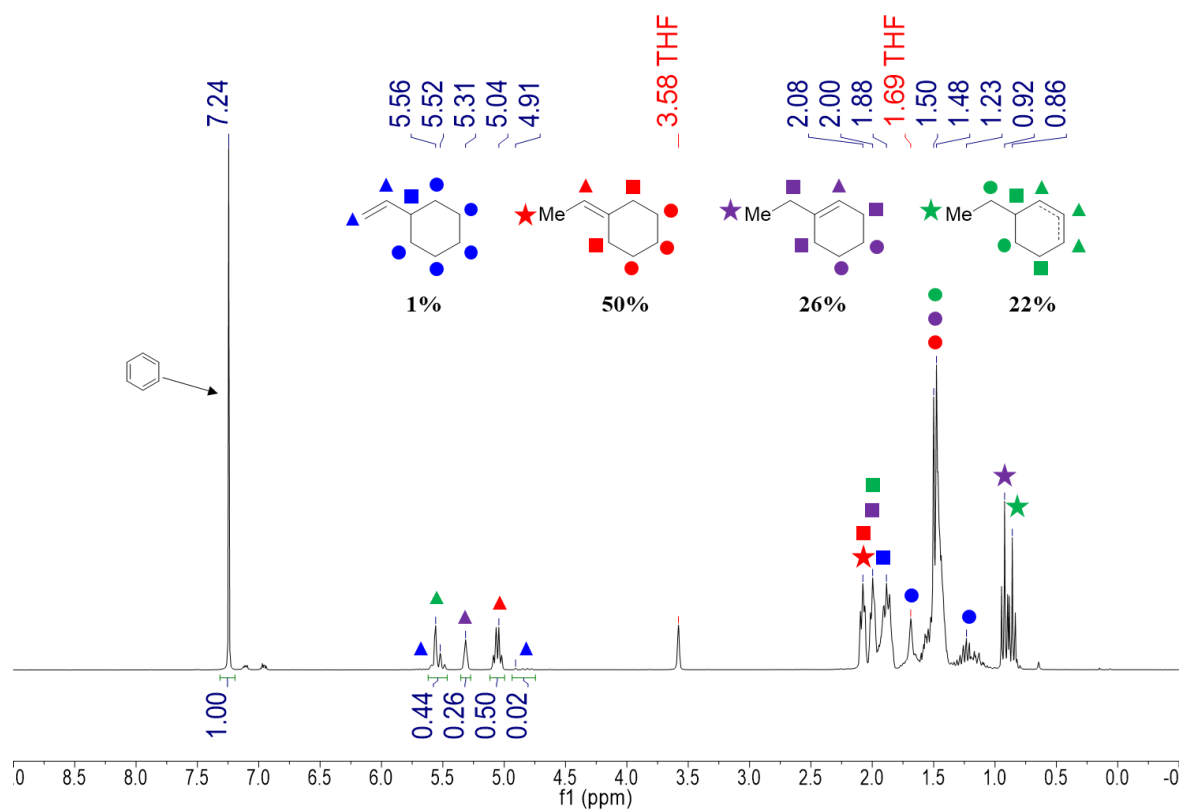


**Figure A17.**  $^1\text{H}$  NMR spectrum in  $\text{thf-}d_8$  of the isomerization of **D** by 1 mol% of **1** at 60 °C,  $t=5.5$  days. Relevant peaks are assigned and benzene served as an internal reference.

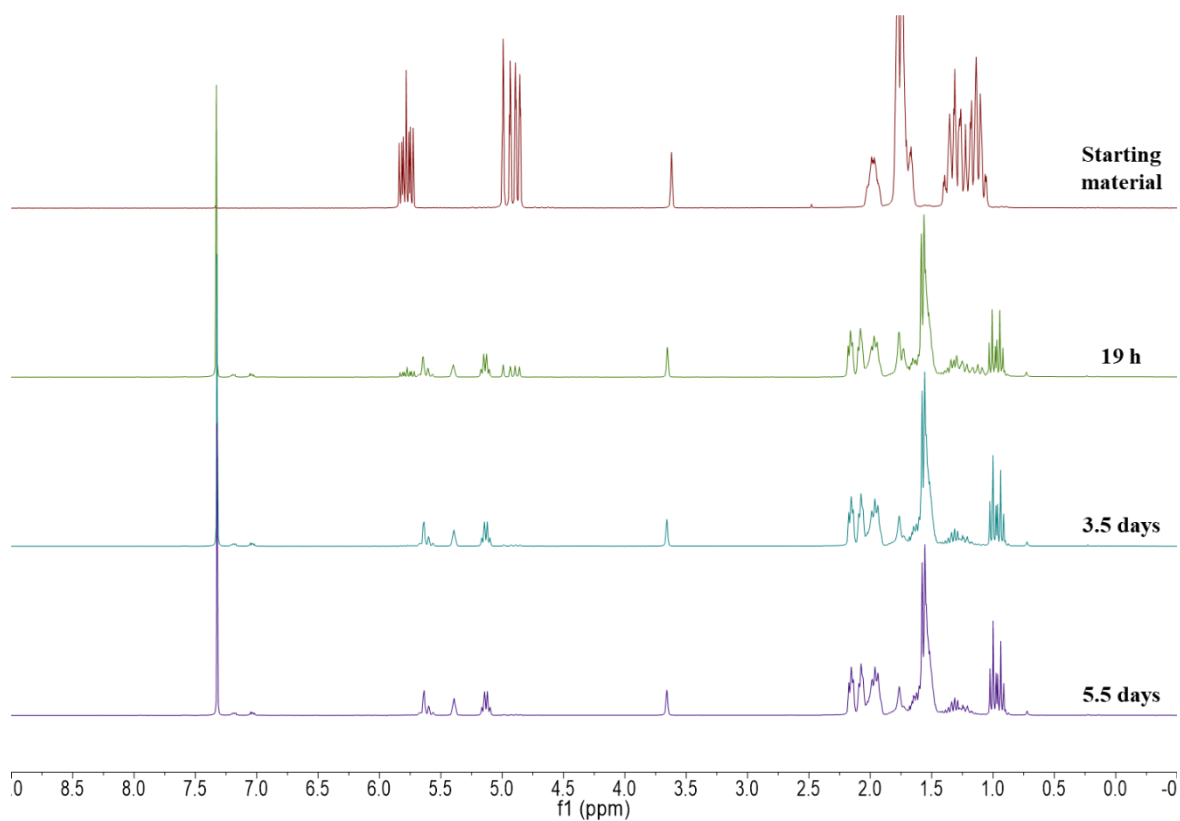


**Figure A18.** Stacked  $^1\text{H}$  NMR spectra in  $\text{thf-}d_8$  of the isomerization of **D** by 1 mol% of **1** at 60 °C, different timings are compared.

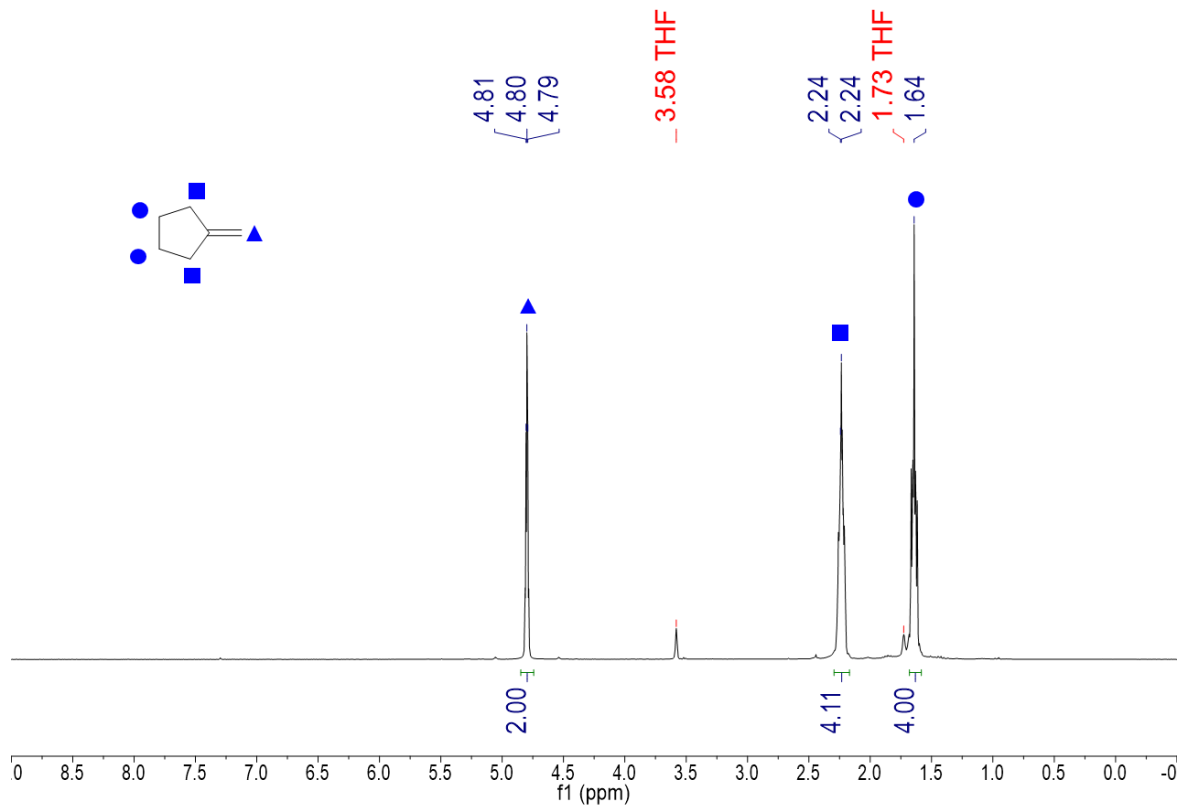


**Figure A19.**  $^1\text{H}$  NMR spectrum in  $\text{thf-}d_8$  of **E**.

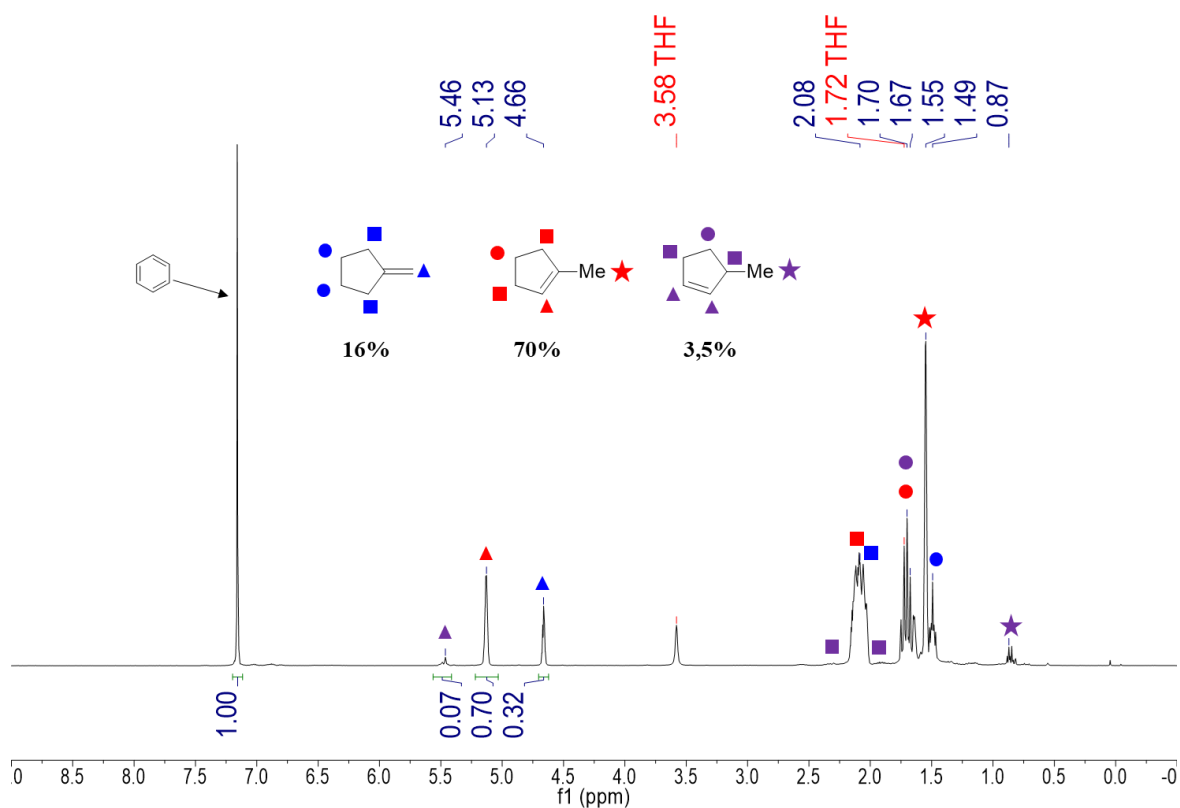


**Figure A20.**  $^1\text{H}$  NMR spectrum in  $\text{thf-}d_8$  of the isomerization of **E** by 1 mol% of **1** at 60 °C,  $t=5.5$  days. Relevant peaks are assigned and benzene served as an internal reference.

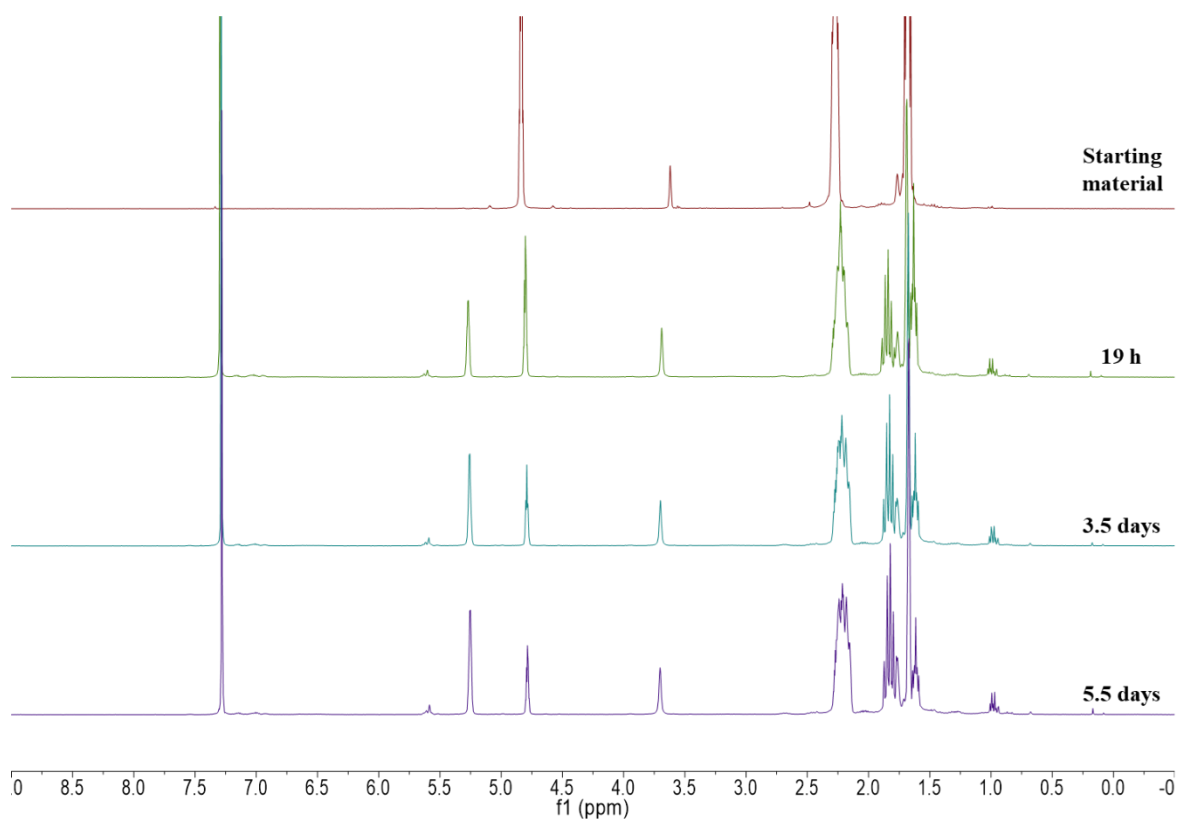


**Figure A21.** Stacked  $^1\text{H}$  NMR spectra in  $\text{thf-}d_8$  of the isomerization of **E** by 1 mol% of **1** at 60 °C, different timings are compared.

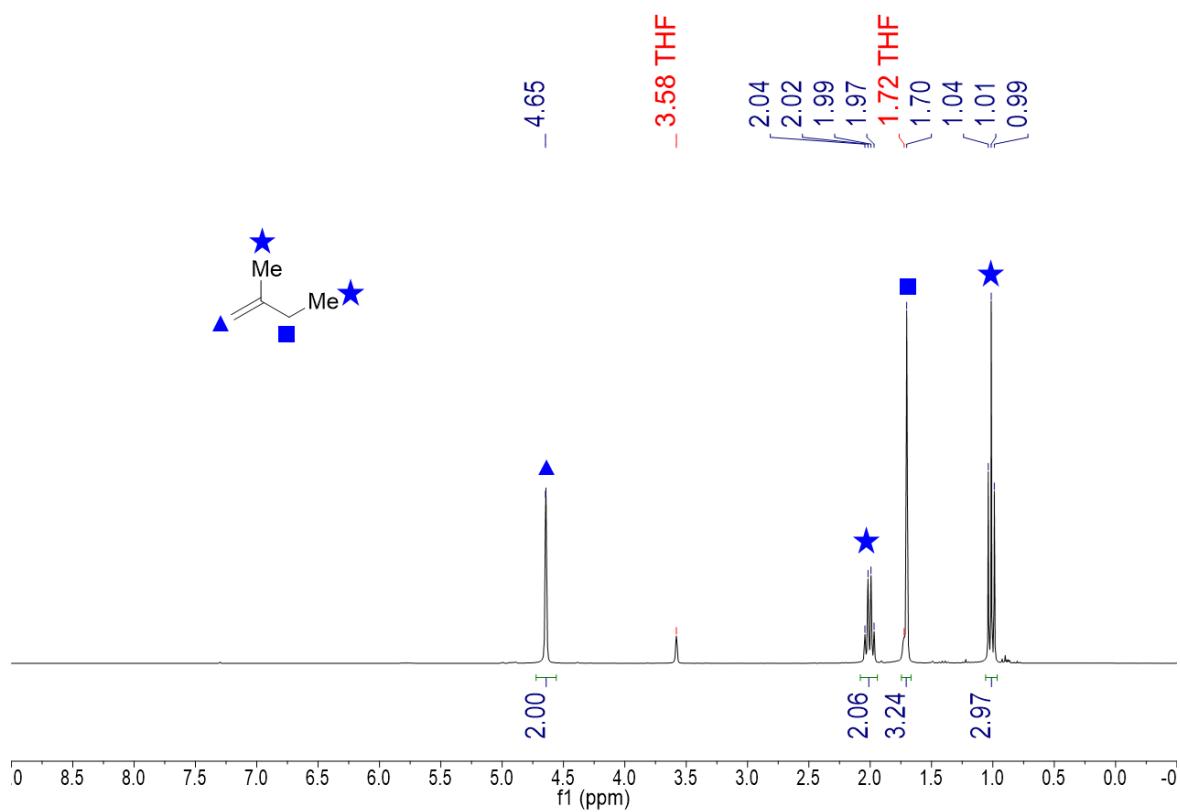


**Figure A22.** <sup>1</sup>H NMR spectrum in thf-*d*<sub>8</sub> of **F**.

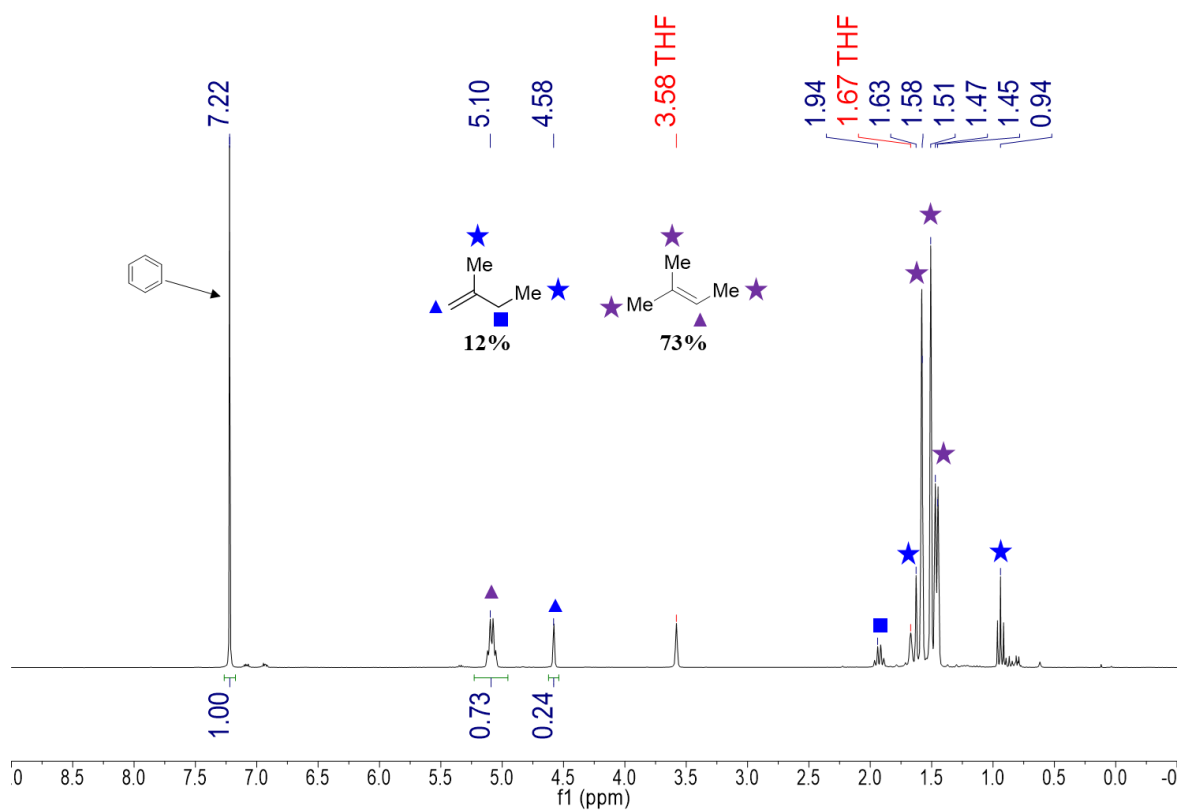


**Figure A23.** <sup>1</sup>H NMR spectrum in thf-*d*<sub>8</sub> of the isomerization of **F** by 1 mol% of **1** at 60 °C, t=5.5 days. Relevant peaks are assigned and benzene serves as internal reference.

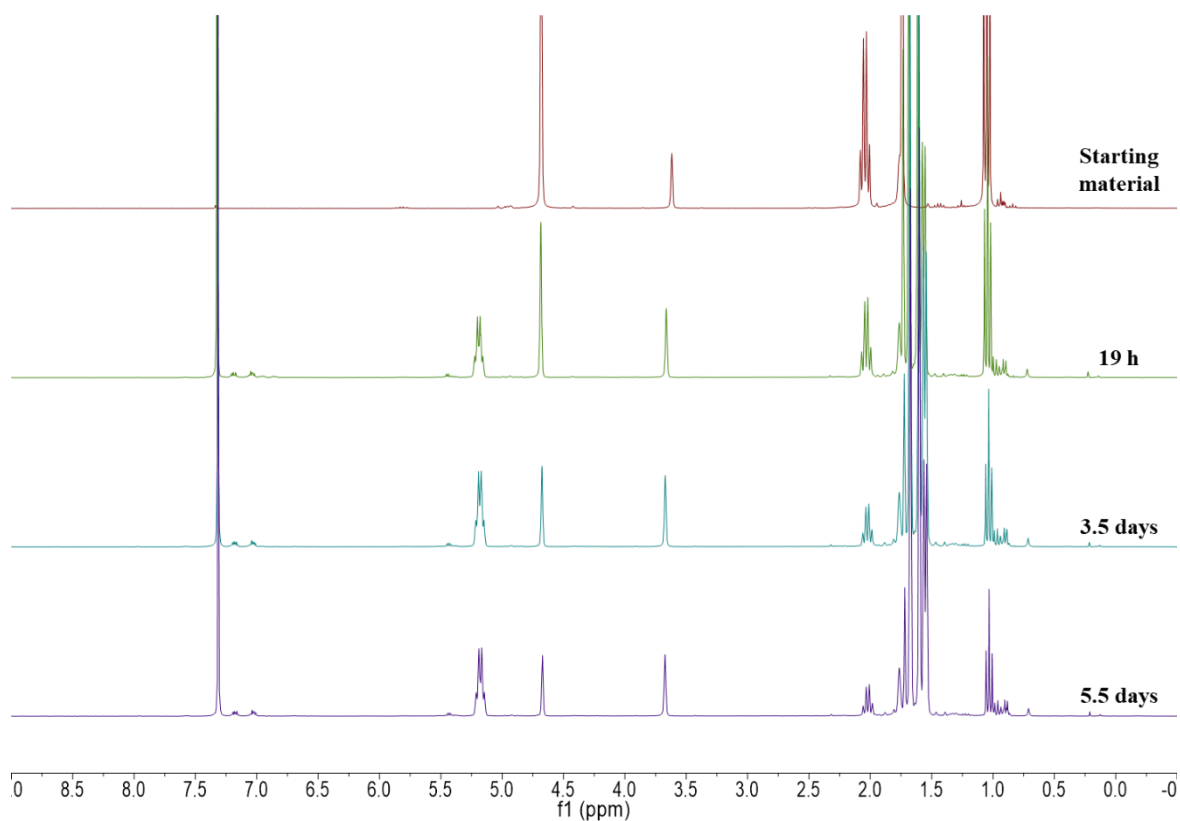


**Figure A24.** Stacked  $^1\text{H}$  NMR spectra in  $\text{thf-}d_8$  of the isomerization of **F** by 1 mol% of **1** at 60 °C, different timings are compared.

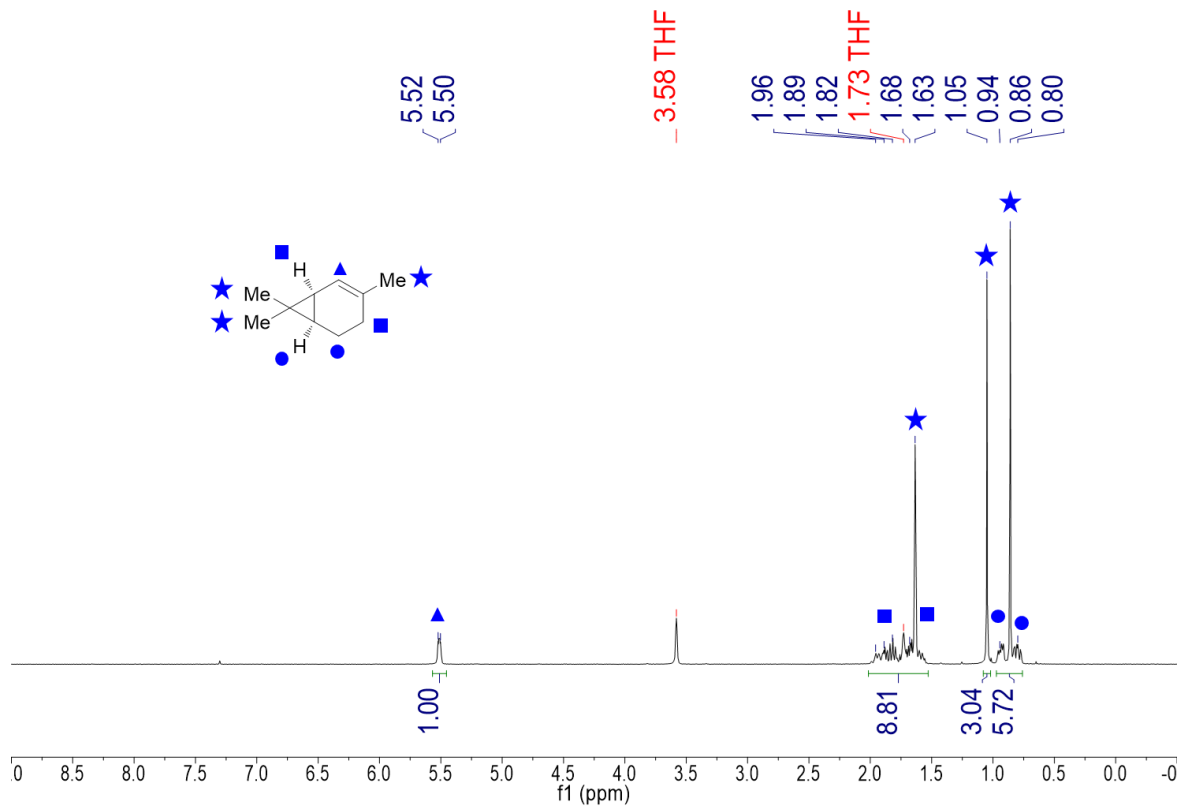


**Figure A25.**  $^1\text{H}$  NMR spectrum in  $\text{thf-}d_8$  of **G**.

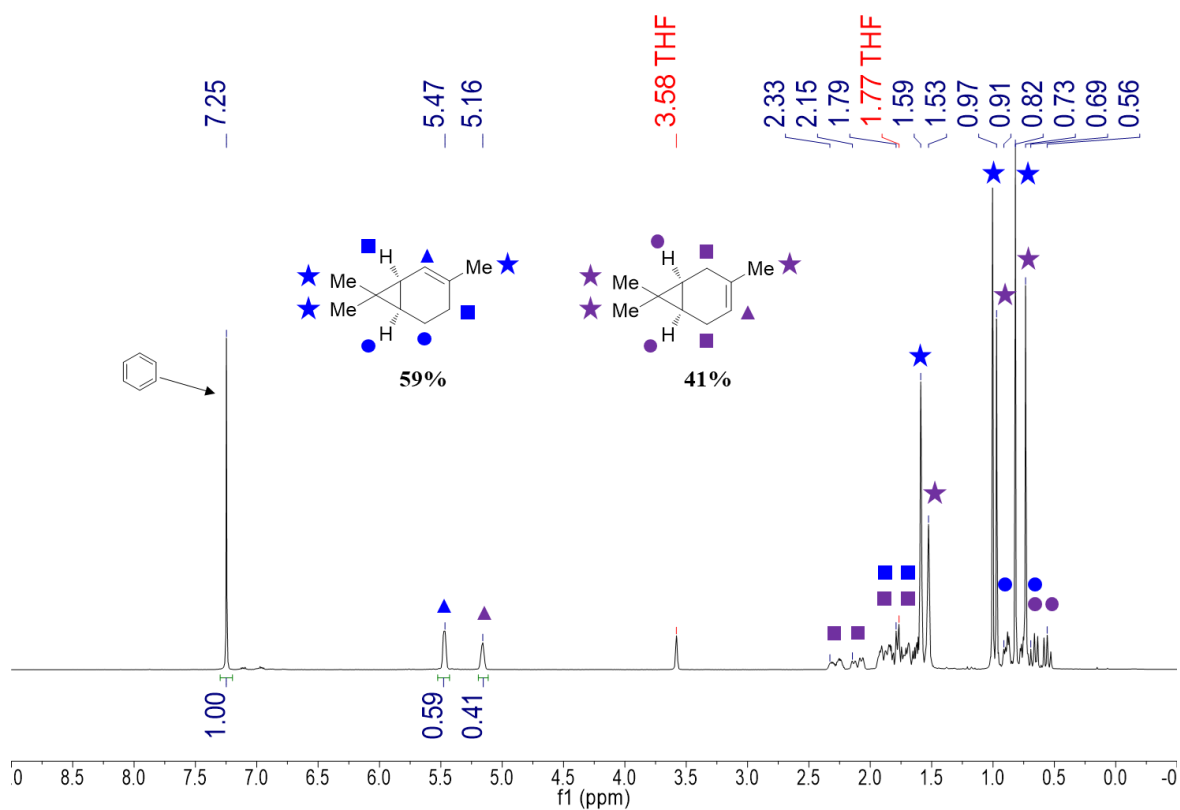


**Figure A26.**  $^1\text{H}$  NMR spectrum in  $\text{thf-}d_8$  of the isomerization of **G** by 1 mol% of **1** at  $60\text{ }^\circ\text{C}$ ,  $t=5.5$  days. Relevant peaks are assigned and benzene served as an internal reference.

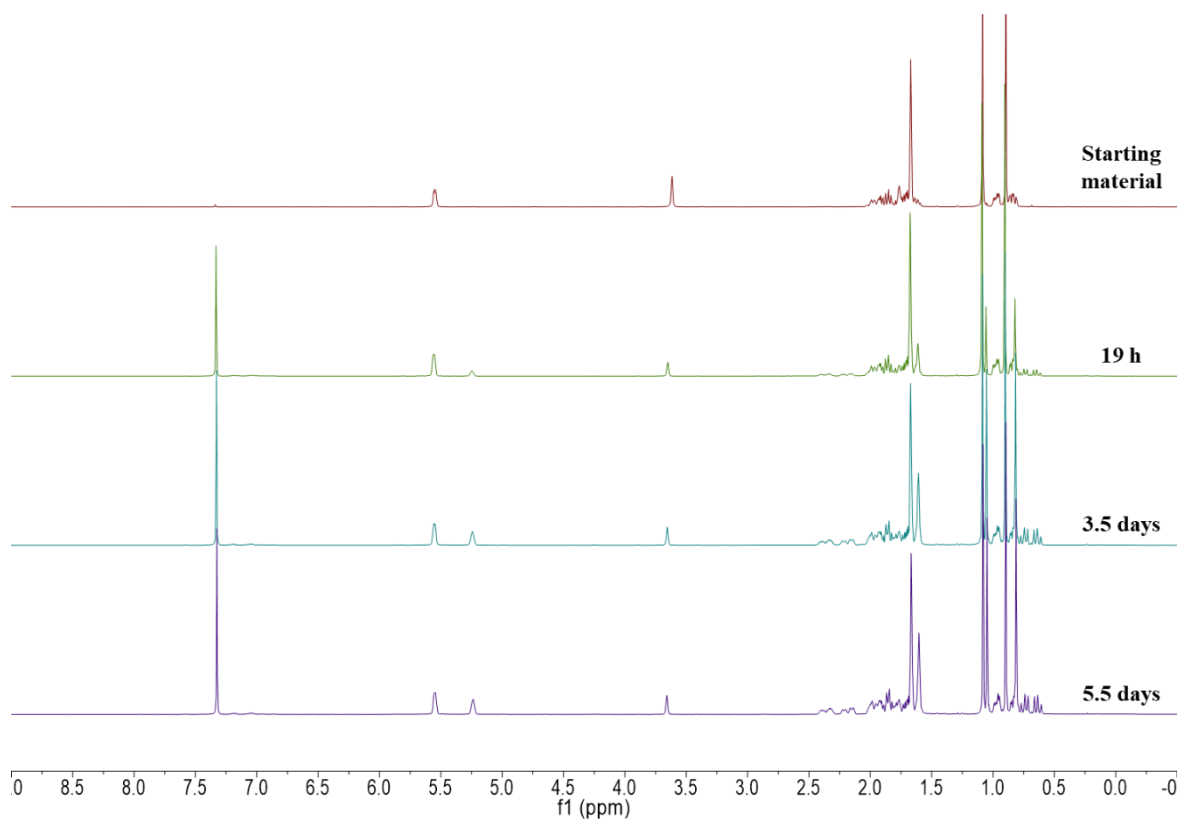


**Figure A27.** Stacked  $^1\text{H}$  NMR spectra in  $\text{thf-}d_8$  of the isomerization of **G** by 1 mol% of **1** at  $60\text{ }^\circ\text{C}$ , different timings are compared.



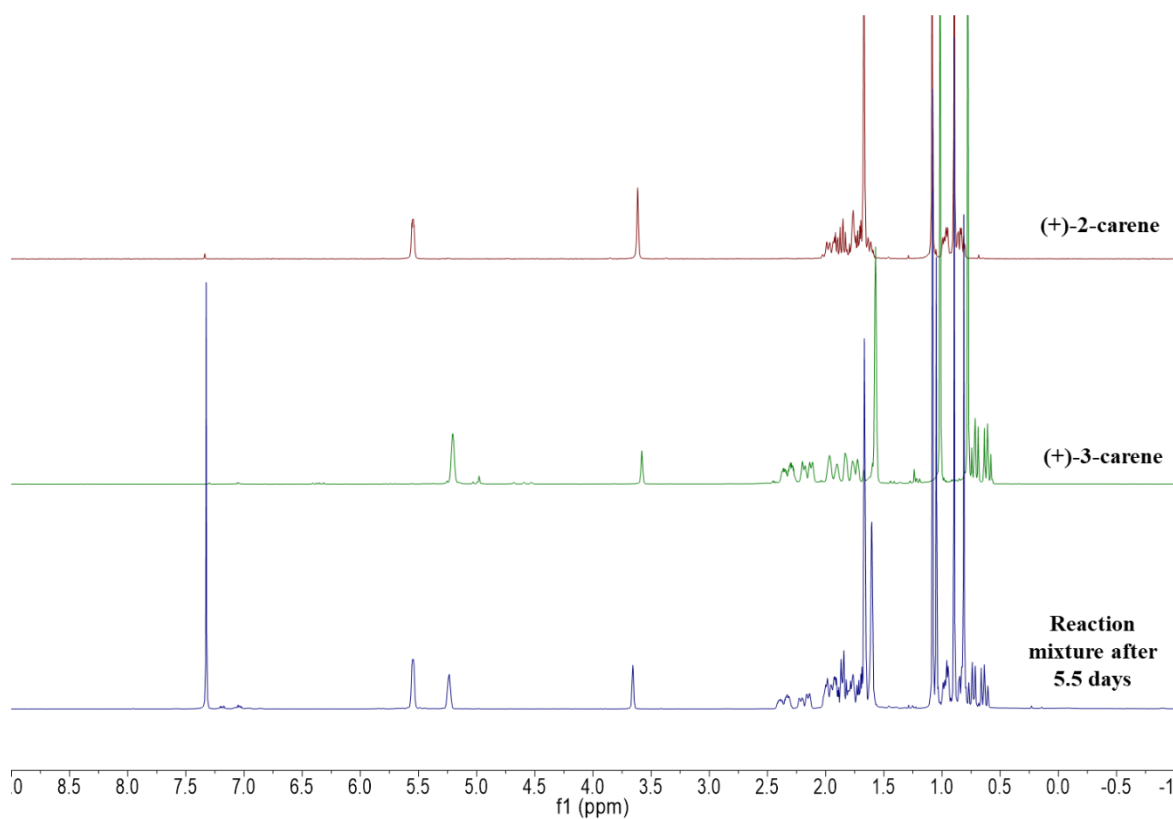


**Figure A28.** Stacked  $^1\text{H}$  NMR spectra in  $\text{thf-}d_8$  of (+)-2-carene, (+)-3-carene and reaction mixture.

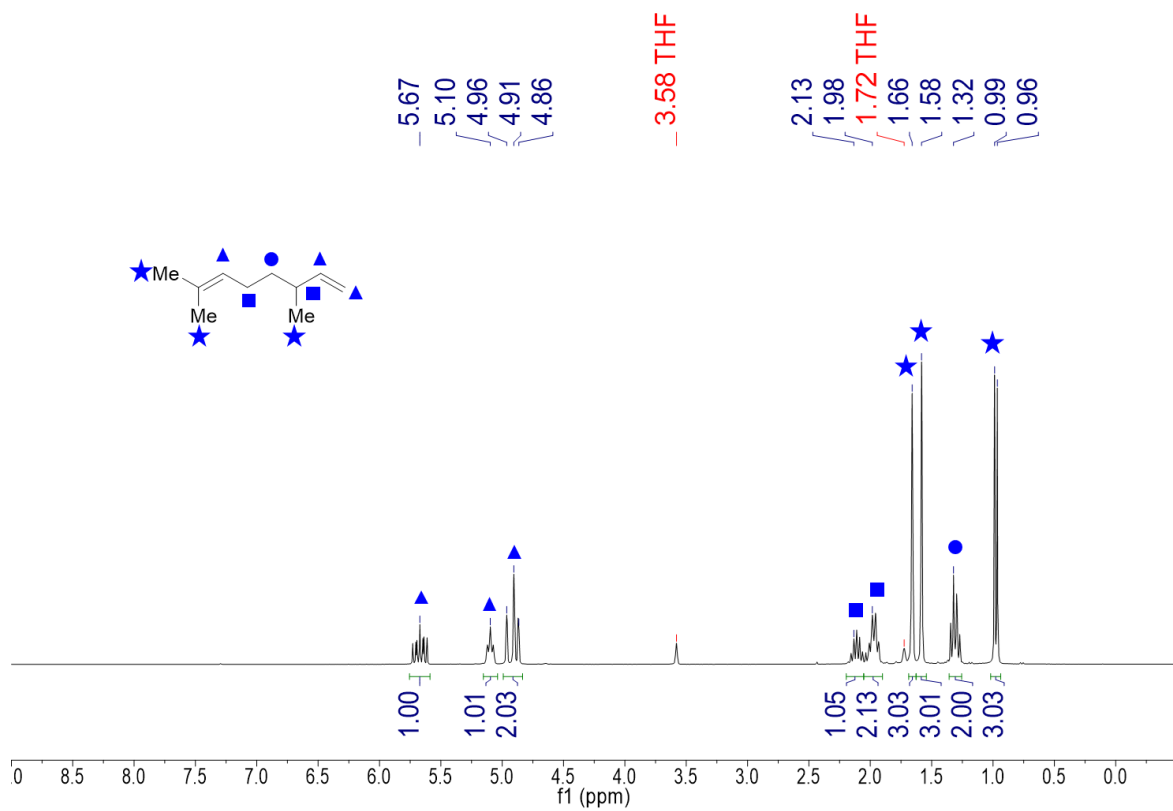


**Figure A29.**  $^1\text{H}$  NMR spectrum in  $\text{thf-}d_8$  of G.

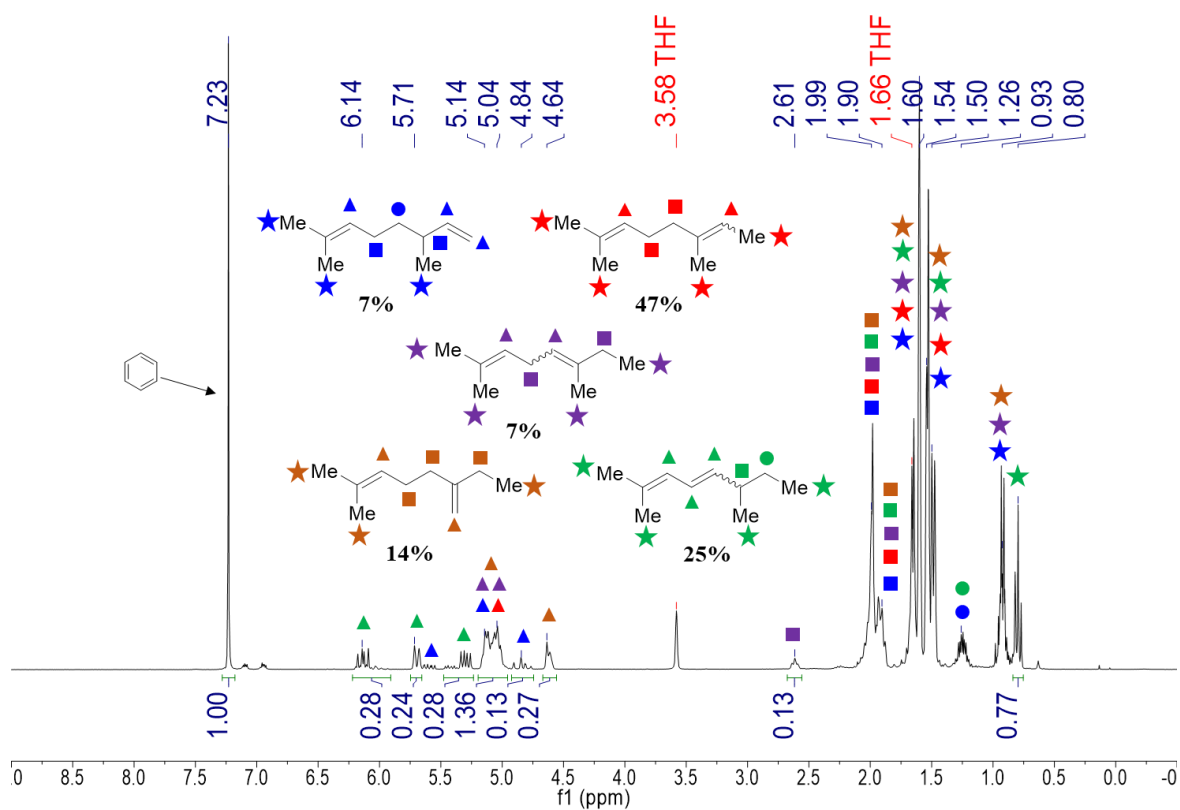


**Figure A30.** <sup>1</sup>H NMR spectrum in thf-*d*<sub>8</sub> of the isomerization of **H** by 1 mol% of **1** at 60 °C, t=5.5 days. Relevant peaks are assigned and benzene served as an internal reference.

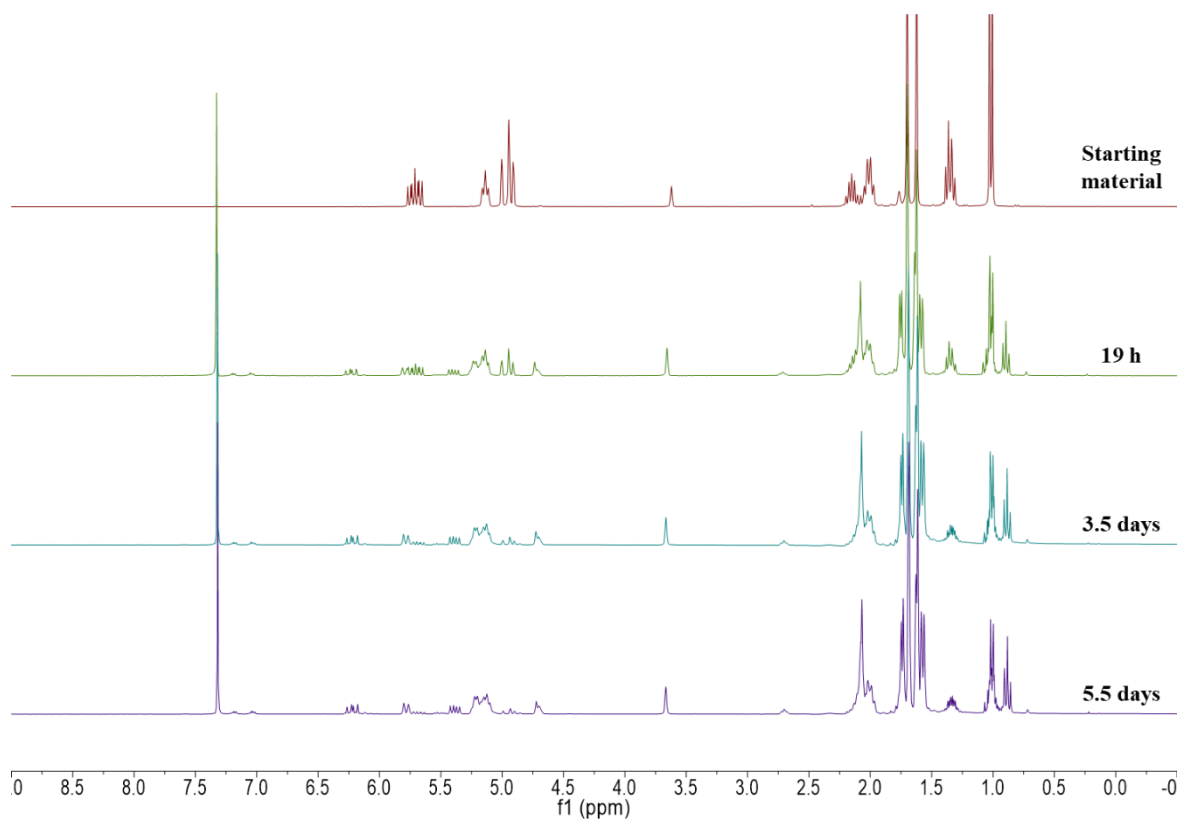


**Figure A31.** Stacked <sup>1</sup>H NMR spectra in thf-*d*<sub>8</sub> of the isomerization of **H** by 1 mol% of **1** at 60 °C, different timings are compared to the starting material.

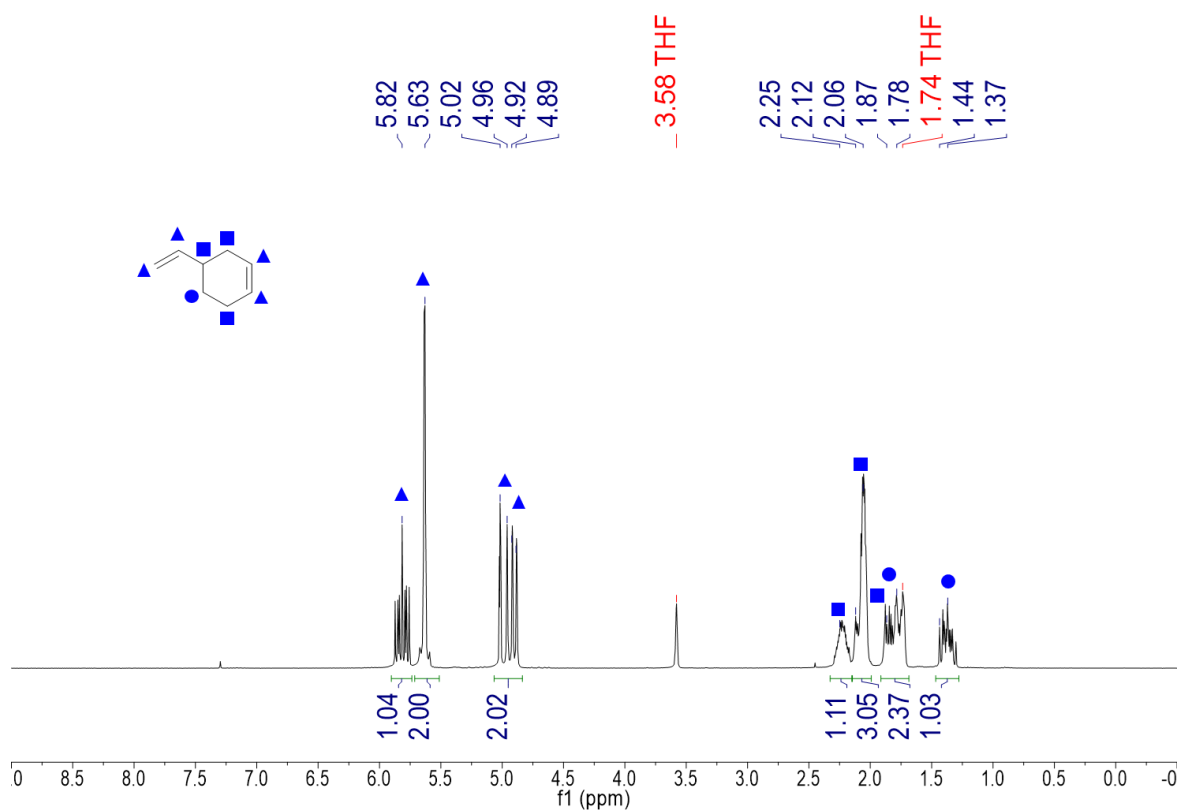


**Figure A32.** <sup>1</sup>H NMR spectrum in thf-*d*<sub>8</sub> of 4-vinylcyclohexene.

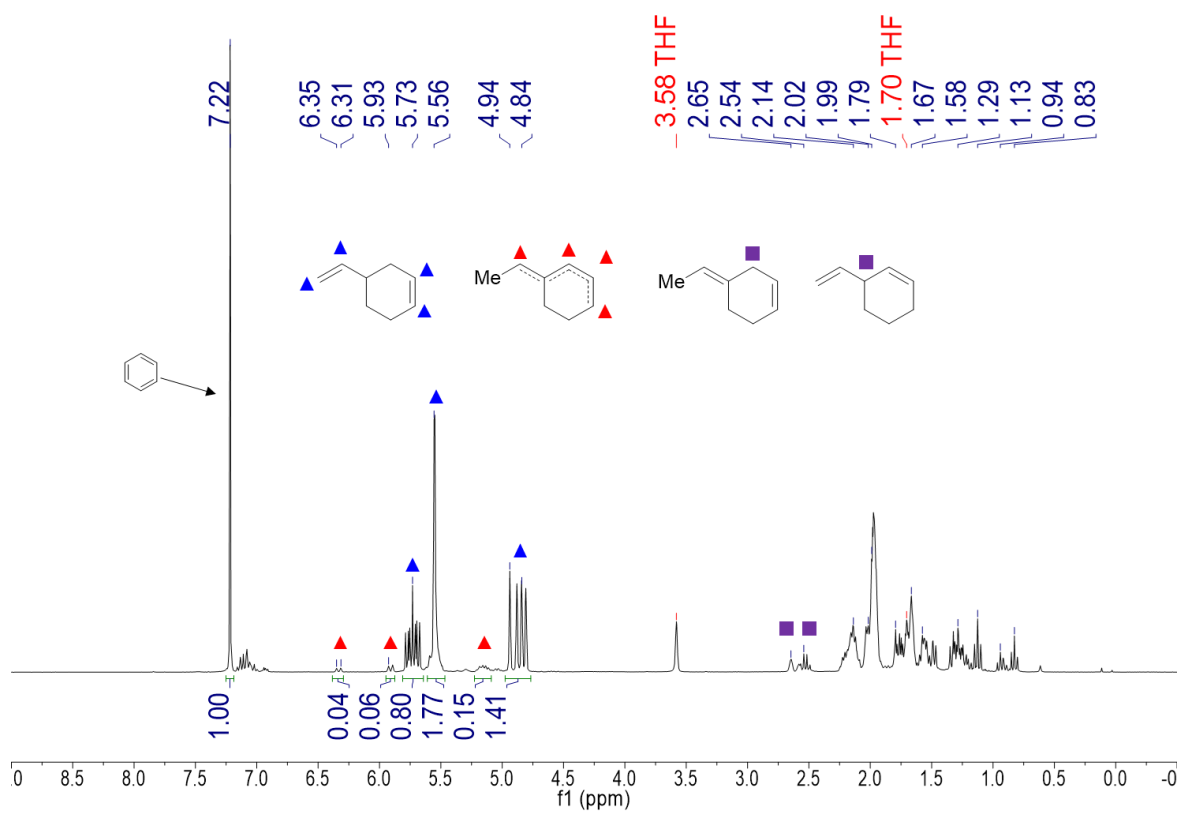


**Figure A33.** <sup>1</sup>H NMR spectrum in thf-*d*<sub>8</sub> of the isomerization of 4-vinylcyclohexene by 1 mol% of **1** at 60 °C, t=5.5 days. Relevant peaks are assigned and benzene served as an internal reference.

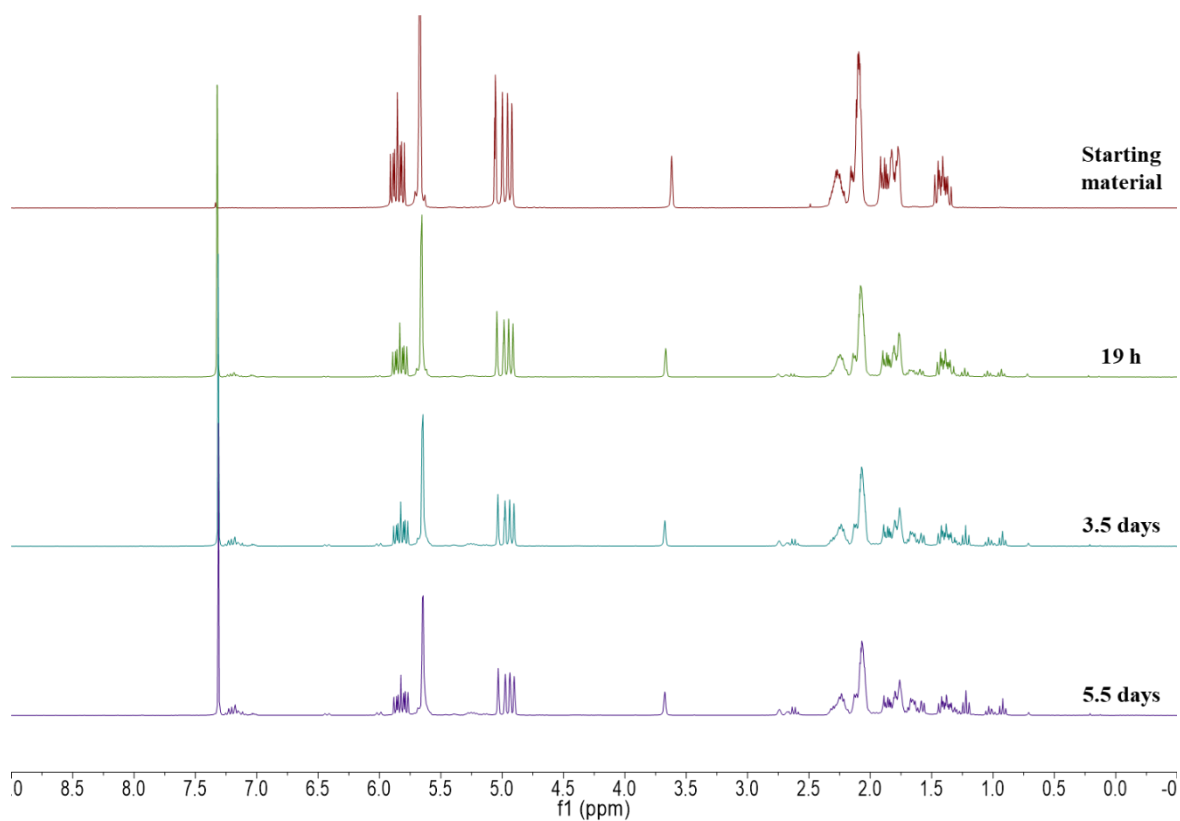


**Figure A34.** Stacked  $^1\text{H}$  NMR spectra in  $\text{thf-d}_8$  of the isomerization of 4-vinylcyclohexene by 1 mol% of 1 at 60 °C, different timings are compared to the starting material.

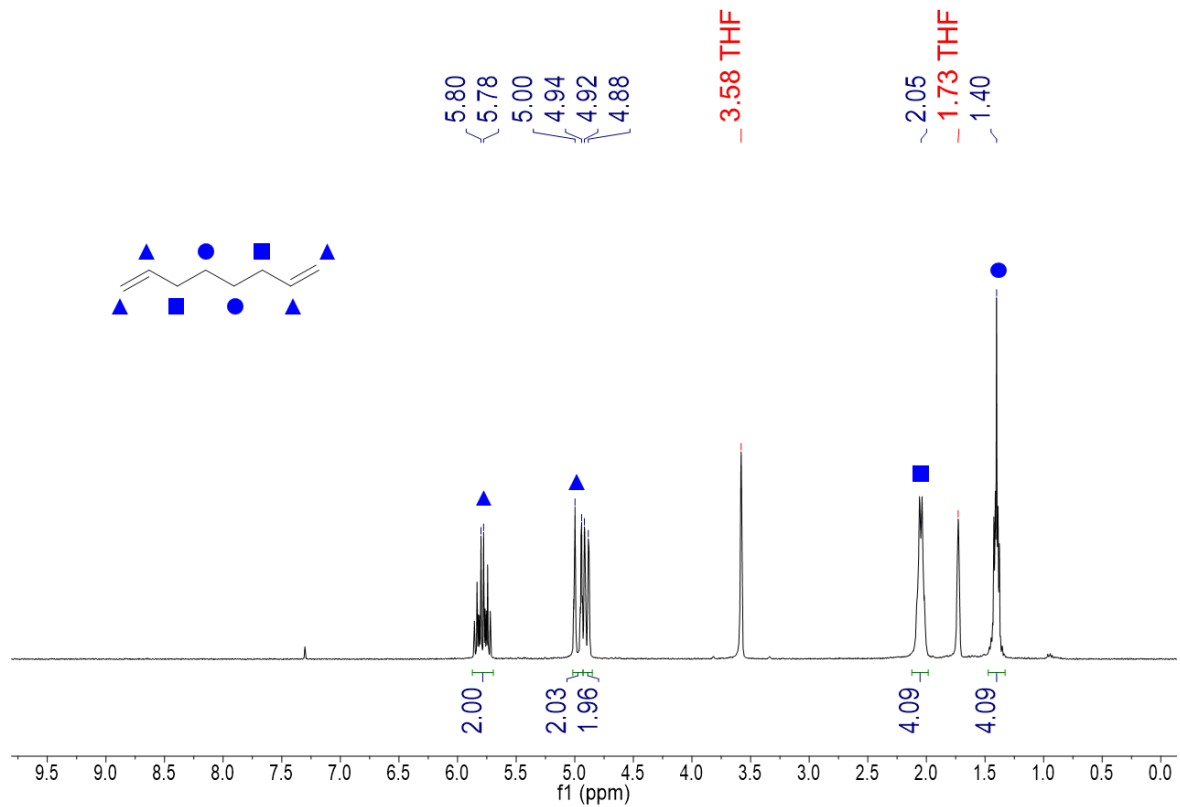


**Figure A35.**  $^1\text{H}$  NMR spectrum in  $\text{thf-d}_8$  of 1,7-octadiene.

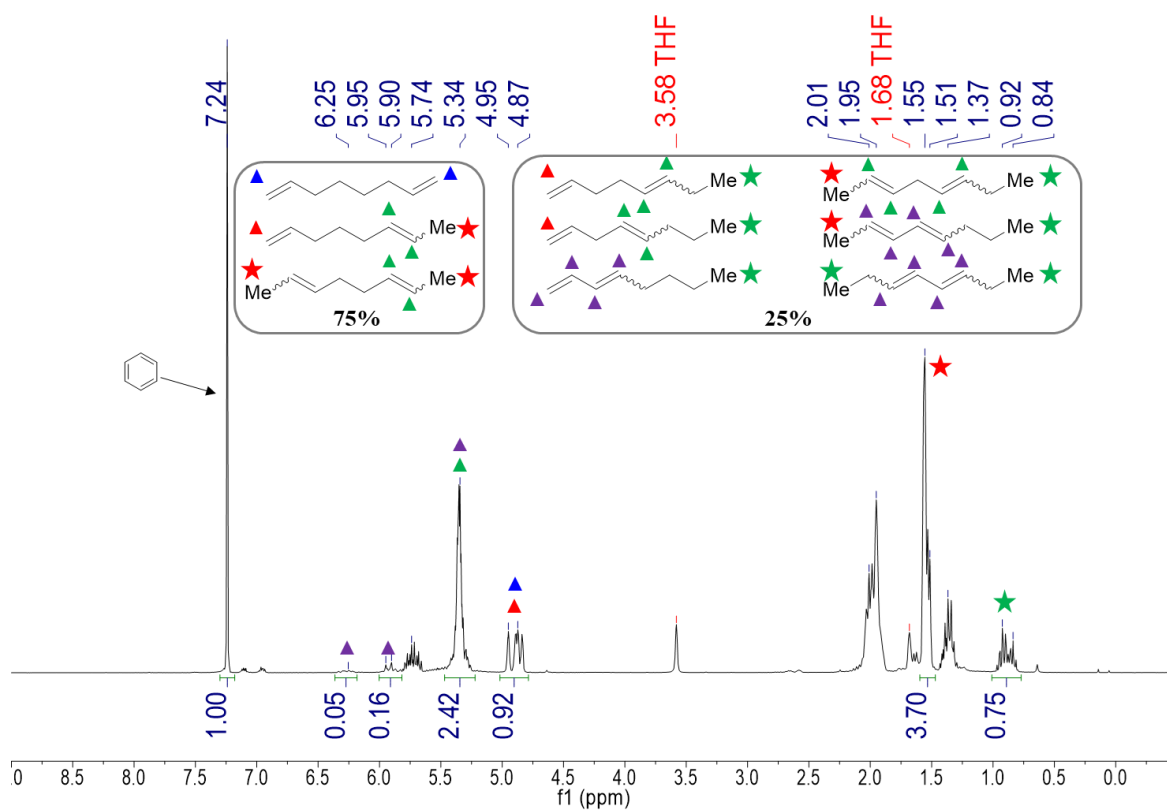


**Figure A36.**  $^1\text{H}$  NMR spectrum in  $\text{thf-}d_8$  of the isomerization of **1,7-octadiene** by 1 mol% of **1** at 60 °C,  $t=5.5$  days. Relevant peaks are assigned and benzene served as an internal reference.

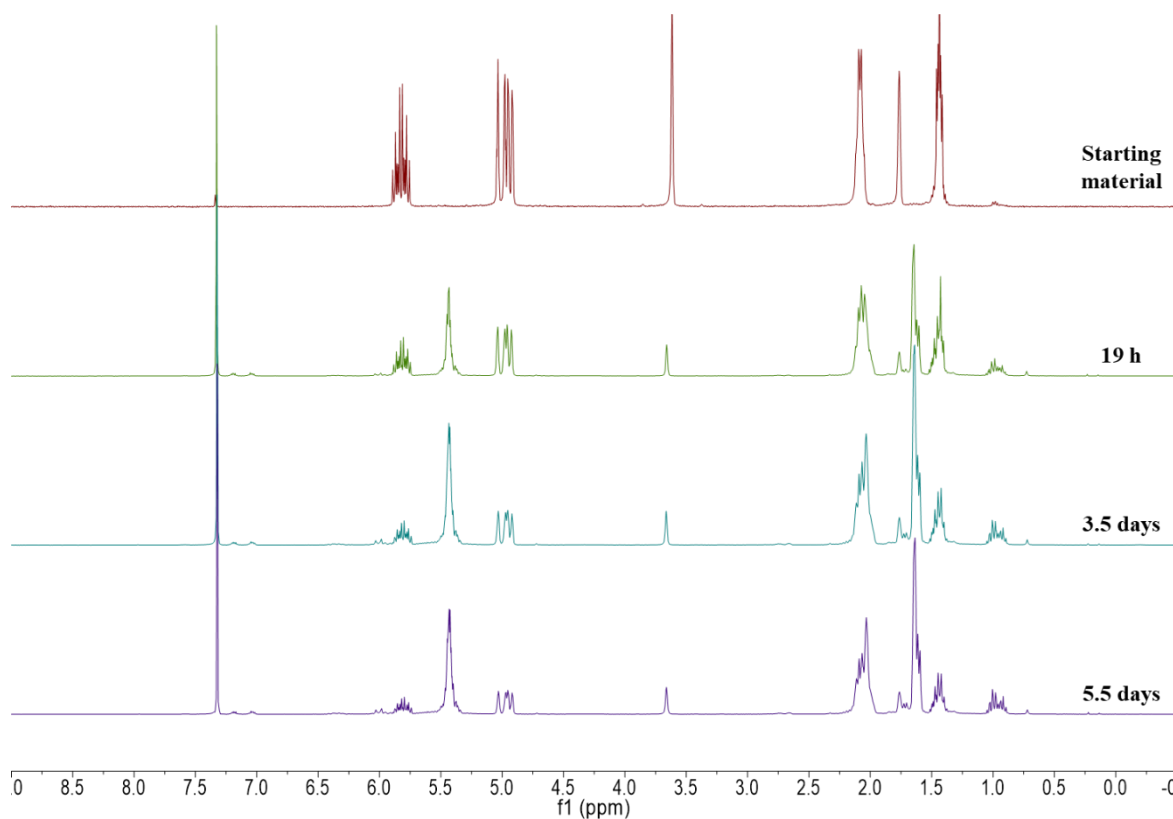


**Figure A37.** Stacked  $^1\text{H}$  NMR spectra in  $\text{thf-}d_8$  of the isomerization of **1,7-octadiene** by 1 mol% of **1** at 60 °C, different timings are compared to the starting material.

■ *Theoretical modelization:*

Methods:

DFT level calculations on the **(bipy)Ni(Cod)** complex were performed using the ORCA 4.1.1. software.<sup>17</sup> The geometry optimizations were done at the PBE level of theory,<sup>18</sup> using scalar relativistic ZORA Hamiltonian with ZORA-def2-TZVP basis set<sup>19</sup> and SARC/J auxiliary basis set for Coulomb fitting.<sup>20</sup> Each time, dispersion corrections were added to the functional used in the D3 framework proposed by Grimme<sup>21</sup> with the addition of the Becke–Johnson damping (D3BJ).<sup>22</sup> Frequencies were calculated analytically to ensure these structures corresponded to an energy minima. Single-point energy calculations starting from PBE optimized geometry with the PBE0<sup>23</sup> functional were then performed in gas phase.

The reaction profiles were computed within a different methodology. The optimization of reactants, transition states, IRC, and products were carried out by employing DFT hybrid functional (B3PW91)<sup>24</sup> along with small core pseudopotential Stuttgart basis set<sup>25,26</sup> for ytterbium, nickel atoms. Pople basis set (6-31G\*\*) were employed for the rest of the atoms.<sup>27–29</sup> Frequency calculations were performed to locate saddle points for transition state structures, minima for the rest of the structures and for obtaining thermal corrections over the energies. All the calculations were performed using Gaussian 09 suite of programs.<sup>30</sup>

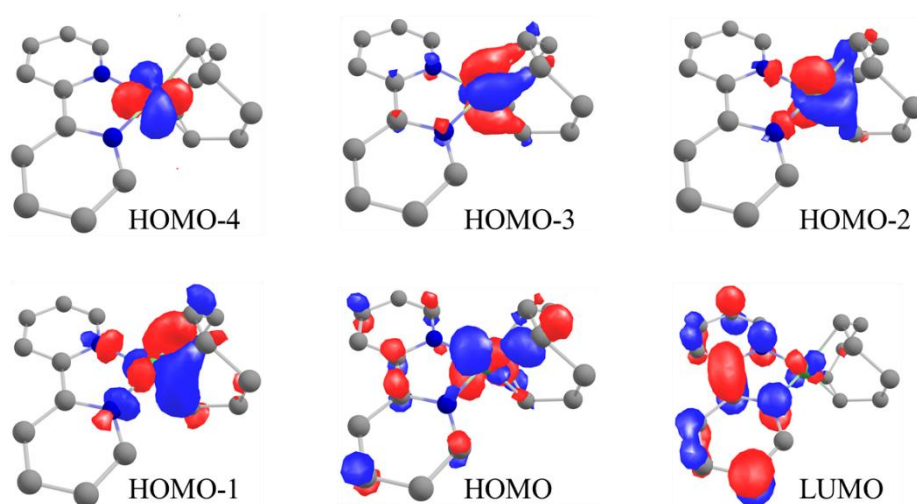


**Figure A38.** Kohn-sham orbitals for **(bipy)Ni(Cod)** obtained by DFT at the PBE0 level.

## Chapter V

### ▪ Syntheses

2,2'-bipyrimidine was purchased from TCI and sublimed prior use. MeI, EtI and CD<sub>3</sub>I were purchased from Sigma Aldrich, degassed and stored at – 40 °C in the glovebox. MeLi was purchased from Sigma Aldrich as a 1.6 M diethyl ether solution from which solid MeLi was obtained as a white powder after evaporation over several hours (10<sup>–3</sup> mbar). All Grignard reagents were prepared as described in literature procedure and titrated by the method of Knochen.<sup>31,32</sup> The palladium precursors (bipym)PdMe<sub>2</sub>, Cp\*<sub>2</sub>Yb(bipym)PdMe<sub>2</sub> and Cp\*<sub>2</sub>Yb(bipym)PdMe<sub>3</sub>I (**1**) were prepared with minor modifications of the reported protocol,<sup>33</sup> reported hereafter, to take into consideration the conditions needed for the synthesis of the tetraalkyl complexes.

**(bipym)PdMe<sub>2</sub>:** No large-scale protocol ensuring a good yield was found to avoid the presence of free 2,2'-bipyrimidine at the end of the reaction. The synthesis was performed in toluene (20 mL) instead of thf with (tmeda)PdMe<sub>2</sub> (935 mg, 3.7 mmol, 1.05 eq.) and 2,2'-bipyrimidine (553 mg, 3.5 mmol, 1 eq.). The resulting brick red suspension was stirred at room temperature for two hours before being left overnight at – 40 °C. The suspension was then filtered on a frit and the solid was washed with toluene (3 x 5 mL) followed by Et<sub>2</sub>O (10 mL) and dried under vacuum to yield a brick-red powder (934 mg, 3.2 mmol, 90%) almost free of unconsumed 2,2'-bipyrimidine (less than 5% impurities), as observed by <sup>1</sup>H NMR in CD<sub>2</sub>Cl<sub>2</sub>.

**Cp\*<sub>2</sub>Yb(bipym)PdMe<sub>2</sub>:** The synthesis was performed in thf instead of toluene as it was found to ease the removal of the formed Cp\*<sub>2</sub>Yb(bipym)YbCp\*<sub>2</sub> dimer considering the impurities mentioned above. A pink solution of Cp\*<sub>2</sub>Yb(OEt<sub>2</sub>) (822 mg, 1.6 mmol, 1 eq.) in thf (5 mL) was added to a brick red suspension of (bipym)PdMe<sub>2</sub> (468 mg, 1.6 mmol, 1 eq.) in thf (3 mL). Almost immediately the reaction mixture turned dark brown and was left stirring for 30 min, time at which it was left to crystallize at – 40 °C overnight. The resulting dark crystals were separated from their mother liquor and washed with cold (– 40 °C) thf (3 x 0.5 mL) and dried under vacuum. <sup>1</sup>H NMR in C<sub>6</sub>D<sub>6</sub> of the resulting solid (1.1 g, 1.5 mmol, 79%) indicated the presence of *ca.* 2 co-crystallized thf molecules and < 1% Cp\*<sub>2</sub>Yb(bipym)YbCp\*<sub>2</sub> dimer.

**Cp\*<sub>2</sub>Yb(bipym)PdMe<sub>3</sub>I (**1**):** The synthesis was performed in thf instead of toluene to avoid the presence of co-crystallized molecules of the latter at the next step. At – 40 °C, to a dark brown suspension of Cp\*<sub>2</sub>Yb(bipym)PdMe<sub>2</sub> (906 mg, 1.2 mmol, 1 eq.) in thf (6 mL) was added MeI (92 µL, 1.5 mmol, 1.2 eq.). The resulting dark brown mixture was left to react for 2h in the fridge while being gently hand-stirred every 30 min to ensure that all the solid reacted. The resulting dark brown crystals

were separated from their mother liquor and washed with cold (-40 °C) thf (3 x 0.5 mL) and quickly dried under vacuum.  $^1\text{H}$  NMR in  $\text{C}_6\text{D}_6$  of the resulting solid (1.1 g, 0.98 mmol, 79%) indicated the presence of *ca.* 3 co-crystallized thf molecule.

**$\text{Cp}^*_2\text{Yb}(\text{bipym})\text{PdMe}_4$  (2):** At -40 °C, to a dark brown solution of  $\text{Cp}^*_2\text{Yb}(\text{bipym})\text{PdMe}_3\text{I}$  (409 mg, 0.37 mmol, 1 eq.) in thf (15 mL) was added a colorless 0.9 M  $\text{Et}_2\text{O}$  solution of  $\text{MeMgI}$  (0.46 mL, 0.41 mmol, 1.1 eq.). Off-white solid appeared almost instantly from the resulting dark brown solution and the reaction was left to react for 1h in the fridge while being gently hand-stirred every 15 min. After filtration the resulting solution was concentrated to 5 mL and filtered a second time before being covered with pentane (10 mL). Dark XRD suitable blocks appeared after only 30 min, time at which the solution was gently stirred. They were separated from their mother liquor after another 30 min, washed with pentane (3 x 2 mL) and quickly dried under vacuum (239 mg, 0.28 mmol, 77%).  $^1\text{H}$  NMR (300 MHz,  $\text{thf-}d_8$ , 20 °C):  $\delta$  (ppm) = 254.66 (s, 2H, bipym), -1.41 (s, 2H, bipym), -149.48 (s, 2H, bipym), -3.51 (s, 6H,  $\text{Pd}(\text{CH}_3)_2$ ), -14.99 (s, 6H,  $\text{Pd}(\text{CH}_3)_2$ ), 5.99 (s, 30H,  $\text{Cp}^*$ ). While **2** was found to be way more stable than **1**, it is still temperature sensitive in the solid state and has to be stored at cold, its half-life at room temperature was roughly estimated to 4 months.

**$\text{Cp}^*_2\text{Yb}(\text{bipym})\text{PdMe}_4(\text{CD}_3)$  (2- $d_3$ ):** The same protocol was used by replacing the 0.9 M solution of  $\text{MeMgI}$  with a 0.7 M solution of  $\text{CD}_3\text{MgI}$ .  $^1\text{H}$  NMR (300 MHz,  $\text{thf-}d_8$ , 20 °C):  $\delta$  (ppm) = 254.42 (s, 2H, bipym), -1.45 (s, 2H, bipym), -149.33 (s, 2H, bipym), -3.52 (s, 6H,  $\text{Pd}(\text{CH}_3)_2$ ), -15.01 (s, 3H,  $\text{Pd}(\text{CH}_3)_2$ ), 5.99 (s, 30H,  $\text{Cp}^*$ ).

**$\text{Cp}^*_2\text{Yb}(\text{bipym})\text{Pd}(\text{CD}_3)_4$  (2- $d_{12}$ ):** The  $(\text{tmeda})\text{Pd}(\text{CD}_3)_2$  precursor was prepared as described in the literature.<sup>34</sup> The following steps were performed with the protocols presented above by replacing  $\text{MeI}$  by  $\text{CD}_3\text{I}$  and the 0.9 M solution of  $\text{MeMgI}$  with a 0.7 M solution of  $\text{CD}_3\text{MgI}$ .  $^1\text{H}$  NMR (300 MHz,  $\text{thf-}d_8$ , 20 °C):  $\delta$  (ppm) = 254.21 (s, 2H, bipym), -1.59 (s, 2H, bipym), -148.93 (s, 2H, bipym), 5.98 (s, 30H,  $\text{Cp}^*$ ).

**$\text{Cp}^*_2\text{Yb}(\text{bipym})\text{PdMe}_2\text{EtI}$  (3):** The protocol presented above for **1** was used by replacing  $\text{MeI}$  with  $\text{EtI}$  and by increasing the reaction time to 48h to ensure completeness of the reaction with this less reactive alkyl halide. XRD suitable crystals were analyzed by  $^1\text{H}$  NMR (300 MHz,  $\text{thf-}d_8$ , 20 °C): two isomers were present, no attribution was made (see the corresponding chapter).

**$\text{Cp}^*_2\text{Yb}(\text{bipym})\text{PdMe}_3\text{Et}$  (4):** The protocol presented above for **2** was used. XRD suitable crystals were analyzed by  $^1\text{H}$  NMR (300 MHz,  $\text{thf-}d_8$ , 20 °C): two isomers were present, no attribution was made (see the corresponding chapter).





**B**

## Crystallographic data

### General details:

All the measured single crystals were mounted on a Kapton loop using a Paratone N oil. All measurements were done on a diffractometer equipped with a kappa goniometer (Nonius, Deft, Netherlands), a Bruker APEX II CCD detector and a graphite Mo-K $\alpha$  monochromator. The temperature at which the data were acquired is specified in the upcoming tables. The structure resolution was accomplished using the SHELXS-97<sup>35</sup> and SHELXT<sup>36</sup> programs and the refinement was done with the SHELXL<sup>37</sup> program. The structure solution and the refinement were performed with the PLATON<sup>38</sup> and OLEX2<sup>39</sup> software programs. Finally, pictures of the compound structure were obtained using the MERCURY<sup>40</sup> and POV-Ray software programs. During the refinement steps, all atoms - except hydrogen atoms - were refined anisotropically. The position of the hydrogen atoms was determined using residual electronic densities, which are calculated by a Fourier difference. Finally, in order to obtain a complete refinement, a weighting step followed by multiples loops of refinement was done.

## Chapter II

**Table B1.** Crystallographic data for the indicated compounds

Compound	Tb(Cot)I(THF) <sub>2</sub>	Ho(Cot)I(THF) <sub>2</sub>	[Lu(Cot)(BH <sub>4</sub> )(THF)] <sub>2</sub>	Tb(Cot)(Cnt) 1 at 150 K	Tb(Cot)(Cnt) 1 at 300 K
Formula	C <sub>16</sub> H <sub>24</sub> TbIO <sub>2</sub>	C <sub>16</sub> H <sub>24</sub> HoIO <sub>2</sub>	C <sub>24</sub> H <sub>40</sub> B <sub>2</sub> Lu <sub>2</sub> O <sub>2</sub>	C <sub>17</sub> H <sub>17</sub> Tb	C <sub>17</sub> H <sub>17</sub> Tb
Crystal size (mm)	0.3 × 0.3 × 0.26	0.22 × 0.08 × 0.08	0.12 × 0.1 × 0.04	0.16 × 0.04 × 0.04	0.18 × 0.02 × 0.02
Crystal system	monoclinic	monoclinic	monoclinic	orthorhombic	orthorhombic
Space group	<i>P</i> 2 <sub>1</sub> / <i>n</i>	<i>P</i> 2 <sub>1</sub> / <i>n</i>	<i>P</i> 2 <sub>1</sub> / <i>c</i>	<i>Pnma</i>	<i>Pnma</i>
Volume (Å <sup>3</sup> )	1766.38(13)	1750.3(2)	1240.90(18)	1345.4(5)	1366.9(13)
a (Å)	8.5442(3)	8.4864(6)	9.5563(9)	11.939(2)	12.002(7)
b (Å)	9.3864(4)	9.3831(7)	11.2696(9)	12.952(3)	13.032(7)
c (Å)	22.2233(10)	22.1744(16)	12.4093(10)	8.7005(17)	8.739(5)
α (deg)	90	90	90	90	90
β (deg)	97.6620(14)	97.579(3)	111.795(3)	90	90
γ (deg)	90	90	90	90	90
Z	4	4	2	4	4
Formula weight (g/mol)	534.17	541.13	732.12	380.22	380.22
Density (calcd) (g/cm <sup>3</sup> )	2.009	2.054	1.959	1.877	1.848
Absorption coefficient (mm <sup>-1</sup> )	5.751	6.297	7.926	5.234	5.152
F(000)	1016.0	1026.0	704.0	736.0	736.0
Temp (K)	219.99	219.99	150	149.99	300.15
diffractometer	Kappa APEX II CCD	Kappa APEX II CCD	Kappa APEX II CCD	Kappa APEX II CCD	Kappa APEX II CCD
Radiation	MoKα (λ = 0.71073)	MoKα (λ = 0.71073)	MoKα (λ = 0.71073)	MoKα (λ = 0.71073)	MoKα (λ = 0.71073)
2θ range for data collection (deg)	5.38 to 60.066	3.706 to 60.064	4.59 to 60.212	5.64 to 58.256	5.612 to 52.044
Absorption correction	Multi-scan	Multi-scan	Multi-scan	Multi-scan	Multi-scan
Total no. reflections	33135	84933	27886	27069	23335
Unique reflections [R <sub>int</sub> ]	5155 [R <sub>int</sub> = 0.0477]	5112 [R <sub>int</sub> = 0.05110]	3654 [R <sub>int</sub> = 0.0766]	1881 [R <sub>int</sub> = 0.1360]	1410 [R <sub>int</sub> = 0.2142]
Final R indices [I > 2σ(I)]	R = 0.0417, R <sub>w</sub> = 0.0841	R = 0.0437, R <sub>w</sub> = 0.0926	R = 0.0330, R <sub>w</sub> = 0.0654	R = 0.0422, R <sub>w</sub> = 0.0986	R = 0.0622, R <sub>w</sub> = 0.1285
R indices (all data)	R = 0.0529, R <sub>w</sub> = 0.0884	R = 0.0485, R <sub>w</sub> = 0.0948	R = 0.0523, R <sub>w</sub> = 0.0717	R = 0.0762, R <sub>w</sub> = 0.1156	R = 0.1247, R <sub>w</sub> = 0.1675
Largest diff. peak and hole (e.Å <sup>-3</sup> )	0.85/-1.82	1.45/-1.54	1.14/-1.17	2.00/-0.94	2.62/-1.77
GooF	1.271	1.343	1.030	1.025	1.041

**Table B2.** Crystallographic data for the indicated compounds

Compound	Dy(Cot)(Cnt) <b>2</b> at 150 K	Dy(Cot)(Cnt) <b>2</b> at 300 K	Ho(Cot)(Cnt) <b>3</b> at 150 K	Ho(Cot)(Cnt) <b>3</b> at 300 K	Er(Cot)(Cnt) <b>4</b> at 150 K
Formula	C <sub>17</sub> H <sub>17</sub> Dy	C <sub>17</sub> H <sub>17</sub> Dy	C <sub>17</sub> H <sub>17</sub> Ho	C <sub>17</sub> H <sub>17</sub> Ho	C <sub>17</sub> H <sub>17</sub> Er
Crystal size (mm)	0.11 × 0.04 × 0.04	0.3 × 0.08 × 0.07	0.16 × 0.07 × 0.04	0.16 × 0.07 × 0.04	0.24 × 0.06 × 0.04
Crystal system	monoclinic	monoclinic	monoclinic	monoclinic	monoclinic
Space group	<i>P</i> 2 <sub>1</sub> / <i>n</i>	<i>P</i> 2 <sub>1</sub> / <i>n</i>	<i>P</i> 2 <sub>1</sub> / <i>n</i>	<i>P</i> 2 <sub>1</sub> / <i>n</i>	<i>P</i> 2 <sub>1</sub> / <i>n</i>
Volume (Å <sup>3</sup> )	671.97(11)	695.1(5)	669.36(13)	689.3(2)	666.72(13)
a (Å)	7.1626(7)	7.253(3)	7.0595(8)	7.1615(13)	6.9928(8)
b (Å)	8.7103(8)	8.808(4)	8.7192(9)	8.7931(16)	8.7303(9)
c (Å)	10.9560(11)	11.070(5)	11.0938(12)	11.163(2)	11.1760(12)
α (deg)	90	90	90	90	90
β (deg)	100.551(4)	100.628(13)	101.409(4)	101.321(7)	102.264(4)
γ (deg)	90	90	90	90	90
Z	2	2	2	2	2
Formula weight (g/mol)	383.80	383.80	386.23	386.23	388.56
Density (calcd) (g/cm <sup>3</sup> )	1.897	1.834	1.916	1.861	1.936
Absorption coefficient (mm <sup>-1</sup> )	5.538	5.353	5.888	5.718	6.271
F(000)	370.0	370.0	372.0	372.0	374.0
Temp (K)	149.99	300.0	150.0	300.0	150.15
diffractometer	Kappa APEX II CCD	Kappa APEX II CCD	Kappa APEX II CCD	Kappa APEX II CCD	Kappa APEX II CCD
Radiation	MoKα (λ = 0.71073)	MoKα (λ = 0.71073)	MoKα (λ = 0.71073)	MoKα (λ = 0.71073)	MoKα (λ = 0.71073)
2θ range for data collection (deg)	7.442 to 60.632	5.95 to 65.148	7.494 to 60.042	6.248 to 54.938	5.974 to 66.238
Absorption correction	Multi-scan	Multi-scan	Multi-scan	Multi-scan	Multi-scan
Total no. reflections	10251	17194	13553	10319	27235
Unique reflections [R <sub>int</sub> ]	1977 [R <sub>int</sub> = 0.0528]	2531 [R <sub>int</sub> = 0.0382]	1959 [R <sub>int</sub> = 0.0517]	1581 [R <sub>int</sub> = 0.0452]	2540 [R <sub>int</sub> = 0.1099]
Final R indices [I > 2σ(I)]	R = 0.0383, R <sub>w</sub> = 0.0783	R = 0.0349, R <sub>w</sub> = 0.0835	R = 0.0514, R <sub>w</sub> = 0.1005	R = 0.0308, R <sub>w</sub> = 0.0637	R = 0.0462, R <sub>w</sub> = 0.1088
R indices (all data)	R = 0.0609, R <sub>w</sub> = 0.0856	R = 0.0461, R <sub>w</sub> = 0.0905	R = 0.0649, R <sub>w</sub> = 0.1042	R = 0.0494, R <sub>w</sub> = 0.0707	R = 0.0620, R <sub>w</sub> = 0.1127
Largest diff. peak and hole (e.Å <sup>-3</sup> )	1.26/-0.73	1.57/-0.54	1.17/-1.48	0.66/-0.39	1.20/-2.01
Goof	1.076	1.074	1.287	1.039	1.307

**Table B3.** Crystallographic data for the indicated compounds

Compound	Er(Cot)(Cnt) <b>4</b> at 300 K	Tm(Cot)(Cnt) <b>5</b> at 150 K	Tm(Cot)(Cnt) <b>5</b> at 300 K	Lu(Cot)(Cnt) <b>6</b> at 150 K	Lu(Cot)(Cnt) <b>6</b> at 300 K
Formula	C <sub>17</sub> H <sub>17</sub> Er	C <sub>17</sub> H <sub>17</sub> Tm	C <sub>17</sub> H <sub>17</sub> Tm	C <sub>17</sub> H <sub>17</sub> Lu	C <sub>17</sub> H <sub>17</sub> Lu
Crystal size (mm)	0.27 × 0.1 × 0.05	0.15 × 0.04 × 0.04	0.2 × 0.04 × 0.02	0.1 × 0.06 × 0.06	0.1 × 0.06 × 0.06
Crystal system	monoclinic	monoclinic	monoclinic	monoclinic	monoclinic
Space group	<i>P</i> <sub>2</sub> <sub>1</sub> / <i>n</i>	<i>P</i> <sub>2</sub> <sub>1</sub> / <i>n</i>	<i>P</i> <sub>2</sub> <sub>1</sub> / <i>n</i>	<i>P</i> <sub>2</sub> <sub>1</sub> / <i>n</i>	<i>P</i> <sub>2</sub> <sub>1</sub> / <i>n</i>
Volume (Å <sup>3</sup> )	687.88(19)	666.12(11)	688.4(3)	665.3(2)	689.6(9)
a (Å)	7.0902(12)	6.9926(7)	7.091(2)	6.9721(12)	7.067(5)
b (Å)	8.8108(13)	8.7084(8)	8.805(3)	8.7073(14)	8.796(6)
c (Å)	11.2593(17)	11.2040(11)	11.287(3)	11.264(2)	11.414(9)
α (deg)	90	90	90	90	90
β (deg)	102.047(6)	102.489(4)	102.343(10)	103.361(7)	103.60(3)
γ (deg)	90	90	90	90	90
Z	2	2	2	2	2
Formula weight (g/mol)	388.56	390.23	390.23	396.27	396.27
Density (calcd) (g/cm <sup>3</sup> )	1.876	1.946	1.883	1.978	1.908
Absorption coefficient (mm <sup>-1</sup> )	6.078	6.637	6.422	7.397	7.136
F(000)	374.0	376.0	376.0	380.0	380.0
Temp (K)	300.0	150.0	300.0	150.0	300.0
diffractometer	Kappa APEX II CCD	Kappa APEX II CCD	Kappa APEX II CCD	Kappa APEX II CCD	Kappa APEX II CCD
Radiation	MoKα (λ = 0.71073)	MoKα (λ = 0.71073)	MoKα (λ = 0.71073)	MoKα (λ = 0.71073)	MoKα (λ = 0.71073)
2θ range for data collection (deg)	7.402 to 58.248	5.98 to 64.054	5.922 to 60.334	5.976 to 65.154	6.198 to 60.06
Absorption correction	Multi-scan	Multi-scan	Multi-scan	Multi-scan	Multi-scan
Total no. reflections	3781	15568	14306	13809	12454
Unique reflections [R <sub>int</sub> ]	1839 [R <sub>int</sub> = 0.0363]	2318 [R <sub>int</sub> = 0.0616]	2020 [R <sub>int</sub> = 0.1199]	2416 [R <sub>int</sub> = 0.0964]	2015 [R <sub>int</sub> = 0.0609]
Final R indices [I > 2σ(I)]	R = 0.0549, R <sub>w</sub> = 0.1217	R = 0.0311, R <sub>w</sub> = 0.0627	R = 0.0447, R <sub>w</sub> = 0.0947	R = 0.0392, R <sub>w</sub> = 0.0757	R = 0.0283, R <sub>w</sub> = 0.0581
R indices (all data)	R = 0.0625, R <sub>w</sub> = 0.1253	R = 0.0461, R <sub>w</sub> = 0.0662	R = 0.0768, R <sub>w</sub> = 0.0993	R = 0.0685, R <sub>w</sub> = 0.0881	R = 0.0461, R <sub>w</sub> = 0.0636
Largest diff. peak and hole (e.Å <sup>-3</sup> )	1.05/-1.00	0.54/-1.00	0.49/-1.17	0.64/-1.14	0.43/-0.51
Goof	1.226	1.122	0.976	1.035	1.024

**Table B4.** Crystallographic data for the indicated compounds

Compound	(Cot)Tb (cis-Cnt) <sub>x</sub> (trans-Cnt) <sub>1-x</sub> <i>x</i> =0.79 1' at 150 K	Tm(Cot)(Cnt) 5 at 100 K	Tm(Cot)(Cnt) 5 at 200 K	Tm(Cot)(Cnt) 5 at 250 K	1/2 Dy(Cot)(Cnt);D y(Cot)(Cnt) (NCMe) at 150 K 2(MeCN)	(Cot)Sm (bipy)(η <sup>5</sup> -Cnt) at 150 K
Formula	C <sub>17</sub> H <sub>17</sub> Tb	C <sub>17</sub> H <sub>17</sub> Tm	C <sub>17</sub> H <sub>17</sub> Tm	C <sub>17</sub> H <sub>17</sub> Tm	C <sub>28.5</sub> H <sub>30.5</sub> Cl <sub>2</sub> Dy <sub>1.5</sub> N	C <sub>27</sub> H <sub>25</sub> N <sub>2</sub> Sm
Crystal size (mm)	0.14 × 0.04 × 0.02	0.21 × 0.04 × 0.02	0.21 × 0.04 × 0.02	0.21 × 0.04 × 0.02	0.3 × 0.1 × 0.03	0.22 × 0.13 × 0.04
Crystal system	orthorhombic	monoclinic	monoclinic	monoclinic	monoclinic	monoclinic
Space group	<i>Pnma</i>	<i>P2<sub>1</sub>/n</i>	<i>P2<sub>1</sub>/n</i>	<i>P2<sub>1</sub>/n</i>	<i>P2<sub>1</sub>/n</i>	<i>P2<sub>1</sub>/c</i>
Volume (Å <sup>3</sup> )	1347.71(16)	661.00(15)	669.4(3)	678.78(10)	2573.5(8)	4327.4(5)
<i>a</i> (Å)	11.9205(8)	6.9750(9)	7.0155(17)	7.0571(6)	8.4461(15)	12.7224(8)
<i>b</i> (Å)	12.9752(9)	8.6935(12)	8.727(2)	8.7567(7)	26.988(5)	17.4447(11)
<i>c</i> (Å)	8.7134(6)	11.1619(14)	11.196(3)	11.2488(10)	11.290(2)	19.6142(13)
$\alpha$ (deg)	90	90	90	90	90	90
$\beta$ (deg)	90	102.413(3)	102.440(10)	102.456(4)	90.128(6)	96.231(2)
$\gamma$ (deg)	90	90	90	90	90	90
<i>Z</i>	4	2	2	2	4	8
Formula weight (g/mol)	380.22	390.23	390.23	390.23	701.69	527.84
Density (calcd) (g/cm <sup>3</sup> )	1.874	1.961	1.936	1.909	1.811	1.620
Absorption coefficient (mm <sup>-1</sup> )	5.225	6.689	6.605	6.513	4.558	2.730
F(000)	736.0	376.0	376.0	376.0	1366.0	2104.0
Temp (K)	150.01	100.15	200.15	250.15	150	149.99
diffractometer	Kappa APEX II CCD	Kappa APEX II CCD	Kappa APEX II CCD	Kappa APEX II CCD	Kappa APEX II CCD	Kappa APEX II CCD
Radiation	MoK $\alpha$ ( $\lambda$ = 0.71073)	MoK $\alpha$ ( $\lambda$ = 0.71073)	MoK $\alpha$ ( $\lambda$ = 0.71073)	MoK $\alpha$ ( $\lambda$ = 0.71073)	MoK $\alpha$ ( $\lambda$ = 0.71069)	MoK $\alpha$ ( $\lambda$ = 0.71069)
2 $\theta$ range for data collection (deg)	5.632 to 77.358	5.994 to 60.036	5.974 to 62.376	5.95 to 61.03	3.018 to 60.058	5.674 to 60.062
Absorption correction	Multi-scan	Multi-scan	Multi-scan	Multi-scan	Multi-scan	Multi-scan
Total no. reflections	48996	13322	11543	12016	7506	76053
Unique reflections [ <i>R</i> <sub>int</sub> ]	3967 [ <i>R</i> <sub>int</sub> = 0.0619]	1932 [ <i>R</i> <sub>int</sub> = 0.0565]	2161 [ <i>R</i> <sub>int</sub> = 0.0518]	2062 [ <i>R</i> <sub>int</sub> = 0.0447]	7506 [ <i>R</i> <sub>int</sub> = undefined]	12649 [ <i>R</i> <sub>int</sub> = 0.0948]
Final <i>R</i> indices [ <i>I</i> > 2 $\sigma$ ( <i>I</i> )]	<i>R</i> = 0.0269, <i>R</i> <sub>w</sub> = 0.0527	<i>R</i> = 0.0484, <i>R</i> <sub>w</sub> = 0.1179	<i>R</i> = 0.0509, <i>R</i> <sub>w</sub> = 0.1149	<i>R</i> = 0.0463, <i>R</i> <sub>w</sub> = 0.1064	<i>R</i> = 0.0391, <i>R</i> <sub>w</sub> = 0.0836	<i>R</i> = 0.0487, <i>R</i> <sub>w</sub> = 0.1030
<i>R</i> indices (all data)	<i>R</i> = 0.0392, <i>R</i> <sub>w</sub> = 0.0575	<i>R</i> = 0.0545, <i>R</i> <sub>w</sub> = 0.1198	<i>R</i> = 0.0645, <i>R</i> <sub>w</sub> = 0.1180	<i>R</i> = 0.0549, <i>R</i> <sub>w</sub> = 0.1087	<i>R</i> = 0.0447, <i>R</i> <sub>w</sub> = 0.0866	<i>R</i> = 0.0805, <i>R</i> <sub>w</sub> = 0.1167
Largest diff. peak and hole (e.Å <sup>-3</sup> )	2.79/-1.37	1.87/-2.46	1.21/-1.98	1.03/-1.38	1.60/-2.85	4.76/-1.22
GooF	1.021	1.416	1.317	1.325	1.133	1.023

## Chapter III

**Table B5.** Crystallographic data for the indicated compounds

Compound	(bipym)NiMe <sub>2</sub> 1 at 150 K	Cp* <sub>2</sub> Yb (bipym)PtMe <sub>2</sub> 2 at 150 K	Cp* <sub>2</sub> Yb (bipym)PtMe <sub>3</sub> I 3 at 280 K	Cp* <sub>2</sub> Yb (bipym)PtMe <sub>4</sub> 4 at 150 K	Cp* <sub>2</sub> Yb (bipym)PtMe <sub>3</sub> OTf 5 at 150 K
Formula	C <sub>10</sub> H <sub>12</sub> N <sub>4</sub> Pt	C <sub>37</sub> H <sub>50</sub> N <sub>4</sub> PtYb	C <sub>34.5</sub> H <sub>49</sub> IN <sub>4</sub> PtYb	C <sub>32</sub> H <sub>48</sub> N <sub>4</sub> PtYb	C <sub>32</sub> H <sub>45</sub> F <sub>3</sub> N <sub>4</sub> O <sub>3</sub> PtSY b
Crystal size (mm)	0.08 × 0.06 × 0.02	0.5 × 0.34 × 0.34	0.38 × 0.04 × 0.04	0.2 × 0.18 × 0.16	0.3 × 0.06 × 0.01
Crystal system	monoclinic	triclinic	monoclinic	orthorhombic	orthorhombic
Space group	<i>P</i> 2 <sub>1</sub> / <i>c</i>	<i>P</i> -1	<i>C</i> 2/ <i>c</i>	<i>F</i> dd2	<i>P</i> nma
Volume (Å <sup>3</sup> )	2114.1(5)	1684.98(17)	7374.3(14)	8696.6(9)	3515.9(13)
a (Å)	13.553(2)	9.5201(6)	21.723(2)	26.5903(18)	27.765(6)
b (Å)	15.545(2)	10.8302(6)	20.665(2)	13.2749(7)	13.696(3)
c (Å)	10.1951(15)	16.8794(10)	17.2799(19)	24.6374(16)	9.246(2)
α (deg)	90	103.235(2)	90	90	90
β (deg)	100.170(4)	94.022(2)	108.076(4)	90	90
γ (deg)	90	93.344(2)	90	90	90
Z	8	2	8	8	4
Formula weight (g/mol)	383.33	918.94	1014.80	856.87	990.91
Density (calcd) (g/cm <sup>3</sup> )	2.409	1.811	1.828	1.309	1.872
Absorption coefficient (mm <sup>-1</sup> )	13.245	6.936	7.175	5.370	6.730
F(000)	1424	896.0	3880.0	3328.0	1920.0
Temp (K)	150.01	150.0	279.56	150.15	150.0
diffractometer	Kappa APEX II CCD	Kappa APEX II CCD	Kappa APEX II CCD	Kappa APEX II CCD	Kappa APEX II CCD
Radiation	MoKα (λ = 0.71073)	MoKα (λ = 0.71073)	MoKα (λ = 0.71073)	MoKα (λ = 0.71073)	MoKα (λ = 0.71073)
2θ range for data collection (deg)	3.054 to 54.968	4.976 to 60.556	4.118 to 52.042	5.768 to 71.258	5.316 to 52.044
Absorption correction	Multi-scan	Multi-scan	Multi-scan	Multi-scan	Multi-scan
Total no. reflections	60495	70405	89877	207149	19564
Unique reflections [R <sub>int</sub> ]	4846 [R <sub>int</sub> = 0.1442]	10000 [R <sub>int</sub> = 0.0459]	7289 [R <sub>int</sub> = 0.0752]	10041 [R <sub>int</sub> = 0.0690]	3623 [R <sub>int</sub> = 0.1032]
Final R indices [I > 2σ(I)]	R = 0.0384, R <sub>w</sub> = 0.0751	R = 0.0263, R <sub>w</sub> = 0.0519	R = 0.0485, R <sub>w</sub> = 0.1038	R = 0.0280, R <sub>w</sub> = 0.1039	R = 0.0384, R <sub>w</sub> = 0.1256
R indices (all data)	R = 0.0759, R <sub>w</sub> = 0.0907	R = 0.0397, R <sub>w</sub> = 0.0604	R = 0.0786, R <sub>w</sub> = 0.1275	R = 0.0786, R <sub>w</sub> = 0.1276	R = 0.0929, R <sub>w</sub> = 0.1424
Largest diff. peak and hole (e.Å <sup>-3</sup> )	1.23/-1.70	3.82/-1.85	1.59/-1.23	1.82/-2.35	1.50/-2.51
GooF	1.043	1.109	1.142	1.069	1.035

**Table B6.** Crystallographic data for the indicated compounds

Compound	[Cp* <sub>2</sub> Yb (bipym)PtMe <sub>3</sub> (py)] <sup>+</sup> OTf <sup>-</sup> <b>5<sup>+</sup>(py) OTf<sup>-</sup></b> at 150 K	[(bipym)PtMe (py)] <sup>+</sup> SbF <sub>6</sub> <sup>-</sup> <b>7<sup>+</sup>(py) SbF<sub>6</sub><sup>-</sup></b> at 150 K	[Cp* <sub>2</sub> Yb (bipym)PtMe <sub>3</sub> (py)] <sup>+</sup> OTf <sup>-</sup> <b>2<sup>+</sup> BPh<sub>4</sub><sup>-</sup></b> at 150 K	Cp* <sub>2</sub> Yb (bipym)PtMe <sub>3</sub> (CD <sub>2</sub> ) <sub>4</sub> OB (C <sub>6</sub> F <sub>5</sub> ) <sub>3</sub> <b>8</b> at 150 K
Formula	C <sub>44</sub> H <sub>58</sub> F <sub>3</sub> N <sub>5</sub> O <sub>3</sub> PtSYb	C <sub>14</sub> H <sub>14</sub> F <sub>6</sub> N <sub>5</sub> PtSb	C <sub>54</sub> H <sub>62</sub> BN <sub>4</sub> PtYb	C <sub>66.5</sub> H <sub>70</sub> BF <sub>15</sub> N <sub>4</sub> O <sub>2</sub> PtYb
Crystal size (mm)	0.12 × 0.08 × 0.03	0.16 × 0.14 × 0.04	0.4 × 0.12 × 0.08	0.46 × 0.4 × 0.06
Crystal system	monoclinic	triclinic	monoclinic	triclinic
Space group	<i>C2/c</i>	<i>P</i> -1	<i>P2/c</i>	<i>P</i> -1
Volume (Å <sup>3</sup> )	9023.7(8)	933.00(16)	2895.2(4)	3262.6(4)
a (Å)	30.6555(12)	6.8846(8)	15.0097(13)	13.3047(10)
b (Å)	14.9962(8)	11.7321(10)	14.0405(11)	15.5530(12)
c (Å)	20.1110(10)	12.3070(10)	14.0400(12)	17.6732(14)
α (deg)	90	75.037(8)	90	78.209(2)
β (deg)	102.572(2)	79.332(4)	101.907(3)	68.289(2)
γ (deg)	90	79.008(3)	90	75.386(2)
Z	8	2	2	2
Formula weight (g/mol)	1162.14	683.14	1146.01	1621.20
Density (calcd) (g/cm <sup>3</sup> )	1.711	2.432	1.315	1.650
Absorption coefficient (mm <sup>-1</sup> )	5.259	9.003	4.051	3.655
F(000)	4576.0	632.0	1134.0	1602.0
Temp (K)	150.0	150.15	150.01	150.01
diffractometer	Kappa APEX II CCD	Kappa APEX II CCD	Kappa APEX II CCD	Kappa APEX II CCD
Radiation	MoKα (λ = 0.71073)	MoKα (λ = 0.71073)	MoKα (λ = 0.71073)	MoKα (λ = 0.71073)
2θ range for data collection (deg)	5.432 to 54.958	3.462 to 55.332	5.804 to 60.066	2.726 to 56.564
Absorption correction	Multi-scan	Multi-scan	Multi-scan	Multi-scan
Total no. reflections	36394	4295	38813	117659
Unique reflections [R <sub>int</sub> ]	10347 [R <sub>int</sub> = 0.0934]	4295 [R <sub>int</sub> = undefined]	8464 [R <sub>int</sub> = 0.0689]	16202 [R <sub>int</sub> = 0.0689]
Final R indices [I > 2σ(I)]	R = 0.0472, R <sub>w</sub> = 0.0929	R = 0.0298, R <sub>w</sub> = 0.0754	R = 0.0561, R <sub>w</sub> = 0.1259	R = 0.0343, R <sub>w</sub> = 0.0723
R indices (all data)	R = 0.0898, R <sub>w</sub> = 0.1081	R = 0.0311, R <sub>w</sub> = 0.0760	R = 0.0711, R <sub>w</sub> = 0.1313	R = 0.0636, R <sub>w</sub> = 0.0880
Largest diff. peak and hole (e.Å <sup>-3</sup> )	1.22/-0.97	1.42/-2.20	4.21/-2.52	2.69/-1.38
GooF	1.004	1.181	1.141	1.085



## Chapter IV

**Table B7.** Crystallographic data for the indicated compounds

Compound	(bipy)NiMe <sub>2</sub> 2 at 150 K	Cp* <sub>2</sub> Eu (bipym)NiMe <sub>2</sub> 3 at 150 K	(4,4'-Me <sub>2</sub> bipy) NiMe <sub>2</sub> 4 at 150 K	(3,3'-Me <sub>2</sub> bipy) NiMe <sub>2</sub> 5 at 150 K
Formula	C <sub>12</sub> H <sub>14</sub> N <sub>2</sub> Ni	C <sub>39</sub> H <sub>51</sub> EuN <sub>4</sub> Ni	C <sub>14</sub> H <sub>18</sub> N <sub>2</sub> Ni	C <sub>14</sub> H <sub>18</sub> N <sub>2</sub> Ni
Crystal size (mm)	0.38 × 0.15 × 0.06	0.16 × 0.08 × 0.04	0.62 × 0.16 × 0.03	0.22 × 0.04 × 0.04
Crystal system	monoclinic	monoclinic	monoclinic	orthorhombic
Space group	<i>C2/c</i>	<i>P2<sub>1</sub>/n</i>	<i>P2/c</i>	<i>Pbca</i>
Volume (Å <sup>3</sup> )	1055.48(12)	3612.5(6)	5129.2(6)	2558.1(4)
a (Å)	17.4134(13)	10.1988(10)	13.8537(11)	10.1597(10)
b (Å)	9.2815(6)	27.869(3)	17.2301(11)	11.1432(11)
c (Å)	7.1570(4)	12.8361(12)	21.8599(15)	22.596(2)
α (deg)	90	90	90	90
β (deg)	114.152(3)	98.045(3)	100.585(3)	90
γ (deg)	90	90	90	90
Z	4	4	16	8
Formula weight (g/mol)	244.96	786.51	273.01	273.01
Density (calcd) (g/cm <sup>3</sup> )	1.542	1.446	1.414	1.418
Absorption coefficient (mm <sup>-1</sup> )	1.802	2.273	1.492	1.495
F(000)	512.0	1616	2304	1152
Temp (K)	150.0	150	149.99	150
diffractometer	Kappa APEX II CCD	Kappa APEX II CCD	Kappa APEX II CCD	Kappa APEX II CCD
Radiation	MoKα (λ = 0.71073)	MoKα (λ = 0.71073)	MoKα (λ = 0.71073)	MoKα (λ = 0.71073)
2θ range for data collection (deg)	7.19 to 71.82	5.61 to 56.564	2.364 to 54.964	3.604 to 56.564
Absorption correction	Multi-scan	Multi-scan	Multi-scan	Multi-scan
Total no. reflections	33136	70248	103453	77109
Unique reflections [R <sub>int</sub> ]	2483 [R <sub>int</sub> = 0.0484]	8958 [R <sub>int</sub> = 0.0811]	11752 [R <sub>int</sub> = 0.0695]	3174 [R <sub>int</sub> = 0.1080]
Final R indices [I > 2σ(I)]	R = 0.0256, R <sub>w</sub> = 0.0647	R = 0.0301, R <sub>w</sub> = 0.0586	R = 0.0562, R <sub>w</sub> = 0.1280	R = 0.0311, R <sub>w</sub> = 0.0639
R indices (all data)	R = 0.0318, R <sub>w</sub> = 0.0678	R = 0.0486, R <sub>w</sub> = 0.0647	R = 0.0738, R <sub>w</sub> = 0.1352	R = 0.0574, R <sub>w</sub> = 0.0729
Largest diff. peak and hole (e.Å <sup>-3</sup> )	0.55/-0.33	0.42/-0.48	0.83/-0.61	0.33/-0.37
GooF	1.063	1.015	1.188	1.019

## Chapter V

**Table B8.** Crystallographic data for the indicated compounds

Compound	Cp* <sub>2</sub> Yb(bipym)PtMe <sub>4</sub> <b>2</b> at 150 K	Cp* <sub>2</sub> Yb(bipym) PtMe <sub>2</sub> EtI <b>4</b> at 150 K	Cp* <sub>2</sub> Yb(bipym) PtMe <sub>3</sub> Et <b>5</b> at 150 K
Formula	C <sub>36</sub> H <sub>56</sub> N <sub>4</sub> OPdYb	C <sub>40</sub> H <sub>63</sub> IN <sub>4</sub> O <sub>2</sub> PdYb	C <sub>37</sub> H <sub>58</sub> N <sub>4</sub> OPdYb
Crystal size (mm)	0.2 × 0.1 × 0.08	0.24 × 0.16 × 0.04	0.24 × 0.2 × 0.16
Crystal system	monoclinic	triclinic	orthorhombic
Space group	<i>P</i> 2 <sub>1</sub> / <i>n</i>	<i>P</i> 1	<i>Pnma</i>
Volume (Å <sup>3</sup> )	10817.0(11)	2288.4(3)	3687.54(14)
a (Å)	13.3945(8)	13.1499(10)	29.4699(6)
b (Å)	28.6680(17)	13.1934(9)	13.3885(3)
c (Å)	28.1932(17)	14.3040(10)	9.3460(2)
α (deg)	90	102.936(3)	90
β (deg)	92.337(2)	99.381(4)	90
γ (deg)	90	103.658(4)	90
Z	12	2	4
Formula weight (g/mol)	840.28	1038.28	854.31
Density (calcd) (g/cm <sup>3</sup> )	1.548	1.507	1.539
Absorption coefficient (mm <sup>-1</sup> )	3.108	3.132	3.041
F(000)	5088.0	1032.0	1728.0
Temp (K)	149.51	150.0	150.0
diffractometer	Kappa APEX II CCD	Kappa APEX II CCD	Kappa APEX II CCD
Radiation	MoKα (λ = 0.71073)	MoKα (λ = 0.71073)	MoKα (λ = 0.71073)
2θ range for data collection (deg)	3.188 to 60.066	4.854 to 56.562	5.492 to 60.416
Absorption correction	Multi-scan	Multi-scan	Multi-scan
Total no. reflections	256027	90024	45763
Unique reflections [R <sub>int</sub> ]	31528 [R <sub>int</sub> = 0.0720]	22589 [R <sub>int</sub> = 0.0605]	5651 [R <sub>int</sub> = 0.0605]
Final R indices [I > 2σ(I)]	R = 0.0410, R <sub>w</sub> = 0.0789	R = 0.0583, R <sub>w</sub> = 0.1526	R = 0.0391, R <sub>w</sub> = 0.0860
R indices (all data)	R = 0.0677, R <sub>w</sub> = 0.0866	R = 0.0714, R <sub>w</sub> = 0.1623	R = 0.0507, R <sub>w</sub> = 0.0911
Largest diff. peak and hole (e.Å <sup>-3</sup> )	1.47/-1.82	6.73/-1.52	2.84/-2.87
GooF	1.062	1.018	1.019

## References:

- (1) Fulmer, G. R.; Miller, A. J. M.; Sherden, N. H.; Gottlieb, H. E.; Nudelman, A.; Stoltz, B. M.; Bercaw, J. E.; Goldberg, K. I. *Organometallics* **2010**, 29 (9), 2176–2179. <https://doi.org/10.1021/om100106e>.
- (2) Bain, G. A.; Berry, J. F. *J. Chem. Educ.* **2008**, 85 (4), 532. <https://doi.org/10.1021/ed085p532>.
- (3) Booth, C. H.; Walter, M. D.; Kazhdan, D.; Hu, Y.-J.; Lukens, W. W.; Bauer, E. D.; Maron, L.; Eisenstein, O.; Andersen, R. A. *J. Am. Chem. Soc.* **2009**. <https://doi.org/10.1021/ja809624w>.
- (4) Booth, C. H.; Kazhdan, D.; Werkema, E. L.; Walter, M. D.; Lukens, W. W.; Bauer, E. D.; Hu, Y.-J.; Maron, L.; Eisenstein, O.; Head-Gordon, M.; Andersen, R. A. *J. Am. Chem. Soc.* **2010**, 132 (49), 17537–17549. <https://doi.org/10.1021/ja106902s>.
- (5) Meihaus, K. R.; Long, J. R. *J. Am. Chem. Soc.* **2013**, 135 (47), 17952–17957. <https://doi.org/10.1021/ja4094814>.
- (6) Xémard, M.; Zimmer, S.; Cordier, M.; Goudy, V.; Ricard, L.; Clavaguéra, C.; Nocton, G. *J. Am. Chem. Soc.* **2018**, 140 (43), 14433–14439. <https://doi.org/10.1021/jacs.8b09081>.
- (7) Hilgar, J. D.; Bernbeck, M. G.; Flores, B. S.; Rinehart, J. D. *Chem. Sci.* **2018**, 9 (36), 7204–7209. <https://doi.org/10.1039/C8SC01361F>.
- (8) Cendrowski-Guillaume, S. M.; Le Gland, G.; Nierlich, M.; Ephritikhine, M. *Organometallics* **2000**, 19 (26), 5654–5660. <https://doi.org/10.1021/om000558f>.
- (9) Fedushkin, I. L.; Bochkarev, M. N.; Dechert, S.; Schumann, H. *Chem. – A Eur. J.* **2001**, 7 (16), 3558–3563. [https://doi.org/10.1002/1521-3765\(20010817\)7:16<3558::AID-CHEM3558>3.0.CO;2-H](https://doi.org/10.1002/1521-3765(20010817)7:16<3558::AID-CHEM3558>3.0.CO;2-H).
- (10) Hill, G. S.; Irwin, M. J.; Levy, C. J.; Rendina, L. M.; Puddephatt, R. J.; Andersen, R. A.; Mclean, L. *Inorganic Syntheses*. January 1, 1998, pp 149–153. <https://doi.org/10.1002/9780470132630.ch25>.
- (11) Straus, D. A.; Zhang, C.; Tilley, T. D. *J. Organomet. Chem.* **1989**, 369 (2), C13–C17. [https://doi.org/10.1016/0022-328X\(89\)88013-1](https://doi.org/10.1016/0022-328X(89)88013-1).
- (12) Scott, J. D.; Puddephatt, R. J. *Organometallics* **1986**, 5 (8), 1538–1544. <https://doi.org/10.1021/om00139a005>.
- (13) Mironov, O. A.; Bischof, S. M.; Konnick, M. M.; Hashiguchi, B. G.; Ziatdinov, V. R.; Goddard, W. A.; Ahlquist, M. M.; Periana, R. A. *J. Am. Chem. Soc.* **2013**, 135 (39), 14644–14658. <https://doi.org/10.1021/ja404895z>.
- (14) Wang, D.; Moutet, J.; Tricoire, M.; Cordier, M.; Nocton, G. *Inorganics* **2019**, 7 (5), 58. <https://doi.org/10.3390/inorganics7050058>.
- (15) Kaschube, W.; Pörschke, K. R.; Wilke, G. *J. Organomet. Chem.* **1988**, 355 (1), 525–532. [https://doi.org/10.1016/0022-328X\(88\)89050-8](https://doi.org/10.1016/0022-328X(88)89050-8).
- (16) Berg, D. J.; Burns, C. J.; Andersen, R. A.; Zalkin, A. *Organometallics* **1989**, 8 (8), 1865–1870. <https://doi.org/10.1021/om00110a006>.
- (17) Neese, F. *WIREs Comput. Mol. Sci.* **2012**, 2 (1), 73–78. <https://doi.org/10.1002/wcms.81>.
- (18) Perdew, J. P.; Burke, K.; Ernzerhof, M. *Phys. Rev. Lett.* **1996**, 77 (18), 3865–3868. <https://doi.org/10.1103/PhysRevLett.77.3865>.
- (19) Weigend, F.; Ahlrichs, R. *Phys. Chem. Chem. Phys.* **2005**, 7 (18), 3297–3305. <https://doi.org/10.1039/B508541A>.
- (20) Weigend, F. *Phys. Chem. Chem. Phys.* **2006**, 8 (9), 1057–1065. <https://doi.org/10.1039/B515623H>.
- (21) Grimme, S.; Antony, J.; Ehrlich, S.; Krieg, H. *J. Chem. Phys.* **2010**, 132 (15), 154104. <https://doi.org/10.1063/1.3382344>.
- (22) Grimme, S.; Ehrlich, S.; Goerigk, L. *J. Comput. Chem.* **2011**, 32 (7), 1456–1465. <https://doi.org/10.1002/jcc.21759>.
- (23) Adamo, C.; Barone, V. *J. Chem. Phys.* **1999**, 110 (13), 6158–6170. <https://doi.org/10.1063/1.478522>.
- (24) Becke, A. D. *J. Chem. Phys.* **1993**, 98 (7), 5648–5652. <https://doi.org/10.1063/1.464913>.

- (25) Andrae, D.; Häußermann, U.; Dolg, M.; Stoll, H.; Preuß, H. *Theor. Chim. Acta* **1990**, *77* (2), 123–141. <https://doi.org/10.1007/BF01114537>.
- (26) Martin, J. M. L.; Sundermann, A. *J. Chem. Phys.* **2001**, *114* (8), 3408–3420. <https://doi.org/10.1063/1.1337864>.
- (27) Ditchfield, R.; Hehre, W. J.; Pople, J. A. *J. Chem. Phys.* **1971**, *54* (2), 724–728. <https://doi.org/10.1063/1.1674902>.
- (28) Hehre, W. J.; Ditchfield, R.; Pople, J. A. *J. Chem. Phys.* **1972**, *56* (5), 2257–2261. <https://doi.org/10.1063/1.1677527>.
- (29) Hariharan, P. C.; Pople, J. A. *Theor. Chim. Acta* **1973**, *28* (3), 213–222. <https://doi.org/10.1007/BF00533485>.
- (30) Frisch, M. J.; Trucks, G. W.; Schlegel, H. B.; Scuseria, G. E.; Robb, M. A.; Cheeseman, J. R.; Scalmani, G.; Barone, V.; Mennucci, B.; Petersson, G. A.; Nakatsuji, H.; Caricato, M.; Li, X.; Hratchian, H. P.; Izmaylov, A. F.; Bloino, J.; Zheng, G.; Sonnenberg, J. L.; Hada, M.; Ehara, M.; Toyota, K.; Fukuda, R.; Hasegawa, J.; Ishida, M.; Nakajima, T.; Honda, Y.; Kitao, O.; Nakai, H.; Vreven, T.; Montgomery Jr., J. A.; Peralta, J. E.; Ogliaro, F.; Bearpark, M.; Heyd, J. J.; Brothers, E.; Kudin, K. N.; Staroverov, V. N.; Kobayashi, R.; Normand, J.; Raghavachari, K.; Rendell, A.; Burant, J. C.; Iyengar, S. S.; Tomasi, J.; Cossi, M.; Rega, N.; Millam, J. M.; Klene, M.; Knox, J. E.; Cross, J. B.; Bakken, V.; Adamo, C.; Jaramillo, J.; Gomperts, R.; Stratmann, R. E.; Yazyev, O.; Austin, A. J.; Cammi, R.; Pomelli, C.; Ochterski, J. W.; Martin, R. L.; Morokuma, K.; Zakrzewski, V. G.; Voth, G. A.; Salvador, P.; Dannenberg, J. J.; Dapprich, S.; Daniels, A. D.; Farkas, Ö.; Foresman, J. B.; Ortiz, J. V.; Cioslowski, J.; Fox, D. J. Gaussian Inc. Wallingford CT **2009**. <https://gaussian.com/>.
- (31) Smith, D. H. *J. Chem. Educ.* **1999**, *76* (10), 1427. <https://doi.org/10.1021/ed076p1427>.
- (32) Krasovskiy, A.; Knochel, P. *Synthesis (Stuttg.)* **2006**, *2006* (05), 890–891. <https://doi.org/10.1055/s-2006-926345>.
- (33) Goudy, V.; Jaoul, A.; Cordier, M.; Clavaguéra, C.; Nocton, G. *J. Am. Chem. Soc.* **2017**, *139* (31), 10633–10636. <https://doi.org/10.1021/jacs.7b05634>.
- (34) De Graaf, W.; Boersma, J.; Smeets, W. J. J.; Spek, A. L.; Van Koten, G. *Organometallics* **1989**, *8* (12), 2907–2917. <https://doi.org/10.1021/om00114a028>.
- (35) Sheldrick, G. M. *Acta Crystallogr. Sect. A* **2008**, *64* (1), 112–122. <https://doi.org/10.1107/S0108767307043930>.
- (36) Sheldrick, G. M. *Acta Crystallogr. Sect. A* **2015**, *71* (1), 3–8. <https://doi.org/10.1107/S2053273314026370>.
- (37) Sheldrick, G. M. *Acta Crystallogr. Sect. C* **2015**, *71* (1), 3–8. <https://doi.org/10.1107/S2053229614024218>.
- (38) Spek, A. L. *J. Appl. Crystallogr.* **2003**, *36* (1), 7–13. <https://doi.org/10.1107/S0021889802022112>.
- (39) Dolomanov, O. V.; Bourhis, L. J.; Gildea, R. J.; Howard, J. A. K.; Puschmann, H. *J. Appl. Crystallogr.* **2009**, *42* (2), 339–341. <https://doi.org/10.1107/S0021889808042726>.
- (40) Macrae, C. F.; Bruno, I. J.; Chisholm, J. A.; Edgington, P. R.; McCabe, P.; Pidcock, E.; Rodriguez-Monge, L.; Taylor, R.; van de Streek, J.; Wood, P. A. *J. Appl. Crystallogr.* **2008**, *41* (2), 466–470. <https://doi.org/10.1107/S0021889807067908>.



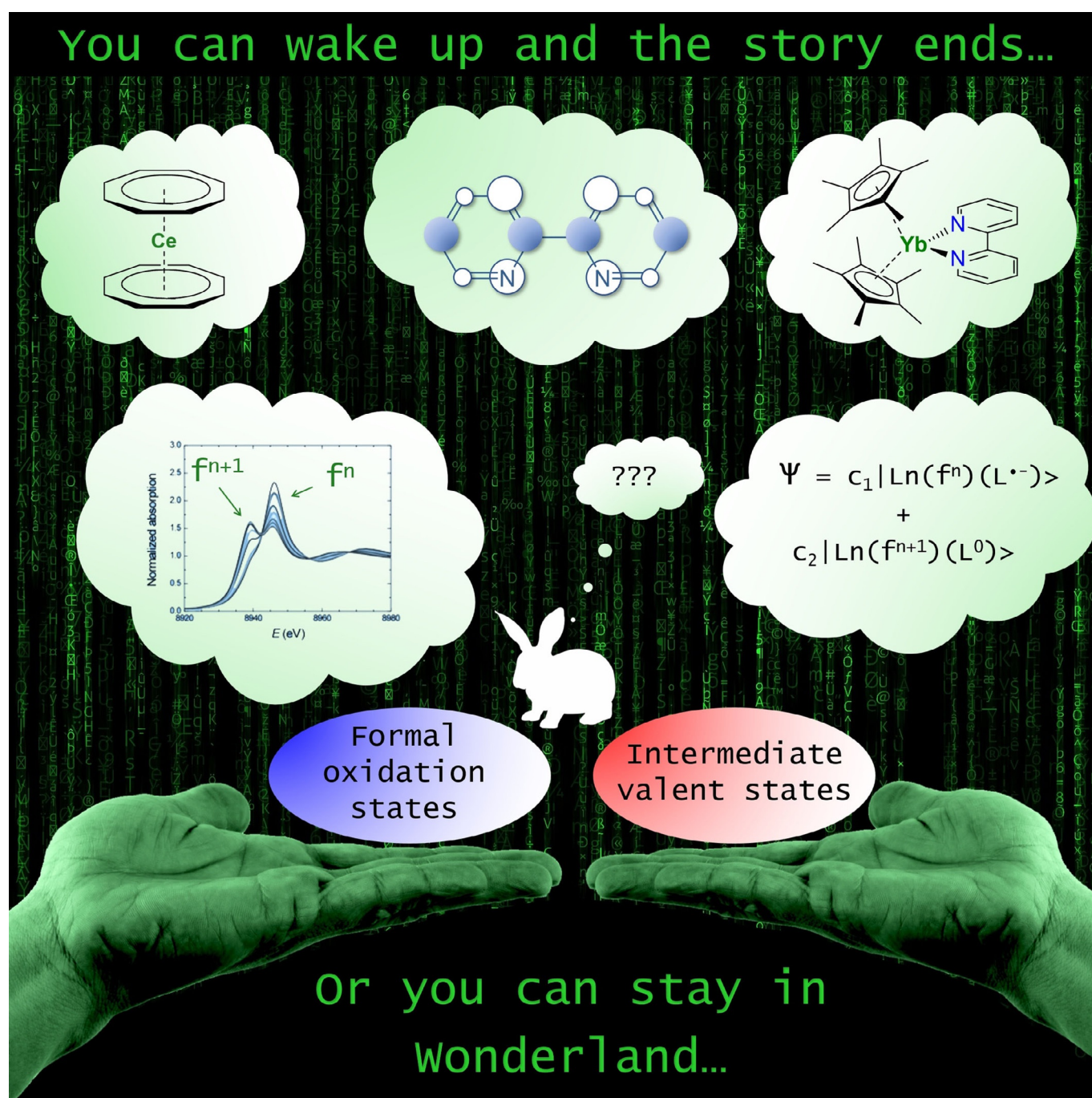
## Published articles



## ■ Lanthanide Complexes

## Intermediate Valence States in Lanthanide Compounds

Maxime Tricoire, Nolwenn Mahieu, Thomas Simler,\* and Grégory Nocton\*[a]

*In memory of Prof. Richard A. Andersen*



**Abstract:** Over more than 50 years, intermediate valence states in lanthanide compounds have often resulted in unexpected or puzzling spectroscopic and magnetic properties. Such experimental singularities could not be rationalised until new theoretical models involving multiconfigurational electronic ground states were established. In this minireview, the different singularities that have been observed among

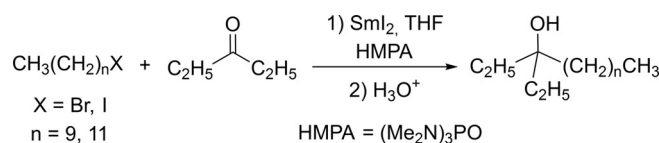
lanthanide complexes are highlighted, the models used to rationalise them are detailed and how such electronic effects may be adjusted depending on energy and symmetry considerations is considered. Understanding and tuning the ground-state multiconfigurational behaviour in lanthanide complexes may open new doors to modular and unusual reactivities.

## 1. Introduction

The chemistry of lanthanide compounds finds a significant number of direct applications especially because of their important and specific optical and magnetic behaviour.<sup>[1–7]</sup> The industry of rare earth elements produces strong magnets for data storage or electrical devices, optics for health and technology and also many materials and molecular complexes for catalysis—including photocatalysis, polymerisation and reductive chemistry.<sup>[7–9]</sup> The physical properties of these species are strongly correlated to high spin-orbit coupling, which is due to relativistic effects in these relatively heavy elements. Thus, the appropriate quantum number is *J* and the ligand field is significantly smaller than the spin-orbit coupling. Moreover, the weak screening of f-electrons leads to contraction of the ionic radius when the atomic number increases. Another important physical property of the f-orbitals is their core nature in the shell. As a consequence, the surrounding ligands often do not play a large role in the energy of those core f-orbitals; minimal spatial overlap occurs between the f-orbitals and the Lewis bases coordinated to the lanthanide ions.<sup>[10]</sup> Finally, except for cerium and europium, the principal formal oxidation state of these elements is trivalent. These textbook properties have, however, been challenged in recent years, in particular as several groups have been able to synthesise divalent complexes for all the lanthanide series (except for the radioactive Pm) with adapted ligand environments,<sup>[11–18]</sup> but also with the number of examples of high-valent molecular compounds increasing rapidly.<sup>[19–23]</sup> The multiple occurrences of these unusual oxidation states ask the question as to whether the physical properties discussed above and the models used to understand them are still valid. If any unexpected properties appear

in those unusual oxidation state species, it would then indicate that some aspects of the metal–ligand bonding nature might have been underestimated. In low-valent species, the participation of the empty 5d-manifold is in question,<sup>[18,24]</sup> as is the role of strongly donating ligands in high-valent species.<sup>[23,25]</sup> This observation notably tends to indicate that the choice of the ligand should not be dictated only by the sterics but also by symmetry and energetic considerations, which is an important paradigm shift in lanthanide chemistry.

In low-valent chemistry, the question of a possible electronic contribution of the ligand to the reduction potential appeared with the important work of Flowers and co-workers on the role of hexamethylphosphoramide (HMPA) addition in reductive chemistry with divalent samarium (Scheme 1).<sup>[26–27]</sup>





**Scheme 1.** Samarium Barbier reaction as described by Flowers and co-workers (adapted from Ref. [27]).

Procter, Maron and co-workers followed this by examining the role of water as solvent in these reactions.<sup>[28]</sup> Aside from the study of organic transformations, in typical synthetic low-valent chemistry, the ligands were often chosen for solubility and stability reasons; the bulkier the ligand, the more stable the complex, even with non-classical divalent lanthanides.<sup>[13]</sup> The use of elaborated ligands to stabilise low-valent lanthanides also generated important information on the influence of the ligand electronics in the reduction reactivity; if most samarium complexes do not reduce N<sub>2</sub> or CO, decamethyl samarocene is thought to do so,<sup>[29,30]</sup> and is capable as well of reducing pyridine to form a C–C coupled dimeric complex whereas the same reactivity was not observed with a similar phospholyl ligand,<sup>[31]</sup> presumably because of a redox potential modulation induced by the ligand. The ligand–metal pair thus takes importance and several electronic effects in the reduction reactivity have been noticed. For instance, a reversible C–C bond coupling was observed,<sup>[32,33]</sup> the free enthalpy of which can be correlated to the redox potential of the reductive lanthanide fragment versus that of the ligand.

This proposition of an adapted energy for the ligand–lanthanide pair is extremely important because it is related to the

[a] M. Tricoire, N. Mahieu, Dr. T. Simler, Dr. G. Nocton  
LCM, CNRS  
Ecole polytechnique  
Institut Polytechnique de Paris  
Route de Saclay, 91128 Palaiseau, cedex (France)  
E-mail: thomas.simler@polytechnique.edu  
gregory.nocton@polytechnique.edu

 The ORCID identification number(s) for the author(s) of this article can be found under:  
<https://doi.org/10.1002/chem.202004735>.

 © 2020 The Authors. Chemistry - A European Journal published by Wiley-VCH GmbH. This is an open access article under the terms of the Creative Commons Attribution Non-Commercial License, which permits use, distribution and reproduction in any medium, provided the original work is properly cited and is not used for commercial purposes.

theory of covalency in metal complexes.<sup>[34]</sup> If an immediate relation with covalency is drawn in the case of a strong overlap between the ligand and the metal orbitals (nephelauxetic effect), the energy gap between them is often neglected. Given that the 4f electrons do not mix to a great extent with ligand orbitals of hard donors—such as oxygen, carbon and nitrogen—most lanthanide complexes are expected to present a purely ionic bonding with no covalency (Figure 1).<sup>[35–37]</sup>

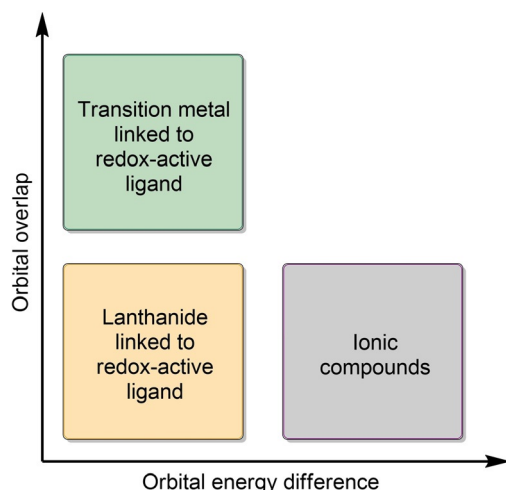


**Figure 1.** Orbital overlap versus orbital energy difference plot and the related compound categories (adapted from Ref. [38]).

However, when the ligand and the metal both possess similar energies, even with a very little overlap, the electron(s), statistically, have similar probabilities of being found on one or the other site. This situation leads to multiple possible configurations, in which the redox state of the metal is different: the metal and the ligand share electrons even with little overlap between the respective orbitals. This situation of multiple configurations is also known in transition-metal complexes when the orbitals are almost orthogonal, resulting in a small-to-zero overlap extent. Notably, the Wieghardt group and some of us have reported transition-metal complexes with multiple configurations, in which the corresponding redox states are different.<sup>[39–46]</sup>

Thus, in lanthanide complexes, when the ligand orbitals and the lanthanide ion are of similar energy, these situations of multiple configurations with different redox states (of both the ligand and the metal ion) can occur, leading to a disturbance in their physical properties. The formal oxidation state is therefore not suitable anymore, as neither one nor the other value is appropriate. The valence is rather intermediate, as discussed in the field by the pioneers, Dolg, Fulde, Maron and Andersen.<sup>[47–51]</sup> Indeed, the computation of multiple states of similar energy requires cautious choices of the methods used and, although density-based methods usually lead to fast analyses, in most cases, it solely points out delocalised density over the metal and ligand orbitals but does not reproduce nor explain the abnormal spectroscopic signatures that were observed. In this area, Field considered in the 1980s the computation of di-

atomic molecules of lanthanides for the better understanding of their non-trivial spectroscopic properties, especially arising from low-lying electronic states, and introduced the concept of “super-configurations”.<sup>[52]</sup> At the time, if the key theoretical milestones of modern theoretical wave-function-based methodologies<sup>[53,54]</sup> and DFT calculations<sup>[55,56]</sup> were known, the large number of electrons in f-element complexes rendered the task

Maxime Tricoire did his studies at Ecole Normale Supérieure (ENS) in Paris. After getting his master's degree from Université Pierre et Marie Curie in Paris (now Sorbonne Université) in 2017, he joined Dr. G. Nocton's group at Ecole polytechnique in 2018 for his Ph.D. project involving lanthanides, redox-active ligands and transition metals.



Nolwenn Mahieu started her studies at the Ecole Normale Supérieure (ENS) Paris-Saclay in 2016. After a stay in Pr. E.J. Schelter's group at the university of Pennsylvania working on imido-thorium complexes, she graduated in 2020 with a master in molecular chemistry from ENS Paris-Saclay. She then joined Dr. G. Nocton's group at Ecole polytechnique for her Ph.D. studies on the synthesis of organolanthanide complexes.



Thomas Simler graduated in 2012 from the Ecole Normale Supérieure in Lyon. He received his Ph.D. in 2016 from the Université de Strasbourg working on functionalised NHC and pincer complexes with Dr. P. Braunstein and Dr. A.A. Danopoulos. He then joined the group of Prof. P.W. Roesky at the Karlsruhe Institute of Technology for a first postdoctoral stay supported by an Humboldt fellowship. Since 2019, he is working as postdoc in the group of Dr. G. Nocton at Ecole polytechnique.

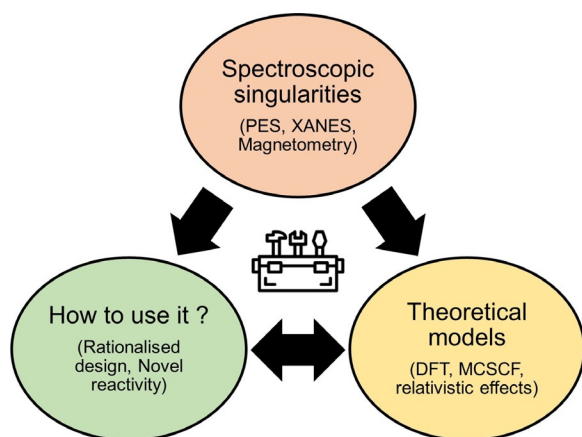


Grégory Nocton was born in Reims, France in 1983. After a master of science at the Universities of Reims and Grenoble (2006), he obtained his Ph.D. in 2009 in Grenoble with Prof. Marinella Mazzanti, working on redox reactivity of uranium. He then joined UC Berkeley for two years working with Prof. R.A. Andersen and was appointed CNRS researcher in 2011 at Ecole polytechnique. He obtained the bronze medal of CNRS in 2016 and he is also associate professor at Ecole polytechnique since 2017.



rather difficult. Similarly, when multiconfigurational methods<sup>[57,58]</sup> appeared, such as multiconfiguration Hartree–Fock/self-consistent field (MCHF/SCF), configuration interaction (CI) methods, many-body perturbation theory (MBPT) and coupled-clusters (CC),<sup>[59–62]</sup> only a few studies were attempted with lanthanide complexes. It is only in the late 1980s that Fulde et al. developed the foundations of the proper understanding of the theoretical approach of such fluctuating systems,<sup>[47,63]</sup> notably rationalising the formation of open-shell singlets and/or low-lying multiplet states by using the interaction between two partners (metal–metal or ligand–metal). This approach provided a possible explanation for several experimental observations based on the analogy with the Kondo singlet-state known in solid-state physics.<sup>[64,65]</sup>

The present review gathers the historical basis that allowed the development of intermediate valence in lanthanide compounds over more than 50 years of spectroscopic singularities and many computational studies. It opens with a rational basis of the symmetry and energetic considerations that can lead to the prediction of these events and, importantly, describes how they may relate to the reactivity of the complexes (Figure 2). With the abundance of low- and high-valent lanthanide compounds isolated in the last few years, this topic is likely to receive broad and increasing attention.

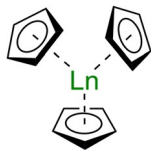


**Figure 2.** Intermediate valence and multiconfigurational ground states in lanthanide compounds: from spectroscopic singularities to the development of new theoretical models and the application in novel reactivity.

## 2. Spectroscopic Singularities

In the 1950s, Wilkinson and Birmingham reported the synthesis of a series of  $[\text{LnCp}_3]$  ( $\text{Cp} = \eta^5\text{-C}_5\text{H}_5$ ) complexes (Table 1).<sup>[66–68]</sup> The latter were obtained as crystalline solids after sublimation under reduced pressure at high temperatures. The ionic nature of the new compounds was evidenced by their reactivity towards ferrous chloride ( $\text{FeCl}_2$ ), resulting in an instantaneous ligand exchange reaction and quantitative formation of ferrocene,  $[\text{FeCp}_2]$ . Such an ionic nature would result from a dominant electrostatic interaction between the highly electropositive metal centres and the Cp rings with well-separated charges.<sup>[69]</sup> The effective magnetic moments for the  $[\text{LnCp}_3]$  com-

**Table 1.** General structure of the  $[\text{LnCp}_3]$  complexes and magnetic data at room temperature (295–300 K) for selected compounds.

 $[\text{LnCp}_3]$				
Ln	Electronic configuration of metal ion	Ground state of metal ion	Exptl. $\mu_{\text{eff}}^{[a]}$	Calcd. $\mu_{\text{eff}}^{[b]}$
Ce <sup>III</sup>	4f <sup>1</sup>	$^2F_{5/2}$	2.46	2.54
Eu <sup>III</sup>	4f <sup>6</sup>	$^7F_0$	3.74 <sup>[c]</sup>	3.40–3.61 <sup>[e]</sup>
Yb <sup>III</sup>	4f <sup>13</sup>	$^2F_{7/2}$	4.00	4.54
Lu <sup>III</sup>	4f <sup>14</sup>	$^1S_0$	diamagnetic	

[a] Values from Ref. [67], unless otherwise stated. [b] Theoretical values in the free-ion approximation. [c] Value from Ref. [71]. [d] Value for the mono-THF adduct, calculated with the data from Ref. [72]. [e] Non-magnetic ground state but presence of thermally populated magnetic excited states,<sup>[73]</sup> estimated values at room temperature from Ref. [74].

plexes were determined experimentally. The overall values were in good agreement with the free-ion values, to the exception of one noticeable discrepancy: the reported magnetic moment of  $[\text{YbCp}_3]$ ,  $4.0 \mu_B$ ,<sup>[67]</sup> differs from the expected value of  $4.5 \mu_B$  for an Yb<sup>III</sup> ion in a  $^2F_{7/2}$  ground state and is significantly lower than the experimental values for other typical Yb<sup>III</sup> coordination compounds.<sup>[70]</sup>

Following this seminal report, in-depth analysis of the electronic and magnetic properties of several  $[\text{LnCp}_3]$  complexes or other lanthanide compounds have been carried out to evaluate and quantify covalency in such compounds, and revealed other spectroscopic singularities that are gathered in this sub-section.

### 2.1. YbCp<sub>3</sub>

Gas-phase photoelectron spectra were recorded for a series of  $[\text{LnCp}_3]$  ( $\text{Ln} = \text{Ce}, \text{Pr}, \text{Nd}, \text{Sm}, \text{Yb}, \text{Lu}$ ) complexes using variable photon energy.<sup>[75–79]</sup> Photoelectron (PE) spectroscopy has especially proved to be a valuable technique to assess the molecular electronic structure of lanthanide complexes and identify ion states resulting from 4f ionisation. In the case of a lanthanide complex featuring a 4f<sup>n</sup> ground-state configuration, the spectrum obtained upon ionisation of a 4f valence electron gives information on the ground and excited states of the corresponding 4f<sup>n–1</sup> cation.

The PE spectrum of  $[\text{LuCp}_3]$ <sup>[80]</sup> can be readily interpreted: upon f-electron ionisation from the closed 4f<sup>14</sup> shell of Lu<sup>3+</sup>, two bands were observed and assigned to the  $^2F_{7/2}$  and  $^2F_{5/2}$  ion states associated with the 4f<sup>13</sup> configuration of Lu<sup>4+</sup>.<sup>[77]</sup> In the case of  $[\text{YbCp}_3]$ , a more complex spectrum was obtained with signals arising from both the 4f<sup>12</sup> and 4f<sup>13</sup> final-state configurations. An important question is whether the presence of both signals is the result of initial or final-state effects, that is, if the multiconfigurational character of the  $[\text{YbCp}_3]^+$  cation ob-



tained upon ionisation does reflect (or not) that of the corresponding neutral  $[\text{YbCp}_3]$  complex. The fact that ytterbium readily forms divalent complexes supports the idea of an initial-state effect, that is, contributions from both  $\text{Yb}^{\text{III}} 4f^{13}$  and  $\text{Yb}^{\text{II}} 4f^{14}$  configurations in the ground state of  $[\text{YbCp}_3]$ . More precisely, the mixed-configuration ground state corresponds to the superposition of a  $\text{Lf}^{13}$  configuration and a  $\text{Lf}^{14}$  charge-transfer configuration involving electronic transfer from the Cp ring to the  $\text{Yb}^{3+}$  ion, where L represents a full ligand shell (the ligand molecular orbitals collectively) and  $\text{L}$  a hole in that shell.<sup>[77]</sup> Careful analysis of the intensities of the bands associated with the two ion states allowed a determination of the relative contributions of the two configurations in the ground state.<sup>[78]</sup> The  $\text{Yb}^{\text{III}} \text{Lf}^{13}$  configuration was determined to account for 88% of the density in the ground state whereas the  $\text{Yb}^{\text{II}} \text{Lf}^{14}$  charge-transfer configuration contributes 12%. Independent estimations of the relative weights of the two configurations were also obtained by thorough EPR investigations.<sup>[78]</sup> Analysis of the  $^{13}\text{C}$  hyperfine coupling, as determined by HYS-CORE (hyperfine sublevel correlation)<sup>[81]</sup> pulsed EPR experiments, revealed an increase of  $12.6 \pm 0.9\%$  in the spin density on the  $^{13}\text{C}$  atoms of the Cp rings. In parallel, a decrease in the  $^{171}\text{Yb}$  hyperfine coupling interaction was observed compared with a series of standard  $\text{Yb}^{3+}$  compounds, indicating a reduced spin density in the 4f shell of the ytterbium atom. The observed  $\text{Yb} \rightarrow \text{Cp}$  spin transfer is linked to the  $\text{Cp} \rightarrow \text{Yb}$  charge transfer associated with the  $\text{Lf}^{14}$  configuration. Finally, the relative weights of the two configurations could also be estimated by analysis of the principal values of the  $g$ -tensor and the axial anisotropy, which is partially quenched owing to the charge-transfer configuration.<sup>[78]</sup>

The presence of two configurations in the ground state of  $[\text{YbCp}_3]$  is expected to have an influence on the magnetic susceptibility of the compound. Therefore, magnetic studies were performed in the solid state in the range 2–305 K.<sup>[77]</sup> Above 20 K, a Curie behaviour was observed over the entire temperature range with an associated magnetic moment of  $3.53 \mu_{\text{B}}$ .<sup>[77]</sup> This low magnetic moment compared with that of typical  $\text{Yb}^{\text{III}}$  complexes can be explained if the ground-state wavefunction includes a  $\text{Lf}^{14}$  charge-transfer contribution, with a largely quenched orbital angular momentum. A slightly lower value for the magnetic moment ( $3.33 \mu_{\text{B}}$ ) was derived from EPR measurements in frozen solution. The higher value obtained from solid-state magnetic measurements can be explained by a higher dielectric constant in the solid state, which stabilises the more polar  $\text{Lf}^{13}$  configuration and reduces the weight of the  $\text{Lf}^{14}$  charge-transfer contribution in the solid state.<sup>[78]</sup> As a result of the Curie behaviour, the magnetic moment showed almost no dependence on the temperature in the range 20–305 K, which can be explained by a negligible thermal population at 300 K of high-lying excited states (higher than  $1000 \text{ cm}^{-1}$ ).<sup>[77]</sup> Below 20 K, substantial departure from the Curie behaviour was observed, which may be interpreted as a structural phase change occurring at a temperature of 20 K.<sup>[77]</sup> As a result of this phase change, the relative weights of the  $f^{13}$  and  $f^{14}$  configurations in the ground state are likely to be perturbed, leading to different magnetic properties.

Anomalous features were also observed in the electronic spectra of  $[\text{YbCp}_3]$ . Such spectra, in the solid state<sup>[82]</sup> and in solution,<sup>[83]</sup> had already been reported in 1967 and 1983, respectively, but remained largely uninterpreted until more recent work by Denning et al. in 2011.<sup>[78]</sup> In the visible/near IR spectrum of  $[\text{YbCp}_3]$ , the f–f region is highly anomalous compared with that of conventional  $\text{Yb}^{3+}$  compounds, such as, for example,  $[\text{Cp}^*_2\text{Yb}(\text{L})]^+(\text{X})^-$  ( $\text{L} = 1,10\text{-phenanthroline (phen)}$  or  $2,2'\text{-bipyridine (bipy)}$ ;  $\text{X} = \text{I}$  or  $\text{PF}_6$ ; see also below, section 2.7).<sup>[84,85]</sup> Indeed, f–f transitions in lanthanide compounds (similarly to d–d transitions for transition-metal complexes) are parity forbidden on the basis of the selection rules. The intensities of the corresponding bands were found to be 20 to 50 times larger than those for typical  $\text{Yb}^{3+}$  compounds and vibronic structures associated with f–f transitions spanned a much larger energy range (ca.  $2000 \text{ cm}^{-1}$  compared with  $597 \pm 185 \text{ cm}^{-1}$ ). Such anomalous features can be explained by charge-transfer transitions supporting a configuration interaction in the ground state.<sup>[78]</sup>

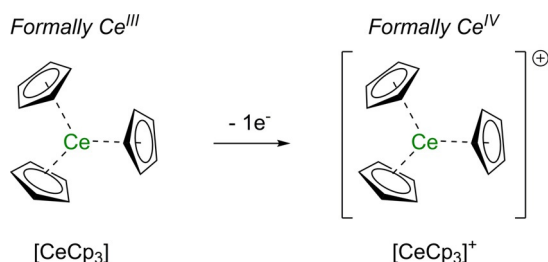
Although routine DFT calculations clearly indicated delocalisation of the spin density away from the Yb atom, they were not appropriate to evaluate the residual spin density on Yb. Using different DFT methods, large differences in the spin density values were obtained. Yet, such computational methods were still useful to give certain insights in the electronic structure, such as the relative orbital energies, and rationalise the experimental electronic and EPR spectra.<sup>[78]</sup>

## 2.2. $\text{EuCp}_3$

The involvement of a  $\text{Cp} \rightarrow \text{Ln}$  charge-transfer contribution similar to that in  $[\text{YbCp}_3]$  is also expected in the more easily reduced  $\text{Eu}^{\text{III}}$  analogue. Indeed, the  $\text{Ln}^{3+}/\text{Ln}^{2+}$  redox potentials versus NHE (NHE = normal hydrogen electrode) are  $-0.35 \text{ V}$  and  $-1.15 \text{ V}$  for Eu and Yb, respectively.<sup>[86]</sup> In the case of europium compounds,  $^{151}\text{Eu}$  Mössbauer spectroscopy is a useful technique to probe the electronic properties at the europium nucleus. The  $^{151}\text{Eu}$  isomer shift strongly depends on the oxidation state of the europium ion whereas the quadrupole interaction gives information about the symmetry of the environment at the metal centre.<sup>[87]</sup> In the  $^{151}\text{Eu}$  Mössbauer spectrum of  $[\text{EuCp}_3(\text{THF})]$ , an unusual isomer shift lying between the typical values for  $\text{Eu}^{\text{II}}$  and  $\text{Eu}^{\text{III}}$  complexes was observed, together with a large negative quadrupole interaction, which is also unusual for europium organometallic compounds.<sup>[88]</sup> To explain such features, a strong interaction between the Eu 4f orbitals and the three Cp ligands, resulting in the transfer of approximately 0.14 electrons from the ligand sphere to the metal, was suggested.<sup>[88]</sup>

## 2.3. $\text{CeCp}_3$

Among  $[\text{LnCp}_3]$  complexes, the cerium analogue was reported to be the most reactive towards oxidation by traces of air, which can be traced back to the easy oxidation of the  $\text{Ce}^{\text{III}}$  centre to  $\text{Ce}^{\text{IV}}$  (Scheme 2).<sup>[66,67]</sup> The reported magnetic moment of  $[\text{CeCp}_3]$  ( $2.46 \mu_{\text{B}}$ ) at room temperature is consistent with



**Scheme 2.** Structures of the formally  $\text{Ce}^{\text{III}}$  complex  $[\text{CeCp}_3]$  and its related  $\text{Ce}^{\text{IV}}$  cation  $[\text{CeCp}_3]^+$ .

that expected for an unperturbed  $\text{Ce}^{\text{III}} 4f^1$  configuration with a  $^2F_{5/2}$  ground state ( $2.54 \mu_B$ , Table 1).<sup>[67]</sup> Insights into the electronic ground state of  $[\text{CeCp}_3]$  and in the optical transition energies of this  $4f^1$  complex were given by non-relativistic and relativistic DFT calculations.<sup>[89]</sup> Analysis of the symmetry of the orbitals revealed that the  $C_{3v}$  ligand environment observed in  $[\text{CeCp}_3]$  is particularly adapted for f-block elements featuring valence f-orbitals, in contrast to transition metals that possess valence d-orbitals. Although the incorporation of relativity into the calculations only had minor effects on the largely ligand-based molecular orbitals (MOs), it did affect the energies of metal-localised atomic orbitals (AOs). Indeed, relativistic effects destabilise the f-orbitals, bringing the Ce 4f and 5d orbitals closer in energy, which has a direct influence on the electronic absorption spectrum. Although both non-relativistic and relativistic calculations predicted a  $4f^1$  ground-state configuration for  $[\text{CeCp}_3]$ , the inclusion of relativity led to a  $6d^1$  ground state for the heavier actinide analogue  $[\text{ThCp}_3]$ . The calculated electronic absorption spectrum of  $[\text{CeCp}_3]$  revealed weak  $f \rightarrow f$  transitions with a more intense low-lying  $f \rightarrow d$  transition.<sup>[89]</sup>

The electronic structures of the neutral complex and of its cationic form  $[\text{CeCp}_3]^+$  were further investigated by variable photon energy photoelectron (PE) spectroscopy in the gas phase.<sup>[75]</sup> Upon ionisation of the single f-electron of  $[\text{CeCp}_3]$ , a simple orbital model would predict only one possible ion state for the corresponding  $4f^0$   $[\text{CeCp}_3]^+$  cation, that is, only one photoelectron band in the PE spectrum. However, two bands separated by a large energy gap (3.2 eV) and associated with two different final states were observed.<sup>[75]</sup> It should be noted that the occurrence of two signals associated with f-ionisation had already been reported in the photoemission spectra of solid inorganic Ce compounds.<sup>[90–92]</sup> In the PE spectrum of  $[\text{CeCp}_3]$ , the lower energy state associated with the first PE band corresponds to the ground state of the gas-phase  $[\text{CeCp}_3]^+$  cation. Its electronic structure was rationalised in terms of an interaction between two different electronic configurations.<sup>[75]</sup> Further studies revealed that, although the ground state of  $[\text{CeCp}_3]^+$  does not possess a Ce-localised f-electron, it has significant f-density arising from population of natural orbitals (NOs) with f-character.<sup>[76]</sup> The higher energy band in the PE spectrum also arises from f-ionisation and is associated with an excited state of  $[\text{CeCp}_3]^+$ . This excited state features significant Ce5d population owing to intramolecular  $\text{Cp} \rightarrow \text{Ce}5d$  charge transfer occurring upon f-ionisation. Insights into the electronic structure of the different states of  $[\text{CeCp}_3]^+$

was provided by ab initio calculations using the complete active space self-consistent field (CASSCF)<sup>[93]</sup>/complete active-space second-order perturbation theory (CASPT2) approach.<sup>[76]</sup> The CASPT2 methodology includes perturbations by additional corrections for dynamic correlation.<sup>[94]</sup>

However, electronic configurations involving canonical CASSCF orbitals were found not to reliably describe the electronic structures of the ground and excited states of  $[\text{CeCp}_3]^+$ . Indeed, the weights of these configurations were highly influenced by the number of states included in the state-averaged (SA) CASSCF calculation (see discussion below on cerocene). The NOs and their occupations (NOOs) are specific to each state and are more informative. They are computed from the reduced density matrix of each state and not from the state-averaged matrix, the latter being used to produce pseudo-NOs in CASSCF/CASPT2 calculations. The f-electron occupancy can then be derived from the NOOs and their f-coefficients for all the active space orbitals. A deviation  $>0.1$  from an integer value for the NOOs ensures the presence of a multiconfigurational state. As a result, in the  $[\text{CeCp}_3]^+$  cation, several configurations were found to compose the wavefunction, resulting in an intermediate-valent ground state. The same conclusion was obtained for the excited states involved in the second PE band. Yet, as no NO is purely f-based in the electronic ground state of  $[\text{CeCp}_3]^+$ , the latter does not possess any metal-localised 4f electron, which supports the description of this cation as formally  $\text{Ce}^{\text{IV}}$ . The significant f-density on the metal centre, similar to that in the formally  $\text{Ce}^{\text{III}}$   $[\text{CeCp}_3]$ , is due to population of delocalised NOs with f-character.<sup>[76]</sup> This conclusion highlights the very core of the semantic issue arising in these kind of systems. How to qualify a Ln ion that shows properties from a different oxidation state than its formal one? The theoretical model supports intermediate valence as it uses multiconfigurational states to define the system but these states may bear no fundamental characteristics of one or the other oxidation state involved (i.e., no pure f-orbital localised electron in this case).

## 2.4. Cerocene and derivatives

Aside from the  $[\text{LnCp}_3]$  complexes, the electronic structure of cerocene,  $[\text{Ce}(\text{Cot})_2]$  ( $\text{Cot} = \eta^8\text{-C}_8\text{H}_8$ ; Figure 3), has been the subject of a great deal of research from both experimental and theoretical points of view.

The successful synthesis of cerocene was first reported in 1976 by Cesca and co-workers, by reaction of  $[\text{Ce}(\text{O}i\text{Pr})_4]$  with  $[\text{AlEt}_3]$  in the presence of excess cyclooctatetraene (Cot).<sup>[95]</sup> Cer-

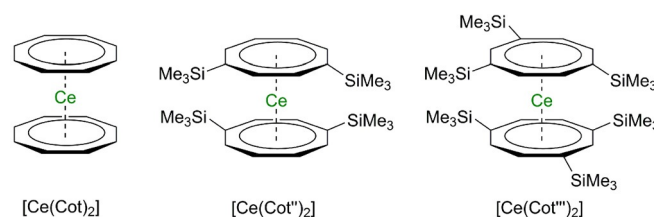


**Figure 3.** Structure of cerocene and its trimethylsilyl-substituted analogues.

ocene combines a strong reducing agent (the  $\text{Cot}^{2-}$  dianion) and a strong oxidising agent (a  $\text{Ce}^{4+}$  ion). Alternative and higher-purity syntheses of  $[\text{Ce}(\text{Cot})_2]^{[96,97]}$  and of several substituted cerocenes have also been described.<sup>[98,99]</sup> In such complexes, the distance between the ring centroid and the Ce metal centre is approximately 1.97 Å, which is approximately 0.10 Å shorter than the corresponding distance in the  $\text{Ce}^{\text{III}}$   $\text{K}[\text{Ce}(\text{Cot})_2]$  diglyme salt.<sup>[100]</sup> Such a shortening is consistent with the smaller ionic radius of the  $\text{Ce}^{4+}$  cation compared with that of the  $\text{Ce}^{3+}$  cation.<sup>[101]</sup> In addition, electrochemical studies and the apparent diamagnetism of cerocene were further pointing to a formal  $\text{Ce}^{\text{IV}}$  complex.

In the gas-phase PE spectrum of  $[\text{Ce}(\text{Cot})_2]$ , no clear sign of f-electron ionisation was observed, also supporting a  $4f^0$  configuration, that is, a +IV oxidation state for the metal centre, similarly to the situation encountered in the heavier 5f thorium analogue.<sup>[102]</sup> In the UV/Vis spectrum, strong absorption bands in the visible region at 469 nm ( $\epsilon$  ca. 8000) with a shoulder at 570 nm ( $\epsilon$  ca. 1000) were assigned to ligand-to-metal charge-transfer transitions. The substituted cerocene  $[\text{Ce}(\text{Cot}'')_2]$  ( $\text{Cot}'' = \eta^8\text{-1,4-(Me}_3\text{Si)}_2\text{C}_8\text{H}_6$ ; Figure 3), first reported in 1994 by Edelmann and co-workers, was obtained by oxidation of the  $\text{Ce}^{\text{III}}$  complex  $\text{Li}[\text{Ce}(\text{Cot}')_2]$  with AgI, and isolated as a deep-purple oil.<sup>[99]</sup> An alternative synthesis, consisting of the oxidation of  $\text{Na}[\text{Ce}(\text{Cot}')_2]$  with allyl bromide, was described by Streitwieser and co-workers and led to the same compound,  $[\text{Ce}(\text{Cot}'')_2]$ , isolated as a dark-brown semisolid material.<sup>[96]</sup> The UV/Vis spectra of  $[\text{Ce}(\text{Cot}'')_2]$  and of other substituted cerocenes ( $[\text{Ce}(\text{C}_8\text{H}_7\text{R})_2]$  with  $\text{R} = \text{Me}, n\text{Bu}, t\text{Bu}, t\text{BuO}$ ) were recorded and revealed a maximum absorption band in the region 470–494 nm.<sup>[96,99]</sup> This band was first attributed to a ligand-to-metal charge-transfer transition occurring in formal  $\text{Ce}^{\text{IV}}$  complexes,<sup>[96]</sup> similarly to the situation in cerocene.<sup>[102]</sup> However, further spectroscopic studies on  $[\text{Ce}(\text{Cot}'')_2]$  at variable temperatures reported by Amberger et al. were more consistent with a  $\text{Ce}^{\text{III}}$  formulation.<sup>[103]</sup> In the luminescence spectrum at low temperature (90 K), two bands were observed with maxima at 14 250 and 17 900  $\text{cm}^{-1}$ , which is typical for  $\text{Ce}^{\text{III}}$  complexes, as, for example,  $[\text{Li}(\text{THF})_4][\text{Ce}(\text{Cot})_2]$ . The separation between the two bands, 3650  $\text{cm}^{-1}$ , is, however, bigger than that usually observed in  $\text{Ce}^{\text{III}}$  complexes (typically 1250–1400  $\text{cm}^{-1}$ ) and is in agreement with the energy separation predicted by calculations corresponding to a  $\text{Ce}^{3+}[(\text{Cot})^{1.5-}]_2$  formulation (see below).<sup>[47–49]</sup> The authors could nonetheless not totally exclude the possibility that some of the luminescence signals detected at a low temperature may arise from  $\text{Ce}^{\text{III}}$  decomposition products under laser irradiation.<sup>[103]</sup>

X-ray absorption near-edge structure (XANES) spectroscopy studies have been carried out to further investigate the oxidation state of Ce in cerocene and its substituted analogues.<sup>[97,104–106]</sup> Through the exposure to high-energy X-rays, core electrons are excited into empty or singly occupied valence orbitals of the metal complex (Figure 4). XANES has been recognised as a useful tool to determine the oxidation state of an atom and has been used to evaluate the degree of f-orbital participation in the bonding of lanthanide and actinide compounds.<sup>[107,108]</sup> The absorption is measured below and above a

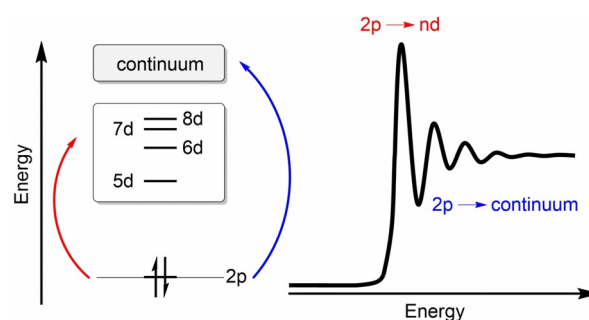


**Figure 4.** Schematic representation of  $L_3$ -edge XANES transitions and their origin. Adapted from Ref. [24].

characteristic X-ray elemental edge. For example, for metal ions, K-, L-, or M-edge X-ray absorption spectroscopy (XAS) has been employed. Some reports focused on ligand K-edge XAS studies on the atoms directly bound to Ln centres to investigate metal/ligand orbital mixing and covalency in lanthanide compounds.<sup>[23,106,109–111]</sup> These different XAS techniques differ by the energy of the transitions involved. Whereas lanthanide K-edge XAS involves high-energy excitations of metal 1s electrons to empty orbitals of p character, lanthanide  $L_3$ -edge XANES studies probe transitions between  $\text{Ln}2p$  orbitals and unoccupied states of 5d character (i.e., transitions from a  $2p^64f^n5d^0$  to a  $2p^54f^n5d^1$  electronic state where  $n$  corresponds to the number of f-electrons in the ground state).<sup>[24]</sup> The energies of the transitions are related to the ground-state  $4f^n$  occupation and the effective nuclear charge on the lanthanide ion.

Recently, lanthanide  $M_{5,4}$ -edge XAS studies, which involve transitions from core-level 3d electrons to empty 4f orbitals, that is, transitions from  $3d^{10}4f^n$  to  $3d^94f^{n+1}$  configurations, have been employed to probe 4f valency in lanthanide ions.<sup>[24,106,109,111]</sup> The energy at which the absorption edge occurs is linked to the metal oxidation state or f-occupancy in intermediate valence systems. In  $\text{Ce}^{\text{III}}$  complexes, the presence of only one initial state with a configuration  $\text{L}2p^64f^1$  (L corresponding to the orbitals of the ligand) results in a single final state of  $\text{L}2p^54f^15d^1$  configuration after L-edge XAS irradiation.

Formal  $\text{Ce}^{\text{IV}}$  compounds, and more generally  $\text{Ln}^{\text{IV}}$  compounds, usually feature a superposition of  $\text{L}f^0$  and  $\text{L}f^1$  ( $\text{L}$  is a ligand hole) configurations in their ground states. It is, for example, the case in  $\text{CeO}_2$ , which is generally considered a strongly mixed-valent compound,<sup>[111–115]</sup> although its electronic ground state is still controversial.<sup>[116]</sup>

In the corresponding XAS spectra, the white line usually displays multiple peaks, typically in the shape of a white line doublet, owing to contributions of the different configurations in the final state. Quantitative analysis of the multiple features observed in the core-level X-ray photoemission (XPS) spectrum of  $\text{CeO}_2$  led to similar conclusions, supporting a mixture of  $\text{L}4f^0$  and  $\text{L}4f^1$  configurations in the ground state.<sup>[112]</sup> However, the physical origin and the interpretation of the white line doublet in Ln XAS measurements is still under debate and the XPS core final states are different from the XANES final states.<sup>[113]</sup> The presence of contributions from both configurations could be the result of either a multiconfigurational ground-state (i.e., ini-

tial-state effects) or final-state effects.<sup>[106,109,111]</sup> Final-state effects would support the presence of a single ground state leading to a doublet feature as the result of transitions to unoccupied 5d states split by the crystal field, or strong perturbation and relaxation effects around the core hole.<sup>[23,113]</sup> However, most studies support initial-state effects. Analysis of the XANES data of the substituted cerocenes [Ce(Cot'')<sub>2</sub>] and [Ce(Cot''')<sub>2</sub>] (Cot''' = η<sup>8</sup>-1,3,6-(SiMe<sub>3</sub>)<sub>3</sub>C<sub>8</sub>H<sub>5</sub>; Figure 3) revealed K-edge shifts at energies similar to those observed in various Ce<sup>3+</sup> model compounds, therefore supporting a Ce<sup>III</sup> oxidation state.<sup>[104]</sup> However, the edge energies were slightly shifted (about 4.5 eV) towards a higher oxidation state in comparison with the edge energies of the corresponding alkali metal Ce<sup>III</sup> adducts. Therefore, XANES data support mixed-valence in substituted cerocenes. The lower electronic density compared with typical Ce<sup>III</sup> compounds was interpreted as an admixture of Ce<sup>III</sup>  $\underline{L}4f^1$  and Ce<sup>IV</sup>  $L4f^0$  configurations in the ground state of cerocene, as predicted in earlier calculations by Dolg, Fulde and co-workers.<sup>[47–49]</sup> Andersen and co-workers reported that, using Ce L<sub>3</sub>-edge (rather than Ce K-edge) XAS, a well-defined white line doublet can be observed in formal Ce<sup>IV</sup> compounds, which allows a more precise estimation of the cerium valence in these compounds.<sup>[105]</sup> The high-resolution Ce L<sub>3</sub>-edge XANES spectrum of [Ce(Cot)<sub>2</sub>] was found to be more consistent with that of a Ce<sup>III</sup> rather than Ce<sup>IV</sup> compound, but still displayed some characteristic Ce<sup>IV</sup> features.<sup>[105]</sup> These data were in agreement with earlier Ce K-edge XANES data recorded by Edelstein and co-workers on the substituted cerocenes [Ce(Cot'')<sub>2</sub>] and [Ce(Cot''')<sub>2</sub>].<sup>[104]</sup> By fitting the Ce L<sub>3</sub>-edge XANES data, the relative contributions of the two configurations can be determined. The f-occupancy,  $n_f$ , is defined in Equation (1) where  $A_{Ln^{3+}}$  is the intensity of the  $\underline{L}2p^{5.4}f^{n+1}5d^1$  final-state contribution and  $A_{Ln^{4+}}$  that of the  $L2p^{5.4}f^n5d^1$  contribution.

$$n_f = \frac{A_{Ln^{3+}}}{A_{Ln^{3+}} + A_{Ln^{4+}}} \quad (1)$$

For cerocene, the estimated value  $n_f = 0.89 \pm 0.03$  supports the calculation predictions of Dolg and co-workers (Figure 5).<sup>[49]</sup> No influence of the temperature on the  $n_f$  value was observed until 400 K, the temperature at which conversion of [Ce(Cot)<sub>2</sub>] to [Ce<sub>2</sub>(Cot)<sub>3</sub>] begins to occur.<sup>[97]</sup> The latter compound, in contrast to [Ce(Cot)<sub>2</sub>], is clearly trivalent with  $n_f = 1$ .

Very recent studies focused on Ce M<sub>5,4</sub>-edge and carbon K-edge XAS to investigate covalency in [Ce(Cot)<sub>2</sub>].<sup>[106]</sup> The Ce M<sub>5,4</sub>-edge XAS data were compared with those obtained by L<sub>3</sub>-edge XAS studies for other formally Ce<sup>IV</sup> ([Ce(Cot)<sub>2</sub>], CeO<sub>2</sub>,

CeCl<sub>6</sub><sup>2-</sup>) and Ce<sup>III</sup> ([Ce(Cot)<sub>2</sub>][Li(THF)<sub>2</sub>] and CeCl<sub>6</sub><sup>3-</sup>) species.<sup>[105,109,111]</sup> It should be noted that, compared with L<sub>3</sub>-XANES, the intensity ratio between M<sub>5,4</sub>-XANES final states are quite different and the deduction of ground-state intermediate valence requires a theoretical description of the final states. Although the Ce M<sub>5,4</sub>-edge XAS spectrum for [Ce(Cot)<sub>2</sub>] is more similar to that of formal Ce<sup>3+</sup> compounds, successful fitting of the data was only possible when including both Ce<sup>IV</sup>  $\underline{L}3d^{10}4f^0$  and Ce<sup>III</sup>  $\underline{L}3d^{10}4f^1$  initial-state configurations, and the corresponding  $\underline{L}3d^94f^1$  and  $\underline{L}3d^94f^2$  final-state configurations. A contribution of 51 % of the charge-transfer Ce<sup>III</sup> configuration to the ground state was established, which is larger than that derived from Ce M<sub>5,4</sub>-edge XAS data on other formally Ce<sup>IV</sup> compounds, such as CeCl<sub>6</sub><sup>2-</sup> (25 %)<sup>[109]</sup> or CeO<sub>2</sub> (ca. 44 %).<sup>[111]</sup> However, this Ce<sup>III</sup> contribution to the ground state is much lower than that established by L<sub>3</sub>-edge XANES spectroscopy (89 %).<sup>[105]</sup>

SQUID magnetic studies revealed that high-purity [Ce(Cot)<sub>2</sub>] displays temperature-independent paramagnetism (TIP) in the range 5–300 K, with the magnetic susceptibility  $\chi$  being slightly positive and temperature independent, which rules out a diamagnetic molecule that would present  $\chi_m < 0$ .<sup>[97,105]</sup> Neumann and Fulde suggested that cerocene may be considered as a molecular analogue of a Kondo singlet.<sup>[47]</sup> The Kondo effect is a term derived from the physics of solid-state materials and arises when paramagnetic sites antiferromagnetically couple to conduction electrons, resulting in cancelation of the local magnetic moment.<sup>[64–65,117]</sup> The term Kondo singlet means that an open-shell singlet is lying lower in energy than the open-shell triplet, as a result of a mixture of two configurations (in this case the Ce<sup>III</sup>  $\underline{L}f^1$  and Ce<sup>IV</sup>  $Lf^0$  configurations, with  $\underline{L}$  and  $L$  corresponding to (Cot<sup>1.5-</sup>)<sub>2</sub> and (Cot<sup>2-</sup>)<sub>2</sub>, respectively). In Kondo systems, the triplet state becomes populated by increasing the temperature until the Kondo temperature at which the spins become uncorrelated. In this case, cerocene behaves as a Kondo singlet in the temperature range 5–300 K but decomposes to [Ce<sub>2</sub>(Cot)<sub>3</sub>] and free Cot before the triplet state begins to be populated.<sup>[97]</sup>

Studies of other [Ln(Cot)<sub>2</sub>]<sup>-</sup> complexes by anion photoelectron spectroscopy revealed a pair of prominent peaks in the PE spectra of the middle-range lanthanide (Ln = Sm, Gd, Tb, Dy and Ho) complexes. In contrast, simpler features were observed for the lighter and heavier lanthanide analogues. These results were rationalised in terms of configuration interaction involving both Ln<sup>3+</sup> and Ln<sup>4+</sup> configurations after photodetachment of one electron.<sup>[118]</sup>

As DFT calculations are not well-adapted for these particular systems, they do not properly describe the multiconfigurational character of [Ce(Cot)<sub>2</sub>]. Yet, broken-symmetry DFT (B3LYP) calculations seemed to reproduce some aspects of the multiconfigurational character observed by CASSCF calculations and revealed an open-shell singlet ground state resulting from an admixture of singlet and triplet states.<sup>[106]</sup> Concerning theoretical models, following the theoretical studies by Rösch and Streitwieser stating that cerocene is at the +IV oxidation state, similarly to uranocene and thorocene,<sup>[119]</sup> Neumann and Fulde were the pioneers who opened cerocene's Pandora box in

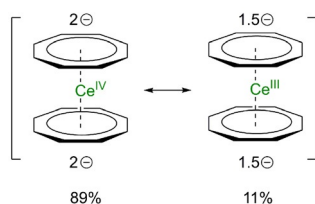


**Figure 5.** Ce<sup>IV</sup> and Ce<sup>III</sup> contributions in cerocene as determined by Andersen and co-workers.<sup>[105]</sup>



which was concealed numerous questions about its oxidation state. With the rise of relativistic pseudo-potentials developed for f-elements in the beginning of the 1990s,<sup>[120–123]</sup> a huge gap was filled, making possible the study of cerocene with complex MCSCF methods. This led to Dolg's works on the topic, validating the fact that cerocene's ground state had to be considered as intermediate valent with two  $^1A_g$  configurations (in  $D_{8h}$  symmetry), the open-shell singlet  $Ce^{III} \underline{1}f^1$  (or  $Ce^{3+}[(Cot)^{1.5-}]_2$ ) and the closed-shell singlet  $Ce^{IV} f^0$  (or  $Ce^{4+}[(Cot)^{2-}]_2$ ), which coexist with the  $Ce^{III}/Ce^{IV}$  ratio being approximately 83:17. This ratio can be noted  $n_f=0.83$  to represent the effective number of f-electrons left on the Ce atom.<sup>[48,49,124]</sup> This initial statement that the ground-state wavefunction of cerocene is multiconfigurational was later endorsed by Kerridge. However, suspicions about the  $Ce^{III}$  character being predominant led in 2009 to SA-CASSCF<sup>[93]</sup> studies coupled with CASPT2<sup>[94]</sup> calculations, which resulted in  $Ce^{II}/Ce^{III}/Ce^{IV}$  contributions to the wavefunction being 9:23:60, respectively.<sup>[125]</sup> One important notion highlighted in this paper is the difference between canonical CASSCF orbitals and natural orbitals. As stated earlier with the  $[CeCp_3]$  study, canonical CASSCF MO coefficients are theoretically and numerically relevant but they are subject to large changes upon modulation of the number of states considered in the SA calculation. The more reliable NOs should be considered to evaluate  $n_f$ , resulting in a value of  $n_f=0.9$  close to that obtained in Dolg's studies and in the experimental ones. Yet, the fact that the NOs remain largely localised on the  $\pi$ -ring system led to the conclusion that this f-density is mostly due to covalency between the Cot and the empty f-orbital on the Ce, which is contradictory with a  $Ce^{III}$  definition. A later update using quantum theory of atoms in molecules (QTAIM) topological analyses<sup>[126]</sup> derived from CASSCF-CASPT2 level of theory studies confirmed the non-negligible covalency arising from electron sharing between the Cot ring and the Ce ion with a charge of approximately 2.9.<sup>[127]</sup> This study enforced the conjecture in which the cerocene ground state is of mixed-valence and closer to the formal oxidation state +IV. The  $n_f$  value being close to 1 (0.95 in this study) mainly originates from Cot–Ce covalency and not from the Ce ion itself. The fact that the first excited state is, however, best defined as  $Ce^{III}$  from both CASSCF and QTAIM with a similar electronic structure is proposed as another reason why experimental measurements are in better agreement with a +III oxidation state. In 2014, Mooßen and Dolg answered these different statements by using the invariance of the CASSCF wavefunction by a unitary transformation in the orbital space.<sup>[128]</sup> Indeed, given this property, by applying the transformation ( $a' = a \cos \alpha + b \sin \alpha$ ) and ( $b' = b \cos \alpha - a \sin \alpha$ ) to any set of starting  $a$  and  $b$  CASSCF orbitals, it is possible to create a new set of orbitals that will end up representing the very same wavefunction but with a different representation and different contributions (see Figure 6). By incrementing this, Mooßen and Dolg highlighted two extreme cases, on the one hand the purest  $\pi$  and 4f orbitals can be created with  $\alpha=25^\circ$  leading to  $a'$  being approximately 95% pure  $\pi$  and  $b'$  approximately 100% pure 4f. The weights of the configurations to the wavefunction are then 80% for  $a'^3b'^1$ , 10% for  $a'^4$  and 10% for  $a'^2b'^2$ , which therefore corre-

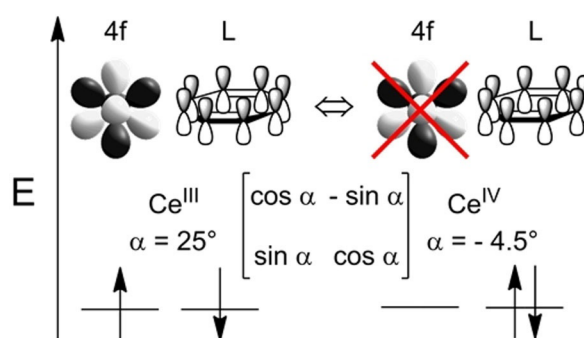


**Figure 6.** Representation of the two extreme cases of orbital rotation highlighted in Mooßen and Dolg's work of 2014.

sponds to a mostly  $Ce^{III}$  intermediate-valent state. On the other hand, the  $a'^4$  configuration contribution is maximised (81%) with  $\alpha=-4.5^\circ$ , resulting in  $a'$  being composed of an 80:20 ratio of  $\pi/4f$  orbitals and  $b'$  the inverse. As a result, a mostly  $Ce^{IV}$  model is obtained but with the resulting orbitals being of mixed character. With these two cases in mind and knowing that an infinite number of combinations may give intermediate results, there is no single best way to describe the formal oxidation state of cerocene. Moreover, all of these combinations are giving a relatively stable  $n_f$  close to 1, which concurs relatively well with the experimental value that remains the absolute reference.

These works enlighten us about why intermediate-valent species are so hard to qualify. Dolg stated in his conclusion that the choice between a +III (where a pure 4f electron is present) and a +IV (where the 4f electron density arises from  $\pi$ -4f covalency) oxidation state is "to a certain extent a matter of taste",<sup>[128]</sup> which, for a pioneer of the field, is quite meaningful.

## 2.5. $[Ce(Pn)_2]$ substituted pentalene

Recently, magnetic and spectroscopic studies have focused on the related substituted pentalene analogues of  $[Ce(Cot)_2]$ , cerium bis(hexamethylpentalene)  $[Ce(Pn^*)_2]$  ( $Pn^* = \eta^8-Me_6C_8$ ) and bis(triisopropylsilyl)pentalene  $[Ce(Pn'')_2]$  ( $Pn'' = \eta^8-(1,4-iPr_3Si)_2C_8H_4$ ) (Figure 7).<sup>[129,130]</sup> In both cases, sharp signals were observed in the  $^1H$  and  $^{13}C$  NMR spectra in solution, suggesting diamagnetic molecules, but with several abnormal chemical shifts revealing some paramagnetic character. The unusual

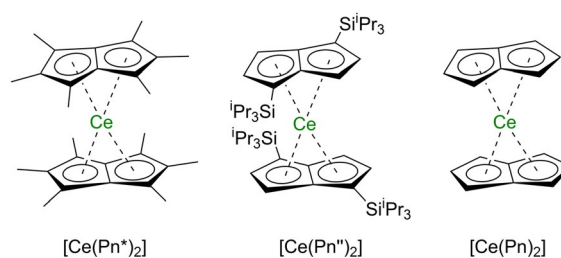


**Figure 7.** Structures of the different Ce pentalene complexes discussed in this section.



NMR chemical shifts were explained by a strongly “mixed-valent” system with  $4f^1$  contributions to the ground state. No appreciable changes in the chemical shifts were observed by variable-temperature NMR studies, implying temperature-independent paramagnetism (TIP). Solid-state magnetic studies revealed a TIP paramagnetism  $((25.0 \pm 0.1) \times 10^{-4}$  and  $(4.5 \pm 0.3) \times 10^{-4} \text{ emu mol}^{-1}$  for  $[\text{Ce}(\text{Pn}^*)_2]$  and  $[\text{Ce}(\text{Pn}^{\prime\prime})_2]$ , respectively) larger than that reported for  $[\text{Ce}(\text{Cot})_2]$   $((1.4 \pm 0.2) \times 10^{-4} \text{ emu mol}^{-1})$ ,<sup>[105]</sup> which was attributed to smaller HOMO–LUMO gaps in the pentalene complexes.<sup>[129,130]</sup> In the UV/Vis spectra, intense absorption bands were detected at 530 nm ( $\epsilon = 17\,000$ ) and 590 nm ( $\epsilon = 5000$ ) for  $[\text{Ce}(\text{Pn}^*)_2]$  and  $[\text{Ce}(\text{Pn}^{\prime\prime})_2]$ , respectively, and were assigned to charge-transfer transitions. The comparative feature in cerocene was observed at 469 nm ( $\epsilon = 8000$ ).<sup>[102]</sup>

For both  $[\text{Ce}(\text{Pn}^*)_2]$  and  $[\text{Ce}(\text{Pn}^{\prime\prime})_2]$  systems, XANES studies revealed intermediate-valent systems, with a formal valence close to  $\text{Ce}^{\text{III}}$ .<sup>[129,130]</sup> In the case of  $[\text{Ce}(\text{Pn}^*)_2]$ , the  $f$ -occupancy was determined by fitting the variable-temperature Ce  $L_3$ -edge XANES spectra. A value  $n_f = 0.87 \pm 0.05$  close to that in  $[\text{Ce}(\text{Cot})_2]$  ( $n_f = 0.89 \pm 0.03$ ) was obtained over the whole temperature range (30–300 K).

DFT calculations were carried out on  $[\text{Ce}(\text{Pn}^*)_2]$  and on the model  $[\text{Ce}(\text{Pn})_2]$  complex.<sup>[129,130]</sup> Although such calculations could not accurately reproduce the observed multiconfigurational ground state, they helped to identify trends in the electronic structure. Contributions from the  $\text{Ce}^{\text{IV}} L^0$  and  $\text{Ce}^{\text{III}} L^1$  configuration were suggested with, in the latter configuration, the  $f$ -electron antiferromagnetically coupled to a hole in the ligand shell ( $L$ ) of the same symmetry. Similarly to what has been discussed in the case of cerocene, the *observed* oxidation state, as determined experimentally from XANES data, is closer to  $\text{Ce}^{\text{III}}$ ,<sup>[129]</sup> whereas the *formal* oxidation state, derived from the redox potential and the apparent diamagnetism, might be better described as  $\text{Ce}^{\text{IV}}$ .<sup>[130]</sup>

Further *ab initio* calculations were carried out independently by the groups of Kaltsoyannis and Dolg.<sup>[131,132]</sup> Using the same methodology as described for the analysis of cerocene (see above),<sup>[125]</sup> CASPT2 calculations were performed to determine the electronic ground state of  $[\text{Ce}(\text{Pn})_2]$ . A particularly large active space correlating 12 electrons in 16 orbitals was used, which allows for occupation of any of the twelve  $4f$  and  $5d$  levels. Although the symmetry of the ground state,  $^1A_1$ , is in agreement with that obtained by DFT calculations, the multiconfigurational character of the ground state is not accurately described by single-configuration DFT calculations. Analysis of the NOOs derived from CASPT2 calculations led to a calculated  $f$ -occupancy  $n_f = 0.78 \pm 0.04$  in good agreement with that obtained experimentally ( $n_f = 0.87 \pm 0.05$ ).<sup>[131]</sup> These calculations also reproduced the energy of the first band in the UV/Vis spectrum of  $[\text{Ce}(\text{Pn}^*)_2]$  with a great accuracy.<sup>[131]</sup>

Similarly to the calculations performed on cerocene,<sup>[48,49]</sup> Dolg investigated the ground-state electronic structure of  $[\text{Ce}(\text{Pn})_2]$  by using advanced CASSCF calculations.<sup>[132]</sup> By means of a rotation of the CASSCF natural orbitals, leaving the wavefunction and total energy invariant, a dominant  $4f^1\pi^1$  configuration based on nearly pure  $\text{Ce} 4f$  and ligand  $\pi$  orbitals was ob-

tained. This description is particularly adapted to illustrate the *observed* oxidation state determined experimentally.

These two substituted pentalene cerium complexes are further examples of self-contained Kondo effect in a single molecule.

## 2.6. Other formally tetravalent lanthanide complexes

Until very recently, no other lanthanide than cerium was reported as a molecular complex in the formal +IV oxidation state.<sup>[23,25]</sup> Also, formal  $\text{Ce}^{\text{IV}}$  complexes are not restricted to organometallic complexes and other coordination compounds have been reported (Figure 8).

Mixed valence in cerium bis(phthalocyaninato)cerium  $[\text{Ce}(\text{Pc})_2]$  (Figure 8) complexes has been established on the basis of IR and Ce3d XPS spectroscopic data. The cerium centre in these complexes is neither tri- nor tetravalent.<sup>[133]</sup> Although similarities in the IR spectra of  $[\text{Ce}(\text{Pc})_2]$  and of trivalent  $[\text{Ln}(\text{Pc})_2]$  complexes supported a formal  $\text{Ce}^{\text{III}}$  view, careful analysis of the different absorption bands revealed discrepancies with other trivalent  $[\text{Ln}(\text{Pc})_2]$  complexes. The absorption band at around  $880 \text{ cm}^{-1}$  was found to be especially sensitive to the ionic radius of the metal within the lanthanide series, and a linear correlation between the band energy and the metal ionic radius was established. The observed absorption band in  $[\text{Ce}(\text{Pc})_2]$  suggested an ionic radius of approximately  $1.01 \text{ \AA}$  for the Ce centre in  $[\text{Ce}(\text{Pc})_2]$ , which is intermediate between the ionic radii of  $\text{Ce}^{\text{III}}$  ( $1.14 \text{ \AA}$ ) and  $\text{Ce}^{\text{IV}}$  ( $0.96 \text{ \AA}$ ) ions in similar coordination environments. Ce3d XPS data further supported a cerium mixed-valent complex with contributions from the  $[(\text{Ce}^{4+})(\text{Pc}^{2-})_2]$  and  $[(\text{Ce}^{3+})(\text{Pc}^{\cdot-})(\text{Pc}^{2-})]$  configurations in the ground state.<sup>[133]</sup> The valence of Ce in a series of tetrapyrrole double-decker complexes bearing (na)phthalocyaninato and porphyrinato ligands with different electronic properties has also been investigated.<sup>[134]</sup> The UV/Vis absorption spectra of the substituted Ce phthalocyaninate complexes displayed two ligand absorption bands (the phthalocyanine Q-bands) at un-

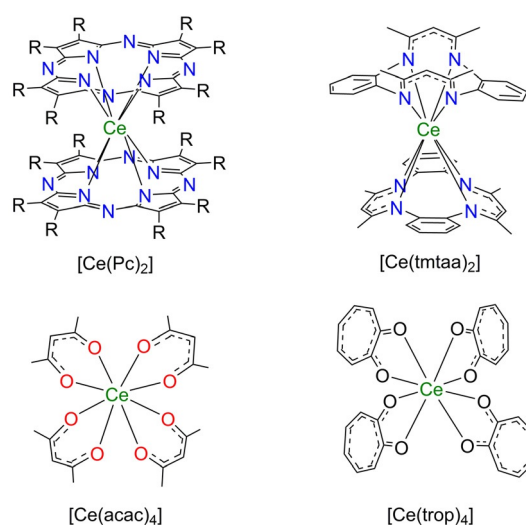


**Figure 8.** Structures of formal  $\text{Ce}^{\text{IV}}$  complexes bearing non-organometallic ligands.

expected wavelengths. Using a similar approach as above, the ionic radius of the Ce centre was estimated through a linear correlation between the energy of the electronic transition and the lanthanide ionic radius. From this study, the ionic radius of the cerium centre was found to be smaller than that expected for a  $\text{Ce}^{\text{III}}$  ion (1.143 Å) and close to that of  $\text{Nd}^{\text{III}}$  (1.109 Å), suggesting an intermediate valence between +III and +IV for the Ce centre.<sup>[134]</sup> Further evidence was given by  $\text{L}_3$ -edge XANES analyses, which revealed two edge absorption peaks corresponding to the  $\text{L}4\text{f}^0$  and  $\text{L}4\text{f}^1$  contributions.

Magnetic susceptibility studies on  $[\text{Ce}(\text{tmtaa})_2]$  ( $\text{tmtaaH}_2$  corresponding to tetramethyldibenzotetraaza[14]annulene), cerium tetrakis(acetylacetonate)  $[\text{Ce}(\text{acac})_4]$  and cerium tetrakis(tropolonate)  $[\text{Ce}(\text{trop})_4]$  (Figure 8) as a function of temperature have shown that these formally  $4\text{f}^0$  complexes exhibit temperature-independent paramagnetism (TIP) with low but positive values of  $\chi$  for the metal centre (after subtraction of the ligand diamagnetic contribution).<sup>[135–137]</sup> The small energy difference between the ground state (open-shell singlet) and the first excited state (open-shell triplet) was found to be responsible for the TIP behaviour. In an applied magnetic field, thermal mixing of the two states occurs with a relative population following the Boltzmann distribution, which results in a small net value of the magnetic moment  $\mu_{\text{eff}}$  (in the range 0.1–0.7  $\mu_{\text{B}}$  at 300 K). The experimental results were therefore not consistent with diamagnetic cerium centres (associated with negative values of  $\chi$ ), which would arise from a single  $4\text{f}^0$   $\text{Ce}^{\text{IV}}$  ground-state configuration. Ce  $\text{L}_3$ -edge XAS studies and ab initio calculations based on multireference wavefunctions further confirmed a  $\text{Ce}^{\text{III}} 4\text{f}^1$  and  $\text{Ce}^{\text{IV}} 4\text{f}^0$  multiconfigurational character in the ground states of these complexes. The calculations were performed by using CASSCF/CAS-SDCI methodologies starting with a relatively large active space (four electrons distributed over five orbitals) further reduced to two active electrons. Averaged orbitals of the  $\text{f}^2\text{L}^6$ ,  $\text{f}^1\text{L}^7$  and  $\text{f}^0\text{L}^8$  states were used in the calculations. Finally, the addition of configuration interaction calculations on top of the CASSCF was necessary to obtain satisfactory results. The combination of one cerium 4f electron and one ligand-based electron can lead to four possible electronic states (Figure 9).

The calculations supported an open-shell singlet ground state. The first excited state, an open-shell triplet, was found to be close in energy and only 40–75  $\text{cm}^{-1}$  higher in energy than the open-shell singlet ground state. In contrast, the  $4\text{f}^0$  closed-shell singlet is much higher in energy (> 400  $\text{cm}^{-1}$ ), and so is the  $4\text{f}^2$  closed-shell singlet.

Ce	L	
$\uparrow\downarrow$	—	closed-shell, $\text{Ce}(\text{II}, \text{f}^2)(\text{L}^{-2/4})_4$
—	$\uparrow\downarrow$	closed-shell singlet, $\text{Ce}(\text{IV}, \text{f}^0)(\text{L}^{-4/4})_4$
$\uparrow$	$\uparrow$	triplet (open-shell), $\text{Ce}(\text{III}, \text{f}^1)(\text{L}^{-3/4})_4$
$\uparrow$	$\downarrow$	open-shell singlet, $\text{Ce}(\text{III}, \text{f}^1)(\text{L}^{-3/4})_4$

Figure 9. Different configurations considered. Adapted from Ref. [136].

Very recently, high-energy-resolution fluorescence detection X-ray absorption spectroscopy (HERFD-XAS) has been used to analyse a formal di-cerium(IV) phenolate complex and confirmed mixed valency with considerable  $4\text{f}^0$  character.<sup>[138]</sup> In addition, the multiconfigurational ground state of formal  $\text{Ce}^{\text{IV}}$  complexes stabilised by imidophosphorane ligands or imidophosphorane-functionalised guanidinate ligands has been established through Ce  $\text{L}_3$ -edge XANES studies.<sup>[139–141]</sup> Notably, the imidophosphorane  $\text{Ce}^{\text{IV}}$  complexes exhibited the lowest reported relative proportion of  $\text{Ce}^{\text{III}} \text{L}^1$  character ( $n_{\text{f}}=0.38(2)$ ). However, some limits to the dominant two-peak model in the analysis of the  $\text{L}_3$ -edge XANES spectra of tetravalent lanthanides were presented.<sup>[140]</sup>

In 2019, access to the first molecular formal  $\text{Tb}^{\text{IV}}$  complexes has been described in independent reports by the groups of La Pierre and Mazzanti by using imidophosphorane and bulky siloxide ligands, respectively (Figure 10).<sup>[19,20]</sup> The use of bulky  $\text{Ph}_3\text{SiO}$  ligands further allowed, in 2020, the synthesis of the first molecular  $\text{Pr}^{\text{IV}}$  complex.<sup>[22]</sup> The reduction potential associated with the  $\text{Pr}^{\text{IV}}/\text{Pr}^{\text{III}}$  couple (+3.4 V) is very close to that of the  $\text{Tb}^{\text{IV}}/\text{Tb}^{\text{III}}$  couple (+3.3 V), which supports that similar ligand environments and procedures might be used to access both  $\text{Tb}^{\text{IV}}$  and  $\text{Pr}^{\text{IV}}$  complexes.<sup>[21,22]</sup>

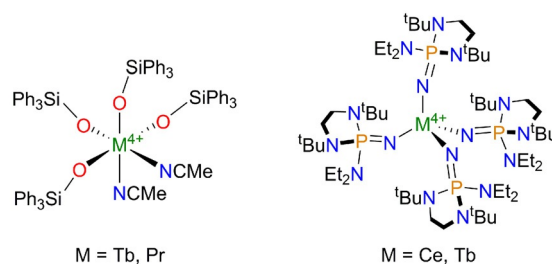


Figure 10. Recent ligand environments used for the stabilisation of formal tetravalent lanthanide compounds including  $\text{Tb}^{\text{IV}}$  and  $\text{Pr}^{\text{IV}}$  complexes.

The electronic structure of the imidophosphorane-stabilised  $\text{Tb}^{\text{IV}}$  complex was investigated by magnetic susceptibility, EPR and XANES studies.<sup>[20]</sup> A multiconfigurational behaviour similar to that observed in  $\text{TbO}_2$  was established by Tb  $\text{L}_3$ -edge XAS measurements. The characteristic double-peak structure was attributed to both  $\text{Tb}^{\text{IV}}$  and  $\text{Tb}^{\text{III}}$  configurations in the final state. The relative amount of the  $\text{Tb}^{\text{III}} \text{L}^1 4\text{f}^0 + 1\text{d}^0$  character in the ground state has been evaluated to be 0.39(4), a value similar to that observed for  $\text{TbO}_2$  (0.42(3)).<sup>[111]</sup> These results indicate that ligand control of the multiconfigurational behaviour is of utmost importance to achieve stabilisation of formal  $\text{Ln}^{\text{IV}}$  complexes.

The multiconfigurational ground state established in these complexes shows that the mixed valency observed in formal  $\text{Ln}^{\text{IV}}$  compounds is not restricted to organometallic complexes but can be extended to other coordination compounds featuring electron-rich donor ligands.

## 2.7. [Cp\*<sub>2</sub>Yb(L)] adducts with L = N-heterocyclic redox-active ligands

The group of Andersen engaged in an in-depth study of the electronic structure and physical properties of ytterbocene adducts by using 2,2'-bipyridyl (bipy), 1,10-phenanthroline (phen) and other diazabutadiene (dad) ligands, which are known to be redox non-innocent or redox-active ligands (Figure 11).<sup>[32,50,51,84,105,142–147]</sup> These compounds provide strong

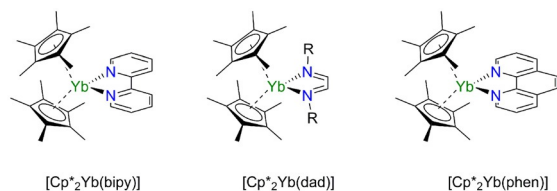


**Figure 11.** Structures of ytterbocene adducts with nitrogen-based redox-active ligands.

magnetic and spectroscopic evidence that both Yb<sup>II</sup> f<sup>14</sup> and Yb<sup>III</sup> f<sup>13</sup> configurations are represented in the ground state. In such complexes, depending on the ytterbocene substituents and on the nature of the ligand (bipy vs. phen), reduction of the redox-active ligand by the Yb<sup>II</sup> centre may occur. The detailed analyses of the reasons allowing the transfer or not will be examined in section 3. In these complexes, the reduced nature of the bipyridyl ligand in [Cp\*<sub>2</sub>Yb(bipy)] can be qualitatively assessed by IR measurements where strong absorption bands in the regions 800–1000 cm<sup>-1</sup> and 1490–1575 cm<sup>-1</sup> are typical for a bipyridyl radical anion.<sup>[84,142]</sup> In addition, analysis of the bond lengths within the bipyridyl ligand in the X-ray structures was indicative of the neutral or reduced character of the ligand and therefore of the ytterbium valence (for example, a variation in the C–C backbone distance of the bipy ligand from 1.49 (Yb<sup>II</sup>) to 1.43 Å (Yb<sup>III</sup>) was observed).<sup>[50,84]</sup> The distance between the Yb and the centroid of the Cp\* ligand was also suggested as an efficient probe of the ytterbium valence, with distances varying continuously from 2.74 (Yb<sup>II</sup>) to 2.59 Å (Yb<sup>III</sup>).<sup>[51]</sup> Raman spectroscopy gave further evidence that the ligands in the [Cp\*<sub>2</sub>Yb(L)] (L = bipy, phen) adducts were reduced radical anions.<sup>[85]</sup> Additionally, in the UV/Vis/near IR electronic absorption spectra of [Cp\*<sub>2</sub>Yb(L)] (L = bipy, phen), f–f transition bands typical of Yb<sup>III</sup> compounds were detected but with some singularities.<sup>[85]</sup> The intensities of the bands in the neutral complexes were 5–10 times greater than those in the corresponding oxidised cationic complexes, revealing unusually large oscillator strengths for f–f transitions. In the case of [Cp\*<sub>2</sub>Yb(phen)], the energies (ca. 11 000 cm<sup>-1</sup>) and separations between adjacent f–f bands (ca. 510 and 780 cm<sup>-1</sup>) were found significantly different from the values found in the cationic oxidised complex [Cp\*<sub>2</sub>Yb(phen)]<sup>+</sup>.<sup>[85]</sup>

Magnetic studies on [Cp\*<sub>2</sub>Yb(L)] (L = bipy, phen) revealed that these complexes were not simple Yb<sup>II</sup> f<sup>14</sup> diamagnetic adducts. The magnetic moments at room temperature were lower than that expected for an Yb<sup>III</sup> ion coordinated by a radi-

cal anionic ligand with non-interacting spins (4.5–5 μ<sub>B</sub>). The low magnetic moment of the ground state can be explained by antiferromagnetic coupling between the Yb<sup>III</sup> centre and the radical anion, and is consistent with the field dependence observed at low temperatures. The effective magnetic moment was also found to depend on the substituents on the cyclopentadienyl rings (Cp\*, Cp<sup>tt</sup> (η<sup>5</sup>-1,3-tBu<sub>2</sub>C<sub>5</sub>H<sub>3</sub>), Cp<sup>rr</sup> (η<sup>5</sup>-1,3-(Me<sub>3</sub>Si)<sub>2</sub>C<sub>5</sub>H<sub>3</sub>)) and reflects the extent of electron transfer from the Yb<sup>II</sup> centre to the N-heterocyclic ligand (see section 3).<sup>[84]</sup> Although the 1/χ versus T plot of the phenanthroline adducts of Cp\*<sub>2</sub>Yb, Cp<sup>tt</sup><sub>2</sub>Yb and (C<sub>5</sub>Me<sub>4</sub>H)<sub>2</sub>Yb featured as expected a linear dependence, a nonlinear shape was observed for [Cp\*<sub>2</sub>Yb(bipy)] and [(C<sub>5</sub>Me<sub>4</sub>H)<sub>2</sub>Yb(bipy)] with a maximum χ value at 380 K. Similarly, analysis of the <sup>1</sup>H NMR spectra of [Cp\*<sub>2</sub>Yb(bipy)] at variable temperatures revealed a nonlinear plot for δ versus 1/T, which cannot be explained by a Curie–Weiss behaviour.<sup>[84]</sup> More generally, variable-temperature analysis of the <sup>1</sup>H NMR chemical shifts of ytterbocene adducts constitutes a useful tool to probe the magnetic behaviour, especially to reveal intermediate valence.<sup>[143,144,146]</sup> Further investigation of the magnetic properties was carried out by using the sealed quartz tube technology, allowing a more precise determination of the magnetic moment for highly air-sensitive and weakly paramagnetic compounds, which feature low but non-zero values of μ.<sup>[142]</sup> This is especially the case for [Cp<sup>tt</sup><sub>2</sub>Yb(bipy)] and [Cp<sup>rr</sup><sub>2</sub>Yb(bipy)], which were found to be weakly paramagnetic. Their 1/χ versus T plots were significantly curved but did not exhibit the unusual behaviour evidenced in [Cp\*<sub>2</sub>Yb(bipy)] and [(C<sub>5</sub>Me<sub>4</sub>H)<sub>2</sub>Yb(bipy)]. To account for the unusual magnetic behaviour observed in bipyridine, phenanthroline and in a related 4'-cyanoterpyridyl adduct of ytterbocene, a thermally induced valence tautomeric equilibrium between paramagnetic 4f<sup>13</sup>–π\*<sup>1</sup> and diamagnetic 4f<sup>14</sup>–π\*<sup>0</sup> forms was first suggested.<sup>[84,85,148]</sup> However, the lack of temperature dependence of the ytterbium valence observed in XANES studies<sup>[50,105,145]</sup> and variable-temperature electronic absorption spectra<sup>[149]</sup> were not consistent with valence tautomerism. Moreover, the higher contribution of the Yb<sup>II</sup> 4f<sup>14</sup>–π\*<sup>0</sup> configuration at low temperature was not consistent either with genuine redox-isomerism in a lanthanide complex. Indeed, valence tautomerism being an entropy-driven process, the isomeric form with the shorter metal–ligand bond lengths, that is, involving the more oxidised Yb<sup>III</sup> ion, should be stabilised at lower temperatures.<sup>[150,151]</sup>

For many ytterbocene adducts, temperature-independent paramagnetism (TIP) was observed at low temperatures, which can be interpreted as a van Vleck interaction between the ground-state singlet and the triplet configuration at some higher energy.<sup>[50]</sup> The magnetic behaviour can be explained by a multiconfigurational singlet ground state, with contributions of both Yb<sup>II</sup> f<sup>14</sup> and Yb<sup>III</sup> f<sup>13</sup> configurations, which is lower in energy than the triplet configuration. When the temperature thermally allows the population of the triplet configuration, the susceptibility initially increases (out of the TIP regime) and then decreases, as in a conventional Curie–Weiss paramagnet.<sup>[50]</sup>

In the case of methyl-substituted bipyridine and phenanthroline adducts of ytterbocene, unusual magnetic susceptibility data were observed and supported a temperature-dependent variation of the Yb valence.<sup>[51,145,147]</sup> In several cases, the presence of inflection points was observed in the plots of  $\chi T$  versus  $T$ , which was rationalised by a multiconfigurational open-shell singlet ground state with low-lying excited states.<sup>[51,146,152]</sup> Especially, different open-shell singlets were found below the triplet state and their thermal population with increasing temperatures accounts for the unusual temperature dependence of the magnetic data (see below). Ab initio calculations were first performed by using the model  $[\text{Cp}_2\text{Yb}(\text{bipy})]$  compound,<sup>[50]</sup> and further improved by using  $\text{Cp}^*$  (instead of Cp) fragments.<sup>[51]</sup> Such calculations typically involve a first DFT geometry optimisation of the molecule using small core Relativistic Effective Core Potentials (RECP)<sup>[120,121,123,153]</sup> followed by CASSCF calculations. After testing active spaces of different sizes and careful comparison of the results, the smallest active space giving the same qualitative results was used for the complete calculations.<sup>[154]</sup> To obtain a better adequation between the calculations and the experimental results, a larger active space that included additional  $\pi^*$  configurations for the substituted bipyridine ligand was used in the computational model and a perturbative PT2 correction was added.<sup>[51]</sup> The calculations revealed that the ground states and first excited states were dependent on the number and position of the methyl substituents.<sup>[51,145,147]</sup> In addition, a correlation between the relative populations of the  $f^{13}$  and  $f^{14}$  configurations and the redox properties of the two fragments (ytterbocene and redox-active ligand) was established.<sup>[145]</sup>

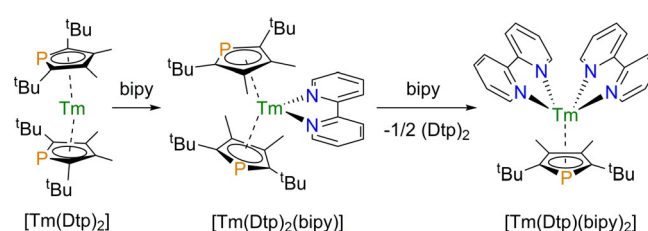
To support the magnetism studies, Yb  $L_{3\text{-edge}}$  XANES data of  $[\text{Cp}^*_2\text{Yb}(\text{bipy})]$  were recorded at different temperatures. The f-hole occupancy ( $n_f$ ), which is directly linked to the ytterbium valence ( $v = 2 + n_f$ ), was estimated to be  $0.80 \pm 0.03$  for  $[\text{Cp}^*_2\text{Yb}(\text{bipy})]$  without any change from 10 K up to decomposition at above approximately 400 K.<sup>[105]</sup> Similar results were obtained for a series of 4,4'-disubstituted bipyridine and 1,4-diazabutadiene (dad) adducts of ytterbocene, which were found to feature between 83 and 95% of trivalent character with no significant change of the lanthanide valence with temperature (in the range 20–300 K).<sup>[50]</sup> In methyl-substituted bipyridine adducts of ytterbocene, depending on the number and position of the methyl substituents, Yb  $L_{3\text{-edge}}$  XANES data revealed different contributions of the  $\text{Yb}^{\text{II}}$  and  $\text{Yb}^{\text{III}}$  forms with temperature and therefore temperature-dependent variation of the Yb valence.<sup>[51,145,147]</sup>

In addition, the coordination of unsubstituted imino-pyridine ligands to  $\text{Cp}^*_2\text{Yb}$  resulted in an electronic transfer reaction and formation of an  $\text{Yb}^{\text{III}}$  complex featuring a radical-anionic ligand.<sup>[155]</sup> Variable-temperature magnetic measurements revealed a maximum at 170 K in the  $\chi_M$  versus  $T$  data, consistent with a multiconfigurational ground state for the Yb ion. Ab initio calculations (CASSCF) using the same methodology as above, supported an open-shell singlet ground state constituted of 78%  $\text{Yb}^{\text{III}}$  and 22%  $\text{Yb}^{\text{II}}$ .

CASSCF and CASPT2 calculations were also carried out on the 1,4-diazabutadiene (dad)  $[\text{Cp}^*_2\text{Yb}(\text{dad})]$  and  $[\text{Ind}_2\text{Yb}(\text{dad})]$  ( $\text{Ind} = \eta^5\text{-C}_9\text{H}_7$ ) complexes.<sup>[156]</sup> Owing to the near degeneracy of the low-lying electronic states, DFT methods were again not appropriate to determine the correct electronic ground state of the system and explain its magnetic properties. Both ligands on the ytterbium centre,  $\text{Cp}^*$  and indenyl on the one hand, bipy and DAB on the other hand, were found to have an effect on the electronic ground-state configuration. Only one of the possible ligand combinations, corresponding to the diamagnetic  $[\text{Ind}_2\text{Yb}(\text{bipy})]$  complex, could be properly studied by using a standard single-configuration DFT approach. Compared with ab initio calculations, DFT calculations are less computationally demanding and can be applied to the real molecules. In contrast, ab initio calculations are typically performed on reduced model systems. The latter should, however, be realistic enough to reproduce the electronic complexity and specificities of the experimental systems.

## 2.8. Other lanthanide complexes with redox-active ligands

Multiconfigurational ground states were also invoked to rationalise the unusual magnetic properties of bipyridine and bisphosphinine (phosphorus analogues of bipyridine) adducts of bis(phospholyl) thulium(II) ( $[\text{Tm}(\text{Dtp})_2]$ , see Scheme 3) but the precise electronic structures of the complexes have remained elusive to date.<sup>[157]</sup>



**Scheme 3.** Synthesis and reactivity of a bipyridine adduct of  $[\text{Tm}(\text{Dtp})_2]$ .<sup>[157]</sup>

Recently, the electronic structures of lanthanide tetrakisbipyridine complexes were investigated.<sup>[158]</sup> Both magnetic susceptibility measurements and  $L_{3\text{-edge}}$  XANES data on the Ce and Yb species were consistent with the metals being trivalent. CASSCF calculations were performed on the closed-shell  $\text{La}^{\text{III}}$  and  $\text{Lu}^{\text{III}}$  ( $f^0$  and  $f^{14}$  configuration, respectively) complexes, as well as on the  $\text{Ce}^{\text{III}}$  and  $\text{Yb}^{\text{III}}$  derivatives featuring one f-electron ( $f^1$ ) or one f-hole ( $f^{13}$ ), respectively. The different multiconfigurational nature of the corresponding ground states helped understand the slight differences observed in their physical properties such as subtle bond length variations and magnetic susceptibility dependencies with temperature. For such systems, multireference calculations,<sup>[57,58]</sup> as opposed to single reference DFT calculations, are often necessary to properly reproduce some of the physical properties such as temperature dependency of the magnetic susceptibility.



## 2.9. Concluding remarks on spectroscopic singularities

The systems presented above can be considered molecules in which the oxidation number is ambiguous and they are representatives of intermediate valence compounds using the term as defined by the physics community. The contribution of the ligand and metal charge transfer configuration will allow the formation of a state, in which the covalency, that is, the electronic delocalisation extent, is substantial. Clearly, in Yb, Eu, Tm and Ce compounds, the redox potential is adapted for these charge transfers with the ligand. It would mean that the energy match or mismatch between ligand and metal orbitals is at the origin of the situation the phenomenon; at least as much as the symmetry consideration for spatial overlap.

## 3. Energy and Symmetry Considerations

All these spectroscopic singularities, reinforced by adapted theoretical computations, clearly established that coordination compounds (or organometallics) of lanthanides can develop intermediate-valent states, that is, multiconfigurational energy states with configurations featuring different oxidation states. In these compounds, the relative ratio between their configurations varies and can be quantified from adapted experimental measurements and confirmed by adapted theoretical computations. An important point going forward is the rationalisation of this ratio from simple symmetric and energetic considerations.

The covalency represents the extent of the electronic delocalisation over both the metallic and ligand sites, as defined by Neidig and co-authors [Equation (2)].<sup>[34]</sup> In this description, to allow a non-zero mixing coefficient, that is, covalency, two parameters are at play: the ligand and metal orbital overlap, and the energy difference between both fragments. In lanthanide compounds, little overlap is expected between these orbitals as f-orbitals are core orbitals. Nevertheless, according to Equation (2), the covalency can also be maximised when the energy gap is minimised. In this situation, the electronic density is statistically delocalised over both the ligand and metal radical, leading to an intermediate-valent charge at the lanthanide centre.

$$\sigma = \frac{\varphi_M + \lambda \varphi_L}{\sqrt{1 + 2\lambda S_{ML} + \lambda^2}} \quad \lambda = \frac{H_{ML}}{E_M^0 - E_L^0} \quad (2)$$

where  $\sigma$  is the mixing metal and ligand orbital from perturbation theory of the ionic limit,  $\varphi_M$  is the metal orbital and  $\varphi_L$  the ligand orbital, both characterised by the metal and ligand energies,  $E_M^0$  and  $E_L^0$ .  $S_{ML}$  is the orbital overlap,  $\lambda$  the mixing coefficient and  $H_{ML}$  the off-diagonal matrix element of the Hamiltonian. Note that in the Hückel theory,  $H_{ML}$  is proportional to  $S_{ML}$ .

For example, if  $[U(\text{Cot})_2]$  and  $[\text{Ce}(\text{Cot})_2]$  are compared,<sup>[106]</sup> the former has greater metal–ligand overlap, whereas the latter has better metal–ligand energy matching, which results in so-called “degeneracy-driven covalency”,<sup>[34]</sup> and participates in the bonding while simultaneously appearing localised.

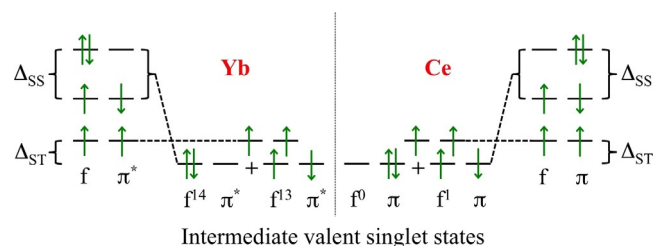


**Figure 12.** Qualitative energy level diagram showing the origin of the intermediate valence states for ytterbium and cerium complexes.

Overall, in Ce and Yb complexes, the description is simpler. They are empty—or full shell—in one configuration and singly occupied—or having only one hole—in the other. The energy diagram of both cases is shown in Figure 12.<sup>[50]</sup> The mixing of the singlet configurations results in a multiconfigurational state of lower energy, in which the two configurations have different valency, leading to intermediate-valent states. It is clear from this energy scheme that the energy difference between the open-shell and closed-shell singlets,  $\Delta_{SS}$ , and the energy gap singlet-triplet  $\Delta_{ST}$  are going to govern the overall electronic structure.

As discussed above, a series of complexes with substituted bipyridine and diazabutadiene ligands with the  $\text{Cp}^*_2\text{Yb}$  fragments has been synthesised in several articles from the Andersen group.<sup>[51,145]</sup> The energy of the ligand fragment and that of the metal fragment,  $E_M$  and  $E_L$ , which is intimately related to  $\Delta_{SS}$ , can be extrapolated from their respective redox potentials.<sup>[50,145]</sup> As written in the previous paragraph,  $L_3$ -edge XANES data indicated an  $n_f$  value of 0.83 for  $[\text{Cp}^*_2\text{Yb}(\text{bipy})]$ , that is, an intermediate-valent ground state composed of 83%  $\text{Yb}^{\text{III}}$  and 17%  $\text{Yb}^{\text{II}}$ . This ratio can evolve depending upon the substituents added to the bipy, which change the ligand redox potential. In other words, when substituents decrease the redox potential, the  $n_f$  value becomes lower and the valency closer to  $\text{Yb}^{\text{II}}$ . Likewise, when substituents increase the redox potential, the  $n_f$  gets closer to 1 and the net valency approaches that of  $\text{Yb}^{\text{III}}$ . This effect can be easily verified by synthesising the 3,3'- $\text{Me}_2\text{bipy}$  adduct of  $\text{Cp}^*_2\text{Yb}$ , which has a  $n_f$  value of 0.17(2) for a reduction potential of the ligand below  $-2.8$  V (Figure 13).

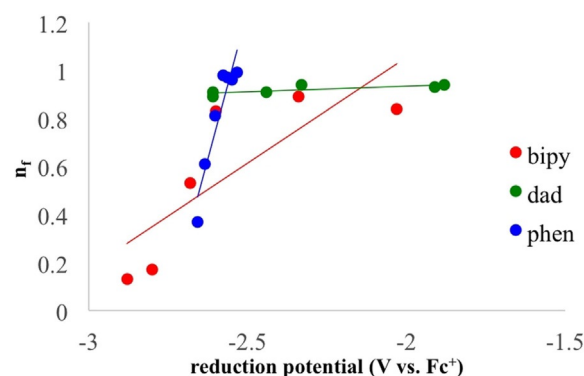


**Figure 13.** Plot of the redox potentials of the (substituted) bipy, phen and dad ligands taken from the literature<sup>[50,145,159,160]</sup> versus the measured  $n_f$  for each series. Linear fitting is only to guide the eye.

This relatively low reduction potential is due to the steric hindrance of the two methyl groups, which are close to each other, inducing a NCCN torsion angle that lowers the reduction potential. As an additional note, when the reduction potential of the metallic fragment is increased, for example, when the Cp\* ligand is replaced by the Cp ligand, the  $n_f$  also decreases; the  $n_f$  of [Cp\*<sub>2</sub>Yb(bipy)] is 0.83(2) whereas that of [Cp<sub>2</sub>Yb(bipy)] is 0.30(1).

The problem became more complex after another series of substituted bipyridine ligands exhibited multiple intermediate valence singlet states below the triplet state. This situation is possible when several low-lying  $\pi^*$  orbitals of the ligand are close enough to accommodate spin density from the Cp\*<sub>2</sub>Yb fragment; each orbital then has a configuration with a given ratio ( $n_f$ ). Figure 14 represents a typical situation. The different natures of the multiple intermediate-valent singlet states were identified thanks to the L<sub>3</sub>-edge XANES data combined with the temperature-dependent magnetic data. As a result of the different ratio in each configuration, the overall  $n_f$  and thus the intermediate valency becomes temperature dependent. The corresponding thermodynamic parameters can be extracted by fitting the temperature-dependent  $n_f$  by using a Boltzmann distribution; these values can be then incorporated in the analysis of the magnetic data.

In the case of 4,5-diazafluorene, the magnetic data indicated three singlet states below the triplet, coming from three low-lying empty  $\pi^*$  orbitals (Figure 14).<sup>[146]</sup>

However, if the energetic consideration described above helped to estimate the  $n_f$  ratio within one series of ligands, a quick look at Figure 13 also indicates that the correlation between the redox potential and the  $n_f$  cannot be generalised and remained true only within each ligand series, the bipy, the phen and the dad series. Additionally, this correlation remained also problematic in the case of the higher energy singlet states (below the triplet) of the substituted bipy ligands. This situation thus tended to indicate that the energy is not the single factor controlling the intermediate valency: the second impor-

tant parameter is the symmetry of the  $\pi$  orbital that accepts the electron. The correlation between redox potential and  $n_f$  value is valid only for orbitals of similar symmetry.

In this matter, the study of the phenanthroline series was of great importance as the ligand is known to possess two empty  $\pi$  orbitals of similar energy that have two very different symmetries.<sup>[161]</sup> In  $C_{2v}$  symmetry, these two orbitals have b<sub>1</sub> and a<sub>2</sub> symmetry (Figure 15): b<sub>1</sub> is similar to the low-lying orbital of bipyridine and has much density located on the nitrogen atoms, which coordinate to the lanthanide metal centre; a<sub>2</sub>, however, has very little density on the nitrogen atoms and a node at the 3,8-position of the phenanthroline. A molecular orbital diagram of the f-shell orbitals indicated that the singly occupied f-orbital possesses b<sub>1</sub> symmetry in  $C_{2v}$ .<sup>[32,147]</sup>

Thus, as opposed to the bipy adduct, the phen adduct was analysed as a triplet, meaning that the symmetry orbital requirements must also be validated to stabilise the intermediate-valent singlet state. Interestingly, depending upon the substituents and their positions, the ground state can be different (triplet or intermediate valent). This means that the relative energy between the different symmetry orbitals can be modulated,<sup>[161]</sup> which then leads to the modulation of the ground state as shown by the temperature-dependent magnetic data and L<sub>3</sub>-edge XANES.<sup>[32,145–147]</sup> An important example is the 3,8-phenanthroline adduct of ytterbocene. Indeed, as the a<sub>2</sub> orbital possesses a node at the 3,8-position, when a methyl replaces the hydrogen at these positions, the energy of the a<sub>2</sub> is not modified whereas that of the b<sub>1</sub> is slightly increased; the ground state is then similar to that of the phen analogue, which is triplet (Figure 16). Accordingly, donating substituents at the 5,6-positions increase the energy of the a<sub>2</sub> and slightly increase that of the b<sub>1</sub>, leading to a situation in which both orbitals have similar energies; the singlet and triplet states have similar energies. Now, when substituents are at the 4,7-positions, the energies of both orbitals are increased but one should note that the coordination of the ytterbium fragment lowers the energy of the b<sub>1</sub> as much density is located in the nitrogen atoms. Thus, the b<sub>1</sub> becomes lower in energy and the ground state is the intermediate-valent singlet (Figure 16).

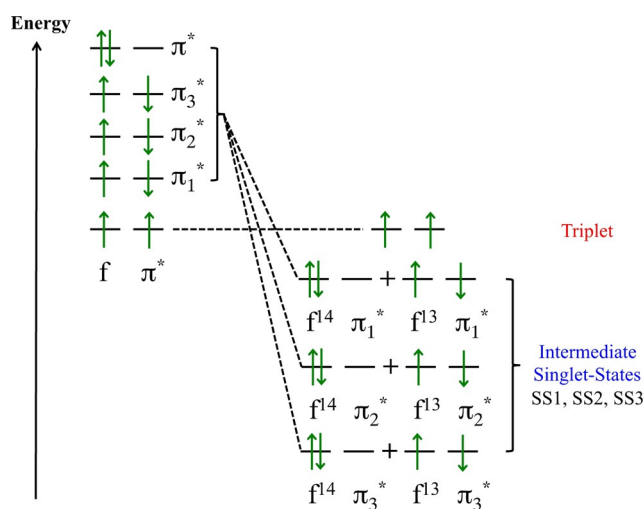


**Figure 14.** Energy scale with multiple  $\pi^*$  orbitals accepting electronic density and forming multiple intermediate-valent singlet states below the triplet.

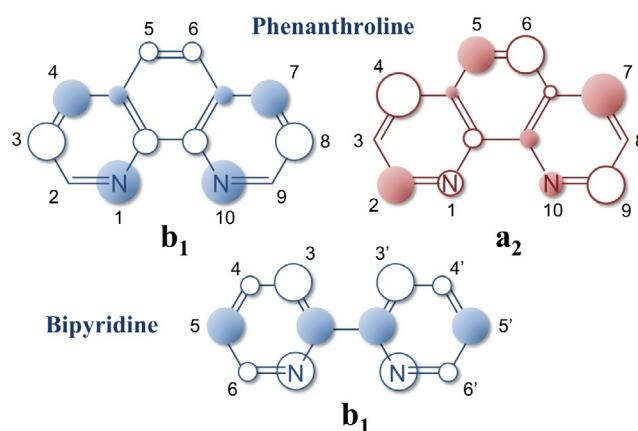


**Figure 15.** Representation of the  $\pi^*$  orbitals for bipy and phen and numbering positions.

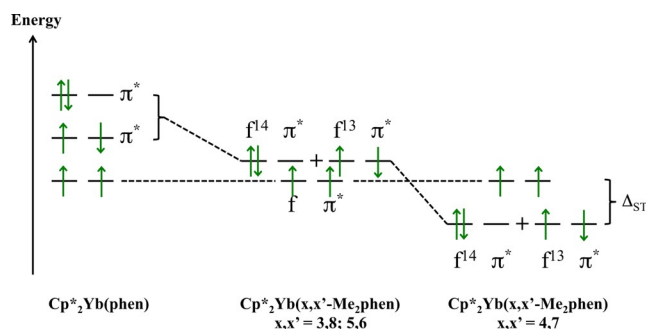
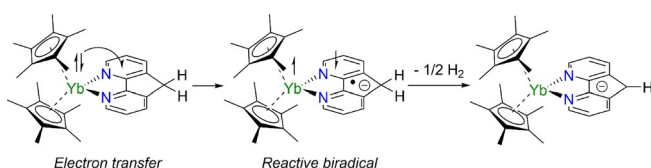


**Figure 16.** Qualitative MO diagrams showing the influence of the nitrogenated ligand on the electronic structure of the resulting complex.<sup>[147]</sup>

As it has been noted early in the literature, intermediate valence state compounds are interesting molecular Kondo systems.<sup>[47]</sup> This phenomenon can occur in nanometre-sized metallic particles and is explained by the presence of paramagnetic impurities, which break the continuous conduction band and creates localised conduction states.<sup>[64,65]</sup> In the case of the Ce and Yb compounds discussed above, the f-moment is cancelled by coupling with extended conjugated  $\pi$  systems such as bipyridine, phenanthroline, but also Cot and tropolonate among others. Additionally, the formation of these intermediate-valent states also demonstrated that the exchange coupling of a radical spin with f-electrons can be rather large, compared with what is usually known in magnetic coupling involving f-elements. Using a model that combined the ligand-to-metal charge transfer energy (Hubbard model), it was possible to determine an exchange coupling value of  $-920 \text{ cm}^{-1}$  for  $[\text{Cp}^*_2\text{Yb}(\text{bipy})]$ .<sup>[162]</sup> This very large value also explains why the use of extended  $\pi$  systems is particularly relevant for the design of compounds with high magnetic coupling between lanthanides. The presence of a  $\pi$ -radical between lanthanide metal centres increases greatly the coupling between them and led notably to performing single molecules magnets.<sup>[163–166]</sup>

## 4. Chemical Ramifications

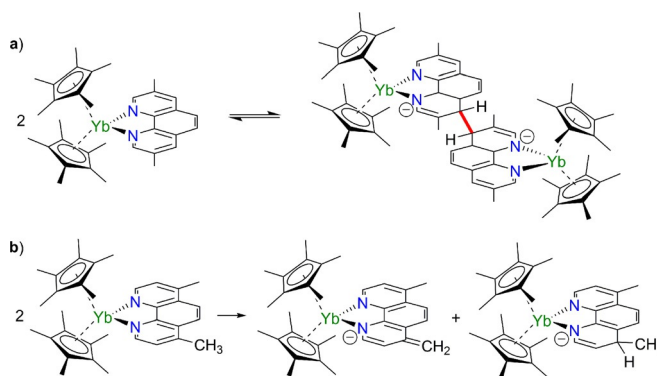
The symmetry of the orbitals became a crucial consideration when talking about reactivity as was demonstrated when the bipy was switched for other di-nitrogenated ligands such as diazafluorene and phenanthroline.<sup>[32,146,147]</sup> The  $[\text{Cp}^*_2\text{Yb}(4,5\text{-diazfluorene})]$  complex was shown by Nocton et al. to slowly release  $\text{H}_2$ , leading to the corresponding  $[\text{Cp}^*_2\text{Yb}(4,5\text{-diazfluorenyl})]$  complex (Scheme 4).<sup>[146]</sup> Experimental and computational studies indicated that the electronic structure of the com-



**Scheme 4.** Elimination of  $\text{H}_2$  from the 4,5-diazfluorene ligand triggered by the intermediate-valent behaviour.<sup>[146]</sup>

pound was similar to that of bipyridine adducts of  $\text{Cp}^*_2\text{Yb}$  with an intermediate-valent ytterbium centre and two open-shell singlet states lying below the triplet state. Analysis of the  $\pi^*$  orbitals of the ligand revealed that the LUMO + 1 orbital of the fluorene was of  $b_1$  symmetry in the  $C_{2v}$  space group and featured non-negligible spin density on the C9 carbon atom. The presence of unpaired spin density at this position helped to rationalise the observed reactivity. It is thought that the electronic structure of  $[\text{Cp}^*_2\text{Yb}(4,5\text{-diazfluorene})]$ , and the formation of a reactive biradical, is responsible for the C–H activation reaction.<sup>[146]</sup> Importantly, the configuration interaction allowed the LUMO + 1 to be substantially populated at room temperature (see Figure 14, energy of SS1, SS2, SS3), the one orbital responsible for the observed reactivity. In contrast, the biradical adducts formed in the case of bipyridine adducts of ytterbocene was more stable and not involved in further chemical evolutions.

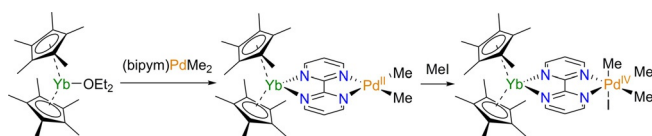
The influence of orbital symmetries on the reactivity was further evidenced in the  $[\text{Cp}^*_2\text{Yb}(\text{phen})]$  complex and its methylated analogues.<sup>[32,147]</sup> Experimental and computational results revealed a triplet ground state with a trivalent ytterbium centre, which contrasts with the open-shell singlet ground state of the bipyridine adducts. Such a different electronic structure has a direct influence on the reactivity of the complexes. Indeed, the  $[\text{Cp}^*_2\text{Yb}(\text{phen})]$  complex, as well as the (3,8)- and (5,6)-di-methylated analogues, dimerised in solution with formation of a reversible C–C bond between the two phenanthroline moieties at the 4,4'-positions (Scheme 5). This unusual reactivity originates in the energy and symmetry of the ligand empty orbitals. In the phenanthroline complex, two  $\pi^*$  orbitals of different symmetry ( $b_1$  and  $a_2$  for the LUMO and LUMO + 1, respectively) are accessible but their respective interaction with either the half-filled 4f orbitals of  $b_1$  symmetry or the empty 5d orbitals of  $a_2$  symmetry results in different cases. As discussed above, on the one hand, if the  $b_1$  orbital is lower in energy than the  $a_2$  orbital, an open-shell singlet ground state is favoured, as is the case in the bipyridine adducts of  $\text{Cp}^*_2\text{Yb}$ . On the other hand, if the ligand  $a_2$  and  $b_1$  orbitals are close in energy, as is the case in the phenanthroline adducts, the final  $a_2$  MO ends up lower in energy, resulting in



**Scheme 5.** Two different reactivities observed for two different phenanthroline derivatives (a) C4–C4' coupling, (b) C4-position-mediated intermolecular HAT.<sup>[32,147]</sup>

stabilisation of the triplet ground state (Figure 16). As this result is based on the energy of the phenanthroline ligand orbitals, it can be tuned by the presence of methyl substituents affecting the  $b_1$ – $a_2$  gap. The population of the  $a_2$  orbital results in an increased spin density in the  $\pi$  system especially at the C4 and C7 positions. The radical character at these positions is responsible for the formation of a reversible C–C bond between the two phenanthroline units (Scheme 5).<sup>[32]</sup> Nonetheless, when the phenanthroline is substituted at the 4,7-positions with methyl groups, a different configuration is observed, with a multiconfigurational open-shell singlet ground state.<sup>[147]</sup> The altered electronic structure, similar to that observed in the bipyridine adducts, results in a different reactivity. In  $[\text{Cp}^*_2\text{Yb}(4,7\text{-Me}_2\text{phen})]$ , accumulation of electronic density at the C4 and C7 positions leads to an intermolecular hydrogen atom transfer (HAT) reaction between two complexes (Scheme 5), reminiscent of the  $\text{H}_2$  elimination reactivity observed in the case of the diazafluorene complex.<sup>[146,147]</sup>

Taking advantage of the particular and tuneable electronic structures of  $[\text{Cp}^*_2\text{Yb}(\text{L})]$  systems, the influence of the ligand was further explored to modulate the chemical reactivity. The possibility of impacting the reactivity of another metal centre was explored through the formation of heterobimetallic complexes using bridging 2,2'-bipyrimidine (bipym) and 4,5,9,10-tetraazaphenanthrene (taphen) ligands instead of bipyridine and phenanthroline ligands. In 2017, the group of Nocton reported the syntheses and electronic structures of the Yb/Pd heterobimetallic complexes  $[\text{Cp}^*_2\text{Yb}(\text{L})\text{PdMe}_2]$  ( $\text{L} = \text{bipym}$  or taphen; Scheme 6).<sup>[152]</sup> Depending on the nature of the ligand, different electronic structures were observed owing to different symmetries for the corresponding LUMOs. In the bipym system, similarly to bipyridine adducts of ytterbocene, the ground state is a multiconfigurational open-shell singlet with a low-lying triplet state populated at room temperature. In contrast, the taphen complex features a triplet ground state, in analogy with the ground-state structure of the phenanthroline adduct of  $\text{Cp}^*_2\text{Yb}$ . The influence of the different electronic structures on the reactivity was exemplified in the reactivity of the complexes towards MeI. In both cases, the addition of MeI triggered an oxidative addition step, resulting in the formation of a  $\text{Pd}^{\text{IV}}$  complex. Although the resulting  $\text{Pd}^{\text{IV}}$  complex rapidly evolved through a reductive elimination process in the taphen system, it presented a much higher stability in the case of the bipym ligand, allowing isolation and characterisation. The increased stability of the  $[\text{Cp}^*_2\text{Yb}(\text{bipym})\text{PdMe}_2]$  complex is mainly due to the spin density mostly held by the N atoms in the  $b_1$  orbital, which support the Pd centre. In the taphen analogue instead, the  $a_2$  orbital is populated and features smaller coefficients on the N atoms. As a result, a lower spin density is



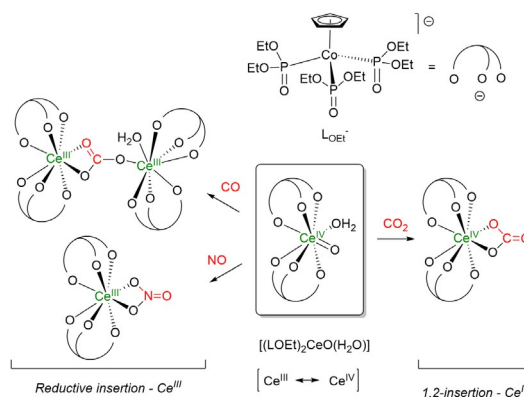
**Scheme 6.** Heterobimetallic Yb–Pd association leading to the stabilisation of a  $\text{Pd}^{\text{IV}}$  oxidation state.<sup>[152]</sup>

present next to the Pd centre, which decreases the stability of the high oxidation state  $\text{Pd}^{\text{IV}}$  complex and triggers a fast reductive elimination step as expected for such  $\text{Pd}^{\text{IV}}$  species.<sup>[152]</sup>

Another chemical ramification of the electronic structure of heterobimetallic complexes was reported with the same  $\text{Cp}^*_2\text{Yb}(\text{bipym})$  backbone using a  $\text{NiMe}_2$  fragment instead of  $\text{PdMe}_2$ .<sup>[167]</sup> Both the monometallic  $[(\text{bipym})\text{NiMe}_2]$  and the heterobimetallic  $[\text{Cp}^*_2\text{Yb}(\text{bipym})\text{NiMe}_2]$  complexes were found to react with CO, resulting in CO insertion reactions in the Ni–C bonds. Kinetic studies revealed that the intermediate-valent lanthanide-bipym fragment led to an increased stabilisation of the expected acyl intermediate through a process similar to that allowing the stabilisation of the  $\text{Pd}^{\text{IV}}$  complex discussed above.<sup>[167]</sup> This result offers a new strategy to stabilise and study reactive metal intermediates for which isolation has remained elusive to date.

The influence of the multiconfigurational character of lanthanide complexes on the reactivity was further exemplified in the case of  $\text{Ce}^{\text{IV}}$  oxo complexes supported by the bulky Kläui oxygen tripodal metallo-ligand  $[\text{CoCp}\{\text{P}(\text{O})(\text{OEt})_2\}_3]^- (\text{L}_{\text{OEt}}^-)$ , Scheme 7).<sup>[168,169]</sup>

The multiconfigurational character of the  $[(\text{L}_{\text{OEt}})_2\text{CeO}(\text{H}_2\text{O})]$  complex was established by CASSCF calculations together with magnetic susceptibility measurements. The combined experimental and theoretical results revealed a multiconfigurational ground state composed of 74% of  $\text{Ce}^{\text{IV}}$  and 26% of  $\text{Ce}^{\text{III}}$ . The reactivity of the oxocerium(IV) complexes was evaluated towards small molecules such as CO,  $\text{CO}_2$ ,  $\text{SO}_2$  and NO. Depending on the substrate, two different types of reactivity for the  $\text{Ce}=\text{O}$  moiety were observed (Scheme 7). Although a classical 1,2-insertion reactivity was observed with  $\text{CO}_2$ , which corresponds to the typical reactivity of  $\text{Ce}^{\text{IV}}$   $f^0$  complexes, the reaction with CO,  $\text{SO}_2$  and NO resulted in an unusual reductive insertion reactivity. As a result, (b)carbonate, hydrogensulfate and nitrate  $\text{Ce}^{\text{III}}$  complexes were isolated, respectively. Such a reductive insertion reactivity is thought to arise from the multiconfigurational nature of the ground state, the  $\text{Ce}=\text{O}$  moiety featuring both some  $\text{Ce}^{\text{IV}}$  oxo and  $\text{Ce}^{\text{III}}$  oxyl character. The  $\text{Ce}^{\text{III}}$  oxyl character results in a radical-like reactivity by forming a singlet metal–ligand biradical similar to the situation in cerocene.<sup>[169]</sup>



**Scheme 7.** Schematic representation of the reactivity of the oxocerium complex  $[(\text{L}_{\text{OEt}})_2\text{CeO}(\text{H}_2\text{O})]$ .<sup>[169]</sup>



## 6. Concluding Remarks

The minireview gathers the spectroscopic singularities that have been reported for lanthanide compounds. In these compounds, the net valency remains ambiguous because of possible redox events with the ligand, whether charge density is transferred from the ligand to the metal or from the metal to the ligand. In addition to physical chemistry reports containing XANES, PES and/or magnetic analysis, adapted theoretical analyses of these peculiar compounds have allowed the rationalisation of their original electronic nature: they are intermediate valent; the wavefunction of the ground and excited state is defined by multiple configurations, in which the valency is of different nature. These observations can be rationalised first from energetic considerations, as the result of the energy difference between both metallic and ligand fragments, and second from the symmetry of both fragments, which needs to be adapted to allow stabilisation of the energy with formation of an intermediate-valent energy state. This typical situation is predominant in lanthanide compounds, in which the spatial orbital overlap is small, whereas in transition metal ions or 5f complexes, the nephelauxetic effect allows the formation of molecular orbitals with delocalised electron density over both the metallic and ligand centres (so-called covalency). Both situations are, however, similar from the perspective of the Pauling electroneutrality principle. As well-established for transition metals and for 5f compounds, the strong electron correlation between a d- and/or f-parentage electron and the  $\sigma$ - and  $\pi$ -electron is then likely to influence the physical properties (relaxation, anisotropy, conductivity) but also the reactivity of these electrons: this review sheds light on several examples of this nature.

## Acknowledgments

This work is part of a project that has received funding from the *European Research Council (ERC)* under *European Union's Horizon 2020 research and innovation program* under grant agreement No 716314. CNRS and Ecole polytechnique are thanked for funding.

## Conflict of interest

The authors declare no conflict of interest.

**Keywords:** intermediate valence • lanthanides • organometallics • spectroscopy • theoretical computations

- [1] J.-C. G. Bünzli, C. Piguet, *Chem. Soc. Rev.* **2005**, 34, 1048–1077.
- [2] S. Cotton in *Lanthanide and Actinide Chemistry*, Wiley, Chichester, **2006**, pp. 61–87.
- [3] E. G. Moore, A. P. S. Samuel, K. N. Raymond, *Acc. Chem. Res.* **2009**, 42, 542–552.
- [4] D. N. Woodruff, R. E. P. Winpenny, R. A. Layfield, *Chem. Rev.* **2013**, 113, 5110–5148.
- [5] J.-L. Liu, Y.-C. Chen, M.-L. Tong, *Chem. Soc. Rev.* **2018**, 47, 2431–2453.

- [6] B. M. Day, F.-S. Guo, R. A. Layfield, *Acc. Chem. Res.* **2018**, 51, 1880–1889.
- [7] R. Pöttgen, T. Jüstel, C. A. Strassert, *Rare Earth Chemistry*, De Gruyter, Berlin, **2020**, pp. 1–654.
- [8] J.-C. G. Bünzli in *Kirk-Othmer Encyclopedia of Chemical Technology*, **2013**, pp. 1–43.
- [9] D. A. Atwood, *The Rare Earth Elements: Fundamentals and Applications*, Wiley, Chichester, **2013**, pp. 1–654.
- [10] P. Pyykko, *Chem. Rev.* **1988**, 88, 563–594.
- [11] M. N. Bochkarev, *Coord. Chem. Rev.* **2004**, 248, 835–851.
- [12] P. B. Hitchcock, M. F. Lappert, L. Maron, A. V. Protchenko, *Angew. Chem. Int. Ed.* **2008**, 47, 1488–1491; *Angew. Chem.* **2008**, 120, 1510–1513.
- [13] F. Nief, *Dalton Trans.* **2010**, 39, 6589–6598.
- [14] M. R. MacDonald, J. E. Bates, M. E. Fieser, J. W. Ziller, F. Furche, W. J. Evans, *J. Am. Chem. Soc.* **2012**, 134, 8420–8423.
- [15] M. R. MacDonald, J. E. Bates, J. W. Ziller, F. Furche, W. J. Evans, *J. Am. Chem. Soc.* **2013**, 135, 9857–9868.
- [16] M. E. Fieser, M. R. MacDonald, B. T. Krull, J. E. Bates, J. W. Ziller, F. Furche, W. J. Evans, *J. Am. Chem. Soc.* **2015**, 137, 369–382.
- [17] C. M. Kotyk, M. E. Fieser, C. T. Palumbo, J. W. Ziller, L. E. Darago, J. R. Long, F. Furche, W. J. Evans, *Chem. Sci.* **2015**, 6, 7267–7273.
- [18] W. J. Evans, *Organometallics* **2016**, 35, 3088–3100.
- [19] C. T. Palumbo, I. Zivkovic, R. Scopelliti, M. Mazzanti, *J. Am. Chem. Soc.* **2019**, 141, 9827–9831.
- [20] N. T. Rice, I. A. Popov, D. R. Russo, J. Bacsá, E. R. Batista, P. Yang, J. Telser, H. S. La Pierre, *J. Am. Chem. Soc.* **2019**, 141, 13222–13233.
- [21] A. R. Willauer, C. T. Palumbo, R. Scopelliti, I. Zivkovic, I. Douair, L. Maron, M. Mazzanti, *Angew. Chem. Int. Ed.* **2020**, 59, 3549–3553; *Angew. Chem.* **2020**, 132, 3577–3581.
- [22] A. R. Willauer, C. T. Palumbo, F. Fadaei-Tirani, I. Zivkovic, I. Douair, L. Maron, M. Mazzanti, *J. Am. Chem. Soc.* **2020**, 142, 5538–5542.
- [23] T. P. Gomba, A. Ramanathan, N. T. Rice, H. S. La Pierre, *Dalton Trans.* **2020**, 49, 15945–15987.
- [24] M. E. Fieser, M. G. Ferrier, J. Su, E. Batista, S. K. Cary, J. W. Engle, W. J. Evans, J. S. Lezama Pacheco, S. A. Kozimor, A. C. Olson, A. J. Ryan, B. W. Stein, G. L. Wagner, D. H. Woen, T. Vitova, P. Yang, *Chem. Sci.* **2017**, 8, 6076–6091.
- [25] N. Li, W.-X. Zhang, *Chin. J. Chem.* **2020**, 38, 1449–1450.
- [26] E. Prasad, B. W. Knettle, R. A. Flowers, *J. Am. Chem. Soc.* **2004**, 126, 6891–6894.
- [27] K. A. Choquette, D. V. Sadasivam, R. A. Flowers, *J. Am. Chem. Soc.* **2010**, 132, 17396–17398.
- [28] X. Zhao, L. Perrin, D. J. Procter, L. Maron, *Dalton Trans.* **2016**, 45, 3706–3710.
- [29] W. J. Evans, J. W. Grate, L. A. Hughes, H. Zhang, J. L. Atwood, *J. Am. Chem. Soc.* **1985**, 107, 3728–3730.
- [30] W. J. Evans, T. A. Ulibarri, J. W. Ziller, *J. Am. Chem. Soc.* **1988**, 110, 6877–6879.
- [31] S. Labouille, F. Nief, X.-F. Le Goff, L. Maron, D. R. Kindra, H. L. Houghton, J. W. Ziller, W. J. Evans, *Organometallics* **2012**, 31, 5196–5203.
- [32] G. Nocton, W. W. Lukens, C. H. Booth, S. S. Rozenel, S. A. Medling, L. Maron, R. A. Andersen, *J. Am. Chem. Soc.* **2014**, 136, 8626–8641.
- [33] G. Nocton, L. Ricard, *Chem. Commun.* **2015**, 51, 3578–3581.
- [34] M. L. Neidig, D. L. Clark, R. L. Martin, *Coord. Chem. Rev.* **2013**, 257, 394–406.
- [35] D. G. Karraker, *J. Chem. Educ.* **1970**, 47, 424.
- [36] K. N. Raymond, C. W. Eigenbrot, *Acc. Chem. Res.* **1980**, 13, 276–283.
- [37] S. Cotton in *Lanthanide and Actinide Chemistry*, Wiley & Sons, Chichester, **2006**, pp. 35–60.
- [38] N. C. Tomson, M. R. Crimmin, T. Petrenko, L. E. Rosebrugh, S. Sproules, W. C. Boyd, R. G. Bergman, S. DeBeer, F. D. Toste, K. Wieghardt, *J. Am. Chem. Soc.* **2011**, 133, 18785–18801.
- [39] K. Ray, T. Weyhermüller, F. Neese, K. Wieghardt, *Inorg. Chem.* **2005**, 44, 5345–5360.
- [40] K. Ray, T. Petrenko, K. Wieghardt, F. Neese, *Dalton Trans.* **2007**, 1552–1566.
- [41] C. C. Scarborough, S. Sproules, T. Weyhermüller, S. DeBeer, K. Wieghardt, *Inorg. Chem.* **2011**, 50, 12446–12462.
- [42] C. C. Scarborough, K. Wieghardt, *Inorg. Chem.* **2011**, 50, 9773–9793.
- [43] N. C. Tomson, K. D. Williams, X. Dai, S. Sproules, S. DeBeer, T. H. Warren, K. Wieghardt, *Chem. Sci.* **2015**, 6, 2474–2487.

- [44] J. England, E. Bill, T. Weyhermüller, F. Neese, M. Atanasov, K. Wieghardt, *Inorg. Chem.* **2015**, *54*, 12002–12018.
- [45] C. Wolff, A. Gottschlich, J. England, K. Wieghardt, W. Saak, D. Haase, R. Beckhaus, *Inorg. Chem.* **2015**, *54*, 4811–4820.
- [46] I. Mustieles Marín, T. Cheisson, R. Singh-Chauhan, C. Herrero, M. Cordier, C. Clavaguéra, G. Nocton, A. Auffrant, *Chem. Eur. J.* **2017**, *23*, 17940–17953.
- [47] C. S. Neumann, P. Fulde, *Z. Phys. B* **1989**, *74*, 277–278.
- [48] M. Dolg, P. Fulde, W. Kühle, C. S. Neumann, H. Stoll, *J. Chem. Phys.* **1991**, *94*, 3011–3017.
- [49] M. Dolg, P. Fulde, H. Stoll, H. Preuss, A. Chang, R. M. Pitzer, *Chem. Phys.* **1995**, *195*, 71–82.
- [50] C. H. Booth, M. D. Walter, D. Kazhdan, Y.-J. Hu, W. W. Lukens, E. D. Bauer, L. Maron, O. Eisenstein, R. A. Andersen, *J. Am. Chem. Soc.* **2009**, *131*, 6480–6491.
- [51] C. H. Booth, D. Kazhdan, E. L. Werkema, M. D. Walter, W. W. Lukens, E. D. Bauer, Y.-J. Hu, L. Maron, O. Eisenstein, M. Head-Gordon, R. A. Andersen, *J. Am. Chem. Soc.* **2010**, *132*, 17537–17549.
- [52] R. W. Field, *Ber. Bunsen-Ges.* **1982**, *86*, 771–779.
- [53] E. Schrödinger, *Ann. Phys.* **1926**, *384*, 361–376.
- [54] M. Born, R. Oppenheimer, *Ann. Phys.* **1927**, *389*, 457–484.
- [55] P. Hohenberg, W. Kohn, *Phys. Rev.* **1964**, *136*, B864–B871.
- [56] W. Kohn, L. J. Sham, *Phys. Rev.* **1965**, *140*, A1133–A1138.
- [57] P. G. Szalay, T. Müller, G. Gidofalvi, H. Lischka, R. Shepard, *Chem. Rev.* **2012**, *112*, 108–181.
- [58] J. W. Park, R. Al-Saadon, M. K. MacLeod, T. Shiozaki, B. Vlaisavljevich, *Chem. Rev.* **2020**, *120*, 5878–5909.
- [59] J. C. Slater, *Phys. Rev.* **1929**, *34*, 1293–1322.
- [60] E. U. Condon, *Phys. Rev.* **1930**, *36*, 1121–1133.
- [61] F. Coester, H. Kümmel, *Nucl. Phys.* **1960**, *17*, 477–485.
- [62] G. Das, A. C. Wahl, *J. Chem. Phys.* **1967**, *47*, 2934–2942.
- [63] P. Fulde, J. Keller, G. Zwignagl in *Solid State Physics, Vol. 41* (Eds.: H. Ehrenreich, D. Turnbull), Academic Press, Cambridge, MA, **1988**, pp. 1–150.
- [64] P. S. Riseborough, *Adv. Phys.* **2000**, *49*, 257–320.
- [65] A. Gilbert, N. S. Vidhyadhiraja, D. E. Logan, *J. Phys. Condens. Matter* **2007**, *19*, 106220.
- [66] G. Wilkinson, J. M. Birmingham, *J. Am. Chem. Soc.* **1954**, *76*, 6210.
- [67] J. M. Birmingham, G. Wilkinson, *J. Am. Chem. Soc.* **1956**, *78*, 42–44.
- [68] H. Schumann, J. A. Meese-Marktscheffel, L. Esser, *Chem. Rev.* **1995**, *95*, 865–986.
- [69] R. A. Andersen, J. M. Boncella, C. J. Burns, J. C. Green, D. Hohl, N. Rösch, *J. Chem. Soc. Chem. Commun.* **1986**, 405–407.
- [70] C. Benelli, D. Gatteschi, *Introduction to Molecular Magnetism: From Transition Metals to Lanthanides*, Wiley-VCH, Weinheim, **2015**, p. 71.
- [71] M. Tsutsui, T. Takino, D. Lorenz, *Z. Naturforsch.* **1966**, *21b*, 1–2.
- [72] S. Manastyrskij, M. Dubeck, *Inorg. Chem.* **1964**, *3*, 1647–1648.
- [73] O. Kahn, *Molecular Magnetism*, VCH, New York, N.Y., **1993**, pp. 31–52.
- [74] M. N. Bochkarev, L. N. Zakharov, G. S. Kalinina in *Organoderivatives of Rare Earth Elements*, Springer Netherlands, Dordrecht, **1995**, pp. 138–249.
- [75] M. Coreno, M. de Simone, J. C. Green, N. Kaltsoyannis, N. Narband, A. Sella, *Chem. Phys. Lett.* **2006**, *432*, 17–21.
- [76] R. Coates, M. Coreno, M. DeSimone, J. C. Green, N. Kaltsoyannis, A. Ker-ridge, N. Narband, A. Sella, *Dalton Trans.* **2009**, 5943–5953.
- [77] M. Coreno, M. de Simone, R. Coates, M. S. Denning, R. G. Denning, J. C. Green, C. Hunston, N. Kaltsoyannis, A. Sella, *Organometallics* **2010**, *29*, 4752–4755.
- [78] R. G. Denning, J. Harmer, J. C. Green, M. Irwin, *J. Am. Chem. Soc.* **2011**, *133*, 20644–20660.
- [79] M. Coreno, M. de Simone, J. C. Green, N. Kaltsoyannis, R. Coates, C. Hunston, N. Narband, A. Sella, *Dalton Trans.* **2014**, *43*, 5134–5141.
- [80] E. O. Fischer, H. Fischer, *J. Organomet. Chem.* **1965**, *3*, 181–187.
- [81] C. Calle, A. Sreekanth, M. V. Fedin, J. Forrer, I. Garcia-Rubio, I. A. Gromov, D. Hinderberger, B. Kasumaj, P. Léger, B. Mancosu, G. Mitrikas, M. G. Santangelo, S. Stoll, A. Schweiger, R. Tschaggelar, J. Harmer, *Helv. Chim. Acta* **2006**, *89*, 2495–2521.
- [82] R. Pappalardo, C. K. Jørgensen, *J. Chem. Phys.* **1967**, *46*, 632–638.
- [83] C. J. Schlessener, A. B. Ellis, *Organometallics* **1983**, *2*, 529–534.
- [84] M. Schultz, J. M. Boncella, D. J. Berg, T. D. Tilley, R. A. Andersen, *Organometallics* **2002**, *21*, 460–472.
- [85] R. E. Da Re, C. J. Kuehl, M. G. Brown, R. C. Rocha, E. D. Bauer, K. D. John, D. E. Morris, A. P. Shreve, J. L. Sarrao, *Inorg. Chem.* **2003**, *42*, 5551–5559.
- [86] L. R. Morss, *Chem. Rev.* **1976**, *76*, 827–841.
- [87] F. Grandjean, G. J. Long in *Mössbauer Spectroscopy Applied to Inorganic Chemistry* (Eds.: G. J. Long, F. Grandjean), Springer US, Boston, **1989**, pp. 513–597.
- [88] G. Depaoli, U. Russo, G. Valle, F. Grandjean, A. F. Williams, G. J. Long, *J. Am. Chem. Soc.* **1994**, *116*, 5999–6000.
- [89] N. Kaltsoyannis, B. E. Bursten, *J. Organomet. Chem.* **1997**, *528*, 19–33.
- [90] Y. Baer, R. Hauger, C. Zürcher, M. Campagna, G. K. Wertheim, *Phys. Rev. B* **1978**, *18*, 4433–4439.
- [91] A. Franciosi, J. H. Weaver, N. Mårtensson, M. Croft, *Phys. Rev. B* **1981**, *24*, 3651–3654.
- [92] J. W. Allen, S. J. Oh, O. Gunnarsson, K. Schönhammer, M. B. Maple, M. S. Torikachvili, I. Lindau, *Adv. Phys.* **1986**, *35*, 275–316.
- [93] B. O. Roos, P. R. Taylor, P. E. M. Sigbahn, *Chem. Phys.* **1980**, *48*, 157–173.
- [94] K. Andersson, P.-Å. Malmqvist, B. O. Roos, A. J. Sadlej, K. Wolinski, *J. Phys. Chem.* **1990**, *94*, 5483–5488.
- [95] A. Greco, S. Cesca, W. Bertolini, *J. Organomet. Chem.* **1976**, *113*, 321–330.
- [96] A. Streitwieser, S. A. Kinsley, C. H. Jenson, J. T. Rigsbee, *Organometallics* **2004**, *23*, 5169–5175.
- [97] M. D. Walter, C. H. Booth, W. W. Lukens, R. A. Andersen, *Organometallics* **2009**, *28*, 698–707.
- [98] T. R. Bousie, D. C. Eisenberg, J. Rigsbee, A. Streitwieser, A. Zalkin, *Organometallics* **1991**, *10*, 1922–1928.
- [99] U. Kilimann, R. Herbst-Irmer, D. Stalke, F. T. Edelmann, *Angew. Chem. Int. Ed. Engl.* **1994**, *33*, 1618–1621; *Angew. Chem.* **1994**, *106*, 1684–1687.
- [100] K. O. Hodgson, K. N. Raymond, *Inorg. Chem.* **1972**, *11*, 3030–3035.
- [101] R. Shannon, *Acta Crystallogr. Sect. A* **1976**, *32*, 751–767.
- [102] A. Streitwieser, S. A. Kinsley, J. T. Rigsbee, I. L. Fragala, E. Ciliberto, *J. Am. Chem. Soc.* **1985**, *107*, 7786–7788.
- [103] H.-D. Amberger, H. Reddmann, F. T. Edelmann, *J. Organomet. Chem.* **2005**, *690*, 2238–2242.
- [104] N. M. Edelstein, P. G. Allen, J. J. Bucher, D. K. Shuh, C. D. Sofield, N. Kaltsoyannis, G. H. Maunder, M. R. Russo, A. Sella, *J. Am. Chem. Soc.* **1996**, *118*, 13115–13116.
- [105] C. H. Booth, M. D. Walter, M. Daniel, W. W. Lukens, R. A. Andersen, *Phys. Rev. Lett.* **2005**, *95*, 267202.
- [106] D. E. Smiles, E. R. Batista, C. H. Booth, D. L. Clark, J. M. Keith, S. A. Kozimor, R. L. Martin, S. G. Minasian, D. K. Shuh, S. C. E. Stieber, T. Tylicszak, *Chem. Sci.* **2020**, *11*, 2796–2809.
- [107] J. L. Sarrao, C. D. Immer, Z. Fisk, C. H. Booth, E. Figueroa, J. M. Lawrence, R. Modler, A. L. Cornelius, M. F. Hundley, G. H. Kwei, J. D. Thompson, F. Bridges, *Phys. Rev. B* **1999**, *59*, 6855–6866.
- [108] T. Vitova, K. O. Kvashnina, G. Nocton, G. Sukharina, M. A. Denecke, S. M. Buterin, M. Mazzanti, R. Caciuffo, A. Soldatov, T. Behrends, H. Geckeis, *Phys. Rev. B* **2010**, *82*, 235118.
- [109] M. W. Löble, J. M. Keith, A. B. Altman, S. C. E. Stieber, E. R. Batista, K. S. Boland, S. D. Conradson, D. L. Clark, J. Lezama Pacheco, S. A. Kozimor, R. L. Martin, S. G. Minasian, A. C. Olson, B. L. Scott, D. K. Shuh, T. Tylicszak, M. P. Wilkerson, R. A. Zehnder, *J. Am. Chem. Soc.* **2015**, *137*, 2506–2523.
- [110] A. B. Altman, J. I. Pacold, J. Wang, W. W. Lukens, S. G. Minasian, *Dalton Trans.* **2016**, *45*, 9948–9961.
- [111] S. G. Minasian, E. R. Batista, C. H. Booth, D. L. Clark, J. M. Keith, S. A. Kozimor, W. W. Lukens, R. L. Martin, D. K. Shuh, S. C. E. Stieber, T. Tylicszak, X.-d. Wen, *J. Am. Chem. Soc.* **2017**, *139*, 18052–18064.
- [112] A. Fujimori, *Phys. Rev. B* **1983**, *28*, 2281–2283.
- [113] A. Bianconi, A. Marcelli, H. Dexpert, R. Karnatak, A. Kotani, T. Jo, J. Petiau, *Phys. Rev. B* **1987**, *35*, 806–812.
- [114] A. Kotani, T. Jo, J. C. Parlebas, *Adv. Phys.* **1988**, *37*, 37–85.
- [115] G. Kaindl, G. Schmiester, E. V. Sampathkumaran, P. Wachter, *Phys. Rev. B* **1988**, *38*, 10174–10177.
- [116] M. V. Ganduglia-Pirovano, A. Hofmann, J. Sauer, *Surf. Sci. Rep.* **2007**, *62*, 219–270.
- [117] A. Kotani, H. Mizuta, T. Jo, J. C. Parlebas, *Solid State Commun.* **1985**, *53*, 805–810.

- [118] N. Hosoya, K. Yada, T. Masuda, E. Nakajo, S. Yabushita, A. Nakajima, *J. Phys. Chem. A* **2014**, *118*, 3051–3060.
- [119] N. Roesch, A. Streitwieser, *J. Am. Chem. Soc.* **1983**, *105*, 7237–7240.
- [120] M. Dolg, H. Stoll, *Theor. Chim. Acta* **1989**, *75*, 369–387.
- [121] M. Dolg, H. Stoll, H. Preuss, *J. Chem. Phys.* **1989**, *90*, 1730–1734.
- [122] W. Küchle, M. Dolg, H. Stoll, H. Preuss, *J. Chem. Phys.* **1994**, *100*, 7535–7542.
- [123] M. Dolg, X. Cao, *Chem. Rev.* **2012**, *112*, 403–480.
- [124] M. Dolg, P. Fulde, *Chem. Eur. J.* **1998**, *4*, 200–204.
- [125] A. Kerridge, R. Coates, N. Kaltsoyannis, *J. Phys. Chem. A* **2009**, *113*, 2896–2905.
- [126] R. F. W. Bader, *Atoms in Molecules: A Quantum Theory*, Clarendon Press, Oxford, **1994**, p. 438.
- [127] A. Kerridge, *Dalton Trans.* **2013**, *42*, 16428–16436.
- [128] O. Mooßen, M. Dolg, *Chem. Phys. Lett.* **2014**, *594*, 47–50.
- [129] A. Ashley, G. Balazs, A. Cowley, J. Green, C. H. Booth, D. O'Hare, *Chem. Commun.* **2007**, 1515–1517.
- [130] G. Balazs, F. G. N. Cloke, J. C. Green, R. M. Harker, A. Harrison, P. B. Hitchcock, C. N. Jardine, R. Walton, *Organometallics* **2007**, *26*, 3111–3119.
- [131] A. Kerridge, N. Kaltsoyannis, *C. R. Chimie* **2010**, *13*, 853–859.
- [132] M. Dolg, O. Mooßen, *J. Organomet. Chem.* **2015**, *794*, 17–22.
- [133] I. Hiroaki, S. Masahiko, *Chem. Lett.* **1992**, *21*, 147–150.
- [134] Y. Bian, J. Jiang, Y. Tao, M. T. M. Choi, R. Li, A. C. H. Ng, P. Zhu, N. Pan, X. Sun, D. P. Arnold, Z.-Y. Zhou, H.-W. Li, T. C. W. Mak, D. K. P. Ng, *J. Am. Chem. Soc.* **2003**, *125*, 12257–12267.
- [135] M. D. Walter, R. Fandos, R. A. Andersen, *New J. Chem.* **2006**, *30*, 1065–1070.
- [136] R. L. Halbach, G. Nocton, C. H. Booth, L. Maron, R. A. Andersen, *Inorg. Chem.* **2018**, *57*, 7290–7298.
- [137] R. L. Halbach, G. Nocton, C. H. Booth, L. Maron, R. A. Andersen, *Inorg. Chem.* **2018**, *57*, 8692.
- [138] P. L. Arnold, K. Wang, S. J. Gray, L. M. Moreau, C. H. Booth, M. Curcio, J. A. L. Wells, A. M. Z. Slawin, *Dalton Trans.* **2020**, *49*, 877–884.
- [139] N. T. Rice, J. Su, T. P. Gompas, D. R. Russo, J. Telser, L. Palatinus, J. Bacsa, P. Yang, E. R. Batista, H. S. La Pierre, *Inorg. Chem.* **2019**, *58*, 5289–5304.
- [140] N. T. Rice, I. A. Popov, D. R. Russo, T. P. Gompas, A. Ramanathan, J. Bacsa, E. R. Batista, P. Yang, H. S. La Pierre, *Chem. Sci.* **2020**, *11*, 6149–6159.
- [141] L. M. Aguirre Quintana, N. Jiang, J. Bacsa, H. S. La Pierre, *Dalton Trans.* **2020**, *49*, 14908–14913.
- [142] M. D. Walter, M. Schultz, R. A. Andersen, *New J. Chem.* **2006**, *30*, 238–246.
- [143] M. D. Walter, D. J. Berg, R. A. Andersen, *Organometallics* **2006**, *25*, 3228–3237.
- [144] M. D. Walter, D. J. Berg, R. A. Andersen, *Organometallics* **2007**, *26*, 2296–2307.
- [145] G. Nocton, C. H. Booth, L. Maron, R. A. Andersen, *Organometallics* **2013**, *32*, 5305–5312.
- [146] G. Nocton, C. H. Booth, L. Maron, R. A. Andersen, *Organometallics* **2013**, *32*, 1150–1158.
- [147] G. Nocton, C. H. Booth, L. Maron, L. Ricard, R. A. Andersen, *Organometallics* **2014**, *33*, 6819–6829.
- [148] J. M. Veauthier, E. J. Schelter, C. J. Kuehl, A. E. Clark, B. L. Scott, D. E. Morris, R. L. Martin, J. D. Thompson, J. L. Kiplinger, K. D. John, *Inorg. Chem.* **2005**, *44*, 5911–5920.
- [149] C. N. Carlson, C. J. Kuehl, L. Ogallo, D. A. Shultz, J. D. Thompson, M. L. Kirk, R. L. Martin, K. D. John, D. E. Morris, *Organometallics* **2007**, *26*, 4234–4242.
- [150] I. L. Fedushkin, O. V. Maslova, E. V. Baranov, A. S. Shavyrin, *Inorg. Chem.* **2009**, *48*, 2355–2357.
- [151] I. L. Fedushkin, O. V. Maslova, A. G. Morozov, S. Dechert, S. Demeshko, F. Meyer, *Angew. Chem. Int. Ed.* **2012**, *51*, 10584–10587; *Angew. Chem.* **2012**, *124*, 10736–10739.
- [152] V. Goudy, A. Jaoul, M. Cordier, C. Clavaguéra, G. Nocton, *J. Am. Chem. Soc.* **2017**, *139*, 10633–10636.
- [153] M. Dolg, H. Stoll, H. Preuss, *Theor. Chim. Acta* **1993**, *85*, 441–450.
- [154] C. E. Kefalidis, L. Castro, A. Yahia, L. Perrin, L. Maron in *Computational Methods in Lanthanide and Actinide Chemistry* (Ed.: M. Dolg), **2015**, pp. 343–373.
- [155] A. A. Trifonov, T. V. Mahrova, L. Luconi, G. Giambastiani, D. M. Lyubov, A. V. Cherkasov, L. Sorace, E. Louyriac, L. Maron, K. A. Lyssenko, *Dalton Trans.* **2018**, *47*, 1566–1576.
- [156] N. A. G. Bandeira, C. Daniel, A. Trifonov, M. J. Calhorda, *Organometallics* **2012**, *31*, 4693–4700.
- [157] L. Jacquot, M. Xémard, C. Clavaguéra, G. Nocton, *Organometallics* **2014**, *33*, 4100–4106.
- [158] R. L. Halbach, G. Nocton, J. I. Amaro-Estrada, L. Maron, C. H. Booth, R. A. Andersen, *Inorg. Chem.* **2019**, *58*, 12083–12098.
- [159] C. V. Krishnan, C. Creutz, H. A. Schwarz, N. Sutin, *J. Am. Chem. Soc.* **1983**, *105*, 5617–5623.
- [160] H. Ferreira, M. M. Conradie, K. G. von Eschwege, J. Conradie, *Polyhedron* **2017**, *122*, 147–154.
- [161] A. Klein, W. Kaim, E. Waldhör, H.-D. Hausen, *J. Chem. Soc. Perkin Trans. 2* **1995**, 2121–2126.
- [162] W. W. Lukens, N. Magnani, C. H. Booth, *Inorg. Chem.* **2012**, *51*, 10105–10110.
- [163] J. D. Rinehart, M. Fang, W. J. Evans, J. R. Long, *Nat. Chem.* **2011**, *3*, 538–542.
- [164] J. D. Rinehart, M. Fang, W. J. Evans, J. R. Long, *J. Am. Chem. Soc.* **2011**, *133*, 14236–14239.
- [165] S. Demir, J. M. Zadrozny, M. Nippe, J. R. Long, *J. Am. Chem. Soc.* **2012**, *134*, 18546–18549.
- [166] C. A. Gould, L. E. Darago, M. I. Gonzalez, S. Demir, J. R. Long, *Angew. Chem. Int. Ed.* **2017**, *56*, 10103–10107; *Angew. Chem.* **2017**, *129*, 10237–10241.
- [167] D. Wang, J. Moutet, M. Tricoire, M. Cordier, G. Nocton, *Inorganics* **2019**, *7*, 58.
- [168] W.-H. Leung, Q.-F. Zhang, X.-Y. Yi, *Coord. Chem. Rev.* **2007**, *251*, 2266–2279.
- [169] L. Castro, Y.-M. So, C.-w. Cho, R. Lortz, K.-H. Wong, K. Wang, P. L. Arnold, K.-C. Au-Yeung, H. H.-Y. Sung, I. D. Williams, W.-H. Leung, L. Maron, *Chem. Eur. J.* **2019**, *25*, 10834–10839.

Manuscript received: October 27, 2020

Accepted manuscript online: December 19, 2020

Version of record online: February 25, 2021



# Size-Controlled Hapticity Switching in $[\text{Ln}(\text{C}_9\text{H}_9)(\text{C}_8\text{H}_8)]$ Sandwiches

Maxime Tricoire,<sup>[a]</sup> Luca Münzfeld,<sup>[b]</sup> Jules Moutet,<sup>[a]</sup> Nolwenn Mahieu,<sup>[a]</sup> Léo La Droitte,<sup>[c]</sup> Eufemio Moreno-Pineda,<sup>[d, e, f]</sup> Frédéric Gendron,<sup>[c]</sup> Jeremy D. Hilgar,<sup>[h]</sup> Jeffrey D. Rinehart,<sup>[h]</sup> Mario Ruben,<sup>[b, d, i, j]</sup> Boris Le Guennic,<sup>[c]</sup> Olivier Cador,<sup>[c]</sup> Peter W. Roesky,<sup>\*,[b]</sup> and Grégory Nocton<sup>\*,[a]</sup>

**Abstract:** Sandwich complexes of lanthanides have recently attracted a considerable amount of interest due to their applications as Single Molecule Magnet (SMM). Herein, a comprehensive series of heteroleptic lanthanide sandwich complexes ligated by the cyclononatetraenyl (Cnt) and the cyclooctatetraenyl (Cot) ligand  $[\text{Ln}(\text{Cot})(\text{Cnt})]$  ( $\text{Ln}=\text{Tb}$ , Dy, Er, Ho, Yb, and Lu) is reported. The coordination behavior of the

Cnt ligand has been investigated along the series and shows different coordination patterns in the solid-state depending on the size of the corresponding lanthanide ion without altering its overall anisotropy. Besides the characterization in the solid state by single-crystal X-ray diffraction and in solution by  $^1\text{H}$  NMR, static magnetic studies and ab initio computational studies were performed.

## Introduction

Many different applications of rare-earth-based compounds originate from their unique physical properties:<sup>[1]</sup> strong spin-orbit coupling, large magnetization and core 4f-orbitals.<sup>[2]</sup> The specific design of compounds adapted to specific applications is facilitated by the small orbital contributions of the ligand-field. This allows the prediction of fundamental physical properties with qualitative electrostatic models.<sup>[3]</sup> These considerations have motivated a large number of fundamental structure/properties studies, especially for luminescent materials,<sup>[4]</sup> MRI contrast agents<sup>[5]</sup> and more recently for the design of high-performance Single Molecule-Magnets (SMMs).<sup>[1a,6]</sup>

In this particular area, the gap from liquid helium (2 K) to liquid nitrogen (77 K) temperatures has recently been closed, and organometallic compounds of lanthanides have played a crucial role in this breakthrough.<sup>[7]</sup> The possible geometries allowed by typical anionic cyclo-aromatic ligands used in organometallic chemistry, such as cyclopentadienyl (Cp),<sup>[6]</sup> cyclooctatetraenyl (Cot)<sup>[8]</sup> and cyclononatetraenyl (Cnt),<sup>[9]</sup> led to unusual arrangements, which can be tuned by the bulk of their substituents. When a linear geometry with localized charge density in the axial position is necessary to get interesting magnetic properties, as in the case of oblate ions such as Dy, small Cp ligands with large bulk are used to provide the localized charge and enforce a nearly linear geometry.<sup>[7a-c,10]</sup>

[a] M. Tricoire, Dr. J. Moutet, N. Mahieu, Prof. G. Nocton  
Laboratoire de Chimie Moléculaire (LCM)  
CNRS, Ecole polytechnique, Institut Polytechnique de Paris  
Route de Saclay, 91120 Palaiseau (France)  
E-mail: gregory.nocton@polytechnique.edu

[b] L. Münzfeld, Prof. Dr. M. Ruben, Prof. Dr. P. W. Roesky  
Institute of Inorganic Chemistry  
Karlsruhe Institute of Technology (KIT)  
Engesserstraße 15, 76131, Karlsruhe (Germany)  
E-mail: peter.roesky@kit.edu

[c] L. La Droitte, Dr. F. Gendron, Prof. Dr. B. Le Guennic, Prof. Dr. O. Cador  
ISCR (Institut des Sciences Chimiques de Rennes)-UMR 6226  
Université de Rennes, CNRS  
35000 Rennes (France)

[d] Dr. E. Moreno-Pineda, Prof. Dr. M. Ruben  
Institute of Nanotechnology (INT)  
Karlsruhe Institute of Technology (KIT)  
Hermann-von-Helmholtz-Platz 1, 76344, Eggenstein-Leopoldshafen (Germany)

[e] Dr. E. Moreno-Pineda  
Depto. de Química-Física, Escuela de Química  
Facultad de Ciencias Naturales, Exactas y Tecnología, Universidad de Panamá, Panamá

[f] Dr. E. Moreno-Pineda  
Panamanian National System of Investigators (SNI, SENACYT), Panama

[h] J. D. Hilgar, Prof. Dr. J. D. Rinehart  
Department of Chemistry and Biochemistry  
University of California-San Diego  
La Jolla, CA (United-States)

[i] Prof. Dr. M. Ruben  
Centre Européen de Science Quantique (CESQ), Institut de Science et d'Ingénierie Supramoléculaires (ISIS)  
Université de Strasbourg  
8, Allée Gaspard Monge, F-67000 Strasbourg (France)

[j] Prof. Dr. M. Ruben  
Institute of Quantum Materials and Technology (IQMT)  
Karlsruhe Institute of Technology (KIT)  
Hermann-von-Helmholtz-Platz 1, 76344, Eggenstein-Leopoldshafen (Germany)

Supporting information for this article is available on the WWW under <https://doi.org/10.1002/chem.202101599>

© 2021 The Authors. Chemistry - A European Journal published by Wiley-VCH GmbH. This is an open access article under the terms of the Creative Commons Attribution License, which permits use, distribution and reproduction in any medium, provided the original work is properly cited.

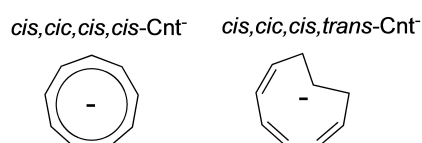


With prolate ions, such as Er, large ligands, such as the Cot dianion and the Cnt anion, are better suited to enhance equatorial ligand field contributions in sandwiched compounds.<sup>[8b,11]</sup>

However, some of these specificities can be antagonistic, making the rational design of such compounds difficult resulting in a narrow edge, at which all the desired properties are maximized. Typically, a bulk increase of the Cp ligand favors linearity while driving away the point charge of the ligand from the metal ion.<sup>[7c,12]</sup> It is thus extremely important to rationalize the dynamic coordination properties of these aromatic ligands in order to be able to control the metal-ligand pair anisotropy.<sup>[11c]</sup> Additionally, because magnetism and luminescent applications often require solid-state measurements, the understanding of how packing forces influence the inner coordination as well as the exact arrangement of the closest neighbors in the crystal lattice is important. Recent studies led by some of us have underlined the importance of the orientation of the anisotropy axes in a series of binuclear Er(Cot) fragments<sup>[11d]</sup> as well as the second sphere environment in divalent [Tm(Cot)<sub>2</sub>]<sup>2-</sup> compounds, when designing performing SMMs.<sup>[11e]</sup>

Among others, the cyclononatetraenyl ligand (Cnt) is a promising ligand for the rational design of SMMs: it allows the formation of perfectly linear homoleptic sandwiches with divalent lanthanides and exhibits labile coordination dynamics in coordinating solvents,<sup>[9a]</sup> contrary to Cot and Cp ligands. In this work, the bis-Cnt [Ln(Cnt)<sub>2</sub>] divalent complexes of Ln=Sm, Eu, Tm and Yb have been obtained in good yields through the use of a mixture of two isomers of the Cnt potassium salt: the *cis-cis-cis-cis* and the *cis-cis-cis-trans* forms (Scheme 1). A step further was the use of this mono-anionic ligand in combination with the dianionic Cot ligand to form neutral sandwiches with linear geometry.<sup>[13]</sup> In this series, the geometry is particularly well adapted for maximizing the anisotropy of the erbium complex and, indeed, the latter was reported to present interesting SMM properties, confirming the adapted Er-Cnt/Cot pair anisotropy. Yet, the specific coordination of the Cnt ligand in various environments, with various bulk, and different lanthanide size remains to be studied to enlarge the scope of Cnt compounds with promising applications.

In the present work, a series of heteroleptic sandwich complexes, [Ln(Cot)(Cnt)], is presented with Ln=Tb, Dy, Ho, Er, Tm, Lu with a focus on their structural aspects, both in the solid-state and in solution. This work reinforces the versatility of the Cnt ligand as a useful candidate for the design of specific geometries needed in organolanthanide chemistry for a given application including magnetism.

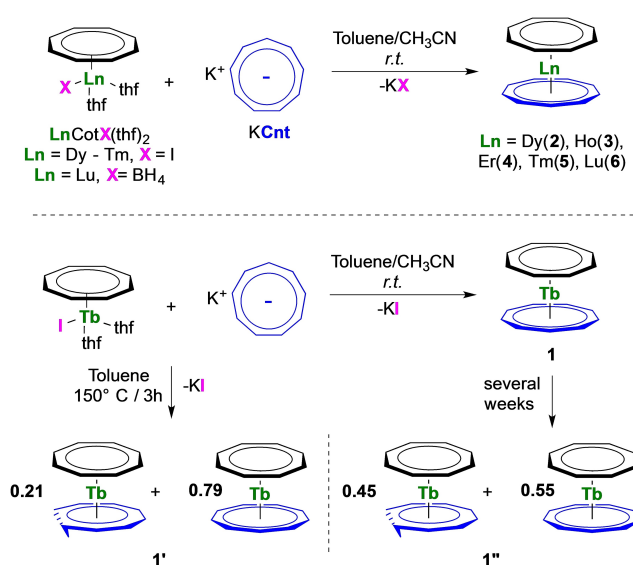


Scheme 1. Isomers of the Cnt ligand

## Results and Discussion

### Synthesis

The heteroleptic trivalent late lanthanide sandwich complexes [Ln(Cot)(Cnt)] (Ln=Tb (1), Dy (2), Ho (3), Er (4), Yb (5), Lu (6)) were synthesized from a toluene/acetonitrile mixture of KCnt and the corresponding [Ln(Cot)I(thf)<sub>2</sub>] complexes (Ln=Tb, Dy,<sup>[13]</sup> Ho, Er,<sup>[11c,13]</sup> Tm) at room temperature (Scheme 2). Due to the facile reduction of Yb<sup>3+</sup> in the presence of the Cot ligand, the Yb compound is not accessible.<sup>[14]</sup> [Ln(Cot)I(thf)<sub>2</sub>] were prepared from K<sub>2</sub>Cot and lanthanide tris-iodides in thf,<sup>[11c]</sup> a faster alternative compared to the elegant procedure proposed by Mashima et al. for the earlier lanthanides.<sup>[15]</sup> The Lu complex is best prepared from the borohydride [Lu(BH<sub>4</sub>)<sub>3</sub>(thf)<sub>3</sub>] precursor<sup>[16]</sup> to afford either the monomeric [Lu(Cot)(BH<sub>4</sub>)(thf)<sub>2</sub>] or the dimeric [Lu(Cot)(BH<sub>4</sub>)(thf)<sub>2</sub>]<sub>2</sub> complex as original compounds depending on the crystallization conditions, similar to the procedure of Ephritikhine for the synthesis of the Nd analogues.<sup>[17]</sup> The three new crystal structures with Ln=Tb, Ho and Lu are discussed in the Supporting Information. The Tm structure was reported by Schumann et al. but was made from direct reaction of TmI<sub>3</sub> with free Cot.<sup>[18]</sup> In the case of Tb, Dy, Ho, Er, and Tm, the potassium salt of the Cnt ligand (both all-*cis* and *cis-cis-cis-trans* isomers can be used)<sup>[9a,19]</sup> is best dissolved in acetonitrile before use. After 12 h of stirring, the suspensions turned to pale-colored solutions with a gradual color change along the lanthanide series (pale yellow for Tb, yellow for Dy,<sup>[13]</sup> pale orange for Ho, orange for Er,<sup>[13]</sup> salmon orange for Tm). The reaction time of 12 h is necessary to complete the isomerization when the more soluble *cis-cis-cis-trans* isomer is used. Synthesis of the lutetium complex [Lu(Cot)(Cnt)] (6) was best performed by heating KCnt and [Lu(Cot)(BH<sub>4</sub>)(thf)<sub>2</sub>] in toluene under reflux for 16 h. Another important step is the removal of all the volatiles and thorough drying of the resulting solid. Several steps of drying and re-suspension in toluene are necessary to



Scheme 2. Synthesis of 1–6.

ensure complete de-coordination of the acetonitrile (or remaining thf molecule in the case of lutetium). If this step is not complete, an acetonitrile adduct of  $[\text{Ln}(\text{Cot})(\text{Cnt})]$  may be isolated, in which the Cnt ligand binds in lower hapticity than  $\eta^9$ . A crystal structure of such a dysprosium complex has been obtained with partial coordination of acetonitrile. The structure is discussed in the Supporting Information (Figure S19–S20). Once the coordinated solvent has been removed, extraction in a large amount of toluene followed by filtration, concentration and cooling ( $-40^\circ\text{C}$ ) allows the crystallization of the title compounds (**1**–**6**) as crystals suitable for X-ray diffraction. The erbium and dysprosium complexes, **2** and **4**, respectively, were already recently published using a different procedure and analyzed by multiple approaches. The  $\eta^9$ -Cnt coordination remained an open question because of a crystallographic disorder.<sup>[13]</sup> For the Tb complex (**1**), several different crystals (crystallized at room temperature and grown over a week) of red color have been analyzed to reveal a mixture of the *cis-cis-cis-cis* and of the *cis-cis-cis-trans* Cnt ligand in a 79:21 ratio (**1'**). The structure is discussed in Supporting Information. However, when the terbium complex was prepared by an alternative method from hot toluene, the crystallized structure was similar to that of **1'** with a ratio of *cis-cis-cis-cis*:*cis-cis-cis-trans* ligand of 55:45 (**1''**). Upon heating, all compounds degraded at higher temperature.

### Solution analysis

Compounds **1**–**6** have been analyzed by  $^1\text{H}$  NMR spectroscopy. Except for the Lu compound (**6**), which is diamagnetic, **1**–**5** are highly paramagnetic but signals have been obtained for all compounds (Figure 1, Supporting Information, Figure S1–S14). The broad signals obtained for the Er (**4**) and Tm (**5**) complexes did not allow distinguishing the Cnt from the Cot ligand on the basis of their relative integrations. The signals appear at  $-5.01$ ,  $-128.7$  ppm and  $-23.2$  and  $-235.8$  ppm, for **4** and **5**, respectively, at room temperature. For **1**–**3** and **6**,  $^1\text{H}$  NMR spectra feature two similar signals with chemical shifts of 245.9, 118.7, 90.5 and 5.83 ppm for the Cot, respectively, and of 101.5, 72.9, 59.2, and 6.54 ppm for the Cnt, respectively. In **1**–**3**, the shapes of the f-electron density in the lanthanide ions are oblate, while in **4**–**5**, they are prolate.<sup>[3b]</sup> The modification in the anisotropy orientation between **3** and **4** is well reflected by the sign change of their chemical shifts for both ligands. Variable temperature  $^1\text{H}$  NMR was performed for **6** but no fluxional behavior<sup>[20]</sup> for both ligands was observed in the range from  $+80$  to  $-80^\circ\text{C}$ .

The crystallization of different terbium complexes, **1**, **1'**, and **1''** with a different configuration for the Cnt ligand was intriguing to us. The free Cnt<sup>−</sup> ligand indeed possesses two different isomers, easily quantified by  $^1\text{H}$  NMR spectroscopy: the *cis-cis-cis-cis* ligand gives rise to one singlet in agreement with  $D_{9h}$  symmetry while the *cis-cis-cis-trans* one features 5 signals in agreement with  $C_{2v}$  symmetry.<sup>[21]</sup> In a previous work, the use of a soluble mixture of these two isomers leads to multiple  $\text{Ln}(\text{Cnt})_2$  sandwich isomers, which were also easily identified by

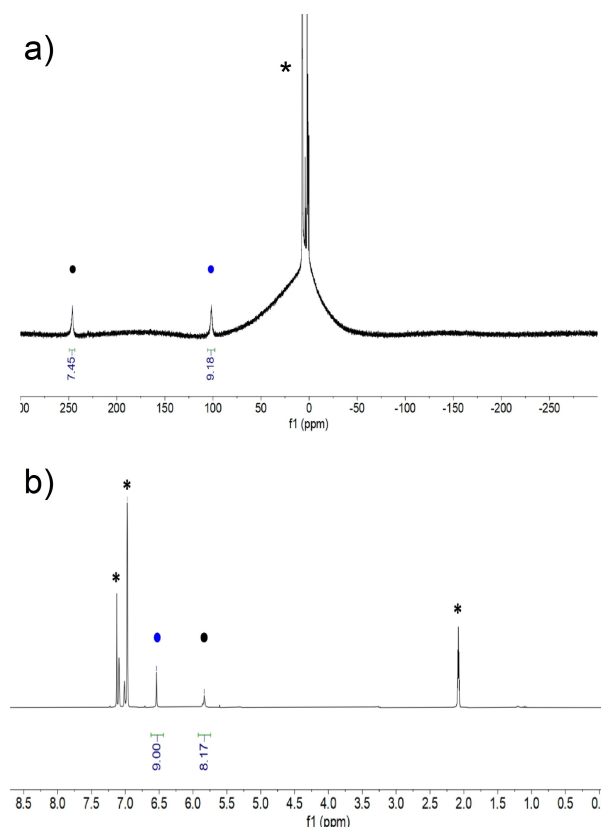
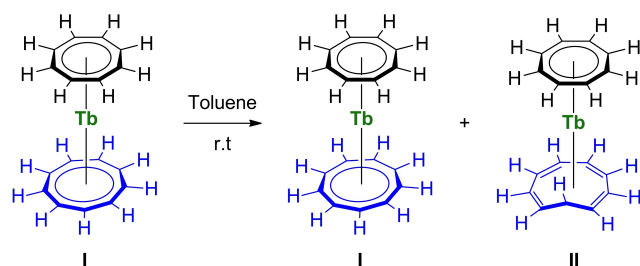


**Figure 1.**  $^1\text{H}$  NMR of **1** (a) and **6** (b) at 293 K in toluene- $d_8$ . Blue mark (●) is for the signals of the Cnt ligand and the black mark (●) for the Cot ligand. \* residual protio signal of the solvent.

$^1\text{H}$  NMR spectroscopy.<sup>[9a]</sup> Additionally, Boche et al. gathered, in a comprehensive series of three articles, useful information on the Cnt ligand synthesis, as well as its topomerization and isomerization.<sup>[19,22]</sup> These studies unveil several questions on the real nature of the isomerization process when assisted by metal complexes. An interesting connection to this is that **1''** in which one ligand is partially isomerized in the *cis-cis-cis-trans* form, is obtained in a relatively high-temperature synthesis ( $150^\circ\text{C}$  for 3 h) from the *cis-cis-cis-cis* ligand, supposedly thermodynamically more stable. In contrast, **1** only contains the *cis-cis-cis-cis* ligand and is prepared under milder conditions (room temperature synthesis). Thus, in order to probe a possible temperature effect on the isomerization of the ligand in the Tb complex, a solution of **1** in toluene- $d_8$  was let stand for several days at room temperature. The resulting  $^1\text{H}$  NMR spectra of this experiment are shown in Figure S14. A new set of 6 signals increases with time at  $\delta$  404.0, 230.1, 203.6, 196.2, 165.1 and  $-169.5$  ppm while the two initial signals of **1** (Scheme 3, I) were still present. The estimated ratio based on integration, 2:8:2:2:1:2, needs to be considered cautiously because of the highly paramagnetic nature of the complex. Yet, it is in full agreement with the formation of a  $[\text{Tb}(\text{Cot})(\text{Cnt})]$  isomer in which the Cnt ligand is in the *cis-cis-cis-trans* configuration (Scheme 3, II). Indeed, the isomerized Cnt ligand in **1'** and **1''** gives rise to 5 distinct proton resonances, as also observed in



**Scheme 3.** Isomerization of I to II in solution.

the free *cis-cis-cis-trans* Cnt ligand,<sup>[9a]</sup> while the Cot signal remains a singlet integrating for 8 protons. The ratio between the isomers I and II is ca. 66:34 after three days and stabilizes over time to approximately 60:40 after 20 days, remarkably close to the ratio found in the solid state structure of 1'' (55:45), while 1', which was obtained from a slow evolution of 1 at room temperature features a higher I:II ratio of 79:21.

This unexpected situation again connects to Boche's findings and shows that the nature of the coordinated metal greatly affects the inter-conversion between topologic isomers of the Cnt ligand. Although this isomerization has only been observed so far in case of the Tb complex 1, a thorough investigation of the Cnt isomerization within the [Ln(Cot)(Cnt)] series (which is outside the scope of this article) would still be necessary to understand whether it is related to size effects or other physical properties.

### X-ray solid-state crystal structure

The crystal structures are isomorphous from Dy to Lu (2–6) and were solved in  $P2_1/n$  irrespective of the data collection temperatures (Figure 2). There is a positional disorder in both ligands, the first one featuring eight carbon atoms (Cot), the second one nine carbon atoms (Cnt). Within this space group, the presence

of these specificities creates a situation in which the final solution has two rings embedded in each other with occupancy of 0.5 on each atom (See Figure S25a). Additionally, for the complexes 2–6, the lanthanide ion is not placed at a special position (i.e. sitting on a symmetry element) but lies close to an inversion center, also with occupancy of 0.5. As a result, the lanthanide ion is not centered with the ligands but is slightly moved away, which seems to point out a possible lower coordination mode (hapticity) of one of the ligands. This situation also drastically complicates the resolution when one wants to separate the ligands from one another since the symmetry generation by the  $P2_1/n$  space group creates two more rings embedded with each other along with an additional lanthanide atom close to the inversion center (See Figure S25b). However, because of the symmetry rules, only two variants exist and it is not possible to mix the two different configurations.

Thus, from a crystallographic point of view, two solutions are possible; viz. a lower hapticity either for the Cot or for the Cnt ligand (See Figure S25d, e). However, it seems that the deviation from planarity observed in the 9-membered ring is in better agreement with a perturbed coordination mode for the Cnt ligand rather than for the Cot ligand. Additionally, the Ln–Ctr (Ctr, centroid) distance with both rings must respect the increased negative charge of  $\text{Cot}^{2-}$  with respect to  $\text{Cnt}^-$  and longer Ln–Cnt distances are therefore expected.<sup>[13]</sup> If the  $\eta^9$ -Cnt coordination mode was preferred, both the Ln–Ctr distances and the coordination mode of Cot are unrealistic from a chemical point of view for the lutetium compound (6) (See Supporting Information). Lowering the symmetry to the  $P1$  symmetry group (See Figure S26) increases the size of the asymmetric unit but does not allow to better define the disorder; it is still necessary to assume either longer Ln–Ctr distances for the Cnt- or for the Cot- ligand. When solving the data, it is also necessary to allow positional freedom to the carbon atoms except for the aromaticity restraint on the C–C distances on both rings in order to avoid scrambling of the carbon atoms between the two ligands moieties upon refinement. If the ring having eight carbon atoms (Cot) ends up relatively planar, in agreement with most Cot ligands coordinated to lanthanide ions in the literature, the one with nine carbon atoms (Cnt) shows a strong deviation from planarity with a curvature at the extremity, which tends to be indicative of a different coordination mode. In 2–6, a closer look to the Ln–C set of distances within the eight values of the eight-membered ring (See Table 1) shows a relatively close set of distances in the range 2.44(2)–2.50(2) Å in 6, 2.43(3)–2.54(3) Å in 5, 2.45(2)–2.55(3) Å in 4, 2.46(2)–2.65(2) Å in 3, and 2.52(2)–2.64(2) Å in 2. In contrast, the variation in the nine membered Cnt ring is much more pronounced (Table 1) with  $\eta(\text{Ln}–\text{C}(\text{Cnt})_{\text{max}}–\text{Ln}(\text{Cnt})_{\text{min}})$  values of 1.426 Å in Lu (6) (2.50(2) to 3.930(9) Å), 1.228 Å in Tm (5) (2.54(3) to 3.769(8) Å), 1.213 Å in Er (4) (2.55(3) to 3.763(15) Å), 0.906 Å in Ho (3) (2.56(2) to 3.47(2) Å), and 0.284 Å in Dy (2) (2.66(2) to 2.96(2) Å).

The space group of the Tb complex (1) is modified from  $P2_1/n$  to  $Pnma$  with the removal of the inversion center on the lanthanide atom, which was confirmed by the analysis of the precession images. An additional symmetry plane that contains

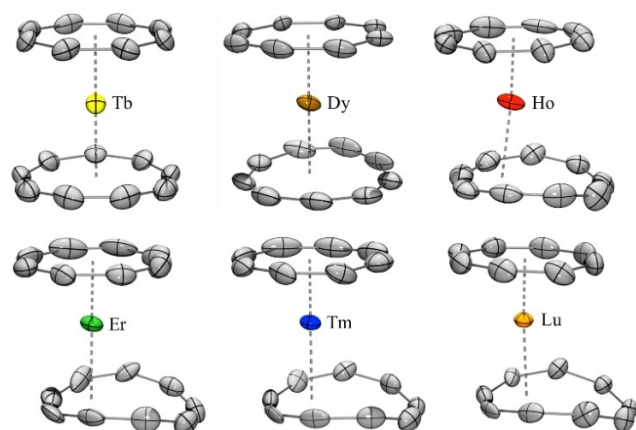


**Figure 2.** ORTEP of 1–6. Thermal ellipsoids are depicted at 50% probability level. Hydrogen atoms and the disorder are omitted for clarity (see main text for the discussion of the coordination mode).

**Table 1.** Main metric parameters for 1–6 at 150 K. [a] Only the carbon atoms formally  $\eta^1$ -coordinated are considered in the average calculation.

	Tb (1, $\eta^9$ )	Dy (2, $\eta^8$ )	Ho (3, $\eta^6$ )	Er (4, $\eta^6$ )	Tm (5, $\eta^6$ )	Lu (6, $\eta^6$ )
Ln–C(Cnt)	2.775(7)	2.68(2)	2.56(2)	2.55(3)	2.54(3)	2.50(2)
	2.775(7)	2.72(2)	2.61(2)	2.59(3)	2.57(2)	2.54(2)
	2.79(1)	2.74(2)	2.62(2)	2.61(3)	2.64(2)	2.6(2)
	2.82(3)	2.74(2)	2.72(2)	2.69(3)	2.73(2)	2.68(2)
	2.83(1)	2.79(2)	2.82(2)	2.88(1)	2.875(13)	2.943(12)
	2.84(2)	2.86(2)	3.02(3)	3.10(2)	3.11(2)	3.14(2)
	2.85(3)	2.86(2)	3.212(14)	3.443(13)	3.449(9)	3.59(10)
	2.85(1)	2.95(2)	3.37(2)	3.60(1)	3.594(12)	3.719(13)
	2.86(2)	2.96(2)	3.47(2)	3.76(2)	3.769(8)	3.930(9)
$\eta(\text{Ln–C(Cnt)})_{\text{max}}\text{–LnC(Cnt)}_{\text{min}}$	0.094	0.284	0.906	1.213	1.228	1.426
Ln–C( $\eta$ -Cnt) <sup>[a]</sup> ave	2.82(3)	2.79(9)	2.73(17)	2.74(21)	2.74(21)	2.73(26)
C( $\eta$ -Cnt)–Ln–C( $\eta$ -Cnt) <sup>[a]</sup>	177.4	172.0	169.6	174.7	173.8	174.2
Ln–C(Cnt) ave	2.82(3)	2.81(10)	2.93(33)	3.02(44)	3.03(44)	3.07(55)
Ln–C(Cot) range	2.57(3)–2.63(2)	2.52(2)–2.64(2)	2.46(2)–2.65(2)	2.45(2)–2.55(3)	2.43(3)–2.54(3)	2.44(2)–2.50(2)
Ln–C(Cot) ave	2.58(2)	2.58(4)	2.55(7)	2.50(4)	2.48(3)	2.46(1)
Ln–C( $\eta$ -all) <sup>[a]</sup> ave	2.71	2.69	2.63	2.60	2.59	2.58

the centroids of both the Cot and Cnt ligands and the Tb metal center is present. The latter thus separates both ligands in two symmetrical sections. The differentiation in the space group between the late lanthanide ions (2–6) and the Tb one (1) could be explained by a hapticity switching of the Cnt ligand in the case of larger lanthanide ions, imposing a different symmetry than that observed in 1. Consequently, the structure visually appears to be in better agreement with a formal  $\eta^9$ -coordination mode. A lower variation in the Ln–C(Cnt) distance range ( $\eta(\text{Ln–C(Cnt)})_{\text{max}}\text{–LnC(Cnt)}_{\text{min}} = 0.094 \text{ \AA}$ ) (See Table 1) is observed. The deformation of the Cnt ligand is minimal.

Several metric parameters help to visualize and quantify the structural modifications (curved vs. planar) and the hapticity modulation of the Cnt ligand in 1–6. First, three main planes were constructed; the plane defined by the Cot ligand (in grey, Figure 3), the mean plane made by the six Cnt carbon atoms that are the closest to the lanthanide ion (in color) and the one set up by three remaining Cnt carbon atoms (in color), which are located further away from the lanthanide ion. The angle between the two Cnt planes decreases from the Lu to the Tb complexes in agreement with a stronger deviation from planarity with smaller lanthanide ions. At low-temperature, the angle is decreasing gradually from  $34.2^\circ$  in Lu (6) to  $4.80^\circ$  in Tb (1), with intermediate values of  $31.3^\circ$ ,  $29.7^\circ$ ,  $23.7^\circ$ , and  $12.4^\circ$  in

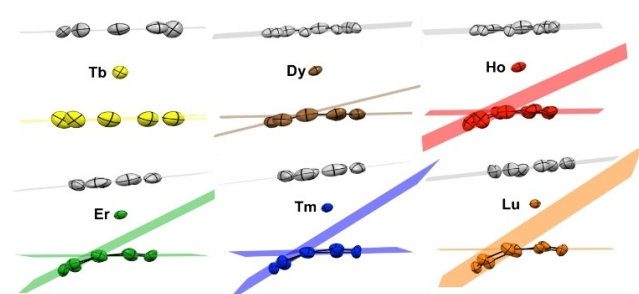


**Figure 3.** Plane constructions in 1–6. The grey plane is constructed with the eight carbon atoms of the Cot ligand. The colored planes are constructed with the six closest carbon atoms and the three remaining carbons of the Cnt ligand, respectively (see main text for limits of this construction)

Tm (5), Er (4), Ho (3) and Dy (2), respectively (Table S8). At room temperature, the decrease is weaker from  $25.3^\circ$  to  $14.8^\circ$  from 6 to 2. Complex 5 has also been recorded at 100 K, 150 K, 200 K, and 250 K with no clear break in the metric parameters.

The plane angle difference between the low- and room-temperature X-ray structures is also significant. This set of angular parameters intends to show how the curvature of the Cnt ligand gradually evolves from Tb to Lu in agreement with the lanthanide contraction of the ionic radius.<sup>[23]</sup>

The plane angle difference between the low- and room-temperature X-ray structures is also significant. This set of angular parameters intends to show how the curvature of the Cnt ligand gradually evolves from Tb to Lu in agreement with the lanthanide contraction of the ionic radius.<sup>[23]</sup>

A second set of useful metric parameters corresponds to the distances and angles from the metal ion to the constructed centroids of both ligands (See Table S8). While the centroid of the Cot ligand is always defined by its eight carbon atoms, three different centroids were constructed for the Cnt ligand: the first with the eight carbon atoms of the Cot ligand and the three others with i) the six atoms closest to the lanthanide ion (Ctr6), ii) the eight atoms closest (Ctr8) and iii) the nine atoms of the Cnt ligand (Ctr9). The Ln–Cot(Ctr) distances (at 150 K) vary from 1.804 Å (1), 1.772 Å (2), 1.735 Å (3), 1.701 Å (4), 1.681 Å (5), to 1.653 Å (6). The overall trend in the distances follows the lanthanide contraction. It is rather informative to compare these distances with those in the mono-Cot iodide or borohydride analogues  $[\text{Ln}(\text{Cot})\text{I}(\text{S})_2]$  ( $\text{S} = \text{thf}$ , pyridine or  $\text{CH}_3\text{CN}$ ) of 1.814 (Tb), 1.80(1) (Dy), 1.78 (Ho), 1.763(12) (Er),<sup>[11c]</sup> 1.750(5) Å (Tm)<sup>[18]</sup> and  $[\text{Lu}(\text{Cot})(\text{BH}_4)(\text{thf})_2]$  of 1.724 Å. Within this series, for Ln = Dy, Ho, Er, Tm, and Lu, the Ln–Cot(Ctr) distances are shorter than those reported for 2–6 while they are similar in 1.

The Ln–Cnt distances are somewhat informative to distinguish three potential coordination modes (See Figure 4): at low-temperature, for the late lanthanides (Ho to Lu), the shortest Ln–Cnt distances are that with Ctr6. In contrast, for Dy and Tb, the shortest Ln–Cnt distances are obtained with Ctr8 and Ctr9, respectively. Similarly, within all the series, the Cot(Ctr)–Ln–Cnt (Ctr) angles are also the largest using the same aforementioned



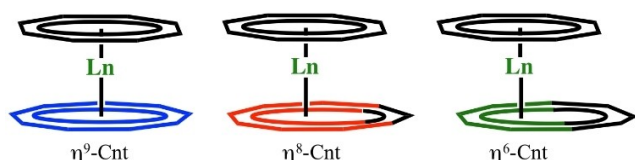


**Figure 4.** Representation of the different limit coordination modes of the Cnt ligand.

Cnt centroids (See Table S8). This set of data would best describe the hapticity of the Cnt ligand as formal  $\eta^6$  for Ho (3) to Lu (6), while the hapticity would be best described as formal  $\eta^8$  for Dy (2) and  $\eta^9$  for Tb (1). Interestingly, at higher temperature, the picture is slightly different and the coordination mode of the Cnt in Ho (3) would be best described as formal  $\eta^8$ . The hapticity of the Cnt in the Er (4), Tm (5) and Lu (6) complexes would remain best described as  $\eta^6$  at room temperature. Thus, the average Ln–C distances on all formally  $\eta$ -coordinated carbon atoms were calculated for 1–6 and are reported in Table 1. A smooth variation with the lanthanide ion size is reported from 2.71 Å for [Tb(Cot)(Cnt)] (1) complex to 2.58 Å for [Lu(Cot)(Cnt)] (6).

Additionally, it is possible to consider the sum of the van der Waals radii as additional information on the nature of the interaction, i.e. distance metrics that are larger than the sum of the van der Waals radii are not expected to size any interaction.<sup>[24]</sup> The range of these van der Waals radii for Tb–Lu is 1.80 to 1.72 Å and that of aromatic C atom is 1.70 Å. Thus the maximum distance is 3.42 Å for 6 (Lu) and 3.47 Å for 1 (Tb). In these considerations 4–6 are  $\eta^6$ , 3 is  $\eta^8$  and 1,2 are  $\eta^9$ . However, these analyses should be taken cautiously because these metrics present the limit forms of coordination ( $\eta^6$  and  $\eta^9$ ) but the real hapticity is probably best found in between these limit forms, as found in solution (See  $^1\text{H}$  NMR). Moreover, from a strict crystallographic point of view, the opposite construction, i.e.  $\eta^9$ -coordination of the Cnt and lower coordination mode of the Cot ligand, remains valid.

### Magnetic measurements

The solid-state magnetic data for compounds 1–3 and 5 are reported in Figure 5. The room temperature  $\chi_{\text{M}}T$  values are equal to 11.34, 14.12, 13.2 and 6.8  $\text{cm}^3\text{Kmol}^{-1}$  for compounds 1–3 and 5 respectively. These values are in fairly good agreement with the calculated Curie constants for the ground state multiplets  $^7\text{F}_6$  (Tb(III), 1, 11.82  $\text{cm}^3\text{Kmol}^{-1}$ ,  $g_J=3/2$ ),  $^6\text{H}_{15/2}$  (Dy(III), 2, 14.17  $\text{cm}^3\text{Kmol}^{-1}$ ,  $g_J=4/3$ ),  $^5\text{I}_8$  (Ho(III), 3, 14.07  $\text{cm}^3\text{Kmol}^{-1}$ ,  $g_J=5/4$ ) and  $^3\text{H}_6$  (Tm(III), 5, 7.15  $\text{cm}^3\text{Kmol}^{-1}$ ,  $g_J=7/6$ ). On cooling,  $\chi_{\text{M}}T$ 's decrease monotonically down to 2 K: 2.52  $\text{cm}^3\text{Kmol}^{-1}$  for 1, 7.2  $\text{cm}^3\text{Kmol}^{-1}$  for 2, 5.1  $\text{cm}^3\text{Kmol}^{-1}$  for 3 and 5.9  $\text{cm}^3\text{Kmol}^{-1}$  for 5. These values reflect the signature of the effect of the crystal field splitting that lifts the degeneracy of the ground state multiplets. The magnetization curves at 2 K are given in the Supporting Information (Figure S15). None of these compounds show slowing down of the relaxation of the

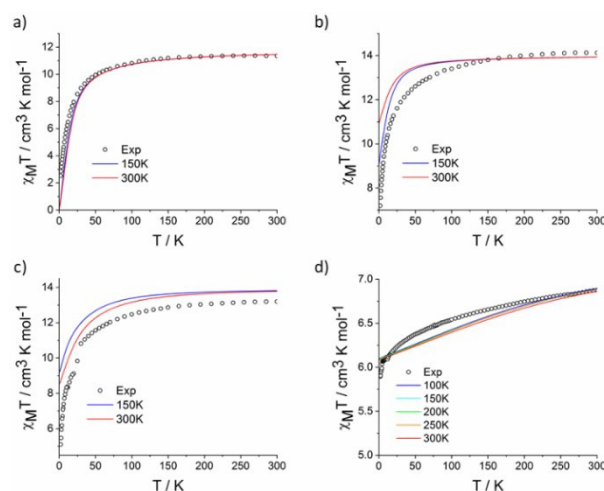


**Figure 5.** Temperature dependent  $\chi_{\text{M}}T$  values for compounds 1 (a), 2 (b), 3 (c) and 5 (d) in dots with the calculated curves from structures at various temperatures.

magnetic moment in the absence of external dc field, which means that they do not behave as Single-Molecule Magnets (SMM) in zero field as opposed to the reported Er complex, 4.<sup>[13]</sup>

### Computational studies

Theoretical computations at the SA-CASSCF/RASSI-SO level have been performed for 1–5 based on the X-ray crystal structures at the different temperatures at which the X-ray data have been obtained (See Supporting Information for computational details). This series of computations can be compared to those done on the basis of the DFT optimized structure of [Er(Cot)(Cnt)] that lead to a perfectly linear structure.<sup>[13]</sup> Ground and excited state wave functions for 1–5 along with the corresponding energy gaps are shown in Tables S30–S34.

Terbium is next to the isotropic gadolinium and is oblate. Tb is a non-Kramers ion, and thus, the crystal field allows the formation of non-degenerated  $m_J$  states. In the geometry imposed by the two large aromatic ligands, the linear geometry does not favor axial anisotropy, which shall allow mixing the  $m_J$  states and/or accounting for  $m_J=0$  ground state. The theoretical treatment needs to take into account this singularity and is then rendered more difficult. Thus, the ground calculated state is then the  $m_J=0$  state and just above the  $m_J=\pm 1$  state, which is not in good agreement with the low temperature data for the above-mentioned considerations.

However, the  $2J+1$  states split on 873  $\text{cm}^{-1}$  and give a reasonable agreement with the experimental data (Figure 5) at higher temperatures.

Following the trend described above, the oblate Dy and Ho ions have similar mixed configurations with principally  $m_J=\pm 15/2$  (65%) and  $\pm 11/2$  (13%) for 2 and principally  $m_J=\pm 8$  (65%) and  $\pm 6$  (14%) for 3, both at 150 K. The  $m_J$  composition evolves at 300 K to be  $m_J=\pm 15/2$  (83%) and  $\pm 11/2$  (12%) for 2 and  $m_J=\pm 8$  (56%),  $\pm 6$  (13%), and  $\pm 7$  (12%) for 3, explaining the

different calculated low temperature magnetic susceptibility data observed (Figure S26 and S27). In **2**, six energy states are found within  $109\text{ cm}^{-1}$ , while in **3**, the overall splitting is only  $397\text{ cm}^{-1}$  with 5 states within  $136\text{ cm}^{-1}$ . The modification of the energy state composition and splitting when different structures are used (X-ray, 150 K, 300 K) is not greatly modulated, and thus the overall calculated magnetic temperature dependent curves is comparable with that of the experiments (Figure 5). These computations rationalize very well the magnetic behavior of **2** and **3**, showing no SMM behavior, as expected from the electrostatic model. Additionally, as expected for oblate ions with large aromatic ligands, the anisotropy orientation is not following the axial symmetry (Figure 6).

For the prolate ions, erbium and thulium, large aromatic ligands are usually well adapted for maximizing the anisotropy compared to the three ions discussed above; they disfavor the mixing of the  $m_J$  states and maximize anisotropy. Accordingly, the ground state is pure  $m_J = \pm 15/2$  for the erbium complex (**4**), while it is pure  $m_J = \pm 6$  for the thulium complex (**5**). For **4**, the first excited state of  $m_J = \pm 13/2$  (98%) and the second excited state, which is principally a mixed configuration of  $m_J = \pm 1/2$  (68.2%) and  $m_J = \pm 3/2$  (19.9%) are located at  $170$  and  $251\text{ cm}^{-1}$ , respectively. In **4**, the relative energy of the  $m_J$  crystal field states varies very little depending upon the structure ( $160$  and  $255\text{ cm}^{-1}$ ) chosen for the computations (X-ray, 150 K, 300 K). However, as expected from the higher symmetry of the structure obtained from DFT optimization, the nature of the energy states differs in the fact that they are pure in symmetric structure but mixed with more realistic solid-states structures. However, despite this, the computed variable temperature magnetic susceptibility curve is very similar to that reported experimentally in previous work.<sup>[13]</sup> In **4**, the anisotropy is typically perpendicular to the aromatic sandwich ligands in agreement with the high symmetry of the complexes. In the case of the X-ray structures, the anisotropy is not perfectly perpendicular to the Cot plane but crosses the two ligands in the approximate position of the  $\eta^8$ -centroid of the Cot ligands and the  $\eta^6$ -centroid of the Cnt ligand (Figure 3). In turn, this does not impact the magnetic properties and the magnetic barrier of  $251\text{ cm}^{-1}$  measured in previous work. According to the computations, the barrier is therefore of good agreement with a thermally accessed QTM via the second excited state.

In **5**, the computations indicate a ground state with pure  $m_J = \pm 6$ , in agreement with the experimental low temperature  $\chi_{\text{MT}}$  value. The first excited state is found  $431\text{ cm}^{-1}$  above and is pure  $m_J = \pm 5$ . The large gap between the ground and first excited state contrasts with the experimental curve shape that increases relatively fast between 2 and 50 K, which would agree with a Boltzmann population of lower excited energy states. The overall splitting is  $770\text{ cm}^{-1}$ .

## Conclusion

In conclusion, we report the synthesis and characterization of a series of heteroleptic late trivalent lanthanide complexes from Tb to Lu with the dianionic Cot and the monoanionic Cnt ligand. The terbium complex adopts a linear structure in which both ligands are aligned and their hapticity is  $\eta^8$  for the Cot and  $\eta^9$  for the Cnt ligand. However, the latter was shown to partially isomerize over time. This yields a structure, in which one of the carbon atoms of the Cnt moves inside the ring, giving a *cis-cis-trans* motif and modifying the overall hapticity of the ligand from nine to eight. The isomerization process has been tracked by  $^1\text{H}$  NMR spectroscopy and X-ray crystallography. From Dy to Lu, the complexes are highly disordered, which makes the analysis more difficult. The solid-state bond metrics show that the Cnt ligand curves with several carbon atoms being moved away from the metal center. The data follow well the ionic contraction of the lanthanide with the Lu complex being the most distorted one. In solution, in the 183–273 K temperature range, the ligand signal is single and remains flexible as observed by  $^1\text{H}$  NMR spectroscopy. The temperature-dependent magnetic data show that the presence of large aromatic ligand suits the prolate ions Er and Tm particularly well. However, only the Er analogue was shown to exhibit SMM behavior.<sup>32</sup> The *ab initio* wavefunction-based computations insist on the role of the ligand geometry on the nature of the ground state and indicate that the deviation of the linearity of the Cnt ligand does not affect the anisotropy in the prolate ions significantly, while this modulates the composition and the ratio of the mixed  $m_J$  states of the non-adapted oblate ions. Together, the data strongly indicate that the coordination versatility of the Cnt ligand might be a great tool for the modulation of the physical properties of lanthanide complexes.

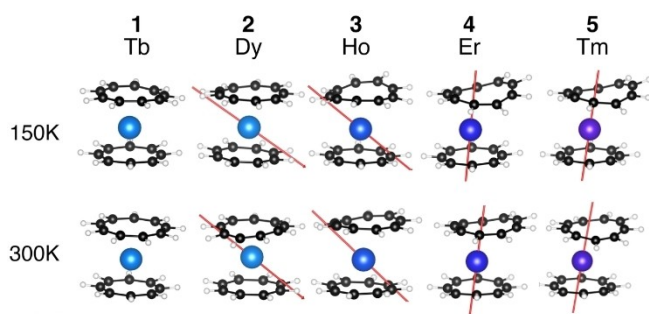


**Figure 6.** Computed structures of **1–5** at 150 and 300 K and ground-state anisotropy axis (not represented for Tb due to planar anisotropy).

## Experimental Section

**General considerations:** All reactions were performed using standard Schlenk-line techniques or in an argon filled glovebox (MBraun). All glassware was dried at  $140^\circ\text{C}$  for at least 12 h prior to use. THF, DME, toluene and toluene- $\text{d}_8$  were dried over sodium, degassed and transferred under reduced pressure in a cold flask.  $\text{TmI}_3$ ,  $\text{ErI}_3$ ,  $\text{HoI}_3$ ,  $\text{DyI}_3$  and  $\text{TbI}_3$  were purchased from Sigma Aldrich and used without further purification. NMR spectra were recorded in 5 mm tubes adapted with a J. Young valve on Bruker 300 MHz Avance III spectrometers. Chemical shifts are expressed relative to TMS in ppm. Infrared (IR) spectra were recorded at room temperature under argon on a Thermo Scientific Nicolet iS5 spectrometer equipped with the iD7 ATR-Diamond unit. Magnetic measurements

were obtained in a Quantum Design MPMS-XL SQUID magnetometer. An applied magnetic field of 2 kOe is used in the temperature range 2–20 K, and 10 kOe for temperatures above 20 K, for the  $\chi_M T$  vs. T curves. To avoid reorientation and sample degradation the microcrystals are trapped and slightly pressed between quartz wool and sealed in quartz tubes or were fixated with dried and degassed eicosane in flame sealed quartz tubes.

**Crystal-structure analysis:** Deposition Numbers 2073511 (for [Tb(Cot)(thf)<sub>2</sub>]), 2073512 (for [Ho(Cot)(thf)<sub>2</sub>]), 2073513 (for [Lu(Cot)(BH<sub>4</sub>)(THF)]<sub>2</sub>), 2073514 (for **1** at 150 K), 2073515 (for **1** at 300 K), 2073516 (for **2** at 150 K), 2073517 (for **2** at 300 K), 2073518 (for **3** at 150 K), 2073519 (for **3** at 300 K), 2073520 (for **4** at 150 K), 2073521 (for **4** at 300 K), 2073522 (for **5** at 150 K), 2073523 (for **5** at 300 K), 2073524 (for **6** at 150 K), 20735325 (for **6** at 300 K), 2073526 (for **1'** at 150 K), 2073527 (for **1''** at 150 K), 2073528 (for **5** at 100 K), 2073529 (for **5** at 200 K), 2073530 (for **5** at 250 K), 2073531 (for **2b** at 150 K) contain the supplementary crystallographic data for this paper. These data are provided free of charge by the joint Cambridge Crystallographic Data Centre and Fachinformationszentrum Karlsruhe Access Structures service.

## Syntheses

**[Er(Cot)I(thf)]:** The complex was synthesized as previously described.<sup>[11c]</sup> A similar procedure was used for the other late lanthanides. [Lu(BH<sub>4</sub>)<sub>3</sub>(thf)<sub>3</sub>] was synthesized using the procedure reported for the Nd analogue.<sup>[17]</sup>

**[Tb(Cot)I(thf)]:** A cold thf solution (−40 °C) of K<sub>2</sub>Cot (4 mL, 117 mg, 0.64 mmol, 1 equiv) was added to a stirred cold (−40 °C) thf suspension of Tbl<sub>3</sub> (3 mL, 346 mg, 0.64 mmol, 1 equiv). The mixture was allowed to warm to room temperature (r.t.) and was stirred for 16 h. The resultant light yellow suspension was filtered through a frit and the filtrate dried under reduced pressure. The solids were suspended in 5 mL thf and heated to 60 °C forming a deep yellow solution. Diethyl ether was layered on the top and the solution was stored at −40 °C. Yellow needles of the desired compound formed slowly (181 mg, 53%). <sup>1</sup>H NMR (300 MHz, thf-d<sub>8</sub>, 293 K): δ (ppm), 194.92 (s br, 8H), *coordinated thf molecules are not visible*. IR (ATR):  $\nu^-$  = 2970 (br m), 2889 (m), 1859 (w), 1753 (w), 1616 (w), 1556 (w), 1444 (br m), 1343 (w), 1309 (w), 1245 (w), 1180 (w), 1011 (vs), 895 (s), 860 (vs), 775 (m), 749 (m), 708 (vs), 667 (s), 573 (m) cm<sup>−1</sup>. Anal. Calcd. for C<sub>16</sub>H<sub>24</sub>IO<sub>2</sub>Tb (534.19): C, 35.97; H, 4.53; Found: C, 35.77; H, 4.56.

**[Dy(Cot)I(thf)]:** A cold thf solution (−40 °C) of K<sub>2</sub>Cot (5 mL, 138 mg, 0.76 mmol, 1 equiv) was added to a stirred cold (−40 °C) thf suspension of Dyl<sub>3</sub> (10 mL, 411 mg, 0.76 mmol, 1 equiv). The mixture was allowed to warm to r.t. and was stirred for 16 h. The resultant light yellow suspension was filtered through a frit and the filtrate dried under reduced pressure. The solids were suspended in 8 mL thf and heated to 60 °C forming a deep yellow solution. Diethyl ether was layered on the top and the solution was stored at −40 °C. Yellow needles of desired compound formed slowly (265 mg, 63%). <sup>1</sup>H NMR (300 MHz, thf-d<sub>8</sub>, 293 K): δ (ppm), 88.66 (s br, 8H), *coordinated thf molecules are not visible*. IR (ATR):  $\nu^-$  = 2951 (br m), 2889 (m), 1858 (w), 1752 (w), 1614 (w), 1554 (w), 1453 (br m), 1343 (w), 1309 (w), 1256 (w), 1178 (w), 1010 (vs), 895 (s), 860 (vs), 750 (m), 705 (vs), 670 (s), 575 (m) cm<sup>−1</sup>. Anal. Calcd. for C<sub>15.4</sub>H<sub>19.2</sub>IO<sub>2</sub>Dy (537.77): C, 33.03; H, 3.91; Found: C, 32.94; H, 4.07. The number of thf was decreased upon drying.

**[Ho(Cot)I(thf)]:** A cold thf solution (−40 °C) of K<sub>2</sub>Cot (5 mL, 223 mg, 1.22 mmol, 1 equiv) was added to a stirred cold (−40 °C) thf suspension of Hol<sub>3</sub> (668 mg, 1.22 mmol, 1 equiv). The mixture was allowed to warm to r.t. and was stirred for 16 h. The resultant light yellow suspension was filtered through a frit and the filtrate dried

under reduced pressure. The solids were suspended in 7 mL thf and heated to 60 °C forming a deep yellow solution. Diethyl ether was layered on the top and the solution was stored at −40 °C. Yellow needles of desired compound formed slowly (583 mg, 88%). <sup>1</sup>H NMR (300 MHz, thf-d<sub>8</sub>, 293 K): δ (ppm), 70.88 (s br, 8H), *coordinated thf molecules are not visible*. IR (ATR):  $\nu^-$  = 2969 (br m), 2888 (m), 1852 (w), 1747 (w), 1601 (w), 1441 (br m), 1343 (w), 1212 (br w), 1008 (vs), 856 (vs), 750 (m), 704 (vs), 645 (s) cm<sup>−1</sup>. Anal. Calcd. for C<sub>16</sub>H<sub>24</sub>IO<sub>2</sub>Ho (540.20): C, 35.57; H, 4.48; Found: C, 35.63; H, 4.53.

**[Tm(Cot)I(thf)]:** A cold solution (−40 °C) of K<sub>2</sub>Cot (3 mL, 32 mg, 0.17 mmol, 1 equiv) was added to a stirred cold (−40 °C) thf suspension of Tml<sub>3</sub> (5 mL, 95 mg, 0.17 mmol, 1 equiv). The mixture was allowed to warm to r.t. and was stirred for 16 h. The resultant light yellow suspension was filtered through a frit and the filtrate dried under reduced pressure. The solids were suspended in 7 mL thf and heated to 60 °C forming a deep yellow solution. Diethyl ether was layered on the top and the solution was stored at −40 °C. Yellow needles of desired compound formed slowly (54 mg, 57%). The <sup>1</sup>H NMR (300 MHz, thf-d<sub>8</sub>, 293 K) remained silent. The compound was previously published by Fedushkin et al.<sup>[18]</sup>

**[Lu(Cot)(BH<sub>4</sub>)(thf)] :** A cold solution (−40 °C) of K<sub>2</sub>Cot (61 mg, 0.33 mmol, 1 equiv) was added to a stirred cold (−40 °C) thf solution of [Lu(BH<sub>4</sub>)<sub>3</sub>(thf)<sub>3</sub>] (145 mg, 0.33 mmol, 1 equiv). The mixture was allowed to warm to r.t. and was stirred for 16 h. The resultant light yellow suspension was filtered through a teflon syringe filter. The filtrate was concentrated under reduced pressure until incipient crystallization and stored at −40 °C to afford the title compound as light yellow crystals (117 mg, 0.27 mmol, 81%). Recrystallization from toluene led to the decoordination of one thf molecule and formation of [(Cot)Lu(BH<sub>4</sub>)(thf)]<sub>2</sub> as colorless crystals suitable for X-ray diffraction studies. <sup>1</sup>H NMR (300 MHz, thf-d<sub>8</sub>, 293 K): δ (ppm), 6.31 (s, 8H, Cot), 3.68–3.59 (m, ca. 4H, OCH<sub>2</sub> coordinated thf), 1.84–1.74 (m, ca. 4H, OCH<sub>2</sub>CH<sub>2</sub> coordinated thf), 0.04 (1:1:1:1 quartet <sup>1</sup>J<sub>BH</sub> = 83.0 Hz, 4H, BH<sub>4</sub>). <sup>13</sup>C<sup>[25]</sup> NMR (75 MHz, thf-d<sub>8</sub>, 293 K): δ (ppm), 92.6 (Cot), 68.0 (OCH<sub>2</sub> coordinated thf), 26.1 (OCH<sub>2</sub>CH<sub>2</sub> coordinated thf). IR (ATR):  $\nu^-$  = 3021 (w), 2989 (w), 2930 (br m), 2889 (m), 2426 (m), 2272 (s), 2239 (s), 2164 (m), 2040 (w), 1855 (w), 1746 (w), 1610 (w), 1494 (w), 1453 (m), 1316 (br m), 1245 (m), 1213 (w), 1092 (s), 1012 (vs), 898 (s), 877 (vs), 752 (m), 706 (vs) cm<sup>−1</sup>. No satisfactory EA was obtained.

**[Tb(Cot)(Cnt)] (1'):** A brown acetonitrile solution of KCnt (2 mL, 42 mg, 0.27 mmol, 1.1 equiv) was added at r.t. to a toluene suspension of [Tb(Cot)I(thf)<sub>2</sub>] (10 mL, 149 mg, 0.25 mmol, 1 equiv). The resulting suspension was left to stir at r.t. for 12 h and was then dried under reduced pressure. The pale-yellow residue was suspended in toluene (5 mL). After 1 h of stirring, the volatiles were removed under reduced pressure and the residue was further dried for 5 h at r.t. and extracted in several crops with large amounts of toluene. The pale-yellow solution was filtered and cooled at −40 °C yielding X-ray suitable pale yellow needles of **1'** (32 mg, 29%). <sup>1</sup>H NMR (300 MHz, toluene-d<sub>8</sub>, 293 K): δ (ppm), 246.3 (s, 8H, Cot), 101.6 (s, 9H, Cnt). The <sup>1</sup>H NMR evolves with time and crystals of **1'** can be obtained after few days. IR (ATR):  $\nu^-$  = 3006 (m) 2920 (s), 2851 (s), 1935 (w), 1853 (w), 1746 (w), 1602 (w), 1551 (w), 1493 (w), 1457 (m), 1375 (w), 1313 (w), 1018 (w), 892 (vs), 846 (w), 772 (m), 747 (s), 704 (vs), 654 (vs) cm<sup>−1</sup>. Anal. Calcd. for C<sub>17</sub>H<sub>17</sub>TbO.2 Toluene (398.67): C, 55.43; H, 4.70; Found: C, 55.35; H, 5.03.

**[Tb(Cot)(Cnt)] (1''):** Toluene (20 mL) was condensed to a mixture of KCnt (30.0 mg, 0.192 mmol, 1 equiv), and [Tb(Cot)I(thf)<sub>2</sub>] (103 mg, 0.193 mmol; 1.01 eq) at −78 °C. The resulting suspension was heated to 150 °C for three hours and immediately passed through a syringe PTFE-filter, while still hot. Upon slowly cooling the orange filtrate to r.t., single crystals of **1''** suitable for X-ray diffraction were obtained. Subsequent decantation of the mother liquor and drying

in vacuo yielded 1'' as orange crystalline solid (30.0 mg, 34%). Raman (solid state, sealed ampule):  $\tilde{\nu}$  [ $\text{cm}^{-1}$ ] = 3044 (vw), 3008 (vw), 1515 (vw), 1495 (vw), 750 (s), 660(s), 366 (vw), 280 (w), 239 (s).

**[Dy(Cot)(Cnt)] (2):** A brown acetonitrile solution of KCnt (2 mL, 47 mg, 0.30 mmol, 1.1 equiv) was added at r.t. to a toluene suspension of [Dy(Cot)(thf)<sub>2</sub>] (10 mL, 146 mg, 0.27 mmol, 1 equiv). The resulting suspension was left to stir at r.t. for 12 h and was then dried under reduced pressure. The yellow residue was suspended in toluene (5 mL). After 1 h of stirring, the volatiles were removed under reduced pressure and the residue was further dried for 5 h at r.t. and extracted in several crops with large amounts of toluene. The yellow solution was filtered and cooled at  $-40^\circ\text{C}$  yielding X-ray suitable yellow needles of **2** (62.5 mg, 60%). <sup>1</sup>H NMR (300 MHz, toluene-d<sub>8</sub>, 293 K):  $\delta$  (ppm), 118.7 (s, 8H, Cot), 72.90 (s, 9H, Cnt). IR (ATR):  $\tilde{\nu}$  = 3005 (br m), 2917 (m), 1970 (w), 1851 (w), 1744 (w), 1601 (w), 1456 (m), 1373 (w), 1313 (w), 1018 (w), 892 (vs), 848 (w), 773 (m), 748 (s), 706 (vs), 654 (vs), 507 (w)  $\text{cm}^{-1}$ . Anal. Calcd. for C<sub>17</sub>H<sub>17</sub>Dy (383.82): C, 53.20; H, 4.46; Found: C, 53.14; H, 4.48.

**[Ho(Cot)(Cnt)] (3):** A brown acetonitrile solution of KCnt (2 mL, 60 mg, 0.39 mmol, 1.05 equiv) was added at r.t. to a toluene suspension of [Ho(Cot)(thf)<sub>2</sub>] (15 mL, 189 mg, 0.35 mmol, 1 equiv). The resulting suspension was left to stir at r.t. for 12 h and was then dried under reduced pressure. The pale-orange residue was suspended in toluene (5 mL). After 1 h of stirring, the volatiles were removed under reduced pressure and the residue was further dried for 5 h at r.t. and extracted in several crops with large amounts of toluene. The pale-orange solution was filtered and cooled at  $-40^\circ\text{C}$  yielding X-ray suitable pale-orange needles of **3** (77.8 mg, 67%). <sup>1</sup>H NMR (300 MHz, toluene-d<sub>8</sub>, 293 K):  $\delta$  (ppm), 90.45 (s, 8H, Cot), 59.17 (s, 9H, Cnt). IR (ATR):  $\tilde{\nu}$  = 3003 (br m), 2920 (m), 1969 (w), 1852 (w), 1745 (w), 1602 (w), 1455 (w), 1374 (w), 1313 (w), 1016 (m), 892 (s), 850 (w), 776 (m), 748 (m), 704 (vs), 656 (vs), 506 (m)  $\text{cm}^{-1}$ . Anal. Calcd. for C<sub>17</sub>H<sub>17</sub>Ho (386.25): C, 52.86; H, 4.44; Found: C, 52.34; H, 4.53.

**[Er(Cot)(Cnt)] (4):** A brown acetonitrile solution of KCnt (2 mL, 65 mg, 0.42 mmol, 1.05 equiv) was added at r.t. to a toluene suspension of [Er(Cot)(thf)<sub>2</sub>] (15 mL, 215 mg, 0.40 mmol, 1 equiv). The resulting suspension was left to stir at r.t. for 12 h and was then dried under reduced pressure. The orange residue was suspended in toluene (5 mL). After 1 h of stirring, the volatiles were removed under reduced pressure and the residue was further dried for 5 h at r.t. and extracted in several crops with large amounts of toluene. The orange solution was filtered and cooled at  $-40^\circ\text{C}$  yielding X-ray suitable orange needles of **4** (73.6 mg, 63%). <sup>1</sup>H NMR (300 MHz, toluene-d<sub>8</sub>, 293 K):  $\delta$  (ppm), -5.01 (br s), -128.7 (br s). IR (ATR):  $\tilde{\nu}$  = 3030 (br m), 2959 (s), 2921 (m), 2851 (m), 1966 (w), 1854 (w), 1748 (w), 1604 (br w), 1451 (w), 1376 (w), 1313 (w), 1259 (s), 1087 (s), 1014 (s), 892 (s), 797 (s), 748 (m), 702 (vs), 657 (vs), 505 (m)  $\text{cm}^{-1}$ . Anal. Calcd. for C<sub>17</sub>H<sub>17</sub>Er (388.58): C, 52.55; H, 4.41; Found: C, 52.80; H, 5.04.

**[Tm(Cot)(Cnt)] (5):** A brown acetonitrile solution of KCnt (2 mL, 65 mg, 0.42 mmol, 1.05 equiv) was added at r.t. to a toluene suspension of [Tm(Cot)(thf)<sub>2</sub>] (15 mL, 217 mg, 0.40 mmol, 1 equiv). The resulting suspension was left to stir at r.t. for 12 h and was then dried under reduced pressure. The salmon-orange residue was suspended in toluene (5 mL). After 1 h of stirring, the volatiles were removed under reduced pressure and the residue was further dried for 5 h at r.t. and extracted in several crops with large amounts of toluene. The salmon-orange solution was filtered and cooled at  $-40^\circ\text{C}$  yielding X-ray suitable salmon-orange needles of **5** (74.6 mg, 48%). <sup>1</sup>H NMR (300 MHz, toluene-d<sub>8</sub>, 293 K):  $\delta$  (ppm), -23.21 (br s), -235.8 (br s). IR (ATR):  $\tilde{\nu}$  = 2998 (br m), 2920 (m), 2852 (m), 1965 (w), 1856 (w), 1753 (w), 1451 (w), 1314 (w), 1259 (w), 1016 (m), 893 (s), 781 (s), 749 (m), 703 (vs), 658 (vs), 505 (m)  $\text{cm}^{-1}$ .

Anal. Calcd. for C<sub>17</sub>H<sub>17</sub>Tm (390.25): C, 52.32; H, 4.39; Found: C, 52.80; H, 4.64.

**[Lu(Cot)(Cnt)] (6):** A mixture of [Lu(Cot)(BH<sub>4</sub>)(thf)<sub>2</sub>] (146 mg, 0.33 mmol) and KCnt (52 mg, 0.33 mmol) in toluene (15 mL) was heated at  $110^\circ\text{C}$  for 16 h and was then dried under reduced pressure for 2 h. The light yellow residue was extracted with hot toluene. The yellow filtrate was stored at  $-40^\circ\text{C}$  yielding yellow needles of **6** suitable for X-ray diffraction studies (44 mg, 0.11 mmol, 34%). <sup>1</sup>H NMR (300 MHz, toluene-d<sub>8</sub>, 293 K):  $\delta$  (ppm), 6.54 (s, 9H, Cnt), 5.83 (s, 8H, Cot). <sup>13</sup>C NMR (75 MHz, toluene-d<sub>8</sub>, 293 K):  $\delta$  (ppm), 107.8 (Cnt), 93.5 (Cot). IR (ATR):  $\tilde{\nu}$  = 2992 (br m), 1963 (w), 1857 (w), 1748 (w), 1604 (w), 1490 (w), 1447 (w), 1375 (w), 1313 (w), 1158 (w), 1018 (w), 892 (vs), 780 (m), 750 (m), 704 (vs), 662 (vs), 502 (w)  $\text{cm}^{-1}$ . Anal. Calcd. for C<sub>17</sub>H<sub>17</sub>Lu (396.29): C, 51.52; H, 4.32; Found: C, 51.16; H, 4.34.

## Acknowledgements

Dr. Louis Ricard is gratefully thanked for his very important insights in the crystal structure analysis. Parts of this work have received funding from the ERC under grant agreement No 716314 and from an ANR (French National Research Agency) granted collaborative project (ANR-19-CE07-0019-1). CNRS and Ecole polytechnique are thanked for financial support. N.M. thanks ENS Paris-Saclay. B.L.G., F.G. and L.L.D. thank the French GENCI/IDRIS-CINES centers for high-performance computing resources. Open access funding enabled and organized by Projekt DEAL.

## Conflict of Interest

The authors declare no conflict of interest.

**Keywords:** cyclononatetraenyl • lanthanides • organometallics • magnetism • single molecule magnets

- [1] a) J.-L. Liu, Y.-C. Chen, M.-L. Tong, *Chem. Soc. Rev.* **2018**, *47*, 2431–2453; b) J.-C. G. Bünzli, C. Piguet, *Chem. Soc. Rev.* **2005**, *34*, 1048–1077; c) D. N. Woodruff, R. E. P. Winpenny, R. A. Layfield, *Chem. Rev.* **2013**, *113*, 5110–5148.
- [2] S. Cotton in *Lanthanide and Actinide Chemistry*, Wiley, **2006**, pp. 9–22.
- [3] a) S. V. Eliseeva, J.-C. G. Bünzli, Vol. 7 (Eds.: P. Hänninen, H. Härmä), Springer Series on Fluorescence, **2010**; b) J. D. Rinehart, J. R. Long, *Chem. Sci.* **2011**, *2*, 2078–2085.
- [4] a) E. G. Moore, A. P. S. Samuel, K. N. Raymond, *Acc. Chem. Res.* **2009**, *42*, 542–552; b) F. Pointillart, B. le Guennic, O. Cador, O. Maury, L. Ouahab, *Acc. Chem. Res.* **2015**, *48*, 2834–2842; c) J. Kido, Y. Okamoto, *Chem. Rev.* **2002**, *102*, 2357–2368.
- [5] a) P. Caravan, J. J. Ellison, T. J. McMurphy, R. B. Lauffer, *Chem. Rev.* **1999**, *99*, 2293–2352; b) M. Bottrill, L. Kwok, N. J. Long, *Chem. Soc. Rev.* **2006**, *35*, 557–571; c) T. J. Clough, L. Jiang, K.-L. Wong, N. J. Long, *Nat. Commun.* **2019**, *10*, 1420.
- [6] B. M. Day, F.-S. Guo, R. A. Layfield, *Acc. Chem. Res.* **2018**, *51*, 1880–1889.
- [7] a) F.-S. Guo, B. M. Day, Y.-C. Chen, M.-L. Tong, A. Mansikkamäki, R. A. Layfield, *Science* **2018**; b) C. A. P. Goodwin, F. Ortu, D. Reta, N. F. Chilton, D. P. Mills, *Nature* **2017**, *548*, 439; c) K. R. McClain, C. A. Gould, K. Chakarawet, S. Teat, T. J. Groshens, J. R. Long, B. G. Harvey, *Chem. Sci.* **2019**; d) A. Chiesa, F. Cugini, R. Hussain, E. Macaluso, G. Allodi, E. Garlatti, M. Giansiracusa, C. A. P. Goodwin, F. Ortu, D. Reta, J. M. Skelton, T. Guidi, P. Santini, M. Solzi, R. De Renzi, D. P. Mills, N. F. Chilton, S. Carretta, *Phys. Rev. B* **2020**, *101*, 174402; e) N. Ishikawa, M. Sugita, T.

- Ishikawa, S.-y. Koshihara, Y. Kaizu, *J. Am. Chem. Soc.* **2003**, *125*, 8694–8695.
- [8] a) W. J. Evans, M. A. Johnston, R. D. Clark, J. W. Ziller, *J. Chem. Soc. Dalton Trans.* **2000**, 1609–1612; b) J. J. Le Roy, I. Korobkov, M. Murugesu, *Chem. Commun.* **2014**, *50*, 1602–1604; c) K. L. M. Harriman, I. Korobkov, M. Murugesu, *Organometallics* **2017**, *36*, 4515–4518.
- [9] a) M. Xémard, S. Zimmer, M. Cordier, V. Goudy, L. Ricard, C. Clavaguéra, G. Nocton, *J. Am. Chem. Soc.* **2018**, *140*, 14433–14439; b) M. D. Walter, G. Wolmershäuser, H. Sitzmann, *J. Am. Chem. Soc.* **2005**, *127*, 17494–17503.
- [10] C. A. Gould, K. R. McClain, J. M. Yu, T. J. Groshens, F. Furche, B. G. Harvey, J. R. Long, *J. Am. Chem. Soc.* **2019**, *141*, 12967–12973.
- [11] a) K. R. Meihaus, J. R. Long, *J. Am. Chem. Soc.* **2013**, *135*, 17952–17957; b) Y.-S. Meng, Y.-S. Qiao, Y.-Q. Zhang, S.-D. Jiang, Z.-S. Meng, B.-W. Wang, Z.-M. Wang, S. Gao, *Chem. Eur. J.* **2016**, *22*, 4704–4708; c) J. D. Hilgar, M. G. Bernbeck, B. S. Flores, J. D. Rinehart, *Chem. Sci.* **2018**, *9*, 7204–7209; d) J. D. Hilgar, M. G. Bernbeck, J. D. Rinehart, *J. Am. Chem. Soc.* **2019**, *141*, 1913–1917; e) J. Moutet, J. Schleinitz, L. La Droite, M. Tricoire, F. Pointillart, F. Gendron, T. Simler, C. Clavaguéra, B. Le Guennic, O. Cador, G. Nocton, *Angew. Chem. Int. Ed.* **2021**, *60*, 6042–6046; *Angew. Chem.* **2021**, *133*, 6107–6111.
- [12] a) G. B. Deacon, C. M. Forsyth, F. Jaroschik, P. C. Junk, D. L. Kay, T. Maschmeyer, A. F. Masters, J. Wang, L. D. Field, *Organometallics* **2008**, *27*, 4772–4778; b) C. Ruspic, J. R. Moss, M. Schürmann, S. Harder, *Angew. Chem. Int. Ed.* **2008**, *47*, 2121–2126; *Angew. Chem.* **2008**, *120*, 2151–2156.
- [13] L. Münzfeld, C. Schoo, S. Bestgen, E. Moreno-Pineda, R. Köppe, M. Ruben, P. W. Roesky, *Nat. Commun.* **2019**, *10*, 3135.
- [14] A. Edelmann, C. G. Hrib, S. Blaurock, F. T. Edelmann, *J. Organomet. Chem.* **2010**, *695*, 2732–2737.
- [15] K. Mashima, Y. Nakayama, A. Nakamura, N. Kanehisa, Y. Kai, H. Takaya, *J. Organomet. Chem.* **1994**, *473*, 85–91.
- [16] a) U. Mirsaidov, I. B. Shaimuradov, M. Khikmatov, *Zh. Neorg. Khim.* **1986**, *31*, 1321–1323; b) M. Ephritikhine, *Chem. Rev.* **1997**, *97*, 2193–2242; c) A. Momin, F. Bonnet, M. Visseaux, L. Maron, J. Takats, M. J. Ferguson, X.-F. Le Goff, F. Nief, *Chem. Commun.* **2011**, *47*, 12203–12205.
- [17] a) S. M. Cendrowski-Guillaume, M. Nierlich, M. Lance, M. Ephritikhine, *Organometallics* **1998**, *17*, 786–788; b) S. M. Cendrowski-Guillaume, G. Le Gland, M. Nierlich, M. Ephritikhine, *Organometallics* **2000**, *19*, 5654–5660.
- [18] I. L. Fedushkin, M. N. Bochkarev, S. Dechert, H. Schumann, *Chem. Eur. J.* **2001**, *7*, 3558–3563.
- [19] B. Gernot, B. Andreas, *Chem. Ber.* **1978**, *111*, 2850–2858.
- [20] F. A. Cotton, *Acc. Chem. Res.* **1968**, *1*, 257–265.
- [21] a) G. Boche, D. Martens, W. Danzer, *Angew. Chem. Int. Ed. Eng.* **1969**, *8*, 984–984; b) G. Boche, H. Weber, D. Martens, A. Bieberbach, *Chem. Ber.* **1978**, *111*, 2480–2496.
- [22] G. Boche, H. Weber, A. Bieberbach, *Chem. Ber.* **1978**, *111*, 2833–2849.
- [23] R. Shannon, *Acta Crystallogr. A* **1976**, *32*, 751–767.
- [24] A. Wells, F. in *Structural Inorganic Chemistry*, 5th ed., Oxford university press, Oxford, **2012**.
- [25] C. Apostolidis, G. B. Deacon, E. Dornberger, F. T. Edelmann, B. Kanellakopulos, P. MacKinnon, D. Stalke, *Chem. Commun.* **1997**, 1047–1048.

Manuscript received: May 5, 2021

Accepted manuscript online: July 1, 2021

Version of record online: August 21, 2021



# Résumé détaillé

Ce manuscrit regroupe mes travaux effectués dans le cadre des recherches menées dans notre groupe sur la synthèse, la caractérisation et l'étude en réactivité de complexes hétérobimétalliques combinant un lanthanide divalent, un ligand rédox-actif et un métal de transition. Afin de mieux comprendre l'intérêt et le potentiel de ces architectures originales, le premier chapitre de cette thèse propose d'étudier un phénomène physico-chimique particulièrement intéressant, la valence intermédiaire dans les composés moléculaires de lanthanide. En effet, grâce à leurs propriétés électroniques atypiques découlant du peuplement des orbitales 4f, certains composés de lanthanide ne peuvent être considérés comme ayant un ion métallique dans un état d'oxydation formel entier mais plutôt comme un mélange de plusieurs configurations, dans lesquelles l'ion peut se présenter à différents degrés d'oxydation. Si ce comportement original a d'abord été considéré par des expérimentateurs pour répondre à de singulières signatures spectroscopiques, il a ensuite créé de nombreux débats chez les chimistes théoriciens comme l'illustre la riche littérature tournant autour du cérocène,  $\text{Ce}(\text{Cot})_2$ . Parmi les exemples marquant de composés à valence intermédiaire, les adduits N-hétérocyclique de l'ytterbocène,  $\text{Cp}^*_2\text{Yb}(\text{L})$  ( $\text{L} = \text{bipy}, \text{phen}, \text{dad}$ ), ont notamment permis de rationaliser et de mettre à profit l'existence de ce phénomène en observant différentes réactivités. Ces changements ont notamment pu être directement corrélés à la modulation de l'énergie relative et de la symétrie des orbitales des deux fragments ytterbium et ligand.

Afin d'aller plus loin dans la compréhension et l'utilisation de ce genre de systèmes, l'ajout d'une troisième entité, un métal de transition, au moyen d'un ligand pontant comme la bipym a constitué le point de départ de nombreux travaux effectués ces dernières années dans notre groupe de recherche, sur la synthèse de composés hétérobimétalliques. Un premier exemple démontrant le potentiel de ces architectures électroniques originales a notamment été publié en 2017 pour présenter la stabilisation remarquable d'un complexe de palladium,  $\text{Cp}^*_2\text{Yb}(\text{bipym})\text{PdMe}_3\text{I}$ , grâce à l'apport de la densité électronique transférée du lanthanide au ligand rédox actif. Plus récemment, la transposition de ce concept à la chimie du nickel a aussi permis de moduler la cinétique d'insertion d'une molécule de CO dans une liaison Ni-Me.

Dans ce contexte, l'objectif des travaux de recherches que j'ai effectués ces dernières années était de continuer à explorer la réactivité des métaux de transition des groupes 9 et 10 lorsqu'incorporés dans ces architectures hétérobimétalliques. Le but ultime étant, d'une part d'améliorer grandement leur capacité d'activation de petites molécules comme le méthane, ainsi que d'étudier la possibilité de développer des systèmes catalytiques bénéficiant de ce phénomène de valence intermédiaire.

Dans un premier temps, afin d'agrandir la gamme de précurseurs de lanthanides à incorporer dans ces assemblages, la synthèse de nouveaux composés hétéroleptiques combinant deux larges ligands aromatiques a été effectuée. Ce travail a permis de mieux comprendre la chimie de coordination du ligand cyclononatétraenyle et de notamment lever le voile sur le changement de son hapticité suivant la taille du lanthanide utilisé. Compte tenu de la géométrie axiale présente dans ces composés, ils ont aussi été étudiés pour leurs propriétés magnétiques afin d'évaluer leur potentiel en tant que molécules-aimants.

Ensuite, afin de compléter la série de composés hétérobimétalliques impliquant les métaux du groupe 10. La synthèse, la caractérisation ainsi que des études de réactivité ont été menées à partir de composés de type  $\text{Cp}^*_2\text{Yb}(\text{bipym})\text{PtMe}_2$ . Grâce à la stabilité du degré d'oxydation +IV du platine, plusieurs espèces présentant chacune un environnement de coordination légèrement différent ont pu être caractérisées, ce qui a permis d'observer une modulation de la valence intermédiaire et d'espérer pouvoir mieux contrôler la réactivité de ces composés hétérobimétalliques, notamment en favorisant la prédominance d'un état électronique plutôt qu'un autre.

Les essais de réactivités menés avec ces composés comportant du platine, ont pu par la suite être transposés à la chimie du nickel. L'activation par un simple produit organique, le catecholborane, du complexe  $\text{Cp}^*_2\text{Yb}(\text{bipym})\text{NiMe}_2$  a été étudiée car constituant une méthode simple et efficace pour obtenir un centre métallique à un bas degré d'oxydation. Afin d'en explorer la réactivité, ce composé à basse valence a été engagé dans un système catalytique d'isomérisation d'alcènes. Si le pré-catalyseur hétérobimétallique s'est montré performant à basse charge catalytique, 1%, son homologue monométallique,  $(\text{bipy})\text{NiMe}_2$ , s'est avéré inefficace. Des études mécanistiques et théoriques ont alors permis d'expliquer cette différence, le nickel se présentant au degré d'oxydation +I dans le premier cas et +0 dans le second.

Enfin, la synthèse et la caractérisation sans précédents d'un complexe palladium tétraméthyle ont été effectuées à partir du complexe  $\text{Cp}^*_2\text{Yb}(\text{bipym})\text{PdMe}_3\text{I}$  et d'un simple réactif de Grignard. L'étude de sa dégradation a permis de confirmer que sa stabilité était accrue grâce à la substitution du ligand iodure, à l'origine de la fragilité des espèces de type  $\text{PdMe}_3\text{I}$ . Le remplacement d'un groupement méthyle par un éthyle a pu aussi être effectué pour confirmer l'absence d'élimination de  $\beta$ -hydrure. Cela a de surcroît, permis d'observer que l'élimination réductrice de propane était favorisée par rapport à celle d'éthane, un résultat peu commun, et de se tourner vers la possibilité d'effectuer des couplages croisés de type alkyle-alkyle via un cycle catalytique  $\text{Pd}^{\text{II}}/\text{Pd}^{\text{IV}}$ .





**Titre :** Valence intermédiaire induite par un lanthanide divalent dans des complexes hétérobimétalliques: Impact sur la réactivité de métaux de transition

**Mots clés :** Valence intermédiaire, Ligands rédox-actifs, Complexes hétérobimétalliques

**Résumé :** L'objectif de ces travaux a été d'étudier de nouveaux composés hétérobimétalliques combinant un lanthanide divalent, un ligand rédox-actif et un métal de transition. Si l'association des deux premiers composants a déjà fait couler beaucoup d'encre, étant donné que ces architectures peuvent induire une valence intermédiaire, seulement un nombre limité de travaux récents ont étudié la possibilité d'ajouter le troisième ingrédient et d'étudier l'impact de ce phénomène sur sa réactivité. Dans un premier temps, afin d'agrandir la gamme de précurseurs de lanthanides à incorporer dans ces assemblages, la synthèse de nouveaux composés hétéroleptiques combinant deux larges ligands aromatiques a été effectuée. Ce travail a permis de mieux comprendre la chimie de coordination du ligand cyclononatetraenyle et de notamment lever le voile sur le changement de son hapticité suivant la taille du lanthanide utilisé. Ces composés ont aussi montré de prometteuses propriétés magnétiques

liées à leur architecture. Afin de compléter une série de composés hétérobimétalliques impliquant les métaux du groupe 10, la synthèse, la caractérisation ainsi que des études de réactivité ont été menées avec du platine ce qui a permis d'observer la modulation de la valence intermédiaire induite par la variation de l'environnement de coordination du Pt. Les essais de réactivités menés avec ces composés ont pu être transposés au nickel menant à un bas degré d'oxydation qui s'est montré efficace quant à l'isomérisation d'alcènes via un mécanisme original, impliquant de multiples transferts mono-électroniques entre les différents fragments du catalyseur. Enfin, la synthèse et la caractérisation sans précédents de complexes de palladium stables, supportés par quatre groupements hydrocarbonés a pu être effectuée et l'étude de sa dégradation a ouvert de nouvelles perspectives quant à son usage pour le couplage de deux atomes Csp<sup>3</sup>.

**Title:** Divalent lanthanide-induced intermediate valence in heterobimetallic complexes: Impact on transition metal reactivities

**Keywords :** Intermediate valence, Redox-active ligands, Heterobimetallic complexes

**Abstract:** This work aimed to widen the scope of accessible heterobimetallic compounds combining a divalent lanthanide, a redox-active ligand and transition metal center. While the association of the first two components was already extensively studied, as such architectures can induce intermediate valence, only a limited number of recent works investigated the addition of the third ingredient to study the impacted transition metal reactivity. In order to extend the possible choice of lanthanide precursors to involve in these assemblies, the synthesis of original heteroleptic trivalent precursors with large aromatic ligands was performed. This work permitted to further study the coordination chemistry of the rarely used cyclononatetraenyl ligand and uncover a lanthanide size-induced hapticity switch in the series of prepared compounds. Such compounds were also found to have a

promising design for slow magnetic relaxation processes. In order to fully cover the group 10 transition metal that can be involved in heterobimetallic complexes, the synthesis as well as extensive characterization and reactivity studies were conducted with platinum and allowed to observe a modulation of the intermediate valence upon the tuning of the coordination environment of the Pt center. The reactivity trials conducted with these compounds led to the investigation of low-valent nickel reactivity toward alkene isomerization and an original mechanism based on the shuttle of electrons between the Yb, the 2,2'-bipyrimidine ligand and the Ni center was elucidated. Finally, the synthesis and characterization of unprecedented tetraalkyl palladium complexes with a high stability was achieved and the study of its degradation opened new perspectives for Csp<sup>3</sup>-Csp<sup>3</sup> coupling reactions.